TM X-58173

N76-23074

APOLLO-SOYUZ TEST PROJECT

Preliminary Science Report

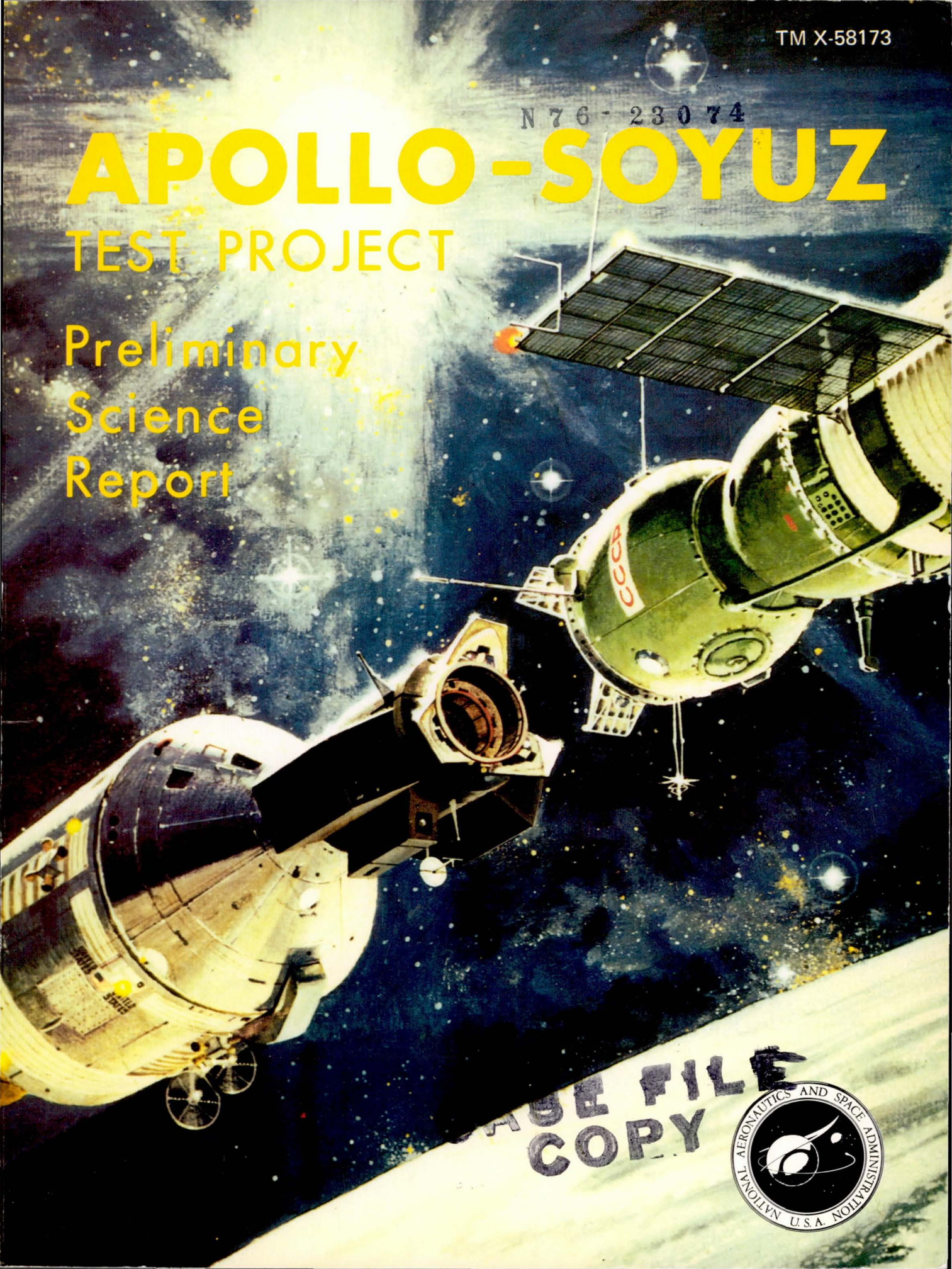

CASE FILE COPY

NATIONAL AERONAUTICS AND SPACE ADMINISTRATION U.S.A.

1. Report No.	2. Government Accession No.	3. Recipient's Catalog No.
NASA TM X-58173		

4. Title and Subtitle	5. Report Date
APOLLO-SOYUZ TEST PROJECT PRELIMINARY SCIENCE REPORT	February 1976
	6. Performing Organization Code: JSC-10632
7. Author(s): NASA Editorial Review Board, R. Thomas Giuli (Chairman)	8. Performing Organization Report No.
9. Performing Organization Name and Address: Lyndon B. Johnson Space Center, Houston, Texas 77058	10. Work Unit No.: 953-36-00-00-72
	11. Contract or Grant No.
12. Sponsoring Agency Name and Address: National Aeronautics and Space Administration, Washington, D.C. 20546	13. Type of Report and Period Covered: Technical Memorandum
	14. Sponsoring Agency Code

15. Supplementary Notes

16. Abstract

This document summarizes the experimental concepts and preliminary analyses (as of December 1975) for each of the 28 scientific experiments conducted during the Apollo-Soyuz Test Project from July 15 to 24, 1975. The scientific topics are X-ray and extreme ultraviolet astronomy, solar astronomy, gamma-ray detectors, Earth studies (including the upper atmosphere, meteorological phenomena, hydrology, oceanography, geology, desert studies, and gravity field studies), microbiology, heavy cosmic particle interaction with live cells, vestibular system studies, and materials processing (including high-temperature and ambient-temperature processing of industrial materials and electrophoretic processing of biological materials).

17. Key Words (Suggested by Author(s))		18. Distribution Statement
Orbital science	Materials processing	STAR Subject Category:
Astronomy	Crystal growth	
Solar physics	Life sciences	88 (Space Sciences, General)
Earth observations	Electrophoresis	
Space applications	Microbiology	

19. Security Classif. (of this report)	20. Security Classif. (of this page)	21. No. of Pages	22. Price*
Unclassified	Unclassified	529	$12.50

*For sale by the National Technical Information Service, Springfield, Virginia 22151

NASA — JSC

JSC Form 1424 (Rev Jul 74)

Apollo-Soyuz crewmen Donald K. Slayton, Thomas P. Stafford, Vance D. Brand, Alexei A. Leonov, and Valeri N. Kubasov

NASA TM X-58173

APOLLO-SOYUZ TEST PROJECT

PRELIMINARY SCIENCE REPORT

U.S. GOVERNMENT PRINTING OFFICE

For sale by the Superintendent of Documents, U.S. Government Printing Office, Washington, D.C. 20402
Stock No.: 033-000-00639-0

EDITORIAL BOARD

The material submitted for the "Apollo-Soyuz Test Project Preliminary Science Report" was reviewed by a NASA Editorial Review Board consisting of the following members: R. Thomas Giuli (Chairman), J. Vernon Bailey, Richard R. Baldwin, Leland J. Casey, P. Donald Gerke, John K. Holcomb, David N. Holman, W. Wilson Lauderdale, Patricia D. Marsden, James M. Sanders, Robert S. Snyder, Orion E. Tollefsbol, and Lyle Vande Zande.

Cover: Drawing by artist Robert McCall, 1974

CONTENTS

Section		Page
	INTRODUCTION . . . . . Chester M. Lee and Glynn S. Lunney	xi
1	SUMMARY OF SCIENTIFIC RESULTS . . . . . R. T. Giuli	1-1
2	MISSION DESCRIPTION . . . . . S. N. Hardee	2-1
3	SOFT X-RAY OBSERVATION - EXPERIMENT MA-048 . . . . S. Shulman, G. Fritz, D. Yentis, R. G. Cruddace, H. Friedman, W. Snyder, and R. C. Henry	3-1
4	EXTREME ULTRAVIOLET SURVEY - EXPERIMENT MA-083 . . . . . S. Bowyer, B. Margon, M. Lampton, F. Paresce, and R. Stern	4-1
5	INTERSTELLAR HELIUM GLOW - EXPERIMENT MA-088 . . . S. Bowyer, J. Freeman, F. Paresce, M. Lampton, and B. Margon	5-1
6	ARTIFICIAL SOLAR ECLIPSE - EXPERIMENT MA-148 . . . . R. T. Giuli, M. D. Jenness, A. N. Lunde, and K. A. Young	6-1
7	CRYSTAL ACTIVATION - EXPERIMENT MA-151 . . . . . J. I. Trombka, E. L. Eller, R. L. Schmadebeck, C. S. Dyer, R. C. Reedy, D. W. Barr, J. S. Gilmore, R. J. Prestwood, B. P. Bayhurst, D. G. Perry, A. R. Smith, R. C. Cordi, R. H. Pehl, J. S. Eldridge, E. Schonfeld, and A. E. Metzger	7-1
8	ULTRAVIOLET ABSORPTION - EXPERIMENT MA-059 . . . . T. M. Donahue, R. D. Hudson, J. Anderson, F. Kaufman, and M. B. McElroy	8-1
9	STRATOSPHERIC AEROSOL MEASUREMENT - EXPERIMENT MA-007 . . . . . T. J. Pepin and M. P. McCormick	9-1
10	EARTH OBSERVATIONS AND PHOTOGRAPHY - EXPERIMENT MA-136 . . . . . Farouk El-Baz and D. A. Mitchell	10-1

Section		Page
11	DOPPLER TRACKING - EXPERIMENT MA-089 . . . . . G. C. Weiffenbach and M. D. Grossi	11-1
12	GEODYNAMICS - EXPERIMENT MA-128 . . . . . F. O. Vonbun, W. D. Kahn, J. W. Bryan, P. E. Schmid, W. T. Wells, and T. D. Conrad	12-1
13	QUANTITATIVE OBSERVATION OF LIGHT FLASH SENSATIONS - EXPERIMENT MA-106 . . . . . T. F. Budinger, C. A. Tobias, E. Schopper, J. U. Schott, R. H. Huesman, F. T. Upham, T. F. Wieskamp, J. M. Kucala, F. S. Goulding, D. A. Landis, J. T. Walton, and R. E. Walton	13-1
14	BIOSTACK III - EXPERIMENT MA-107 . . . . . H. Bücker, R. Facius, D. Hildebrand, G. Horneck, G. Reitz, U. Scheidemann, M. Schäfer, C. Thomas, B. Toth, A. R. Kranz, E. H. Graul, W. Rüther, M. Delpoux, H. Planel, J. P. Soleilhavoup, C. A. Tobias, T. Yang, E. Schopper, J. U. Schott, E. Obst, O. C. Allkofer, K. P. Bartholomä, R. Beaujean, W. Enge, W. Heinrich, H. François, G. Portal, R. Kaiser, J. P. Massué, R. Pfohl, C. Jacquot, E. V. Benton, and D. D. Peterson	14-1
15	ZONE-FORMING FUNGI - EXPERIMENT MA-147 . . . . . T. D. Rogers, G. R. Taylor, and M. E. Brower	15-1
16	MICROBIAL EXCHANGE - EXPERIMENT AR-002 . . . . . G. R. Taylor, K. D. Kropp, M. R. Henney, S. S. Ekblad, T. O. Groves, T. C. Molina, J. G. Decelle, C. F. Carmichael, N. J. Gehring, and E. L. Young	16-1
17	CELLULAR IMMUNE RESPONSE - EXPERIMENT MA-031 . . . B. S. Criswell	17-1
18	THE EFFECTS OF SPACE FLIGHT ON POLYMORPHONUCLEAR LEUKOCYTE RESPONSE - EXPERIMENT MA-032 . . . . . R. R. Martin	18-1
19	KILLIFISH HATCHING AND ORIENTATION - EXPERIMENT MA-161 . . . . . H. W. Scheld, J. F. Boyd, G. A. Bozarth, J. A. Conner, V. B. Eichler, P. M. Fuller, R. B. Hoffman, J. R. Keefe, K. P. Kuchnow, J. M. Oppenheimer, G. A. Salinas, and R. J. von Baumgarten	19-1

Section		Page
20	ELECTROPHORESIS TECHNOLOGY - EXPERIMENT MA-011 . . . . . R. E. Allen, G. H. Barlow, M. Bier, P. E. Bigazzi, R. J. Knox, F. J. Micale, G. V. F. Seaman, J. W. Vanderhoff, C. J. Van Oss, W. J. Patterson, F. E. Scott, P. H. Rhodes, B. H. Nerren, and R. J. Harwell	20-1
21	ELECTROPHORESIS EXPERIMENT - EXPERIMENT MA-014 . . . . . K. Hannig and H. Wirth	21-1
22	MULTIPURPOSE ELECTRIC FURNACE - EXPERIMENT MA-010 . . . . . A. Boese, J. McHugh, and R. Seidensticker	22-1
23	SURFACE-TENSION-INDUCED CONVECTION - EXPERIMENT MA-041 . . . . . R. E. Reed	23-1
24	MONOTECTIC AND SYNTECTIC ALLOYS - EXPERIMENT MA-044 . . . . . C. Y. Ang and L. L. Lacy	24-1
25	INTERFACE MARKINGS IN CRYSTALS - EXPERIMENT MA-060 . . . . . H. C. Gatos and A. F. Witt	25-1
26	ZERO-G PROCESSING OF MAGNETS - EXPERIMENT MA-070 . . . . . D. J. Larson, Jr.	26-1
27	CRYSTAL GROWTH FROM THE VAPOR PHASE - EXPERIMENT MA-085 . . . . . H. Wiedemeier, H. Sadeek, F. C. Klaessig, and M. Norek	27-1
28	HALIDE EUTECTIC GROWTH - EXPERIMENT MA-131 . . . . A. S. Yue, B. K. Yue, and J. Y. M. Lee	28-1
29	MULTIPLE MATERIAL MELTING - EXPERIMENT MA-150 . . . . . R. S. Snyder and A. Boese	29-1
30	CRYSTAL GROWTH - EXPERIMENT MA-028 . . . . . M. D. Lind	30-1

Section | Page

31 SCIENCE DEMONSTRATIONS 31-1
R. S. Snyder, K. S. Clifton, B. Facemire,
A. F. Whitaker, P. G. Grodska, and S. Bourgeois

APPENDIX A — ABBREVIATIONS AND ACRONYMS A-1

APPENDIX B — UNITS AND UNIT-CONVERSION FACTORS B-1

APPENDIX C — HARDWARE VENDORS C-1

APPENDIX D — POINTS OF CONTACT D-1

INTRODUCTION

Chester M. Lee and Glynn S. Lunney

International cooperation was the keynote of the Apollo-Soyuz Test Project. In the 3 years since the project was initiated in the U.S.-U.S.S.R. Agreement Concerning Cooperation in the Exploration and Use of Outer Space (signed by the U.S. and U.S.S.R. Heads of State on May 24, 1972), the great effort expended in coordination, communication, and integration culminated in the highly successful flight from July 15 to 24, 1975. The 9-day flight marked the first time that manned spacecraft of two nations have met in space for joint engineering and scientific investigations.

The principal objective of the project was to develop a compatible docking system and rendezvous and crew transfer procedures that might be appropriate for future international manned space missions. This objective was successfully accomplished.

An additional objective of major importance was the program of scientific investigations conducted during the mission. A science program was planned by NASA that made abundant use of the experimental opportunities afforded by the mission parameters and spacecraft capabilities. The 2-day docked phase of the flight was used to conduct three experiments that required joint scientific activities within the two spacecraft. Subsequent to the docked phase, two additional joint scientific experiments were conducted that required involved, precise maneuvering of the Apollo spacecraft relative to, and in the proximity of, the Soyuz spacecraft. The remaining unilateral phases of the mission were likewise used effectively by each country to perform scientific experiments on a unilateral basis. In addition to the five joint U.S.-U.S.S.R. experiments, the Apollo crewmen conducted 23 unilateral experiments. Two of these were provided by the Federal Republic of Germany — a further illustration of the international scope of the mission. Not only was scientific research served by this mission, but worldwide space-science awareness was promoted through extensive home television broadcasting and filming of flight experimentation and in-flight science demonstrations.

This report discusses the joint experiments and the U.S.-conducted unilateral experiments. It provides detailed descriptions of the scientific concepts and experiment design and operation. The results of scientific analyses are preliminary. Although much analysis remains to be done by the scientists involved in this program, the preliminary results indicate significant scientific achievements. The Summary Science Report, to be published in the latter part of 1976, will contain more detailed results of the experiment analyses. The scientific value of this international venture will contribute significantly to the development of future international science collaboration on the Space Shuttle flights and other projects.

1. SUMMARY OF SCIENTIFIC RESULTS

R. T. Giuli[a]

The Apollo-Soyuz Test Project (ASTP) experiments package comprised 28 separate experiments. Twenty-one were unilateral U.S. experiments, five were joint U.S.-U.S.S.R. experiments (i.e., involving participation by both Apollo and Soyuz crewmembers), and two were unilateral West German experiments (i.e., funded by the Federal Republic of Germany). Together, these experiments formed a well-integrated program of complementary scientific objectives. In several cases, related experiments used different experimental techniques in pursuit of the same or similar scientific objectives. A comparison of the scientific results from these experiments may be useful in defining the best technique to pursue in future space missions.

The individual experiments are grouped in this report according to category and topic. The space sciences experiments are presented in order of the distance away from the center of the Earth that the objects of study lie. The soft X-ray objects lie deep in our galaxy and even beyond our galaxy. The extreme ultraviolet (EUV) objects lie within a few hundred light-years from the solar system, whereas the portion of the interstellar medium investigated by the helium glow experiment lies within a few astronomical units. The corona photographed during the artificial solar eclipse lay within approximately 50 solar radii from the Sun. Two crystal detectors that have potential application for future gamma-ray astronomy payloads were carried onboard the Apollo spacecraft to measure their susceptibility to radioactivation by cosmic particle bombardment. The tenuous Earth atmosphere at the spacecraft altitude was investigated by ultraviolet absorption, and the aerosol component of the atmosphere below the spacecraft was investigated by stratospheric aerosol measurements. Features of the Earth surface were observed and photographed by the Apollo crew, and the structure of the Earth below the surface was investigated by two spacecraft-spacecraft Doppler techniques.

The life sciences experiments addressed three primary topics. One was the effects of cosmic particle bombardment on live cells: the human eye retina (light flash), dormant eggs and seeds (biostack), and growing fungi (zone-forming fungi). (The fungi experiment also studied the effects of space-flight factors on biorhythm.) The second topic was the effects of space flight on the human immune system from the aspect of microbial transfer and ability to cause infection and from the aspect of the ability of the immune system to resist infection. The third topic was the effects of reduced gravity on the calcium metabolism of the killifish vestibular system. The purpose was to assess the feasibility of using the killifish vestibular system as a model for future investigations of space-flight effects on human calcium metabolism.

---

[a]NASA Lyndon B. Johnson Space Center.

The materials processing effort addressed two topics: the separation of live cells and the improvement of physical properties of solid materials. The live cell separation was performed by each of two electrophoresis methods in which an electric field was applied through a buffer solution containing a mixture of cells with different biological functions (and hence with different negative surface charges). The cells separated into groups of cells with like biological function, each group being characterized by a unique value of cell surface charge. Each group thus acquired a unique speed through the buffer solution. The solid materials were processed both by a high-temperature (melting) technique and an ambient-temperature (crystal growth from solution) technique.

The subsequent sections in this report describe in detail the conceptual, instrumental, and operational aspects of each experiment and include a preliminary assessment of scientific results. This section describes the major preliminary results of a few of the experiments (astronomy, Earth atmosphere, Earth observations, biological materials processing, and solid materials processing) as known in December 1975.

ASTRONOMY

The first known pulsar outside our galaxy was discovered (jointly with a rocket experiment by the same investigator) by the Soft X-ray Experiment (MA-048). The pulsar is contained in a binary star system in the Small Magellanic Cloud, which is a companion galaxy located approximately 200 000 light-years from our own. It is the most luminous pulsar known, by at least a factor of 10, and it radiates predominantly at X-ray energies greater than 2 kiloelectronvolts. Its period is 0.7 second, which is half that of the next fastest binary pulsar. Only two other binary pulsars are known.

Extreme ultraviolet radiation from four stars was positively detected by the Extreme Ultraviolet Survey Experiment (MA-083). Two of the stars are very strong sources of EUV radiation; they are very hot, nearby white dwarf stars HZ 43 and Feige 24. Although these stars were previously known by means of their visible radiation, their extremely high temperatures (approximately 100 000 K) were not previously known. The star HZ 43 was also detected by the Soft X-ray Experiment, which confirmed the high temperature. The soft X-ray preliminary results imply a temperature as high as 150 000 K, as compared with the EUV result of 110 000 K. There is thus no doubt that HZ 43 is the hottest white dwarf known.

EARTH ATMOSPHERE

The space application of absorption spectroscopy as a technique for measuring the very tenuous abundances of the atomic constituents of the Earth atmosphere at spacecraft altitudes was successfully pioneered by the Ultraviolet Absorption

(UVA) Experiment (MA-059). The results compare excellently with results obtained previously by less direct means:

UVA results	Previous results
2.5 billion oxygen atoms/cm^3	2.3 billion oxygen atoms/cm^3
6 million nitrogen atoms/cm^3	5 to 6 million nitrogen atoms/cm^3

The comparison is encouraging for the continued development of an expanded absorption spectroscopy concept for application in the Space Shuttle Program, in which a greater number of constituents may be measured over a greater portion of the atmosphere.

The layering of aerosols in the stratosphere was successfully measured by the Stratospheric Aerosol Measurements Experiment (MA-007). The concentration of aerosols was 1.5 to 2 times greater in the Northern Hemisphere than in the Southern Hemisphere, and the peak concentration of the layers occurred at an altitude of 19 to 20 kilometers in the Northern Hemisphere (somewhat lower in the Southern Hemisphere). This was the pioneering space application of the solar extinction technique for monitoring atmospheric particulates. The technique, which uses appropriately filtered photometers to measure the extinction of infrared sunlight as it passes through the atmosphere during orbital sunrise and sunset, is being developed to monitor molecular constituents (such as ozone) as well.

The absorption spectroscopy and the solar extinction methods are complementary. Eventually, they may be used for long-term monitoring of the atomic, molecular, and particle composition of the atmosphere.

EARTH OBSERVATIONS

An extensive northward extension of the Red Sea rift system was successfully identified and recorded during the Earth Observations and Photography Experiment (MA-136). The Red Sea rift system branches into three well-established fault lines from a point situated north of Beirut. The photographs led to the interpretation that the primary motion of the Arabian subplate is counterclockwise rotation about the branch point of the fault lines. The Arabian subplate was previously believed to be translating eastward. This is the first observational detection of rotational plate motion.

The crew also detected and photographed an extensive system of internal ocean waves off the western coast of Spain. The wavefronts were approximately 60 kilometers long, were parallel to the coastline, and were apparently not associated with any islands. The wavelength was approximately 2 kilometers. Detection of the waves was very dependent on the Sun angle and look angle; the waves appeared suddenly and disappeared shortly thereafter. The detection of internal ocean waves is an example of how rapid crew reactions can be utilized to great advantage.

BIOLOGICAL MATERIALS PROCESSING

The static-column method of electrophoretic separation of mixtures of different live cells into zones of like cells was successfully demonstrated by the Electrophoresis Technology Experiment (MA-011). This experiment marks the first time that all three phases of a complete electrophoresis operation (preflight cell preservation, microgravity processing, and postflight cell preservation) were successfully addressed. Additionally, a commercial firm participated in the experiment to investigate the enhancement of urokinase production over that obtainable by ground-based methods. Urokinase is an enzyme with major potential application for future treatment of persons with thrombotic conditions. Urokinase is cultured from a particular type of kidney cell, and the objective of this experiment was to isolate pure samples of that type cell to be used as starters for the culturing process. The objective was successfully achieved, as evidenced by enhanced urokinase production from laboratory cultures of the ASTP samples. A significant spinoff from this experiment has been achieved in connection with the attempt to separate different types of lymphocytes. The electrophoresis attempt was unsuccessful (the cells lost viability before they could be processed); however, in preparation for the experiment, sterilization techniques were developed that may eventually permit family members of leukemia victims to donate blood years in advance of its intended use rather than requiring them to donate with sometimes less than 2 days' notice, as is the current practice.

SOLID MATERIALS PROCESSING

The Multipurpose Electric Furnace (MA-010) was used to conduct several experiments. The ASTP experiment on Crystal Growth From the Vapor Phase (MA-085) completed an experiment begun on Skylab (M-556) in which greatly enhanced growth rates (7 to 10 times the ground-based rates) were obtained for crystals being grown from the vapor phase. The Skylab experiment demonstrated that no existing model for vapor transport phenomena is adequate for microgravity conditions. The ASTP experiment completed the parameter variations for the experiment and yielded crystal growth rates of 3 to 4 times those of ground-based rates. Preliminary analysis indicates the existence of thermochemical effects in vapor transport that become dominant in microgravity conditions.

The Interface Marking in Crystals Experiment (MA-060) successfully used a complex laboratory technique to reveal the changes in speed with which a solid/liquid interface travels during a solidification process. The purpose was to correlate the microsegregation of materials that occurs at the interface with the interface speed. The interface speed was determined to increase continuously during the solidification. Correlation with microsegregation is currently under analysis.

2. MISSION DESCRIPTION

S. N. Hardee[a]

ABSTRACT

The Apollo-Soyuz mission was the first manned space flight conducted jointly by two nations. The United States and the U.S.S.R. achieved a substantial degree of success in (1) obtaining flight experience for rendezvous and docking of manned spacecraft and developing a docking system that would be suitable for use as a standard international system, (2) demonstrating in-flight intervehicular crew transfer, and (3) conducting a series of science and applications experiments. The Apollo and Soyuz spacecraft, with minor exceptions, were similar to those flown on previous missions, but a new Apollo module, the docking module, was built specifically for this mission. The mission started with the Soyuz launch on July 15, 1975, followed by the Apollo launch on the same day. Docking of the two spacecraft occurred on July 17, and joint operations were conducted for 2 days. Both spacecraft landed safely and on schedule; the Soyuz landing in the U.S.S.R. occurred on July 21, and the Apollo landing near Hawaii occurred on July 24. Twenty-eight science experiments were performed during the mission.

INTRODUCTION

The first international manned space flight, the Apollo-Soyuz Test Project (ASTP) (fig. 2-1), was highly successful. The primary objectives of the joint U.S.-U.S.S.R. project were to test systems for manned spacecraft rendezvous and docking that would be suitable for use as a standard international system and to demonstrate crew transfer between spacecraft. An additional objective was to conduct a program of science and applications experimentation. Joint and unilateral experiments that provided data and experience in the fields of Earth resources, Earth gravity, Earth atmosphere, astronomy, solar science, life sciences, and space processing were conducted. (The arrangement of these experiments within this report is given in the Table of Contents.) Some of these experiments were conducted in pioneering fields. For example, the first measurements of atomic nitrogen in the Earth atmosphere at orbit altitudes were made, and a search for discrete sources of 5- to 100-nanometer (50 to 1000 angstrom) extreme ultraviolet (EUV) radiation outside the solar system was made for the first time. In addition, space science awareness was promoted through extensive commercial television (TV) broadcasting and filming of flight experimentation and through in-flight science demonstrations.

---

[a]NASA Lyndon B. Johnson Space Center.

SPACECRAFT DESCRIPTION

An overview of the two spacecraft and the docking module (DM) is shown in figure 2-2, and the ASTP experiment locations are shown in figure 2-3.

Apollo Spacecraft Description

The Apollo spacecraft used for this mission was similar in most respects to those employed to ferry crews to and from the Skylab space station, but it differed in some significant aspects that will be pointed out in this discussion. The significant differences among four generations of Apollo spacecraft are summarized in table 2-I.

Command and service module.- The Apollo command and service module (CSM) flown on the Apollo-Soyuz mission was closely similar to the command and service modules used for the Skylab flights, but some modifications were made to fit mission needs. Additional controls for the docking system and special CSM-to-DM umbilicals were added together with experiment packages and their controls. Also, the steerable high-gain antenna used for deep-space communications during the Apollo lunar missions but not needed for the Skylab missions was reinstalled on the Apollo-Soyuz command and service module. The antenna was used to establish a relay link with Applications Technology Satellite 6 (ATS-6) in synchronous orbit to provide communications with the Mission Control Center for 55 percent of each orbit.

Docking module.- The docking module was basically an airlock that permitted the crewmen to transfer between the two spacecraft, which had different internal pressures and atmosphere constituents. The docking module had docking facilities on each end that enabled rigid coupling of the Apollo and Soyuz spacecraft and was a cylindrical pressure vessel with an internal diameter of 1.42 meters and an overall length of 3.15 meters between the docking interfaces.

The principal external attachments to the docking module were a Doppler transmitter antenna for the Doppler Tracking Experiment, an ultraviolet spectrometer for the Ultraviolet Absorption Experiment, a docking target that enabled the Soyuz crew to observe the Apollo docking approach through the Soyuz periscope, three very-high-frequency (VHF) antennas, three adapter mountings, a vent housing, and four gas storage tanks. The external and internal arrangements of the docking module are shown in figure 2-4.

Soyuz Spacecraft Description

The Soyuz spacecraft consisted of three modules, which are discussed in the order of their proximity to the Apollo spacecraft when docked.

The orbital module, which provided the Soyuz portion of the compatible docking system, was used for work and rest by the crew during orbit. The module contained a side hatch for crew entry before launch, a forward hatch for crew

transfer to and from the docking module, and an aft tunnel for crew transfer to the descent vehicle. Two windows were provided: one forward of the side hatch for earthward viewing, and the other on the opposite side of the module for outward viewing.

The descent vehicle, with the main controls and crew couches, was occupied by the cosmonauts during launch, dynamic orbital operations, descent, and landing.

The instrument assembly module, which contained subsystems required for power, communications, propulsion, and other functions, was located at the aft end of the Soyuz spacecraft. Two sets of winglike solar battery panels were mounted 180° apart on the exterior of the module.

TRACKING AND COMMUNICATIONS

Flight control personnel maintained contact with the Apollo and Soyuz spacecraft through the Spaceflight Tracking and Data Network (STDN). This network consisted of a complex of fixed ground stations, portable ground stations, specially equipped aircraft, and an instrumented ship. The mission was supported by 14 Spaceflight Tracking and Data Network stations, as well as by a U.S.S.R. network consisting of 7 ground stations and 2 ships. Communications opportunities with the use of the Spaceflight Tracking and Data Network alone encompassed 17 percent of the mission time; but, for the first time, an Applications Technology Satellite that increased the total communications coverage to 63 percent was employed (fig. 2-5). The increased coverage with the ATS-6 was of significant importance to several science experiments. The Apollo-Soyuz Test Project communications are shown schematically in figure 2-6.

NARRATIVE FLIGHT SUMMARY

Launch and Rendezvous Maneuvers Phase

The Soyuz spacecraft, manned by Alexei A. Leonov, commander, and Valeri N. Kubasov, flight engineer, was launched from the Baykonur, Kazakhstan, launch complex at 12:20 GMT on July 15, 1975. It was launched in a northeasterly direction and was inserted into a 186- by 222-kilometer orbit at an inclination of 51.8°. On the fourth orbit after lift-off, the first of two maneuvers to circularize the Soyuz orbit at 223 kilometers was initiated. The second circularization maneuver occurred on the 17th Soyuz orbit.

Seven and one-half hours after the Soyuz launch, the Apollo spacecraft, manned by Thomas P. Stafford, commander, Vance D. Brand, command module pilot, and Donald K. Slayton, docking module pilot, was launched from the NASA John F. Kennedy Space Center in a northeasterly direction and was inserted into a 149- by 168-kilometer orbit, also with an inclination of 51.8°. One hour fourteen minutes after lift-off, the Apollo command and service module was separated from the Saturn-IVB stage, and the crew began the transposition and docking procedure

to extract the docking module from the launch vehicle. Although these operations were generally normal, the removal of the docking probe was hindered by a misrouted pyrotechnic connector cable. A corrective procedure given to the crew was used successfully to remove the probe, and extraction was completed at 22: 24 GMT. After performance of an evasive maneuver to avoid recontact with the launch vehicle, a circularization maneuver at the third apogee, and additional phasing and plane correction maneuvers, the first day of maneuver activities was concluded for both crews.

Before the end of the day, several science experiment operations were performed. The Zone-Forming Fungi (ZFF) Experiment, which had been photographed at 12-hour intervals beginning July 13, 1975, was again photographed at 12: 30 Soyuz ground elapsed time (GET). Simultaneously, the Biostack Experiment was activated for approximately 12 hours of operation. The first Geodynamics Experiment data take was initiated at 15: 12 GET and continued through the next three ATS-6 passes by the Apollo spacecraft. Major mission events and data collection periods are shown in figure 2-7.

The second day was devoted primarily to predocking checkout activities, rendezvous maneuvers, and science experiments. The first biostack data take was concluded at 25: 38 GET, and the killifish experiment was initiated at 27: 18 GET. Earth observations activities were initiated after starting the killifish experiment and extended into the period of Ultraviolet Absorption (UVA) Experiment lamp burn-in, which started at 27: 40 GET. Multipurpose furnace experiment preparations were also made during the lamp burn-in period, and the ultraviolet absorption crew optical alinement sight calibrations were made. After another Geodynamics Experiment data take, multipurpose furnace operations were started with the Surface-Tension-Induced Convection Experiment cartridges. Simultaneously, the Electrophoresis Experiment (EPE) was prepared and operated; the Extreme Ultraviolet Survey, Helium Glow (HeG), and Soft X-Ray Experiments were checked out; several geodynamics data takes were made; and zone-forming fungi photographs were taken. Unfortunately, a malfunction developed in the Soft X-Ray Experiment after only 10 minutes of normalcy during the initial operation of the experiment on the second day of flight. However, good data were obtained again, intermittently, during the sixth through eighth days of flight.

Joint Phase

Docking occurred on the 36th Soyuz orbit and the 29th Apollo revolution. The time of docking was 51 hours 49 minutes Soyuz GET on July 17, 1975. The Apollo and Soyuz spacecraft remained docked for approximately 2 days.

After docking, hatch 1 was opened, and several transfers of both crews, television tours of both spacecraft and of the United States and the U.S.S.R., a news conference, and official ceremonies were conducted. The Surface-Tension-Induced Convection Experiment in the multipurpose furnace was continued during this period, and the collection of microbial samples for the Microbial Exchange Experiment was accomplished by the two crews. The multipurpose furnace was shut down at 58: 05 GET and was reinitiated for the U.S.S.R. Multiple-Material Melting Experiment at 58: 45 GET.

Several other science experiments were conducted during this first docked phase. The Zone-Forming Fungi Experiment was photographed again; several Earth observations and geodynamics data takes were made; the Microbial Exchange Experiment was conducted; the U.S.S.R. multiple-material melting was concluded; and the zero-g processing of magnets in the multipurpose furnace was conducted.

After the two spacecraft had been docked for nearly 44 hours, the first undocking was performed normally, and the joint Artificial Solar Eclipse Experiment was performed. A second docking was then performed at 96:14 GET to test the docking system with the Soyuz docking system active.

Final undocking was at 99:06 GET, after which the Ultraviolet Absorption Experiment was conducted to conclude the joint phase of the flight. The Apollo spacecraft began stationkeeping 18 meters ahead of the Soyuz spacecraft. The Apollo spacecraft then was maneuvered to a 150-meter displacement out of the Soyuz orbital plane. At 99:40 GET, a 10-minute data take was performed as the command and service module swept through a 30° arc at the 150-meter radius from the Soyuz spacecraft. Similarly, a 500-meter out-of-plane data take was made starting at 101:18 GET. After the 500-meter data take, the command and service module was positioned back into the Soyuz orbital plane, and an in-plane final evasive maneuver was begun at 102:22 GET.

During the 150-meter data take, no reflected signal was detected by the spectrometer. Assessment of the problem by ground personnel indicated a contaminated Soyuz side reflector or possible locking of the star tracker onto a different light source. Therefore, the Soyuz aft reflector was used for the 500-meter data take.

Soyuz Deorbit and Landing

The Soyuz deorbit maneuver was performed at 141:50 GET. The reentry vehicle was brought to a safe landing in Kazakhstan at 10:51 GMT on July 21, 1975, after a flight of 142 hours 31 minutes.

Apollo Orbit Continuation Phase

The Apollo spacecraft continued in orbit for approximately 5 days after separation from the Soyuz spacecraft. Following the ultraviolet absorption joint phase data takes, one revolution of Apollo out-of-plane data was obtained and a spacecraft test roll maneuver of 360° was performed to measure resonant fluorescence background and ambient atmosphere gas pileup. The experiment was shut down at 107:07 GET.

The multipurpose furnace zero-g processing of magnets was concluded at 106:50 GET, and the Halide Eutectic Experiment was initiated in the furnace at 109:20 GET. In the interim, zone-forming fungi photographs and Earth observations were made; the Crystal Growth Experiment (CGE) was initiated; and a raster scan for the extreme ultraviolet survey was made. After several Geodynamics Experiment data takes and several Earth observations, the extreme ultraviolet experiment was started. The Crystal Growth and Zone-Forming Fungi Experiments were

then examined and photographed before the Helium Glow Experiment scans were made. Helium glow data-take periods consisted of sweeping the 15° field of view across regions of the celestial sphere by rolling the Apollo spacecraft about the longitudinal axis. Several excellent roll scan data takes were made. The killifish observations were again made during this period.

Extreme ultraviolet and helium glow scans, Earth observations, geodynamics data takes, and crystal growth and zone-forming fungi observations were continued at intervals; the multipurpose furnace Crystal Growth From the Vapor Phase Experiment was conducted; and the Biostack Experiment was turned on at 132: 00 GET. The Electrophoresis Technology Experiment was initiated at 147: 30 GET and was shut down at 152: 10; it was started again 18 hours later. The Stratospheric Aerosol Measurements (SAM) Experiment operations were initiated at 154: 30 GET, and shutdown occurred at 158: 00 GET. The multipurpose furnace Interface Marking in Crystals Experiment was also conducted during this period, as was the Monotectic and Syntectic Alloys Experiment.

During revolution 109, an extreme ultraviolet finding of special significance was made when an intense EUV source was discovered. This discovery was the first known detection of a cosmic source of extreme ultraviolet radiation. The Light Flash Experiment (LFE) was also initiated during revolution 109. The unmanned portion of this experiment started at 179: 13 GET, and the manned portion was initiated during the following revolution. These times were selected so that the two data-take periods would include passage through the South Atlantic Anomaly and would be descending passes (i.e., from northwest to southeast) to provide data at the maximum available geomagnetic latitude and to provide South Atlantic Anomaly data. Periodic zone-forming fungi, geodynamics, crystal growth, Earth observations, helium glow, killifish experiment, soft X-ray, and electrophoresis technology operations were also conducted during this period.

The docking module was jettisoned at 199: 27 GET to prepare for the Doppler Tracking Experiment, which required a 300-kilometer separation of the command and service module from the docking module. After jettison, the Apollo crew photographed the docking module and then maneuvered the command and service module to the same orbit as the docking module at a range of 300 kilometers. The data-take period began at 204: 20 GET and continued for approximately 14 hours with intentional command and service module attitude changes during the interim. During these 14 hours, periodic crystal growth, zone-forming fungi, geodynamics, and Earth observations operations were continued.

Apollo Deorbit and Landing

The Apollo deorbit maneuver was performed at 224: 17 GET, and, after a flight of 217 hours 28 minutes, the command module landed approximately 1.3 kilometers from the target point. The time of splashdown was 21: 18 GMT on July 24, 1975. The command module assumed the Stable II attitude for approximately 4.5 minutes after splashdown. The crew remained in the command module during recovery operations and were onboard the U.S.S. New Orleans approximately 41 minutes after splashdown.

After shipboard ceremonies, during which the crewmen appeared to be in good condition, it was learned that they had been exposed to oxidizer vapors for several minutes when an arming function and a manual backup function were overlooked during the entry phase of the mission. The crewmen were immediately given intensive medical care. The necessary changes in medical examination schedules and the therapy given the crew potentially affected the Cellular Immune Response Experiment and the Polymorphonuclear Leukocyte Response Experiment. These experiments were complementary experiments that were conducted by preflight and postflight blood sampling and analysis. Despite this impact, scientifically useful results were obtained in these experiments.

TABLE 2-I.- SIGNIFICANT APOLLO SPACECRAFT CONFIGURATION DIFFERENCES

System	Area of difference	Mission			
		ASTP	Skylab	[a]Apollo 11 to 14	[b]Apollo 15 to 17
Command module					
Electrical power system	Lunar module umbilicals			X	X
	Skylab tunnel umbilical		X		
	Docking module umbilicals	X			
	Drag-through umbilical	X	X		
Experiments	Stowable	X	X	X	X
	Coldplate mounted	X			
Television	Cameras and monitors	X	X	X	X
	Video tape recorder	X			
Communications	Speaker box	X	X		
	ATS-6 equipment	X			
Environmental control system (ECS)	Extravehicular activity capability		X		X
Displays and controls	Experiments	X	X		X
	Docking module	X			
	Compatible docking system	X			
	ATS-6 communications	X			
Stowage	Apollo Block II			X	X
	Skylab		X		
	Modified Skylab	X			
Service module					
Experiments	Scientific instrument module	X			X
	Lunar sounder				X
	Doppler tracking receiver	X			
	Remotely controlled doors	X			X
	Extravehicular retrieval capability				X
Service propulsion system	Propellant utilization gaging system (flight)			X	X
	Propellant utilization gaging system (ground)	X	X		
	Four propellant, two pressurant tanks			X	X
	Two propellant, one pressurant tank	X	X		
Environmental control system	Heaters deactivated	(c)	X		
	Coldplates for experiment cooling and ATS-6 equipment	X			

[a]Lunar-landing missions.

[b]Lunar-landing missions with expanded scientific data return capability.

[c]ECS radiator heater motor switches placed in open position before launch.

TABLE 2-I.- Concluded

System	Area of difference	Mission			
		ASTP	Skylab	[a]Apollo 11 to 14	[b]Apollo 15 to 17
Service module - concluded					
Reaction control system (RCS)	Propellant storage module	X	X		
	RCS quad heaters	X	X		
Thermal protection	Increased cork insulation	X	X		
	[d]Additional cork insulation	X			
Communications	Rendezvous radar transponder			X	X
	ATS-6 power amplifier system	X			
	High-gain antenna	X		X	X
Electrical power system	Two fuel cells		X		
	Three fuel cells	X		X	X
	Descent batteries		X		
	Extra water tank		X		
	Increased cryogenic storage capacity			X	X
	Return enhancement battery			X	X
Spacecraft adapter					
Panels	Jettisonable	X		X	X
	Deployable		X		
Structural support	Lunar module			X	X
	Docking module	X			

[a]Lunar-landing missions.

[b]Lunar-landing missions with expanded scientific data return capability.

[d]For long-duration RCS firings.

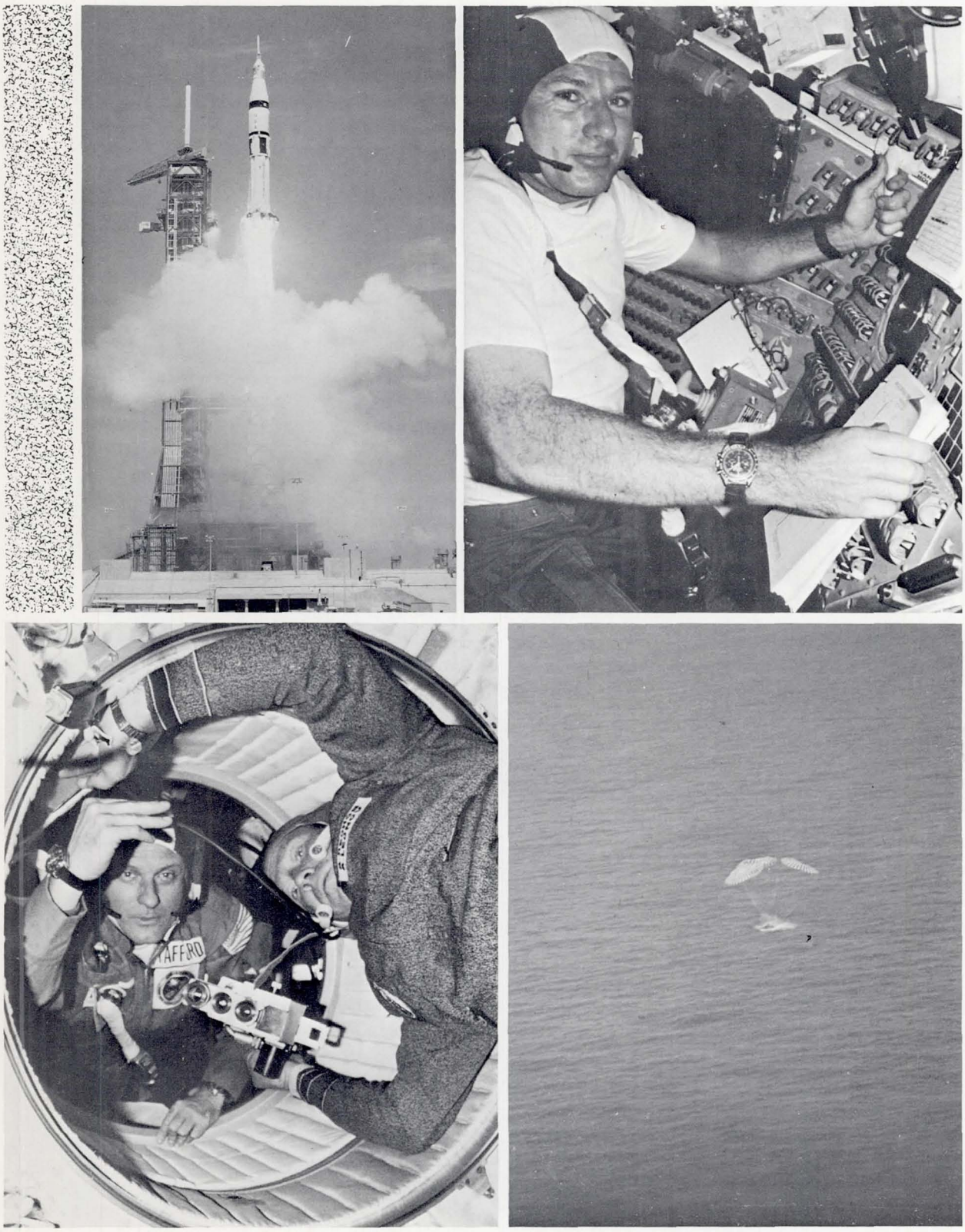

Figure 2-1.- Pictorial summary of Apollo-Soyuz mission.

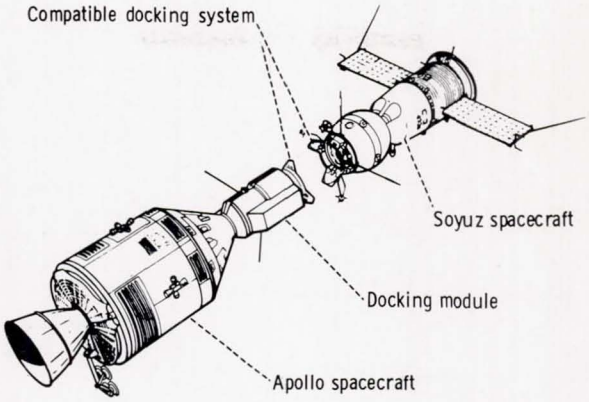

Figure 2-2.- Apollo Soyuz rendezvous and docking configuration.

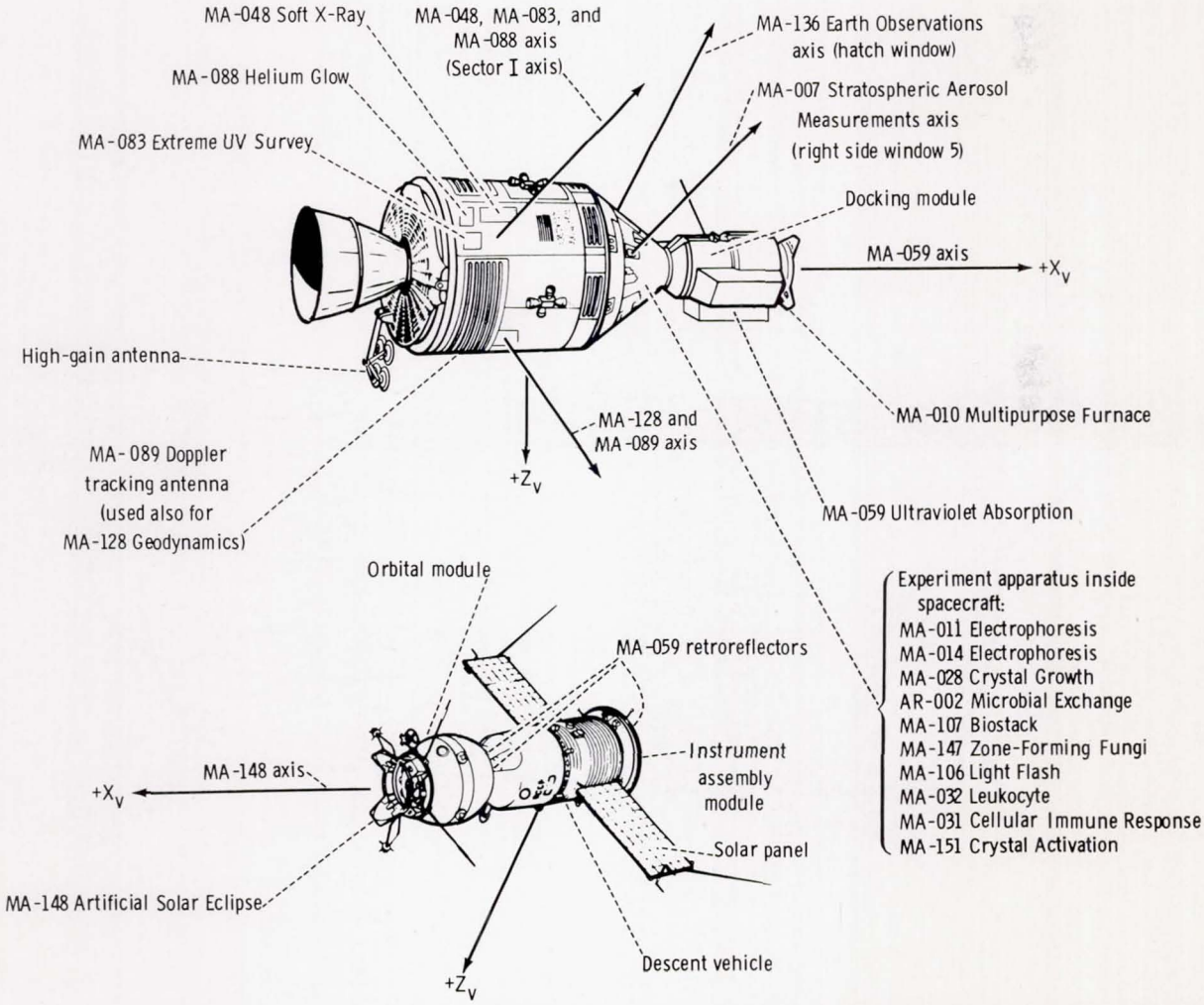

Figure 2-3.- ASTP experiment mounting locations.

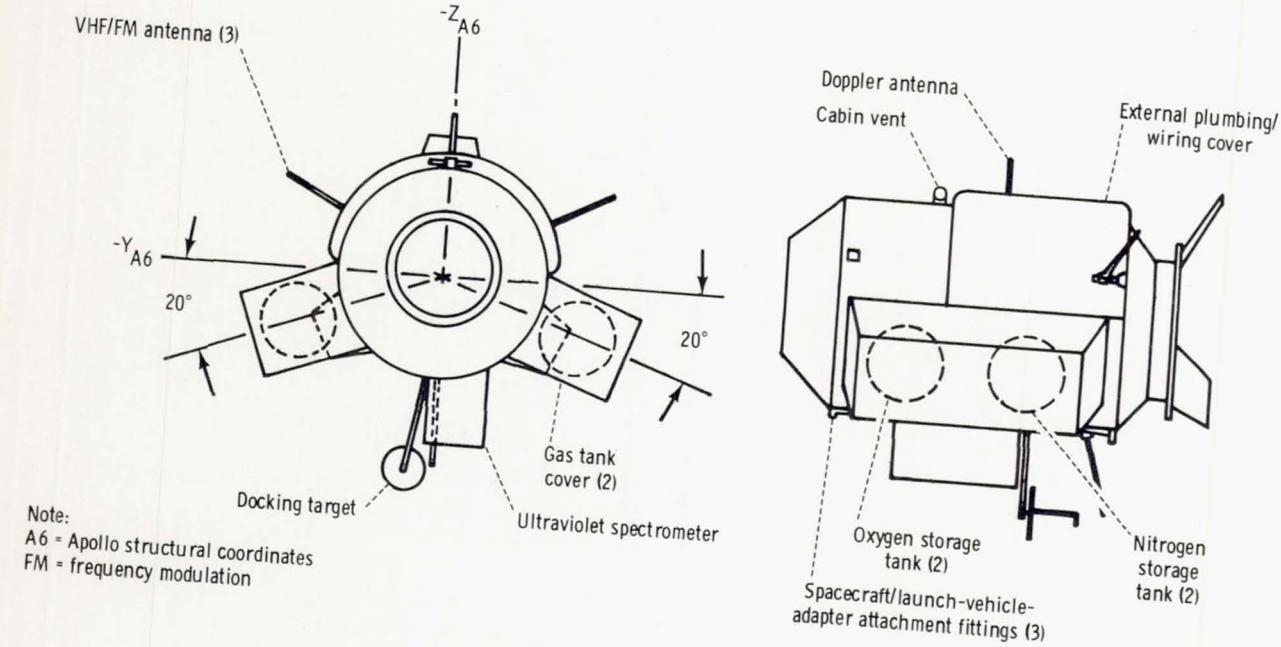

(a) Exterior.

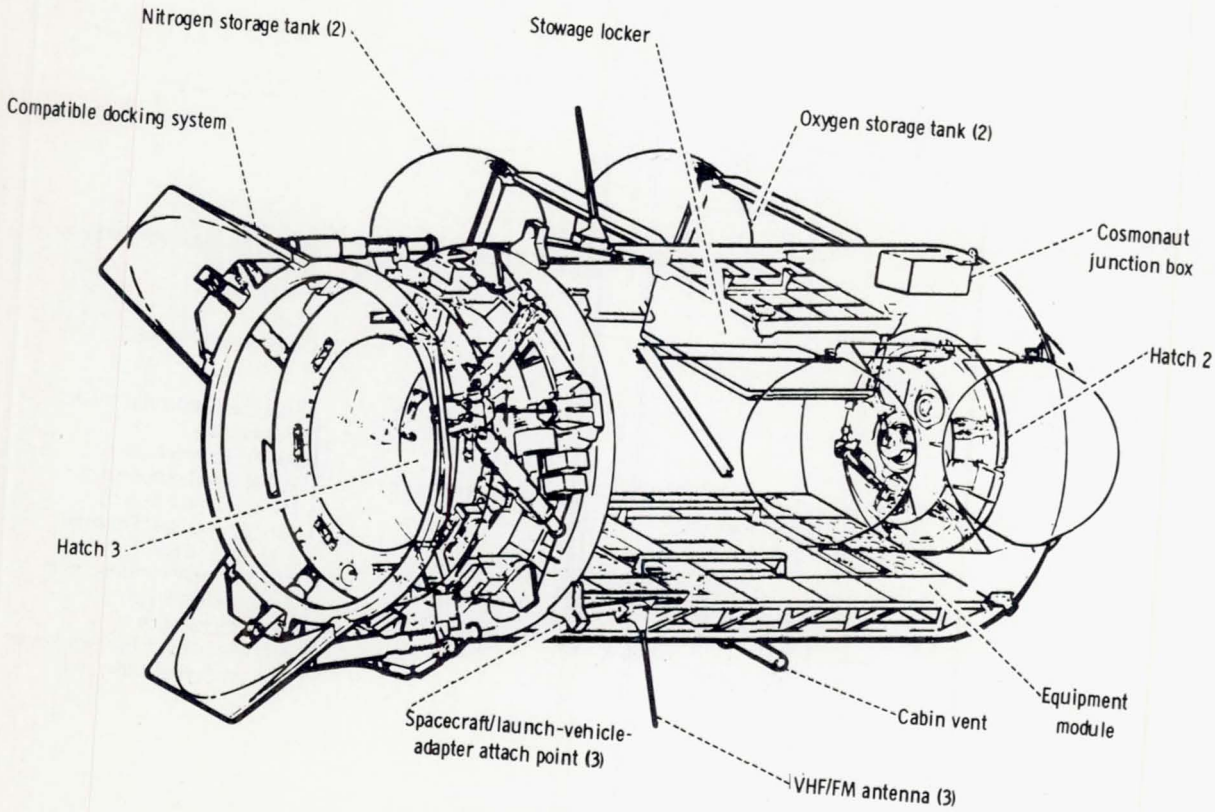

(b) Interior.

Figure 2-4.- Docking module.

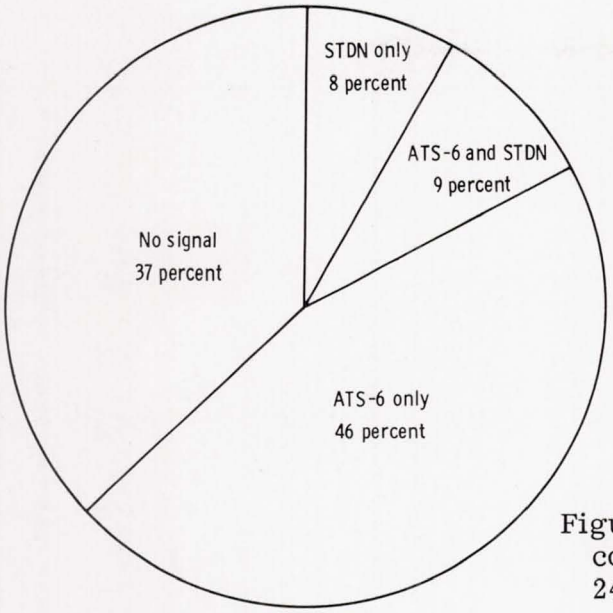

Figure 2-5.- Communications with command and service module for 24-hour period.

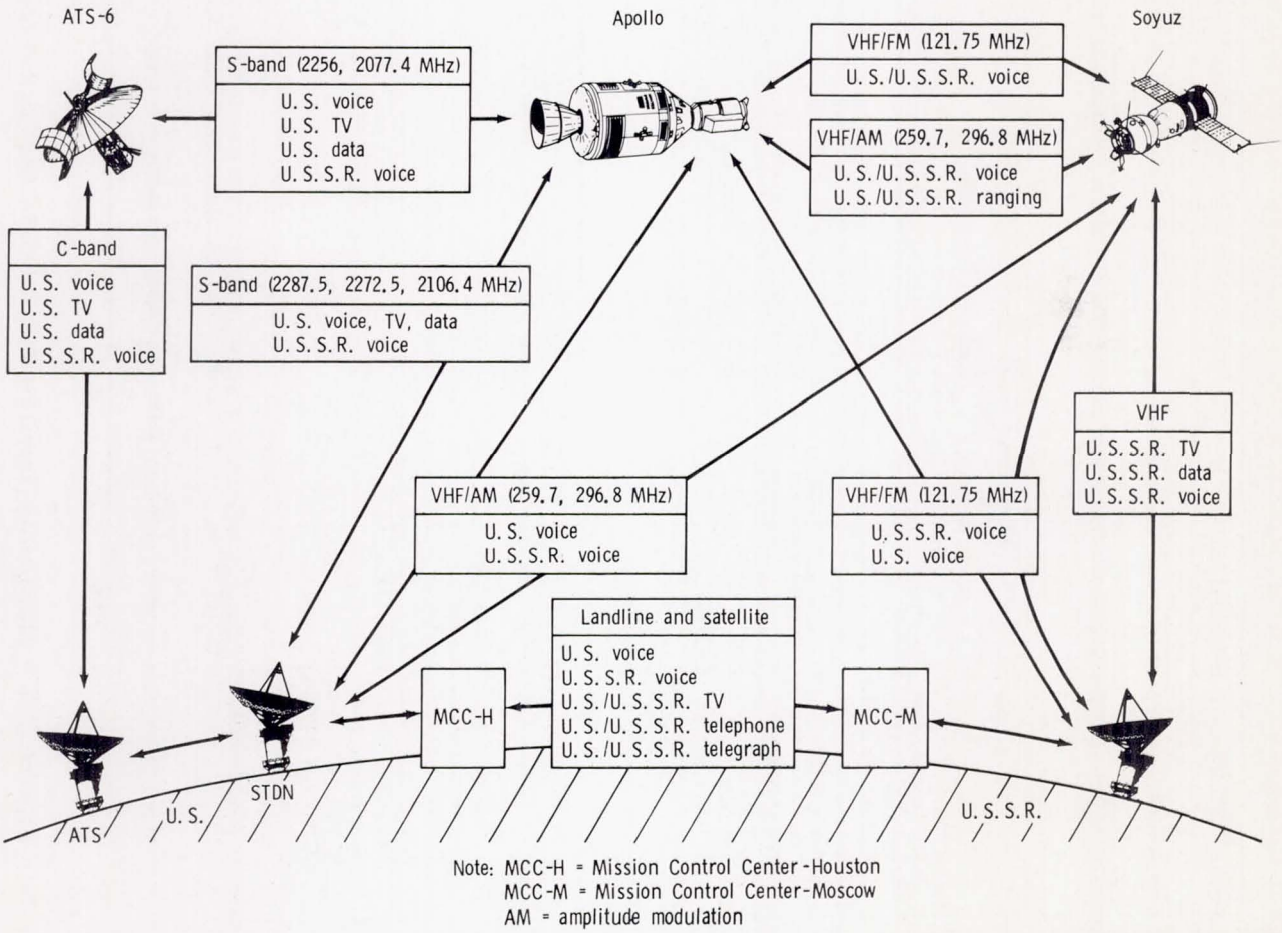

Note: MCC-H = Mission Control Center-Houston
MCC-M = Mission Control Center-Moscow
AM = amplitude modulation

Figure 2-6.- Apollo-Soyuz communication overview.

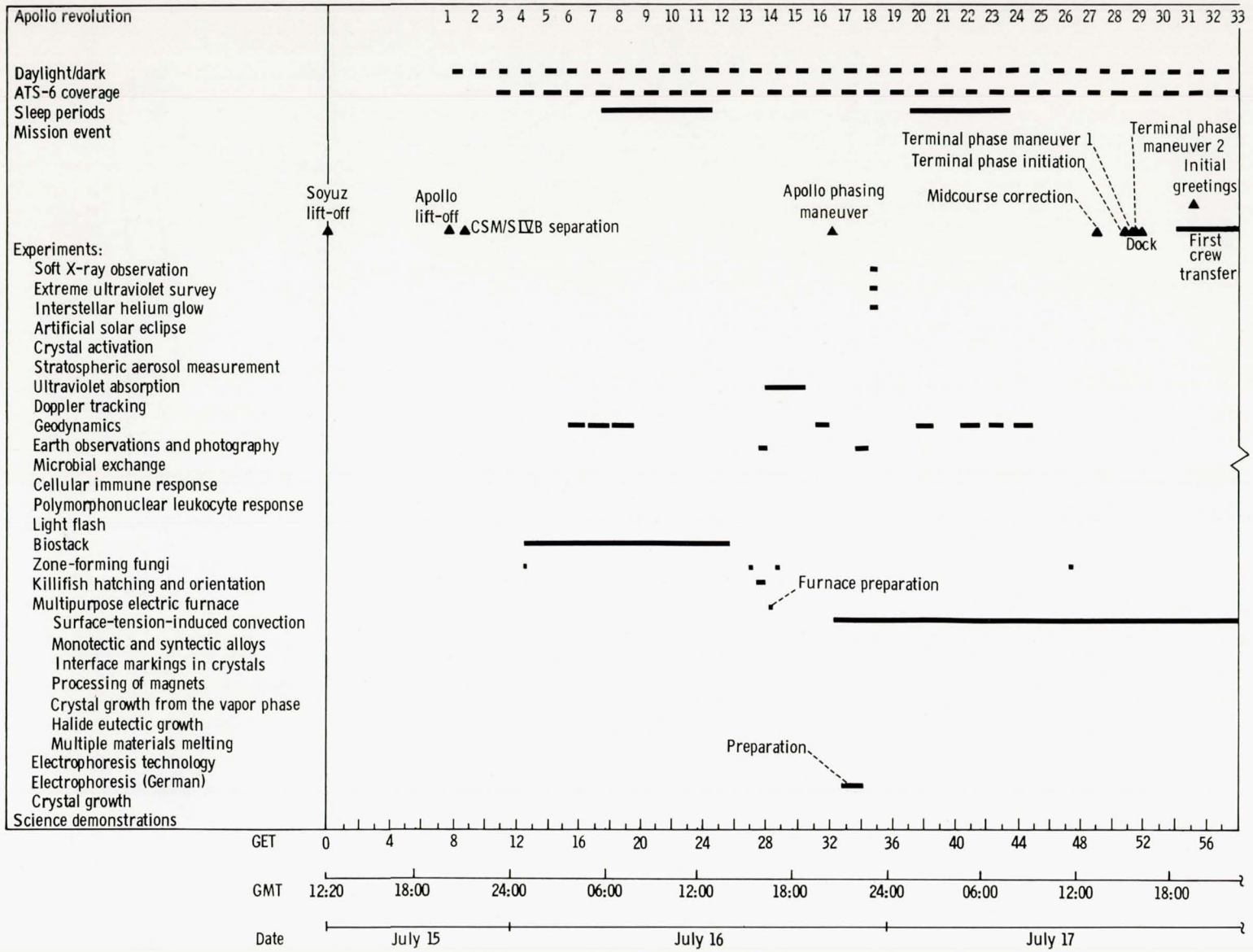

Figure 2-7.- Major mission events and data collection periods correlated to GMT and GET.

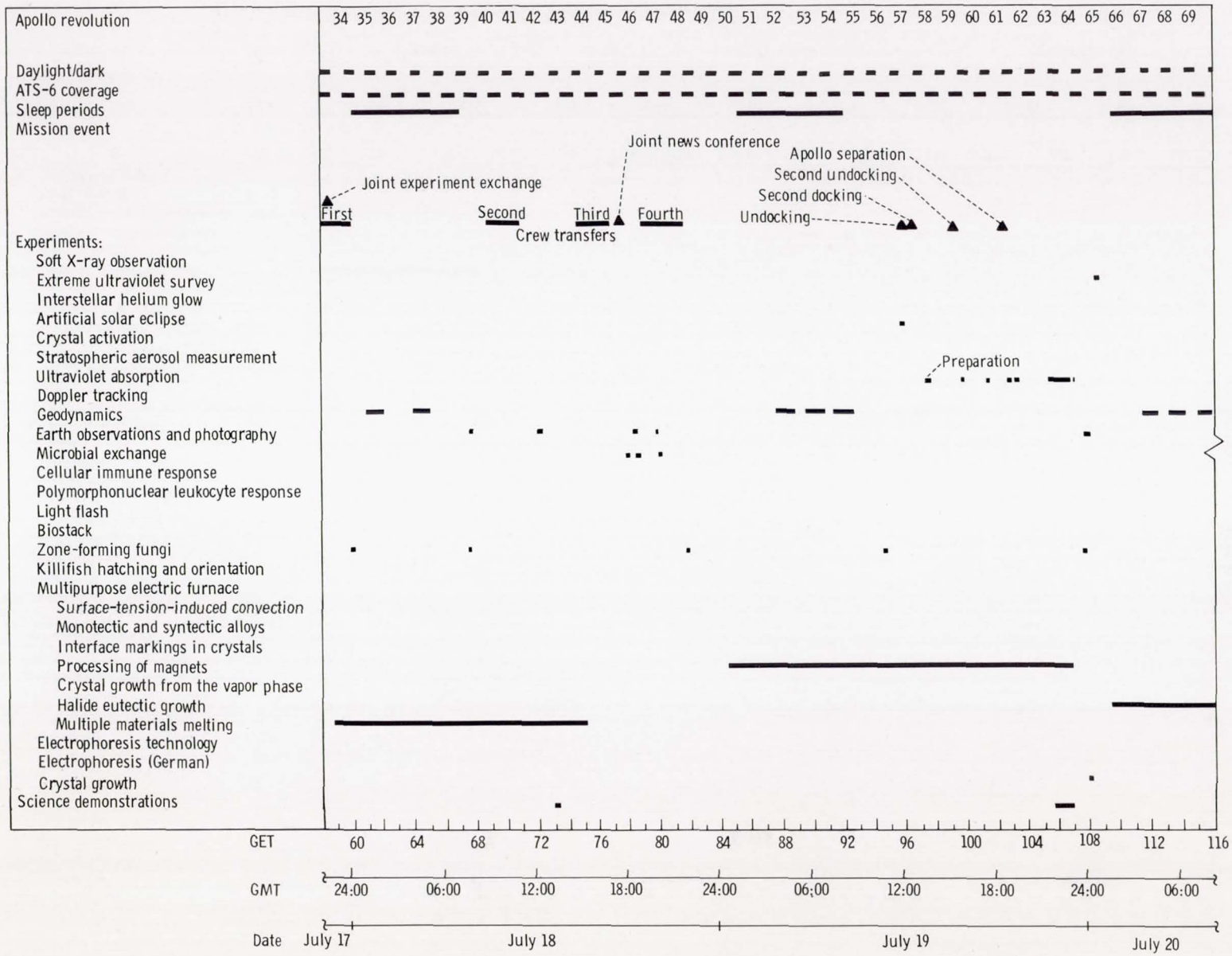

Figure 2-7.- Continued.

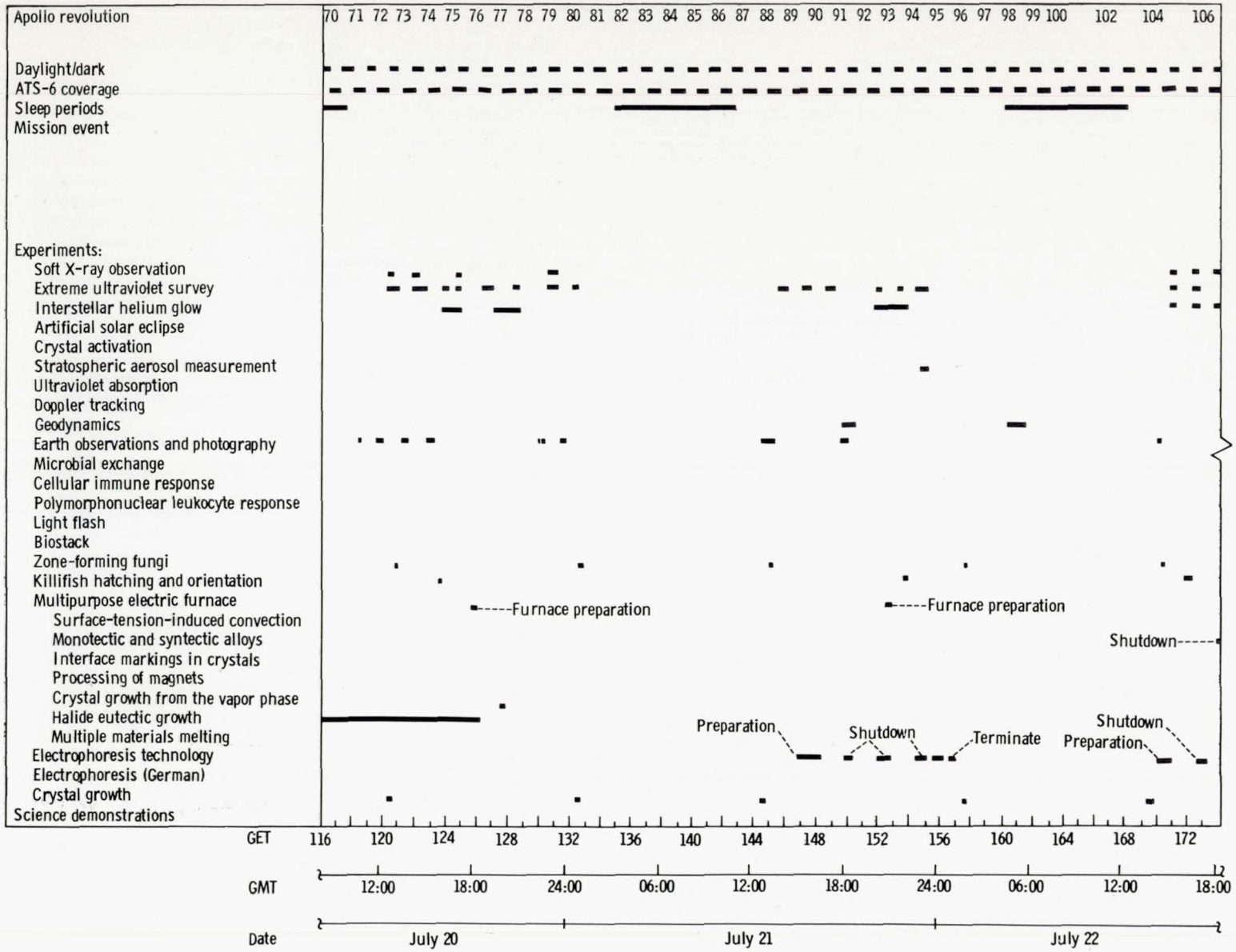

Figure 2-7.- Continued.

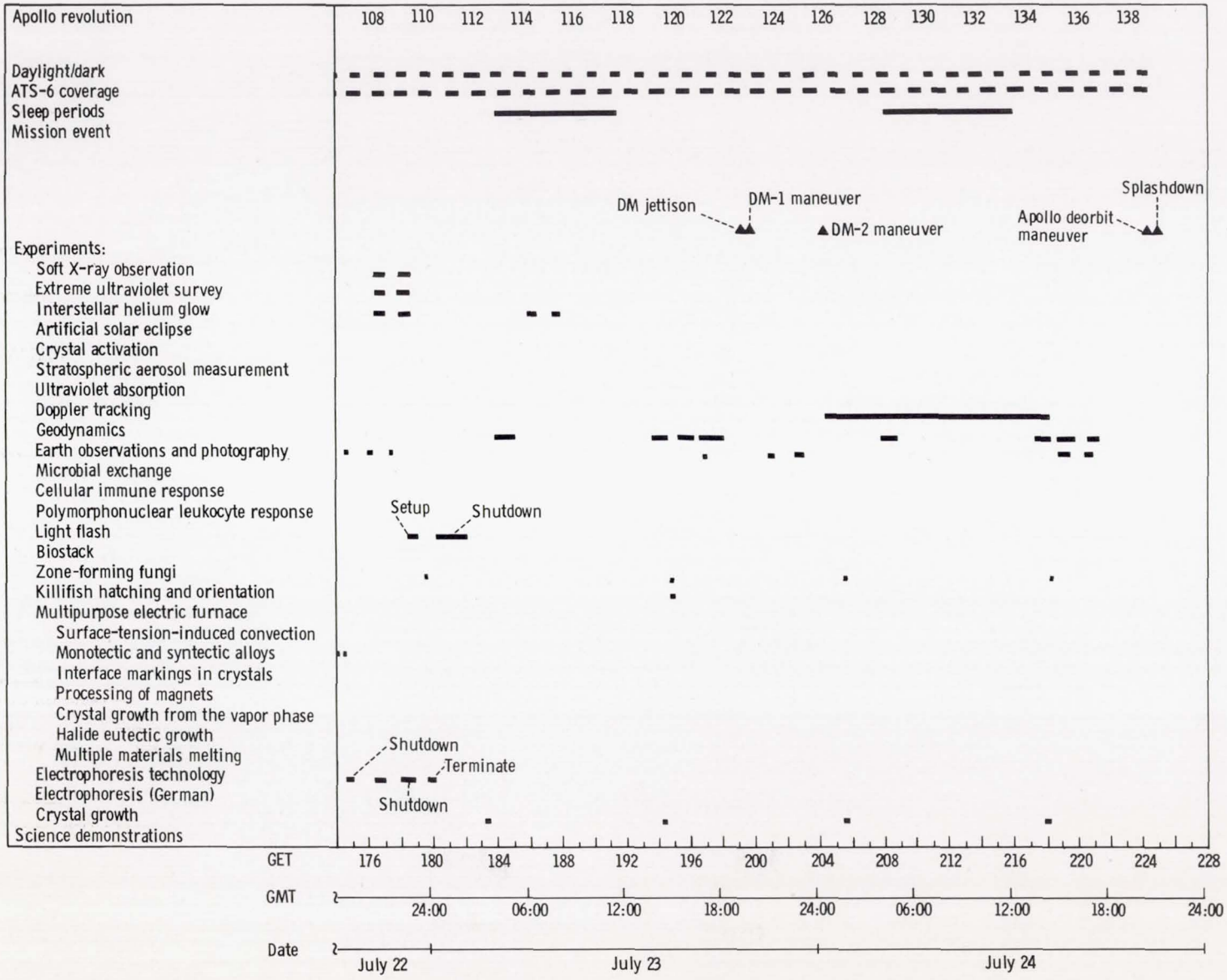

Figure 2-7.- Concluded.

3. SOFT X-RAY OBSERVATION

EXPERIMENT MA-048

S. Shulman,[a] G. Fritz,[a] D. Yentis,[a] R. G. Cruddace,[a]
H. Friedman,[a†] W. Snyder,[b] and R. C. Henry[b]

ABSTRACT

The Apollo-Soyuz Test Project Soft X-ray Experiment was designed to observe celestial X-ray sources in the energy range from 0.1 to 10 kiloelectronvolts. The instrument that was used in the experiment obtained energy and fast-timing data to characterize both the spectrum and the variability of known X-ray sources. Data were obtained on approximately 12 sources. During the mission, the instrument developed an intermittent high-voltage discharge problem that resulted in the loss of approximately 75 percent of the anticipated data, including the scans intended for mapping of the low-energy diffuse X-ray background.

OBJECTIVES

The objectives of the Apollo-Soyuz Test Project (ASTP) Soft X-ray Experiment were to study the spectra of a large number of known celestial X-ray sources in the range from 0.1 to 10 kiloelectronvolts, to search for periodicities and other variability in these sources, and to more precisely map the soft X-ray diffuse background. Celestial X-ray sources have been observed from rockets and satellites for approximately a decade, and more than 200 sources have been located. Figure 3-1 is a map of the sky in galactic coordinates showing the sources located by the Uhuru small astronomy satellite (SAS-1). The concentration in the galactic plane indicates a class of sources within the galaxy, and the uniform distribution at high latitudes indicates a class of extragalactic objects.

The objective of spectral measurements in the range from 0.1 to 10 kiloelectronvolts is twofold. First, detailed comparison of the spectra of many sources would provide the capability to classify X-ray sources more precisely in terms of the X-ray emission mechanism and the relevant physical parameters such as size, density, temperature, magnetic field strength, and relativistic particle content.

---

[a]Naval Research Laboratory.

[b]Johns Hopkins University.

[†]Principal Investigator.

Second, the low-energy parts of the spectra (less than 2 kiloelectronvolts) are affected by absorption in the intervening interstellar material. A measure of the absorption can be used to establish a fairly precise distance scale for the X-ray sources. The distances in turn yield the absolute luminosities and the relationship to other features of galactic structure such as the spiral arms.

The search for periodicities and fast-time variability was conducted by recording the counts in 3-microsecond intervals for three broad energy bands. The objective was to search for new pulsars (presumably rotating neutron stars) and for other types of sources where intensity variations on a fast-time scale might provide information on the source structure, size, and emission mechanisms.

The third objective of the experiment was to map the soft X-ray background. At energies of approximately 0.25 kiloelectronvolt, there is an observable diffuse emission from all directions in the sky. Figure 3-2 is a map obtained from data taken during an Aerobee rocket flight. To map a significant portion of the sky during the 5-minute flight, a wide field of view (10° by 10°) and a rapid scan rate were used. As a result, the statistical precision of the map is poor, and the minimum contrast features that can be detected are quite bright. The increased observing time available with the ASTP instrument provided the opportunity to use a 4° by 4° field of view and to obtain approximately 10 times as much data in each resolution element. With increased resolution, an attempt is being made to determine the origins of the soft X-ray diffuse background.

INSTRUMENT DESCRIPTION

The X-ray instrument is a large-area proportional counter very similar to those that have been flown on sounding rockets by several groups. The proportional counter detects individual X-ray photons when they interact in the detector gas. This interaction produces photoelectrons that drift toward a high-voltage anode and produce secondary electrons. In the high electric field region near the anode, the secondary electrons initiate an electron avalanche, which produces an electronic pulse that can easily be amplified and detected. In the proportional counter (as opposed to the Geiger counter), the total charge in the avalanche pulse is proportional to the original number of secondary electrons; thus, information about the energy of the detected X-ray is preserved.

The detector gas is a standard mixture of 90 percent argon and 10 percent methane (P10 gas) at 111 457.5 N/m^2 (1.1 atmospheres). The detector anodes are nominally operated at 2700 volts, and the instrument contains a feedback system to adjust this voltage to keep the gain constant during variations in detector temperature. The gas is contained by a 2-micrometer polycarbonate window that requires an elaborate support structure to withstand the 111 457.5-N/m^2 (1.1 atmosphere) pressure. This thin window is necessary to permit the detection of X-rays in the 0.1- to 2-kiloelectronvolt energy range: these X-rays would be absorbed by more conventional window materials such as 50-micrometer beryllium. Aluminum honeycomb is part of the window support structure and also provides the instrument collimation that gives a circular field of view with a full-width half-maximum (FWHM)

response of 4° . The effective area for X-ray detection is 1200 square centimeters. The front face of the detector, including the honeycomb and support ribs, is shown in figure 3-3.

Because a thin window is required for the low-energy X-ray observations, a gas supply is required to replenish gas that escapes through small pinholes in the window. Typical leak rates into vacuum range from 10 to 100 cm^3 Pa/min (10 to 100 cm^3 atm/min). A 30.5-centimeter (12 inch) diameter reservoir tank was incorporated into the experiment and was pressurized to 17 237 kN/m^2 (170.115 atmospheres), approximately 35 days before launch. With this gas supply system, the detector could also be completely emptied and refilled by astronaut command to remove atmospheric contaminants that diffused into the detector before launch. The gas tank is a prominent feature in the rear view of the instrument shown in figure 3-4.

The electronic design of the instrument is shown in figure 3-5. There are two sets of anodes in the detector, one for X-ray data and one for the veto of charged particles. Each set has a separate preamplifier and discriminator. A data pulse is accepted and analyzed only if no pulse is detected within a few microseconds in the veto section. Data pulses that are accepted are then pulse height analyzed, and the pulse height is stored for telemetry readout. The analysis is accomplished by a 9-bit analog-to-digital (A-D) converter that uses a successive approximation scheme. Each pulse height is also sorted into one of three energy bins for accumulation in the 3-microsecond fast-timing bins. The electronics are mounted on the rear of the detector as shown in figure 3-4.

The crucial parameters of gain and resolution were measured during laboratory calibrations. These parameters are required to determine the spectrum of X-rays incident on the detector. The detector response is convolved with the incident photon spectrum to give the counts observed in each pulse height bin of the spectral data. Mathematically, this is described as follows:

$$N(V_1,V_2) = \int_{E_1=G(V_1)}^{E_2=G(V_2)} dE \int_0^{\infty} T(E')\,A(E')\,R(E',E)\,N(E')\,dE'$$

where N is the counting rate, V_1 and V_2 are the boundaries of the pulse-height channel, $T(E')$ is the window transmission as a function of energy, $A(E')$ is the gas absorption as a function of energy, $R(E',E)$ is the resolution function, $N(E')$ is the incident photon spectrum, and $G(V)$ is the pulse-height gain function. The functions T and A can be calculated from measurements made at a number of different laboratories. The gain $G(V)$ and the resolution function $R(E',E)$ are determined by laboratory calibrations with monochromatic X-rays incident on the detector. The peak in the spectral data yields the gain, and the shape of the spectral data yields the resolution function. At most energies, the resolution function is

Gaussian; however, at low energies, a Poisson function gives a better fit because the parameters must all be greater than zero.

The gain calibration is given in figure 3-6. Energy is plotted as a function of channel number rather than channel voltage. The instrument gain is linear to within 10 percent over the entire range from 0.1 to 8 kiloelectronvolts. A significant nonlinearity of approximately 10 percent is noticeable at the higher energies. The resolution function averaged over the entire sensitive area of the detector at an energy of 5.98 kiloelectronvolts (Mn_K) is shown in figure 3-7. The FWHM of the function is approximately 27 percent. The FWHM at any single point in the detector is considerably better (approximately 20 percent), but slight gain variations from point to point broaden the average resolution. The FWHM resolution is plotted as a function of energy in figure 3-8.

A quick in-flight calibration was provided by two radioactive sources mounted on rotary solenoids, which could be switched into the detector field of view by astronaut command. The housings for these assemblies are shown mounted to the end ribs in figure 3-3.

The flight window was installed on the detector in April 1975. The leak rate measured in vacuum was approximately 3 cm^3 Pa/min (3 cm^3 atm/min). This rate remained stable through testing, installation, and launch. No degradation was observed during the flight.

IN-FLIGHT ANOMALIES

The X-ray experiment was activated together with the other scientific instrument module (SIM) bay experiments approximately 35 hours after launch. Several minutes after the initial activation and calibration, an excessively high count rate was noted in the lowest spectral channels. This pattern of several minutes of normal operation followed by a period of high count rates was observed several times during the mission. The problem apparently was caused by a high-voltage breakdown. Problems with high-voltage breakdown in proportional counters have been evident in all programs using these detectors. In addition to the usual problems of component failures and potting breakdowns, the gas gain region of the detector amplifies any discharge or breakdown caused by sharp points, metal chips, or inadequate spacing of elements. The following paragraphs give a brief operating history for the flight.

The X-ray experiment was operated on day 5 during the raster scan for the Extreme Ultraviolet Survey (EUV) Experiment. The count rates went full scale, and a gas purge was scheduled in anticipation of a possible instrument problem. After purging, the instrument was operated on the sixth day of flight, and 25 minutes of satisfactory data were obtained before the problem reappeared. On day 7, a test was performed in which the instrument was operated with the high voltage on for 2 minutes and then off for 2 minutes. The instrument operated properly for approximately 3 of the 5 minutes during which the high voltage was on. The experiment operation procedure for day 8 was revised to incorporate the 2-minute-on mode of operation, and at least 30 more minutes of satisfactory data were obtained.

On days 8 and 9, an engineering test was performed in an attempt to determine the cause of the instrument malfunction. At the end of the data take on day 8, the instrument was left in a "contingency powerdown" mode, which evacuated the gas volume of the detector. The detector was allowed to pump down to a hard vacuum overnight, and, on day 9, the high voltage was turned on with no gas in the detector. No counts at all were observed for 30 minutes or longer. This result indicated that the malfunction occurred in the gas gain volume of the detector. High-voltage potting, power supplies, and the other high-voltage components external to the gas volume of the detector were thus eliminated as possible causes of the malfunction.

The high voltage was turned off, the detector gas volume was refilled to a nominal pressure of 111 457.5 N/m^2 (1.1 atmospheres) and the high voltage was activated again. The detector malfunction reappeared in approximately 2 minutes, thus reaffirming the conclusion that the malfunction occurred in the gas volume of the detector.

The available data are currently being interpreted to hopefully obtain a better understanding of this malfunction. Several hypotheses have been suggested, and some laboratory tests may be needed to determine whether the characteristics of the problem can be reproduced. At present, however, no simple hypothesis convincingly explains both the intermittent nature and the preponderance of low-energy spectral counts.

Another instrumental anomaly occurred during the flight when a calibration source stuck in the field of view of the detector. The problem first occurred during the initial activation on July 21. The calibration source retracted after several momentary applications of power by the astronauts; however, the source was observed in the field of view again several orbits later, apparently because of inadvertent crew operations. No further efforts were made to dislodge the source because of the astronaut workload and the number of changes that would have been required to the Flight Plan.

In contrast to the high-voltage breakdown, the calibration source was viewed as a relatively minor problem. In analyzing the data, most of the X-ray counts caused by the calibration source can be subtracted because they occur in a narrow spectral range. (The source was iron-55, which emits Mn_K X-rays at an energy of 5.9 kiloelectronvolts). The subtraction, however, does introduce some additional statistical uncertainties into the results.

PRELIMINARY DATA[1]

Analysis of the X-ray experiment data has been slowed considerably by the high-voltage breakdown problem because considerable care is required to find the times during which the detector was functioning properly. Extensive real-time mission replanning was required. Without this coordinated effort, the scientific return would have been far less than was achieved.

---

[1]Also see section 1.

The spectral data are first plotted as shown in figure 3-9. Each plot gives the count rate in a certain X-ray energy band as a function of time. Each point represents an integration of 2.784 seconds, the spectral data accumulation time. The high-voltage problems are readily identifiable as places where the 0.18- to 0.28-kiloelectronvolt count rates average more than 10 000 counts/2.784 sec. To thoroughly examine the good low-energy data, the data must be replotted on a greatly expanded scale. The data from figure 3-9 are shown replotted in figure 3-10. Note that the X-ray source Cygnus X-2 is more readily apparent in the 0.5- to 2-kiloelectronvolt plot. A detailed spectrum of the source can also be obtained from the data as shown in figure 3-11. The incident spectrum that gives the best fit to the data is also shown.

One of the most exciting observations was made during the final orbit of prime data. Both the EUV telescope and the soft X-ray instrument were pointed at HZ 43, a white dwarf. Both instruments detected the object in their respective energy ranges. From the EUV measurements, the spectrum appears to be that of a black body with a temperature of 100 000 K. The X-ray count rate in the lowest energy range, 0.18 to 0.28 kiloelectronvolt, is shown in figure 3-12. (The occasional spikes appear to be due to a milder form of the high-voltage breakdown.) At the time the astronauts began maneuvering the instruments away from the target, a marked decrease in the count rate is seen. The counts attributable to the source can be found by subtracting the background level (dotted line) from the source level (solid line). The result is approximately 10 counts/sec. This count rate appears to be consistent with the upper range of black-body temperatures derived from the EUV data, which was approximately 150 000 K.

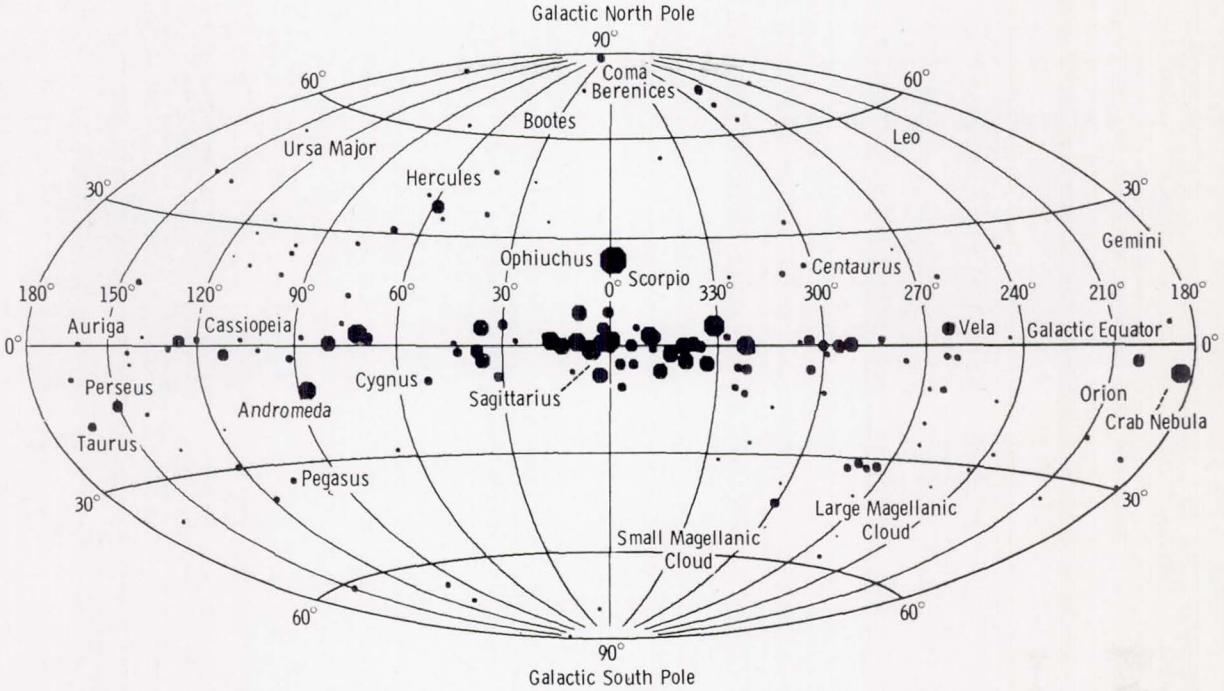

Figure 3-1.- A map of 2- to 10-kiloelectronvolt X-ray sources as determined by the Uhuru satellite.

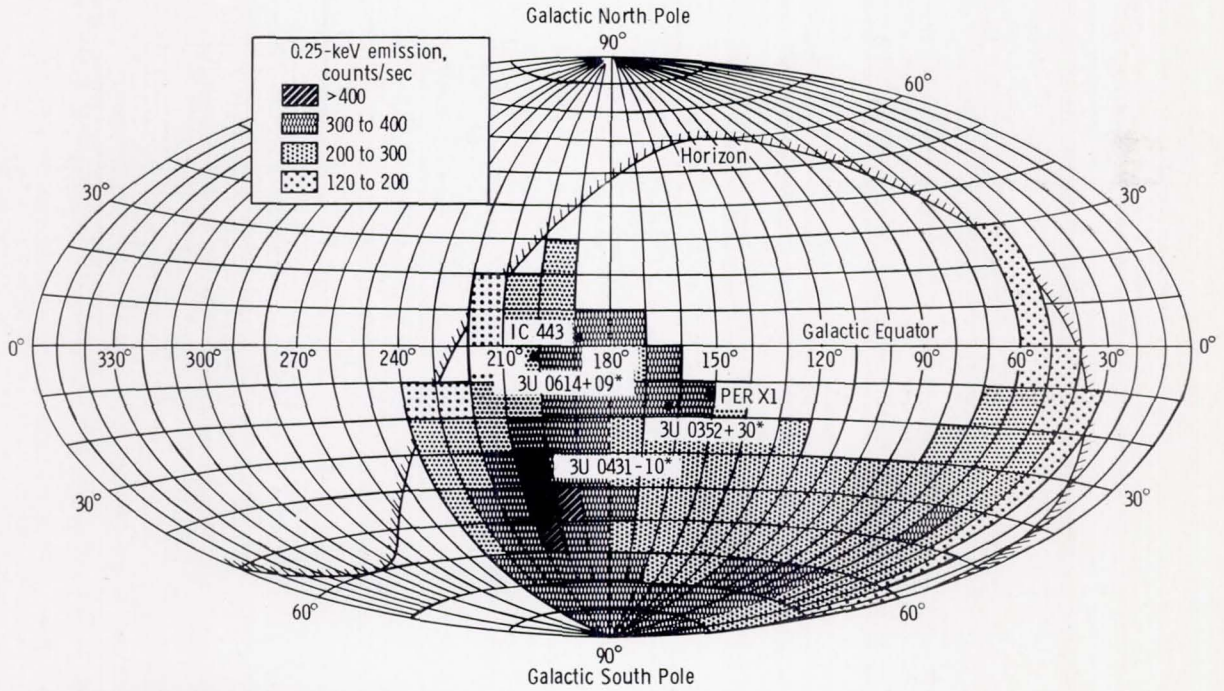

*Source designations from the Uhuru catalog.

Figure 3-2.- A map of diffuse 0.25-kiloelectronvolt X-ray emission from a Naval Research Laboratory (NRL) rocket observation.

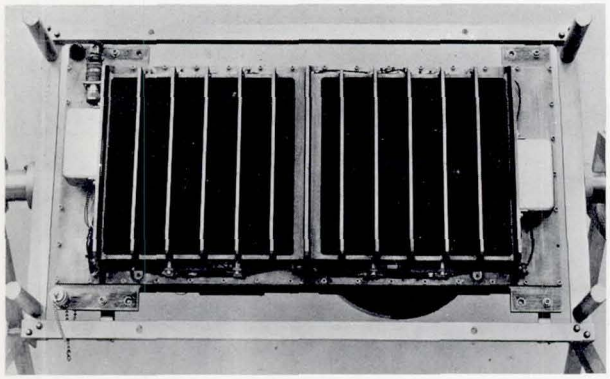

Figure 3-3.- Front view of the ASTP X-ray detector.

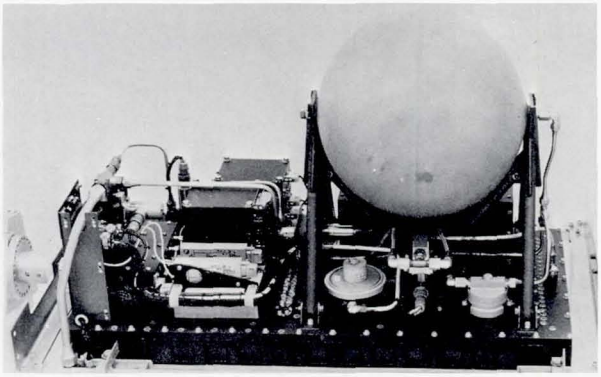

Figure 3-4.- Rear view of the ASTP X-ray detector with the electromagnetic interference shield removed.

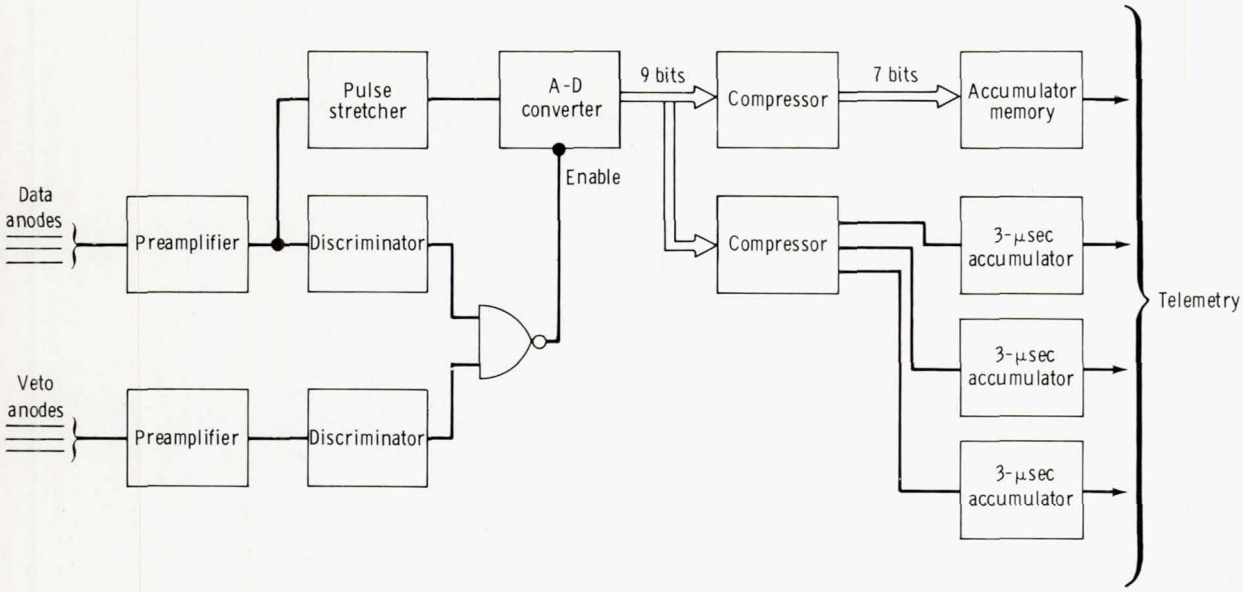

Figure 3-5.- Simplified block diagram of the detector electronics.

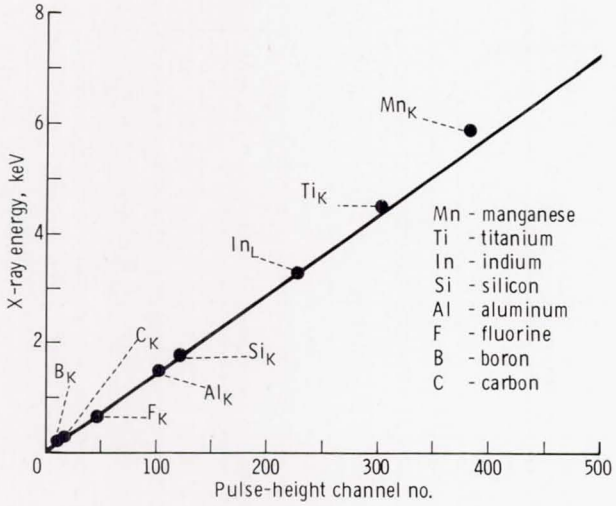

Figure 3-6.- Laboratory gain calibration of the ASTP detector.

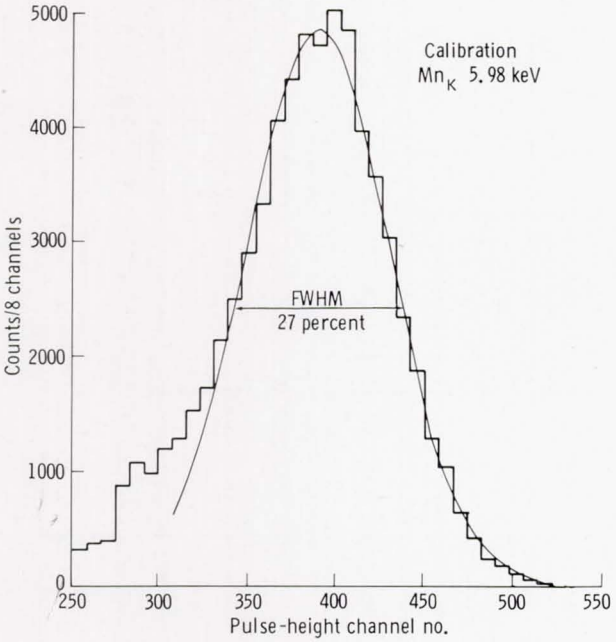

Figure 3-7.- Laboratory calibration spectrum of the Mn_K X-ray line at 5.98 kiloelectronvolts.

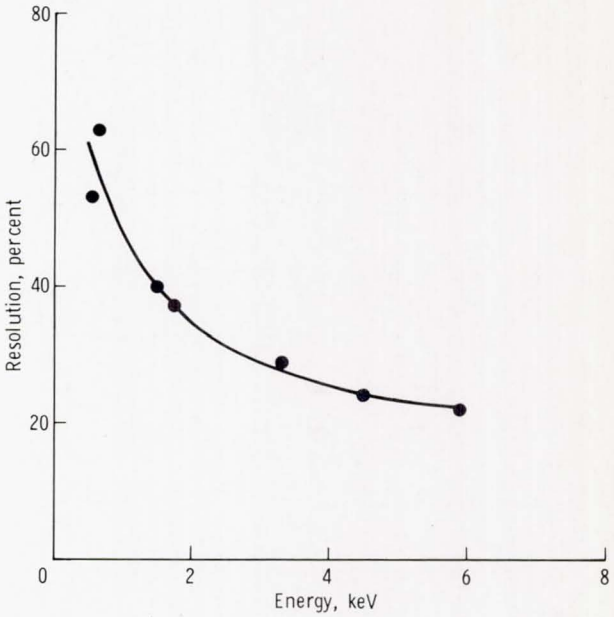

Figure 3-8.- Detector resolution as a function of energy calibration.

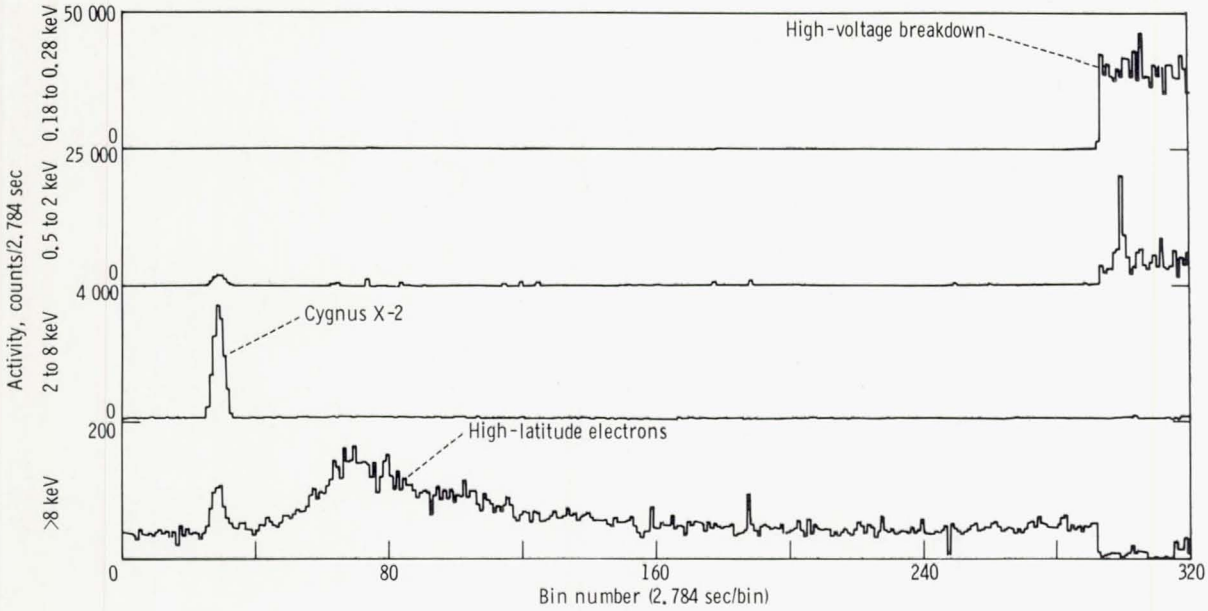

Figure 3-9.- Count rates as a function of time during the flight.

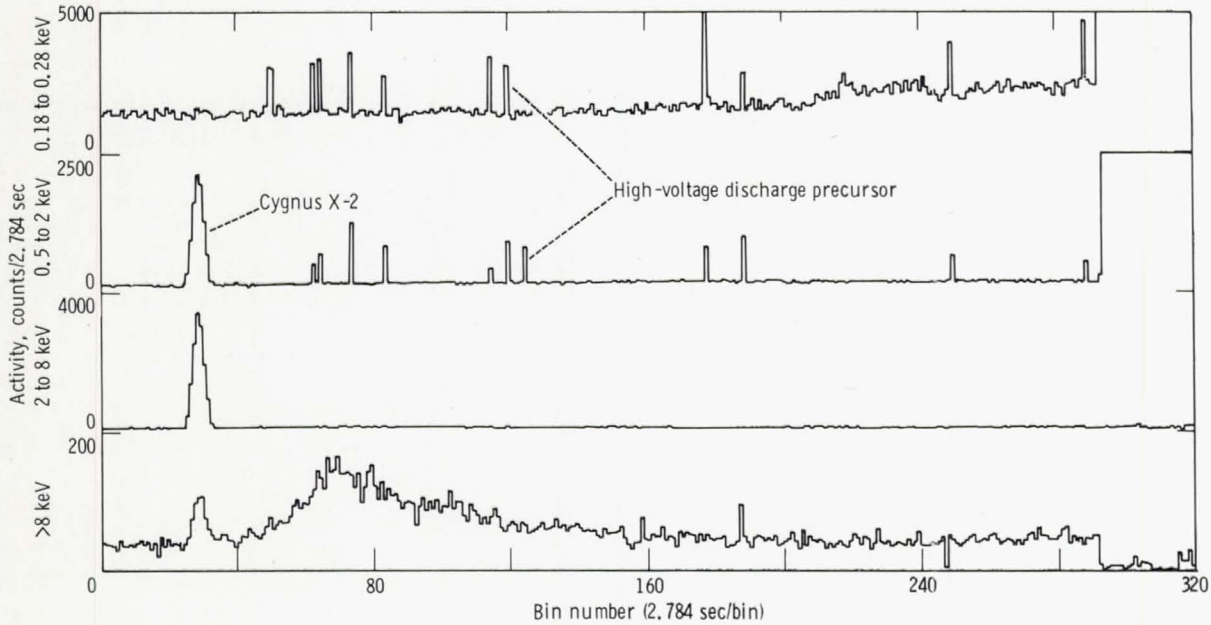

Figure 3-10.- Replotted count rates as a function of time during the flight.

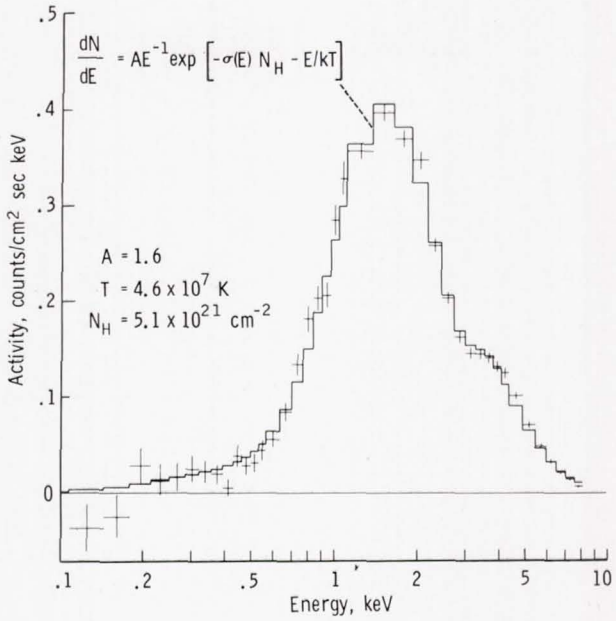

Figure 3-11.- Observed spectrum of Cygnus X-2.

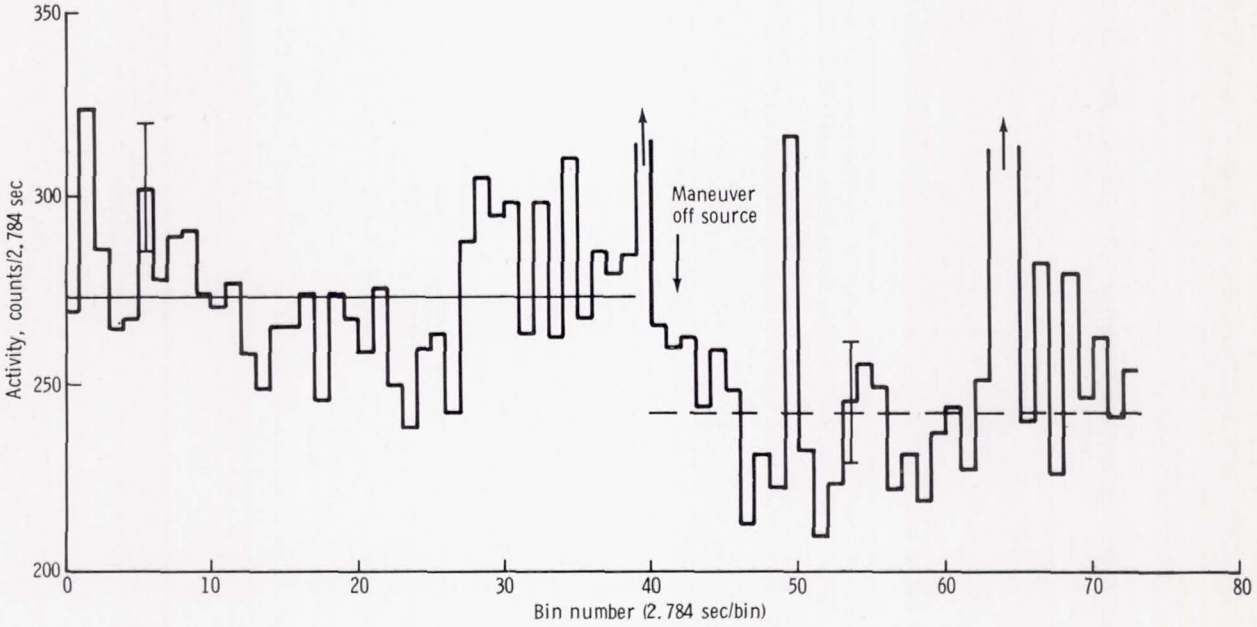

Figure 3-12.- Count rates as a function of time during the observation of the white dwarf HZ 43 (0.18 to 0.28 kiloelectronvolt).

4. EXTREME ULTRAVIOLET SURVEY

EXPERIMENT MA-083

S. Bowyer,[a†] B. Margon,[a] M. Lampton,[a] F. Paresce,[a] and R. Stern[a]

ABSTRACT

A grazing incidence telescope sensitive to radiation in the 5- to 100-nanometer (50 to 1000 angstrom) band was flown in the Apollo service module. On 10 nighttime revolutions, the command and service module was maneuvered to point the instrument at 30 different stellar targets for periods of 1 to 20 minutes, thus constituting the first sensitive search for extreme ultraviolet radiation from nonsolar sources. Several hours of supplementary data were also obtained during nighttime orbits when other experiments in the scientific instrument module bay were operating.

Preliminary analysis of a small fraction of the total data indicates the definite detection of a strong source of extreme ultraviolet radiation during observations made during revolution 109. The source is located in Coma Berenices at $\alpha = 13^h13^m$, $\delta = +29°$. Positive detections have been made in the 17- to 62-, 11.4- to 15-, and 5.5- to 15-nanometer (170 to 620, 114 to 150, and 55 to 150 angstrom) wavelength bands. The intensity is 4 pW/m^2 (4×10^{-9} $ergs/cm^2sec$) in the 17- to 62-nanometer (170 to 620 angstrom) band. The suggested optical identification is the white dwarf HZ 43. If this association is correct, the star has the highest temperature of any known white dwarf. Regardless of the optical identification, however, this object is the first nonsolar source to be detected in the extreme ultraviolet band.

INTRODUCTION

Astronomical observations of nonsolar sources in the extreme ultraviolet (EUV) region of the electromagnetic spectrum (10 to 100 nanometers (100 to 1000 angstroms)) are of profound significance for studies of stellar evolution, stellar atmospheres, and the interstellar medium. The existence of stars producing predominantly ionizing radiation (wavelengths less than 91.2 nanometers (912 angstroms)) has been postulated to explain the ionization state of the interstellar medium. Such stars might represent a very hot phase of stellar evolution (refs. 4-1 and 4-2). Effective surface temperatures greater than 20 000 K have been observed, for example, among O stars, among white dwarfs of classes DAn and DAwk, among the subdwarf OB stars (ref. 4-3), and among the ultraviolet (UV) excess objects observed from the European TD-1A satellite (ref. 4-4). A major deterrent to previous attempts at celestial

---

[a]University of California at Berkeley.

[†]Principal Investigator.

EUV observations has been the opacity of the interstellar gas resulting from photoelectric absorption by neutral hydrogen and neutral and singly ionized helium. However, recent spectroscopic studies of interstellar matter toward nearby stars (refs. 4-5 to 4-7) indicate that in many directions neutral hydrogen concentrations are as low as 0.01 to 0.1 atom/cm^3. Then, the absorption cross sections given in reference 4-8 indicate that direct EUV observations of sufficiently hot stars should be possible to distances of 20 to 100 parsecs.

Preliminary surveys at EUV wavelengths have been made from sounding rockets and have set upper limits of approximately 10^{-10} W/m^2 (10^{-7} ergs/cm^2sec) for sources in limited regions of the sky (refs. 4-9 to 4-11). However, significant constraints on stellar emission models would require improvements in sensitivity of perhaps two orders of magnitude. The Apollo-Soyuz mission offered the opportunity to make extended observations of numerous candidate stars with an EUV telescope that had the requisite sensitivity. Ten nighttime orbits were used to obtain data on 30 preselected stars, 1 planet, and the EUV background radiation. A preliminary analysis of quick-look data has indicated that one target exhibited a particularly intense EUV flux. A second target was also detected at a statistically significant level above the background. Computer processing of the production data will make weaker flux level targets also detectable.

EQUIPMENT

The EUV telescope (ref. 4-12) consisted of a 37-centimeter-diameter grazing incidence mirror assembly, a continually rotating (10 rpm) six-position filter wheel, and a pair of channel electron multiplier detectors. A schematic view of the instrument is shown in figure 4-1.

The parabolic optics were fabricated from aluminum coated with a nickel alloy and then overcoated with a fine layer of gold. The filter wheel included an opaque filter that permitted nearly continuous monitoring of the detector background during the mission. The field of view of the instrument was circular with selectable diameters of 2.5° or 4.3° full width at half maximum obtained by commanding either detector into the focal position. The detailed construction of the detector modules is described in reference 4-13. The detector not at the focal position was also monitored to establish further the stability of the background count rates. Count rates from both detectors were telemetered each 0.1 second together with the filter wheel position and other auxiliary information.

The entire system was calibrated in the laboratory with collimated radiation at numerous wavelengths between 4.4 and 265 nanometers (44 and 2650 angstroms). Absolute intensities were established by using National Bureau of Standards-calibrated vacuum-photodiode secondary standards above 20 nanometers (200 angstroms) and propane proportional counters below 20 nanometers (200 angstroms). The various filters, in combination with the efficiency characteristics of the mirror assembly and detector, defined the wavelength bands illustrated in figure 4-2. The detailed response of the system is summarized in table 4-I. The filters and their bandpasses at 10 percent of peak transmission, the energy-integrated effective area,

or grasp $G = \int A(E)dE$, and the effective energy $E_e = \frac{\int EA(E)dE}{G}$ are given in table 4-I.

The experiment was mounted to a shelf in bay 1 of the service module (SM). A protective cover enclosed the instrument assembly at all times when the experiment was not in operation. At appropriate times in the Flight Plan, the crew activated a switch in the command module (CM) to open the cover. The remaining experiment controls consisted of a POWER ON/OFF switch and a two-position detector-selection switch. Both switches were located in the CM and operated by the crew.

The observing procedure consisted of opening the experiment cover, waiting 10 seconds to permit the ambient pressure in the SM bay to vent to vacuum, and then turning the instrument power on. The crewmember then selected the appropriate detector to ensure that the proper channel multiplier was always in the focal plane. The filter wheel operated automatically and continuously whenever the instrument power was on.

The telescope was oriented at preselected targets by using the spacecraft command module computer (CMC) for guidance and orientation and by using the normal Apollo reaction control system thrusters for maneuverability to point the instrument line of sight at the desired position on the celestial sphere for predetermined lengths of time. The typical target observation sequence consisted of spending equal amounts of time pointing at a target and at two background points located 3° on each side of the target. Any statistically significant differences between the average count rates when observing target and background are then attributable to EUV emission from the object under study. Target observations lasting from 1 to 20 minutes were executed.

RESULTS[1]

The EUV telescope functioned perfectly during the entire mission. The background count rates remained low and reproducible, and analysis of quick-look data shows no evidence of degradation in instrument sensitivity from the laboratory-measured values.

On revolution 65 at 108 hours 26 minutes ground elapsed time, a preplanned raster scan maneuver was executed using a special erasable memory program in the CMC. This maneuver consisted of slewing the telescope in a zigzag pattern back and forth across a star of known brightness in the far UV (~130 nanometers (~1300 angstroms)) where the barium fluoride filter has maximum sensitivity. Because the target position is known in celestial coordinates, a comparison of the time history of the barium fluoride count rates during this maneuver with the known command and service module (CSM) attitude enables the calculation of the actual (in-flight) alinement of the experiment with respect to the CM inertial measuring unit. This information could then be used to recompute CSM pointing data for mission targets to

[1]Also see section 1.

compensate for any changes in alinement from the nominal values caused by vibration or thermal stresses. However, analysis of the revolution 65 raster scan data, obtained on the stars ι Aql and κ Aql, indicated, to an accuracy of 0.3°, that no change from the nominal alinement occurred.

Observation of the targets proceeded normally with occasional small deviations from the observing list caused by time-line anomalies. The rationale for target selection is discussed in reference 4-12. A list of the targets actually observed appears in table 4-II. This list is composed of 30 distinct targets. Seven targets were observed twice during the mission, one target was observed three times, and one target was observed during an extended crew sleep period while the spacecraft was in a fixed inertial attitude. During the mission, considerable real-time planning enabled additional high-quality science data to be obtained. For example, on day 4 of the mission, the American Association of Variable Star Observers advised that the dwarf nova SS Cygni had undergone an optical outburst. As a result, additional observations of this target were obtained on revolutions 80 and 105.

The most interesting target data examined thus far were obtained on revolution 109. As part of the observing schedule, the ultrasoft X-ray source in Coma Berenices (refs. 4-14 to 4-16) was observed for 7 minutes starting July 22, 1975, at 22:26 GMT. After taking background data for 1 minute, a 3° spacecraft roll maneuver brought the center of the instrument line of sight to a point 1° north of the intended target. Thus, the target was just at the edge of the 2° field of view of the instrument. Several roll and pitch motions of approximately 0.5° resulted from spacecraft motion within the attitude dead-band box and moved the field of view off and on the source. Finally, additional sky background data were obtained 3° off the target.

During these maneuvers, obvious increases and decreases in the detector count rates were immediately recognized. A plot of the count rate as opposed to time is shown in figure 4-3 for the 5.5- to 15-, 11.4- to 15-, 17- to 62-, 50- to 78-, and 135- to 154-nanometer (55 to 150, 114 to 150, 170 to 620, 500 to 780, and 1350 to 1540 angstrom) bands with each point representing the average count rate during an 0.8-second time interval. Also shown is the count rate in the opaque filter position, which indicates that the observed instrumental background remained steady at 0.6 count/sec.

A crude estimate of the spectral energy distribution of an object can be made by dividing the observed count rate in each band by the appropriate energy-integrated effective area. Such an estimate is exact for continua having constant photon fluxes per unit frequency. Listed in table 4-I are the observed background-subtracted count rates for the Coma source and the estimated continuum fluxes, both raw and corrected for atmospheric attenuation at E_e based on the Committee on Space Research International Reference Atmosphere 1965 model 2 reference atmosphere, appropriate for the observing conditions. The total energy flux in the 17- to 62-nanometer (170 to 620 angstrom) band is approximately 4 pW/m^2 (4×10^{-9} $ergs/cm^2$ sec).

These intensities have been plotted as a function of wavelength in figure 4-4. Also shown is the 4.4- to 16.5-nanometer (44 to 165 angstrom) detection and 1 kilo-electronvolt upper limit reported in reference 4-16. The data appear compatible and

support the identification of the EUV object with the Coma soft X-ray source. This figure clearly indicates that the spectrum peaks in the EUV band at approximately 30 nanometers (300 angstroms).

A more precise description of the spectrum can be provided by using the observed count rates to constrain parameters of emission models. The simple continuum models chosen for these calculations had photon number per unit energy functions of the following forms: power law, $N(E) = AE^n \exp(-N_H\sigma)$; exponential, $N(E) = AE^{-1} \exp(\frac{-E}{kT}) \exp(-N_H\sigma)$; and blackbody, $N(E) = AE^2[\exp(\frac{E}{kT})-1]^{-1} \exp(-N_H\sigma)$. In each case, the energy-dependent attenuation cross section per hydrogen atom σ has been taken from reference 4-8 with normal abundances, no ionization, and no molecular hydrogen.

The collected data can be satisfactorily fit by any of these trial spectra provided that the free parameters are appropriately chosen. Figure 4-5 shows the derived parameter constraints for these models. In each case, contours are drawn at the $\chi^2_{min} + 6.25$ level appropriate for 90 percent statistical confidence with three free parameters (ref. 4-17). These constraints are compatible with, but much stricter than, the parameter regions derived from the soft X-ray rocket data given in reference 4-16.

Positional information on this source can be derived from the fact that, as the spacecraft pointing varies, the count rates are occasionally interrupted. Telemetered data on the CSM aspect have been combined with in-flight data on the experiment alinement to obtain four independent position zones for the source. These zones define a common region that is shown in figure 4-6 superposed on the relevant star field.

The Small Astronomy Satellite-3 observations reported in reference 4-15 have given a positional error box for the soft X-ray source that is compatible with the EUV position and is also shown in figure 4-6. It is highly probable that one object is responsible for the soft X-ray and EUV emissions. It has been suggested (ref. 4-15) that the soft X-ray object is the hot white dwarf HZ 43 at $\alpha(1950) = 13^h14.0^m$, $\delta(1950) = +29°22'$. This object is also marked on figure 4-6, and the EUV position is compatible with this suggestion.

If this identification is correct, it is of interest to determine whether any of the simple EUV spectra in figure 4-5 are compatible with the optical brightness of the star HZ 43. Magnitudes for HZ 43 have been published in reference 4-18 and are given as V = 12.86, B = 12.76, and U = 11.62 where V, B, and U are brightnesses in the standard astronomical photoelectric system. The power law and exponential spectra, if extended to visible wavelengths, would give magnitudes much redder and brighter than observed. However, the blackbody spectra would be compatible at $\simeq$110 000 K. If this simple model is correct, the stellar radius is 7800 D_{100} kilometers, where D_{100} is the distance to the star in units of 100 parsecs, and the corresponding luminosity is 17 D_{100}^2 $L_\odot$, where $L_\odot$ is the solar luminosity,

3.83×10^{33} ergs/sec. These parameters are in reasonable agreement with white dwarf models. Although these data do not uniquely require a blackbody stellar spectrum, with this explanation and identification, HZ 43 has the highest temperature of any known white dwarf.

Additional observations obtained on revolution 109 indicate the probable detection of EUV radiation from an additional target. Although detailed aspect data are still being reduced, it appears that the source may be the M-dwarf star Proxima Centauri. Detections appear in the 5.5- to 15-nanometer (55 to 150 angstrom) band and possibly the 11.4- to 15-nanometer (114 to 150 angstrom) band. Both detections are at an intensity substantially less than the Coma source.

Data from targeted observations on revolutions other than 109 have not been processed but will have sensitivity similar to that described previously. In addition, a substantial volume (several hours) of supplementary data was obtained by the EUV telescope while it was being used with the Helium Glow Detector or the Soft X-ray Experiments. These data will be processed to search for discrete sources of EUV radiation and to derive information on the spectrum, intensity, and isotropy of the ultrasoft X-ray/EUV cosmic diffuse background radiation. The data are the most extensive ever obtained on the latter problem.

SUMMARY

All the primary goals of the EUV Survey Experiment were achieved. Data were obtained on 30 different targets belonging to a variety of different classes of stars. Extensive and sensitive data on the EUV background radiation were also acquired. Preliminary analysis of the data indicates the detection of at least one strong source of EUV radiation, which is the first nonsolar source to be detected in the EUV band and proves the feasibility and value of astronomical observations at the wavelengths indicated in this report.

REFERENCES

4-1. Hills, J. G.: An Explanation of the Cloudy Structure of the Interstellar Medium. Astron. & Astrophys., vol. 17, 1972, pp. 155-160.

4-2. Rose, W. K.; and Wentzel, D. G.: Ultraviolet Stars and the Interstellar Gas. Astrophys. J., vol. 181, 1973, pp. 115-123.

4-3. Greenstein, J. L.; and Sargent, A. I.: The Nature of Faint Blue Stars in the Halo. II. Astrophys. J. Supp. Series, vol. 28, no. 259, 1974, pp. 157-210.

4-4. Carnochan, D. J.; Dworetsky, M. M.; Todd, J. J.; Willis, A. J.; and Wilson, R.: A Search for Ultraviolet Objects. Phil. Trans. Roy. Soc. London, A, vol. 279, 1975, pp. 479-485.

4-5. Rogerson, J. B.; York, D. G.; Drake, J. F.; Jenkins, E. B.; Morton, D. C.; and Spitzer, L.: Spectrophotometric Results From the Copernicus Satellite. III. Ionization and Composition of the Intercloud Medium. Astrophys. J. (Letters), vol. 181, 1973, pp. L110-L115.

4-6. Bohlin, R. C.: Copernicus Observations of Interstellar Absorption at Lyman Alpha. Astrophys. J., vol. 200, 1975, pp. 402-414.

4-7. Dupree, A. K.: Ultraviolet Observations of Alpha Aurigae From Copernicus. Astrophys. J. (Letters), vol. 200, 1975, pp. L27-L31.

4-8. Cruddace, R.; Paresce, F.; Bowyer, S.; and Lampton, M.: On the Opacity of the Interstellar Medium to Ultrasoft X-rays and Extreme Ultraviolet Radiation. Astrophys. J., vol. 187, 1974, pp. 497-504.

4-9. Riegler, G. R.; and Garmire, G. P.: Observations of the Extreme Ultraviolet Nightglow. J. Geophys. Res., vol. 79, 1974, pp. 226-232.

4-10. Henry, P.; Bowyer, S.; Cruddace, R.; Lampton, M.; and Paresce, F.: An Extreme Ultraviolet Search of the Galactic Anticenter Region. Bull. American Astron. Soc., vol. 6, no. 4, part I, 1974, p. 446.

4-11. Henry, P.; Cruddace, R.; Paresce, F.; Bowyer, S.; and Lampton, M.: An Extreme Ultraviolet Search of the North Galactic Polar Region. Astrophys. J., vol. 195, 1975, pp. 107-110.

4-12. Margon, B.; and Bowyer, S.: Extreme Ultraviolet Astronomy From Apollo-Soyuz. Sky and Telescope, vol. 50, no. 1, 1975, pp. 4-9.

4-13. Hoshiko, H. H.: Helical Channel Multiplier Package Design for Space Instrumentation. Rev. Sci. Instr., vol. 46, no. 3, 1975, pp. 331-332.

4-14. Hayakawa, S.; Murakami, T.; Nagase, F.; Tanaka, Y.; and Yamashita, K.: Transient Soft X-ray Sources. Proc. IAU/COSPAR Symposium on Fast Transients in X- and Gamma-Rays, XVIIIth Plenary Meeting of COSPAR (Varna, Bulgaria), May 1975.

4-15. Hearn, D. R.; and Richardson, J. A.: New Soft X-ray Source. IAU Circulars, no. 2890, June 17, 1975.

4-16. Margon, B.; Malina, R.; Bowyer, S.; Cruddace, R.; and Lampton, M.: An Ultrasoft X-ray Source in Coma Berenices. Astrophys. J. (Letters), vol. 203, 1976, pp.L5-L8.

4-17. Margon, B.; Lampton, M.; Bowyer, S.; and Cruddace, R.: Soft X-ray Spectroscopy of Three Extragalactic Sources. Astrophys. J., vol. 197, 1975, pp. 25-29.

4-18. Eggen, O. J.; and Greenstein, J. L.: Spectra, Colors, Luminosities, and Motions of the White Dwarfs. Astrophys. J., vol. 141, 1965, pp. 83-108.

TABLE 4-I.- EUV PHOTOMETRIC DATA

Instrument characteristics					Data	Derived fluxes		
Filter material	Bandpass		Grasp, $cm^2 eV$	Effective energy,	Coma source observation count rate,[a] counts/sec	Uncorrected, $ph(cm^2 sec\ eV)^{-1}$	Corrected for atmosphere	
	eV	nm (A)					$ph(cm^2 sec\ eV)^{-1}$	mfu[b]
Parylene N	83 to 225	5.5 to 15.0 (55 to 150)	590	142	22 ± 1	0.037	.039	3.7
Beryllium	83 to 109	11.4 to 15.0 (114 to 150)	60	100	8 ± 0.5	.13	.15	9.9
Aluminum plus carbon	20 to 73	17 to 62 (170 to 620)	270	46	160 ± 3	.59	1.0	30
Tin	16 to 25	50 to 78 (500 to 780)	108	21	<50	<.46	<1.2	<17
Barium fluoride	8.0 to 9.2	135 to 154 (1350 to 1540)	0.47	9	<25	<53	<53	<325

[a]Errors quoted are $\pm 1\sigma$.

[b]mfu = 10^{-26} ergs/cm^2sec Hz.

TABLE 4-II.- TARGETS OBSERVED BY THE ASTP EUV TELESCOPE

Revolution	Target
72	EV Lac, AE Aqr, NGC 7293, ε Eri
73	VW Cep, DQ Her, 70 Oph, α PsA
80	EV Lac, SS Cyg, DQ Her, θ Oph, α Cen
88	α CMa B
89	NGC 6853, PSR 1929, α Aql, UV Cet, Feige 24
90	SS Cyg, 61 Cyg, BD +24° 4811, Jupiter
94	HZ 29, i Boo, Prox Cen
105	SS Cyg, BD +24° 4811
108	Wolf 424, α Cen, Z Cha, VW Hyi, UV Cet
109	CP 1133, HZ 43, Prox Cen, PSR 1451, β Hyi
113 to 117	Wolf 424

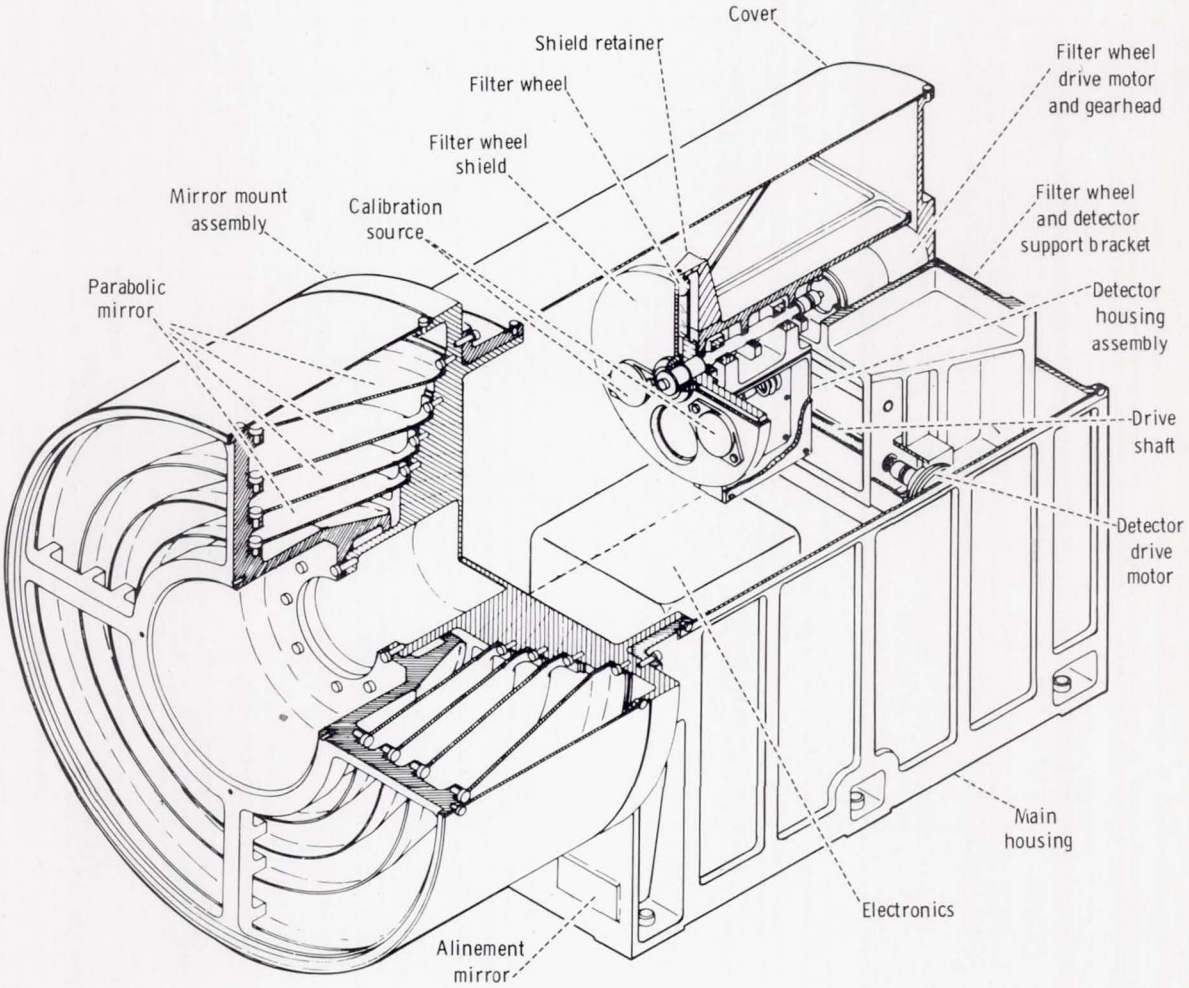

Figure 4-1.- A schematic diagram of the EUV telescope.

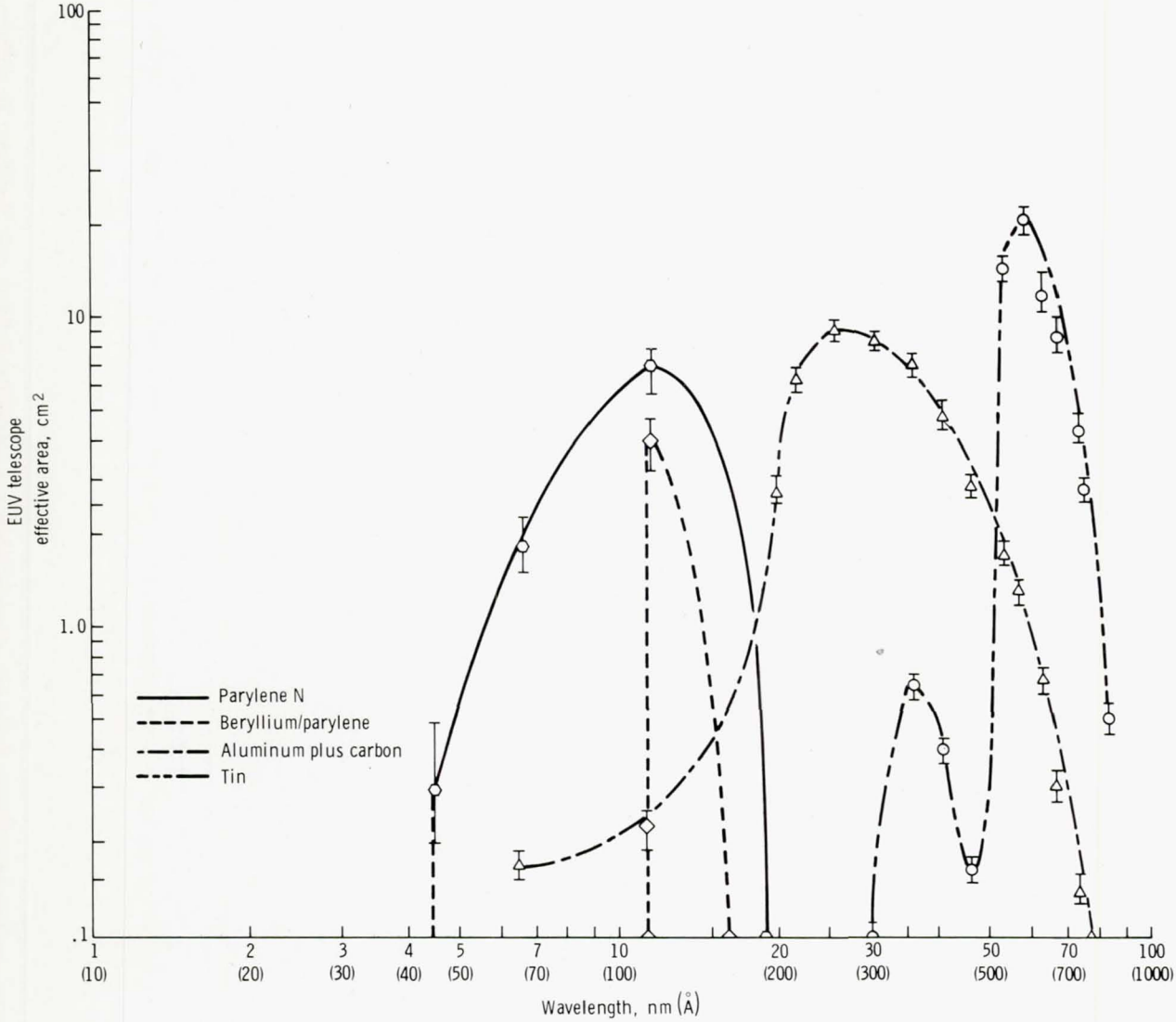

Figure 4-2.- Effective area of the EUV telescope as determined by laboratory calibration data. (The response of the barium fluoride bandpass, which was used primarily for instrument alinement determination, is given in table 4-I.)

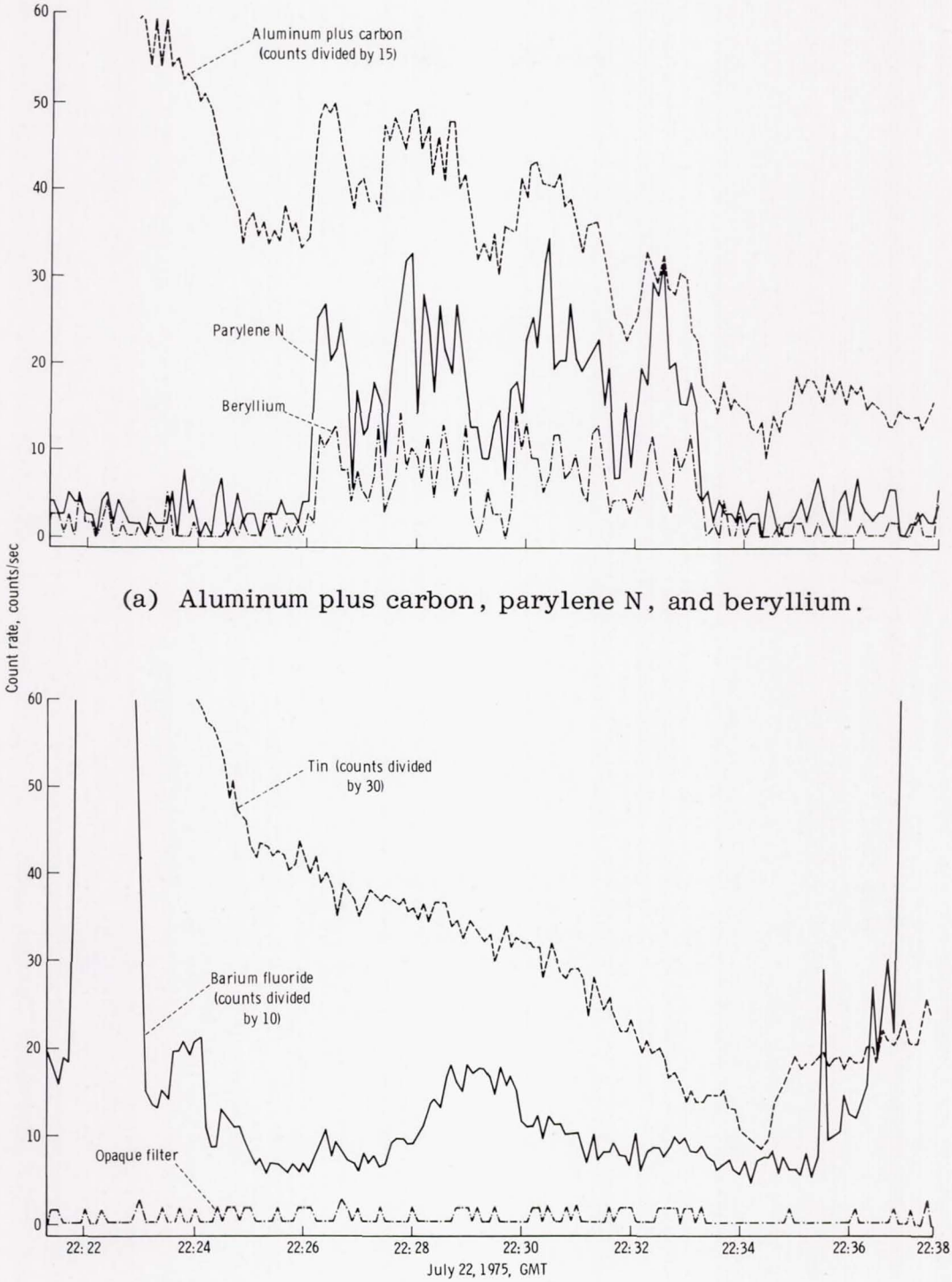

(a) Aluminum plus carbon, parylene N, and beryllium.

(b) Tin, barium fluoride, and the opaque filter.

Figure 4-3.- The EUV data obtained during a portion of revolution 109. The trends in the aluminum and tin band passes are due to the spatial variations in the geocoronal foreground radiation. This behavior was repeated on numerous orbits. The barium fluoride count rates are dominated by the occasional observations of known blue stars.

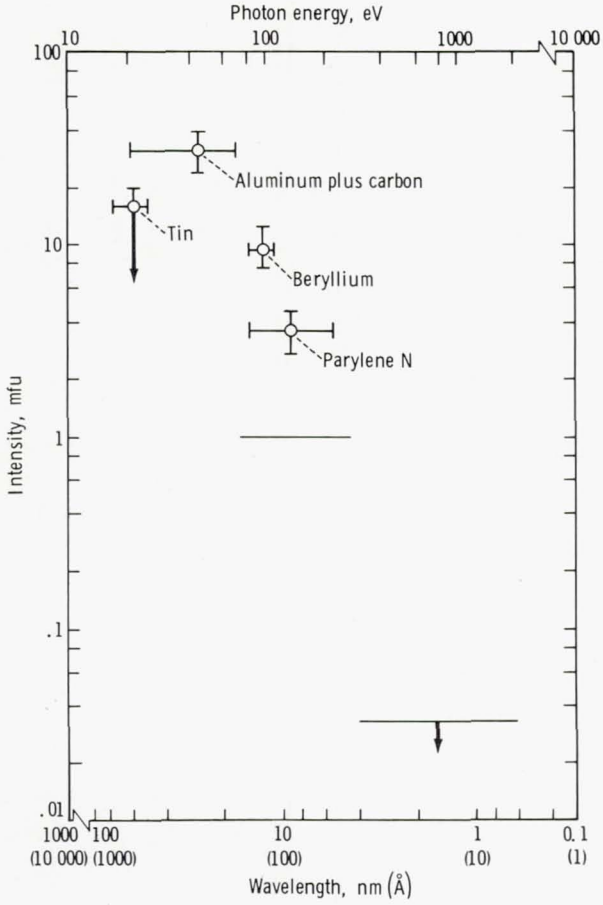

Figure 4-4.- Spectral intensities derived from the EUV data on the source in Coma Berenices. Soft X-ray data (ref. 4-16) are also shown.

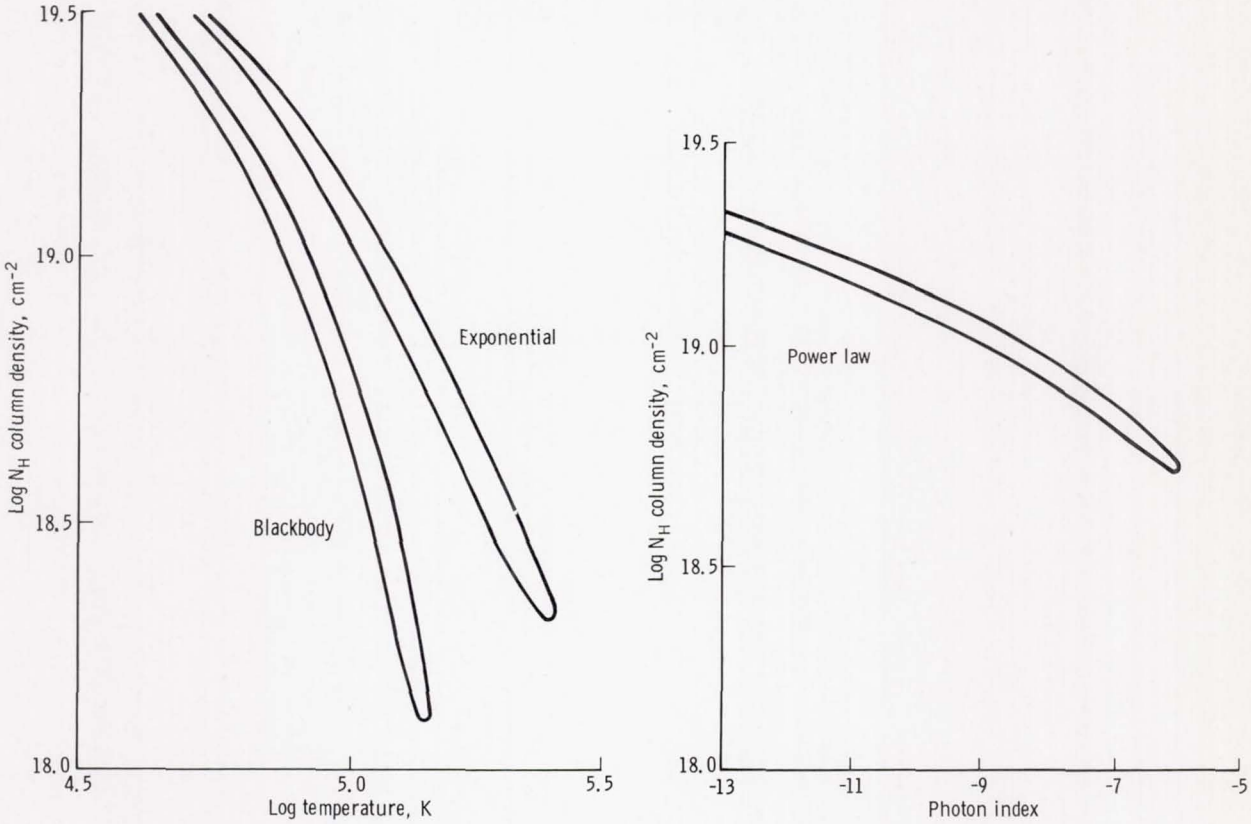

(a) Blackbody and exponential contours.

(b) Power law spectra contour.

Figure 4-5.- Contours of constant χ^2 for the fits of blackbody, exponential, and power law spectra. Each contour has been drawn at the $\chi^2_{min} + 6.25$ level appropriate for 90 percent statistical confidence with three adjustable parameters (ref. 4-17).

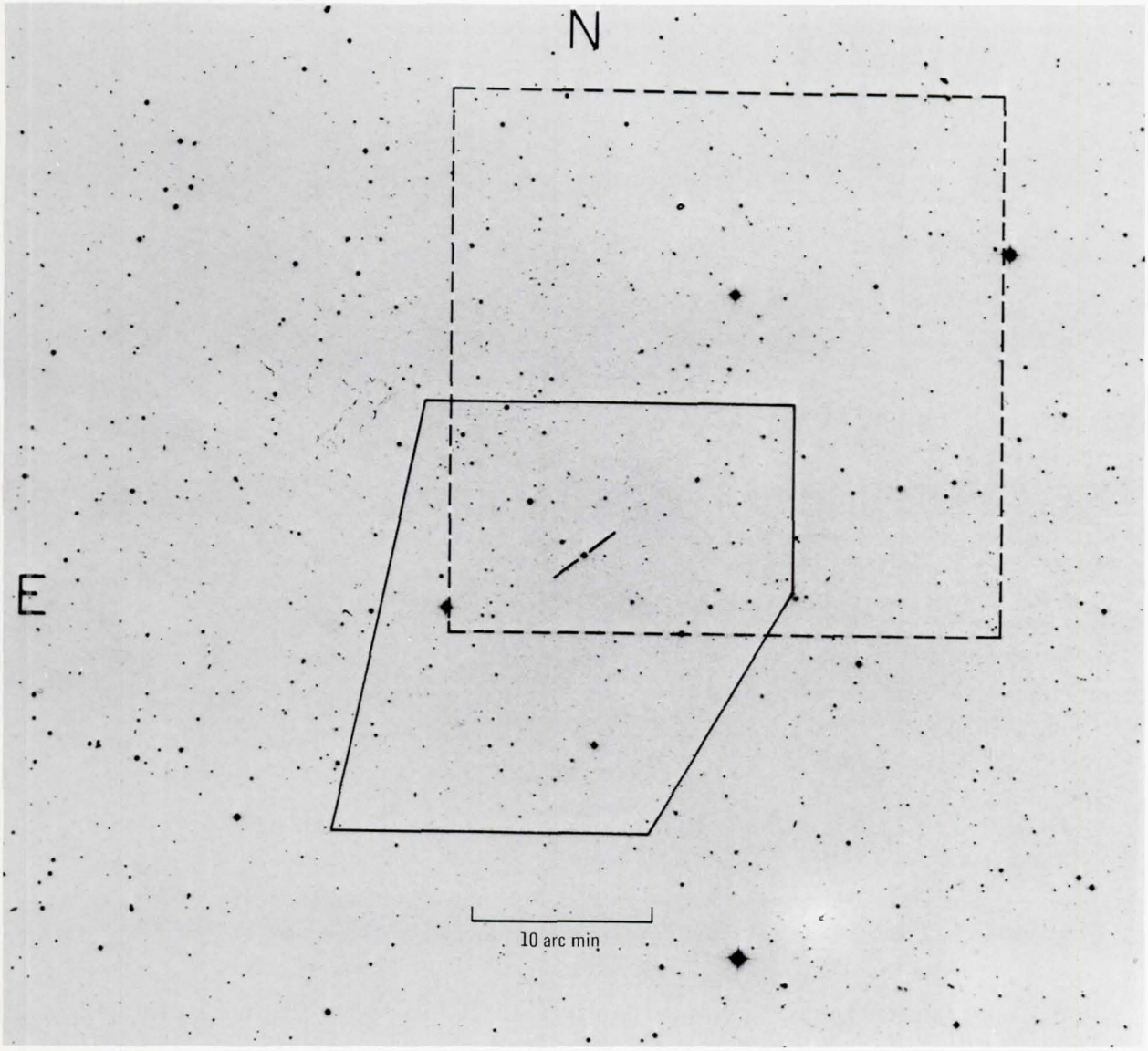

Figure 4-6.- Positional error box for the EUV source in Coma Berenices derived from the revolution 109 data (solid line). The broken line is the error box for the soft X-ray source observed from Small Astronomy Satellite-3 (ref. 4-15). The white dwarf HZ 43 is also marked in the center of the photograph. Enlargement is from the blue Sky Survey plate (copyright by the National Geographic Society - Palomar Observatory Sky Survey; reproduced by permission of the Hale Observatories).

5. INTERSTELLAR HELIUM GLOW

EXPERIMENT MA-088

S. Bowyer,[a†] J. Freeman,[a] F. Paresce,[a]
M. Lampton,[a] and B. Margon[a]

ABSTRACT

The Apollo-Soyuz Test Project Interstellar Helium Glow Experiment (MA-088) studied the motion of helium in the local interstellar medium as that medium passed through the solar system to determine several poorly known properties of the local interstellar gas. The instrument used was a photometer sensitive to two solar extreme ultraviolet spectral lines that are resonantly scattered by helium gas. The instrument surveyed the entire celestial sphere during a series of slow, rolling maneuvers by the Apollo spacecraft. The equipment operated properly, and usable data were obtained.

INTRODUCTION

Most knowledge of the structure and properties of the interstellar medium (ISM) has been obtained by observations with radio telescopes and optical telescopes that average the properties of the ISM over distances of 10^{18} meters or more. Measurements averaged over these distances do not permit the study of smaller scale variations in the ISM or the determination of the properties of the ISM in the immediate vicinity of the Sun. Furthermore, these measurements have left considerable doubt about fundamental ISM parameters such as density, speed, and temperature.

As the Sun moves through the local ISM, the motion of gas atoms in that medium is affected by the pressure of sunlight and by solar gravitation. The resulting patterns of gas motion and distribution are determined not only by the effects of these two forces but also by the initial conditions of temperature, velocity, and density that the gas possessed before entering the solar system. The primary goal of the helium glow experiment was to determine those initial conditions by observing the local distribution of interstellar helium gas over the entire sky.

---

[a]University of California at Berkeley.

[†]Principal Investigator.

BASIC THEORY

Motion of the ISM Near the Sun

Axford, Blum and Fahr, Holzer and Axford, Wallis, and Johnson (refs. 5-1 to 5-5) have described the dynamics of the local ISM as it passes through the solar system. If the interstellar gas is sufficiently cold that the thermal speeds of gas atoms are negligible compared to the bulk speed of the gas with respect to the Sun, then the number density of a specific atomic species at a given point in the solar system may be determined as follows.

Let V be the bulk speed of the distant ISM with respect to the Sun, G be the gravitational constant, M be the solar mass, and μ be the absolute value of the ratio of the pressure of sunlight to the force of gravity on a gas atom. Let $C = V^2/[GM(1 - \mu)]$.

In any plane containing the Sun and the bulk velocity vector of the distant ISM, choose polar coordinates r and ψ, with the Sun at $r = 0$ and with $\psi = 0$ pointing toward the direction from which the ISM approaches. Each point (r,ψ) in this plane is the intersection of two gas atom orbits. Atoms moving in these two orbits will have angular momentum per unit mass

$$P_j = \frac{1}{2} V \left\{ r \sin \psi + (-1)^{j+1} \left[r^2 \sin^2 \psi + \frac{4r(1 - \cos \psi)}{C} \right]^{\frac{1}{2}} \right\} \tag{5-1}$$

where $j = 1,2$.

Let $b_j = p_j/V$ be the impact parameters corresponding to the two orbits. Let β_0 be the rate at which atoms of the selected species are ionized by sunlight at a distance from the Sun equal to the radius r_e of the Earth orbit. Let $r_i = \beta_0 r_e^2/V$, and let N be the number density of the gas atoms in question, far from the Sun.

Now choose spherical coordinates (r,θ,φ) such that $0 \leq \theta \leq \pi$ and $0 \leq \varphi \leq 2\pi$, with the Sun at $r = 0$, with $\theta = 0$ pointing toward the approaching ISM, and with $\varphi = 0$ arbitrarily chosen. For these coordinates, the number density of the gas atoms in question is

$$n(r,\theta,\varphi) = \sum_{j=1}^{2} \frac{N b_j^2 \exp\left(\frac{-r_i \theta_j}{|b_j|} \right)}{r \sin \theta \left[r^2 \sin^2 \theta + \frac{4r(1 - \cos \theta)}{C} \right]^{\frac{1}{2}}} \tag{5-2}$$

where $\theta_j = \theta$ if $p_j \geq 0$, and $\theta_j = 2\pi - \theta$ if $p_j < 0$.

If μ is less than 1 (as is the case for helium), equation (5-2) diverges as θ approaches π. This divergence is a straightforward consequence of neglecting the thermal motions of the gas atoms; in this case, the orbit of every atom crosses a line drawn outward from the Sun in the direction toward which the gas moves. Blum, Pfleiderer, and Wulf-Mathies (ref. 5-6) have described a modification to equation (5-2) for θ near π by which gas thermal speeds that are nonzero but that are still small compared to V are properly considered. They find that near $\theta = \pi$, the gas density has a maximum the detailed shape of which depends on the gas temperature. Variations in equation (5-2) that are due to larger gas thermal motions and to such other effects as nonionizing collisions involve more elaborate analyses, such as those of Danby and Camm (ref. 5-7) and Wallis (ref. 5-8), and detailed numerical modeling of the gas motion. Discussion of these topics is beyond the scope of this preliminary report. A detailed discussion of current theory of the behavior of the local ISM as it flows through the solar system can be found in reference 5-9.

Photometric Observations of the Gas

The Sun emits strong, broad spectral lines at 30.4 and 58.4 nanometers that are resonantly scattered by singly ionized helium and neutral helium, respectively. A general formalism describing the radiation in the ISM is well established (ref. 5-10). An observer viewing the gas through a spectral filter that transmits all of one of these lines would see I photons per second per square meter per steradian, where I is given by

$$I = \sum_{j=1}^{2} \int_{s} \int_{\nu} F(\nu,s) a_j(\nu,s) p(s) n_j(s) d\nu \, ds \tag{5-3}$$

The outer integral is taken along the ray from the observer toward infinity along the observer's line of sight. Points along this ray are specified by their distance s from the observer. The inner integral is taken over frequency ν, between limits sufficiently far from the line center to allow for the combined effects of solar line width, thermal-Doppler line broadening, and Doppler shifts due to radial motions between the Sun and the gas and between the gas and the observer.

The quantity $F(\nu,s)$ is the flux of solar photons having frequency ν at a point $P(s)$, which is s away from the observer on the line of sight. It is given by

$$F(\nu,s) = \frac{\pi F_0}{\sqrt{2\pi}\,\sigma} \left[\frac{r_e}{r(s)}\right]^2 \exp\left[\frac{-(\nu - \nu_0)^2}{2\sigma^2}\right] \tag{5-4}$$

in which πF_0 is the total solar photon flux in the spectral line of interest at the radius r_e of the Earth orbit, σ is the standard deviation of the Gaussian profile of the solar line, $r(s)$ is the distance from the Sun to the point $P(s)$, and ν_0 is the frequency at the line center. In equation (5-3), the quantity $a_j(\nu,s)$ is the scattering cross section per atom at frequency ν and point $P(s)$, given by

$$a_j(\nu,s) = \frac{q_e^2}{4\varepsilon_0 m_e c} \bullet f \bullet \frac{1}{\Delta\nu} \bullet \frac{1}{\sqrt{\pi}} \exp\left[-\left(\frac{\nu - \nu_0'}{\Delta_\nu}\right)^2\right] \tag{5-5}$$

in which q_e is the absolute value of the electron charge, ε_0 is the permittivity of free space, m_e is the electron mass, c is the speed of light, and f is the oscillator strength for the transition in question.

Furthermore, the quanity $\Delta\nu$ is a measure of thermal broadening of the scattered line:

$$\Delta\nu = \frac{\nu_0}{c}\sqrt{\frac{2kT}{m}} \tag{5-6}$$

where k is the Boltzmann constant, T is the gas temperature, and m is the mass of one gas atom. The quantity ν_0' is defined

$$\nu_0' = \nu_0\left[1 + \frac{V_{r,j}(s)}{c}\right] \tag{5-7}$$

in which $V_{r,j}(s)$ is the radial velocity of an atom on orbit j at the point $P(s)$.

The quantity $p(s)$ is

$$p(s) = \frac{3}{4}\left\{1 + \cos^2[\theta(s)]\right\} \tag{5-8}$$

in which $\theta(s)$ is the angle included between the Sun, the point $P(s)$, and the observer.

Equation (5-3) may be numerically integrated to give the fluxes produced by various theoretical models of the ISM.

The Problem of the Terrestrial Geocorona

Observations of the local behavior of interstellar helium are complicated by the presence of substantial concentrations of neutral helium and singly ionized helium in the Earth geocorona, retained respectively by the terrestrial gravitational field and the magnetic field. This helium also scatters solar radiation of wavelengths 58.4 and 30.4 nanometers, respectively. The local concentrations of helium extend to several Earth radii above the surface. Therefore, even if the observer is located within the Earth shadow (viz, nighttime), fluxes scattered from the geocorona will still be observed. If the observer's line of sight happens to point down the axis of the Earth shadow, these fluxes will be minimized; but even then, they will not necessarily be zero because photons may scatter twice, as is shown in figure 5-1, and thereby reach the observer from outside the shadow. In any case, only a small portion of the celestial sphere can be viewed by looking down the shadow.

The 58.4-nanometer flux scattered from the geocorona can be eliminated easily. The average geocoronal temperature of 10^3 K (ref. 5-11) corresponds to a helium thermal speed of approximately 2 km/s, which yields approximately 0.6-picometer thermal-Doppler broadening of the scattered 58.4-nanometer line at full width half maximum. On the other hand, the bulk speed of the local ISM with respect to the Sun is 5 to 20 km/s (ref. 5-9) and the orbital speed of the Earth is 30 km/s. Hence, there are large solid angles, the configuration of which varies throughout the year, within which the radial velocities of local interstellar helium with respect to the Earth are several tens of kilometers per second. These velocities correspond to Doppler shifts in the 58.4-nanometer line of several picometers, or many times the width of the geocoronal line. Therefore, a gas absorption cell containing neutral helium at an appropriate column density will absorb the geocoronal 58.4-nanometer flux while transmitting most of the flux scattered from the local ISM.

A detailed calculation shows that a column of helium 0.1 meter long at a temperature of 300 K and a pressure of 130 N/m^2 absorbs more than 99 percent of the geocoronal flux over a band approximately 3.5 picometers full width, centered on the 58.4-nanometer line. The width of this absorption band is sufficient to block the geocoronal 58.4-nanometer line even when that line is also Doppler shifted by the 8-km/s speed of a spacecraft in low Earth orbit.

If the observer does use a gas absorption cell, equation (5-3) must be modified to include a third integral, taken over the cell transmission as a function of radial speed between the observer and the gas.

EQUIPMENT

The helium glow detector (HGD) onboard the Apollo spacecraft during the Apollo-Soyuz Test Project flight is shown in figure 5-2. The unit was approximately cubical, 0.35 meter on each side, and had a mass of 23 kilograms. It was mounted below the bay 1 shelf of the service module, close to the instruments for the soft X-ray and extreme ultraviolet survey experiments, as shown in figure 5-3.

A small door in the spacecraft skin protected the instrument during ascent and during the in-flight venting of liquids and gases and was opened by the astronauts for observations. The HGD consisted of three main subassemblies: the detector (including the helium gas system), the electronics, and the instrument housing and mechanical structures.

Detector Subsystem

The detector subsystem was composed of four similar channels, each of which detected photons by means of a channel electron multiplier. Channels 1 and 3 were identical, as were channels 2 and 4. Channels 1 and 3 observed the 58.4-nanometer radiation through helium gas absorption cells. Each cell was 0.10 meter long and was capped with two thin metal filters, one tin and one aluminum. Layers of these elements a few hundred nanometers thick are transparent in the extreme ultraviolet (EUV) spectral region, and the particular combination of filters used defines a bandpass approximately 10 nanometers wide, containing the 58.4-nanometer line.

Each gas absorption cell was alternately filled with helium to a pressure of approximately 130 N/m^2 and evacuated. The pressure cycles of the two cells were exactly out of phase, so that one cell was full when the other was empty. Each cell was equipped with a thermocouple-type pressure gage and with a thermistor for measuring temperature.

Figure 5-4 is a schematic diagram of the helium gas subsystem. Helium was supplied to the cells from a tank at a pressure of approximately 6000 kN/m^2. The gas flowed through a master solenoid valve to a regulator, where the pressure was reduced to approximately 10 kN/m^2. The gas then flowed through adjustable needle valves into small transfer manifolds. To pressurize either gas cell, the cell fill valve was opened briefly, releasing into the cell the gas in the transfer manifold plus a small amount that leaked through the needle valve. The transfer manifold volume was chosen to contain insufficient helium to fill a cell to design pressure, and the needle valve was adjusted until the total amount of gas released produced the correct pressure.

Detector channels 2 and 4 observed the 30.4-nanometer radiation. The bandpass for this wavelength was defined by a single thin filter, composed of a layer of aluminum and a layer of carbon. Each of the four channels had a field of view of approximately 15° full width at half maximum.

Electronics Subsystem

The HGD electronics subsystem is shown schematically in figure 5-5. Timing and synchronization were controlled by the central control logic subsystem, which was itself synchronized to the spacecraft 1.0-hertz clock. The power system converted spacecraft 28-volt direct-current (dc) power into various regulated low voltages for electronics subsystems and into regulated high voltages for the channel

electron multipliers. To minimize single-point failures, each detector had an independent high-voltage power supply (HVPS).

The amplifier (A) system for each detector channel accepted signals as small as 10^{-14} coulomb at a maximum random rate of 10^5 seconds^{-1}. To stay within a reasonable threshold level for the discriminator, a 10X interstage amplifier was used. A pulse pair resolution of 1.0 microsecond ensured that statistical counting losses remained below 10 percent, even at the maximum count rate.

The compressor and register for each channel accepted serial event pulses from the discriminator and produced an 8-bit output word representative of the number of events detected in each 0.1-second accumulation interval. The binary word was then converted by the digital-to-analog (D-A) converter to an analog voltage compatible with the Apollo telemetry system. The output voltage was updated every 0.1 second in synchronization with the sampling of that voltage by the telemetry system.

Data compression was necessary because the 8-bit word employed by the telemetry system allowed only 256 distinct output signals, whereas the event rates from the detector ranged as high as 10^4 per sampling interval. The system chosen produced an output word that varied approximately as the logarithm of the detector count rate.

Several "housekeeping" voltages, measuring various performance parameters of the instrument, were also sampled and telemetered. The parameters were gas absorption cell pressures, average absorption cell temperature, gas storage tank pressure, and a current measurement reflecting the condition of the high-voltage power supplies.

Mechanical Structures

Major mechanical structures of the instrument included instrument housing and covers, gas absorption cells, collimators for detector channels 2 and 4, detector housings and mountings, helium plumbing and control mechanisms, and electronics subassemblies. Figure 5-6 shows a general view of the instrument, with the cover removed.

Calibration

Careful calibration of the HGD was vital for successful interpretation of the data telemetered from orbit. A complete calibration facility was established at the University of California. It included a vacuum chamber large enough to contain the instrument, a grazing-incidence monochromator, several sources of EUV radiation, reference diodes calibrated by the National Bureau of Standards, ion and electron guns, and such supporting equipment as pumps, manipulators, collimators, laminar flow benches, and dehumidifiers.

The sensitivity of each of the 4 detector channels was measured at approximately 20 wavelengths from 25.6 to 143.5 nanometers. Extreme ultraviolet light

was provided by a gas discharge lamp using argon, helium, hydrogen, and neon to provide strong spectral emission lines (ref. 5-12).

The shape and angular response of the sensitive area of each detector was determined by shining a narrow monochromator beam into the entrance pupil while tilting and translating the HGD with a manipulator. In this way, a detailed map of the detector response was produced.

The behavior of the gas absorption cells was studied by recording the detector response with the cell full while the monochromator wavelength was slowly swept across the 58.4-nanometer spectral line. The observed response agreed well with the response calculated from theory.

Intense sources of ions and electrons were used to verify that the detectors would not respond to the high fluxes of charged particles in the Earth ionosphere. Various combinations of visible light and ultraviolet light were shined into the vents and viewports of the instrument to make certain that photoemission of electrons from internal sources would not cause false counts.

Ground-Support Equipment

The ground-support equipment for the HGD was composed of electrical checkout equipment (ECE), a helium fill apparatus, and shipping containers. A schematic diagram of the ECE is shown in figure 5-7. This apparatus simulated all the inputs to the HGD from the spacecraft and sampled the HGD output voltages in the same manner as the spacecraft telemetry system. It also sampled many additional housekeeping voltages, which were not telemetered during flight, as an aid to ground testing and calibration of the instrument. The apparatus was housed in a portable chassis that was approximately 0.7 meter long on each side. It was used for initial testing of the HGD by the manufacturer, for calibration and further testing at the University of California, and for final installation and checkout in the spacecraft at the NASA John F. Kennedy Space Center.

The helium fill apparatus was used to service the helium tank in the HGD. The fill apparatus contained a large cylinder of high-pressure, high-purity helium, plus the regulator, valves, hoses, and plumbing necessary to purge the HGD tank and fill it to its operating pressure.

Design Philosophy

A great deal of technology and experience from previous space missions was available for design of the HGD. Approximately 70 percent of the electronic circuits used in the HGD and its ground-support equipment had been previously developed, tested, and produced for other programs, including the Atmosphere Explorer Satellite and the Skylab Apollo telescope mount SO55A spectrophotoheliograph. Some mechanical components, such as the HGD helium tank and the instrument shipping containers, were Government-furnished equipment from earlier Apollo missions.

To reduce drafting and manufacturing costs and to facilitate maintenance, the HGD was designed with a high level of interchangeability of parts. For example, the electronics modules containing the channel electron multipliers were interchangeable, as were the gas filter cells and the collimators. Furthermore, the design similarities between the HGD and the instrument for the EUV survey, which had the same Principal Investigator, made possible the design of a single ECE unit to support both instruments.

FLIGHT OPERATIONS

The HGD and its protective door were controlled by switches and circuit breakers in the Apollo command module. When data were to be taken, the astronauts opened the door, waited a few moments to allow the pressure in the instrument area to drop from approximately 0.1 to 1.0 N/m^2 (door closed) to 0.001 N/m^2 or less (door open), and turned on the helium glow experiment power. The short wait before activation was necessary to avoid possible corona discharge from the high-voltage electronics at pressures greater than 0.1 N/m^2.

The astronauts also controlled a switch that could interrupt the flow of helium to either gas absorption cell. This switch would have been used if declining tank pressure or corona discharge had indicated a leak in either gas cell. Corona discharge would have been detected as a very high spurious count rate in one or more detectors.

The HGD was pointed at selected areas of the sky by maneuvering the spacecraft. These maneuvers were carefully and elaborately planned before the flight and consisted mostly of slow rolls about the spacecraft long axis, with that axis pointing in a specified, fixed direction. In the course of many such rolls, the HGD surveyed most of the celestial sphere, with particular attention given to the region in which the pronounced helium density increase mentioned previously was predicted to occur. At the time of flight, that region was approximately 30° from the side of the Sun opposite the Earth, as shown in figure 5-8; therefore, because of perspective, the region was less than 30° from the Sun in the spacecraft sky. Particular attention was also given to the patch of sky, approximately 30° in diameter, that can be viewed while looking down the shadow cast by the Earth in the geocorona, as shown in figure 5-1. These latter observations provided especially significant data from the 30.4-nanometer detectors.

Data useful for in-flight checks of instrument calibration and sensitivity to unwanted wavelengths of light were taken while the instrument viewed the Earth and the horizon. Finally, at the last turnoff of the HGD, the instrument was intentionally operated with the door closed, in a successful attempt to doublecheck the background count rate with no light at all reaching the detectors.

DISCUSSION

The instrument operated satisfactorily. One 30.4-nanometer detector failed during the flight, but adequate data in that channel were returned throughout the mission by the other 30.4-nanometer detector. One 58.4-nanometer detector exhibited a somewhat high background rate. Data taken during in-flight calibration checks seem to indicate that these extra counts could be satisfactorily explained by degradation of the metal filters and consequent increased sensitivity to Lyman-alpha radiation at a wavelength of 121.6 nanometers. Possibly, much of the data from this channel will be usable; in any case, the other 58.4-nanometer detector worked well and returned satisfactory data.

Detailed reduction of the scientific data requires taped records of spacecraft position and attitude while the data were being taken. Computer programs for the prediction of observed count rates as a function of ISM parameters, using equations (5-1) to (5-8) and associated limits, have been developed. Comparison of such predictions with the distribution of helium glow actually observed during the flight will clarify the ISM parameters involved in the predictions.

One interesting possibility for extracting additional information from the data deserves mention. The 58.4-nanometer count rate seen with the gas cell empty is the sum of the contributions from the ISM and the geocorona. The rate seen with the cell full includes no geocoronal term. Thus, the ratio of the rates seen with the cell full and with the cell empty is a lower bound for the value of that same ratio that would have been seen with no geocoronal flux present. The no-geocorona cell-full count rate can be predicted by a modification of equation (5-3), and the no-geocorona predicted ratio can be calculated. This ratio turns out to be a moderately sensitive indicator of the dispersion in radial speeds of helium along the line of sight, whether caused by thermal motions, collisions, or turbulence. A lower bound on the ratio may thereby possibly provide additional insight into the dynamical state of the local interstellar medium.

SUMMARY

The goals of the helium glow experiment were to observe the patterns of concentration of interstellar helium as it flows through the solar system, and to deduce therefrom several uncertain properties of the local interstellar medium. A four-channel extreme ultraviolet photometer, sensitive at spectral lines of neutral and ionized helium, mapped the sky from orbit during the Apollo-Soyuz Test Project flight. The instrument used helium gas absorption cells to eliminate from the observations any contribution due to photons scattered from neutral helium in the Earth geocorona. The experiment operated satisfactorily, and adequate usable data were produced.

REFERENCES

5-1. Axford, W. I.: The Interaction of the Solar Wind With the Interstellar Medium. Solar Wind. NASA SP-308, 1972, pp. 609-660.

5-2. Blum, P. W.; and Fahr, H. J.: Interaction Between Interstellar Hydrogen and the Solar Wind. Astron. & Astrophys., vol. 4, no. 2, 1970, pp. 280-290.

5-3. Holzer, T. E.; and Axford, W. I.: Interaction Between Interstellar Helium and the Solar Wind. J. Geophys. Res., vol. 76, no. 28, Oct. 1971, pp. 6965-6970.

5-4. Wallis, Max K.: Local Hydrogen Gas and the Background Lyman-Alpha Pattern. Monthly Notices Roy. Astron. Soc., vol. 167, Apr. 1974, pp. 103-119.

5-5. Johnson, H. E.: Backscatter of Solar Resonance Radiation — I. Planet. & Space Sci., vol. 20, no. 6, June 1972, pp. 829-840.

5-6. Blum, P. W.; Pfleiderer, J.; and Wulf-Mathies, C.: Neutral Gases of Interstellar Origin in Interplanetary Space. Planet. & Space Sci., vol. 23, no. 1, Jan. 1975, pp. 93-105.

5-7. Danby, J. M. A.; and Camm, G. L.: Statistical Dynamics and Accretion. Monthly Notices Roy. Astron. Soc., vol. 117, 1957, pp. 50-71.

5-8. Wallis, Max K.: Collisional Heating of Interplanetary Gas: Fokker-Planck Treatment. Planet. & Space Sci., vol. 23, no. 3, Mar. 1975, pp. 419-430.

5-9. Fahr, H. J.: The Extraterrestrial UV-Background and the Nearby Interstellar Medium. Space Sci. Rev., vol. 15, Feb. 1974, pp. 483-540.

5-10. Paresce, F.; and Bowyer, S.: Resonance Scattering From Interstellar and Interplanetary Helium. Astron. and Astrophys., vol. 27, 1973, pp. 399-406.

5-11. Jacchia, L. G.: Revised Static Models of the Thermosphere and Exosphere With Empirical Temperature Profiles. SAO-SR-332, Smithsonian Institution Astrophysical Observatory, Cambridge, Mass., 1971.

5-12. Paresce, F.; Kumar, S.; and Bowyer, C. S.: Continuous Discharge Line Source for the Extreme Ultraviolet. Appl. Opt., vol. 10, no. 8, 1971, pp. 1904-1908.

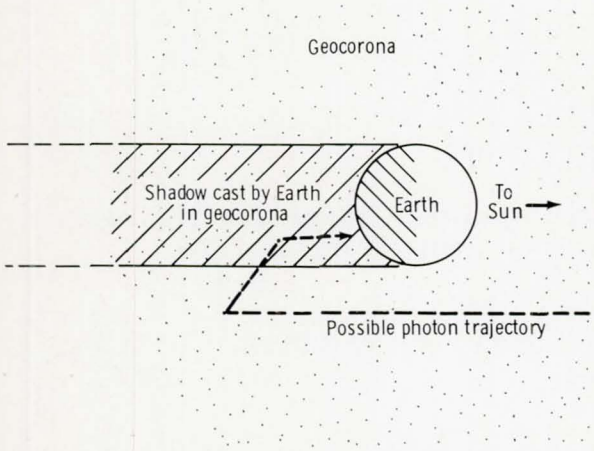

Figure 5-1.- The Earth geocorona, showing the shadow of the Earth and a multiply scattered photon that could reach an observer from the shadow.

Figure 5-3.- The interior of the Apollo scientific instruments bay 1. The HGD is mounted below the shelf at the lower left.

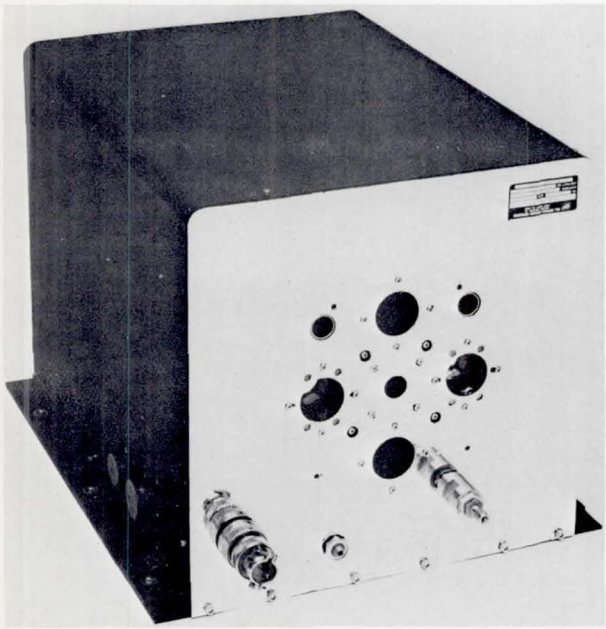

Figure 5-2.- The helium glow detector. The four large holes are the viewports for the four photometer channels.

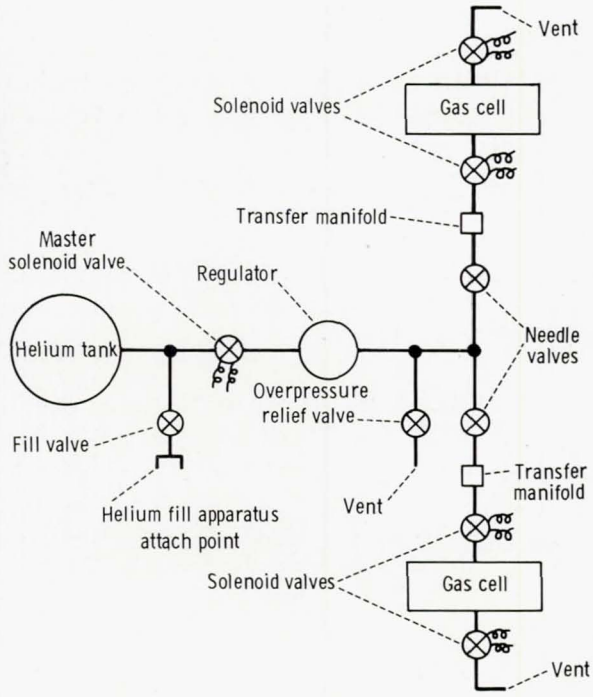

Figure 5-4.- Schematic diagram of the HGD gas subsystem.

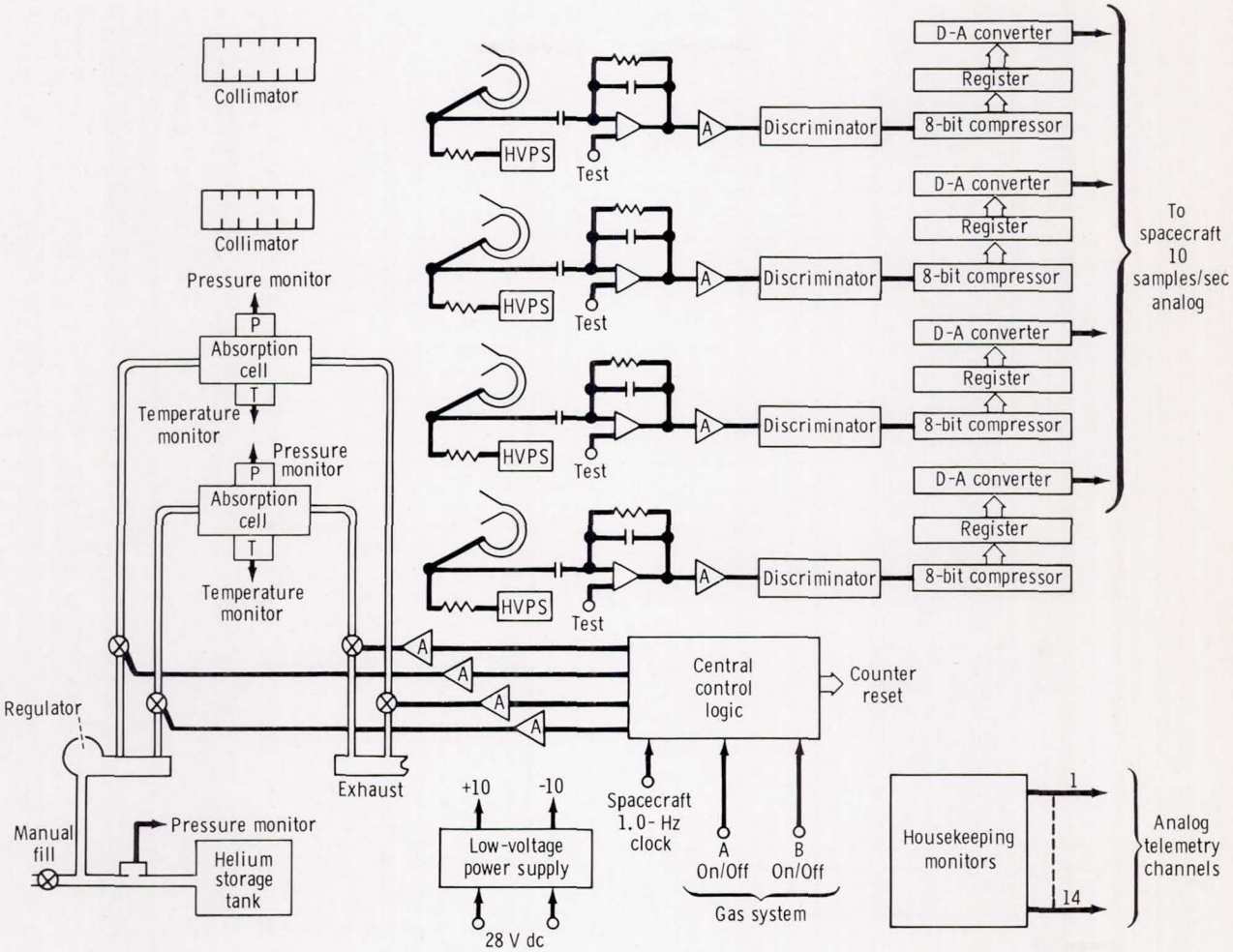

Figure 5-5.- Schematic diagram of the HGD electronics subsystem.

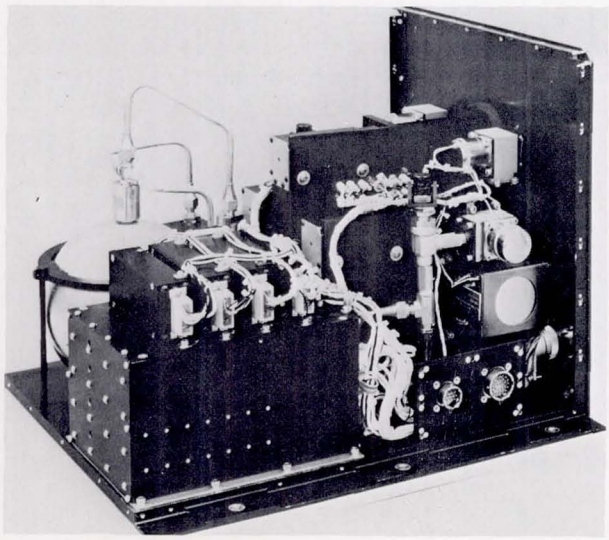

Figure 5-6.- The HGD with cover removed. Left rear, helium tank; left front, electronics modules; right rear, detector housings (only three visible).

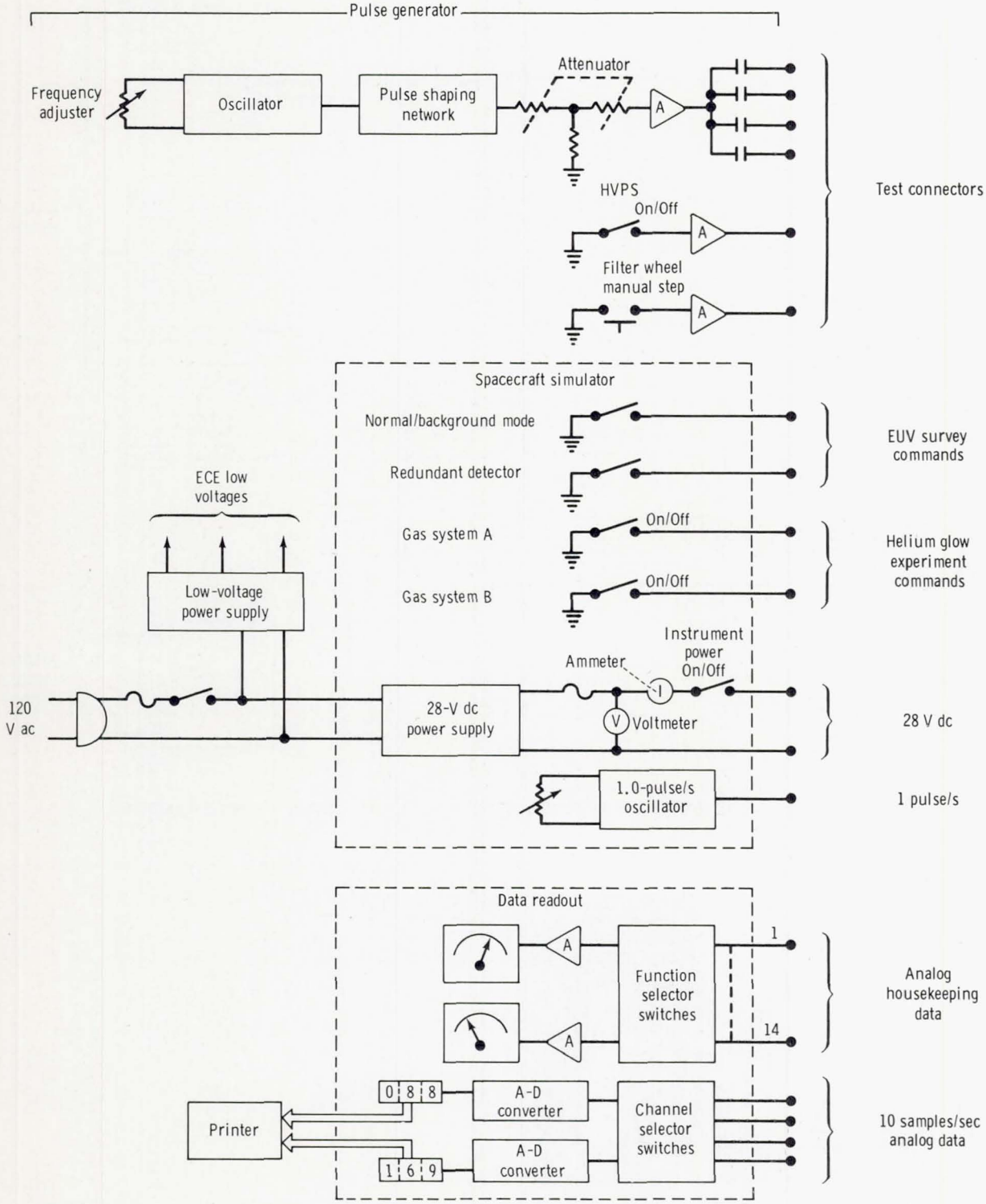

Figure 5-7.- Schematic diagram of the ground-support electrical checkout equipment.

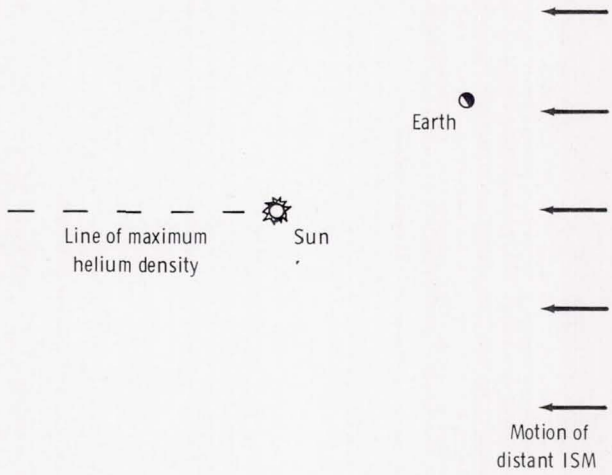

Figure 5-8.- The Sun, the Earth, and the local ISM velocity vector at the time of flight. The helium density concentration occurs along the dashed line downstream of the Sun.

6. ARTIFICIAL SOLAR ECLIPSE

EXPERIMENT MA-148

R. T. Giuli,[a] M. D. Jenness,[a] A. N. Lunde,[a] and K. A. Young[a]

ABSTRACT

On July 19, 1975, the Apollo spacecraft successfully occulted the solar disk from the field of view of a camera mounted in the Soyuz spacecraft while performing a spacecraft separation maneuver to permit the outer solar corona to be viewable by the Soyuz camera. The camera operated automatically, and 55 frames were developed for scientific analysis.

INTRODUCTION

The Artificial Solar Eclipse Experiment is one of the five experiments that incorporated joint activities between the U.S. and U.S.S.R. crews during the Apollo-Soyuz Test Project (ASTP) mission. In this U.S.S.R.-proposed experiment, the Apollo crew was responsible for performing the required spacecraft maneuvers and for photographing the eclipse shadow on the Soyuz vehicle, and the Soyuz crew was responsible for photographing the corona. As agreed, the U.S.S.R. investigators are responsible for the scientific analysis of the experiment and publication of the scientific results within 1 year after the ASTP mission. This preliminary report contains a description of the experiment background, equipment, and operations.

BACKGROUND

The solar corona is the extended atmosphere of the Sun. Whereas the Earth atmosphere extends above the Earth surface to a distance of less than 1 Earth radius, the solar corona extends to many solar radii. The inner corona is about 1 million times fainter than the bright surface of the Sun, and the outer coronal regions are hundreds to millions of times more faint. Thus, to observe the structure of the extended corona, the intense radiation coming directly from the surface of the Sun must be excluded from view, and the corona must be observed against as dark a background as possible. Both of these conditions occur during a natural, total solar eclipse, in which the Moon occults the Sun and significantly reduces the intensity of the local daylight. An artificial eclipse of the Sun above the Earth atmosphere may reduce the daylight much further and permit the most extensive possible detection of the

---

[a]NASA Lyndon B. Johnson Space Center.

corona. The ASTP Artificial Solar Eclipse Experiment provided this opportunity on July 19, 1975, at approximately noon GMT. The objective of this experiment was to detect the extended region of the corona by photographing it from the Soyuz spacecraft against the black space background while the disk of the Sun was occulted by the Apollo spacecraft.

EQUIPMENT AND OPERATIONS

The artificial solar eclipse was effected by separating the Apollo from the Soyuz shortly after orbital sunrise in such a way that Apollo occulted the Sun from view of the orbital module (OM) hatch window. Apollo backed away from Soyuz toward the Sun to a separation distance at which the apparent diameter of Apollo was about 2 solar diameters. Apollo totally occulted the Sun during the separation maneuver, and Soyuz performed automatic sequence photography in the solar direction during the entire separation maneuver.

Before orbital sunrise, the Soyuz crew set up a camera on the inside of the closed OM hatch window. The 50-millimeter camera had a 90-millimeter focal length lens with no filter. The photographs were taken in "white" light over the wavelength range of approximately 400 to 750 nanometers. A mechanized magazine containing highly sensitized Kodak 2485 film was mounted to the back of the camera. On the outside of the hatch window, the Apollo crew deployed a U.S.S.R. light baffle designed to minimize the amount of scattered and reflected light that entered the optical path of the camera. The Soyuz crew retreated to the descent module, and the Apollo crew retreated to the command module (CM). The Apollo crewmen oriented the docked spacecraft with the longitudinal (X) axes alined to the Sun-spacecraft direction, as depicted in figure 6-1. At 75 seconds after orbital sunrise, the Apollo undocked and coasted for 15 seconds. The undocking occurred at 95:43:20 ground elapsed time (GET), or 12:03:20 GMT, July 19. At position 2 (fig. 6-1), the reaction control system (RCS) of the Apollo spacecraft was fired in the four-jet mode for 3 seconds to back away (minus-X direction) from the Soyuz spacecraft. A second coast period of 12 seconds was followed by another four-jet, RCS, minus-X firing (position 3, fig. 6-1). The two-thrust sequence was adopted to expedite achieving the desired separation rate of approximately 1 m/sec, while respecting thermal constraints associated with RCS gases impinging on the Soyuz spacecraft. At 4 minutes after undocking, the separation of the two spacecraft was approximately 220 meters, at which time the Apollo fired the RCS (four-jet) in the plus-X direction for 16 seconds (fig. 6-1, position 5) to return to Soyuz. During the entire separation time, the spacecraft maintained attitude hold with both X-axes alined in the solar direction. The sequence of events is listed in table 6-I, and the views from the Soyuz hatch window at the beginning and end of the 1-m/sec separation phase are given in figures 6-2(a) and 6-2(b), respectively. The field of view from Soyuz (fig. 6-2) was determined by the light baffle; the vignetting in the Earth direction was intended to minimize the light that entered the optical path of the Soyuz camera from the illuminated crescent of the Earth beyond the terminator. The Soyuz camera operated during the entire separation phase in an automatic sequence of exposures of 0.1, 0.3, 1, 3, and 10 seconds. Each cycle lasted 27 seconds, and the cycles were repeated continuously.

Also during separation, the 16-millimeter Apollo data acquisition camera (DAC) was mounted in a CM window to view along the Apollo plus-X axis. The 75-millimeter focal length lens of the DAC automatically operated at 12 frames/sec, exposing SO-242 color film at 1/125 second. The purpose of the DAC photography was to monitor the motion of the umbra on the Soyuz spacecraft. The DAC photographs reveal that the edge of the umbra did not reach the Soyuz docking ring until 120 to 150 seconds after undocking. The light baffle was not apparent in the photographs, but the Apollo crew reported seeing the edge of the umbra reaching the light baffle at approximately 170 seconds after undocking.

In mid-November, the U.S.S.R. submitted a mission report to the U.S. Technical Director that contained the following statement:

> Photography of the solar corona and "atmosphere" around the Apollo spacecraft began at 95: 43: 41 GET (21 seconds after undocking). The process of photography lasted 12 minutes 47 seconds. Preliminary analysis of the pictures and telemetry data showed that all the equipment involved in the experiment functioned nominally.
>
> 125 frames were taken in the process of the artificial solar eclipse experiment; 23 of them were exposed during the time from undocking to the crossing by the spacecraft of the dawn terminator plane. This portion of the orbit was chosen in accordance with procedure as the primary one.
>
> The frames taken during the time from terminator crossing to 280 seconds [referred to undocking] are practically exposed by the illuminated Earth reflected from the Apollo CM cone. The frames taken from 280 seconds through 440 seconds (24 frames) contain scientific information.
>
> Approximately 442 seconds after undocking, the Soyuz spacecraft drifted from the shadow made by the Apollo. Therefore, the conditions of artificial solar eclipse were disturbed from that moment.
>
> Before redocking (starting from 630 seconds), the conditions of artificial solar eclipse were restored. The last eight frames gave additional scientific information. Thus, 55 frames suitable to be developed were taken during the experiment.
>
> A great deal of scientific data on the solar corona (within the limits of 25 through 50 solar radii) and atmosphere around the spacecraft was obtained. Absolute photometric calibration of the obtained data was made with the reference to α CMi and γ Gem stars and Mercury; many frames contain the images of these bodies.
>
> Of great importance was an experimental confirmation of the effectiveness of a new method for research of the solar corona and "atmosphere" around spaceships. Detailed analysis of experimental data coupled with the Apollo RCS duty cycle and record of the Soyuz darkening conditions will be made later.

TABLE 6-I.- SEQUENCE OF EVENTS FROM FIRST UNDOCKING TO SECOND DOCKING

GET	Event description
95:42:05	Orbit sunrise
95:43:20	Delta-V of 0.10 m/sec along Soyuz minus-X axis and 0.05 m/sec along Apollo minus-X axis because of spring-release mechanism
95:43:35	Apollo performs first 4-jet, minus-X, 0.38-m/sec separation maneuver (initiated after a 15-sec coast period) along line of sight to Sun direction and maintains inertial attitude hold
95:43:38	RCS engines cut off
95:43:50	Apollo performs second 4-jet, minus-X, 0.50-m/sec maneuver after a 12-sec coast period; range, 9.6 m
95:43:54	RCS engines cut off; range, 12.8 m; range rate, 1.03 m/sec
95:47:20	Apollo achieves 220-m separation distance from Soyuz and performs a 2-m/sec, 4-jet, plus-X RCS maneuver to null the separation rate and return the Apollo vehicle to the redocking position
95:47:36	RCS engines cut off
95:50:58	Apollo achieves a relative range <17 m and performs a 1-m/sec, 4-jet, minus-X RCS maneuver to null the closing range-rate component

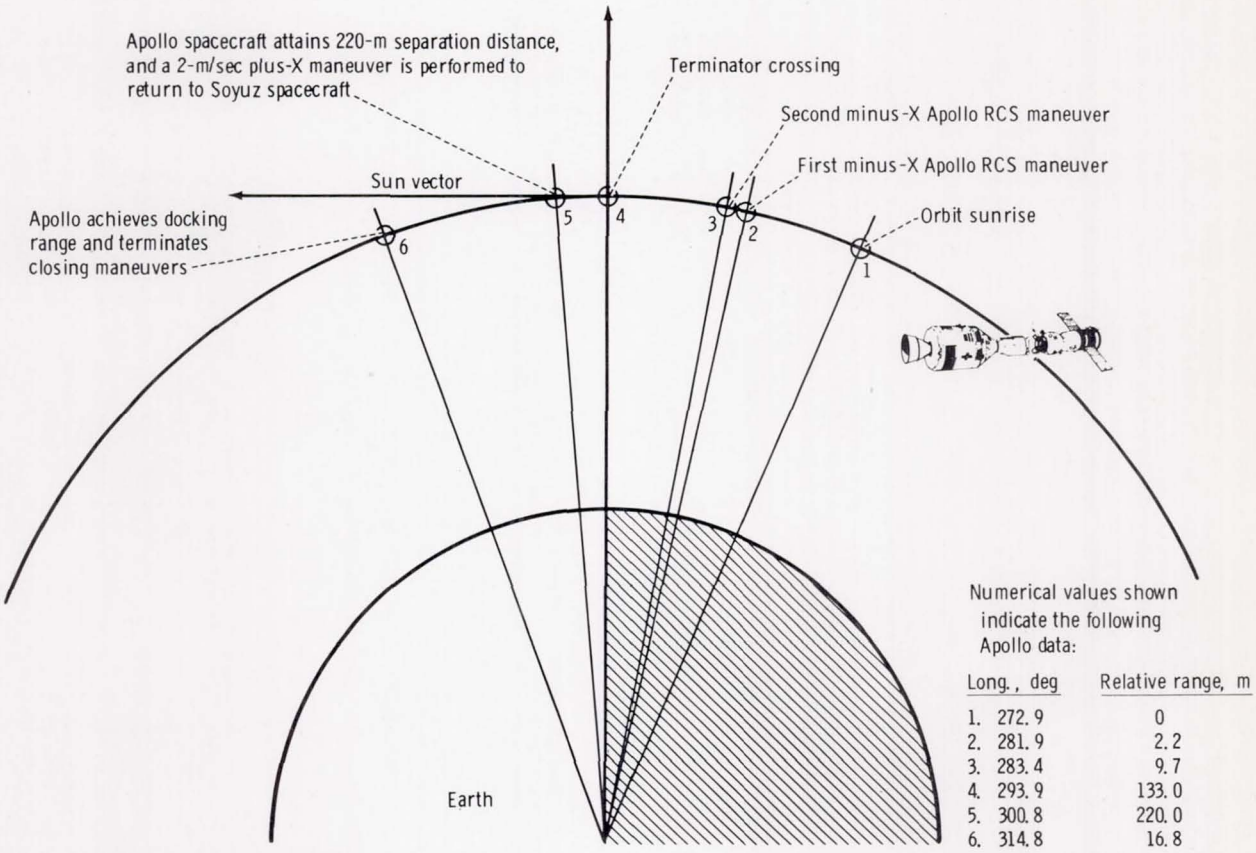

Figure 6-1.- Artificial solar eclipse orbit profile during the 57th revolution of the Apollo spacecraft and the 65th orbit of the Soyuz spacecraft.

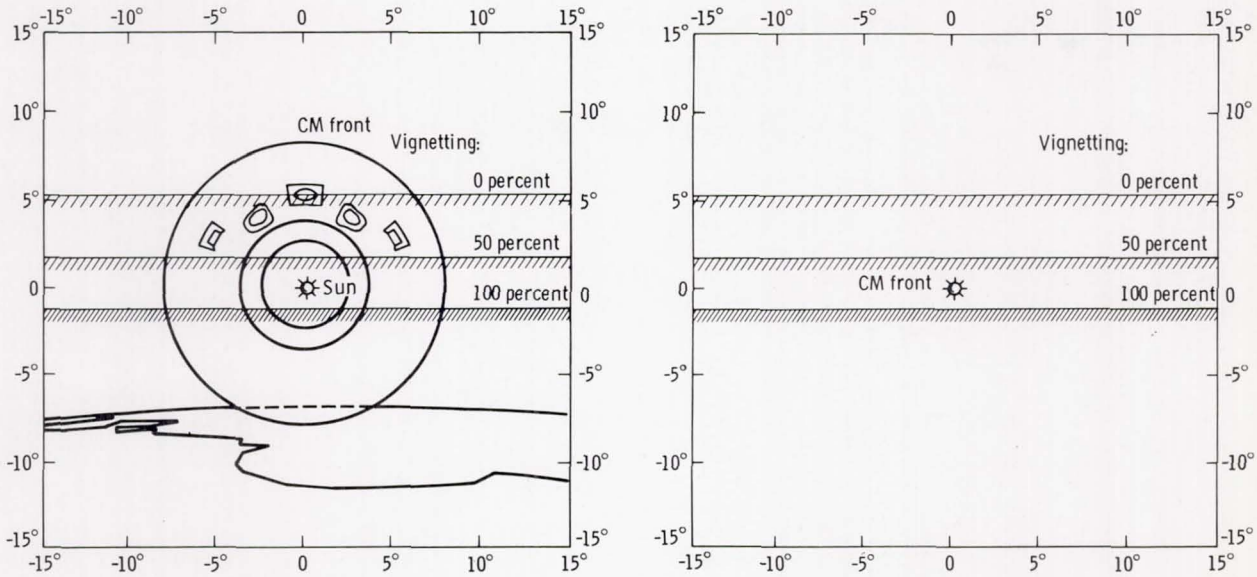

(a) 12.8 m from Soyuz.

(b) 220 m from Soyuz.

Figure 6-2.- View of the Apollo spacecraft after the second RCS burn as seen from the Soyuz spacecraft. The field of view is 30° with the Sun in the center of the view.

7. CRYSTAL ACTIVATION

EXPERIMENT MA-151

J. I. Trombka,[a†] E. L. Eller,[a] R. L. Schmadebeck,[a] C. S. Dyer,[b]
R. C. Reedy,[c] D. W. Barr,[c] J. S. Gilmore,[c] R. J. Prestwood,[c]
B. P. Bayhurst,[c] D. G. Perry,[c] A. R. Smith,[d] R. C. Cordi,[d]
R. H. Pehl,[d] J. S. Eldridge,[e] E. Schonfeld,[f] and A. E. Metzger[g]

ABSTRACT

The Crystal Activation Experiment consisted of two sample packages that were flown in the command module and returned to Earth for analysis of the radioactivity induced in them during the flight. The objective of the experiment was to define the background caused by detector activation that interferes when gamma radiation is measured in the 0.02- to 10-megaelectronvolt range from Earth orbit. These measurements, together with accelerator beam activation measurements and theoretical calculations, will be used to estimate this background for future or planned experiments. To aid the calculations, metals selected for their cross sections for specific neutron and proton energies were included in the samples in addition to the germanium and thallium-activated sodium iodide (NaI(Tl)), which are the usual detectors for low-energy gamma-ray measurements.

Preliminary results show that the activation of the NaI(Tl) crystal was a factor of 3 below that from a similar measurement on Apollo 17. The identification of certain species and the level of activation observed show an important contribution from the interactions of thermal and energetic neutrons produced as secondaries in the spacecraft. That the activation was reduced by only a factor of 3 compared with the Apollo 17 experiment, despite the geomagnetically shielded orbit, possibly indicates more efficient secondary neutron production by the more energetic cosmic rays.

---

[a]NASA Robert H. Goddard Space Flight Center.

[b]University of Maryland.

[c]Los Alamos Scientific Laboratory.

[d]Lawrence Berkeley Laboratory.

[e]Oak Ridge National Laboratory.

[f]NASA Lyndon B. Johnson Space Center.

[g]NASA Jet Propulsion Laboratory.

[†]Principal Investigator.

INTRODUCTION

Significant background components to X-ray and gamma-ray measurements performed in space can be attributed to X-ray and gamma-ray emission induced in the spacecraft surrounding the detector and within the detector itself. Varying detector-spacecraft geometries (such as those obtainable with an extendable boom) can provide an indication of the spacecraft contribution, but in-flight measurements cannot separate the cosmic-ray-induced detector background from counts caused by the external photon flux.

Previous measurements were made on an NaI(Tl) crystal flown on Apollo 17. For that flight, the activation was mainly induced by cosmic-ray protons and by secondary neutrons produced in the spacecraft material. Because of the low-altitude Earth orbit on the Apollo-Soyuz Test Project (ASTP) mission, the Apollo-Soyuz spacecraft was exposed to a proton flux that was less intense. However, the protons had a higher average energy and therefore could have been more efficient in producing secondary neutrons. Neither the particle flux inside the spacecraft nor the cross sections for production of radioactive isotopes in the detector materials are well known. Therefore, in addition to NaI(Tl) and germanium detector crystals, the sample package included a number of metals that have good cross sections for specific energy ranges of neutrons and protons.

SCIENTIFIC BACKGROUND

One of the major difficulties in measuring 0.02- to 10-megaelectronvolt gamma radiation from space lies in distinguishing the radiation emitted by cosmic and planetary sources from the high rate of background gamma radiation produced by cosmic-ray and trapped-proton interaction with the spacecraft and the detector materials. Of these effects, the most difficult to isolate is the delayed decay of a radioactive nucleus produced by a spallation interaction within the detector material. These effects particularly complicate measurements of the diffuse sky-background gamma radiation in a spectral band that could contain important information on cosmology and the role of antimatter in the universe. The experimental confusion and theoretical possibilities have been recently reviewed by Horstman, Cavallo, and Moretti-Horstman (ref. 7-1). It is evident that advances in the field require improved knowledge of local activation effects and optimization of detector design and location against such a background.

Radioactive background has been observed in all cosmic gamma-ray experiments that have been carried into regions of trapped radiation such as in the Orbiting Space Observatory (OSO) series of spacecraft. Such effects have been successfully explained (ref. 7-2) by a model proposed by Dyer and Morfill (ref. 7-3) in which the direct proton interactions in scintillators lead to radioactive spalled nuclei, the decay products of which are indistinguishable from an external gamma ray. The work by Dyer and Morfill and that by Fishman (ref. 7-4) demonstrated that similar interactions due to cosmic rays could also cause contamination, and this has been verified by the gamma-ray NaI(Tl) spectrometers carried onboard Apollo 15 and Apollo 16 (ref. 7-5). As a result, an identical crystal was flown and returned on Apollo 17. Application of the spallation-activation calculation to those results

showed that the level of activation was considerably enhanced by significant fluxes of secondary neutrons produced in the heavy spacecraft by cosmic-ray proton interactions (ref. 7-6). Results from activation packages flown on Skylab (ref. 7-7) also showed the presence of secondary neutrons but indicated less thermalization of this flux than that indicated by the Apollo 17 data.

For these reasons, it was considered important to include an activation package onboard the Apollo-Soyuz spacecraft to obtain further data from near-Earth orbit. In that orbit, part of the primary cosmic-ray flux was shielded by the Earth's magnetic field. The very low Apollo-Soyuz altitude minimized trapped-proton effects, although further calculations are required before their contribution can be considered negligible.

EQUIPMENT AND EXPERIMENTAL PROCEDURE

The two assemblies shown in figures 7-1 and 7-2 were flown in the command module of the Apollo spacecraft during the Apollo-Soyuz mission. An NaI(Tl) crystal (fig. 7-1) physically identical to those flown on the Apollo 15 and 16 missions was used in this experiment. This assembly did not include the photomultiplier, the proton anticoincidence mantle, and the thermal shield that were used during the Apollo 15 and 16 missions, but it was identical to the assembly used on the Apollo 17 mission. Thus, direct comparison of the results from the two missions can be made. The detector was a 7- by 7-centimeter right-cylindrical crystal, hermetically sealed in a steel cylinder with a glass plate at one end. Magnesium oxide was used as an optical reflector inside the crystal assembly except at the glass window. This assembly made possible the simple procedure for optically coupling the crystal to a photomultiplier tube after flight. The second assembly (fig. 7-2) consisted of a 724-gram sample of high-purity germanium; a small intrinsic germanium detector 32 millimeters in diameter by 8.75 millimeters thick, with a 0.12-millimeter layer of indium on one face; and 100-gram foil disks of yttrium (Y), scandium (Sc), and depleted uranium (U) sealed in a cylinder identical to that used for containing the NaI(Tl) crystal. The lid of the container in this second assembly was made of 55 grams of titanium rather than steel.

Before the mission, background counts were taken on all materials in the laboratories where postflight low-level counting was anticipated. After splashdown, the flight (i.e., activated) NaI(Tl) was returned to the recovery ship and optically mounted on a photomultiplier tube, and pulse height spectra were obtained. The crystal counting was started approximately 2 hours after atmospheric entry of the command module. Before splashdown, a control (unactivated) crystal was optically sealed to the same photomultiplier tube, and the background was determined in the steel shield.

A 10.2- by 10.2-centimeter NaI(Tl) detector was used to measure the gamma-ray emission flux from the NaI(Tl) crystal and from the germanium after removal from its container. These measurements were also performed inside the steel shield, starting approximately 1.5 hours after atmospheric entry of the command module. Counting continued for 4 hours onboard the recovery carrier.

The detectors, bulk germanium, and foil disks were then returned to laboratories in the United States for further counting. The intrinsic germanium detector was returned to the Lawrence Berkeley Laboratory where the detector material was mounted on a cryostat, cooled, and low-level-counted. The foil disks and the steel container were delivered to the Los Alamos Scientific Laboratory for analysis. The NaI(Tl) crystals and the bulk germanium material were taken to the Oak Ridge National Laboratory, where the internal NaI(Tl) measurements were continued, and lithium-activated germanium (Ge(Li)) and low-level coincidence spectra were accumulated on both materials. High-resolution Ge(Li) spectra were also taken of the bulk germanium at the NASA Lyndon B. Johnson Space Center.

RESULTS

Recovery Ship Measurements

The internal NaI(Tl) spectrum taken onboard the recovery ship approximately 4 hours after splashdown is compared with the equivalent data from the Apollo 17 experiment in figure 7-3. The radionuclides identified from the Apollo 17 data are shown. Although the statistics are poorer, the Apollo-Soyuz data have the same general shape and are lower in intensity by a factor of approximately 3. The bulk germanium data did not show any identifiable lines but indicated a low-energy excess consistent with the presence of gallium-67 (^{67}Ga) identified in the data taken at the Lawrence Berkeley Laboratory.

Lawrence Berkeley Laboratory

The detector was successfully brought into operation on the first attempt and showed the same noise and resolution characteristics that had been observed during preflight tests. Counting commenced at the Lawrence Berkeley Laboratory approximately 24 hours after splashdown.

The earliest spectra showed some excess count rates in continuum regions up to at least 1000 kiloelectronvolts, and perhaps as high as 2000 kiloelectronvolts; however, counting statistics will severely limit the quantitative results that can be obtained from these spectral distributions. Simple hand analysis indicated decay with (probably) more than one half-life, in the few-tens-of-hours range, but definitely shorter than the 78-hour half-life of ^{67}Ga.

The prominent X-ray peak at approximately 10 kiloelectronvolts (fig. 7-4) shows a composite decay curve that has been graphically resolved into two components, appropriate to 78-hour ^{67}Ga and 12-day germanium-71 (^{71}Ge). Identification of ^{67}Ga is conclusive, based on the aforementioned evidence, the decay of a 93-kiloelectronvolt gamma ray with a single half-life of about 80 hours, the decay of a gamma ray with apparent energy of about 195 kiloelectronvolts (the sum of the 185 kiloelectronvolt gamma ray and the X-ray) having approximately the same

half-life, and the delayed-coincidence results described in a later paragraph. Identification of ^{71}Ge is also considered conclusive, although it is based on less evidence, namely observation of the appropriate energy X-ray peak, which decays with (nearly) the ^{71}Ge half-life.

Identification of the 78-hour half-life radionuclide ^{67}Ga was confirmed from early spectra using delayed-coincidence measurements. In ^{67}Ga decay, the lowest level (93 kiloelectronvolts) in the stable daughter zinc-67 (^{67}Zn) has a half-life of 9.3 microseconds; thus, the gamma ray that de-excites this level is almost always delayed in time with respect to emission of zinc fluorescent X-rays. Delayed-coincidence analysis was performed, using the X-ray events to generate a gate delayed 9 microseconds and of 27-microsecond width. A delayed-coincidence spectrum acquired during 2175 minutes of data accumulation that started 4 days after splashdown shows only the 93-kiloelectronvolt peak and a scattering of lower energy partial absorption events. No events were stored in any of the 1420 channels above the peak region. This spectrum cannot be reconciled with any decay scheme other than that of ^{67}Ga.

The most recent data indicate the appearance of at least two X-rays at energies below 10 kiloelectronvolts, which may indicate the presence of ^{65}Zn and one (or more) of the long-lived cobalt isotopes ^{56}Co, ^{57}Co, and ^{58}Co.

Los Alamos Scientific Laboratory

The metal foil disks arrived at Los Alamos Scientific Laboratory 23 hours after splashdown. Analysis of the exposed foils was conducted as follows.

1. The scandium disk was nondestructively counted for ^{46}Sc to determine the thermal neutron-capture product.

2. Neptunium-239 (^{239}Np) was chemically separated from uranium and counted to determine the epithermal neutron-capture product.

3. Molybdenum-99 (^{99}Mo) was also chemically separated to measure the fission component.

4. The yttrium disk was dissolved and analyzed for ^{87}Y, an energetic neutron- and proton-induced reaction product, and for zirconium-89 (^{89}Zr), a low-energy-proton reaction product.

5. The titanium lid was chemically processed for scandium radionuclides produced by 1- to 20-megaelectronvolt neutrons.

6. The stainless steel can was nondestructively analyzed for activities produced from iron.

Preliminary results are as follows. The thermal neutron flux was 0.26 neutron/cm^2 sec and the epithermal neutron flux was 0.004 neutron/cm^2 sec. Energetic neutron and proton fluxes were much lower than previously observed on Apollo and Skylab missions. The neutron plus proton flux on this mission as determined from the $^{238}U(n,f)^{99}Mo$ reaction was a factor of 3 to 4 less than that observed in the Skylab mission by solid-state track detectors. A limit on the fast neutron (1 megaelectronvolt) flux of 2 neutrons/cm^2 sec was established from the absence of positive results for the high-energy activation reaction. These preliminary results will be tentatively correlated with the neutron spectra from the track detectors flown onboard the Apollo-Soyuz spacecraft.

Oak Ridge National Laboratory and NASA Lyndon B. Johnson Space Center

Direct measurements of induced radionuclides were made by optically sealing a photomultiplier tube to the activated NaI(Tl) crystal. Pulse height spectra of the internal response were obtained beginning approximately 26 hours after splashdown. Such measurements are continuing to characterize the long-lived components. Indirect measurements of the induced radionuclides were made by using Ge(Li) detectors and a large anticoincidence-shielded NaI(Tl) spectrometer in the low-level facility at Oak Ridge National Laboratory (ref. 7-8).

Preliminary results from the low-level spectrometer system (4π system) yielded positive identification of iodine-124 (^{124}I), ^{126}I, and ^{24}Na in the NaI flight detector. Tentative identification of ^{22}Na was also made, but verification must await refinement of the spectral analysis. Semiquantitative disintegration-rate values are approximately one-third to one-half those found in the Apollo 17 experiment (ref. 7-6) for ^{124}I, ^{126}I, and ^{24}Na.

Gamma-gamma coincidence data on the germanium experiment from the 4π system indicated the presence of at least one short-lived positron-emitting radionuclide. Decay-curve analysis of the positron-positron coincidences yielded a half-life value of 29 hours. The early measurements also show apparent gamma-gamma coincidences of 0.5 with 0.8-megaelectronvolt photon and of 0.8 with 1.4-megaelectronvolts photon. The radionuclide most closely fitting these characteristics is arsenic-72 (^{72}As), a 26.0-hour positron emitter with a 0.834-megaelectronvolt gamma ray in coincidence with its major positron branch. The positron-positron counting rate corrected to splashdown is approximately 2.7 counts/min with a corresponding system background of 0.1 count/min. At 41 days after splashdown, the positron-positron counting rate was only 50 percent above background. Detailed analysis of Ge(Li) spectra shows a tentative identification of ^{67}Ga, a 78-hour radionuclide that decays by electron capture.

DISCUSSION OF APOLLO-SOYUZ RESULTS

Both internal and external monitoring of the NaI crystal show an activation spectrum similar to that shown by the Apollo 17 crystal but at approximately one-third the intensity. Gallium-67 has been positively identified in the intrinsic germanium as well as in the external counting of the bulk germanium. Germanium-71 has been tentatively identified internally and ^{72}As, externally.

The quantities of all positively identified radionuclides are considerably in excess of prediction based on preliminary estimates of the cosmic-ray fluence. Compilations of trapped-proton fluences for orbits similar to that of Apollo-Soyuz (222-kilometer altitude, 51.8° inclination) indicate that this contribution to the activation should be very small. However, exact orbital integrations are required to assess this component, particularly in view of the possible ^{72}As identification, indicative of low-energy (p,xn) interactions.

At present, the most probable explanation of these results is a considerable flux of secondary neutrons produced in the heavy spacecraft, as was the case on Apollo 17 (ref. 7-6). A considerable flux of thermal neutrons is again shown by the ^{24}Na result and the scandium activation. The relatively low epithermal neutron flux determined from the uranium foil disk is consistent with the low ^{128}I: ^{24}Na ratio found in the Apollo 17 crystal. To produce the other species presented here, an energetic (20 to 100 megaelectronvolt) neutron flux of about 2 cm^{-2} sec^{-1} is required.

The reduction of activation between Apollo 17 and Apollo-Soyuz is less than preliminary estimates of the reduction of primary cosmic-ray intensity due to geomagnetic shielding, possibly indicating the increased efficiency of the more energetic cosmic rays in producing secondary neutrons. However, further work is required to define the exact cosmic-ray and trapped-proton fluences before this conclusion can be made with great certainty.

The production of secondary neutrons in heavy spacecraft and their efficient thermalization in Apollo modules again emphasize the necessity for developing codes to assess neutron production and transport, and demonstrate that gamma-ray spectrometers are best used far removed from heavy material.

The calculations used here will be improved by comparison with controlled monoenergetic irradiation experiments, which will also yield important information on the short half-life radionuclides missed by such return procedures.

REFERENCES

7-1. Horstman, H. M.; Cavallo, G.; and Moretti-Horstman, E.: La Rivista del Nuovo Cimento, vol. 5, 1975, p. 255.

7-2. Dyer, C. S.; Dunphy, P. P.; Forrest, D. J.; and Chupp, E. L.: Proceedings of the 14th International Cosmic Ray Conference, 1975, p. 3122.

7-3. Dyer, C. S.; and Morfill, G. E.: Contribution to the Background Rate of a Satellite X-Ray Detector by Spallation Products in a Cesium Iodide Crystal. Astrophys. & Space Sci., vol. 14, no. 1, 1971, pp. 243-258.

7-4. Fishman, G. J.: Cosmic-Ray Effects on Diffuse Gamma-Ray Measurements. Astrophys. J., vol. 171, 1972, pp. 163-167.

7-5. Trombka, J. I.; Metzger, A. E.; Arnold, J. R.; Matteson, J. L.; et al.: The Cosmic Gamma-Ray Spectrum Between 0.3 and 27 MeV Measured on Apollo 15. Astrophys. J., vol. 181, 1973, pp. 737-746.

7-6. Dyer, C.; Trombka, J. I.; Schmadebeck, R. L.; Eller, E.; et al.: Radioactivity Observed in the Sodium Iodide Gamma-Ray Spectrometer Returned on the Apollo 17 Mission. Space Sci. Instrum. 1, vol. 3, 1975.

7-7. Fishman, G. J.: Neutron and Proton Activation Measurements from Skylab. AIAA/AGU Paper 74-1227, Nov. 1974.

7-8. Eldridge, J. S.; O'Kelley, G. D.; Northcutt, K. J.; and Schonfeld, E.: Nondestructive Determination of Radionuclides in Lunar Samples Using a Large Low-Background Gamma-Ray Spectrometer and a Novel Application of Least-Squares Fitting. Nucl. Instr. & Meth., vol. 112, 1973, pp. 319-322.

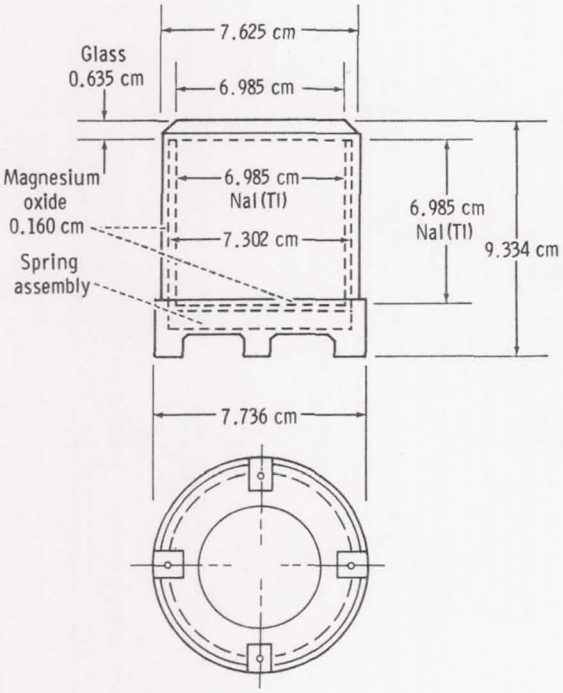

Figure 7-1.- The Apollo NaI(Tl) crystal assembly.

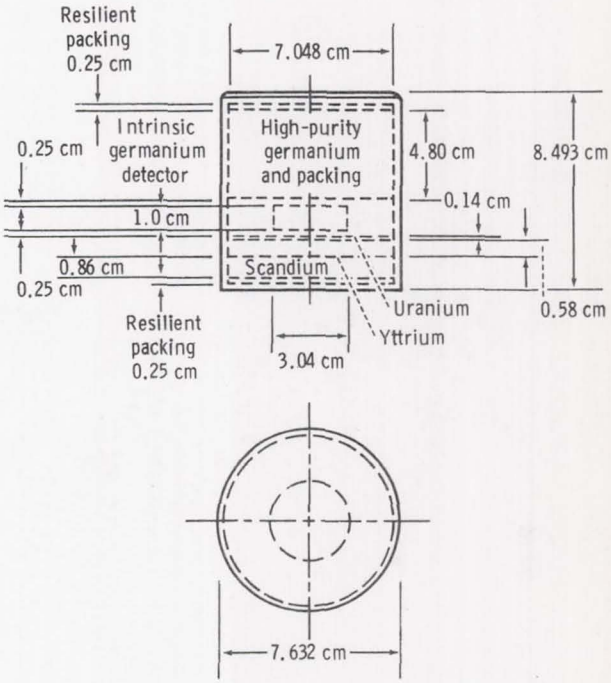

Figure 7-2.- Sample package showing location of metals and intrinsic germanium detector.

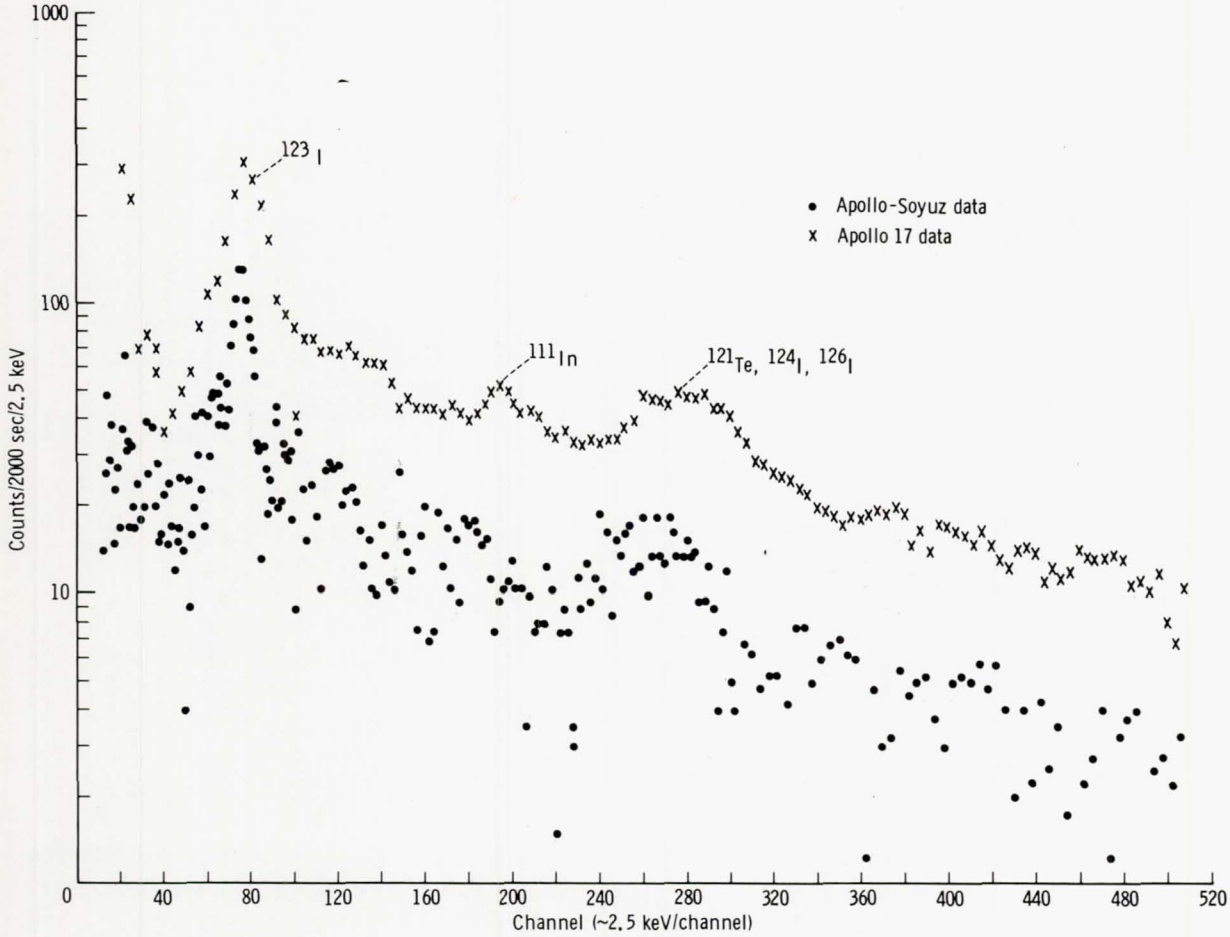

Figure 7-3.- Comparison of Apollo 17 and Apollo-Soyuz internal NaI(Tl) spectra taken 4 hours after splashdown.

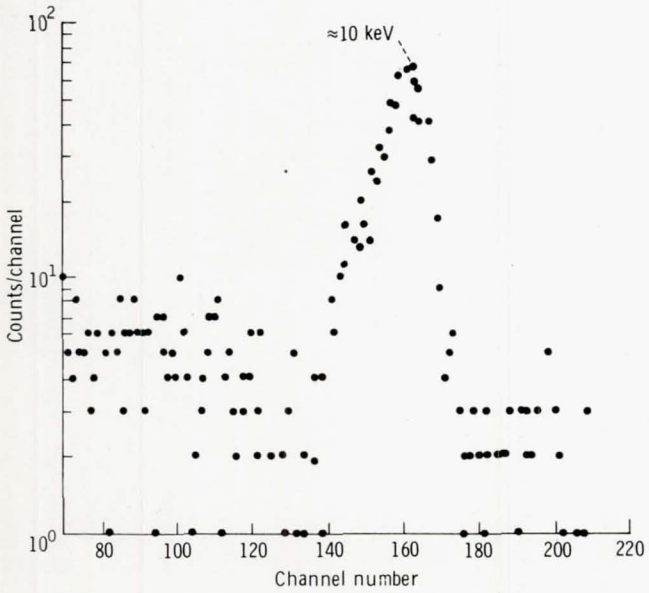

Figure 7-4.- Internal germanium spectrum showing doublet structure of 10-kiloelectronvolt peak contributed by ^{67}Ga and ^{71}Ge (440-minute count time at 0.066 keV/channel).

8. ULTRAVIOLET ABSORPTION

EXPERIMENT MA-059

T. M. Donahue,[a†] R. D. Hudson,[b†] J. Anderson,[a]
F. Kaufman,[c] and M. B. McElroy[d]

ABSTRACT

The Ultraviolet Absorption Experiment performed during the Apollo-Soyuz mission involved sending a beam of atomic oxygen and atomic nitrogen resonance radiation (130.4 and 120.0 nanometers), strong unabsorbable oxygen and nitrogen radiation (135.6 and 149.3 nanometers), and visual radiation, all filling the same 3°-wide field of view from the Apollo to the Soyuz. The radiation struck a retroreflector array on the Soyuz and was returned to a spectrometer onboard the Apollo. Lock on the retroreflector was maintained by the visual light and a star tracker. The density of atomic oxygen and atomic nitrogen between the two spacecraft was measured by observing the amount of resonance radiation absorbed when the line joining Apollo and Soyuz was perpendicular to their velocity with respect to the ambient atmosphere. By allowing the Apollo spacecraft to drift at fixed ranges of 150, 500, and 1000 meters through an arc of ±15° with respect to the perpendicular to the velocity vector, the temperature of the gas was obtained; i.e., the Doppler line profile was scanned. Information concerning oxygen densities was also obtained by observation of resonantly fluorescent light. The absorption experiments for atomic oxygen and atomic nitrogen were successfully performed at a range of 500 meters, and abundant resonance fluorescence data were obtained.

INTRODUCTION

The Apollo-Soyuz Test Project (ASTP) Ultraviolet Absorption (UVA) Experiment provided an opportunity for the realization of a technique devised to permit the measurement of atmospheric species concentrations. This experiment involved the application of the most reliable and specific laboratory technique available for

---

[a]University of Michigan.

[b]NASA Lyndon B. Johnson Space Center.

[c]University of Pittsburgh.

[d]Harvard University.

[†]Co-Principal Investigator.

measuring the concentration of a given gaseous species — atomic absorption spectroscopy. This method is probably the most reliable available tool for quantitative analysis if the cross sections or oscillator strengths for absorption are known, if proper precautions are taken to ascertain the frequency dependence (or line shapes) of light sources and absorbers, if optical properties of the measuring devices are measured, and if corrections are made for absorption by other species (or impurities). A complementary technique, the quantitative observation of resonance fluorescence in which atomic or molecular species scatter resonance radiation from a light source into a detector, is a powerful one and was used in the ASTP UVA experiment. The species chosen for detection and measurement were neutral atomic oxygen (O) and neutral atomic nitrogen (N). The first was selected for several reasons.

1. Strong resonance light sources are available that produce radiation in the resonance triplet at 130.2, 130.5, and 130.6 nanometers, hereafter referred to as 130.4-nanometer radiation.

2. The absorption cross section or oscillator strength of O for the energy-state transition producing or absorbing this radiation ($^3P_{2,1,0}$ $^3S_1$) is accurately known.

3. Although O is the most abundant atmospheric species at the experiment altitude (225 kilometers), to detect the species cleanly in a mass spectrometer is difficult because of its propensity to recombine into molecular oxygen (O_2) upon colliding with the walls of a spectrometer ion source. At lower altitudes, this recombination has caused difficulties that leave the actual density of O near 120 kilometers uncertain by a factor of 5 or more. At an altitude of 225 kilometers, the uncertainty is probably not very great, but it is interesting to attempt to verify other measurement methods by a new one or to prove the new method by comparison with ground truth.

Atomic nitrogen was interesting because, as of a year or so ago, the direct measurement of this species in the thermosphere had probably not yet been performed successfully. A satellite mass spectrometer result (ref. 8-1) obtained at an altitude of 400 kilometers suggested that the partial pressure of N exceeded that of molecular nitrogen (N_2), but the result was flawed by low mass resolution. A rocketborne mass spectrometer result by Ghosh and others (ref. 8-2) suggested that, at an altitude of 185 kilometers, the density of N was 6 percent that of N_2, although Hickman and Nier (ref. 8-3) showed that this is an upper limit.

The problems in measuring atomic nitrogen mass spectrometrically are similar to those of obtaining atomic oxygen measurements but are more serious because the density ratio of N to N_2 in the thermosphere is small. The N_2 can be dissociatively ionized in the spectrometer ion source; like O, N is highly reactive and can recombine not only to form N_2 on instrument chamber walls but can form other compounds such as NO.

PRINCIPLE OF THE UVA EXPERIMENT

The principle of the UVA measurement was to produce fairly well collimated beams of 130.4- and 120.0-nanometer radiation (resonance for O and N), and 135.6- and 149.3-nanometer radiation (forbidden lines of O and N that are very weakly absorbed by these species). The forbidden line radiation originated in the same sources as the resonant line radiation and hence defined the beam geometry, the reflectivity, and the transmission of the optical instrument for the resonance radiation independently of resonance absorption. The light was produced by radiofrequency-driven lamp sources and collimated by mirrors on the Apollo spacecraft. The light beams illuminated an array of corner reflectors mounted on the Soyuz spacecraft at a known distance x from the Apollo UVA light source. Thus, the portion of the beam striking the retroreflectors returned to a collecting mirror near the Apollo collimating mirror. From this mirror array, the radiation was focused on the entrance slit of a 0.75-meter Ebert-Fastie scanning spectrophotometer by an auxiliary mirror. The spectral range from 120.0 to 149.3 nanometers was scanned every 12 seconds through 1.5-nanometer ranges centered on 120.0, 130.4, 135.6, and 149.3 nanometers. The bandwidth of the spectrometer was approximately 1.15 nanometers. The spectrometer was a modified backup unit for the one used on the Apollo 17 experiment (ref. 8-4).

In its simplest terms, the principle of the UVA experiment is illustrated in figure 8-1. A known flux of resonance radiation F is radiated into a solid angle Ω. At a distance x from the source, the irradiance is $F/\Omega x^2$. If the reflectivity of each surface of the retroarray is r and the retroarray surface area is A, an amount of radiation $r^3FA/\Omega x^2$ is returned to point O and passes through a well-defined and limited region determined by the shape of the collimating mirror, the shape of the corner reflectors, and the geometry of the retroreflector array. Essentially, light from each point on the collimating mirror that strikes a given retroreflector returns through a region of the same shape but twice the linear dimensions of the corner reflector. The pattern of light sent from a point source to a corner reflector that is a distance x from the source and back to the source is analogous to the pattern of light sent from the point source to a hole in an opaque screen at a distance x of the same shape as the reflector and then on through the aperture to a screen that is a distance $2x$ from the source. If a fraction of this returned light f is sent to a spectrometer having a throughput QT, where Q is the quantum efficiency and T is the transmission, the counting rate R of a detector in the spectrometer will be

$$R = r^m (FA/\Omega x^2) e^{-2\bar{\sigma} x n} fQT \tag{8-1}$$

where m is the number of reflections, six in the present case; $\bar{\sigma}$ is the mean absorption cross section; and n is the attenuation coefficient. Obviously, r is assumed to be the same at each surface for a given wavelength.

The flux F of 130.4-nanometer radiation was 5×10^{13} photons/sec into a solid angle Ω of 0.75 steradian. Typical values for the other terms in the equation are as follows.

$r = 0.75$

$m = 6$

$A = 55$ square centimeters

$f = 0.2$

$T = 0.2$

$Q = 0.12$ electron/photon

$\bar{\sigma} = 10^{-13}$ square centimeter

Thus

$$R \simeq 3 \times 10^{12}\, x^{-2} e^{-2\bar{\sigma}xn} \tag{8-2}$$

The unattenuated counting rate R_0 is $3 \times 10^{12}\, x^{-2}$, or $3 \times 10^{2}\ \mathrm{sec}^{-1}$ even at a range of 1 kilometer. It was assumed that the minimum absorption that could be detected was 10 percent; i.e., $e^{-2\bar{\sigma}xn} = 0.9$, or $xn = 2 \times 10^{12}\ \mathrm{cm}^{-2}$. Thus, at 100 meters, an absorber density of $2 \times 10^{9}\ \mathrm{cm}^{-3}$ should be detectable and, at 1 kilometer, a density of $2 \times 10^{7}\ \mathrm{cm}^{-3}$ should be detectable. In this case, the counting rate will be 270 counts/sec, compared with the unabsorbed rate of 300 counts/sec.

In an experiment such as this, the spacecraft velocities are greater than the average thermal velocities of the gas particles at 1000 K (by a factor of 8 for oxygen). Hence, the frequency of the lamp signal will be shifted far away from the absorption frequency of the atoms by the Doppler effect if the light is radiated in the approximate direction of the Apollo velocity vector. It is therefore necessary to conduct the experiment with the vector between the spacecraft nearly perpendicular to the spacecraft velocity vectors. A simple calculation shows that, if the angle between the direction of emission of the light signal and the Apollo velocity vector were 78° with the two spacecraft 100 meters apart, the absorption by 4×10^{9} atoms/cm^{3} of oxygen would be only 30 percent compared to 82 percent if the angle were 90°. This effect could, however, readily be turned into an advantage if the experiment were performed in such a way that one spacecraft (for example, Apollo) slowly drifted past the other at a fixed range and the angle between them varied through approximately 30° centered on the normal to the orbital velocity vector. The reasons are twofold. First, it would not be necessary to determine by some independent measurement when the angle of observation was 90° to the direction

of the relative wind. This information would automatically be determined as the point at which the counting rate became minimum. Second, the change in counting rate with angle would define the Doppler line shape of the absorbing atom. Hence, the functional form of this variation would enable measuring the temperature of the absorbing atoms.

In practice, it is necessary to consider the fact that the light flux F varies with wavelength λ for each fine structure component of the resonance lines, and that the absorption cross section σ is also a function of wavelength. Thus, the term $Fe^{-2\bar{\sigma}nx}$ in equation (8-1) must be replaced for each fine structure component by

$$\int_i F_i(\lambda)\exp\left[-2xn\sigma(\lambda)\right]d\lambda \tag{8-3}$$

where $F_i(\lambda)$ depends on the effective lamp temperature T_L and $\sigma(\lambda)$ values depend on the gas temperature T_G. When there is no relative motion between source and absorber, the functional form of $F(\lambda)$ may be written

$$\left(mc^2/2\pi kT_L\lambda_{0i}^2\right)^{1/2}\exp\left[-mc^2\left(\lambda-\lambda_{0i}\right)^2/2kT_L\lambda_{0i}^2\right] \tag{8-4}$$

where λ_{0i} is the line center wavelength of the i-th fine structure component, m is the atomic mass of the gas species, c is the speed of light, and k is the Boltzmann constant. When u is the component of the atmospheric velocity along the light beam in the coordinate system in which the Apollo vehicle is at rest, $\sigma(\lambda)$ becomes

$$\sigma_0\exp\left\{\frac{-mc^2\left[\left(\lambda-\lambda_0\right)c-u\lambda_0\right]^2}{2kT_G\lambda_0^2c^2}\right\} \tag{8-5}$$

Finally, because the spectrometer does not resolve the fine structure components in the spectrum, it is necessary to sum over fine structure components to obtain the predicted counting rate.

$$R = \Sigma R_i \tag{8-6}$$

The spectral parameters for the gases involved in this experiment are shown in table 8-I.

Figures 8-2(a) and 8-2(b) show the counting rates as a function of spacecraft separation when $u = 0$ for atomic oxygen and atomic nitrogen, respectively, at typical gas concentrations. Figures 8-3(a) and 8-3(b) show, for various values of T_G, the variation in atmospheric transmission as a function of the angle between the direction of observation and the perpendicular to the wind velocity vector in the coordinate system in which the Apollo spacecraft is at rest. The lamp output (integrated over wavelength of all spectral components) is assumed to be 10^{13} photons/sec for the oxygen 130.4-nanometer triplet and 3×10^{12} photons/sec for the nitrogen 120.0-nanometer triplet.

A practical complication is introduced in performing this experiment because the resonance radiation in the emitted beam can be scattered resonantly by the gas to be studied. Some of this radiation will be emitted in a direction to enter the spectrometer slit, although it is a relatively small amount of the total scattered light because the scattering is virtually isotropic. If one considers the light traveling in a certain direction from the light source (treated as a point source) and calls the number of photons crossing unit area per second at a distance x from the source $I_L(\lambda)$, the number of these scattered per second will be

$$\int_{x_0}^{\infty} \int_0^{\infty} I_L(\lambda) n\sigma(\lambda) \exp\left[-2n\int_0^x \sigma(\lambda)dx'\right] d\lambda \frac{dx}{4\pi x^2} \tag{8-7}$$

where x_0 is the distance from the light source at which the outgoing beam crosses the spectrometer field of view. To evaluate the actual counting rate due to these scattered photons, it is necessary to evaluate the overlap of the outgoing beam with the effective spectrometer field of view. For example, the field of view is filled gradually and not abruptly at a distance x_0 along the beam. This evaluation is being conducted for the instrument actually flown. A reasonable approximation for the counting rate from resonance fluorescence R_F is

$$R_F = \frac{FA_M A_{SM} A_S r^3 QT}{4\pi p^2 \Omega} \int_{x_0}^{\infty} \frac{dx'}{x^2} \int_0^{\infty} I_L(\lambda) n(x)\sigma(\lambda) \exp\left[-\int_0^x 2n\sigma(\lambda)dx\right] d\lambda \tag{8-8}$$

where A_M = the lamp collimating mirror area (3.3 by 5.7 centimeters)

A_{SM} = the area of the collecting mirror (5.5 by 3.7 centimeters)

A_S = the area of the spectrometer slit (0.2 by 5.7 centimeters)

p = the focal length of the collecting mirror (16.5 centimeters)

x_0 = 75 centimeters

The contribution of resonance fluorescence under the same conditions assumed in the absorption calculation is shown in figure 8-2. The fluorescence contribution varies with the angle between direction of observation and velocity vector and reaches a maximum where the transmitted light reaches a minimum; i.e., when the wind velocity component in the direction of observation is zero. The resonance fluorescence contribution to the observed counting rate as a function of time (or angle) must be evaluated independently so that it can be subtracted from the total counting rate to obtain the contribution due to transmitted (or absorbed) radiation alone; also to be subtracted are background signals from airglow.

The heart of the experimental apparatus is the Apollo 17 Ebert-Fastie spectrometer. It was equipped with a new grating drive cam that rotated the grating to scan from 129.65 to 131.15 nanometers in 2.5 seconds, from 119.25 to 120.75 nanometers in 4.5 seconds, from 129.65 to 131.15 nanometers again in 2 seconds, from 134.85 to 136.35 nanometers in 1.25 seconds, and from 148.55 to 150.05 nanometers in 1.25 seconds. The light output of each lamp was pulsed with a pulse duration of 0.1 second; the sequence was the O lamp alone, the N lamp alone, and both lamps off.

The resonance lamp light sources, the retroreflector array, and the optical transmitting and receiving systems had to be designed around the spectrometer in such a way as to maximize the signals received. The spectrometer choice was governed by availability and by the schedule for experiment preparation. The instrument has an entrance slit of 0.2 by 5.7 centimeters, with an f/5 collecting aperture corresponding to a solid angle of 12° by 12°. The ultraviolet lamps have a 1-centimeter source diameter and emit into a solid angle of approximately 56° full width, or 0.74 steradian. The flux from each lamp is collimated by a mirror placed 12 centimeters from the lamp. Because the source diameter in the lamps is 1 centimeter, the beam leaves the collimating mirror with a spread of approximately 5°.

In designing the corner reflector array, it was necessary to consider that the optimum diameter of the mirror that focuses the returned light on the spectrometer slit equals the width of an individual corner reflector. The corner reflectors must be packed efficiently into an array of convenient diameter. The arrangement adopted was a 10-centimeter array diameter, and each reflector was 3.3 centimeters wide (fig. 8-4). In this case, the focusing mirror diameter was 3.3 centimeters, and the mirror was placed 16.5 centimeters from the slit to fill the slit aperture laterally.

The geometry of the optical transmitting and collecting system is defined in figure 8-5. Light originating from a point on a collimating mirror will return from the corner reflector and pass through a region centered at that point on the mirror but twice as large in linear dimensions as the corner reflector (neglecting diffraction effects). For example, light originating from point x on mirror O in figure 8-6 will return through the 6.6-centimeter dashed-line region (hexagonal). It is reasonable to put the collecting mirror in the space bounded by the collimating mirrors and allow the dimensions to be 3.3 by 5.7 centimeters. The contribution

to the collected light originating from point x is then the shaded overlap of the collecting mirror and the hexagonal area 6.6 centimeters in diameter and centered at point x. The size of the return beam from all points on the collimating mirror O is shown by the broken line. The collecting mirror must be protected from stray light coming from the lamps by means of baffling because the most intensely illuminated region is that adjacent to the collimating mirror.

Figure 8-7 shows how the fluorescence and transmitted signals should vary with wavelength around 130.4 nanometers. This calibration was done by convoluting the previously computed signal intensities in each of the three components of the oxygen triplet with the spectrometer slit function. The latter was assumed to be triangular with a full width of 1.15 nanometers at half maximum. The case shown is for an Apollo-Soyuz separation of 100 meters, an oxygen density of 4×10^9 cm^{-3}, a lamp temperature T_L of 600 K, and a gas temperature T_G of 1050 K. The curves are normalized. The difference in wavelength at the peak occurs because most of the transmitted signal is in the weaker 130.5- and 130.6-nanometer components, whereas most of the fluorescence signal is from the 130.2-nanometer line.

A third light source was incorporated in the apparatus to provide bright visual light illuminating the same field of view as the ultraviolet sources. The collimating lamp, marked "Visible" in figure 8-6, provided input to a star tracker with output in the spacecraft to indicate to the astronaut whether the retroreflector array was being illuminated by the lamp beams, and, more importantly, whether the retroarray was in the spectrometer field of view (±0.35° in pitch). A backup to the star tracker was provided by the crew optical alinement sight (COAS), through which the retroreflector could be seen. The COAS was provided with a reticle marked in degrees in the pitch and yaw directions.

A door was provided that was closed when data were not being taken. The inside surface of the door was blackened. However, small reflecting cylinders, one for each of the ultraviolet sources, were fitted in the door. These cylinders provided a means of in-flight calibration. The counting rate as a function of grating position was obtained with the flight unit during thermal-vacuum (TV) checks of the instrument for comparison with calibration runs made during flight.

The reflectivity of the retroreflectors was measured as a function of wavelength. The transmission T of the full receiving system, the external optics, and the telescope was also measured at the Johns Hopkins University with the cooperation of W. G. Fastie. The quantum efficiencies of the detectors Q for both flight and backup units were also measured. Pertinent data are shown in tables 8-II to 8-V.

The flight lamps and backup lamps were calibrated to determine the flux of photons emitted. For this calibration, a monochromator and a double ionization chamber (for the 120.0- and 130.4-nanometer lines) were used, and a measurement of the photocurrent in the monochromator detector (for the 135.6- and 149.3-nanometer lines) was made. The data obtained for the flight lamps were reduced to absolute intensities by comparison with similar measurements made with the same system on another lamp that had been absolutely calibrated at the University of Pittsburgh. The detector used at Pittsburgh to calibrate the standard lamp had

been calibrated by a measurement of its response to radiation at the four wavelengths in question emitted from a beam of O and N atoms of known density excited by electron impact. The flux from the flight lamp is given in table 8-III.

The effective lamp temperatures T_L were also measured at the University of Pittsburgh by measuring the absorption of their resonance radiation by a column of atoms of known concentration at a temperature of 300 K. The surprising result was that typical effective temperatures for the oxygen lamps were very large, from 2200 to 3700 K. The high temperature is presumed to be caused by the presence of many atoms that have been dissociatively excited from O_2 into high radiating states of O, and have cascaded into the resonantly radiating state before undergoing many collisions. This was not the case for the nitrogen lamps. The flight lamp temperatures were 2500 K for the oxygen lamp and 400 K for the nitrogen lamp. The UVA experiment was mounted on the Apollo docking module with the field of view forward (plus-X axis).

RESULTS[1]

The first exercises of the UVA experiment began when the lamps were turned on at 27:00 ground elapsed time (GET) on Wednesday, July 16, 1975. The counting rate as a function of cam position closely reproduced that obtained with the door closed in the last thermal-vacuum tests before the apparatus left the laboratory (table 8-IV). At 28:30 GET, the cover was opened and the spacecraft was pointed toward the star Vega. The purpose of this exercise was to calibrate the COAS and to test the star-tracker system designed to lock the field of view on a target. During this test, the obtaining of resonance fluorescence signals in the oxygen 130.4-nanometer channels was verified. One problem was discovered, however; the star tracker indicated lock while the COAS indicated star movement from 3° to the right to 2.5° to the left. This difference occurred because a spacer was inserted between the lens and aperture of the star tracker to increase the size of the light spot on the photocathode and thereby to change the slope of the star-tracker response curve. This change moved the focal point approximately 0.25 centimeter in front of the aperture and enlarged the star-tracker field of view to the limits of the star-tracker tube, 5.5°, due to vignetting. To avoid operating with the retroreflector out of the field in yaw (even though the star tracker indicated it was in the field), the chart on the COAS reticle was marked at ±1.5° and the crew was instructed to prevent straying of the retroreflector image beyond these limits. In fact, the crew was asked to keep the retroreflector as near as possible to the center of the COAS.

Five additional data-taking exercises were performed. After the final undocking on July 19, 1975, the Apollo vehicle assumed a stationkeeping position 18 meters ahead of the Soyuz vehicle as the two spacecraft approached the morning terminator. The UVA power was turned on at approximately 98:55 GET, 30 minutes before the first observational exercise, to permit stabilization of the lamps and the photomultiplier tube. During this period, calibration data were obtained using the door reflectors. Table 8-IV presents results for comparison with those obtained during

---

[1]Also see section 1.

the final thermal-vacuum tests conducted at the Applied Physics Laboratory of Johns Hopkins University. The counting rates during flight were approximately 0.8 those obtained on the ground. This effect can be attributed to use of the detector head from the backup unit to replace that of the flight unit on the launch pad shortly before flight because of an electronics problem. A comparison of the ground-test product of QT values for the two units (table 8-IV) shows that the ratios are about the same as the flight to ground-based counting rate ratios. At 99:25 GET, the Soyuz crew activated circuits to unlatch covers over the Soyuz retroreflector arrays. Two arrays were mounted on top of the vehicle, one facing upward and the other facing starboard. A third array was mounted on the rear of the spacecraft facing aft. The Apollo crew verified with binoculars that the covers on the top-mounted retroreflectors had opened. (If the starboard array had not opened, a contingency plan would have permitted a Soyuz yaw so that its aft-mounted retroreflectors could be used in the experiment.) Power to the UVA was briefly turned off while the door of the instrument was opened after the terminator had been passed. (The powerdown precaution was necessary so that large flashes of light would not damage the detectors as the door was being opened or closed.) Beginning 18 minutes before the data-gathering run, the Apollo vehicle moved out of the orbital plane (fig. 8-8) until it was 150 meters from the Soyuz vehicle and oriented so that the retroreflector could be illuminated. At this time, the angle between the perpendicular to the Soyuz velocity vector and the Apollo vehicle was 15°. The Apollo vehicle then was maneuvered through a 33° circular arc sweep passing through the normal to the velocity vector while the crew attempted to keep the retroreflector illuminated following procedures described previously. Both the star-tracker output and the COAS observations indicated that a lock was obtained. A problem occurred during the first several minutes of the run because the Soyuz flashing beacons and orientation lights were not extinguished. After the data-taking maneuver (lasting 10 minutes) was completed, the Apollo vehicle returned to a stationkeeping position 50 meters from the Soyuz vehicle but facing in the direction of motion, as the Soyuz yawed 180° to face the Apollo.

For reasons still not understood, no clearly identifiable reflected ultraviolet radiation was detected during this pass. There was a strong 130.4-nanometer signal that was almost surely resonance fluorescence, but there were no counts above background in the 135.6-, 149.3-, or 120.0-nanometer channels. The Apollo crew reported that both the Soyuz window and the retroreflector were illuminated, and two possible explanations for failure were considered. One was that the reflectivity of the retroreflector had been seriously degraded during the flight. The other was that a window reflection was registered by the star tracker as a reflection from the retroreflector. The second explanation is not consistent with the fact that, through the COAS, an illuminated retroreflector was seen centered in the field of view. It was decided, therefore, not to risk using the side-looking retroreflector during the scheduled run at 500 meters separation but to request performance of a Soyuz 90° yaw maneuver to enable use of the aft-looking reflector.

The procedure followed during the 500-meter data take was very similar to that described at 150 meters (fig. 8-9). It occurred during the next eclipse period. Calibration data with the door closed were obtained starting at 100:30 GET (about 35 minutes before the run). The Apollo vehicle maneuvered, as shown in the figure, to a position 500 meters from the Soyuz vehicle out of the orbital plane and 15° behind. The Apollo vehicle then executed a circular sweep through 32° (-15° to +17°) in a horizontal plane that contained the Soyuz vehicle; the maneuver

required 10 minutes. Very early in this maneuver, clear indication was obtained in all UV channels that reflected radiation was being received by the UVA spectrometer. Reflected data were received (as indicated in the 135.6-nanometer channel) throughout the sweep. Figure 8-10 is an example of the strip-chart records showing a complete spectral scan taken during the sweep for comparison with a spectrum obtained from the UVA door just before the sweep (fig. 8-11). The observed ratio of the counting rates at 130.4 and 135.6 nanometers was 5.7 ± 0.5 from 101: 17: 38.13 to 101: 17: 40.25 GET. (The sweep began at 101: 17: 37 GET.) The ratio obtained from the door (after correction for the reflectivity of the door) was 5.72. The ratio of 130.3 to 135.6 nanometers obtained during the run is shown in figure 8-12. There was an anomaly during the run; the 135.6-nanometer counting rate dropped by a factor of 5.5 from a plateau of about 250 counts to about 45 counts between 101: 17: 39.37 and 101: 17: 41.49 GET. It remained at 45 counts thereafter. A similar effect occurred in the 149.3-nanometer channel. These anomalies are being analyzed. Because the returned 130.3-nanometer signal contains a strong component of resonance fluorescence and because time and spacecraft attitude have not been correlated, there are no reliable estimates of O or N densities currently.

During the warmup period for the next eclipse pass, the signals reflected from the door were normal during the first several minutes; this observation indicates that no change in the lamp output, collimating mirror reflectivity, or receiver QT was responsible for the drop in signal during the second part of the 500-meter pass. However, the calibration signal dropped by a factor of approximately 4 in all channels during the last several minutes of the warmup period and remained low after the door was opened for the 1000-meter data take. As shown in figure 8-13, these data were obtained in the orbital plane during separation of the Apollo and Soyuz vehicles. The upward-looking retroreflector was used, and the range varied from 800 to 1300 meters during the sweep from +15° to -15° with the vertical.

Some reflected signals were detected, although the retroreflector was only in the field of view sporadically. Use of the COAS and the star tracker was very difficult because bright moonlight was illuminating the top of the Soyuz spacecraft. An attempt was made to use the COAS to keep the Apollo vehicle pointed toward the Soyuz beacon and navigation lamps instead of trying to lock on the retroreflector as in the out-of-plane observations.

After the Apollo departed the neighborhood of the Soyuz, two resonance exercises were performed. During an eclipse phase, the Apollo X-axis was oriented normal to the orbital plane and one full orbit (from 105: 10 to 106: 46 GET) of resonance fluorescence and airglow background data was obtained. This exercise was followed during the next eclipse phase (from 106: 55 to 107: 10 GET) with an observation of the resonance fluorescence signal obtained with the Apollo X-axis still oriented normal to the orbital plane and with the Apollo vehicle executing a slow roll through 360°. The purpose of this exercise was to determine the variation in population of thermal oxygen atoms between the ram side of the docking module and the lee side (fig. 8-14). The atoms near the aperture consist of ambient undisturbed atmosphere and atoms that have been scattered from the vehicle. Obviously, the higher density will be on the ram side of the vehicle. Some of the atoms striking the vehicle will have become thermalized, and then reflect. Some will recombine and become O_2 molecules. The recombining fraction should be determinable from

the data obtained, because the 130.4-nanometer fluorescence signal was found to depend strongly on the roll orientation.

It is too early in the analysis of data to report O or N densities measured during this experiment. However, it can be stated with confidence that the data are sufficient to determine those densities.

REFERENCES

8-1. Philbrick, C. R.; and McIsaac, J. P.: Measurements of Atmospheric Composition Near 400 KM. Space Research XII, vol. 1, Academie-Verlag (Berlin), 1972, pp. 743-749.

8-2. Ghosh, S. N.; Hinton, B. B.; Jones, L. M.; Leite, R. J.; et al.: Atomic Nitrogen in the Upper Atmosphere Measured by Mass Spectrometers. J. Geophys. Res., vol. 73, no. 13, July 1968, pp. 4425-4426.

8-3. Hickman, David R.; and Nier, Alfred O.: Measurement of the Neutral Composition of the Lower Thermosphere Above Fort Churchill by Rocket-Borne Mass Spectrometer. J. Geophys. Res., vol. 77, no. 16, June 1972, pp. 2880-2887.

8-4. Fastie, William G.; Feldman, Paul D.; Henry, Richard C.; Moos, H. W.; et al.: A Search for Far-Ultraviolet Emissions From the Lunar Atmosphere. Science, vol. 182, no. 4113, Nov. 1973, pp. 710-711.

8-5. Lin, Chorng-Lieh; Parkes, David A.; and Kaufman, Frederick: Oscillator Strength of the Resonance Transitions of Ground-State N and O. J. Chem. Phys., vol. 53, no. 10, Nov. 1970, pp. 3896-3900.

TABLE 8-I.- SPECTRAL PARAMETERS FOR ATMOSPHERIC ABSORPTION EXPERIMENT

Species	Spectral line, nm	Absorption cross section at 300 K (σ_0), cm^2 (a)	Relative lamp intensity F_i	Relative atmospheric populations at 1050 K
O	130.217	1.6×10^{-13}	0.542	[b]0.613
	130.487	1.6	.337	[b].297
	130.601	1.6	.120	[b].090
N	119.955	3.8	.500	1.000
	120.022	2.5	.333	1.000
	120.071	1.3	.167	1.000

[a]$\sigma_0(T_G) = \sigma_0(300\ K)\sqrt{300/T_G}$. The values of $\sigma_0(300\ K)$ are calculated from the oscillator strengths given in reference 8-5.

[b]The relative atmospheric populations for atomic oxygen are calculated from the following formulas.

$$n_{130.2}/n_{total} = 5/(sum)$$

$$n_{130.5}/n_{total} = \left[3 \exp\ (-228.24/T_G)\right] \Big/ (sum)$$

$$n_{130.6}/n_{total} = \left[\exp\ (-326.16/T_G)\right] \Big/ (sum),$$

$$\text{where } (sum) = 5 + \left[3 \exp\ (-228.24/T_G)\right] + \left[\exp\ (-326.16/T_G)\right]$$

TABLE 8-II.- PRODUCT OF QUANTUM EFFICIENCY AND TRANSMISSION QT FOR FLIGHT AND BACKUP UNITS

Wavelength, nm	Backup unit QT	Flight unit QT
130.4	0.0258	0.0307
120.0	.0129	.0264
130.4	.0272	.0397
135.6	.0258	.0311
149.3	.0151	.0172

TABLE 8-III.- FLIGHT LAMP FLUXES INTO 0.74 STERADIAN

Flight lamp	Wavelength, nm	Flux, photons/sec
O	130.4	10.4×10^{13}
	135.6	1.78
N	120.0	.634
	149.3	1.45

TABLE 8-IV.- COMPARISON OF COUNTING RATES FOR FLIGHT AND BACKUP UNITS

Wavelength, nm	Activity, counts/sec, for -			
	TV test of flight unit	During flight with backup unit	Ratio flight/ TV test	Ratio QT backup unit/QT flight unit
130.4	27 310	21 260	0.78	0.84
120.0	21 788	18 359	.84	.78
130.4	27 771	21 709	.78	.69
135.6	6 363	4 268	.67	.83
149.3	13 527	11 881	.88	.88

TABLE 8-V.- RETROREFLECTOR REFLECTIVITIES

Wavelength, nm	Reflectivity from -	
	Aft	Top
130.4	0.60	0.57
120.0	.56	.54
135.6	.55	.52
149.3	.52	.49

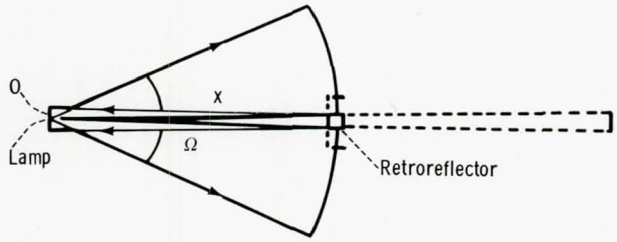

Figure 8-1.- Basic geometry of the UVA experiment.

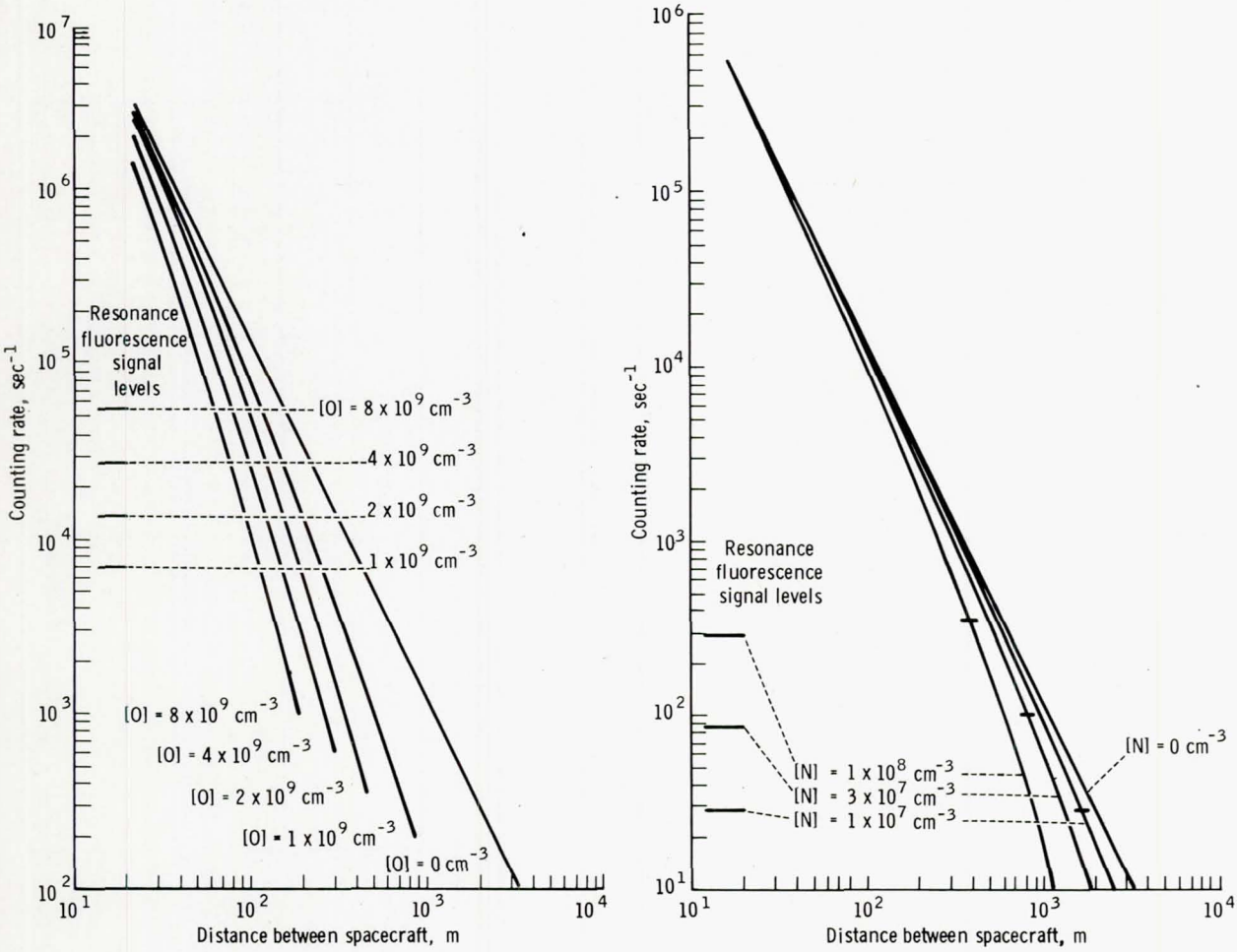

(a) Oxygen atoms.

(b) Nitrogen atoms.

Figure 8-2.- Spectrometer signal as a function of spacecraft separation distance.

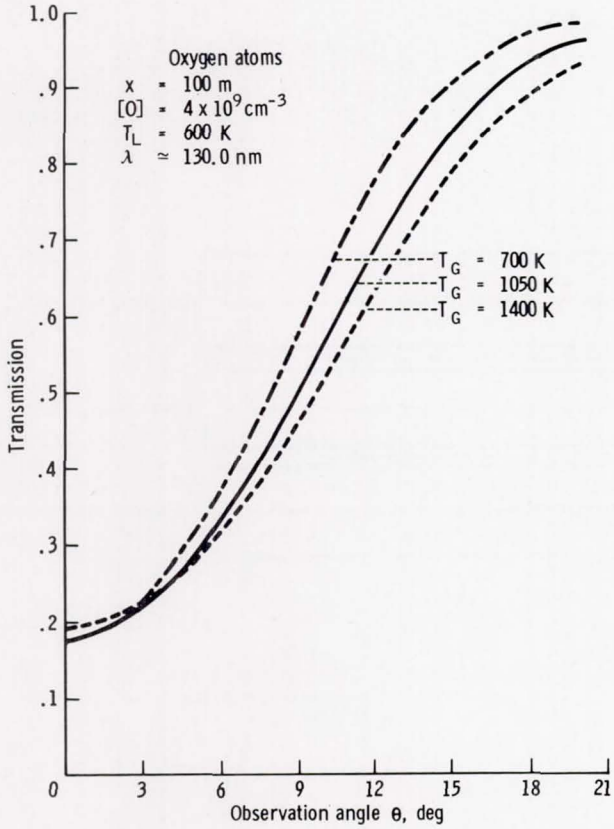

(a) Oxygen atoms.

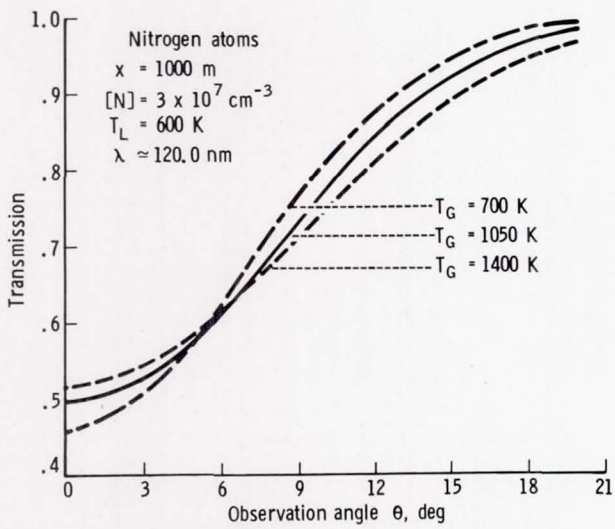

(b) Nitrogen atoms.

Figure 8-3.- Variation of atmospheric transmission as a function of the observation angle.

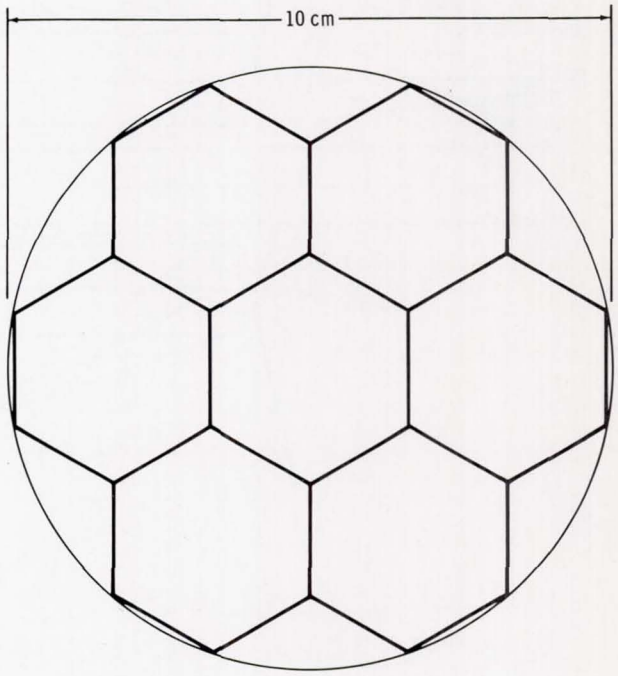

Figure 8-4.- Arrangement of mirrors in the retroreflector array.

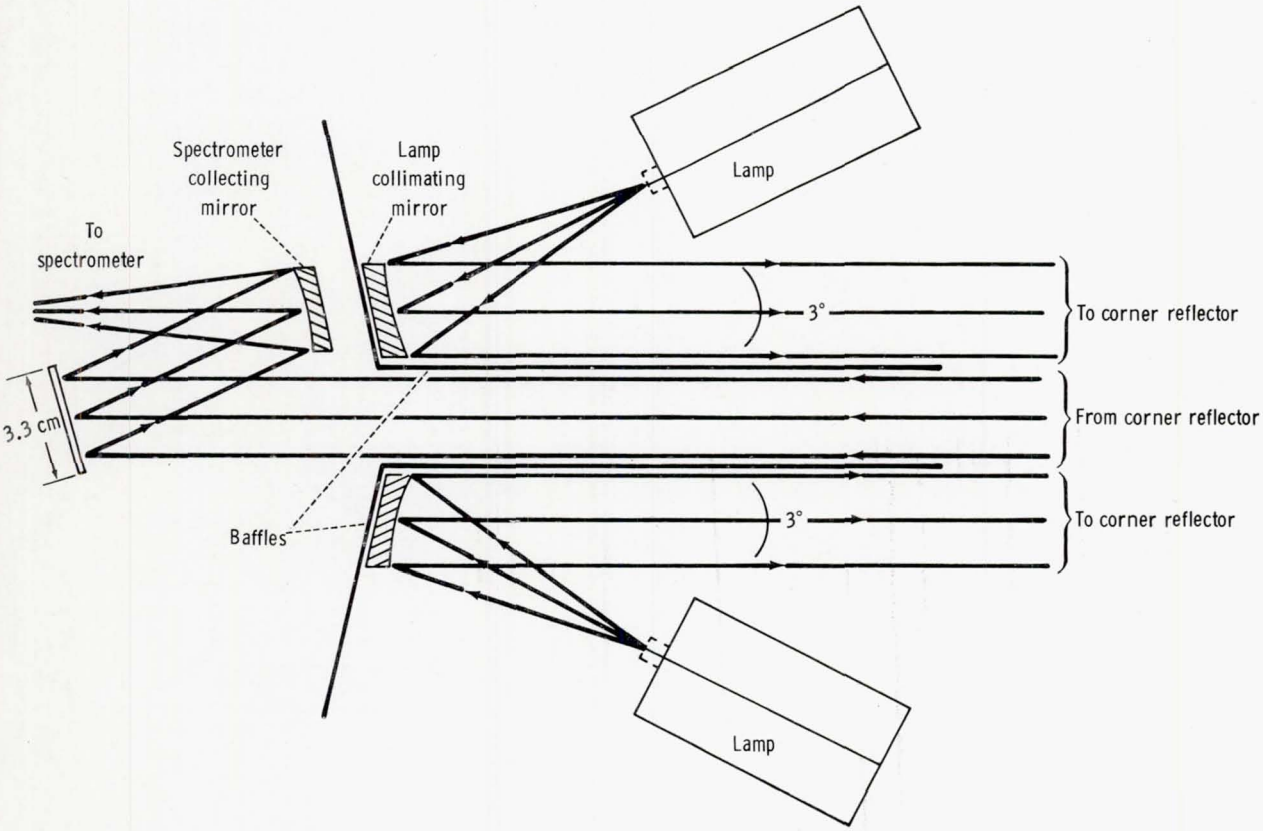

Figure 8-5.- Schematic diagram of optical transmitting and collecting system.

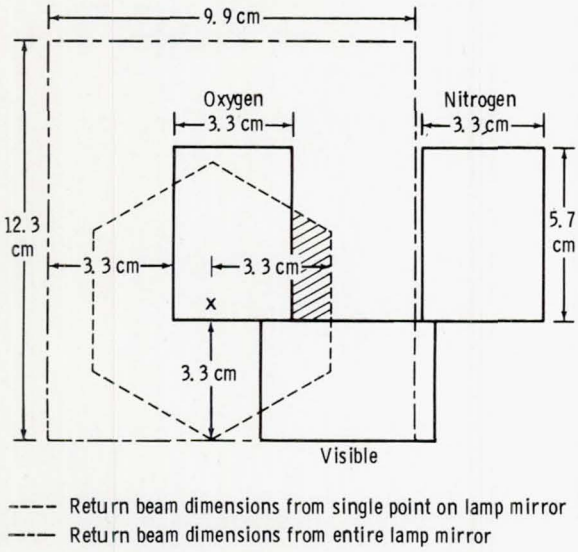

Figure 8-6.- Geometry of return beam from the retroreflector array.

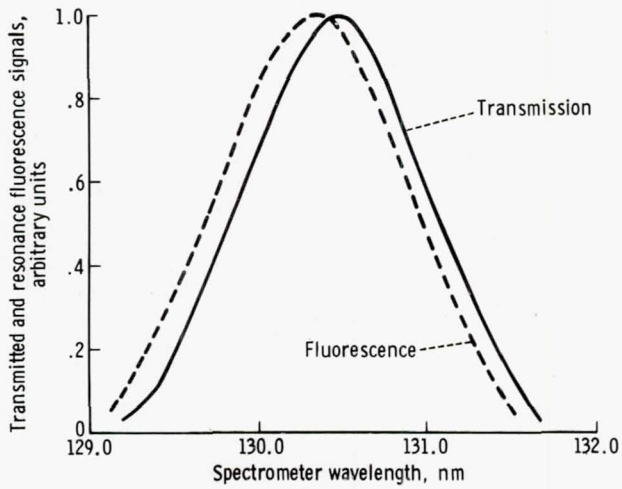

Figure 8-7.- Transmitted and resonance fluorescence signals as a function of spectrometer wavelength setting.

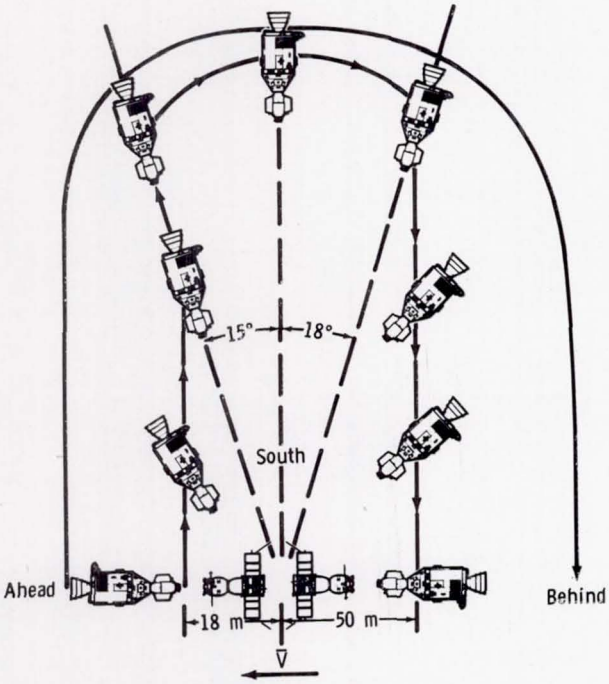

Figure 8-8.- Illustration of the 150-meter out-of-plane data take. The symbol $\overline{V}$ represents the velocity vector.

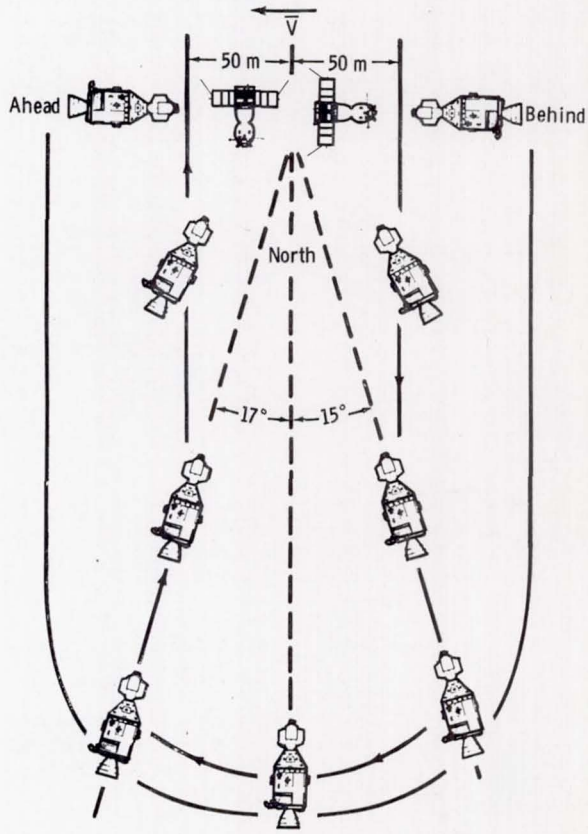

Figure 8-9.- Illustration of the 500-meter out-of-plane data take; $\overline{V}$ is velocity vector.

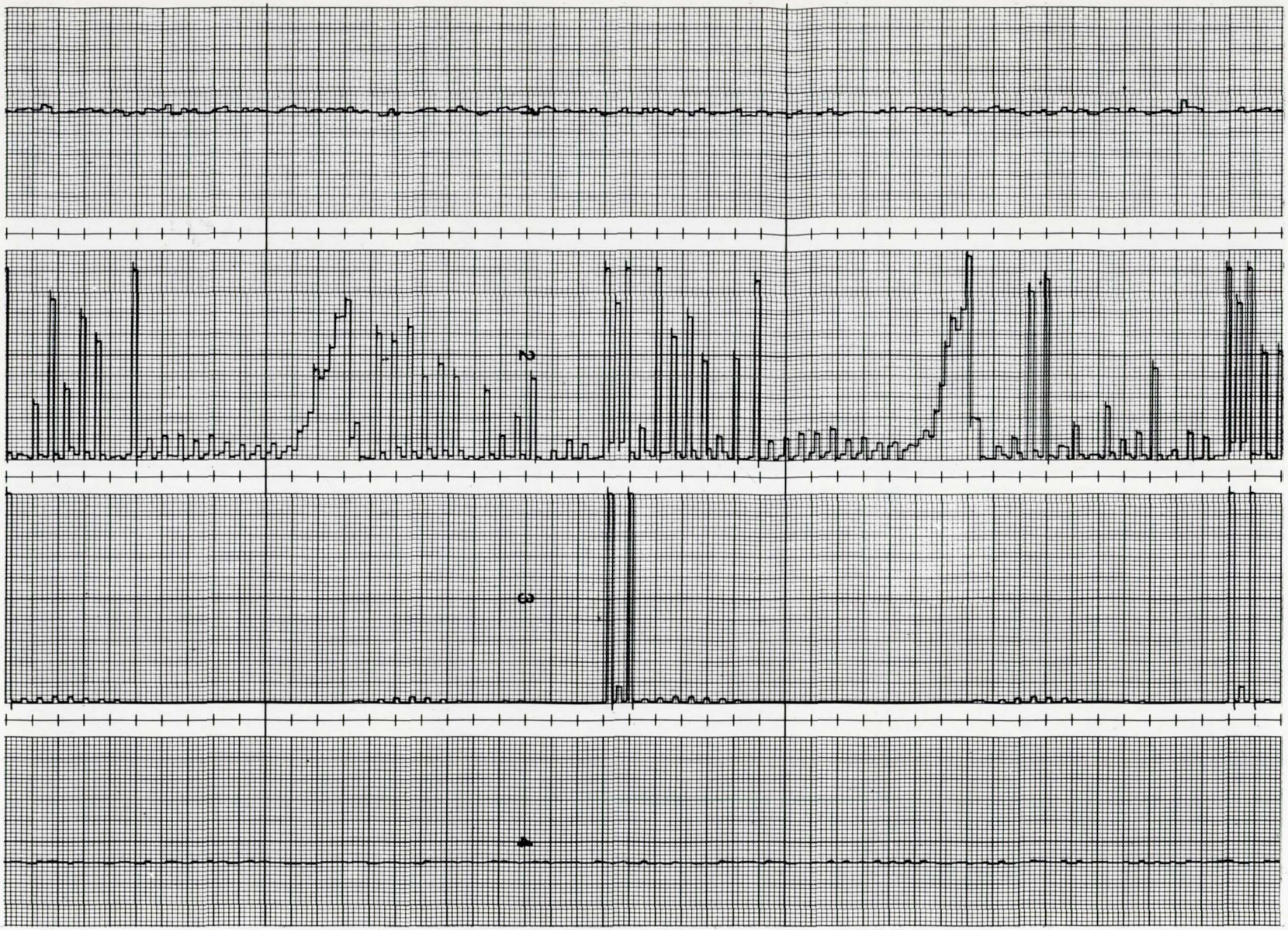

Figure 8-10.- Strip-chart record taken during the 500-meter data take.

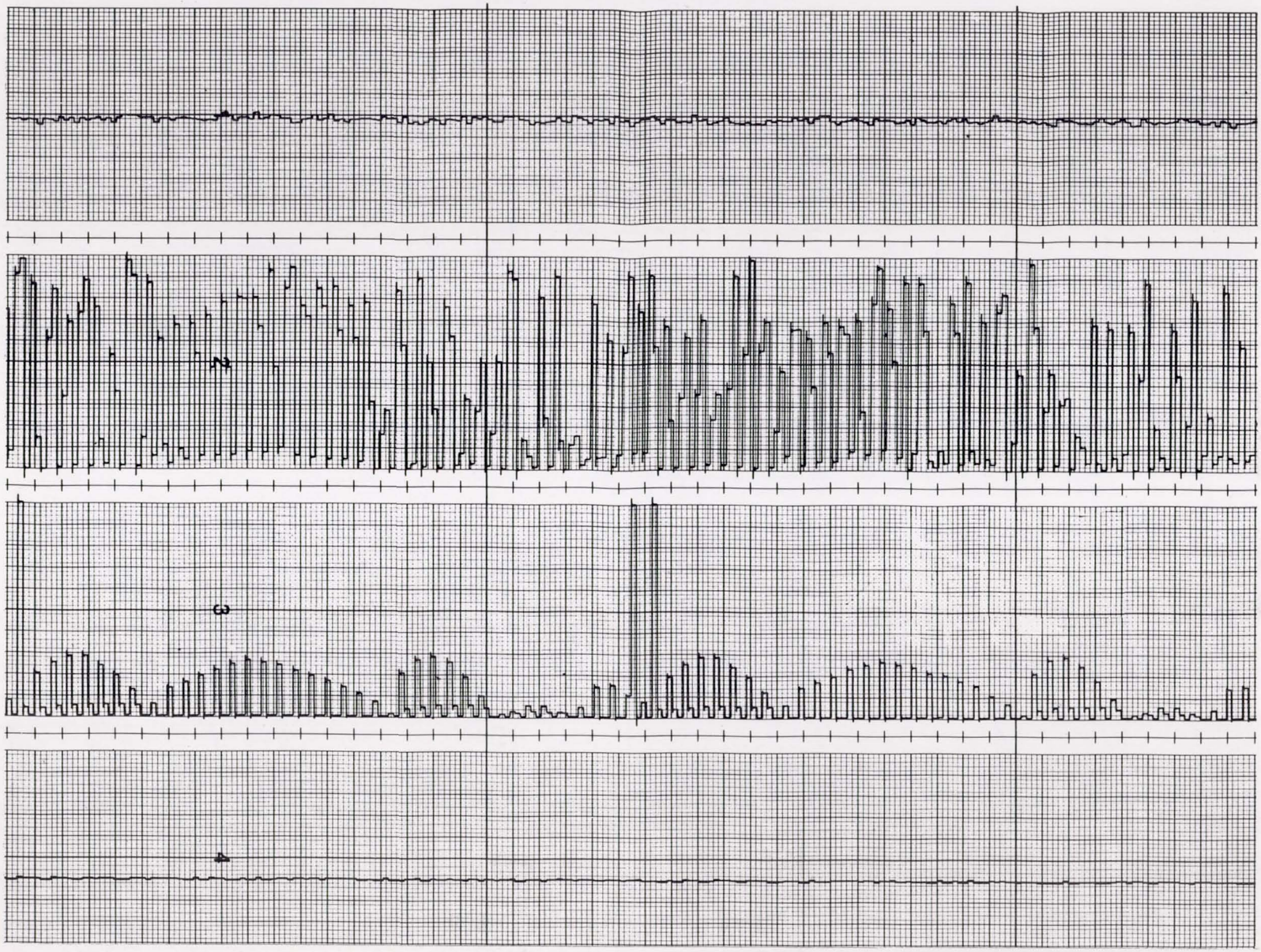

Figure 8-11.- Strip-chart record taken just before the 500-meter data take with door closed.

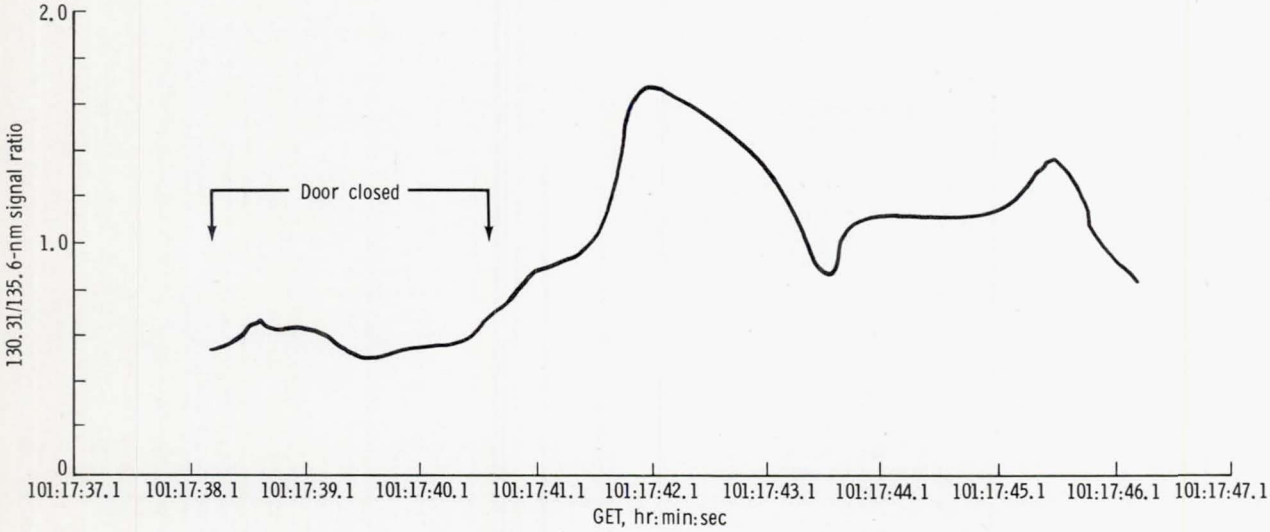

Figure 8-12.- Ratio of the 130.3- to 135.6-nanometer signal during the 500-meter data take.

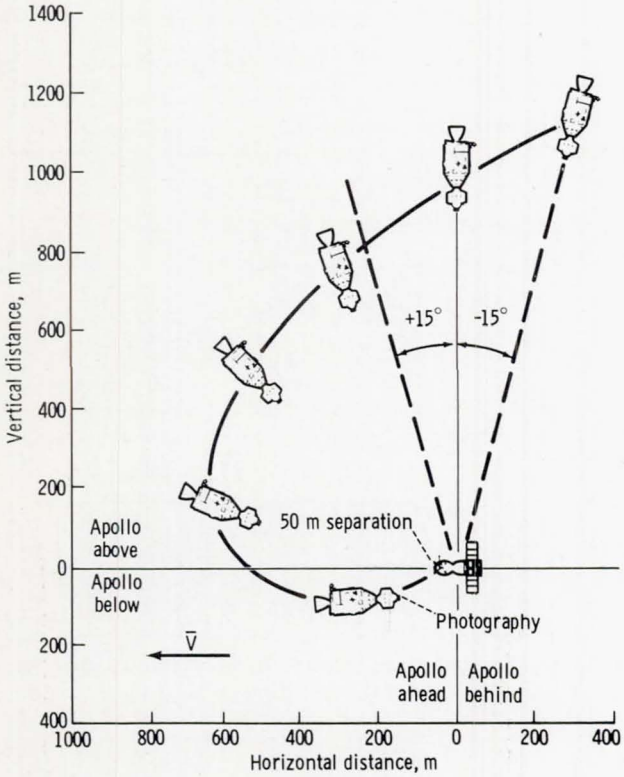

Figure 8-13.- Illustration of the 1000-meter in-plane data take; $\overline{V}$ is velocity vector.

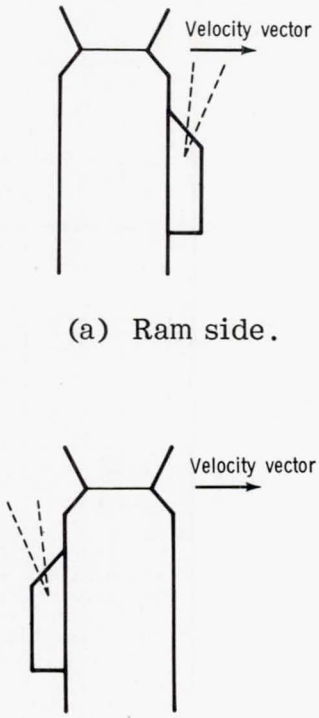

(a) Ram side.

(b) Lee side.

Figure 8-14.- Collecting aperture orientation on Apollo docking module.

9. STRATOSPHERIC AEROSOL MEASUREMENT

EXPERIMENT MA-007

T. J. Pepin[a†] and M. P. McCormick[b]

ABSTRACT

The Apollo-Soyuz Test Project Stratospheric Aerosol Measurement Experiment was flown to demonstrate that direct solar occultation measurements by photometers and photographs can be used for defining stratospheric aerosol concentrations. Supporting ground-truth data were provided by laser radar and balloon-borne dustsonde. Initial results show a significant difference in aerosol concentrations between the Northern and Southern Hemispheres.

INTRODUCTION

This experiment was designed to demonstrate the feasibility of remotely sensing aerosols in the stratosphere from a low-orbiting manned spacecraft. Increasing interest in the stratosphere has led to the investigation of methods for remote sensing from Earth-orbiting satellites. Information gained from the Stratospheric Aerosol Measurement (SAM) Experiment performed during the Apollo-Soyuz Test Project (ASTP) mission will be used in the design of remote-sensing equipment for future satellite missions.

The instrument used for making these stratospheric aerosol measurements consisted of a photometer and associated electronics that provided a signal to the command module (CM) telemetry system. A Hasselblad data camera (HDC) equipped with special infrared (IR) film and filter was used to photograph the sunset and sunrise events. The experiment technique involved directly measuring solar intensity (photometer) and Sun shape (photographs) in the spectral region centered at approximately 0.84 micrometer. Immediately before satellite night, as the spacecraft approached the shadow of the Earth, the line of sight to the Sun passed first through the upper layers of the stratosphere and then steadily down into the lower layer of the troposphere. During the 1.5 minutes (approximately) required for the instrument line of sight to pass through the lower 150 kilometers of the atmosphere, the solar intensity was recorded by the photometer, and solar disk shape changes were recorded in photographs. The same set of measurements was made at satellite dawn as the spacecraft emerged from the shadow of the Earth.

---

[a]University of Wyoming.

[b]NASA Langley Research Center.

[†]Principal Investigator.

The total extinction coefficient was obtained from the variation of the solar intensity as a function of total airmass distributed along the line of sight. At the effective wavelength of the photometer and the photographic system, the extinction was principally produced by the atmospheric aerosols; the measurements are being used to determine the aerosol concentration.

To verify the performance of the SAM Experiment, ground-truth data were acquired by a balloon-borne aerosol optical counter and a ground-based laser radar (lidar) system. The balloon-borne counter was flown from the Richards-Gebaur Air Force Base (lat. 39° N, long. 95° W) near Kansas City, Missouri, at the same time and place of the ASTP second sunset SAM. The lidar measurements were also made from Richards-Gebaur Air Force Base on Earth nights bracketing and during the second sunset SAM.

THE SAM INSTRUMENT

The photometer (fig. 9-1) used for the SAM Experiment utilizes a pin diode detector having a 10° field of view (FOV), which was used to look at the Sun through the CM window at a wavelength centered at approximately 0.84 micrometer. The detector was used in the photovoltaic mode to detect the solar signal, and samples were taken at a rate of 10 samples/sec using a 12-bit analog-to-digital converter. The signal output of the converter was recorded and transmitted by the CM data system.

The photometer was equipped with a projection sight system consisting of a post whose shadow was projected onto a grid that could be observed by the astronaut to ensure that the photometer system was properly alined with respect to the Sun. The instrument also included a green light to verify that the power was properly connected and a switch that the astronaut could activate to send a known signal over the telemetry system to verify proper installation of the photometer in the CM.

CAMERA SYSTEM

The photographic portion of the experiment consisted of a series of timed IR photographs of spacecraft sunrises and sunsets taken through the CM window with an HDC. The 250-millimeter focal length (12.5° by 12.5° FOV), f/5.6 lens was fitted with a quality glass IR filter capable of obtaining at least three orders of magnitude blocking in the visible and the ultraviolet. Kodak multispectral IR aerial film (ESTAR-AH base) SO-289 was used in two 70-millimeter Hasselblad magazines. Each magazine contained film for 50 frames with an additional 1 meter reserved for sensitometric calibration exposures. The HDC had a self-contained battery power supply for shutter activation and film advance. An onboard intervalometer provided a contact closure to the HDC every 2.5 seconds during the experiment to trigger the camera automatically. Timing with SAM data was to be provided by an audio channel of the spacecraft tape recorder.

THE BALLOON-BORNE "DUSTSONDE"

Figure 9-2 is a schematic drawing of the University of Wyoming balloon-borne dustsonde used in this program for the ground-truth in situ aerosol measurement that was made from the Richards-Gebaur Air Force Base. The mode of operation of the dustsonde is described in the following discussion.

Air sampled on balloon ascent and parachute descent is pumped at approximately 0.75 liter/min in a well-defined stream through the focal point of the condenser lens in the 2.5-liter scattering chamber where individual particles scatter light into the microscopes. The light pulses that can be observed with the microscopes are detected and amplified by the photomultipliers. By pulse-height discrimination and careful laboratory calibration with aerosols of known size and index of refraction, the integral concentration of aerosol particles larger than 0.3 micrometer and 0.5 micrometer in diameter can be determined.

Two photomultipliers were used to enhance the signal-to-noise ratio by requiring coincident events from the two detectors. The background noise for the system was mainly due to Rayleigh scattering from the air molecules in the chamber at low altitude and from cosmic-ray scintillation in the photomultiplier glass at high altitudes. The background was measured approximately every 15 minutes during the flight by passing filtered air through the chamber. For the system used in the Kansas City flight, the background was negligible above a 10-kilometer altitude. Corrections for the background have been used below this altitude. The dustsonde was also equipped with a rawinsonde temperature element for recording the atmospheric temperature profile.

LIDAR

Ground-based lidar measurements were used as part of the ground truth for the experiment. Generally, laser radars operate in the following manner. A Q-switched laser emits a pulse of nearly monochromatic light approximately 30 nanoseconds in duration. Molecules and suspended particulate matter (aerosols) scatter and/or absorb this radiation as the pulse propagates through the atmosphere. A small portion of this light is scattered directly back toward the laser. A receiver composed of mirrors and/or lenses collects this backscattered radiation and diverts it onto a photodetector the output of which is measured as a function of elapsed time after laser emission, or range. The backscattered energy incident on the photodetector is examined spectrally at or near the laser output wavelength with color filters, interference filters, or spectrometers. This enhances the signal-to-noise ratio by reducing unwanted background radiation and determines whether elastic or inelastic techniques will be used.

The lidar measurements for the SAM experiment were provided by the Langley Research Center (LaRC) 122-centimeter (48 inch) laser radar system (fig. 9-3), which consists of two temperature-controlled lasers (ruby and neodymium-doped glass) mounted on either side of an f/10 cassegrainian-configured telescope composed of a 122-centimeter (48 inch) diameter, f/2, all-metal primary and a 25.4-centimeter (10 inch) diameter secondary. The output from the detector package is

recorded by a high-speed data acquisition system. Analog signals are amplified and bandwidth limited, digitized at a 5- or 10-megahertz rate with 8-bit accuracy, and recorded on magnetic tape. A 16-bit-word storage computer is used to control the data acquisition system and to process the data. An X-band microwave radar, coincident with the laser system axis, is used to ensure safe operation in the atmosphere. A rotating shutter reduces laser fluorescence after Q switching. The entire system is mobile and can scan in elevation and azimuth at a slew rate of 1°/sec.

PRELIMINARY RESULTS

The SAM Experiment was designed to observe four events. In the 95th revolution, measurements were made of a sunset observation off the coast of New Jersey (lat. 39° 10' N, long. 72° 45' W)[1] and of a sunrise observation over the Indian Ocean off the coast of Australia (lat. 43° S, long. 99° 55' E). In the 96th revolution, a sunset observation was taken over Kansas City, Missouri (lat. 38° 57' N, long. 95° 06' W), followed by a sunrise observation over the Indian Ocean (lat. 42° 55' S, long. 77° 39' E). The SAM photometer was used to obtain radiometric measurements during each of these four events. Preliminary inversions of the data for two of the events are shown in figure 9-4. Because the final spacecraft ephemeris was only recently received, these data may shift in altitude or be extended in altitude when the final analysis is complete. Notice that the total extinction is greater in the Northern Hemisphere than in the Southern Hemisphere. This difference in aerosol content is believed to be due to the injection of material from the Volcan de Fuego in Guatemala (lat. 14.5° N) that erupted in October 1974. The general meridional circulation of injected mass into the atmosphere would normally be northward at this time of the year. This movement reverses in the summer with the buildup of aerosols in the Southern Hemisphere. This was just beginning at the time of the ASTP mission. The slight difference in altitude of the peak extinction is believed to be due to seasonal differences in the height of the tropopause.

Photographs were made of the first sunrise and the second sunset with the HDC. Figure 9-5 is a composite of several of the photographs taken during the first sunrise and shows the observed refracted images of the solar disk superimposed on a grid showing the horizon and tangent altitudes of the Earth. These photographs confirm that, at spacecraft altitude, the refracted image of the Sun must be a factor in the design of future solar occultation experiments.

Ground-truth data were obtained with the Wyoming dustsonde and the LaRC lidar. Data from the Kansas City balloon flight (lat. 38.8° N, long. 94.7° E) launched on July 21, 1975, at 23:58 GMT are shown in figures 9-6 and 9-7. Figure 9-6 presents the measured temperature profile, and figure 9-7 presents the measured aerosol concentration for particles larger than 0.3 micrometer in diameter. The LaRC lidar system was used during the nights of July 21 and July 22 to obtain laser

---

[1]These are the geometric coordinates of the tangent point of the 0-kilometer high-grazing ray to the Sun.

backscatter measurements of the stratospheric aerosols above Kansas City. Figure 9-8 shows the backscatter ratios[2] obtained during one of these measurements made above Kansas City on July 22 at 04:51 GMT. Note the agreement in the altitude of the peak aerosol concentration obtained by three different techniques.

CONCLUSIONS[3]

The SAM Experiment was performed by the ASTP crewmen as planned. The experiment demonstrated that solar occultation is a viable remote-sensing technique for measuring the vertical concentration of stratospheric aerosols. The solar photographs corroborated the refraction model needed for future solar occultation experiments. The inversion process that was used to reduce the SAM data was confirmed by the agreement with the ground-truth lidar and dustsonde measurements, and these data show that the solar occultation, lidar, and dustsonde data agree in altitude distribution. In addition, the inversions from the SAM Experiment show a significant difference between the Northern and Southern Hemispheres in the peak aerosol concentration, with the Northern Hemisphere having a factor of at least 1.5 greater than that of the Southern Hemisphere.

---

[2]Backscatter ratio is the ratio of total observed backscatter to the Rayleigh backscatter.

[3]Also see section 1.

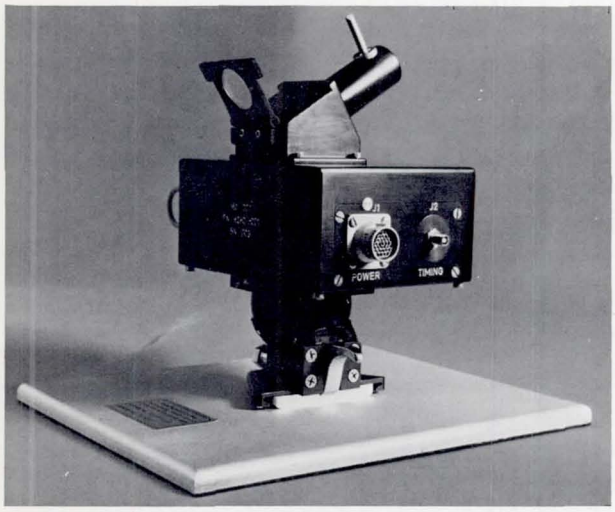

Figure 9-1.- The photometer used for making stratospheric aerosol measurements.

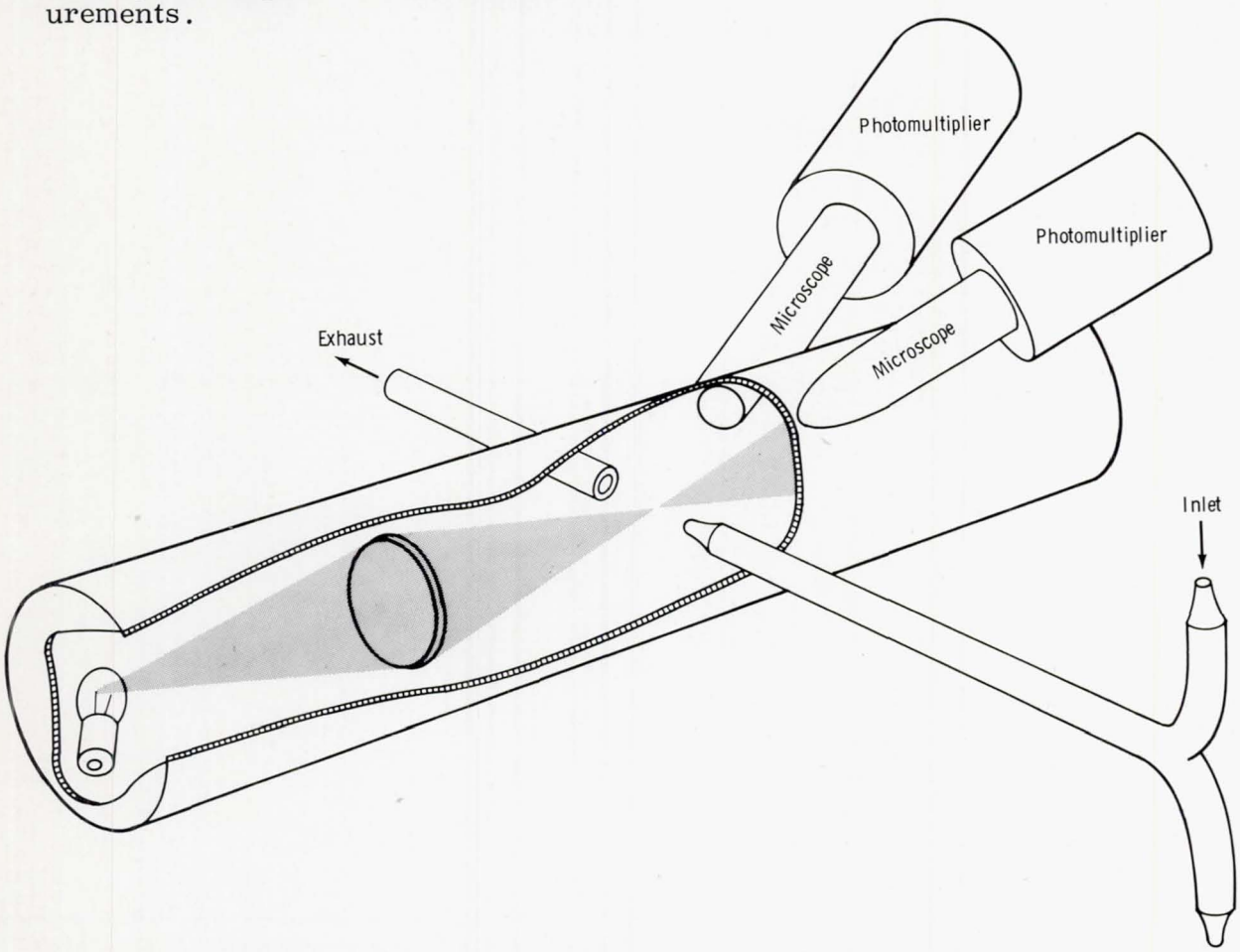

Figure 9-2.- Schematic drawing of the University of Wyoming dustsonde used for ground-truth measurements.

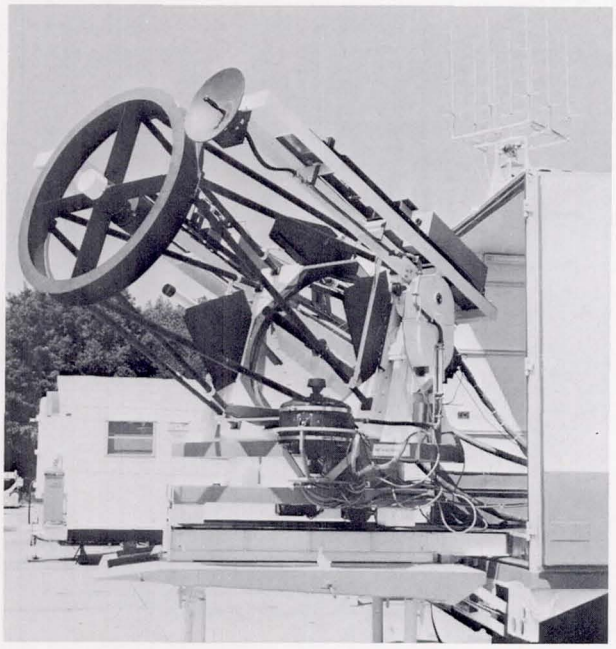

Figure 9-3.- The NASA Langley Research Center 122-centimeter (48 inch) lidar system.

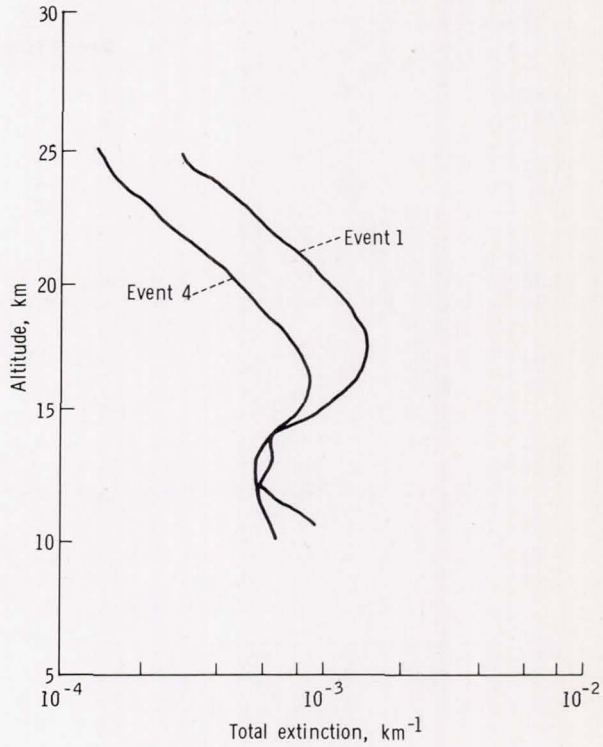

Figure 9-4.- Inverted SAM data of extinction as a function of altitude. Event 1 (lat. 39°10' N, long. 72°45' W) was measured at sunset (07: 04 GMT) on July 22, 1975. Event 4 (lat. 42°55' S, long. 77°39' E) was measured at sunrise (02: 14: 39 GMT) on July 22, 1975.

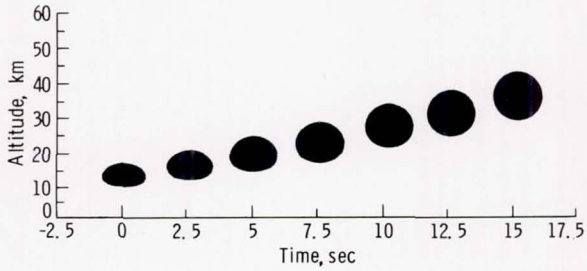

Figure 9-5.- Composite of photographs taken during the first sunset.

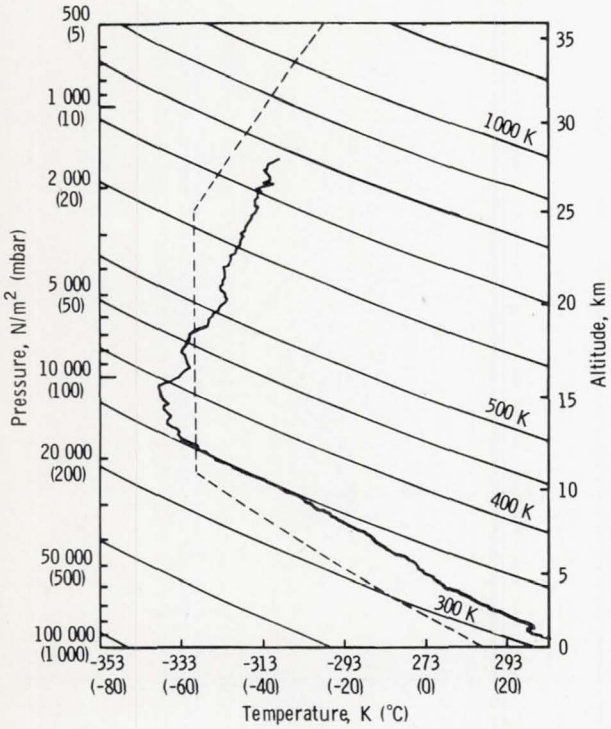

Figure 9-6.- Measured temperature profile above Kansas City, Missouri.

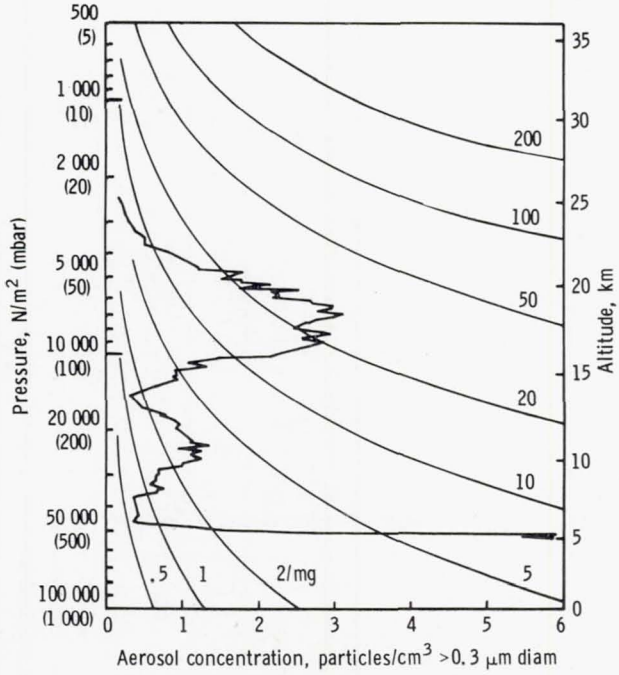

Figure 9-7.- Measured dustsonde aerosol concentration (>0.3 μm diameter) above Kansas City, Missouri. Curved lines indicate moving ratio.

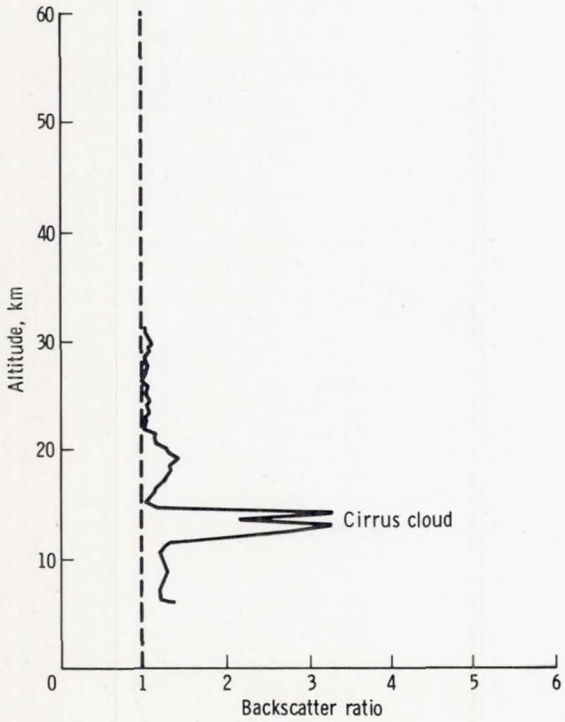

Figure 9-8.- Lidar aerosol profile taken above Kansas City, Missouri, on July 22, 1975, at 04:51 GMT.

10. EARTH OBSERVATIONS AND PHOTOGRAPHY

EXPERIMENT MA-136

Farouk El-Baz[a†] and D. A. Mitchell[a]

ABSTRACT

The Gemini, Apollo, and Skylab missions showed that orbiting astronauts can provide valuable data composed of visual observations and photographs. For this reason, the primary objectives of the Earth Observations and Photography Experiment of the Apollo-Soyuz Test Project were to photograph various terrestrial structures and to use the capabilities of man as a trained observer in visually studying Earth features and phenomena. Man's special capabilities include the sensitivity of the eye to subtle color variations and the speed with which the eye-brain system can interpret what is seen and select targets for photography.

Real-time astronaut observations constitute a useful complement to orbital photographs and greatly aid in their interpretation. Targets for mapping and hand-held photography were selected on the basis of their value to specialists in the Earth sciences including geology, oceanography, desert study, hydrology, meteorology, and environmental science.

INTRODUCTION

Background

The experiences of the Gemini, Apollo, and Skylab Programs proved that scientifically interesting features can be selected and photographed by observers in space. Photographic records of these programs include a plethora of valuable scenes taken from orbital altitudes, both from Earth orbit (e.g., refs. 10-1 to 10-4) and from lunar orbit (e.g., refs. 10-5 to 10-7).

During the Apollo Program, it became apparent that the orbiting astronauts could see more than what was recorded on film. To test this capability, plans were made, beginning with the Apollo 13 crew, to train Moon-bound astronauts to make visual observations. However, because the Apollo 13 mission was aborted, the first attempt at making visual observations from lunar orbit was made on Apollo 14. The results were encouraging (ref. 10-8), and a program was developed for the systematic acquisition of scientifically relevant data on Apollo 15 (refs. 10-9 and 10-10), Apollo 16 (refs. 10-11 and 10-12), and Apollo 17 (refs. 10-13 and

---

[a]National Air and Space Museum, Smithsonian Institution.

[†]Principal Investigator.

10-14). Emphasis was placed on the command module pilot (CMP) of each Apollo mission because he spent more time in lunar orbit than did his crewmates. Also, premission training and data acquisition were limited to the field of lunar geology during the Apollo missions.

The Skylab Program provided the first opportunity to pursue a systematic visual study of the Earth. However, this study was done only on the last of three missions, Skylab 4. Because of the nature of the Earth, the Skylab visual observations program included geology, oceanography, hydrology, meteorology, etc. (ref. 10-15). The long duration of the mission (84 days) allowed repeated observations of the same area and during different seasons. Observations on Skylab 4 and their documentation with photographs proved to be a very worthwhile effort and resulted in significant findings (ref. 10-15). During the Apollo-Soyuz Test Project (ASTP), selected features of interest from the Skylab Earth observations program were reexamined and viewed from a different altitude, 2 years later in time.

Visual Observation Team

To assist in the planning and implementation of the ASTP Earth Observations and Photography Experiment, a team of experts in the fields of geology, oceanography, desert study, hydrology, meteorology, and environmental science was assembled. The Earth observations team (table 10-I) was composed of 42 individuals, including the Principal Investigator (PI) and 12 Co-Investigators (Co-I). The responsibilities of this team of experts and support personnel were as follows.

1. To collect and compile problems to be solved in support of ongoing research in the Earth sciences.

2. To evaluate and select achievable goals based on experience and level of crew training.

3. To recommend and pursue a training program of mutually acceptable procedures and sites.

4. To identify Flight Plan requirements and tools necessary to achieve the objectives.

5. To support the mission operations for nominal and contingency flight plans.

6. To report the results and the possible applications to future space flight.

Earth Observation Sites

The primary objective of the ASTP Earth Observations and Photography Experiment was to use the Apollo and Skylab experiences in acquiring photographs of specific Earth features, processes, and phenomena and in making visual observations from orbit to complement photographic data. Visual sightings are needed because the extensive dynamic range and color sensitivities of the eye cannot be matched by any one film type and also because, in special cases, on-the-scene interpretations of obscured features and phenomena are necessary.

To achieve the primary objective, both photographic mapping and visual observation sites were included in the Flight Plan. A total of 11 mapping sites (table 10-II) and 12 visual observation sites (fig. 10-1) were selected. The 12 visual observation sites were chosen according to geographic localities and included 60 specific targets of prime scientific interest (table 10-III). This method of target identification made it possible for both planners and astronauts to easily discuss and locate targets selected for scientific investigations.

Crew Training

One of the main objectives of the Earth Observations and Photography Experiment was to utilize the capabilities of man as a trained observer in orbit. In accordance with this goal, an extensive training program consisting of classroom sessions and flyover exercises was initiated 1 year before the mission.

Classroom training was conducted by Earth scientists from various disciplines. These specialists briefed the astronauts on the types of Earth features they would observe from orbit. The first lectures on geology, hydrology, oceanography, desert studies, and meteorology consisted of background on theory and familiarization with terminology. Subsequent lectures were scheduled on the basis of crew interest. Other sessions, conducted mainly by the Principal Investigator, covered (1) operational procedures and viewing conditions and constraints and (2) groundtrack familiarization and specific photographic and observational requirements. The crew received approximately 60 hours of classroom training during 20 sessions. A schedule of the training sessions is given in table 10-IV.

The flyover exercises were designed to give the astronauts practical experience in target acquisition and site selection and to familiarize them with the types of features they would observe from Earth orbit. The astronauts were also able to practice verbalizing about and handling onboard equipment, including cameras, lenses, the color wheel, and the tape recorder. Each flyover exercise consisted of a predetermined flight route with a visual observations book designed for that particular flight and similar to the one to be used during the actual mission. Seven high-altitude flyover exercises (table 10-V) were planned over areas of the United States. The California flyover was repeated twice and the Florida flyover once for a total of 10 flyover exercises. During these flights, the astronauts observed both sites scheduled for observation during ASTP and examples of the various types of ocean features and landforms they would view from Earth orbit.

These flyovers were valuable in showing the astronauts how to select the optimum conditions for observations and photography. For example, they found that sunglint was especially important in observing ocean features such as currents, eddies, and internal waves. On land, high Sun angles were best for observing color variations, whereas a low Sun angle enhanced relief and facilitated observations of faults and sand dunes. The flyover exercises gave the crew valuable practice in making visual observations and acquiring photographs.

METHODS AND TECHNIQUES

Photographic Systems

Three types of imaging systems (video, cameras, and scanners) have been successfully used in Earth-orbital surveys. The ASTP photographs of observation and mapping sites were made with a video tape recorder (VTR), a 70-millimeter Hasselblad reflex camera (HRC), a 70-millimeter Hasselblad data camera (HDC), a 35-millimeter Nikon camera (with exposure control), and a 16-millimeter data acquisition camera (DAC).

The 70-millimeter HDC was usually bracket mounted and could accept both 60-millimeter and 100-millimeter lenses. An intervalometer was used, and the frequency of frame usage was calculated to provide stereoscopic coverage with a 60-percent overlap. The HDC was equipped with a reseau plate to improve geometric accuracy and to allow the construction of controlled photomosaics. In general, the photographs obtained with the HDC are excellent, with the exceptions of a few short segments of unplanned photography that were out of focus and one mapping pass over the northeastern United States in which the wrong lens was used.

In addition to mapping strips, photographs of approximately 60 observation sites were made using either the hand-held HRC with the 50- or 250-millimeter lens or the HDC. However, most of the visual observation targets were photographed with the HRC. The HRC has a single lens reflex mechanism that allows the astronaut to see what he is photographing. The crew reported that light loss through the 250-millimeter lens made it difficult to locate the target and to center it within a frame. However, all photographs taken with this lens are excellent. The 16-millimeter DAC was used to acquire photographic data over the western Sahara and to provide a sequential film of color zone transitions in the largest sand sea in the world.

Real-time television transmissions were also scheduled, and images of the daylight portion of revolution 124 over the Pacific Ocean were recorded on the VTR. These color television images of the Earth are potentially capable of providing new data in poorly studied areas and in areas such as the Pacific Ocean, which is too vast for conventional oceanographic surveys. They can give scientists an astronaut's perspective of target acquisition and tracking and also provide imagery that can possibly be reformatted for stereographic and radiometric analysis.

Thirteen magazines of color film were used for the scheduled mapping sites (type SO-242) and observation targets (type SO-368). The SO-368 film was specially coated with the equivalent of a Wratten 2A filter to improve the color sensitivity of the film by eliminating the effects of short wavelengths. Two magazines of type 2443 color infrared film were also used to facilitate identification of features such as volcanic rocks and red tide blooms.

Visual Observation Aids

The human eye-brain system is similar to a camera in that it has a lens and an iris, it generates images with good resolution and geometric fidelity (the resolving power of the unaided human eye is 0.0003 radian or approximately 0.60° (ref. 10-9)), and it is sensitive to electromagnetic radiation in the visible region. Under laboratory conditions, the eye is estimated to be able to distinguish 1×7.5^6 color surfaces, a precision that is 2 to 3 times better than most photoelectric spectrophotometers (ref. 10-16).

The eye can easily distinguish subtle color variations to a greater extent than any commercially manufactured film, but the brain cannot recall these after a given period of time has elapsed. Real-time calibration of desert and water colors was achieved by the use of a two-sided color wheel composed of carefully selected Munsell colors (fig. 10-2 and table 10-VI). These colors can be compared to the photographs to apprise users of the color sensitivity and fidelity of the film. However, the crew indicated that it was sometimes difficult to make good comparisons because variable lighting conditions inside the spacecraft often resulted in the color wheel being in the shade.

To assist in the acquisition and location of visual observation targets, the use of 20-power binoculars was originally planned. However, after the crew tested the binoculars during flyover exercises, a change was made to use a 16-power monocular. The crew believed the monocular would provide a more convenient means of checking the eye's resolution and of locating targets. During postmission evaluation, the astronauts indicated that the usefulness of the spotting scope was curtailed by the speed with which a target passed outside their field of view.

The principal onboard aid was the "Earth Observations Book." This book was divided into three major sections. The first section contained (1) a time line summarizing the visual observation tasks and mapping camera configurations and (2) a stowage list and a review of operational procedures. Information in the second section pertained to specific visual observation targets and was arranged according to site numbers. For each site, there was a summary page with a map showing revolution groundtracks followed by a page (one for each target) that included specific questions, appropriate diagrams and photographs, and camera settings. The last section was a reference appendix that included maps of the distribution of volcanoes, ocean currents, July cloud cover, etc., and diagrams of various Earth features such as drainage patterns, ocean phenomena, dune types, and faults.

Flight Planning

Earth observations and photography mission tasks required approximately 12 hours of crew time. These tasks were planned during 24 revolutions and assigned to specific crewmembers. The task assignments for the mapping sites and the visual observation targets are listed in table 10-VII.

Planning for the ASTP mission also included simulations of real-time activities. The Earth observations team participated in three mission simulations to practice interaction with other Mission Control Center personnel and with the

crew. These proved to be very useful exercises because the need existed for verbal communications with the astronauts during the mission. The Earth observations team supported the mission and was in contact with ground-truth data collection parties on a 24-hour basis throughout the mission.

RESULTS

Ground-Truth Data

During the real-time operations of the ASTP mission, the largest air, sea, and ground support team of any manned mission collected ground truth to expedite the postmission interpretation of orbital observations and photography (fig. 10-3). This support included the acquisition of metric and multispectral photography by high-altitude aircraft. Aerial photography was acquired simultaneously during several ASTP photographic passes to link ground-based studies with Earth-orbital observations. Ocean research vessels obtained data on sea surface temperatures, salinity, water color, current directions, and cloud types and heights. On land, ground-truth teams collected data to support geological, hydrological, and desert research projects in India, Guatemala, Mexico, the United States, and Egypt. A summary of the reported support operations follows.

ANZUS Eddy (site 11D).- The Australian ship Bombard, stationed in the Tasman Sea, surveyed the warm water ANZUS (Australia-New Zealand-United States) Eddy. Oceanographic data indicated that the nearly circular eddy was 145 to 160 kilometers in diameter with surface temperatures 2° warmer than the surrounding water. Ship personnel also reported a cumulus cloud formation over the center of the eddy and a number of trawlers fishing for tuna within the eddy.

Caribbean (site 7G).- To support crew observations and photography of the extent of organic acid outflow from the Orinoco River, the Bellairs Research Institute of McGill University sponsored three cruises from the island of Barbados on July 21, 22, and 23. Observations and measurements were made of sea state, water color, sea surface temperature, salinity, chlorophyll content, cloud cover, and wind speed and direction.

Egypt (sites 9E and M7).- For the revolution 71 mapping pass over Egypt, geologists from the Ain Shams University in Cairo will provide ground-truth data to be used in support of a photogeological investigation of the Western Desert of Egypt. Field work will be carried out at Abu Râwash, Oweinat Mountain, and the Faiyûm, Baharîya, and Farâfra Oases (fig. 10-4). Ground investigations include detailed mapping, characterization of the structural and topographic setting, and studies of desert erosion patterns and grain transportation. The major objective is to use the geological data in verifying color zonation and other features recorded on the ASTP film.

England (sites 6A and 6B).- The Royal Air Force flew a 3-day sequence over ocean waters off southern Ireland and England. Expendable bathythermographs (XBT's) were dropped from the planes to provide data on water temperature as a function of depth.

Gulf of Mexico (site 5A).- The National Oceanic and Atmospheric Administration (NOAA) research vessel Virginia Key made a transect of the Gulf of Mexico from Miami to the Yucatan peninsula and obtained data on the location of the Gulf Loop Current. Approximately 20 NOAA ships were also stationed around the Mississippi River Delta.

New Zealand (site 1).- The Royal New Zealand Air Force flew P-3 airplanes along the revolution 17 groundtrack starting from East Cape, New Zealand, then north-northeast over the Pacific Ocean to obtain photographic data and to plot cloud types and heights. A New Zealand Navy research vessel made a transit along the same line and acquired oceanographic data, including water temperatures and sound velocity measurements.

Strait of Gibraltar (sites 9K and 9J).- The U.S. Navy research vessel Kane obtained oceanographic data along a line paralleling the revolution 73 groundtrack from the Canary Islands to Spain. These data were obtained to support crew observations of a current boundary extending north and south off the western coast of Portugal. The Navy also flew a P-3 aircraft along this line dropping XBT's. East of the strait in the Mediterranean Sea, the carrier U.S.S. Kennedy obtained oceanographic and meteorological data.

United States (sites 2A, 4A, 4B, 5B, 5E, and 5F).- Several high-altitude flights were flown over the United States with a B-57 aircraft based at the NASA Lyndon B. Johnson Space Center and a U-2 aircraft based at the NASA Ames Research Center. Metric and multispectral photography was obtained with a metric RC-10 camera and a multispectral Vinten System A camera. Sensor data are provided in table 10-VIII. Photographic coverage was acquired over the East Coast (coastal areas of New York, Massachusetts, and Maine), Florida (coastal areas), the northwestern United States (Washington, Idaho, and Oregon), and the southwestern United States (from Kingman, Arizona, to Santa Maria, California).

In addition to the aircraft support, ocean research vessels made measurements in the Gulf Stream and along the New England coast. The U.S.S. Preserver collected data in the Gulf Stream north of Jacksonville, Florida, on the distribution, size, and velocities of eddies. The ship also released four drifting buoys that had transmitters to the Nimbus-F satellite. The buoys were positioned about once a day throughout the mission and provided data on current direction and velocity.

In New England, two Bigelow Laboratory research vessels (the Bigelow and the Challange) made a traverse of the Gulf of Maine from Portland to the Bay of Fundy and also southward to Cape Cod. Data were obtained on the size, shape, and location of red water patches due to toxic phytoplankton and included measurements of sea surface temperature, salinity, chlorophyll content, and water color. In addition to the red tide observations off the coast of Maine, support ships and sampling stations of the Commonwealth of Massachusetts acquired water color, salinity, and biological content data. A high chlorophyll content in the coastal waters off New England was reported and was possibly the result of abnormally heavy rains carrying an increased amount of biota into the sea.

Mission Data

A total of 11 mapping passes and 60 visual observation sites was scheduled. Only one mapping pass was canceled (on revolution 15/16) because of problems in the Flight Plan. Approximately 20 percent of the 100 planned observations of the 60 sites were not performed because of bad weather, making the overall success measure of the experiment approximately 80 percent. The summary results of the photographic mapping sites and the visual observation targets are given in tables 10-IX and 10-X, respectively.

DISCUSSION

The quality of photographic data obtained in previous Earth-orbital surveys has firmly established their value as basic tools in the evaluation of terrestrial features and in the reconnaissance of remote locations. Before the ASTP mission, several types of photographic systems were successfully used in spacecraft. On the Skylab missions, the Earth resources experiment package included a multispectral array of six cameras (with various film/filter combinations in the visible and infrared) as well as a high-resolution Earth terrain camera.

Two of the more obvious advantages of such orbital systems over aerial photography are the large regional coverage and the speed with which data can be obtained. These advantages facilitate the preparation of base maps because mosaics of large areas can be rapidly prepared with orbital photographs. The ASTP planning for visual observations and photography utilized these advantages to their maximum. For example, several mapping passes were scheduled over areas where general land surveys (including a classification of terrain, mineral resources, and land use) are either nonexistent or inadequate. Targets were also selected for photography in oceans and deserts, where size and inaccessibility make conventional surveys impractical.

The large regional coverage of orbital photographs also provides a more efficient method for the observation of large-scale phenomena, such as color transitions within deserts and ocean currents. Orbital photographs have a greater perspective and are useful in the study of broad distributions and regional structure; two examples are major fault zones (such as the San Andreas system and the Levantine Rift) and snow cover and drainage patterns (as in the Cascade Mountains). One other advantage is the stability of spacecraft as a platform for Earth-looking photography. Variations in velocity and attitude are minimal and flightpaths can be determined with great precision. The following is a discussion of some of the ASTP tasks and results in the fields of Earth science selected for emphasis on this mission.

Geology

Geological investigations on the ASTP mission included observations of major active fault zones, river deltas, volcanoes, and astroblemes (ancient impact scars). Studies of global tectonic patterns were made by observation and photography of some major areas of continental crustal fracturing. One of these areas

was the Levantine Rift, a fault complex formed as a result of the motion of the Arabian subplate. The crew was asked to observe the northern extensions of this rift and to obtain photographs necessary to an understanding of the locations and mechanisms of displacement. Excellent photographs were obtained of the entire area (e.g., fig. 10-5). The photographs support the theory that motion of the Arabian subplate is counterclockwise drift rather than eastward rotation. Astronaut observations of the area provided additional data:

> The one thing I noticed was that if you look at the 9G map [fig. 10-6], the dotted line on the left up near the end of it, makes a bend to the left and follows a new tectonic line or fault which goes along parallel to the Turkish coast. In other words, the one on the left, number 1, goes up . . . and then makes a left turn and parallels the Turkish coast. Two seems to be obscured and it just ends in a lot of jumbled country up somewhere slightly beyond where the number 2 is, and it seems to end right in this jumbled area. Three, I could trace clear up to a river which - I'll have to see a map later. But I could trace the faults out, going rather eastward. You could see them through the valley silt, clear up to a river which must be inland in either Syria or Turkey. So the overall pattern of these is a fan; three going almost eastward, and one bending finally to the north, and two going to the northeast. (CMP)

Photographs of river deltas were also acquired. In the geologic record, deltaic sediments are often a source of natural gas and oil accumulation; an understanding of the growth of deltas might have applications in the future development of these resources. Several major river deltas were photographed, including the Orinoco (fig. 10-7), Rhone, Nile (fig. 10-8), Fraser, Danube, and Yellow Rivers. These photographs will be compared with previous orbital photographs in an effort to document the rate and direction of growth of modern deltas.

A study was also made of astroblemes, or ancient impact scars, to increase knowledge of the interaction of the Earth and meteoritic bodies and to locate new areas for possible economic exploitation. Photography of this type of feature was obtained in Libya near the Kufra Oasis (fig. 10-9). Resolution was excellent. The central dome and ghost ring of one known feature, the BP structure, were easily recognized. Another circular feature, possibly a twin site, was also identified.

Oceanography

In the field of oceanography, a study was made of major ocean features such as eddies, currents, and internal waves. Because large areas can be rapidly surveyed, the global view of oceans from space is especially useful. As previously stated, extensive ground-truth data collection (fig. 10-3) was coordinated with

photographic passes to aid in postmission data interpretation. Areas of prime scientific interest include the following.

Area	Interest
Coral Sea	Interaction of currents with the Great Barrier Reef Eddies in the Coral Sea
ANZUS Eddy	Support of an Australian-New Zealand-United States oceanographic study of a 200-kilometer-wide eddy east of Sydney, Australia
Caribbean Sea	Ocean currents and their relation to fisheries Eddies and their relation to the Gulf Stream
Gulf of Mexico	Development of the Gulf Loop Current Eddies and currents in the Yucatan Channel
Mediterranean Sea	Observation and photography to support oceanographic study by U.S. Sixth Fleet research team Effects of reduction of freshwater from the Nile River

Investigations of these features will provide a better understanding of dynamic ocean phenomena and will have potential applications to trade, shipping, and the identification of environmental parameters affecting fisheries.

The crewmen remarked that the ease with which oceanographic targets were discerned was a function of several factors; Sun glitter was identified as the most influential parameter. For example, the following remarks concerned the visual identification of internal waves west of the Strait of Gibraltar (fig. 10-10):

> I was looking for all these things and suddenly they popped out within a second right there. Just suddenly when the Sun angle changed, everything was there, the waves and the boundary were all there and we just snapped a series on them. But before that, there was nothing but just solid blue water and then they just suddenly popped . . . You have to be ready and the Sun angle has to be just right. And it's there for just a short period of time and then it's gone. (ACDR)

A study was also made of red tide occurrences off the New England coast. The crew was informed during the mission that support ships off the coast of Maine had located a zone of discolored water near the mouth of the Damariscotta River. This area was observed by the crew, and the DMP later reported:

> Per ground request we just shot a few frames here up through the New England area ending on magazine CX-10 with frame 35. Trying to pick up the red tide around Boothbay, and we did see a lot of red coloration in the water there. However, some of it

looked to me like it was coming out of the river mouths and is really sediment. And I hesitate to term it red tide. We shot some pictures; maybe we can psych it out later.

Examination of the returned photographs suggests that the DMP photographed the area of the Bay of Fundy (fig. 10-11). This area shows the same features that were expected around Boothbay Harbor, mainly discolored reddish water caused by sediments from coastal rivers.

To aid oceanographers in the identification and location of ocean features, the crew was asked to provide the ground-elapsed time (GET) when a target was observed. However, during the postmission debriefings, the crew indicated that time was probably insufficient to identify the exact location of an observed ocean site because they could see such a broad area.

Desert Studies

Deserts occupy nearly one-sixth of the Earth's land masses, but first-order surveys of most desert regions are inadequate. Size, remoteness, and inaccessibility make conventional aerial surveys impractical and costly. Photographs acquired from space, however, can provide reliable data that are useful in the preparation of base maps and in the evaluation of eolian landforms. Orbital images of large areas can be rapidly acquired for the construction of mosaics and for distribution analysis of large-scale phenomena such as color variation and sand dune patterns. As part of the ASTP investigation of deserts and arid lands, visual observations and photography of the following types of features were scheduled.

Feature	Interest
Eolian landforms	Dune shape, size, and distribution Dune patterns and their relation to topography, wind, moisture, and vegetation
Desert color	Color transitions within a homogeneous desert Comparison of equatorial desert color with that of high-latitude deserts
Processes of desertification in the Sahel	Land use Evolution of dune patterns and effect on cultivation

Excellent photographs of deserts in Africa, the Arabian Peninsula, Australia, and Argentina were acquired. Photography over the Sahara is extensive and includes two mapping passes over Algeria, Chad, Libya, and Egypt; a strip of 16-millimeter photography over the western Sahara; and numerous hand-held photographs. This photography will be used in an investigation of eolian geomorphology primarily to evolve a classification scheme for deserts in North Africa. In

addition, a mosaic to be constructed from the mapping photography of Egypt will be used in a study of the Western Desert of Egypt by a team of geologists from Ain Shams University, Cairo.

Synoptic photography and astronaut observations also provided valuable information on desert color. Deserts often contain a significant amount of iron compounds that, because of weathering, oxidize into red-colored ferrous oxides. Photography of color zonation within a desert where the sand is derived from the same source (e.g., fig. 10-12) can be used to determine relative age. The crew used the color wheel to calibrate variations in the color of North African sand seas. During photography of the western Sahara with the 16-millimeter DAC, the DMP made the following observation:

> We discovered a large expanse of fairly homogeneous sand desert. No obvious dune patterns . . . We're now coming to the rocky volcanic hills of the northeast edge of the big sand desert. Some very red sand to the north. In fact, it looks almost like a massive parabolic sand dune, black with red sand behind it. And we're coming up on a large band of very black barren-looking hills with great red areas interspersed between them . . . Okay, and at 119:50, we're coming up into a couple of areas where the dunes are now a little better defined; they look like old domes. They're certainly not stars and they're not linear either. And we get farther into the north, there is a little linear pattern, but it's mostly of dome appearances, very homogeneous.

Excellent photographs of the Simpson Desert in Australia were also obtained (e.g., fig. 10-13). Visual observations were made on several passes over the area, and the crew was able to identify dune patterns and desert color.

> We're going over the Simpson Desert right now. And it's just fantastic. It's got dunes in it, looks like they are very long, and they look like road tracks, there are so many of them - like hundreds of parallel road tracks, it's just plain spectacular. (CMP)

> Yeah, and the long red streaks are matching about color 10, I would say on [the color] wheel and some of those long sand streaks, could have either gone to the 9, between 9 and 10, about like 9A. (ACDR)

In Argentina, the crew photographed a little-known dune field (fig. 10-14) and made visual observations of dune shape and the relation of the dune field to the surrounding topography. The following is an excerpt from the discussion of this occurrence during the postmission crew debriefings.

ACDR Okay, it's right over the edge of the Andes Mountains . . . And you could really see how they were crescents; it looked like occasionally maybe the head of the crescent would wash out, and it would tend to be a linear one with lineations on the side. There are all those other little crescents up on the left. That was the area that you wanted me to look at?

PI Yes, that's the only one that we thought existed. We didn't know that there were two dune fields.

ACDR I'd remembered that there was some type of linear feature. There were two rays. One was on this edge down here, which is nearly linear. But the big thing was those huge crescents; then something else linear caught my eye. I see what it is now, those very minor ones in the center left part of the picture.

Co-I This is a particular variety that I haven't seen anywhere else. I have seen a lot of varieties of this generally crescentic dune pattern, but nothing where you have these linear dunes superimposed right on the crescent and they're oriented in this way. That's totally unlike anything I have ever seen anywhere else, so this really is the prize picture as far as desert dune observations went.

ACDR On that little field up there, it's just the way the boundary was very well defined, as opposed to the other where this kind fades out into like a dry lake bed.

Co-I One of the things that is very obvious is the relationship between the edge of the alluvial fan and the beginning of the dune fields; it's very, very sharp. That's not a very red dune field, is it?

ACDR No, it's not.

Co-I Does it look about like the ones you see in the southwestern United States in terms of color?

DMP I would say so. We had a fairly early morning light.

ACDR I think it's close. We have early morning light there and low Sun angles. It didn't have the redness like the Simpson does or anything like that.

Hydrology

Hydrological investigations included photography of snow cover and drainage patterns as well as visual observations of glaciers, firn lines, and closed water basins. Mapping of snowpack distribution is important in the estimation of the

volume of water reaching drainage systems for use in irrigation and the control of floods. Targets for snow cover photography included the Cascade Mountains in the northwestern United States (fig. 10-15), the Andes Mountains in South America, and the Himalaya Mountains in southern Asia. Coverage of the Cascades and Andes was acquired; however, the Himalayan photography was not successful because of cloud cover.

Visual observations of glaciers and firn lines were also scheduled to test the limits of the eye's resolution. The crew was successful in distinguishing firn lines and remarked that this was a function of both texture and color. The following remarks were made during the postmission debriefings.

CMP The best case, I believe, was in the Alberta-British Columbia area. I very easily saw a firn line on one big glacier up there.

PI How did you make the distinction? Why do you think you were able to see that? Because of color or texture?

CMP Texture and color and even shininess, you might say. Surface texture, I guess.

PI The ice being more gray?

DMP Kind of a gray compared to pure white.

ACDR Yes, it goes from white to gray. And the firn line wasn't just a straight line; it was kind of jagged. It wasn't a clear line.

DMP But I thought I could see texture down below it also, that sort of looked like flow patterns going parallel with the glaciers.

A study was also made of major lakes including Lake Chad, the Great Salt Lake, Lake Eyre, and the Caspian Sea. Lake Chad, once one of Africa's largest lakes, lies in the Sahel region between the savanna land and the sandy desert. To the northeast, it is bounded by fossil dunes; from the south, tropical rivers flow into the lake, bringing sediment and freshwater. The rapid decrease in lake size has been attributed to three factors: the influx of sand from the Sahara, the accumulation of sediments deposited by inflowing rivers from the south, and the evaporation of surface waters.

The possibility that Lake Chad might eventually dry up presents a problem because the southern part of the lake is biologically productive and rich in fish. The ASTP photography will be compared to Skylab data to determine the rate of change in the size of Lake Chad. Many more dunes are now visible within the lake (fig. 10-16).

The ASTP photography of the Great Salt Lake in the United States will also be compared to Skylab imagery. Construction of a railroad causeway in 1956 has essentially divided the lake into two basins. Almost 90 percent of the lake's inflow now enters the southern half, resulting in a rise in water level and a decrease in salinity in that half. Conversely, waters in the northern basin have become oversaturated with salts and minerals. This change in salinity is easily detected from orbit because the presence of different types of algae has given each half a different color. These factors have had a serious effect on both the ecology of the lake region and industrial development.

Meteorology

Meteorological investigations were made in a study of cloud features and tropical storms. Photography of cloud features includes Bénard cells, Kármán vortices, mountain waves (rotor clouds), atmospheric bow waves in the lee of islands, and cumulonimbus buildups. The crew also obtained photography of a developing tropical storm in the Caribbean Sea. The following is an excerpt of real-time observations over the storm:

> It doesn't seem to cover so much area, but it does have a rather swirling "V" appearance. I don't see an eye, but I can see where an eye would be. (CMP)

Photographs and visual observations will help meteorologists develop computer models of hurricanes and tropical storms. Stereophotographs of a dissipating storm were also taken and will be used in making a three-dimensional stereoscopic model of the storm to help decipher its "topography." The stereoscopic model in turn will affect theoretical models of storm development and dissipation. Excellent photography of thunderstorms was also acquired and will be used in studies of severe storm development (fig. 10-17).

Unusual photographs of large-scale intersecting cloud streaks were obtained (fig. 10-18). During postmission debriefings, the crew reported that these features were too large to be contrails and had a wedge-shaped appearance:

DMP We saw an awful lot of contrails over the North Atlantic and it's nothing like that. They just don't get that big.

CMP Contrails were lines; these are wedges practically.

QUERY Remember from Skylab, when they took a picture and they thought it was the hot air coming from a ship going through a very low scattered deck about like that, and there was a plume going right across the apparent trend of the clouds. Do you think that maybe that was this same thing?

CMP It's a possibility, I suppose, but at the time it looked natural.

Environmental Studies

Environmental investigations included photography of sources of atmospheric and water pollution and potential sites for sea farming. The crew recognized and observed several different sources of atmospheric pollutants, both manmade and natural. These sources included volcanic plumes, duststorms in the Sahara and the U.S.S.R., brush fires in Africa, oil fires in the Middle East, ship trails, and contrails. Astronaut observations were useful in determining the extent and geographic locations of these features.

Sources of water pollution include suspended sediments, oil spills, and organic compounds. The occurrence of two types of water pollution was documented with photography of the Orinoco River Delta (fig. 10-7). In addition to sediments, the Orinoco River outflow includes a high concentration of humic compounds that result in the discoloration of the ocean waters for hundreds of kilometers. The ASTP information, combined with real-time ground-truth data collection, will allow a better understanding of this phenomenon and its effect on local fisheries.

In cooperation with the International Maritime Commission, observations of oil slicks in North Atlantic ship routes were planned, but cloud cover and the lack of sunglint prevented the acquisition of data. However, observations were made and photographs were taken of oil slicks in the Mediterranean Sea and the Persian Gulf.

The crew was also asked to observe and photograph several areas designated by Jacques Cousteau as potential sites for "sea farming." Three sites were scheduled in real time and included the Adriatic Sea, the waters south of Cuba, and the Strait of Georgia.

CONCLUSIONS

Preparation and execution of the ASTP Earth Observations and Photography Experiment was a highly rewarding experience. The many hours spent in training the crew, both in flyover exercises and in the classroom, brought significant results that attest to the value of man in space flight. The astronauts are enthusiastic about their contributions, and the participating scientists have a considerable amount of new data to be interpreted and analyzed. This analysis will further our vistas in numerous fields of Earth science.

From the results of this experiment, several conclusions can be drawn in regard to the most tangible scientific results and the role of man in space.

Tangible Scientific Results

Evaluation of the scientific return of ASTP observations of the Earth has just begun. It is difficult, at this stage, to determine the most significant contributions. The following are only examples of what has been learned in the considered fields of Earth science.

Geology.- Although many fault systems were studied from orbit, the observations and photographs of the Levantine Rift zone are most prominent. Three major faults were traced to their northernmost extremities where very little was known about them. These faults appear to branch out in north and northeast directions. Branching appears to start at a pivot point for the counterclockwise rotation of the Arabian crustal subplate relative to the African crustal plate. This indicates that fractures in that zone are not simply the result of a rip-apart motion but a complex rotation of the entire Arabian peninsula. The results of detailed mapping of these faults from the ASTP data will add significant insight into the tectonic regime of the Middle East.

Oceanography.- One of the most significant ASTP findings establishes that ocean features such as eddies and internal waves are more common than previously thought. The ASTP crew also established that viewing direction, as well as Sun angle, is extremely significant in observing internal waves. Viewing conditions will be thoroughly documented to allow better planning and preparation for similar activities in the future.

Deserts.- Perhaps the most significant contribution of the experiment is that the ASTP data will help define (1) relative ages of desert areas based on color and (2) direction of desert growth using sand dune patterns in North Africa. The implications of these results, particularly to the African drought problem, include the ability to distinguish, from photographs, areas of recent desert formation and to establish the directions of desert growth. Also, two new unique patterns of dune morphologies were observed: star dunes atop linear dunes in the Gobi Desert and a fish-scale pattern of dense sand dunes overlain by thin linear dunes in Argentina.

Hydrology.- Snow cover over the Cascade Mountains was photographed on separate days to permit studies of melt patterns. These photographs will also be compared to previous images of the same area to establish trends in snow accumulation and melting for hydrological projects.

Meteorology.- The most significant result in the field of meteorology appears to be the photography of a developing storm northeast of Florida and of a dissipating storm over the Atlantic Ocean. Stereoscopic models of these storms will be studied to improve theoretical models of tropical storm development and dissipation.

Environment.- The outflow of the Orinoco River into the Atlantic Ocean was described, and the observations were documented with photographs. In addition to sediments, the Orinoco River outflow includes an unusually high concentration of humic compounds that result in the discoloration of the ocean waters for hundreds of kilometers. The ASTP information combined with real-time ground-truth data collection will allow a better understanding of this phenomenon.

Role of Man in Space

From the ASTP experience, the following conclusions may be made.

1. Man in space can help design instruments or film to be used on unmanned probes. An example is the use of a color wheel to establish the actual range of visible colors of deserts and oceans.

2. A trained observer is probably essential to the study of features and phenomena characterized by transient visibility. An example is internal waves that are visible only under very restricted conditions.

3. An observer in orbit can make immediate interpretations that significantly contribute to solving the problem under investigation; for example, the explanation of the tectonic setting of the Levantine Rift area.

4. A human observer is essential if the purpose of the study is to explore the unknown. A trained observer will scan an entire region and select targets for photography that will draw attention to the significant aspects.

5. From the information learned about deserts on this mission, it is concluded that much more can yet be attained from orbital surveys in this field. Desert study will also be important in comparative planetological studies; many of the features of Mars are similar to those of the Earth's deserts.

6. Earth observations and photography tasks require a flexible platform where viewing angles and interior lighting conditions can be controlled. The design of instrumentation should allow control of imaging systems by the observer.

7. For the successful performance of Earth observations tasks, the observer must be well prepared and well trained. The exercise must be pursued systematically; otherwise, significant features and phenomena may be overlooked.

REFERENCES

10-1. Earth Photographs From Gemini III, IV, and V. NASA SP-129, 1967.

10-2. Earth Photographs From Gemini VI through XII. NASA SP-171, 1968.

10-3. Cortright, Edgar M., ed.: Exploring Space With a Camera. NASA SP-168, 1968.

10-4. Lowman, Paul D., Jr.: The Third Planet. Weltflugbild. Reinhold A. Muller (Zurich, Switzerland), 1972.

10-5. Musgrove, R. G.: Lunar Photographs From Apollos 8, 10, and 11. NASA SP-246, 1968.

10-6. Kopal, Zdenek: A New Photographic Atlas of the Moon. Taplinger Publishing Co. (New York), 1971.

10-7. El-Baz, Farouk: New Geological Findings in Apollo 15 Lunar Orbital Photography. Proceedings of the Third Lunar Science Conference, vol. 1, MIT Press (Cambridge, Mass.), 1972, pp. 39-61.

10-8. El-Baz, Farouk; and Roosa, S. A.: Significant Results From Apollo 14 Lunar Orbital Photography. Proceedings of the Third Lunar Science Conference, vol. 1, MIT Press (Cambridge, Mass.), 1972, pp. 63-83.

10-9. El-Baz, Farouk; and Worden, A. M.: Visual Observations From Lunar Orbit. Sec. 25, Part A, of the Apollo 15 Preliminary Science Report. NASA SP-289, 1972.

10-10. El-Baz, Farouk; Worden, A. M.; and Brand, V. D.: Astronaut Observations From Lunar Orbit and Their Geologic Significance. Proceedings of the Third Lunar Science Conference, vol. 1, MIT Press (Cambridge, Mass.), 1972, pp. 85-104.

10-11. Mattingly, T. K.; El-Baz, Farouk; and Laidley, Richard A.: Observations and Impressions From Lunar Orbit. Sec. 28 of the Apollo 16 Preliminary Science Report. NASA SP-315, 1972.

10-12. Mattingly, T. K.; and El-Baz, Farouk: Orbital Observations of the Lunar Highlands on Apollo 16 and Their Interpretation. Proceedings of the Fourth Lunar Science Conference, vol. 1, MIT Press (Cambridge, Mass.), 1973, pp. 49-56.

10-13. Evans, R. E.; and El-Baz, Farouk: Geological Observations From Lunar Orbit. Sec. 28 of the Apollo 17 Preliminary Science Report. NASA SP-330, 1974.

10-14. El-Baz, Farouk; and Evans, R. E.: Observations of Mare Serenitatis From Lunar Orbit and Their Interpretation. Proceedings of the Fourth Lunar Science Conference, vol. 1, MIT Press (Cambridge, Mass.), 1973, pp. 139-147.

10-15. Kaltenbach, J. L.; Lenoir, W. B.; McEwen, M. C.; Weitenhagen, R. A.; and Wilmarth, V. R., eds.: Skylab 4 Visual Observations Project Report. NASA TM X-58142, 1974.

10-16. Committee on Colorimetry: The Science of Color. The Optical Society of America (Washington, D.C.), 1963, p. 129.

TABLE 10-I.- EARTH OBSERVATIONS TEAM

Name	Discipline	Affiliation
J. R. Apel	Oceanography	National Oceanic and Atmospheric Administration (NOAA)
J. C. Barnes[a]	Snow mapping	Environmental Research and Technology, Inc.
P. G. Black[a]	Meteorology	NOAA
G. Borstad	Oceanography	Bellairs Research Institute, McGill University, Canada
C. S. Breed[a]	Deserts	Museum of North Arizona and U.S. Geological Survey (USGS)
N. S. Brill	Red tide	Commonwealth of Massachusetts
W. J. Campbell[a]	Hydrology	University of Puget Sound
R. Citron	Short-lived phenomena	Smithsonian Institution
J. Cousteau	Sea farming	Cousteau Society
R. Dietz[a]	Marine geology	NOAA
L. Dunkelman	Atmosphere	University of Arizona and Goddard Space Flight Center (GSFC)
F. El-Baz[b]	General	Smithsonian Institution
G. Ewing	Oceanography	Woods Hole Oceanographic Institute
R. K. Holz	Demography	University of Texas at Austin
W. A. Hovis	Oceanography	GSFC
R. C. Junghans	Environment	NOAA
J. L. Kaltenbach	Skylab results	Lyndon B. Johnson Space Center (JSC)
W. B. Lenoir	Skylab results	JSC
N. H. MacLeod	Deserts and Agriculture	American University
G. A. Maul[a]	Oceanography	NOAA
M. C. McEwen	Skylab results	JSC
E. D. McKee[a]	Deserts	USGS
S. McLafferty	General	Smithsonian Institution
D. A. Mitchell	General	Smithsonian Institution
J. A. Murphy	General	Smithsonian Institution
W. R. Muehlberger[a]	Geology	University of Texas at Austin

[a]Co-Investigator.

[b]Principal Investigator.

TABLE 10-I.- Concluded

Name	Discipline	Affiliation
K. M. Nagler	Weather patterns	NOAA
D. K. Odell	Oceanography	University of Miami
D. M. Pirie	Oceanography	Army Corps of Engineers, California
P. R. Pisharoty[a]	Hydrology	Indian Space Research Organization (ISRO), India
D. E. Pitts	Color Science	University of Houston
R. O. Ramseier	Hydrology	Department of the Environment, Canada
J. W. Sherman	Meteorology	NOAA
L. T. Silver[a]	Geology	California Institute of Technology
R. E. Stevenson[a]	Oceanography	Scripps Institute of Oceanography
F. M. Suliman	Deserts	College of Education, Qatar
G. A. Swann	Geology	USGS
V. R. Wilmarth	Skylab results	JSC
R. Wolfe	General	Smithsonian Institution
S. P. Vonder Haar	Oceanography	University of Southern California
C. Yentsch[a]	Red tide	Bigelow Laboratory, Maine
M. Youssef	Deserts	Ain Shams University, Egypt

[a]Co-Investigator.

TABLE 10-II.- PHOTOGRAPHIC MAPPING SITES

Site	Name	Objective
M1	Gulf Stream	The Gulf Loop Current and the Gulf Stream from eastern Florida to its confluence with the Labrador Current
M2	New Zealand	The Alpine Fault in South Island and the coastal waters between the two islands and north of North Island
M3	Southern California	Coastal waters off California, the San Andreas Fault system, and the Mohave Desert
M4	Himalaya Mountains	Ocean features in the Indian Ocean and Arabian Sea, the flood plain of the Indus River, drainage patterns, and snow cover in the Himalayas
M5	Arabian Desert	The Afar Triangle, dune patterns in Ar-Rub Al-Khali, and coastal processes at Doha, Qatar
M6	Australia	Dune patterns and erosional features in the Simpson Desert, the Great Barrier Reef, and eddies in the Coral Sea
M7	African drought	Vegetation and land use patterns in the Sahel, desert colors in northeastern Africa, the Nile River Delta, and the Levantine Rift
M8	Falkland Current	The Falkland Current and its confluence with the Brazil Current east of South America
M9	Sahara	Vegetation and land use patterns in the Sahel, desert colors and dune patterns in the Sahara, and the coastal waters off Tripoli
M10	Northern California	Coastal waters off northern California and subsystems of the San Andreas Fault
M11	New England	Eddies and gyres in the Gulf of Mexico, the Mississippi River Delta, Chesapeake Bay, and coastal waters off New England

TABLE 10-III.- VISUAL OBSERVATION TARGETS

Site no.	Target
1	New Zealand
2	Southwestern United States
	2A Southern California
	2B Baja California
	2C California Current
	2D Great Salt Lake
	2E Guadalajara
3	Weather Belt
	3A Cloud features
	3B Tropical storms
	3C Hawaii
	3D Kuroshio Current
4	Northern North America
	4A Snow peaks
	4B Puget Sound
	4C Superior iron
	4D Sudbury nickel
5	Eastern North America
	5A Gulf of Mexico
	5B Gulf Stream
	5C Labrador Current
	5D Central American structures
	5E Florida red tide
	5F New England red tide
	5G Chesapeake Bay
6	Northern Atlantic
	6A Oil slicks
	6B London
7	Northern South America
	7A Humboldt Current
	7B Nazca Plain
	7C Internal waves
	7D Peruvian desert
	7E Orinoco River Delta
	7F Galapagos Islands
	7G Caribbean Sea
8	Southern South America
	8A Falkland Current
	8B Chilean Andes
	8C Dune field
	8D Paraná River
	8E Circular structures
9	Africa and Europe
	9A Afar Triangle
	9B Arabian Peninsula
	9C Guinea Current
	9D Desert colors
	9E Oweinat Mountain
	9F Nile Delta
	9G Levantine Rift
	9H Niger River Delta
	9I Algerian Desert
	9J Tripoli
	9K Strait of Gibraltar
	9L Alps
	9M Danube Delta
	9N Anatolian Fault
	9O Volcanics
	9P Bioluminescence
10	Africa and India
	10A Great Dike
	10B Somali Current
	10C Arabian Sea
	10D Himalaya Mountains
	10E Takla Makan Desert
11	Australia
	11A Playas
	11B Coral Sea
	11C Simpson Desert
	11D ANZUS Eddy
12	Antarctican ice
	12A Icebergs

TABLE 10-IV.- CLASSROOM TRAINING

Date	Subject	Lecturer
Aug. 5, 1974	Plan for Earth observations and photography	F. El-Baz
Aug. 16	Global tectonics and astroblemes	R. Dietz
Oct. 10	Background, terminology, and Skylab 4 results (oceanography)	S. P. Vonder Haar
Oct. 18	Snow and ice	J. C. Barnes, W. J. Campbell, and R. O. Ramseier
Nov. 6	Southwest U.S. tectonics Site selection procedures	L. T. Silver F. El-Baz
Nov. 15	Ocean currents and eddies Sites for observation	G. A. Maul R. E. Stevenson and G. Ewing
Dec. 3	African rift system and Central America	W. R. Muehlberger
Dec. 20	Deserts and sand dune patterns	E. D. McKee and C. S. Breed
Jan. 7, 1975	Cloud features and tropical storms	P. G. Black
Jan. 31	Groundtracks and sites	F. El-Baz
Mar. 5	Onboard site book	F. El-Baz
Mar. 18	Visual observation sites	F. El-Baz
Mar. 19	Ocean observation tasks	Oceanography Team
Apr. 1	Groundtracks and sites	F. El-Baz
Apr. 9	Groundtracks and sites	F. El-Baz
May 20	Review of observation tasks	F. El-Baz
June 2	Review of observation tasks	F. El-Baz
June 20	Review of observation tasks	F. El-Baz
July 8	Review of observation tasks	F. El-Baz
July 13	Review of observation tasks	F. El-Baz

TABLE 10-V.- FLYOVER EXERCISES

Flyover	Observation targets
Houston to Los Angeles	Texas coastal plain Karst topography Basin and range topography Volcanic features Sonora and Mohave Deserts (site 2A) San Andreas Fault system (site 2A)
California	San Andreas Fault (site 2A) Garlock Fault (site 2A) Desert varnished hills (site 2A) Sand dunes in the Algodones Desert Ocean features in waters off California (site 2A)
Gulf Coast	Coastal sediments Mississippi River Delta Gulf Loop Current (site 5A) Red tide off the western coast of Florida (site 5E)
Florida	Gulf Stream (site 5B) Red tide (site 5E)
East Coast	Gulf Stream (site 5B) Sediment and pollution in Chesapeake Bay (site 5G) Internal waves Sand dunes on Cape Cod Red tide off Massachusetts and Maine (site 5F)
Southwestern United States	Dune patterns at White Sands and Great Sand Dunes National Monuments Circular structures in the San Juan Mountains Copper mines
Northwestern United States	Fault systems in northern California (site 2C) Metamorphic foothills of the Sierra Nevadas (site 2C) Snow-covered peaks in Washington (site 4A) Blue Glacier and Southern Cascades Glacier Sediments in Puget Sound

TABLE 10-VI.- MUNSELL COLOR DESIGNATIONS[a]

OF THE ASTP COLOR WHEEL

Color wheel no.	Desert colors[b]		Color wheel no.	Ocean colors[c]	
	A	B		A	B
1	2.5R 6/6	2.5R 7/8	28	10BG 4/4	10BG 5/6
2	2.5R 5/8	2.5R 6/10	29	10BG 5/4	10BG 6/6
3	5R 4/10	5R 5/12	30	10BG 6/4	10BG 7/6
4	5R 5/8	5R 6/10	31	2.5B 6/6	2.5B 7/8
5	5R 6/6	5R 7/8	32	2.5B 5/6	2.5B 6/8
6	7.5R 6/6	7.5R 6/8	33	2.5B 4/6	2.5B 5/8
7	7.5R 5/8	7.5R 6/10	34	5B 4/4	5B 5/6
8	7.5R 4/10	7.5R 5/12	35	5B 5/4	5B 6/6
9	10R 4/8	10R 5/10	36	5B 6/4	5B 7/6
10	10R 5/6	10R 6/8	37	7.5B 6/6	7.5B 7/8
11	10R 6/4	10R 7/6	38	7.5B 5/6	7.5B 6/8
12	2.5YR 7/6	2.5YR 8/8	39	7.5B 4/6	7.5B 5/8
13	2.5YR 6/8	2.5YR 7/10	40	10B 4/8	10B 5/10
14	2.5YR 6/10	2.5YR 6/12	41	10B 5/6	10B 5/8
15	5YR 5/8	5YR 6/10	42	10B 6/6	10B 6/8
16	5YR 6/6	5YR 7/8	43	2.5PB 5/6	2.5PB 6/8
17	7.5YR 6/6	7.5YR 7/8	44	2.5PB 4/6	2.5PB 5/8
18	7.5YR 5/8	7.5YR 6/10	45	2.5PB 3/6	2.5PB 4/8
19	10YR 5/6	10YR 6/10	46	5PB 3/8	5PB 4/10
20	10YR 6/6	10YR 7/8	47	5PB 4/8	5PB 5/10
21	10YR 7/4	10YR 8/6	48	5PB 5/6	5PB 6/8
22	2.5Y 8/6	2.5Y 8.5/6	49	7.5PB 5/8	7.5PB 6/10
23	2.5Y 8/4	2.5Y 7/4	50	7.5PB 4/10	7.5PB 5/12
24	7.5YR 8/4	7.5YR 7/4	51	7.5PB 3/10	7.5PB 4/12
25	2.5YR 8/4	2.5YR 7/4	52	5P 2.5/4	5P 3/10
26	7.5R 8/4	7.5R 7/4	53	5RP 2.5/4	5RP 3/6
27	2.5R 8/4	2.5R 7/4	54	5R 2.5/4	5R 3/4

[a]Each designation indicates hue, value, and chroma in the form H V/C. Hue is divided into 10 groups (red, yellow-red, yellow, green-yellow, green, blue-green, blue, purple-blue, purple, and red-purple); each group is further subdivided by use of numerals (2.5, 5, 7.5, and 10 for the ASTP color wheel). Value is specified on a numerical scale from 1 (black) to 10 (white). Chroma is indicated numerically from 0 to 12 (for the ASTP color wheel).

[b]See fig. 10-2(a).

[c]See fig. 10-2(b).

TABLE 10-VII.- MISSION TASK ASSIGNMENTS

Revolution	Mapping tasks		Visual observation tasks	
	Site	Crewmember (a)	Site	Crewmember (a)
15	M1	ACDR	5A, 5B, 5C	DMP
17	M2, M3	DMP	12A, 1, 3A, 2A, 4C, 5C	CMP
39	M4	DMP	10A, 10B, 10C, 10D, 10E	DMP
40	M5	DMP	9A, 9B	DMP
42			8A, 3A, 9H, 9I, 9J	DMP
45			5D, 5A, 5E, 5F, 5C	DMP
46			2E, 4D	CMP
64	M6	ACDR	11C, 11B, 3A	CMP
71	M7	DMP	9C, 9D, 9E, 9F, 9G	CMP
72	M8, M9	ACDR	12, 8A, [b]9H, [b]9I, [b]9J	DMP
73			3A, 9K, 9L	ACDR
74			7B, 7C, 6A, 6B	ACDR
78			3C, 4A	DMP
79			11A, 11B, 3A	DMP
88			8B, 8C, 8D, 8E, 3A, 9K, 9L	ACDR
90			5D, 5A, 5E, 5G, 5F, 5C, 6A, 9P	DMP
104			7A, 7D, 7E	ACDR
106			3B, 2B, 2E, 4D	CMP
107	M10	CMP	2C, 2D	CMP
108			3C, 4B	CMP
123			11D	DMP
124			4A, 4C, 4D	CMP
134			7F, 7G, 6A, 6B, 9M, 9N, 9P	ACDR
135	M11	DMP	3B, 5A, 5G, 5F, 6A, 9L, 9O, 9P	CMP

[a]ACDR, Apollo commander; DMP, docking module pilot; CMP, command module pilot.
[b]DAC.

TABLE 10-VIII.- AIRCRAFT SUPPORT SENSOR DATA

Sensor type	Lens focal length, cm (in.)	Film type	Filtration	Spectral band, nm	Percent of overlap
Vinten	4.45 (1.75)	Panatomic-X, 3400	Schott GG 475 and Schott BG 18	475 to 575	60
Vinten	4.45 (1.75)	Panatomic-X, 3400	Schott OG 570 and Schott BG 38	580 to 680	60
Vinten	4.45 (1.75)	Infrared Aerographic, 2424	Schott RG 645 and Corning 9830	690 to 760	60
Vinten	4.45 (1.75)	Aerochrome Infrared, 2443	Wratten 12	510 to 900	60
RC-10	15.24 (6)	Aerial color, SO-242	2.2AV	400 to 700	60

TABLE 10-IX.- PHOTOGRAPHIC MAPPING RESULTS

Mapping pass	Description	Remarks
M1 Gulf Stream	Fracture pattern of a micro-crustal plate that includes the Yucatán Peninsula Eddies and currents in the Yucatan Channel Red tide off western coast of Florida Eddies and gyres of Gulf Stream	Mapping camera photography was canceled on revolution 15/16 because of Flight Plan problems.
M2 New Zealand	Photography of Alpine Fault Internal waves Plankton blooms Eddies in South Pacific	Alpine Fault photography was not successful because of cloud cover; however, all other objectives were achieved.
M3 Southern California	Ocean water color Red tide off coast of California Subsystems of San Andreas Fault Desert colors and processes in the Mohave Desert	The ocean part of the mapping strip was partly cloudy; excellent photography was obtained of the land part.

TABLE 10-IX.- Continued

Mapping pass	Description	Remarks
M4 Himalaya Mountains	Shoreline processes at Zambezi River Delta margin Sediment plumes in Somali Current Ocean currents in Arabian Sea Flood plains of the Indus River Drainage patterns of foothills of Himalayas Photography of snow cover	Excellent photography was acquired over the Indian Ocean and Arabian Sea; however, most of India (and particularly the Himalayas) was completely cloud covered.
M5 Arabian Desert	Afar Triangle Structures on border of Red Sea rift Dune patterns in Ar-Rub Al-Khali Coastal processes at Doha, Qatar	Scattered clouds covered the western part of the Afar Triangle, but the weather was clear from eastern Afar to Qatar and good photography was acquired.
M6 Australia	Playas in the Lake Eyre region Dune patterns in Simpson Desert Great Barrier Reef Eddies in the Coral Sea	The weather was good all along the revolution 64 groundtrack, and excellent photographs of Australia and the Coral Sea were obtained.

TABLE-10-IX.- Continued

Mapping pass	Description	Remarks
M7 African drought	Guinea Current Lake Chad region, vegetation and land use patterns Desert colors in northeastern Africa Sand dune patterns and their relation to vegetation and wind Nile River Delta Levantine Rift: structures of Golan Heights and southern Turkey	Photography of the Guinea Current was not successful because of cloud cover; however, the weather was clear from Lake Chad to the Levantine Rift and excellent photographs were obtained.
M8 Falkland Current	Continental-shelf waters Falkland Current and its relationship to fisheries	The spacecraft attitude for this pass was not nominal and resulted in oblique photography with the horizon occupying much of the frames.
M9 Sahara	Niger River Delta: dune patterns and land use of the Inland Delta for comparison with Skylab data on the Sahel Desert color and relation to age Desert dunes and their relation to topography, moisture, and vegetation Coastal processes at Tripoli Eddies in waters between Tripoli and Sicily	South of the Niger River Delta, cloud cover obscured much of the terrain, but the weather was clear north of the delta. Photographs of the Sahara are slightly overexposed, but those over the land-water interface at Tripoli are excellent.

TABLE 10-IX.- Concluded

Mapping pass	Description	Remarks
M10 Northern California	Ocean water color Red tide occurrences Subsystems of San Andreas Fault Metamorphic foothills of Sierra Nevadas	Photographs of northern California are good, although some frames are slightly over-exposed.
M11 New England	Mexican volcanoes Sediment patterns in Gulf of Mexico waters Eddies and gyres in Gulf of Mexico Mississippi River Delta Potomac River pollution Red tide occurrences off coast of Massachusetts and Maine	Mapping pass photography on revolution 135/136 is out of focus, probably because the 80-mm lens (used for the electrophoresis experiment) was substituted for the 60-mm lens.

TABLE 10-X.- VISUAL OBSERVATION RESULTS

Target designation		Description	Remarks
1	New Zealand	Alpine Fault photographs Internal waves between North and South Islands Plankton blooms Pacific water color	The Alpine Fault was cloud covered, but visual observations of ocean waters northeast of New Zealand were recorded. The color wheel was used, and the crew reported that the ocean color was close to 47-B.
2A	Southern California	Current boundaries Red tide off coast Gran Desierto color Desert varnished hills	Cloud cover obscured much of the ocean, but interesting cloud waves were observed in the lee of the Channel Islands. A color wheel reading of 16-A was given to the Gran Desierto.
2B	Baja California	Pacific water color Bahía Concepción Fault Internal waves in Gulf of California Gray rock exposures	Oblique photographs were obtained over the Baja peninsula, but there were no crew comments.
2C	California Current	Pacific water color Faults west of San Andreas Foothill metamorphic range	There was some cloud cover over the ocean, but a color reading of 47-B was taken for the coastal waters just offshore from San Francisco.

TABLE 10-X.- Continued

Target designation		Description	Remarks
2D	Great Salt Lake	Bonneville track Color boundaries and sediment plumes in lake Bingham copper mine Snow cover on the Wasatch Range	Excellent photographs of the Great Salt Lake were acquired. In addition, the crew reported that the Bonneville track could be easily detected.
2E	Guadalajara	Major fault lines Big Bend structures	No visual observations were made or photographs taken of the Guadalajara area; however, good photography was obtained of a part of the Mexican volcanic belt southeast of Guadalajara.
3A	Cloud features	Photographs of convective clouds	A number of excellent photographs were obtained including Benard cells, atmospheric bow waves, rotor clouds, and severe thunderstorms.
3B	Tropical storms	Storm centers Texture of storms	Good data were acquired on both developing and dissipating tropical storms.
3C	Hawaii	Upwellings, bow waves, island wakes Kilauea Volcano	No photographs were taken of the Hawaiian islands, but excellent data were obtained of eddies and currents southeast of the islands.
3D	Kuroshio Current	Ocean current boundary Plankton blooms	Some photography was acquired in the South China Sea.
4A	Snow cover	Snow-peaked mountains Glaciers and firn lines	Excellent photographs were obtained of glaciers and snow-peaked mountains in both the Cascade and Canadian Rocky Mountains.

TABLE 10-X.- Continued

Target designation		Description	Remarks
4B	Puget Sound	Suspended sediments Gyres Glaciers and firn lines	Valuable photographic and verbal data were obtained of sediments and gyres in the Puget Sound.
4C	Superior iron	Color oxidation zones	No photographs were taken but visual observation comments were made on color oxidation zones in the Superior region.
4D	Sudbury nickel	Color oxidation zones	Photography of the Sudbury area was unsuccessful because of cloud cover.
5A	Gulf of Mexico	Eddies in Yucatan Channel Florida Current Gulf Loop Current Internal waves in Gulf	Excellent data were obtained, including photography of eddies in the Yucatan Channel and current boundaries in the Gulf of Mexico.
5B	Gulf Stream	Ocean current boundary Internal waves Confluence with Labrador extension	This target was canceled on revolution 15/16 because of Flight Plan problems.
5C	Labrador Current	Ocean current boundary Confluence with Gulf Stream	The ocean northeast of Newfoundland was cloud covered and no photographs were taken.
5D	Central American structures	Bartlett Fault extension Graben valley structures	Central America was usually cloud covered and visual observations of fault structures could not be made.

TABLE 10-X.- Continued

Target designation		Description	Remarks
5E	Florida red tide	Red tide location Color and shape of bloom	The crew reported cloud cover over the Florida peninsula during every visual observation pass.
5F	New England red tide	Red tide location Color and shape of bloom	Boothbay Harbor in Maine was always cloud covered, but excellent photographs of coastal waters of Massachusetts and Canada were taken.
5G	Chesapeake Bay	Sediment gyres Pollution in Potomac River	Valuable photographic and verbal data were obtained of sediment gyres and pollution plumes in the Chesapeake Bay.
6A	Oil slicks	Oil slick extent Color and location	No oil slicks were observed in the North Atlantic, but some photographs of slicks were acquired over the Persian Gulf and the Mediterranean Sea.
6B	London	Sediments and boundaries in English Channel London Harbor area	England was usually cloud covered, but some photographs were taken along the coasts of England and France.
7A	Humboldt Current	Ocean current boundary Gyres in water	Photography of the Humboldt Current was successful.
7B	Nazca Plain	Nazca Plain markings Peruvian desert landforms	Some photography was obtained of the Nazca region, but the crew could not definitely confirm visual sightings of the Nazca Plain markings.
7C	Internal waves	Photographs of internal waves	Excellent photographs were taken of internal waves off Thailand and west of Spain.
7D	Peruvian desert	Dune fields Nazca Plain markings	Valuable photographic data of dune fields in the Peruvian desert were acquired.

TABLE 10-X.- Continued

Target designation		Description	Remarks
7E	Orinoco River Delta	Photographs of delta Water color near Barbados	Photographic and verbal data of the Orinoco River Delta included excellent photography of ocean waters between the delta and Barbados as well as visual observations of the extent of "brown water" outflow from the delta.
7F	Galapagos Islands	Upwellings Bow waves Island wakes Internal waves	Excellent photography was acquired of the volcanic calderas on the Galapagos and of the complex atmospheric wave patterns surrounding the islands.
7G	Caribbean Sea	Eddies Gulf Stream	A number of photographs were taken of the Caribbean waters and the islands of Cuba and Jamaica.
8A	Falkland Current	Ocean current boundary Plankton blooms Confluence with Brazil Current	The spacecraft attitude was not nominal for the revolution 72 pass, and the viewing angle out window 3 was very oblique.
8B	Chilean Andes	Color oxidation Structures and lineaments	The Chilean Andes were cloud covered and only a few very high peaks were visible.
8C	Dune field	Dune field color Dune pattern and orientation Relation with topography	Excellent photography was obtained of this little-known dune field and of a smaller unknown field to the east.

TABLE 10-X.- Continued

Target designation		Description	Remarks
8D	Paraná River	Photographs of dam sites	The weather over Paraguay and Brazil was amazingly clear, and excellent data were acquired of potential dam sites on the Paraná and Paraguay Rivers. Additional photographs were taken of the Amazon River.
8E	Circular structures	Photographs of two structures	Excellent photography of one possible astrobleme was obtained.
9A	Afar Triangle	Ethiopian Plateau scarp Red Sea mountains	The Afar Triangle was mostly cloud covered. The infrared photography is out of focus.
9B	Arabian Peninsula	Structures normal to Red Sea Desert color Dune types Coastline of Qatar	Infrared photography of the Arabian Peninsula is out of focus.
9C	Guinea Current	Ocean current boundary Gyres in water	Currents and gyres in the Gulf of Guinea could not be observed because of cloud cover.
9D	Desert colors	N'Djamena photographs Desert colors Dune patterns	Excellent photography was obtained of the Lake Chad area and of desert colors and dune patterns in the Libyan Desert.
9E	Oweinat Mountain	Photographs of mountain Structures in mountain Color oxidation zones	Valuable data were obtained over the Oweinat Mountain, including excellent photography and verbal observations of structural features and color zonations.

TABLE 10-X.- Continued

Target designation		Description	Remarks
9F	Nile Delta	Observation of pyramids Photographs of Cairo Gulf of Suez structures	A number of photographs were acquired over the Nile Delta and included excellent near-vertical photography of the Cairo area.
9G	Levantine Rift	Arcuate fault photographs Terminations of faults	Excellent data were obtained on the arcuate terminations of the Levantine Rift.
9H	Niger River Delta	Dune generations Vegetation patterns	Photography of the Niger River Delta was not successful because of cloud cover.
9I	Algerian Desert	Desert colors Dune patterns Interdune areas Desert and vegetation relationship	Good photography was taken of the Algerian Desert; observations of color zones and sandstorms were also made.
9J	Tripoli	African coastline Eddies, gyres, current boundaries, internal waves in Mediterranean Sea	Data for this target included good photography of the land-water interface at Tripoli and of current boundaries in the Mediterranean Sea.
9K	Strait of Gibraltar	Coastline at Casablanca Atlas Mountains Ocean current boundaries Internal waves	Excellent photography of the Strait of Gibraltar was acquired, and the crew was successful in observing internal waves and current boundaries. Good photographic data were also acquired of central and southern Spain.

TABLE 10-X.- Continued

Target designation		Description	Remarks
9L	Alps	Snow cover Glaciers and firn lines	Photographs of snow cover on the Alps were not obtained because of cloud cover.
9M	Danube Delta	Photographs of delta Sediment plumes in Black Sea	The crew was successful in photographing the Danube Delta but reported that most of the area was very hazy.
9N	Anatolian Fault	Photographs of fault Snow cover on mountains	Good low-Sun-angle photography was acquired of fault zones in Turkey, including excellent data east of Lice (epicenter of the recent earthquake).
9O	Volcanics	Photographs of Vesuvius Dark-colored volcanic rocks	Excellent infrared photographs were taken of igneous terrain in Italy.
9P	Bioluminescence	Brightening of tracks or zones in the Red Sea, Persian Gulf, and Arabian Sea that may be due to biological factors (nighttime observation)	The crew was not successful in observing bioluminescence in the Red Sea and remarked that they were still in sunglint. However, that was 2 min before the scheduled observation and they were still over the Mediterranean Sea. Earlier in the mission, the mission clocks had been updated 2 min, and the crew was probably using the old ground-elapsed time (GET).
10A	Great Dike	Color of Great Dike and surrounding rock	Photography and visual observations of this target were not successful.
10B	Somali Current	Zambezi River Delta Coastal sediment plumes Current boundaries Internal waves	Infrared photography of the delta was out of focus, but observations were made of sediment plumes and gyres along the coast.

TABLE 10-X.- Continued

Target designation	Description	Remarks
10C Arabian Sea	Ocean current boundaries	The crew was successful in observing a current boundary, but farther north, high cirrus clouds obscured much of the Arabian Sea.
10D Himalaya Mountains	Photographs of northwestern India	The Himalayas were cloud covered and photographs were out of focus.
10E Takla Makan Desert	Desert colors Dune patterns	The infrared photography of the Takla Makan was out of focus, but observations were made of what was probably a sandstorm over the desert.
11A Playas	Lake Eyre deposits Desert erosion and dune patterns Great Dividing Range	Excellent data were acquired of playas in the Lake Eyre region and included an unusual photograph of the normally dry Lake Eyre with much water.
11B Coral Sea	Coastal sediment plumes Great Barrier Reef Water eddies	Valuable photography was obtained of ocean features in the Coral Sea, and the crew was very successful in locating and describing eddies. They also observed the Great Barrier Reef and remarked that coastal sediments did not extend as far as the reef.
11C Simpson Desert	Desert colors Dune fields Dune types	Excellent photography was obtained that clearly illustrates the characteristic linear dune patterns and the red color of the Simpson Desert.

TABLE 10-X.- Concluded

Target designation	Description	Remarks
11D ANZUS Eddy (Tasmanian Sea)	ANZUS Eddy	Most of the area was cloud covered, but the crew did observe several eddies, one of which may have been the ANZUS Eddy.
12A Icebergs	Photographs of bergs Berg rotation Edge of Antarctica	No icebergs were observed in the Southern Hemisphere; however, the crew did see several large bergs in the North Atlantic and attempted to photograph them.

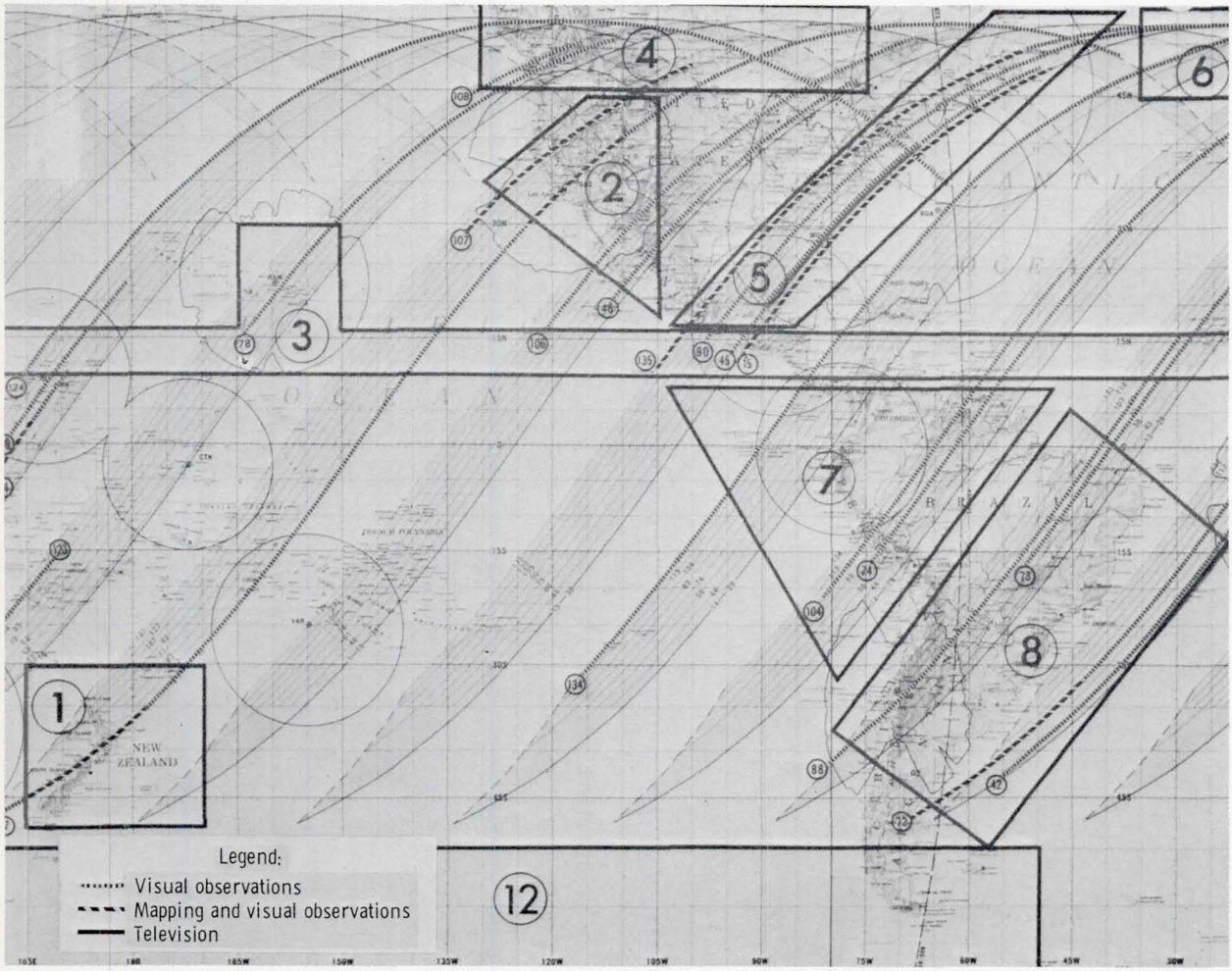

(a) Western Hemisphere.

Figure 10-1.- Maps showing the broad locations of the Earth observation sites. Small circled numbers represent revolution groundtracks for photographic mapping and visual observation tasks; large circled numbers represent the Earth observation sites.

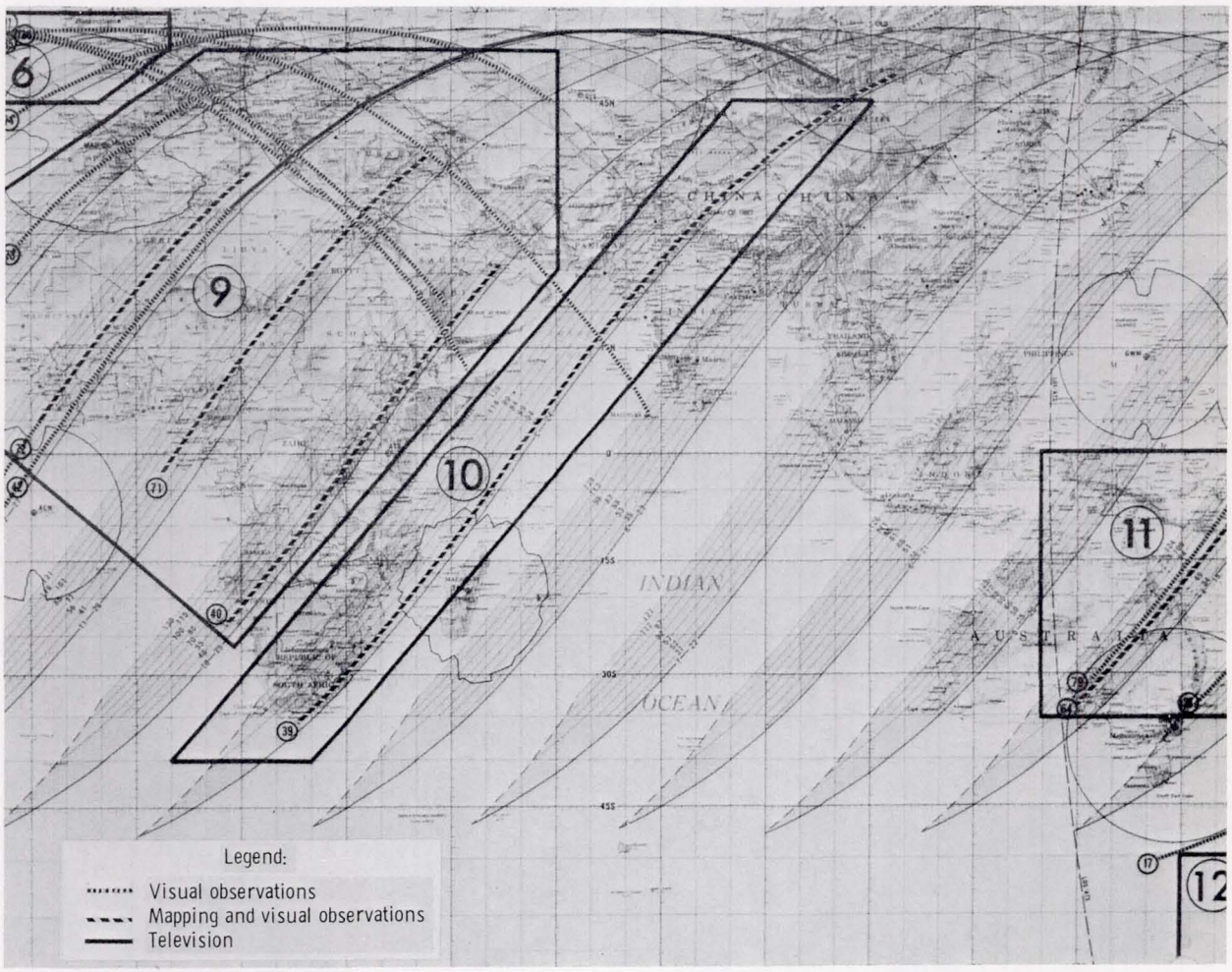

(b) Eastern Hemisphere.

Figure 10-1.- Concluded.

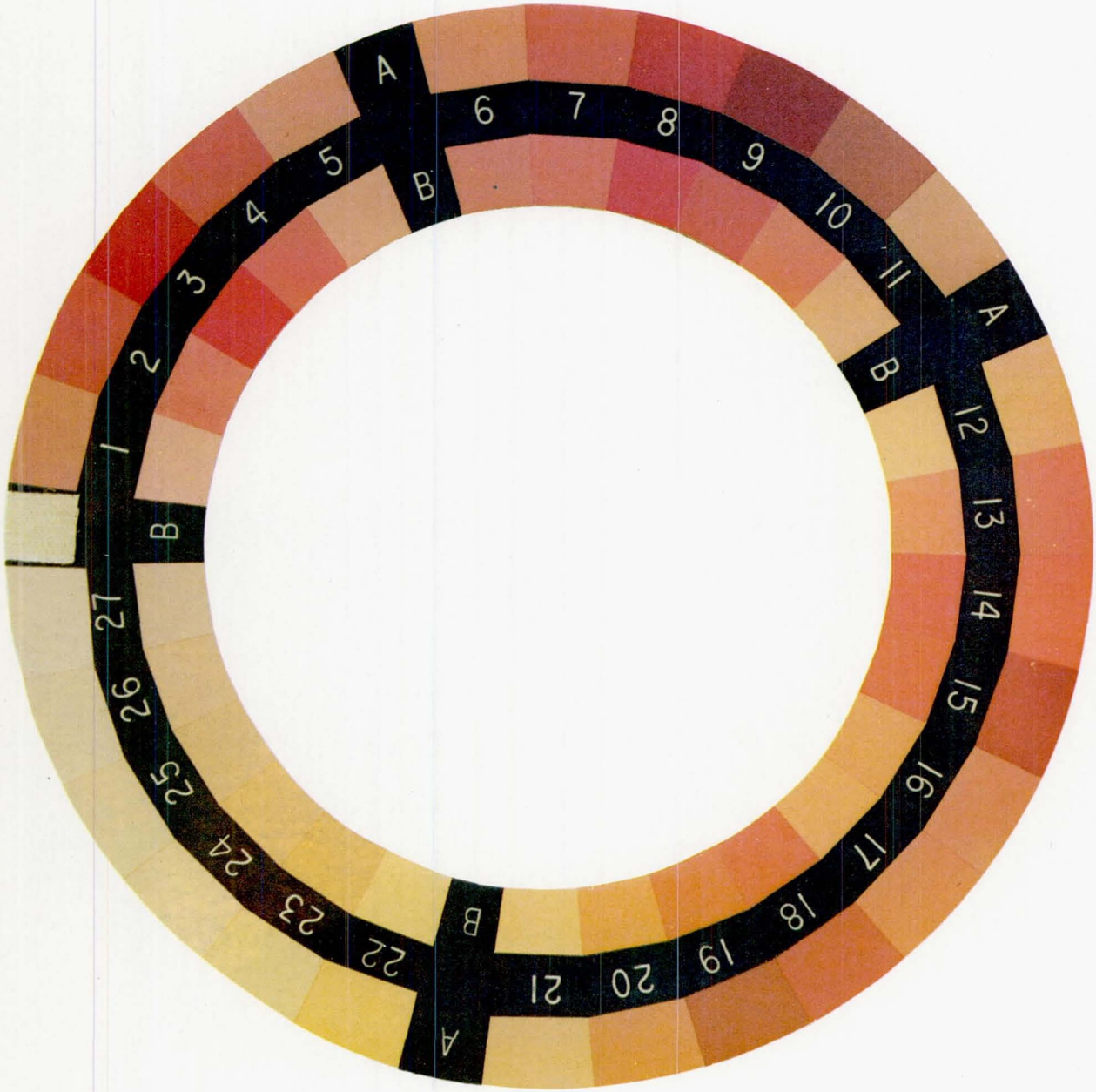

(a) Desert colors.

Figure 10-2.- Color wheel used for assigning desert and ocean colors during the ASTP visual observations. The color chips are from the Munsell color system (see table 10-VI), and their grouping resulted from testing during flyover exercises.

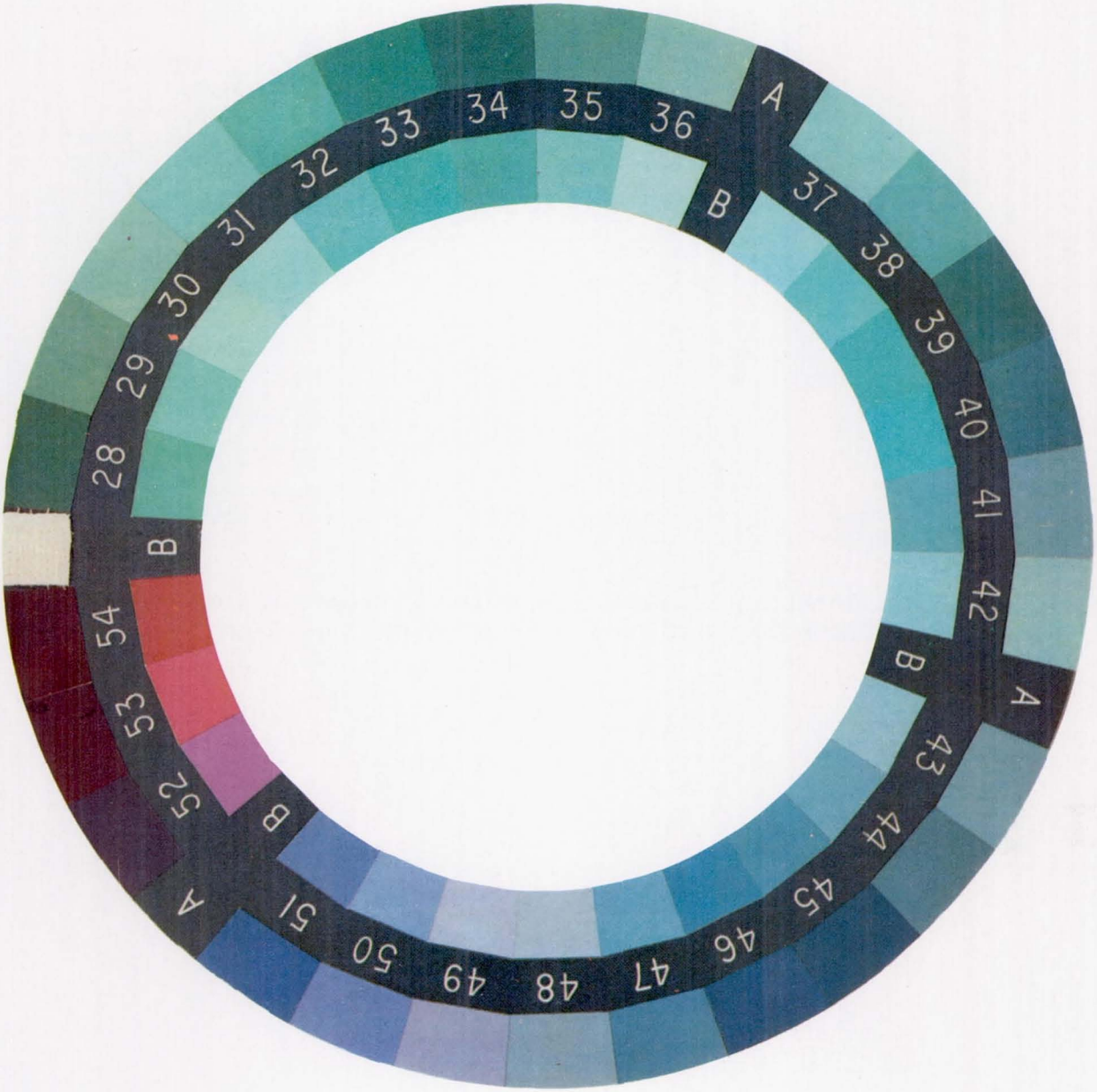

(b) Ocean colors.

Figure 10-2.- Concluded.

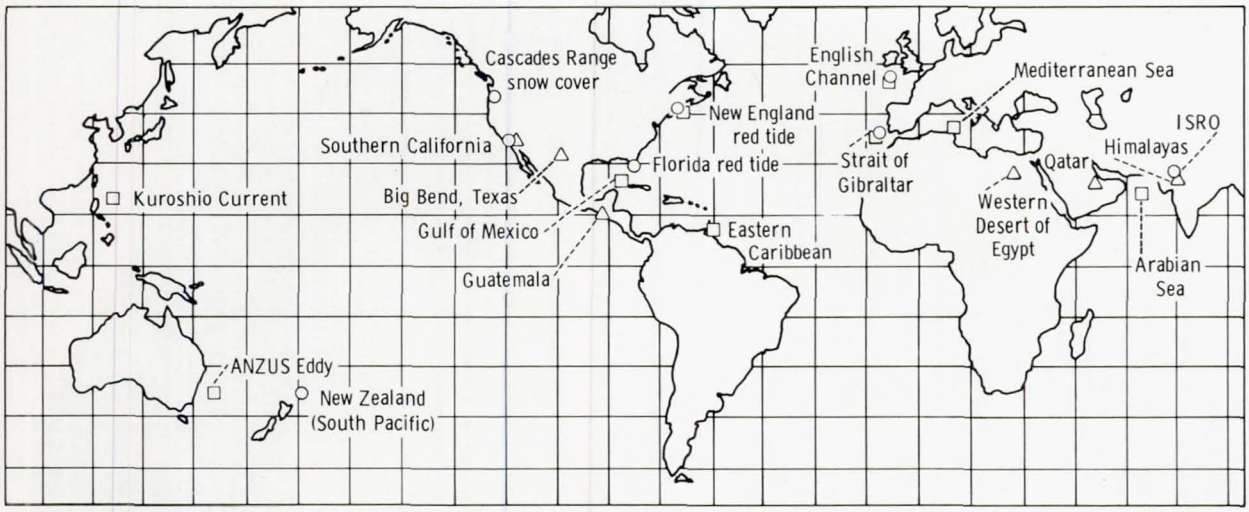

○ Aircraft support
□ Oceanography support
△ Ground support

ISRO - Indian Space Research Organization
(aircraft support)

Figure 10-3.- World map illustrating locations of support efforts of the ASTP Earth Observations and Photography Experiment.

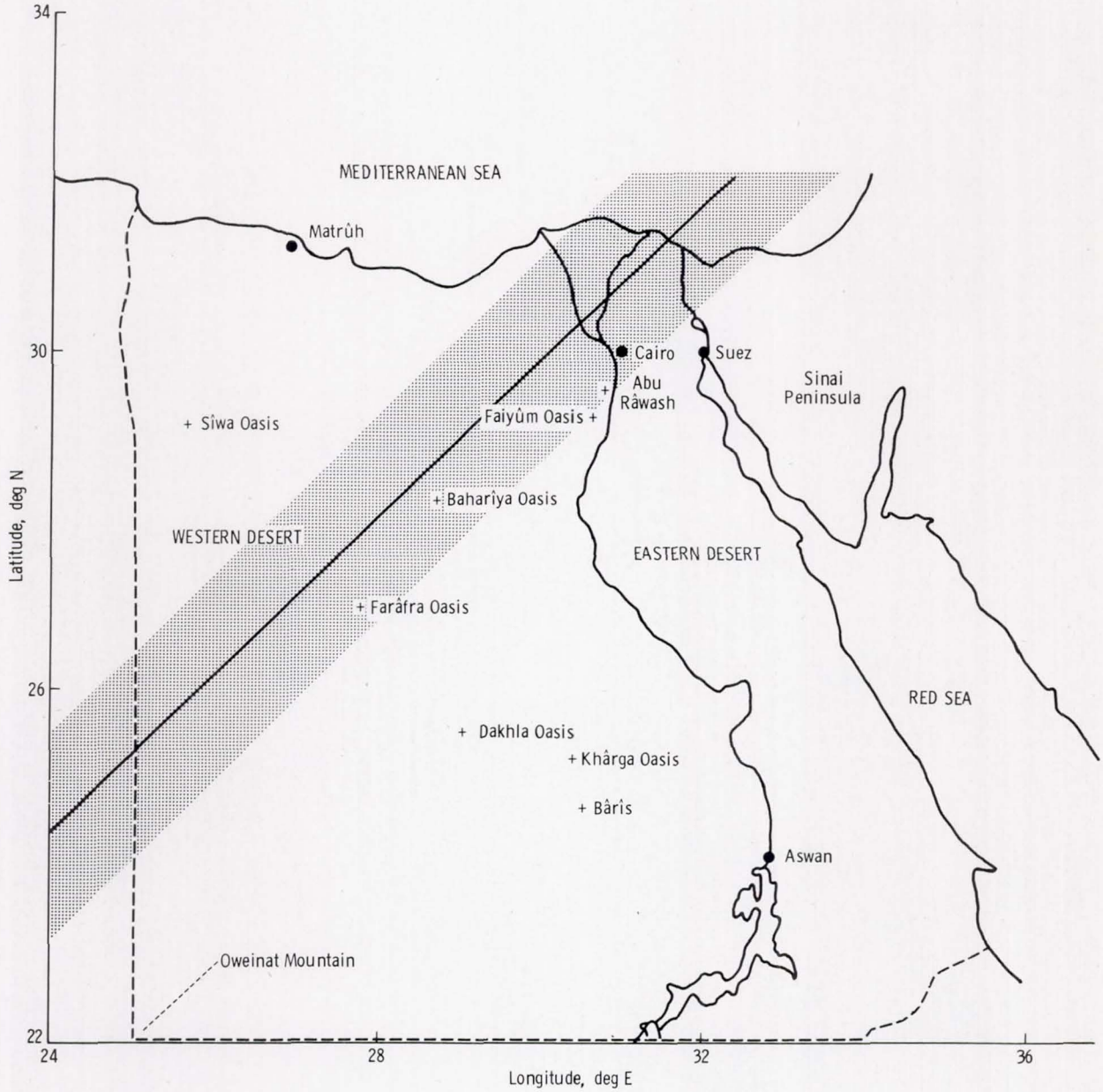

Figure 10-4.- Sketch map of Egypt showing the extent of photographic coverage (dotted area) by the mapping camera on revolution 71 (solid line). A support team from the Ain Shams University in Cairo will provide ground-truth data from the Oweinat Mountain area; the Farâfra, Bahariya, and Faiyûm Oases; and the Abu Râwash region.

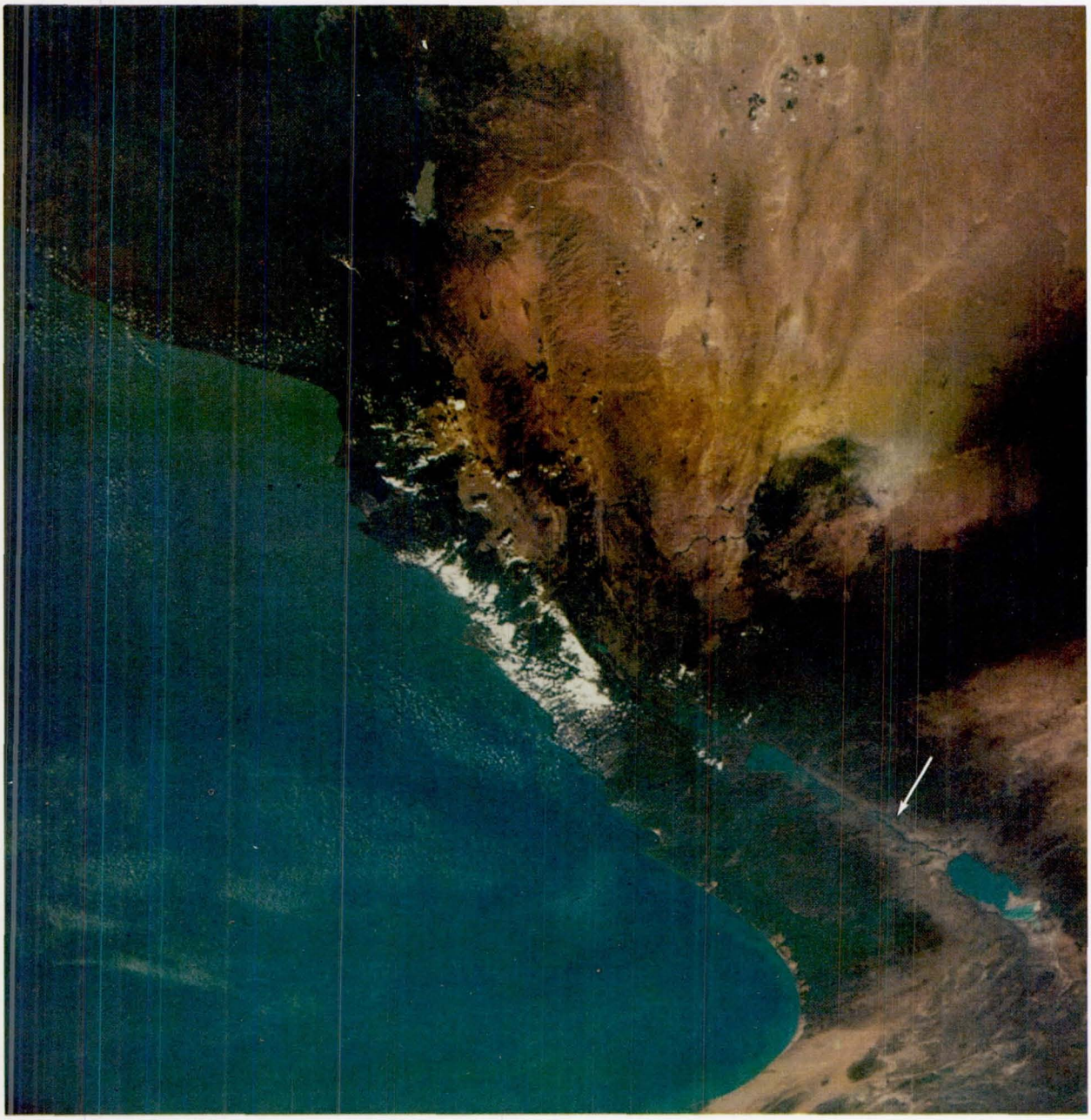

Figure 10-5.- The southern part of the Levantine Rift, extending from the Dead Sea to the Sea of Galilee, is distinguished by the linearity of the Jordan River Valley (arrow). To the north, a "fan shaped" complex system of arcuate faults characterizes the rift. One prominent fault parallels the Syrian coast and then makes a noticeable bend to the northwest (AST-9-564).

LEVANTINE RIFT

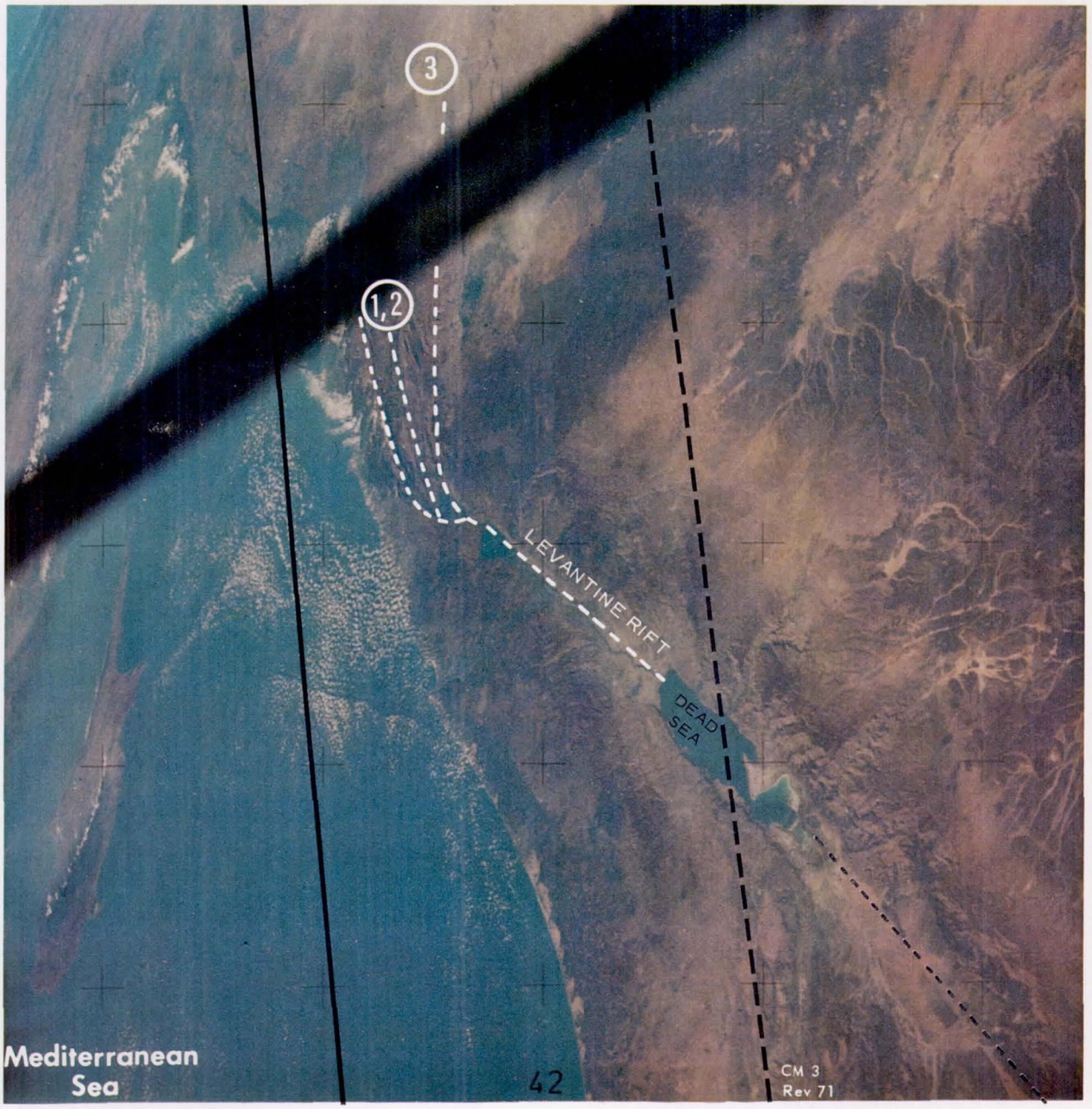

71

1. OBTAIN 3 STEREO PHOTOGRAPHS OF THE ARCUATE TERMINATIONS OF THE LEVANTINE RIFT.
2. CAN YOU DISTINGUISH RELATED GROUPS OF FAULTS?
3. WHERE IS THE NORTHERNMOST TERMINATION OF THIS FAULT COMPLEX?

REV 71: CM3/SILVER/250/CX12(f8,1/500) 3FR,[RECORD LAST FR NO: PAGE 4]

Figure 10-6.- One page from the Earth Observations Book (visual observation target 9G) that was used by the crew to visually study the Levantine Rift area.

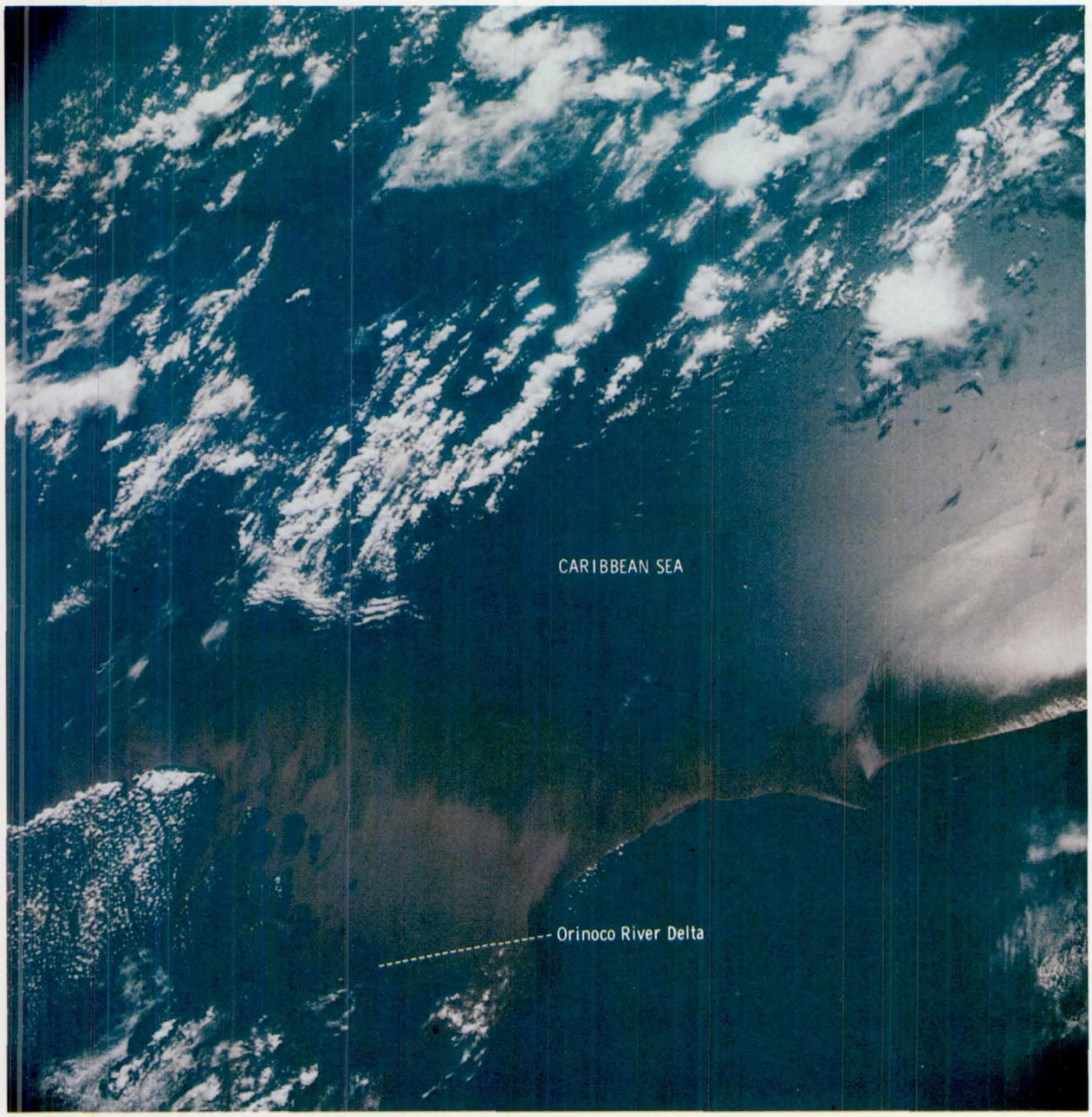

Figure 10-7.- The deep-brown color of the Orinoco River outflow is caused by both sediments and humic compounds. This turbid water was observed by the crew farther north than the island of Barbados (AST-21-1685).

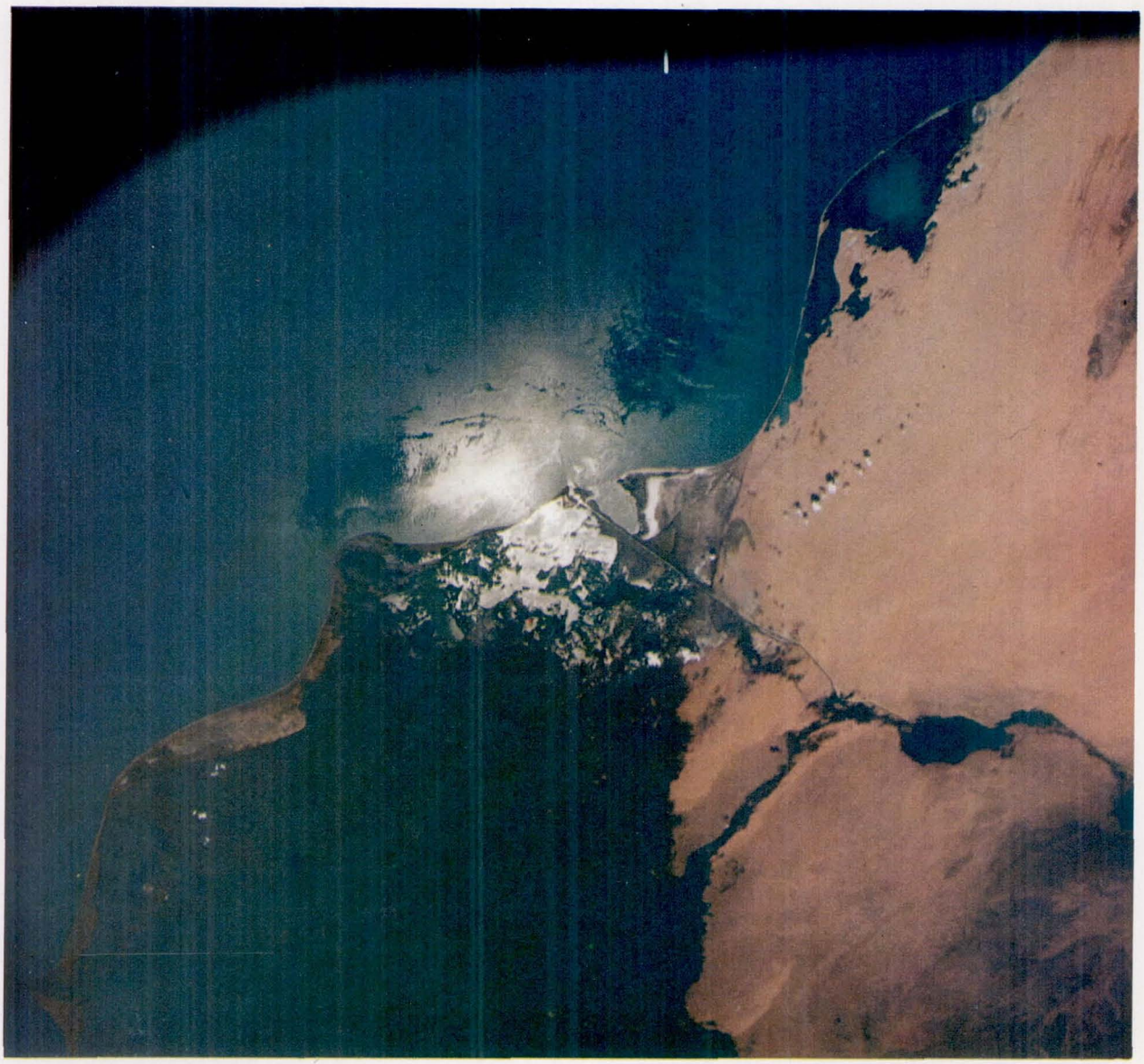

Figure 10-8.- The Nile Delta is an excellent example of a triangular-shaped arcuate delta. Patterns of surface texture and boundary layers, easily seen in the Sun's reflection, possibly result from a density difference between the freshwater from the Nile and the more saline water of the Mediterranean Sea (AST-9-558).

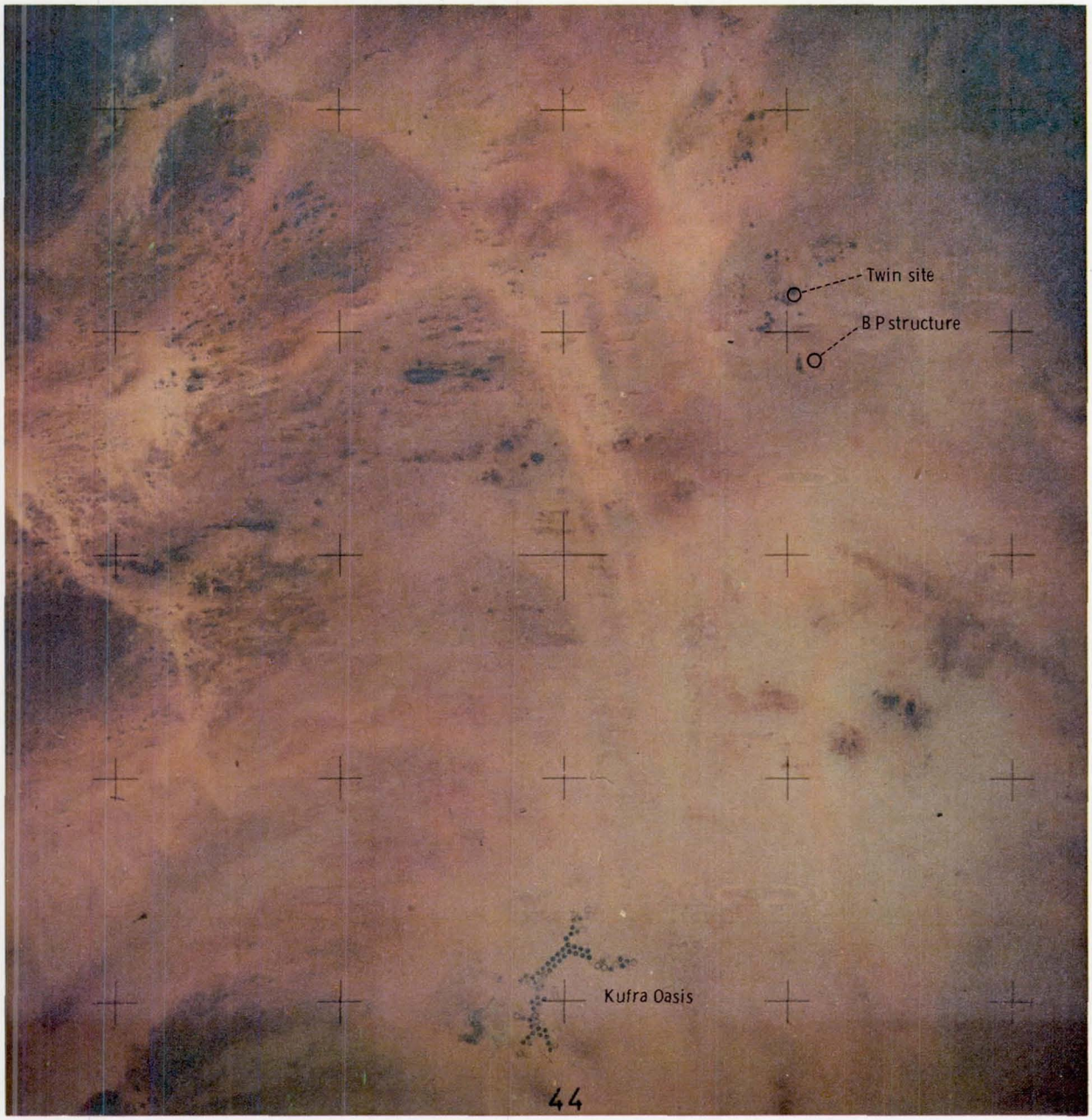

Figure 10-9.- The Kufra Oasis, in the lower half of the photograph, is characterized by circular irrigation patterns. To the north, two faint rings (arrows) are possible astroblemes (AST-16-1244).

(a) The Atlantic Ocean appears homogeneous with no visible ocean features in this oblique photograph looking toward the Strait of Gibraltar (AST-27-2365).

Figure 10-10.- The Strait of Gibraltar.

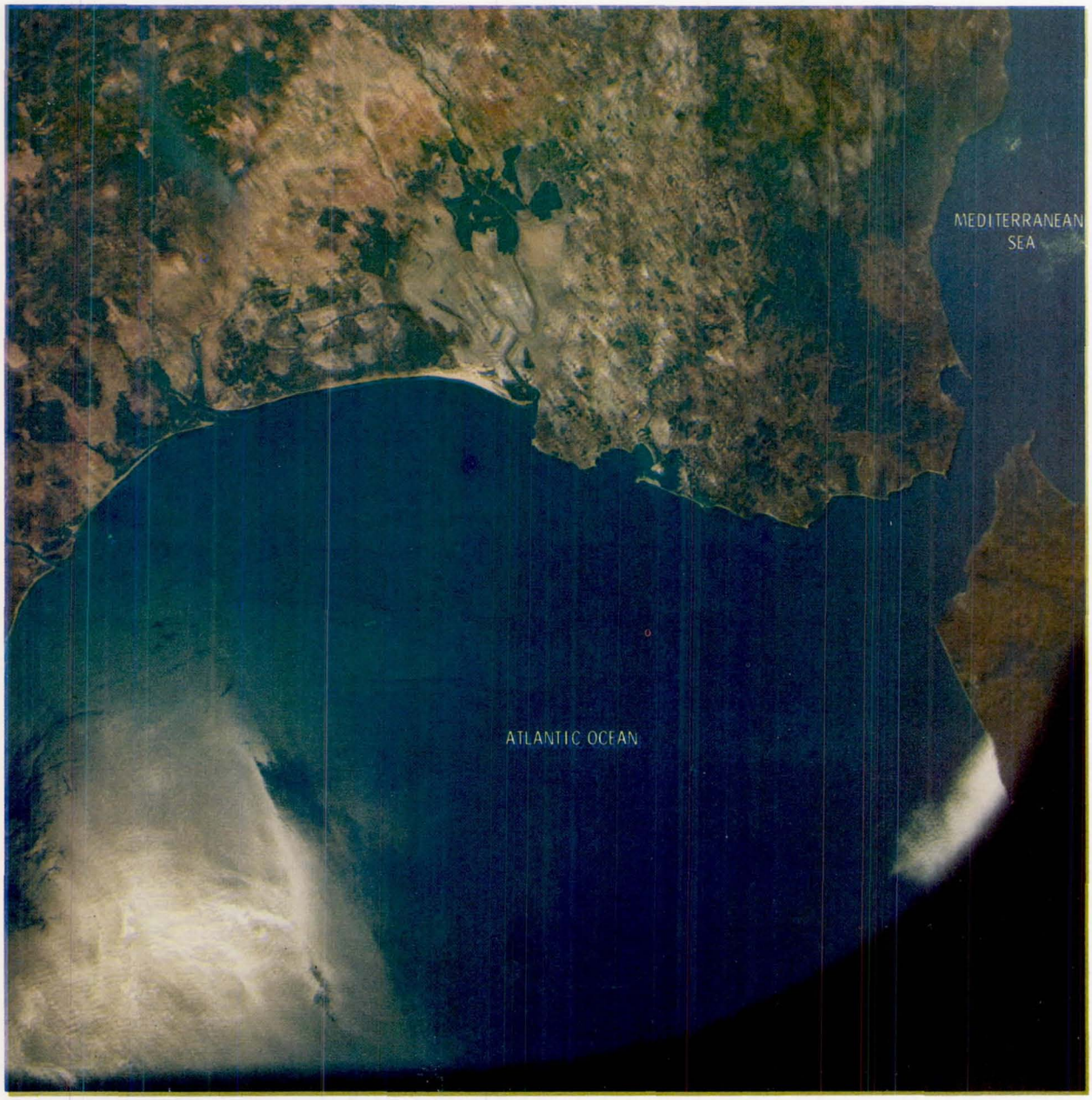

(b) The change in Sun angle in this photograph, taken shortly after figure 10-10(a), has made a number of features visible. Orbital photography of the oceans has revealed that the occurrence and magnitude of internal waves is greater than expected. The internal waves in this photograph are approximately 50 to 60 kilometers long (AST-27-2367).

Figure 10-10.- Concluded.

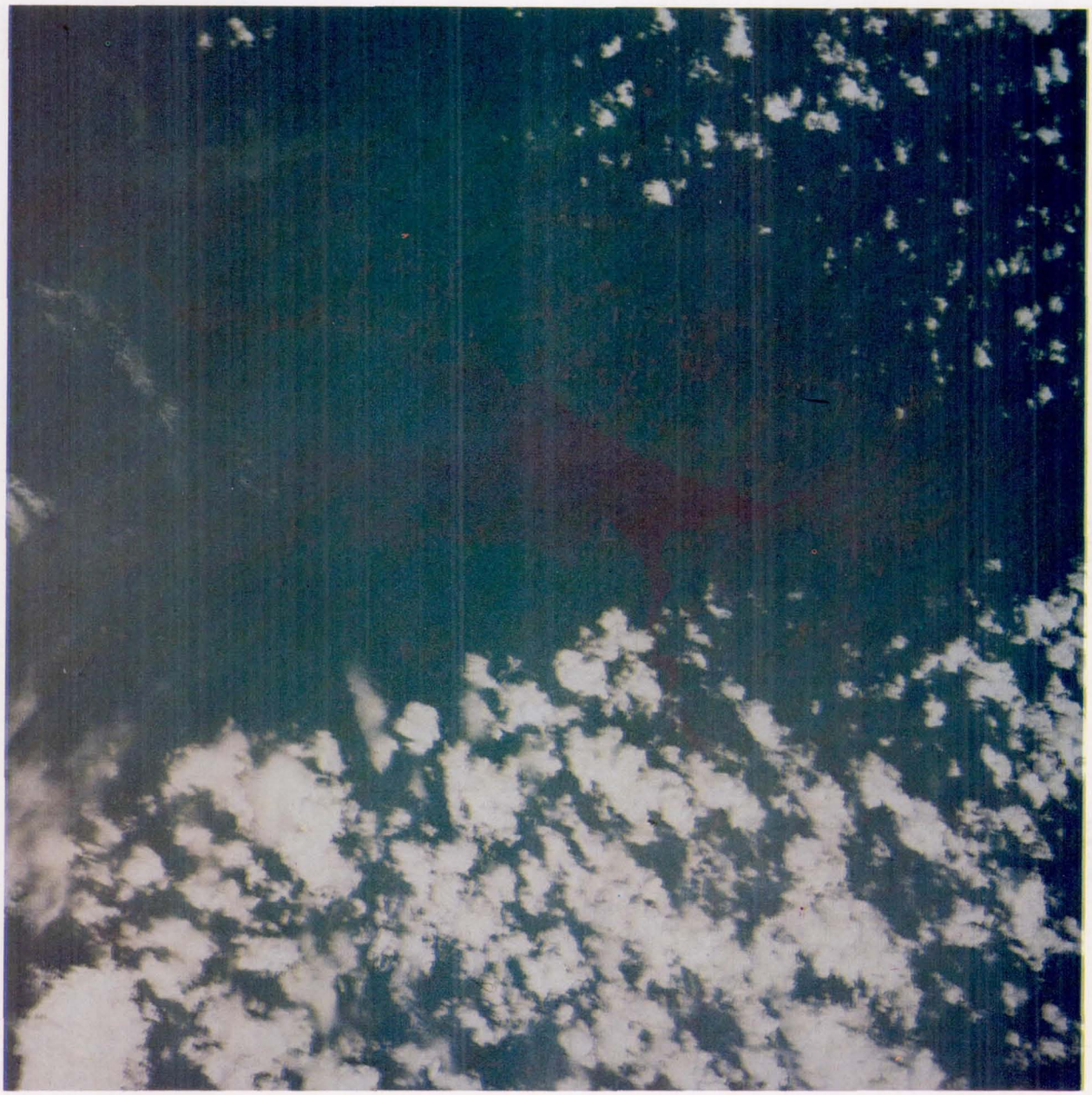

Figure 10-11.- In this photograph of the Bay of Fundy, the red water color is probably due to the deposition of red clays by inflowing rivers. There is a fairly heavy sediment load in the bay; high tidal activity maintains water turbulence (AST-1-67).

Figure 10-12.- This vertical photograph was taken with the mapping camera over the Western Desert of Egypt. A sharp color change marks the boundary between the younger, yellow sand sea to the north and the older, orange-red desert associated with the Gilf el Kebîr region in the lower part of the photograph (AST-16-1247).

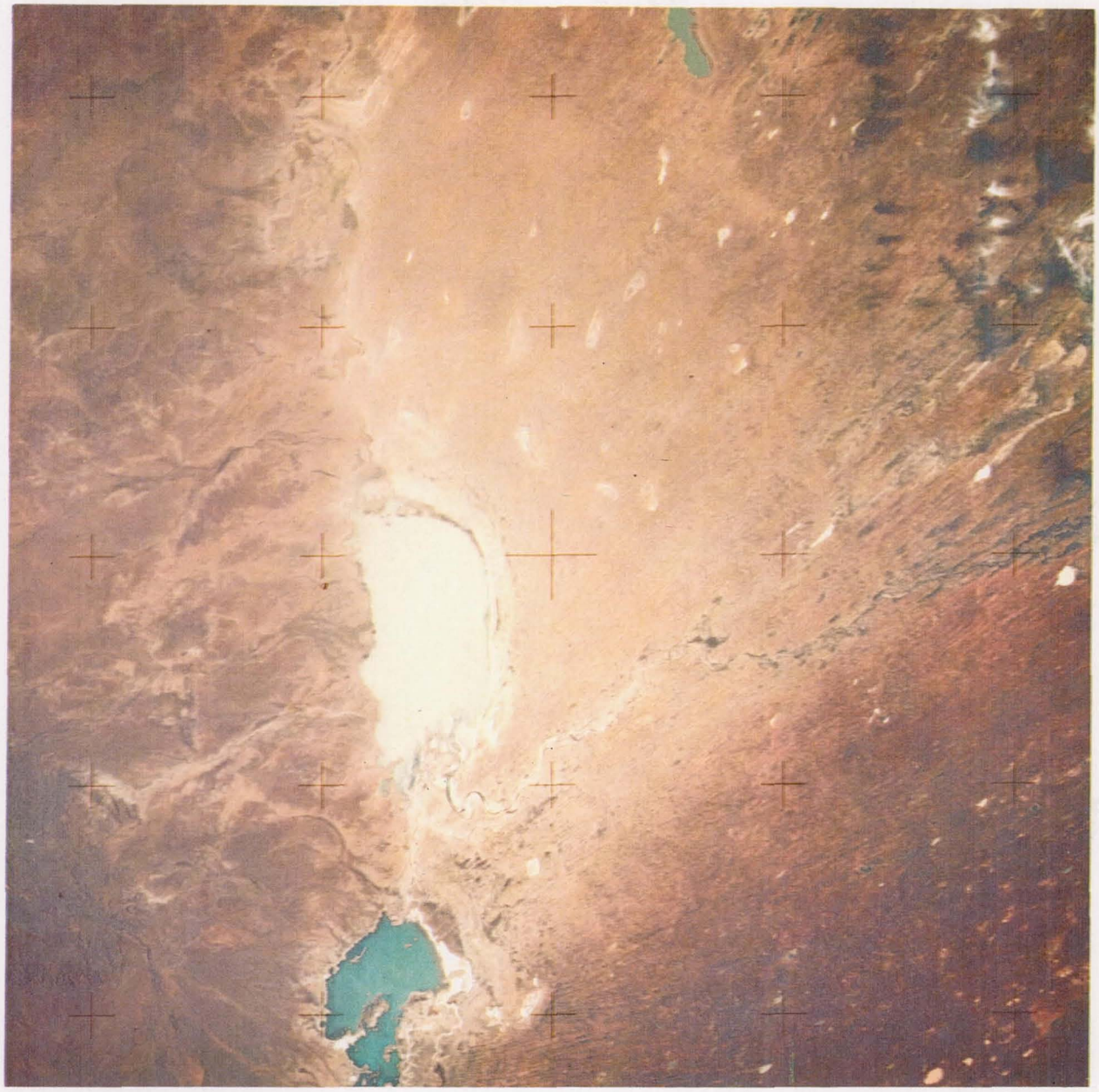

Figure 10-13.- The color difference between the dark-red Simpson Desert and the yellow Western Desert of Egypt in figure 10-12 is readily apparent. The radiating linear dunes in this photograph, described by the crew as "hundreds of parallel road tracks," seem to constitute the characteristic dune pattern in this region (AST-16-1133).

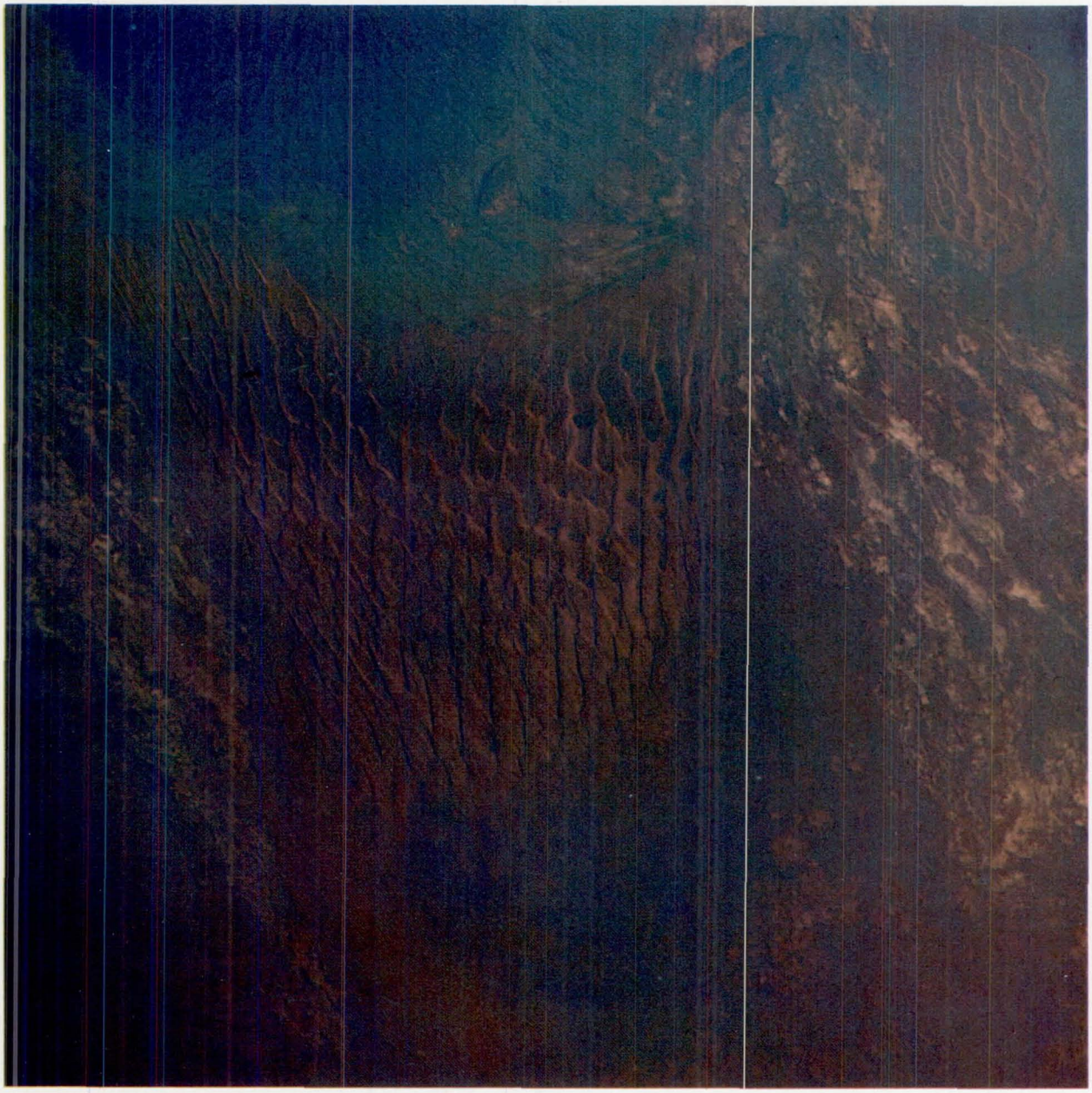

Figure 10-14.- In this excellent photograph of a little-known dune field in Argentina, the transition between the alluvial fan at the base of the mountain and the dune field is very sharp. The general dune pattern is crescentic with a superimposed secondary linear pattern. To the east of the dune field is a smaller field, the existence of which was previously unknown (AST-27-2340).

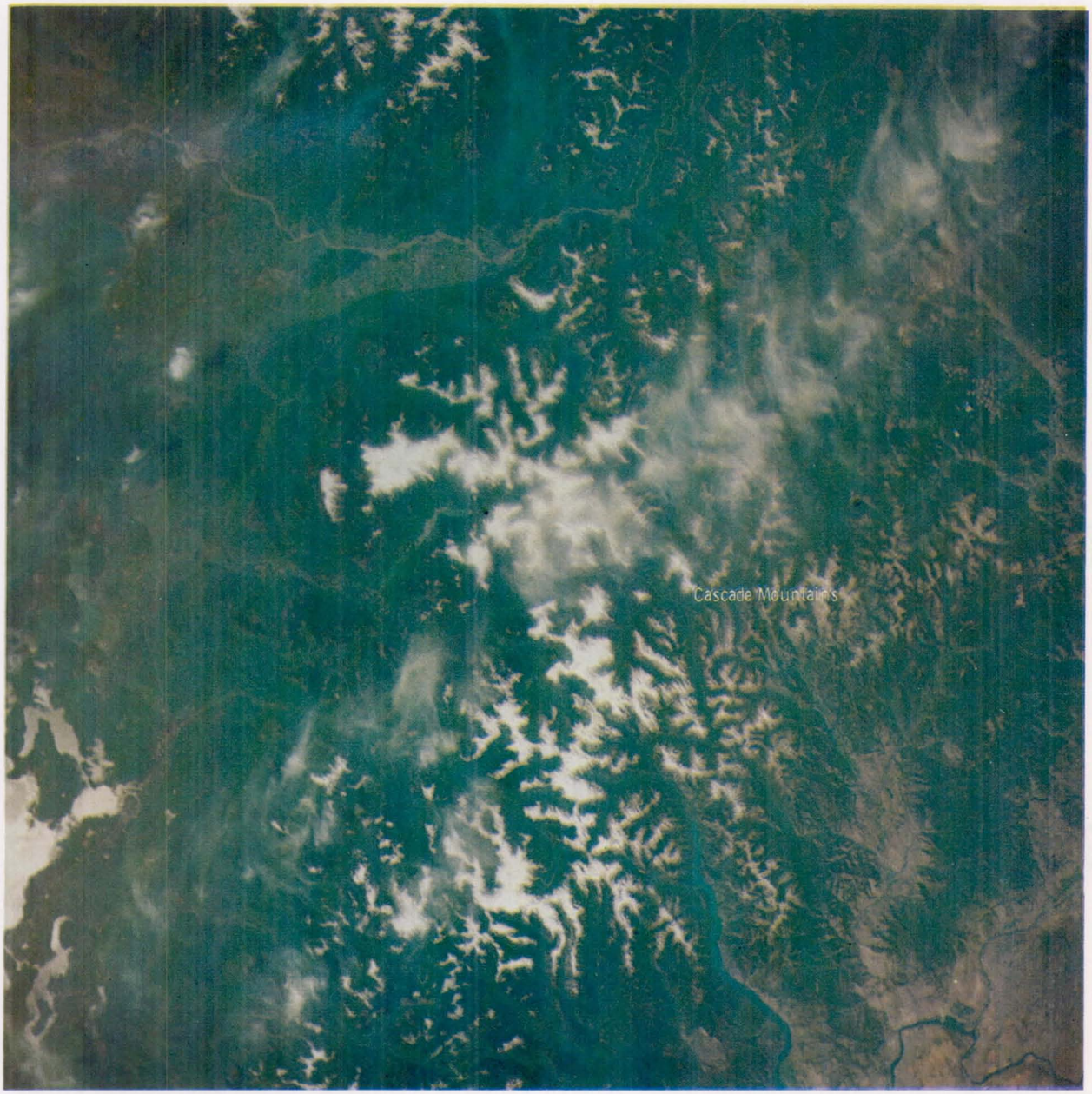

Figure 10-15.- This photograph of the July snow cover was taken over the Cascades in the State of Washington. Snowpack distribution is being mapped to estimate the volume of water reaching drainage systems for use in irrigation (AST-19-1540).

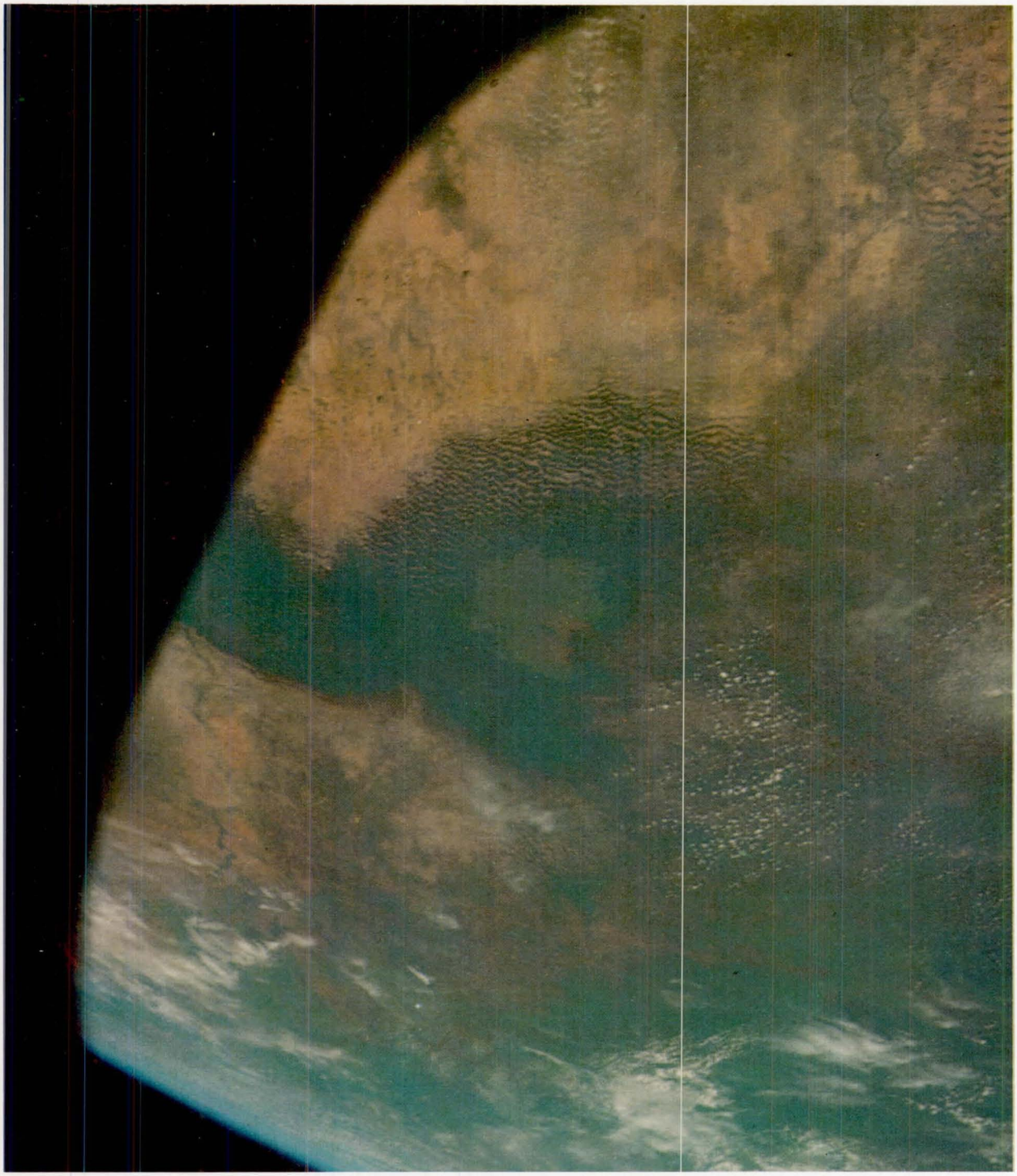

Figure 10-16.- In this photograph of Lake Chad, the number of emergent dunes within the lake attest to the fact that the lake was once considerably larger. However, various factors, such as the influx of sand from the Sahara, have contributed to a significant decrease in its size (AST-9-550).

Figure 10-17.- This photograph of an unusual cumulonimbus convective system was taken along the western coast of Mexico over the Gulf of California (AST-9-545).

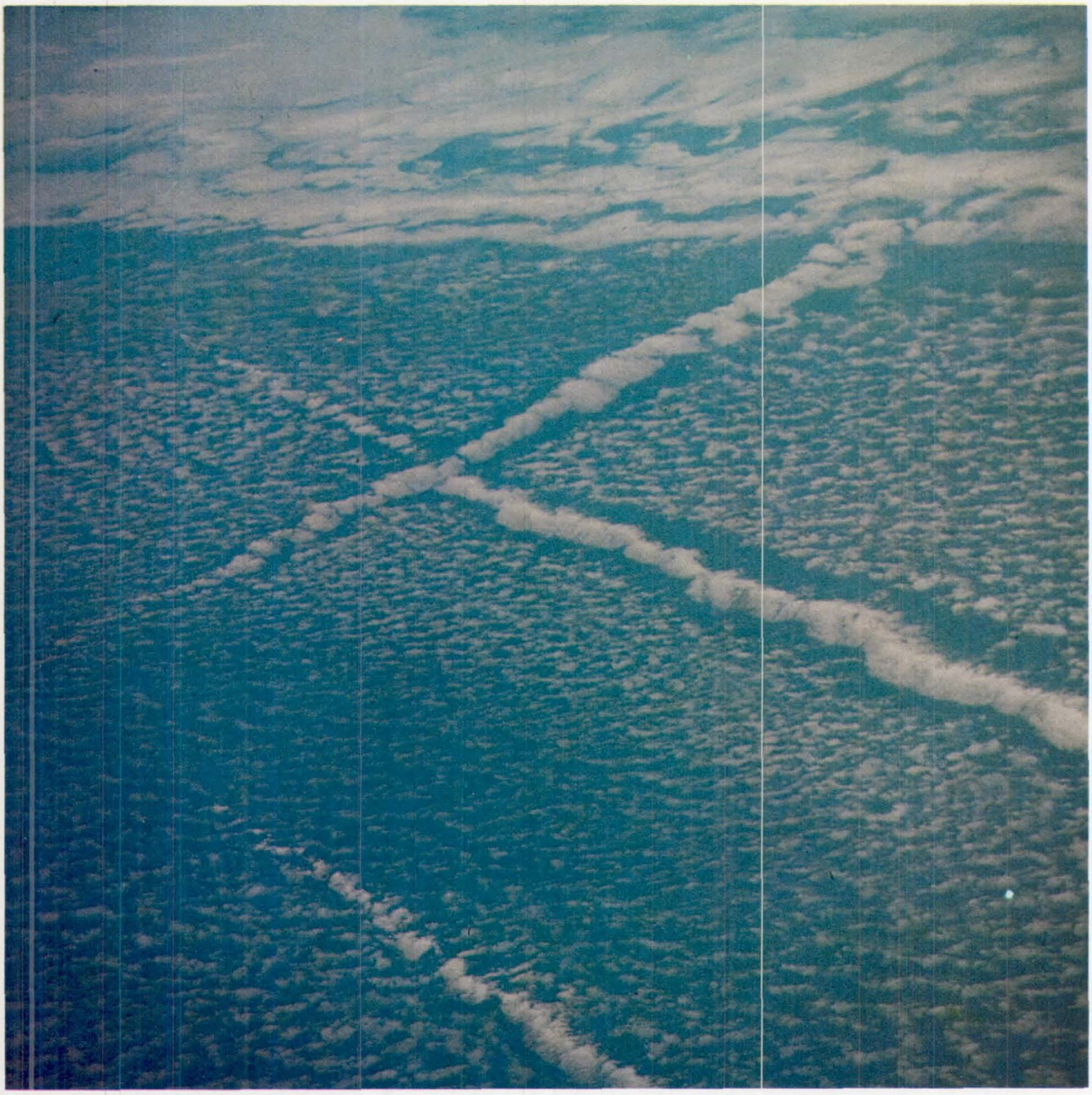

Figure 10-18.- The unique, wedge-shaped linear features in this photograph taken over the Pacific Ocean west of southern California are significantly larger than contrails. Their mode of formation is not yet understood (AST-1-42).

11. DOPPLER TRACKING

EXPERIMENT MA-089

G. C. Weiffenbach[a†] and M. D. Grossi[a]

ABSTRACT

The Doppler Tracking Experiment was designed to test the feasibility of improved mapping of Earth gravity field anomalies by means of the low-low satellite-to-satellite tracking method. All prescribed data have been retrieved and are currently being reduced and analyzed. Baseline data taken while the docking module was still attached to the command and service module indicated that the equipment operated satisfactorily. The efficacy of the two-frequency ionospheric-correction method has been demonstrated, and preliminary reduction of a data sample has successfully removed extraneous signatures down to the 50-millihertz level, where the rotational motion of the docking module is revealed. Photographs of the docking module, taken shortly after jettison, show that its rotation was stable.

INTRODUCTION

Interest has recently focused on mass density anomalies with scale sizes of 100 to 700 kilometers in the subcrustal region of the Earth, the asthenosphere. It is likely that these anomalies are important factors in the physics of the mantle and plate tectonics and in the reconstruction of important aspects of the evolution of the Earth, such as continental drift. Small-scale anomalies near the surface of the Earth have been studied for many years by means of surface gravimetry; and large-scale anomalies, greater than 2000 kilometers, have been investigated for almost 20 years by observing artificial-satellite orbit perturbations. The spacecraft-to-spacecraft Doppler Tracking Experiment conducted by the Smithsonian Astrophysical Observatory (SAO) during the Apollo-Soyuz Test Project (ASTP) mission was designed to determine gravity features having an intermediate horizontal scale of 250 to 1000 kilometers. The ASTP mission was particularly suitable for this experiment because it provided two platforms with a controlled separation within the same orbit at an altitude low enough for enhanced sensitivity to these short-wavelength gravity anomalies.

---

[a]Smithsonian Astrophysical Observatory.

[†]Principal Investigator.

The experiment consisted of measuring, by means of a phase-coherent, dual-frequency, very-high-frequency link, the relative velocity, or Doppler shift, between the docking module (DM) and the command and service module (CSM). Both orbiting at a height of 220 kilometers, these two modules had an initial separation of 317 kilometers which increased to 475 kilometers by the end of the data take. From their relative-velocity data, localized anomalies in the Earth gravitational field can be measured with a threshold sensitivity of better than 0.15 mm/sec^2 (15 milligals). The geometric range-rate error induced by the ionosphere can be removed by applying the dual-frequency (162 and 324 megahertz) correction.

A secondary goal of the experiment was to measure the integrated electron concentration and other ionospheric properties along a radio path between the CSM and the DM, and between the DM and the ground.

THEORY

Measuring the Earth Gravity Field

The structure of the Earth gravity field has been of considerable scientific interest for some time because it provides one of the few available clues to the internal distribution of mass in the Earth. The recent development of the plate-tectonics hypothesis has placed added emphasis on the need for information on specific features in the gravity field that have horizontal wavelengths of 100 to 700 kilometers.

Evidence from studies of seismic-wave propagation shows that the outer portion of the Earth consists of (1) a high-velocity zone, the lithosphere, which generally includes the crust and uppermost mantle, has significant strength, and is approximately 50 to 80 kilometers thick under the oceans and somewhat thicker under the continents; (2) a low-velocity zone, the asthenosphere, which is a layer of low effective strength on a geologic time scale and extends from the base of the lithosphere to a depth of several hundred kilometers; and (3) the lower remaining portion of the mantle, the mesosphere, which may have strength and is relatively passive in tectonic processes.

The plate-tectonics concept is based on the observation that large blocks or plates of the rigid lithosphere, some thousands of kilometers in horizontal extent, appear to be moving ("floating" on the yielding asthenosphere) with respect to one another at average long-term rates of approximately 1 to 15 cm/yr (ref. 11-1). One manifestation of this plate motion is continental drift. Most large earthquakes, volcanic activity, mountain building, and tsunami generation, plus some terrestrial mineral resources, are located at the boundaries of the lithospheric plates. In fact, nearly all large-scale geological and geophysical phenomena occurring on the Earth surface appear to be intimately related to this global pattern of plate motions. Thus, the subject of plate tectonics is of much scientific and practical interest. However, no satisfactory theory of the mechanisms producing plate motion is currently available. It is very probable that both thermal convection and chemical convection in the asthenosphere are involved in some way; most current theories include one or both processes. However, there is little question that knowledge of the density

field in the upper portion of the Earth, to a depth of 700 kilometers or so, would be of considerable importance in determining the basic mechanisms underlying plate motion.

The distribution of mass within the Earth uniquely determines the external gravity field. Hence, measurements of the external gravity field contain information on the density field, although the external field does not define the unique internal mass distribution. Generally, a density anomaly within the Earth will produce a lateral variation in the external gravity field of a scale comparable to the depth of the anomaly. Thus, the density field within the upper mantle at depths of 100 to 700 kilometers will generally be reflected in horizontal variations of the gravity field having wavelengths of 100 to 700 kilometers. These results indicate that measurements of intermediate-wavelength (100 to 1000 kilometer) features in the gravity field will be fundamental to advancing the understanding of plate tectonics.

The intermediate-wavelength structure of the Earth gravity field is interesting for another reason. The surface of the ocean contains topographic signatures of current systems, eddies, storm surges, tsunamis, barometric loading, etc., all of which are of considerable practical importance. There is great interest in developing methods for maintaining frequent surveillance of these phenomena over the ocean. One very promising approach is to map the topography of the ocean with satellite-borne radar altimeters. The third Geodynamics Experimental Ocean Satellite, launched by NASA in April 1975, has such an altimeter. However, the mean-sea-level surface also contains the topographic imprint of the Earth gravity field; i.e., the geoid. Geoid undulations must be mapped and removed from the measured ocean topography before it will be possible to uniquely identify the signatures of oceanographic parameters. All the previously mentioned oceanic features have topographic structures with significant lateral components in the range 100 to 1000 kilometers. The estimated geoid accuracy needed for this purpose is 10 centimeters in geoid height.

Measuring the Earth gravity field has been a continuing occupation of geodesists for many years. The traditional method has been to use gravimeters at fixed locations in land areas and on ships, submarines, and, more recently, aircraft. This method provides accurate measurements of the detailed structure of the gravity field, particularly on land. However, surface gravimetry has several deficiencies: the cost and time involved in covering large geographic areas (particularly in rough terrain), the reduced accuracy of gravimeters on mobile platforms, and the loss in accuracy of large-scale gravity variations synthesized from gravimeter data.

More recently, the structure of the gravity field has been calculated using orbital dynamics from accurate tracking of artificial satellites. Because satellite orbits are uniquely determined by the forces acting on the satellite and because gravity is by far the dominant force, the gravitational force can be inferred from the observed orbits and an appropriate orbit theory. This orbital-dynamics approach has been used successfully to measure the large-scale structure of the gravity field with considerable accuracy. However, the orbital-dynamics approach is not suitable for measuring intermediate- or short-wavelength gravity-field features. Specifically, spherical-harmonic terms of a degree higher than 20 are impractical, both because of the rapidly increasing complexity of the theory and its computer mechanization and because of the need for many more satellites in different orbits. Thus,

this method is restricted, for practical reasons, to gravity features having horizontal wavelengths greater than 2000 kilometers.

The Gravity Field From Satellite-to-Satellite Velocity Measurements

Another method using artificial satellites can be used to measure intermediate-sized gravity features. Used in the SAO Doppler Tracking Experiment, the method is based on calculating the gravitational force acting on a spacecraft directly from changes in its measured velocity. Figure 11-1 is a simple diagram of this method; it pictures a satellite in Earth orbit. The density of the model Earth is assumed to be homogeneous except for an excess mass M at some point under the orbit. As the satellite approaches M, the added gravitational force exerted by M will accelerate the satellite. As the satellite moves away from M, the corresponding retarding force will reduce the satellite velocity. By measuring the time history of the velocity variation during the period when the satellite is under the influence of M, the size, position, and magnitude of the excess mass M can be deduced. This approach was used to discover and measure lunar mascons (ref. 11-2).

Of course, the actual situation for the experiment is more complex, not only because of the internal mass distribution of the Earth and its effects on the satellite trajectory, but also because the velocity of the satellite must be measured from another satellite. A detailed analysis of more realistic cases has been reported by Schwarz (ref. 11-3).

From surface-gravimeter data for the United States, Schwarz constructed arrays of 1° by 1°, 2° by 2°, and 5° by 5° gravity anomalies and computed the theoretical range-rate variations that would be observed between two spacecraft in orbit over these simulated gravity fields. Orbit altitudes of 200, 300, and 700 kilometers and satellite-to-satellite separations of 200 to 600 kilometers were used in various combinations. Noise was added to the computed range-rate data. Schwarz then inverted the process to determine the accuracy with which the simulated gravity anomalies could be recovered from the computed, noisy, range-rate (Doppler) data.

The results of Schwarz's computer experiments are briefly summarized as follows.

1. The structure of the gravity field can be determined from measurements of the variations in range rate between two spacecraft in the same nominal orbit.

2. The lateral scale of the shortest wavelength gravity feature that can be recovered using this method is approximately equal to the orbital altitude.

3. The accuracy of the recovered gravity anomalies is approximately 0.1 mm/sec^2 (10 milligals), for an accuracy of 0.5 mm/sec (1 standard deviation) in range rate between the spacecraft, where each measurement is averaged over 16 to 32 seconds.

4. The ephemerides of the two spacecraft need not be determined to high accuracy; orbit errors as large as 1000 meters have little effect on the solutions.

Schwarz's computer experiments suggest rather convincingly that the ASTP Doppler Tracking Experiment should produce accurate determinations of gravity anomalies having horizontal wavelengths in the range of 300 to 1000 kilometers over those geographic regions for which measurements are obtained. The lunar-mascon experiment confirms this conclusion even though the geometry was somewhat different because one of the "spacecraft" terminals was located on the Earth.

Useful data can be obtained when the spacecraft are within line of sight of each other, when the line between them lies above the troposphere, and when their separation is greater than 200 kilometers. It is important to note that gravity field information is obtained only for geographic regions in which Doppler measurements are made. The scientific usefulness of the experiment thus depends on the geographic coverage.

The accelerations produced by atmospheric drag and radiation pressure on the spacecraft contribute to the measured range rates and thus constitute systematic errors in the determination of the gravity field. The acceleration caused by radiation pressure was computed for solar flux incident on the side of the spacecraft. In this case, the area-to-mass ratio is approximately $0.02\ cm^2/g$. The pressure exerted by direct solar radiation was taken as $0.45 \times 10^{-9}\ N/cm^2$ $(4.5 \times 10^{-5}\ dyn/cm^2)$; therefore, the resulting acceleration is approximately $1 \times 10^{-6}\ cm/sec^2$, which is negligible.

The acceleration produced by atmospheric drag a was computed for the case in which the spacecraft velocity vector is parallel to its long axis, with an effective area-to-mass ratio A/m of $0.005\ cm^2/g$. The following equation was used.

$$a = \frac{C_d}{2} \frac{A}{m} \rho v^2 \tag{11-1}$$

where the drag coefficient C_d is 2, ρ is the atmospheric density, and v is the spacecraft velocity. When $\rho = 2.8 \times 10^{-13}\ g/cm^3$ at an altitude of 200 kilometers, an acceleration of $0.0084\ mm/sec^2$ is obtained. For the 10-second averaging time of the Doppler observations, the velocity change is thus 0.084 mm/sec for each data sample period.

If drag accelerations are reasonably smooth, as is expected, it should be possible to separate the gravity variations satisfactorily even at a spacecraft altitude of 200 kilometers. Alternatively, the drag forces appear small enough that they can be modeled to sufficient accuracy. However, the drag effects are large enough that they must be computed accurately by using the measured orbital and altitude motions of both spacecraft.

Ionospheric Studies Using Satellite-to-Satellite Doppler Data

If a radiofrequency (RF) Doppler link is used between two spacecraft to obtain range-rate data, information about the electron concentration between the spacecraft can be obtained. In fact, the effects of the ionosphere must be identified before accurate range rates can be determined. Consequently, a secondary goal of the Doppler Tracking Experiment is to analyze the resulting ionospheric information. In addition, it should be possible to probe traveling ionospheric disturbances with the satellite-to-satellite link and to detect the boundaries of turbulent regions of the ionosphere.

The analysis of the ionospheric information is an extension of well-known methods (differential Doppler and Faraday rotation) of measuring the integrated electron concentration and other properties of the ionosphere along a radio path between a terminal moving within or above the ionosphere and a station on the ground. Before artificial satellites were flown, these techniques were used in suborbital rocket flights to measure ionospheric parameters (refs. 11-4 and 11-5). Since 1957, much information based on the use of multifrequency Doppler links between satellites and ground stations has been published (refs. 11-6 to 11-14).

A fundamental problem in space-to-ground Doppler links is that the differential Doppler shift between two coherent, harmonically related frequencies is connected to the time derivative of the columnar electron content and not to the columnar content itself. This difficulty can be removed if simultaneous measurements are made of Faraday rotation. When Faraday rotation is not observed, the problem is not adequately determined, and inversion of differential Doppler data into columnar content strongly depends on the presence of horizontal gradients in that region of the ionosphere swept by the space-to-ground radio path while the spaceborne terminal is in motion.

The ASTP Doppler Tracking Experiment measured horizontal gradients between two spacecraft in the same orbit.

In the case of a probe transmitting at frequency ω_1 through the ionosphere with a receiver on the ground

$$\Phi_1(t) = \frac{\omega_1}{c} \int_0^{r(t)} n_1(r)\, dr \tag{11-2}$$

when the spacecraft is at a height $r(t)$. The symbol Φ denotes the phase shift imparted to the transmitted signal due to passage through the ionosphere, and its time derivative is

$$\dot{\Phi}_1(t) = \frac{\omega_1}{c}\frac{d}{dt}\int_0^{r(t)} n_1(r)\,dr \tag{11-3}$$

where c is the velocity of light in free space, $n(r)$ is the index of refraction at height r, and Φ is the frequency shift due to ionosphere passage. The change of the phase path with time is due in part to the spacecraft motion and in part to temporal changes of the index of refraction along the vertical path between the spacecraft and the ground. If there are no temporal changes along the path and the spacecraft is assumed to be at height r_0 at time t_0, the resulting equation is

$$\dot{\Phi}_1(t_0) = \frac{\omega_1}{c}\,\dot{r}(t_0)\,n_1(r_0) \tag{11-4}$$

If there are temporal changes, equation (11-3) becomes

$$\dot{\Phi}_1(t_0) = \frac{\omega_1}{c}\left[\dot{r}(t_0)n_1(r_0) + \int_0^{r(t)} \frac{\partial n_1(r)}{\partial t}\,dr\right] \tag{11-5}$$

where the term

$$\int_0^{r(t)} \frac{\partial n_1(r)}{\partial t}\,dr$$

represents the temporal variation of the columnar refractivity in the entire vertical path between the spacecraft and the ground. If this temporal variation is not determined, the inference of $n_1(r_0)$ from $\dot{\Phi}_1(t_0)$ will be erroneous.

When the effects of the Earth magnetic field and the collision frequency on the index of refraction are disregarded, equation (11-4) can be rewritten as

$$\dot{\Phi}_1(t_0) = \frac{\omega_1}{c}\,\dot{r}(t_0)\left(1 - \frac{2\pi e^2 N}{m\omega_1^{\,2}}\right) \tag{11-6}$$

where $\dot{N}$ is the electron density and e and m are the charge and the mass of the electron, respectively; $2\pi e^2/m = 1587.6$, if N is expressed in electrons per cubic meter and if ω_1 is expressed in radians per second. From equation (11-4), the local index of refraction, and hence the electron density, can be determined at the spacecraft height by monitoring the received Doppler shift and by knowing, independently, the velocity of the spacecraft and the frequency radiated. With a single frequency, it is necessary to know these two parameters very accurately. However, by adding a second frequency ω_2, the equation of the differential Doppler shift in the spacecraft-to-ground link, when temporal changes are neglected, becomes

$$\begin{aligned}
\delta\dot{\Phi} &= \dot{\Phi}_1(t) - \frac{\omega_1}{\omega_2}\,\dot{\Phi}_2(t) \\
&= \frac{\omega_1}{c}\,\frac{d}{dt}\int_0^{r(t)} \left[n_1(r) - n_2(r)\right] dr \\
&= \frac{\omega_1}{c}\,\dot{r}(t_0)\left[n_1(r_0) - n_2(r_0)\right]
\end{aligned} \tag{11-7}$$

If the refractive effects of the Earth magnetic field and the collision frequency are disregarded, the results are

$$\delta\dot{\Phi} = \frac{\omega_1}{c}\,\dot{r}(t_0)\,\frac{2\pi e^2 N}{m}\left(\frac{\omega_1^{\,2} - \omega_2^{\,2}}{\omega_1^{\,2}\omega_2^{\,2}}\right) \tag{11-8}$$

Equation (11-8) indicates that the contribution to the measurement error arising from an error in estimating the link frequencies is virtually eliminated.

Equation (11-6) indicates that an error in frequency contributes directly to the error in $\dot{\Phi}_1(t_0)$. However, equation (11-8) shows that the error in frequency must now be multiplied by the quantity $(n^2 - 1)/\omega_1^2$, which is usually very small. For instance, if $\omega_1/\omega_2 = n = 2$ and if $\omega_1 = 2\pi \times 300 \times 10^6$ rad/sec, then $(n^2 - 1)/\omega_1^2 = 8.6 \times 10^{-19}$; therefore, the influence of the frequency error in the overall error of $\dot{\Phi}_1(t_0)$ is eliminated.

When the spacecraft trajectory is not vertical, other analytical expressions, which have already been developed by several authors, must be used. For the case in which horizontal gradients of the electron content are negligible, the following can be written (ref. 11-8).

$$\delta\dot{\Phi}(t) = a_0 \left[-\frac{\dot{z}_s}{\cos\varphi_s} N_s + \left(\dot{r}_s + \frac{\dot{z}_s}{\cos\varphi_s}\right)\bar{N} \right] \tag{11-9}$$

where the velocity component $\dot{z}_s$ corresponds to the transmitter height z_s (measured along the local vertical z) and N_s is the local value of the electron concentration at that height; φ_s is the angle of incidence at the source measured from the local vertical z. The parameter

$$\bar{N} = \frac{1}{z_s} \int_0^{z_s} N \, dz \tag{11-10}$$

is the mean value of the integrated electron concentration in a column having a cross section of 1 square centimeter. The coefficient a_0 is

$$a_0 = \frac{2\pi e^2}{m} \frac{\omega_1}{c} \left(\frac{1}{\omega_1^2} - \frac{1}{\omega_2^2} \right) \tag{11-11}$$

In figure 11-2, r_s denotes the time-dependent radius vector joining the point of observation O to the moving source C, which is assumed to be approaching the observer and located at height z_s. The radial, horizontal, and vertical

velocity components of the source are denoted, respectively, by $\dot{r}_s$ (along the line of sight), $\dot{x}_s$, and $\dot{y}_s$ and $\dot{z}_s$.

In the general case, the electron concentration can be written as

$$\begin{aligned} N &= N(R,\theta,\chi,t) \\ &= N(z,x,y,t) \end{aligned} \tag{11-12}$$

where (fig. 11-2)

$$\left.\begin{aligned} R &= R_0 + z \\ x &= R_0\theta \\ y &= R_0\chi \end{aligned}\right\} \tag{11-13}$$

and (z,θ,χ) is a variable coordinate in a spherical orthogonal coordinate system along the wave-propagation trajectory joining the point of observation $(0,0,0)$ and the point (z_s,θ_s,χ_s) at which the transmitter is located at time t; these points are denoted by O and C, respectively, in figure 11-2. The difference in the Doppler frequency shifts for the two coherent radio waves can then be written in the form

$$\delta\dot{\Phi}(t) = a_0 \frac{d}{dt} \int_{R_0}^{R_s(t)} N(x,y,z,t) \frac{dz}{\cos\varphi(t)} \tag{11-14}$$

If certain conditions are satisfied, as in the Doppler Tracking Experiment, the results (ref. 11-8) obtained will be

$$\delta\dot{\Phi} = a_0 \left[-N_s \frac{\dot{z}_s}{\cos\varphi_s} + \bar{N}_x \left(\dot{r}_s + \frac{\dot{z}_s}{\cos\varphi_s} \right) - \bar{N}_y \dot{y}_s - N_t \right] \tag{11-15}$$

When the further simplifying assumption is made that the medium is plane parallel (i.e., neglecting Earth sphericity), the various parameters of equation (11-15) (ref. 11-8) are defined as follows.

$$\left.\begin{aligned}
\bar{N}_x &= \frac{1}{z_s}\int_0^{z_s} N\,dz + \frac{1}{z_s \sin\varphi_0 \cos\varphi_0}\int_0^{z_s} \frac{\partial N}{\partial x}\, z\,dz \\
\bar{N}_y &= \frac{1}{z_s \cos\varphi_0}\int_0^{z_s} \frac{\partial N}{\partial y}\, z\,dz \\
N_t &= \frac{1}{\cos\varphi_0}\int_0^{z_s} \frac{\partial N}{\partial t}\,dz
\end{aligned}\right\} \qquad (11\text{-}16)$$

Even in the planar approximation, the problem is inadequately determined. The difficulty is partly alleviated in this experiment by the fact that the DM-to-CSM dual-frequency link measures the quantity $\partial N/\partial x$ (the horizontal gradient in the orbital plane) at the ASTP orbital height.

$$\begin{aligned}
\delta\dot{\Phi} &= \dot{\Phi}_1(t) - \frac{\omega_1}{\omega_2}\dot{\Phi}_2 \\
&= \frac{\omega_1}{c}\frac{\partial}{\partial t}\left[\int_{DM}^{CSM} n_1(x)\,dx - \int_{DM}^{CSM} n_2(x)\,dx\right]
\end{aligned} \qquad (11\text{-}17)$$

Assuming the two spacecraft remain at a constant separation (have a relative velocity of zero), the results obtained will be

$$\delta\dot{\Phi} = \frac{\omega_1}{c}\int_{DM}^{CSM} \frac{\partial}{\partial x}\left[n_1(x) - n_2(x)\right]\frac{\partial x}{\partial t}\,dx \qquad (11\text{-}18)$$

By neglecting the refractive effects of the Earth magnetic field and the collision frequency, equation (11-18) can be rewritten as follows.

$$\delta\dot{\Phi} = \frac{\omega_1}{c}\,\frac{2\pi e^2}{m}\left(\frac{\omega_1^{\,2} - \omega_2^{\,2}}{\omega_1^{\,2}\omega_2^{\,2}}\right)\int_{DM}^{CSM} \frac{\partial N}{\partial x}\,\frac{\partial x}{\partial t}\,dx \qquad (11\text{-}19)$$

where $\partial x/\partial t$ is known from orbital-mechanics considerations and $\partial N/\partial x$ can therefore be obtained from the measured values of $\delta\Phi$ in the DM-to-CSM path. Before it can be used in equation (11-16), however, $\partial N/\partial x$ must be known all along the vertical z. In fact, what is needed is the function

$$\int_0^z (\partial N/\partial x)(z)\,dz$$

and not just $\partial N/\partial x$ at the ASTP orbital height of 220 kilometers. Therefore, a model must be constructed of $(\partial N/\partial x)(z)$ in the lower ionosphere, with the constraint of satisfying both the value measured at 220 kilometers by the DM-to-CSM link and a value equal to zero measured at the bottom of the ionosphere. A linear variation of the gradient between these two values thus seems to be an acceptable assumption.

In the DM-to-CSM link, the transmitting antenna is linearly polarized and the receiving antenna is circularly polarized. Therefore, the Faraday rotation (rotating Doppler) phenomenon cannot be observed.

EQUIPMENT

The two major Doppler Tracking Experiment components are the transmitter (fig. 11-3), located on the DM, and the receiver (fig. 11-4), complete with the Doppler processor, located on the CSM. Each weighs approximately 7 kilograms.

The transmitter consists of a highly stable crystal oscillator, frequency multipliers, amplifiers, and a diplexer. The diplexer combines the two frequencies for transmission from a single antenna. Figure 11-5 is a block diagram of the transmitter. To save battery power for the operational phase of the experiment, the transmitter was powered directly from the spacecraft during the 50-hour warmup period required by the oscillator. The frequency of the oscillator is set for 5.06 megahertz. Its excellent stability (1.5 parts in 10^{12}, over both 10- and 100-second averaging intervals) is preserved by carefully insulating it from environmental changes. A single multiplier chain multiplies, amplifies, and filters the oscillator

output and drives a power divider. One power-divider output drives the 162-megahertz input of a diplexer; the second power-divider output is frequency-doubled, then drives the 324-megahertz diplexer input. The diplexer provides input isolation and filtering. At least 100 milliwatts of output power is delivered to the dual-frequency antenna at each of the two frequencies.

The receiver, shown in block diagram form in figure 11-6, provides a Doppler output that is compatible with transistor-to-transistor logic for each input frequency to the processor. The frequency and phase variations of the 162- and 324-megahertz inputs are retained through the use of second-order phase-lock loops. Thus, the receiver outputs are actually bandpass-filtered and constant-amplitude replicas of the input signals, translated from 162 and 324 megahertz to 1 kilohertz. The choice of 1 kilohertz as the center frequency for the processor represents a compromise between a desire for high accuracy, which means a low frequency, and the need to avoid the ambiguity that could result if the Doppler signal shifted this frequency negatively by more than 1 kilohertz. Because the maximum anticipated Doppler shift is approximately 350 hertz, a 1-kilohertz center frequency leaves an adequate margin without significantly degrading the attainable measurement accuracies.

The receiver is powered internally by means of dc-to-dc converters, regulators, and filter circuitry. Less than 50 watts of spacecraft power is required to operate both the receiver and the experiment tape recorder.

Both the transmitting and the receiving antennas are dual-frequency units. The former is a vertical monopole that acts as a quarter-wave antenna at frequencies of 162 and 324 megahertz. At 324 megahertz, an inductor near the midpoint of the antenna isolates the top section from the bottom section; at 162 megahertz, the inductor acts as a small loading coil. The receiving antenna is approximately 1 meter square and contoured to fit against the side of the service module. It is a strip-line conformal array in which tuned stubs are used to couple its sections at 162 megahertz and to isolate the sections at 324 megahertz.

A 5.0-megahertz reference frequency input to the synthesizer and the timing reference for the Doppler processor are supplied by an oscillator that is identical, except for its frequency, to that in the transmitter. The synthesizer, having output frequencies, derived by frequency multiplication and division, that are phase coherent with the reference, provides all local-oscillator injections and phase-detector references. When required, bandpass filters are used to obtain outputs of sufficient spectral purity.

A diplexer at the receiver input divides the single input from the dual-frequency antenna into two channels. A preamplifier and a mixer follow the diplexer. These stages have a noise figure of less than 8 decibels and a first intermediate-frequency (IF) image-rejection capability of greater than 60 decibels. For each channel, a second IF image-rejection capability of at least 60 decibels is achieved by means of a crystal filter. The first IF amplifier includes two automatic-gain-controlled stages, and the second includes four active filters with amplitude limiting at each stage. The second IF amplifier is followed by sine and cosine phase detectors and filters; the first develops the loop filter voltage fed to the voltage-controlled oscillator (VCO), and the second provides both the automatic-gain-control voltage for the first IF amplifier and a lock/out-of-lock signal to the Doppler

processor. The VCO module output fed to the first mixer is derived by multiplying and filtering the output of a crystal VCO having a frequency of 22.5 megahertz.

If an out-of-lock signal is received, the processor responds by supplying the phase-detector module with one signal to change the phase-lock-loop bandwidth from 5 to 100 hertz and another signal to inject a sweep voltage into the loop. The difference between the sweep (±5 and ±2.5 kilohertz at 324 and 162 megahertz, respectively) and the expected Doppler shift allows for changes in the central-voltage-to-frequency transfer characteristics of the oscillator. When lock is acquired, the signal voltages change state, the sweeping voltage is removed, and the loop bandwidth is restored to 5 hertz.

The processor receives Doppler frequency information from the receiver, extracts the desired information, and records and stores this information simultaneously on two tape recorders in the CSM (fig. 11-7). The Doppler frequency averaging interval counted by the processor is shown in figure 11-8. A 10-second counter identifies the time instants t_0, $t_2 = t_0 + 9.996$ seconds, $t_0' = t_0 + 10$ seconds, $t_2' = t_2 + 10$ seconds, etc. The points t_1 and t_3 are determined by the first positive-going zero crossing that occurs after times t_0 and t_2, respectively. For each channel, an associated vernier up/down counter is enabled at time t_0 and counts the number of 1-microsecond clock pulses observed before it is disabled at time t_1. It is enabled again at time t_2, when it down-counts the number of clock pulses in the interval $t_2 - t_3$. Simultaneously, zero-crossing counters count the number of positive-going zero crossings in the interval $t_0 - t_2$ for each channel. These time counts and zero-crossing counts constitute the raw data associated with each observation interval. The counters are reset and the entire process begins again at time t_0'.

The average frequency $\hat{f}$ observed during a processor cycle can be determined from these tape-recorded data by dividing the number of zero crossings Z by the observation time.

$$\hat{f} = \frac{Z}{9.996 - \Delta t} \tag{11-20}$$

where Δt represents the contents of the vernier counter. Because the zero-crossing counters and the vernier counters are 15 and 13 bits wide, respectively, an unambiguous measurement of any Doppler frequency shift less than or equal to ±750 hertz is ensured.

The Doppler processor also performs other functions. For example, it monitors lock/out-of-lock signals from the receiver. If an out-of-lock condition occurs, the processor reestablishes lock status and loads out-of-lock data into a format that can be detected during subsequent data reductions. In addition, the Doppler processor supplies 324-megahertz phase-lock status information to the astronauts by

means of a panel meter, and supplies that information plus frame numbers to telemetry. Based on this phase-lock status information, spacecraft maneuvers can be performed to regain 324-megahertz lock if required. (If the 324-megahertz channel is locked, the 162-megahertz channel probably also is locked, because of its higher signal-to-noise ratio.) From the telemetered frame number, the tape-recorded data can be correlated with the position of the CSM/DM pair relative to the Earth. In another function, data on roll, pitch, and yaw rates of the CSM are received by the processor and tape-recorded to enable compensation for the effect of the CSM motion on the Doppler shift during data reduction. Finally, 7-bit parity words are generated by the processor as a protection against substitution and synchronization errors.

Every 10 seconds, a data word is formatted by means of a random-access memory, shift registers, a frame counter, and a microprogramed controller. This data word consists of the number of zero crossings and the Δt values for both the 162-megahertz and the 324-megahertz channels, plus information on roll, pitch, and yaw rates and parity. After 73 words have been stored as a frame, the frame number is appended and the data are serially transferred to the tape recorders at a 972-hertz bit rate through a biphase encoder. Approximately 5.2 seconds of recording is required per frame.

RESULTS

The experiment produced 108 Doppler data frames, each containing 73 data words; each data word is a 10-second sample of an integrated Doppler shift. The total data span was 21 hours 54 minutes. The CSM/DM separation occurred during data frame 16. The CSM orbital changes, to attain the intended 300-kilometer CSM/DM separation, ended with data frame 40. The prime data take included frames 40 to 108; thus, the prime data span covered 13 hours 47 minutes, or approximately nine orbital revolutions.

The CSM Doppler receiver lost lock twice during the prime data take (shown in the plot of Doppler signals from the prime data take): once over eastern Siberia, where ground transmitters having the same frequency used in the experiment are known to be operating, and once during an incorrect CSM maneuver, which turned the CSM Doppler antenna away from the DM line of sight. (The maneuver was intended to aim the high-gain unified S-band (USB) antenna at Applications Technology Satellite 6 after a sleep period.)

To avoid occultation of the transmitting antenna by the DM, that antenna was mounted parallel to the planned axis of rotation (the Z-axis). In a series of slightly more than 100 frames of 16-millimeter motion picture film taken by the astronauts showing the DM shortly after separation, the DM appears to be rotating as predicted at a rate of approximately 1.0 rpm about the Z-axis. Some precession is seen, which was probably caused by undetermined separation forces and enhanced by the near equality of the moments of inertia about the Y-axis and the Z-axis.

Two hundred and thirty-five passes of DM tracking support were arranged with the Defense Mapping Agency (DMA). The transmitter frequencies for the experiment were selected specifically for compatibility with the DMA tracking network

so that an accurate DM orbit could be calculated. The USB tracking of the CSM resulted in data that will be used by SAO for computing a CSM orbit. By means of spacecraft telemetry, SAO has accurate times for the start of several data frames; these times provide a correlation between the Doppler data and the orbital position of the spacecraft.

Doppler data taken before CSM/DM separation were intended to give measurements of relative (transmitter compared to receiver) oscillator stability and a check of correct operation of the flight hardware. When the two spacecraft are docked, neither Doppler shift nor ionospheric effects can occur. Thus, the time variation in the sequence of 10-second integrated-frequency measurements at each frequency is a measure of the stability of the transmitter oscillator relative to that of the receiver oscillator. The difference between simultaneous 324- and 162-megahertz observations is a test of the balance of the flight circuitry.

The 324-megahertz data for the time before separation are plotted in figure 11-9. Figure 11-10 is an expanded plot of the 3×10^{-10} frequency shift visible in figure 11-9 2000 seconds after the start of the data take. It is clear that the two channels track closely; therefore, the frequency shift must be attributed to one of the two oscillators. A shift of this kind is not unusual in a crystal oscillator that has not attained its designed operating temperature; the shift probably results from the inadvertent turnoff of the Doppler transmitter for an interval of 10 minutes after the 50-hour warmup period and before the start of the data take. The 4×10^{-11} excursion at 10 000 seconds, just before separation (fig. 11-9), may be the result of vehicle spinup, which applies a small gravitational load to the oscillator crystals. The slope of the curve in figure 11-9 between 3000 and 9000 seconds indicates a relative drift of 1.6×10^{-9} per day between the transmitter and the receiver oscillators. This drift is sufficiently small to be considered insignificant.

Before separation, the fluctuations between successive Doppler data points had a root-mean-square value of 3×10^{-12}, which is slightly better than the level obtained in preflight tests. The differences between simultaneous frequency measurements for the 324- and 162-megahertz channels have a root-mean-square value of 4×10^{-12}, which again is consistent with preflight test results.

In summary, the frequency measurements made while the CSM and the DM were rigidly attached indicate that the flight hardware for this experiment was operating properly, with the exception of a 250-second oscillator excursion of 3×10^{-10}. Such an excursion is not likely to have been repeated during the prime data take some 8 hours later.

Figure 11-11 illustrates the clear Doppler signatures of DM jettison and CSM-orbit-adjust rocket firing. The 1.40-hertz step change in frequency corresponds to a 1.30-m/sec initial separation velocity.

Figures 11-12 and 11-13 display the Doppler data acquired during the prime data take. These data have been corrected for ionospheric propagation effects. A comparison of these graphs with figures 11-14(a) to 11-14(d) illustrates the efficacy

of the two-frequency ionospheric correction; the large (as great as 6 hertz peak to peak) ionospheric signals of figure 11-14 are absent from figures 11-12 and 11-13.

The large, nearly sinusoidal oscillations shown in figure 11-12 have a period identical to the spacecraft orbital period and are the result of differences between the CSM and the DM orbits. The fact that these oscillations diminish in amplitude and show an increasing departure from a sinusoid indicates that the difference between the two orbits varied with time and very likely resulted from atmospheric drag, which would affect the two spacecraft differently because of their different area-to-mass ratios. These orbit differences will be verified by using the USB tracking data to calculate an accurate CSM orbit for comparison with the DM orbit derived from the DMA tracking network data.

Figure 11-13 displays a sample of the ionosphere-corrected data with long-period (orbital) variations removed to permit an examination of short-period noise. The short-period variations are attributed to DM rotation. Because this effect was anticipated, the DM transmitting antenna was positioned to be parallel to, but offset from, the DM rotation axis. It appears that the actual antenna offset is essentially zero. However, the photographs of the DM taken just after separation show a precession of the DM spin axis of approximately 20°, which would generate a periodic Doppler modulation at the DM rotation rate with a peak-to-peak amplitude of approximately 70 to 80 millihertz (fig. 11-13). A fast Fourier analysis is being performed to identify all frequency components that may be present in the Doppler data. This analysis will provide a positive identification of all periodic components generated by DM rotation.

The preliminary results for the secondary goal of the Doppler Tracking Experiment are as follows. The traces of $\delta\dot{\Phi}$ obtained after the orbit adjustments show quite large excursions — as great as 6 hertz peak to peak — on successive orbits. This value is approximately 10 times greater than any simulated value obtained from the average ionospheric model. However, if an averaging interval equal to that used in the simulation were applied to the measured $\delta\dot{\Phi}$, the amplitude variation would be of the same order of magnitude. Differential Doppler measurements for four consecutive revolutions are shown in figures 11-14(a) to 11-14(d).

Calculations to accurately establish the CSM orbit have not yet been performed. Until the baseline length and directions have been more precisely determined, it is difficult to assign visible features of the $\delta\dot{\Phi}$ record to known or expected ionospheric conditions. It does appear, from examining the periods between peaks in $\delta\dot{\Phi}$, that the baseline is somewhat shorter than the nominal 300 kilometers. It also appears that traveling ionospheric disturbances were repeatedly intersected by the DM/CSM Doppler baseline.

REFERENCES

11-1. Isacks, Bryan; Oliver, Jack; and Sykes, Lynn R.: Seismology and the New Global Tectonics. J. Geophys. Res., vol. 73, no. 18, Sept. 15, 1968, pp. 5855-5899.

11-2. Muller, P. M.; and Sjogren, W. L.: Mascons: Lunar Mass Concentrations. Science, vol. 161, no. 3843, Aug. 16, 1968, pp. 680-684.

11-3. Schwarz, C. R.: Gravity Field Refinement by Satellite to Satellite Doppler Tracking. NASA CR-117404, 1970.

11-4. Jackson, John E.; and Seddon, J. Carl: Ionosphere Electron Density Measurements With the Navy Aerobee Hi Rocket. J. Geophys. Res., vol. 63, no. 1, Mar. 1958, pp. 197-208.

11-5. Seddon, J. C.: Propagation Measurements in the Ionosphere With the Aid of Rockets. J. Geophys. Res., vol. 58, 1953, pp. 323-335.

11-6. Alpert, Ya. L.: A Method for Investigating the Ionosphere With Artificial Satellites. Uspekhi Fizicheskikh Nauk, vol. 64, 1958, p. 3.

11-7. Alpert, Ya. L.: On the Results of Ionosphere Investigations With the Help of Coherent Radio Waves Emitted by Satellites. Space Research V, Proceedings of the Fifth International Space Science Symposium, D. S. King-Hele, P. Muller, and G. Righini, eds., North-Holland Publishing Co. (Amsterdam), 1965, pp. 652-686.

11-8. Alpert, Ya. L.: Radio Wave Propagation in the Ionosphere. The Ionosphere. Second ed. Vol. I, Consultants Bureau (New York), 1973, pp. 61-77.

11-9. Alpert, Ya. L.: On Radio Methods of Ionospheric Investigations by Means of Coherent Radio Waves Emitted by Satellites. Paper presented at COSPAR/URSI Symposium on Beacon Satellite Investigations of the Ionosphere Structure and ATS-6 Data (Moscow), Nov. 1974.

11-10. Garriott, Owen K.: The Determination of Ionospheric Electron Content and Distribution From Satellite Observations, Part 1. Theory of the Analysis. J. Geophys. Res., vol. 65, no. 4, Apr. 1960, pp. 1139-1150.

11-11. Garriott, Owen K.: The Determination of Ionospheric Electron Content and Distribution From Satellite Observations, Part 2. Results of the Analysis. J. Geophys. Res., vol. 65, no. 4, Apr. 1960, pp. 1151-1157.

11-12. De Mendoza, F.: Ionospheric Studies With the Differential Doppler Technique. Radio Astronomical and Satellite Studies of the Atmosphere, J. Aarons, ed., American Elsevier (Amsterdam), 1963, pp. 289-312.

11-13. Misyura, V. A.; Solodovnikov, G. K.; and Migunov, V. M.: Gradients of the Integral Electron Content in the Ionosphere. Geomagn. & Aeron., vol. 4, 1964, pp. 872-874. (Primary source — Geomagn. i Aeronomiya, vol. 4, 1964, pp. 1124-1126.)

11-14. Tyagi, T. R.: Determination of Total Electron Content From Differential Doppler Records. J. Atmos. Terrestrial Phys., vol. 36, July 1974, pp. 1157-1164.

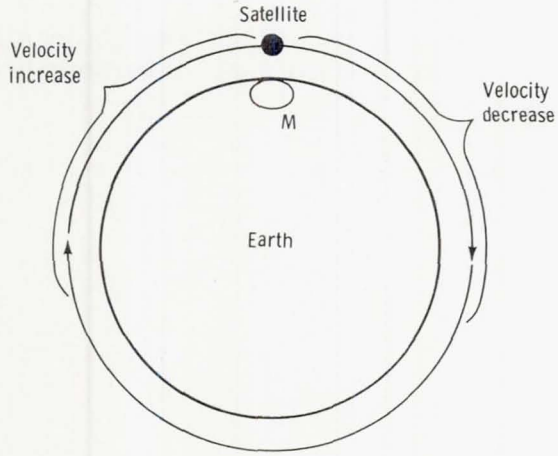

Figure 11-1.- Velocity changes associated with a gravity anomaly.

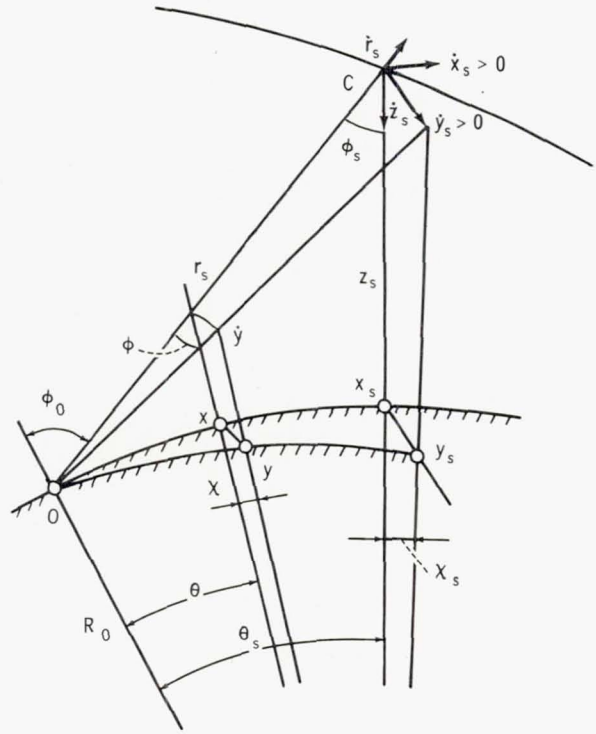

Figure 11-2.- Schematic diagram of terms used in equations (11-12) to (11-16).

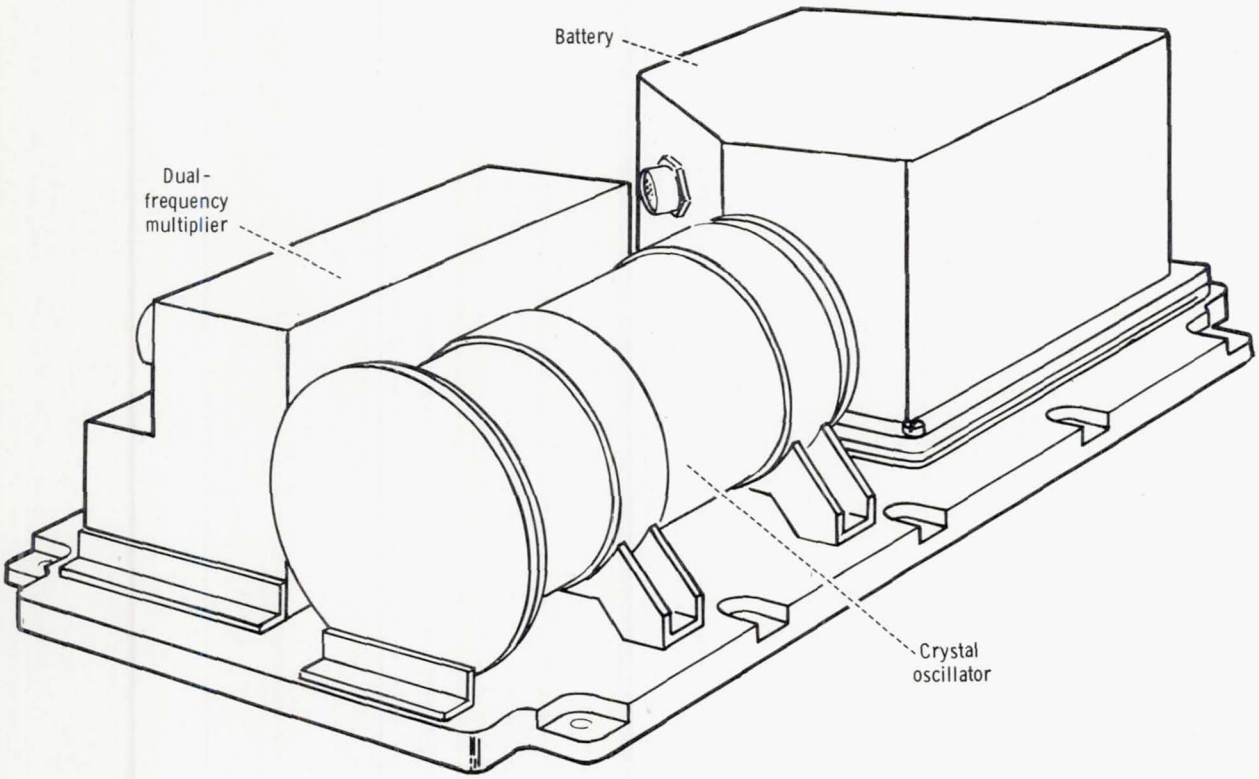

Figure 11-3.- The Doppler tracking transmitter.

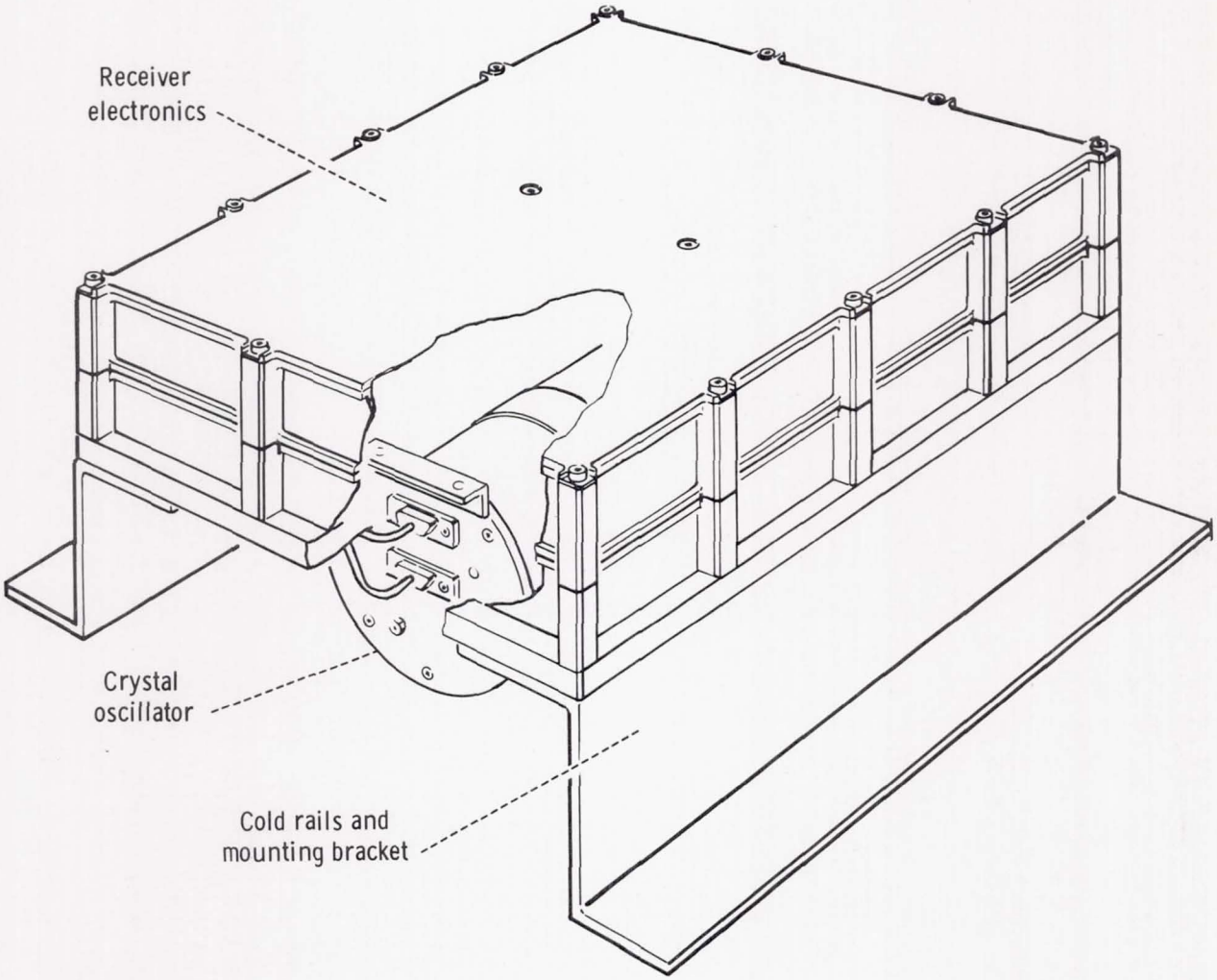

Figure 11-4.- The Doppler tracking receiver.

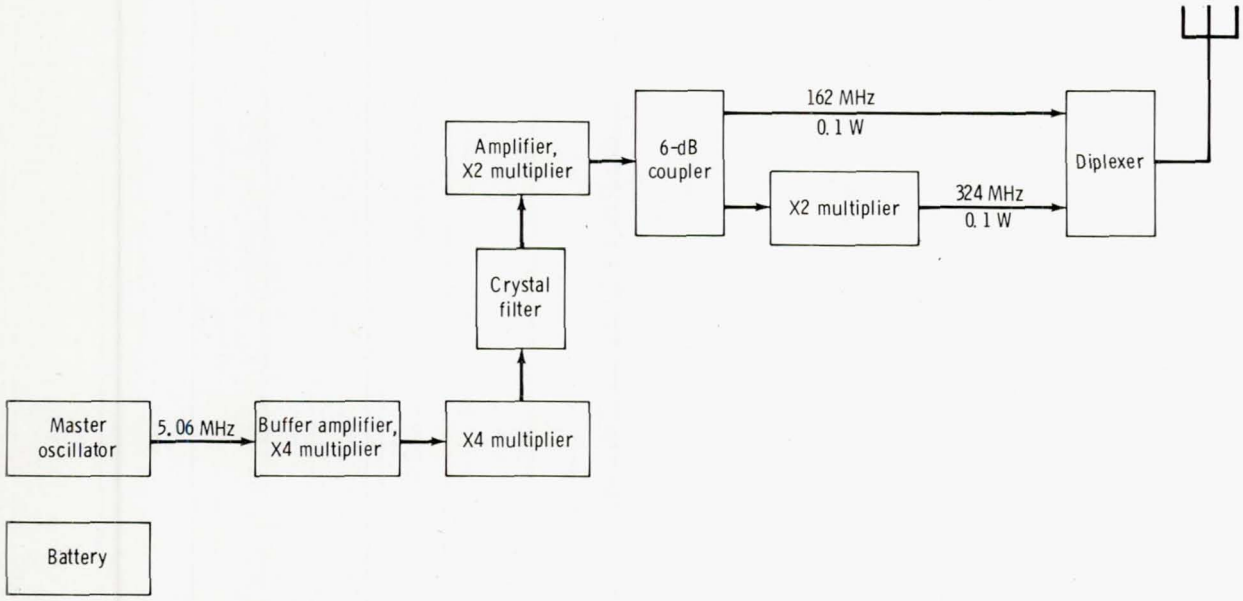

Figure 11-5.- Block diagram of the transmitter.

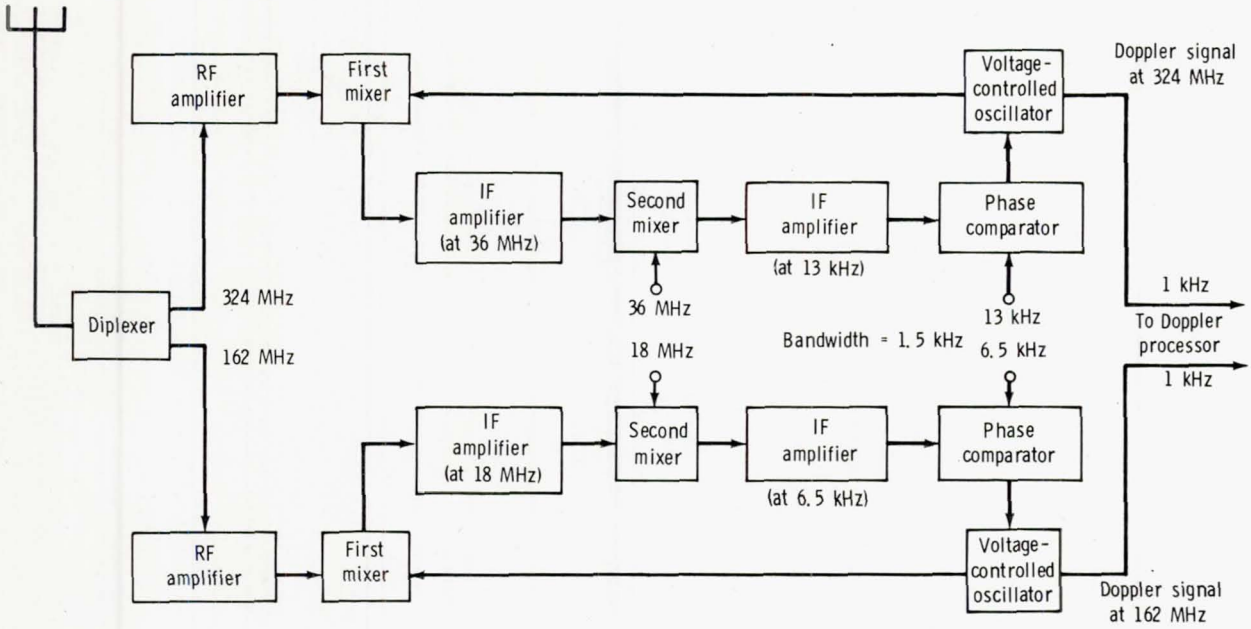

Figure 11-6.- Block diagram of the receiver.

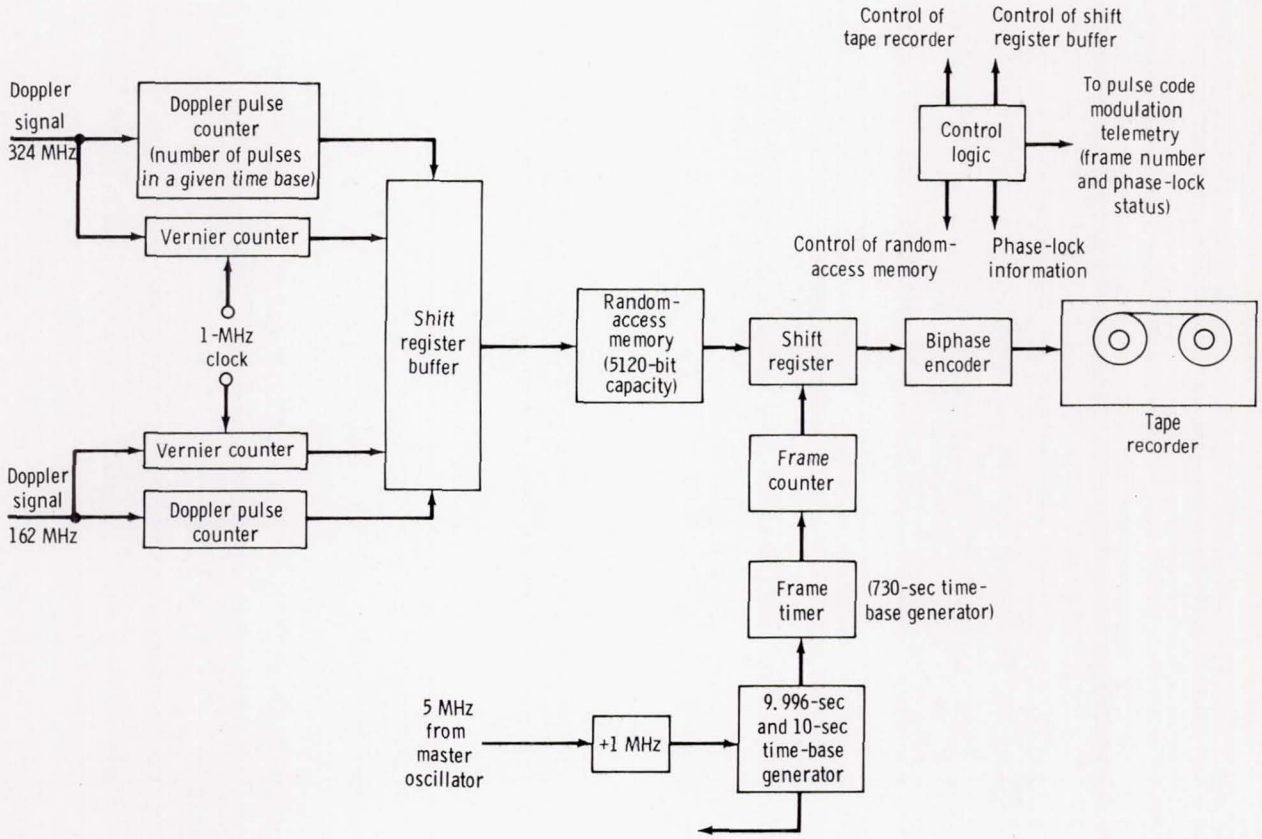

Figure 11-7.- Block diagram of the Doppler processor.

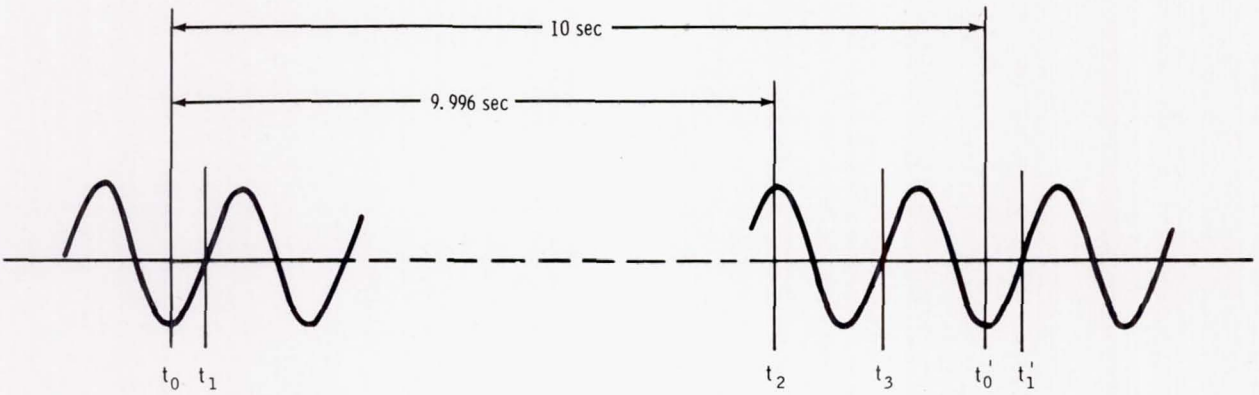

Figure 11-8.- Counting interval of the Doppler processor.

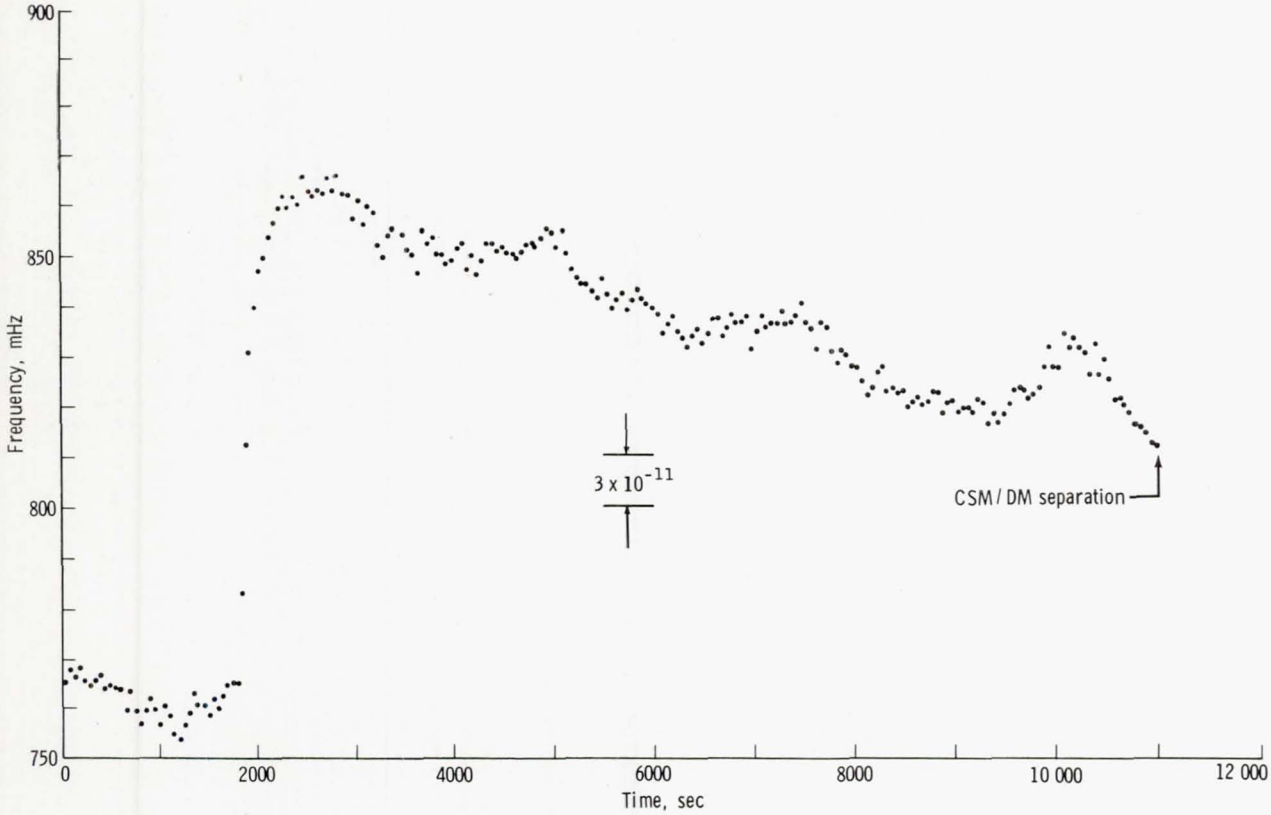

Figure 11-9.- Initial 11 000 seconds of 324-megahertz Doppler data. Vertical scale shows the output of the receiver Doppler processor with a 1020-hertz instrument bias subtracted.

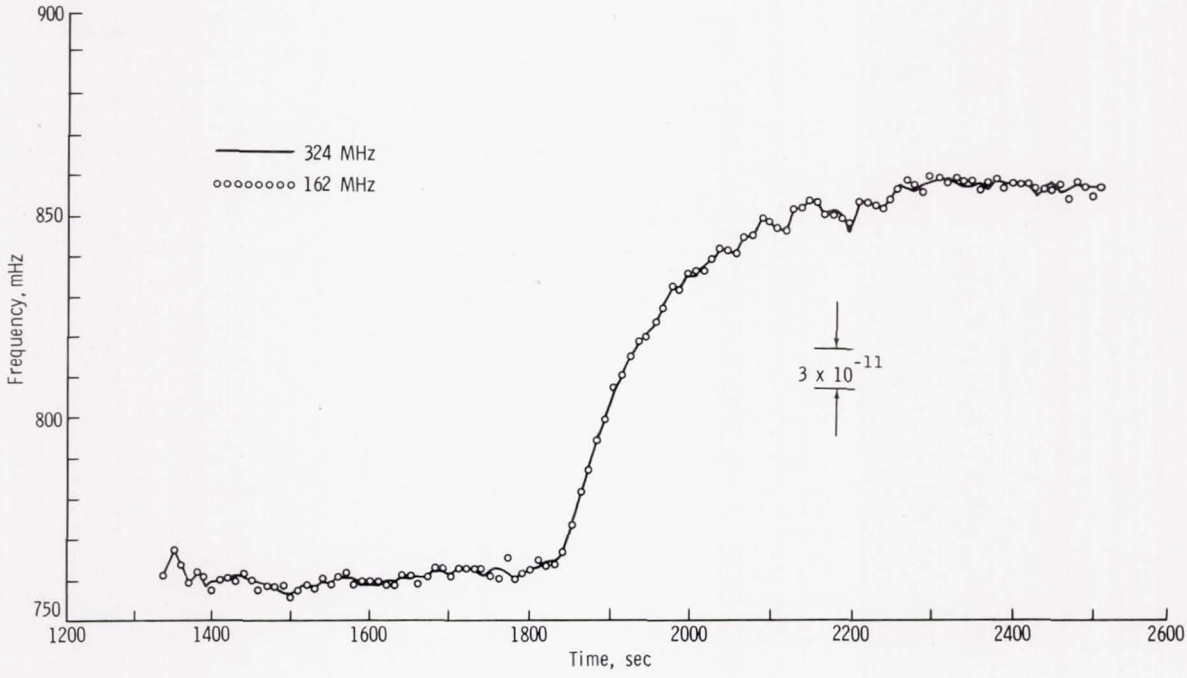

Figure 11-10.- Expanded plot of frequency shift seen shortly after start of the data take. Vertical scale shows the output of the receiver Doppler processor with a 1020-hertz instrument bias subtracted.

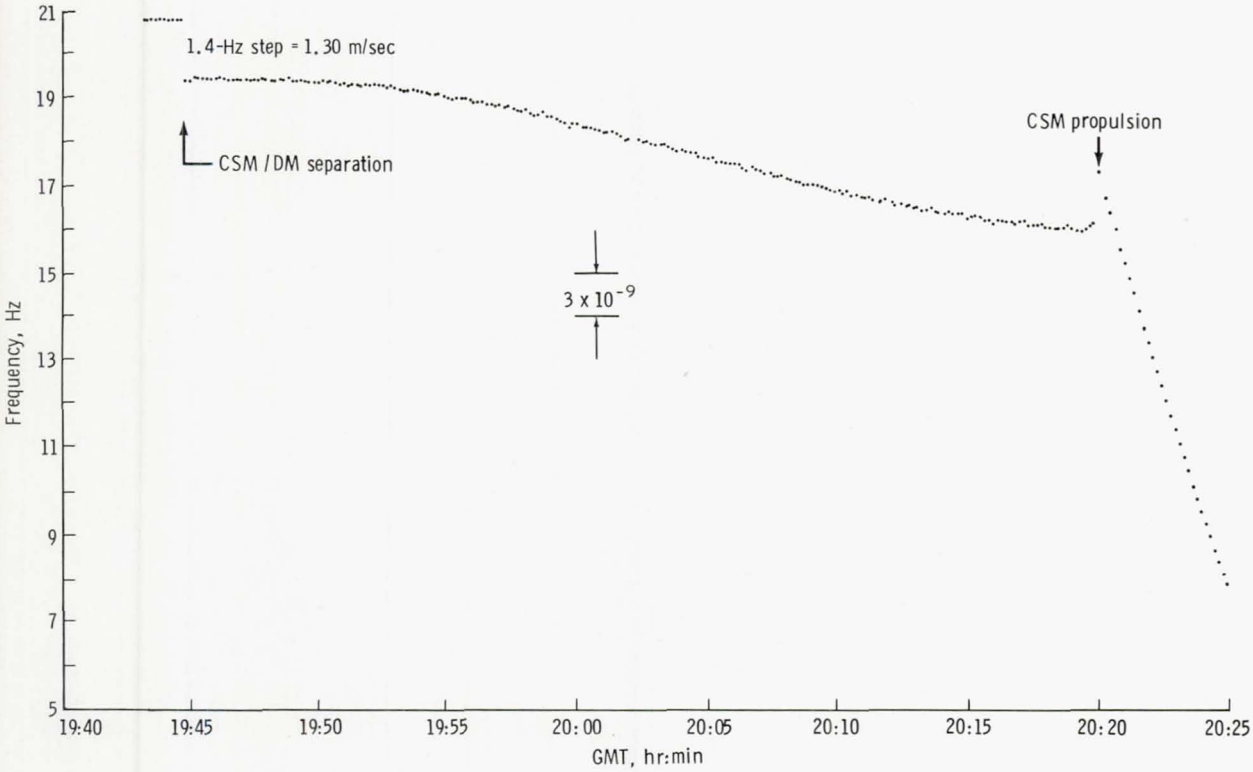

Figure 11-11.- Doppler signatures of DM jettison and CSM-orbit-adjust rocket firing. Vertical scale shows the output of the receiver Doppler processor with a 1000-hertz bias subtracted (July 23, 1975).

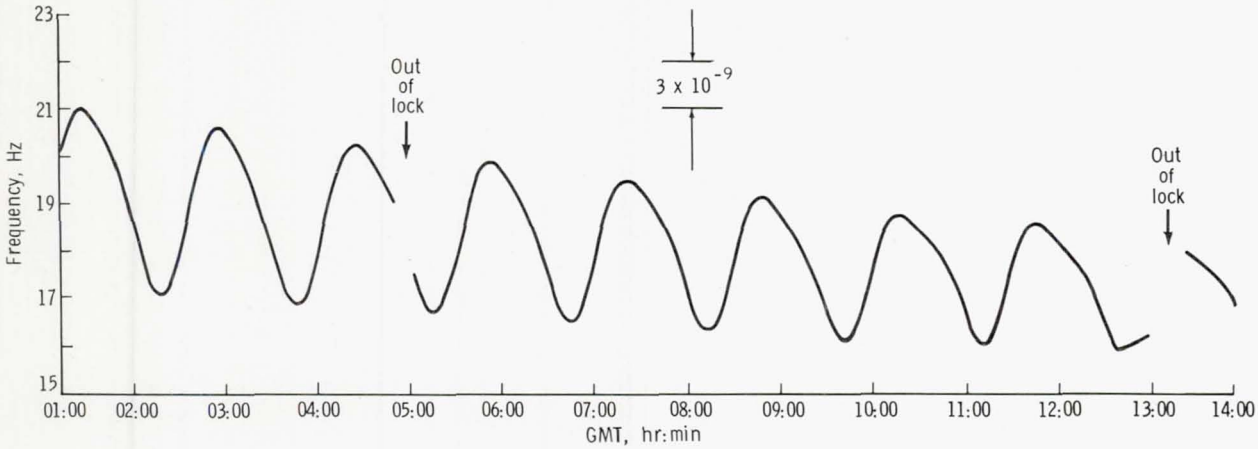

Figure 11-12.- Doppler signals from prime data take, corrected for ionospheric propagation effects. Vertical scale shows the output of the receiver Doppler processor with a 1000-hertz bias subtracted (July 24, 1975).

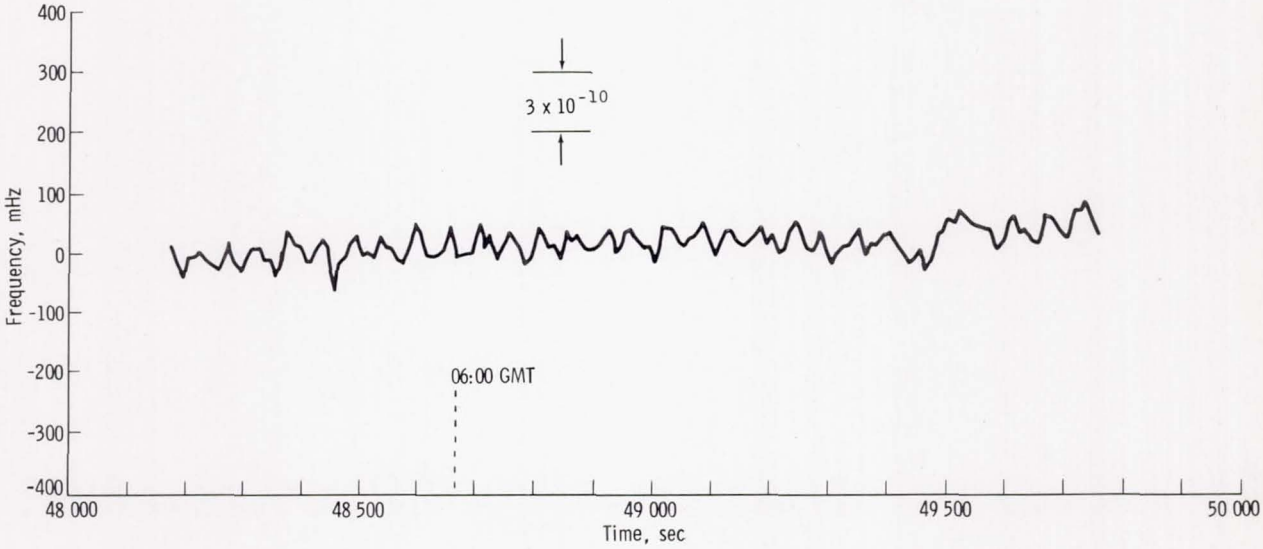

Figure 11-13.- Doppler data corrected for ionospheric propagation effects; long-period variations have been removed (July 24, 1975).

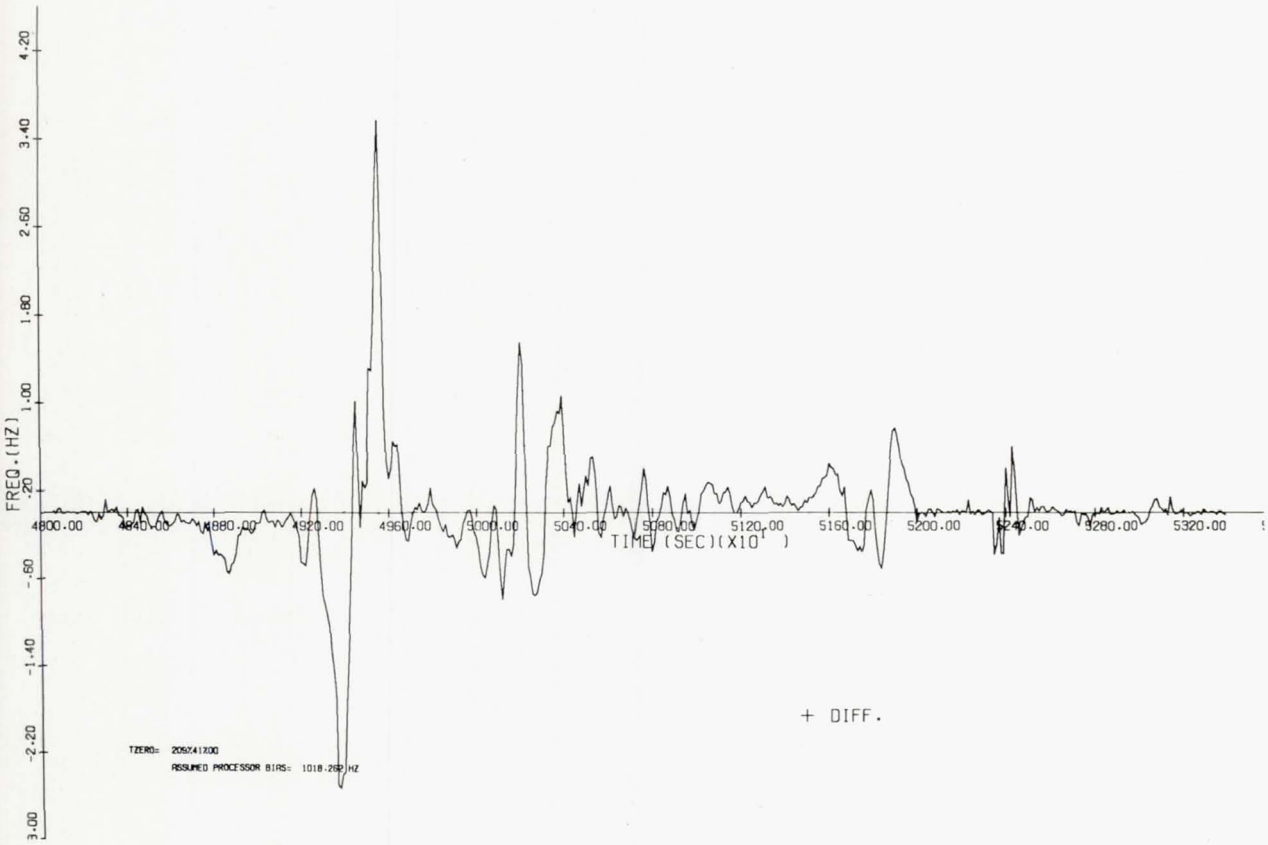

(a) Revolution 129.

Figure 11-14.- Differential Doppler shift, which is due to the ionosphere, for four consecutive orbital revolutions.

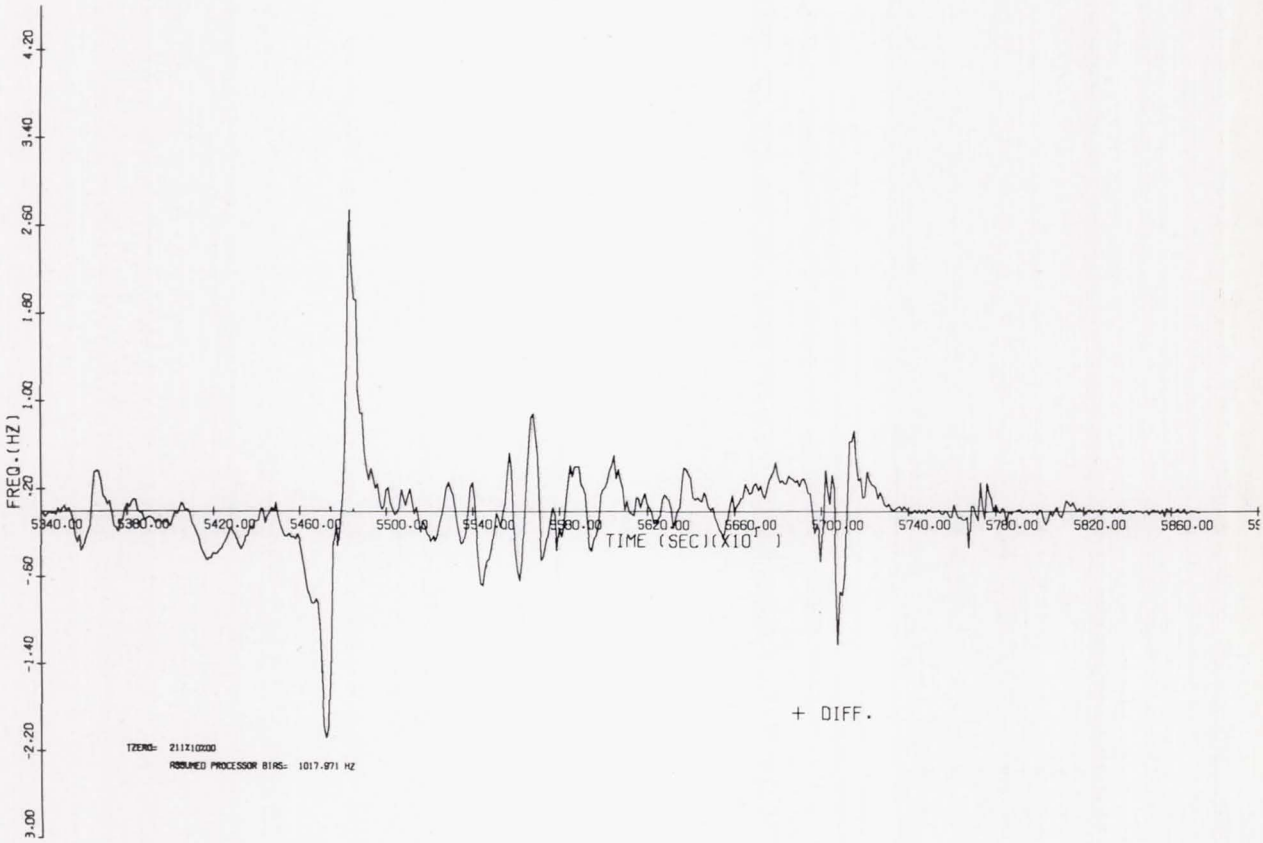

(b) Revolution 130.

Figure 11-14.- Continued.

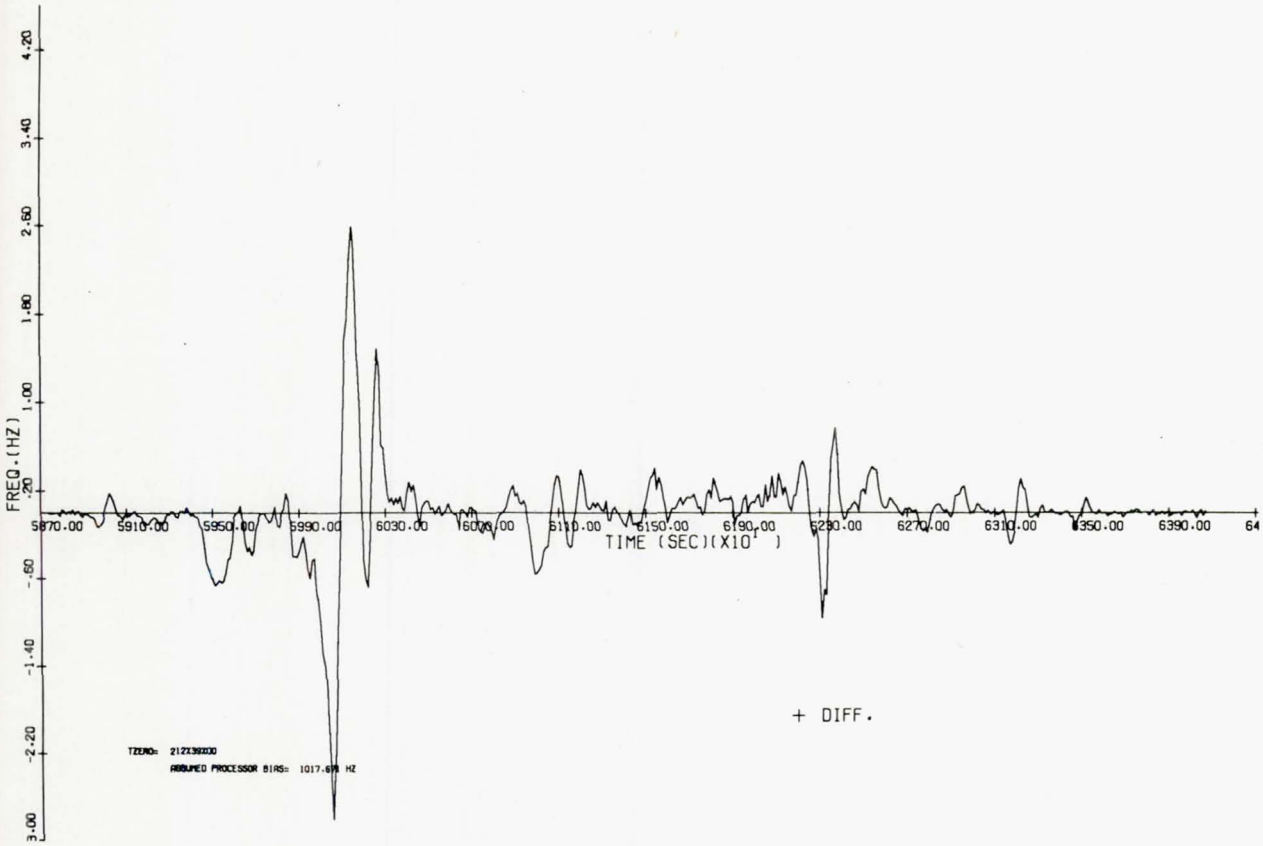

(c) Revolution 131.

Figure 11-14.- Continued.

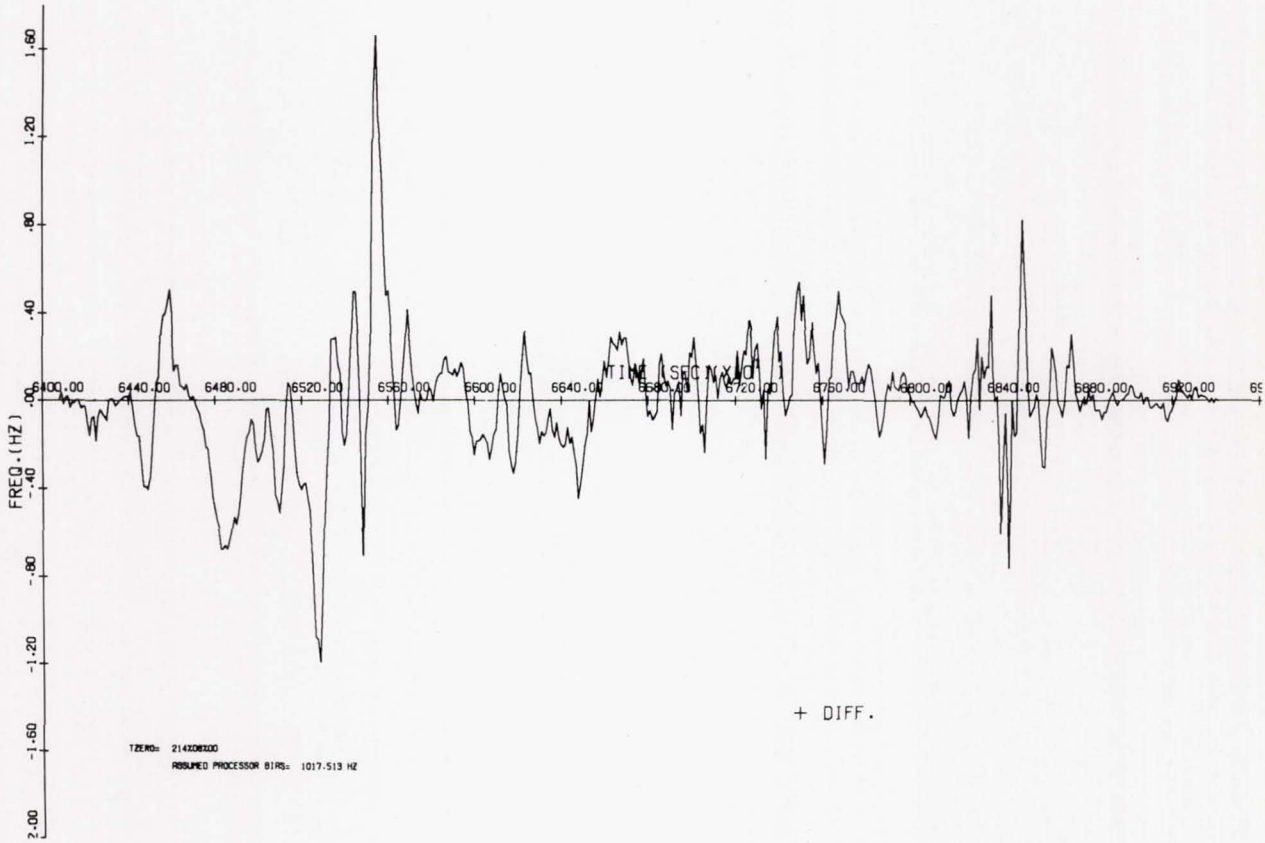

(d) Revolution 132.

Figure 11-14.- Concluded.

12. GEODYNAMICS

EXPERIMENT MA-128

F. O. Vonbun,[a†] W. D. Kahn,[a] J. W. Bryan,[a] P. E. Schmid,[a]
W. T. Wells,[b] and T. D. Conrad[b]

ABSTRACT

The Apollo-Soyuz Test Project Geodynamics Experiment was performed to assess the feasibility of tracking and recovering high-frequency components of the Earth gravity field by utilizing a synchronous orbiting tracking station such as Applications Technology Satellite 6. Gravity anomalies of 5 milligals or larger having wavelengths of 300 to 1000 kilometers on the surface of the Earth are important for geologic studies of the upper layers of the Earth crust. Two prime areas of data collection were selected for this experiment. The first area is the center of the African Continent, and the second area is the Indian Ocean Depression centered at latitude 5° N and longitude 75° E.

Preliminary results show that the detectability objective of the experiment has been achieved in both areas as well as in several additional anomalous areas around the globe. Gravity anomalies of the Karakoram and Himalayan mountain ranges, of ocean trenches, and of the Diamantina Depth are specific examples. Further analyses are planned to demonstrate the usefulness of range-rate signatures for recovery of gravitational anomalies and for determining the surface distribution of the anomalies.

INTRODUCTION

The objectives of the Apollo-Soyuz Test Project (ASTP) Geodynamics Experiment were threefold.

1. To demonstrate the detectability of short-wavelength (i.e., 300 kilometers and larger) features of the Earth gravity field

2. To evaluate the "high/low" satellite-to-satellite tracking (SST) concept for geodynamics applications

---

[a]NASA Goddard Space Flight Center.

[b]Washington Analytical Services Center, Inc., Riverdale, Maryland.

[†]Principal Investigator.

3. To test the recoverability of short-wavelength features of the Earth gravity field

This experiment was the culmination of an effort to utilize synchronous orbiting tracking stations for NASA missions (ref. 12-1). The use of a low-orbiting (approximately 230 kilometers) spacecraft, such as Apollo-Soyuz, continuously tracked by a synchronous satellite has, for the first time, led to the detection of short-wavelength Earth gravity anomalies (ref. 12-2).

The Apollo-Soyuz spacecraft, flying in a low orbit, is particularly sensitive to gravity anomalies. For example, the ratio of sensitivity to the 25th-degree terms of the Earth gravity potential having a wavelength of approximately 1600 kilometers is approximately 13 to 1 when going from a Geodetic Earth Orbiting Satellite 3 type orbit (840 kilometers) to the lower Apollo orbit (230 kilometers). Thus, the ASTP mission presented an excellent opportunity to test the SST concept. Normal satellite perturbation methods used previously for computing the Earth gravity field cannot be used for such short wavelengths because this would require a spherical harmonic expansion to an order and degree of 120 or larger.

MATHEMATICAL METHODS

The gravitational field of the Earth is generally represented in terms of a finite spherical harmonic series expansion having coefficients determined from a combination of satellite ground tracking data and surface gravimetric data. Such a limited representation of the global geopotential does not adequately "model" local variations in the gravity field because the short wavelengths of these local variations would require a field expansion to a degree and order of approximately 100 to 200. This is considered impractical if not impossible. However, rather small local gravity anomalies are important for geologic investigations of the upper crust as well as for studies of the ocean topography.[1] This experiment provided an opportunity to improve knowledge of the terrestrial gravitational field in localized areas by directly measuring local gravity variations through detection of small velocity changes (1 to 10 mm/sec) of the low-orbiting spacecraft. Before the gravity anomaly analyses are discussed, some basic information about the tracking system will be presented. Figure 12-1 is a schematic of the Applications Technology Satellite 6 (ATS-6)/Apollo communication links. The Apollo spacecraft was connected with Madrid by two links: the ATS-6 link and a direct ground link. This provides a total loop for the measurements that will be used to reduce the errors in the system. The emphasis in this report is on the link from Madrid to ATS-6 to Apollo and back. Figure 12-2 depicts the range rates that were actually measured during the experiment. The system was constructed to measure the total range rate between the ground station (in this case Madrid) and the Apollo spacecraft in Earth orbit. The total range rate is the sum of the range rates between Madrid and ATS-6 $\dot{r}_1$, ATS-6 and Apollo

[1] F. O. Vonbun, et al., "Sea Surface Determination From Space," Report X-900-75-216, Goddard Space Flight Center, 1975.

$\dot{r}_2$, Apollo and ATS-6 $\dot{r}_3$, and ATS-6 and Madrid $\dot{r}_4$ (ref. 12-3). This analysis concentrates only on variations of the range rate between Apollo and ATS-6 $\dot{\rho}_A$, which is a dot product of the spacecraft velocity vector $\vec{v}$ and the unit vector between Apollo and ATS-6 $\vec{\rho}^{\,0}$ as seen in figure 12-2.

$$\dot{\rho}_A = \left(\vec{\rho}^{\,0} \bullet \vec{v}\right) \tag{12-1}$$

One of the first experiment tasks was to evaluate the noise characteristics of the total system. An analysis performed before the experiment was the basis for a predicted range-rate noise level of approximately 0.05 cm/sec using a 10-second integration time (fig. 12-3). The actual experimental range-rate noise level, approximately 0.03 cm/sec, was lower than predicted. These values were obtained using a small portion of an orbit to minimize possible orbit modeling errors. These noise values have been rather consistent throughout all the experimental arcs analyzed.

Two approaches were taken to test the detectability of gravity anomalies. The first approach consisted of assuming a single mass anomaly Δm and of computing, in a simple analytical manner, the expected variation of the spacecraft velocity Δv due to this anomaly (ref. 12-2). The velocity variations in the radial and horizontal components, respectively, are then

$$\Delta v_\rho = -\frac{\Delta m}{m} v_{horiz} \left\{ \frac{1+x}{2(1-x)^2} \frac{\Delta\theta}{\sqrt{1 + \frac{x}{(1-x)^2}\Delta\theta^2}} + \frac{1}{2\sqrt{x}} \ln\left[\frac{\sqrt{x}}{1-x}\Delta\theta + \sqrt{1 + \frac{x}{(1-x)^2}\Delta\theta^2}\right] \right\} \tag{12-2a}$$

$$\Delta v_\theta = v_{horiz} \frac{\Delta m}{m} \left(\frac{1}{\sqrt{1 + x^2 - 2x\cos\Delta\theta}} - 1 \right) \tag{12-2b}$$

where $x = \left(\frac{R - d}{R + H}\right)$

$\Delta\theta = v \bullet t$

$t \doteq 0$ to 150 seconds

R = radius of the Earth

d = anomaly depth

H = satellite altitude

Equations (12-2a) and (12-2b) assume that the spacecraft travels directly over the anomaly and are only valid for variations in true anomaly of as much as ±5°, which corresponds to approximately 1.5 minutes of flight time. The dashed curve in figure 12-4 represents the radial velocity variation due to a 5-milligal anomaly (4° by 4°). The size of the anomaly block is roughly twice the orbital height and represents the area of sensitivity of a spacecraft in orbit to an anomaly on the ground (ref. 12-4). Because of the extremely low noise in the data and the actual geometry (i.e., the spacecraft was not directly over the mass and it was an extended mass rather than a point mass), a second approach, using computer simulation techniques, was necessary to improve the analytical results.

The dotted line in figure 12-4 depicts the result of the computerized analysis. As shown in figure 12-2, the value $\dot{\rho}$ is defined as (ref. 12-5)

$$\dot{\rho} = \dot{r}_1 + \dot{r}_2 + \dot{r}_3 + \dot{r}_4 \tag{12-3}$$

This is the range rate as actually measured at the Madrid Applications Technology Satellite Ranging (ATSR) station. However, only the range rate between the Apollo spacecraft and the ATS-6 spacecraft $\dot{\rho}_A$, which is the dot product of the spacecraft orbital velocity vector $\vec{v}$ and the unit vector $\vec{\rho}^0$ between Apollo and ATS-6, is of interest (eq. (12-1)). The ATS-6 orbit is almost independent of any gravity variations because of its extreme height (36 000 kilometers); therefore, the range rate between ATS-6 and Madrid can simply be subtracted from the measured range rate. That is,

$$\dot{\rho}_A \doteq \dot{\rho} - \dot{\rho}(\text{ATS-6/Madrid}) \tag{12-4}$$

which reduces to one the quantity needed for further analyses. This range rate is, however, a function of the state vectors and the gravity field.

$$\dot{\rho}_A = f\left(X_A, X_{ATS}, G\right) \tag{12-5}$$

where X_A and X_{ATS} are the Apollo and ATS-6 state vectors, respectively, and G represents the gravity field. The major aim in this experiment was to determine the relationship between surface gravity anomalies Δg and the Apollo/ATS-6 range-rate variations $\Delta\dot{\rho}_A$. Again, because only the variation in $\dot{\rho}_A$ is of interest, equation (12-5) is varied as follows.

$$\Delta\dot{\rho}_A \approx \frac{\partial f}{\partial X_A} \cdot \frac{\partial X_A}{\partial X_A^0} \Delta X_A^0 + \frac{\partial f}{\partial X_{ATS}} \cdot \frac{\partial X_{ATS}}{\partial X_{ATS}^0} \Delta X_{ATS}^0 + \frac{\partial f}{\partial X_A}\left(\frac{\partial X_A}{\partial G}\right)\Delta G \tag{12-6}$$

Also, $\Delta\dot{\rho}_A \doteq (\Delta\vec{v}_\theta + \Delta\vec{v}_\rho) \bullet \vec{\rho}^0$ = observed-computed range rate.

The sensitivity coefficient $(\partial X_A/\partial G)$ is now contained in equation (12-6) together with ΔG, and thus relates the actual measurements with the gravity potential variation ΔG. Because local anomalies are being observed over a very brief time (as seen in fig. 12-2, approximately a few minutes), the first two terms on the right side of the series expansion can be neglected. Thus, equation (12-6) reduces to

$$\Delta\dot{\rho}_A \approx \frac{\partial f}{\partial X_A}\left(\frac{\partial X_A}{\partial G}\right)\Delta G \tag{12-7}$$

This sensitivity coefficient can now be computed using Newton's equation of planetary motion.

$$\ddot{X}_A = \frac{\partial V}{\partial X_A} = f\left(X_{A_1}, G\right) \tag{12-8}$$

Differentiating equation (12-8) with respect to G yields

$$\frac{\partial \ddot{X}_A}{\partial G} = \frac{\partial f}{\partial X_A}\frac{\partial X_A}{\partial G} + \frac{\partial f}{\partial G} \tag{12-9}$$

Because $(\partial X_A/\partial G)$ is the variable to be determined, equation (12-9) can be rewritten in the following manner, assuming interchangeability of differential operators; that is

$$\left(\frac{\partial \ddot{X}_A}{\partial G}\right) = \frac{d^2}{dt^2}\left(\frac{\partial X_A}{\partial G}\right)$$

$$= \frac{\partial}{\partial X_A}\left(\frac{\partial V}{\partial X_A}\right) \cdot \frac{\partial X_A}{\partial G} + \frac{\partial}{\partial G}\left(\frac{\partial V}{\partial X_A}\right) \qquad (12\text{-}10)$$

where $V = U + T$

U = the normal potential of the Earth gravity field in spherical harmonics

$T = \frac{R}{4\pi} \iint_{\sigma} \Delta g S(\psi)\, d\sigma$

$\Delta g = \Delta G + \Delta g_{LOC}$ using Δg_{LOC} as the local average anomaly of a block (4° by 4°, as an example)

T = the disturbing potential due to the anomalies Δg

R = the radius of a sphere having a volume equal to that of the spheroid

$S(\psi)$ = the Stokes function

σ = an element of surface area

Introducing U and T into equation (12-10) yields

$$\frac{d^2}{dt^2}\left(\frac{\partial X_A}{\partial G}\right) = 2\,\frac{\partial^2}{\partial X_A}(U + T)\,\frac{\partial X_A}{\partial G} + \frac{\partial^2}{\partial X_A \partial G}(U + T) \qquad (12\text{-}11)$$

Equation (12-11) is now solved for the sensitivity coefficient $(\partial X_A/\partial G)$ by numerical integration. Using equation (12-7), the computed sensitivity coefficient is correlated and the relationship between $\Delta\dot{\rho}_A$ and ΔG is established. The following procedures were used in detecting the gravity anomalies.

An orbit of one to one and one-half revolutions was computed for the Apollo spacecraft using the Preliminary Goddard Solution 108 (PGS-108) gravity field and all available tracking data (ground station as well as SST). From these Apollo orbits, together with the ATS-6 orbit, the range rates $\dot{\rho}_A$ between ATS-6 and Apollo were computed. These computed range rates were subtracted from the actual measured ones to yield the $\Delta\dot{\rho}_A$ shown in figures 12-5 and 12-6. These values of $\Delta\dot{\rho}_A$ are finite rather than zero because the gravity field, which would necessarily include all the gravity anomalies, is not known to a very high accuracy. To obtain more precise knowledge of the gravity field, of course, is the essence of this experiment.

PRELIMINARY RESULTS

Experimental data were collected in the Eastern Hemisphere region where the Apollo-Soyuz spacecraft was in range of the ATS-6 satellite, which is positioned over the Equator at approximately longitude 35° E to perform the Indian Communications Experiment. The duration of each Apollo orbit visible to ATS-6 was approximately 50 minutes, or slightly greater than one-half an orbital revolution. To minimize atmospherically disturbed data, the actual SST data passes used were limited to approximately 40 minutes. All data were successfully collected using the ATS-6 spacecraft and the Madrid ATSR station as the prime ground station. Preliminary results confirm that the range-rate noise of 0.05 cm/sec computed before the experiment was improved by the experimental data, which show an average noise of approximately 0.03 cm/sec (fig. 12-3). Figure 12-7 shows the groundtrack of Apollo revolution 115, which coincidentally passed over two anomalies in the African area. The gravity variations shown resulted from the difference between Goddard Earth Models 7 and 8 (GEM-7 and GEM-8). The even-numbered models are constructed using ground and satellite data, whereas the odd-numbered models are constructed only from satellite data. Thus, this difference reflects essentially the surface gravity anomalies, which are somewhat filtered by the models. These two anomalies have a variation of approximately ±5 milligals. Figure 12-5 depicts the theoretical variations of a 5-milligal anomaly (fig. 12-5(b)) and superimposed model data (fig. 12-5(c)) resulting in a total characteristic signature one would expect. Figure 12-5(c) also depicts the observed radial velocity variations. A fairly good agreement exists between the simulated and observed variations of the radial component of the spacecraft velocity except for a time delay. The dashed line shows the time-shifted simulated variation of $\Delta\dot{\rho}_A$.

For this analysis, the PGS-108 field of order and degree of 25 was used. In that particular case, the gravity anomalies of approximately 5 milligals extended over 300 to 2000 kilometers and were actually observed because the wavelength of the gravity anomaly and the resolution of this field are roughly compatible. Thus, the usefulness of SST data for resolving anomalies of approximately ±5 milligals on the Earth surface is demonstrated.

The second test area (the Indian Ocean Depression) is shown in figure 12-8 using GEM-6 augmented with 1° by 1° surface gravity data. In figure 12-6(a), four orbital passes (revolutions 8, 23, 83, and 113) are plotted. These orbits pass over

the Indian Ocean Depression as well as the Himalayan mountain range. Figures 12-6(b) to 12-6(e) depict the actual measurement residuals obtained; that is, the observed minus the computed values. Both the Indian Ocean Depression and the anomaly in the Himalayan area can easily be "seen" in the actual data. The shape of the range-rate variations from the Indian Ocean Depression actually fits the expected shape computed in a similar manner to those shown in figure 12-5. Detectability of the gravity field perturbations has thus been demonstrated to be manifested in the expected form of small spacecraft velocity variations. The peak values of these variations could, in most cases, be closely correlated with anomalies shown on the detailed map of the global geoid. Other features may have been detected but cannot be verified at this time because of a lack of surface gravimetric data in these areas, particularly in the southern portion of the globe. One may assume, however, that the detected gravity signatures in the southern part of the Earth represent existing anomalies that are not well known.

Orbit determination required for the proper analysis of the experimental data involves the use of SST range-rate data together with direct ATS-6 tracking data and unified S-band tracking data. The error analysis performed indicates that one- and two-revolution arcs are superior for minimizing the effects of unmodeled error in the detection and recovery of gravity anomalies. Longer arcs seem to introduce larger errors because the influence of the Earth gravity field errors on the orbit errors becomes more pronounced as the arc length increases. Shorter arcs, however, also have rather large errors because not enough tracking data are available. Thus, the use of one- to two-orbit revolutions for the analyses seems to be a good optimum. Air-drag corrections have been used for Apollo-Soyuz orbit determination. The SST data were used only during those periods judged free of onboard propulsion activities. Because the antenna is separated from the spacecraft axis by approximately 3 meters, any attitude motion (correction) of the spacecraft (rotation of the spacecraft) is transformed into a range rate between the Apollo-Soyuz spacecraft and the ATS-6 spacecraft. One could therefore quite wrongly interpret a spacecraft rotation as a gravity anomaly. Detailed analysis of attitude control has not yet been performed; however, attitude data are available and will be used to further refine the range-rate residuals measured between the Apollo-Soyuz and ATS-6 vehicles.

CONCLUDING REMARKS

The high/low satellite-to-satellite tracking technique can be utilized for Earth gravity anomaly detection. Anomalies having dimensions equal to or longer than the height of the low spacecraft and having values of approximately 5 milligals have been detected with a good 10:1 signal-to-noise ratio. The 0.05-cm/sec range rate conservatively computed before the experiment was actually improved by the measured noise of 0.03 cm/sec. For all the passes examined, it was possible to correlate the measured range-rate residuals with known geoidal features of short wavelength (approximately 300 kilometers). It was further demonstrated that the range-rate signatures could be repeated orbit by orbit; thus, confidence in the experimental data has been increased.

REFERENCES

12-1. Vonbun, F. O.; and Mengel, J. T.: Tracking and Communications for Planetary Manned Missions. J. Spacecraft & Rockets, vol. 5, no. 5, July 1968, pp. 863-865.

12-2. Vonbun, F. O.: The ATS-F/Nimbus-E Tracking Experiment. Rotation of the Earth, Paul Melchoir and Shigeru Yumi, eds., D. Reidel Publ. Co. (Dordrecht, Holland), 1972, pp. 112-120.

12-3. Schmid, P. E.; and Vonbun, F. O.: The ATS-F/Nimbus-F Tracking and Orbit Determination Experiment. 1974 IEEE Intercon Technical Program Papers, 1974, pp. 34/6-1 and 34/6-2.

12-4. Schwarz, Charles R.: Gravity Field Refinement by Satellite to Satellite Doppler Tracking. NASA CR-117404, 1970.

12-5. Bryan, J.: ATS-F/GEOS-C Satellite to Satellite Tracking Data Processing Consideration. NASA TM X-70736, 1974.

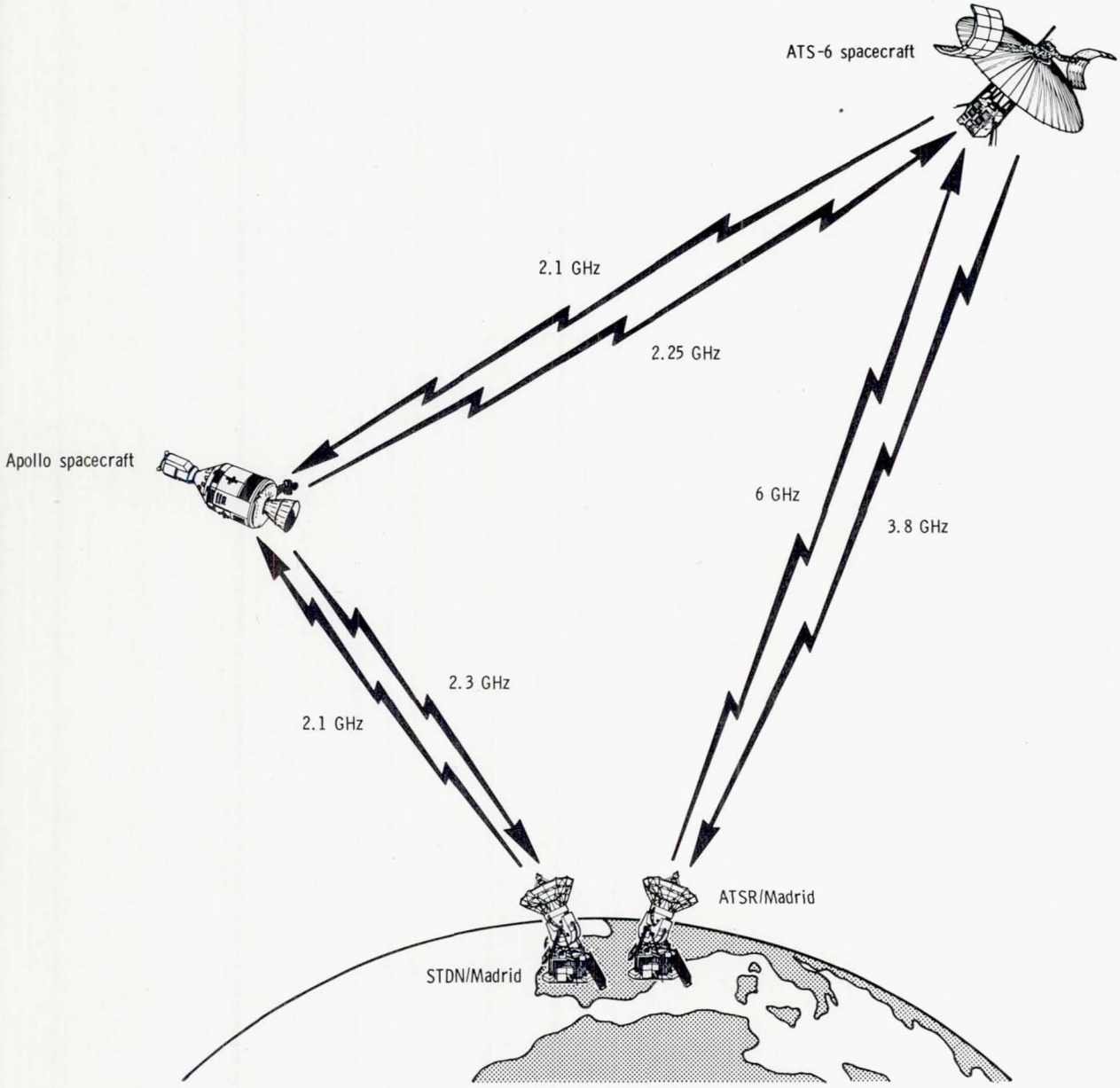

Figure 12-1.- Schematic of the ATS-6/Apollo communication links for operations with ATS-6 in the Eastern Hemisphere. The ATS Ranging station is designated ATSR; the Spaceflight Tracking and Data Network station is designated STDN.

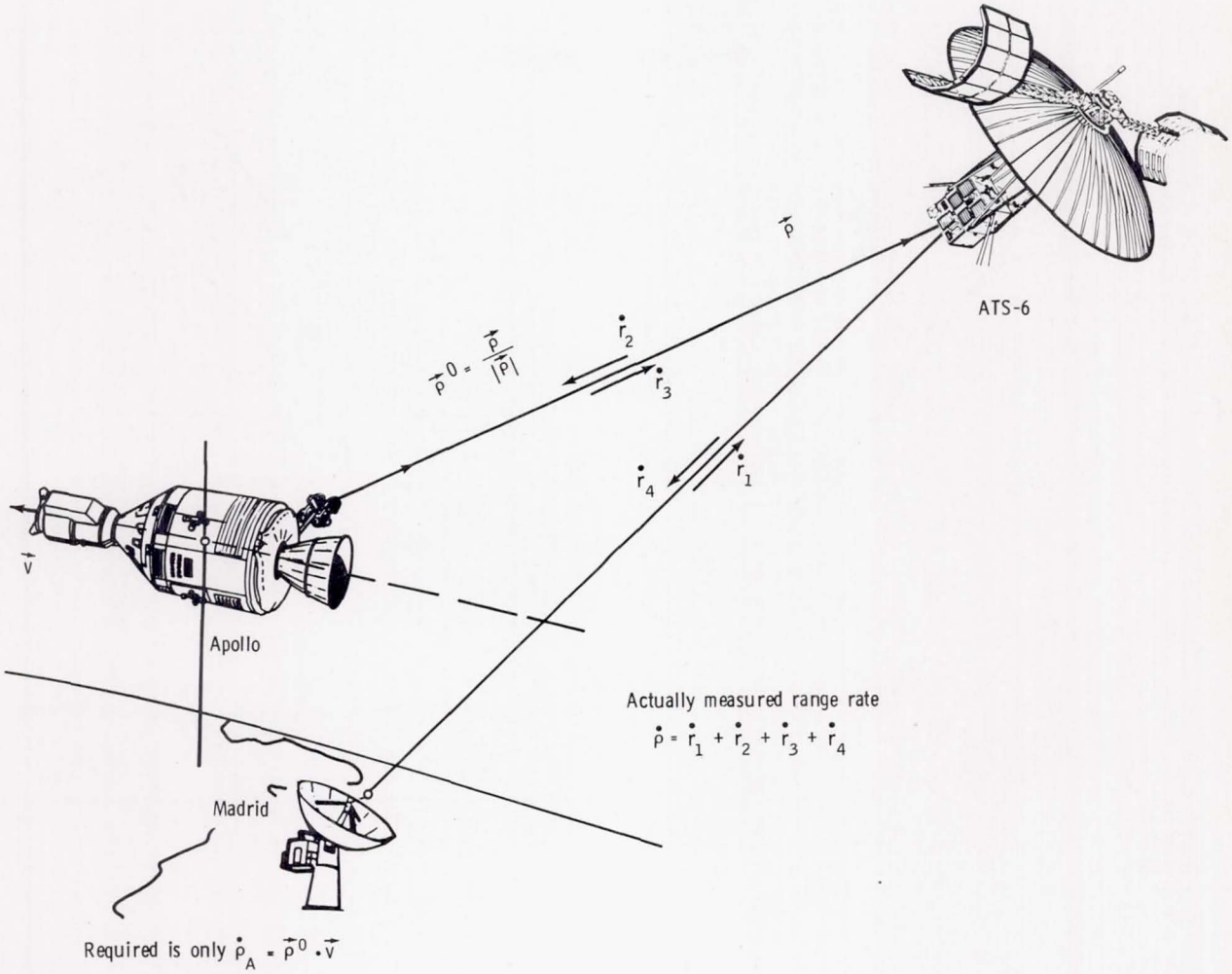

Figure 12-2.- Schematic showing range-rate measurement for the ATS-6 and Apollo vehicles.

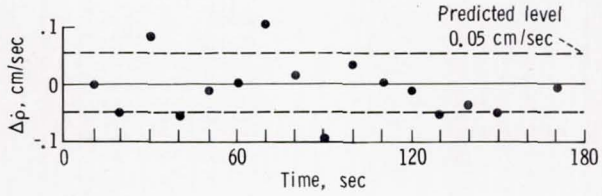

Figure 12-3.- Tracking systems range-rate noise characteristics measured from Madrid to ATS-6 to Apollo-Soyuz to ATS-6 to Madrid.

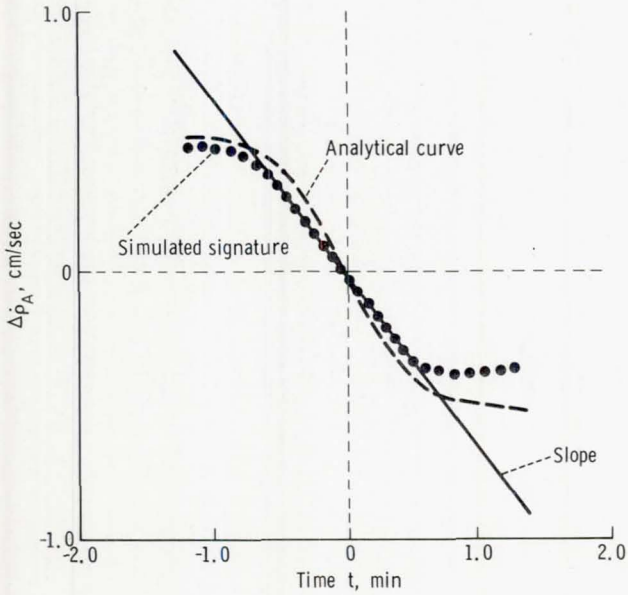

(a) Plot.

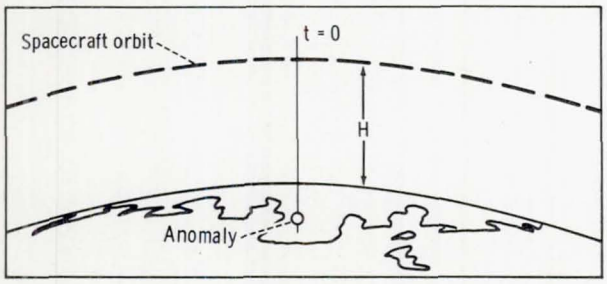

(b) Schematic.

Figure 12-4.- Analytical and computer-simulated range-rate signature for a 4° by 4°, 5-milligal anomaly.

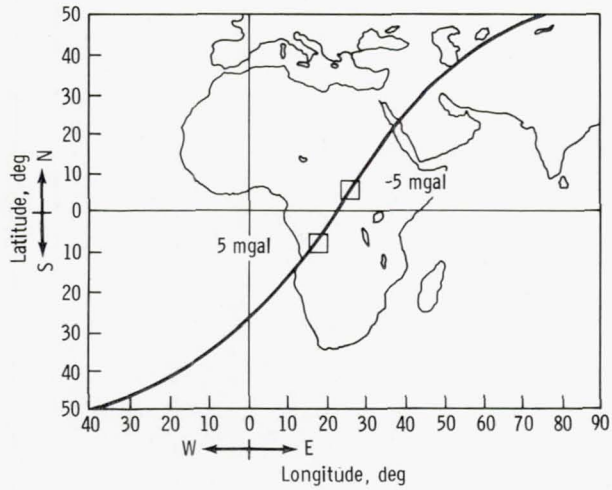

(a) Groundtrack.

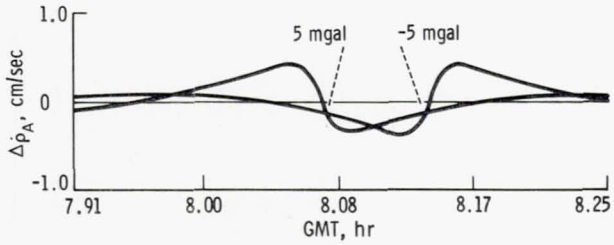

(b) Independent computed range-rate signatures due to each anomaly.

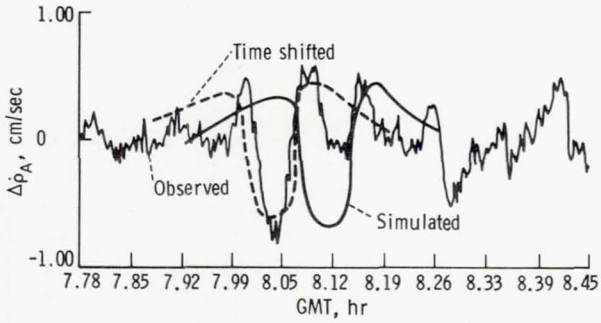

(c) Comparison of observed and simulated range-rate signatures. The observed signature was based on PGS-108 gravity field (degree and order 25).

Figure 12-5.- Revolution 115 4° by 4° anomalies simulation in Africa, July 23, 1975.

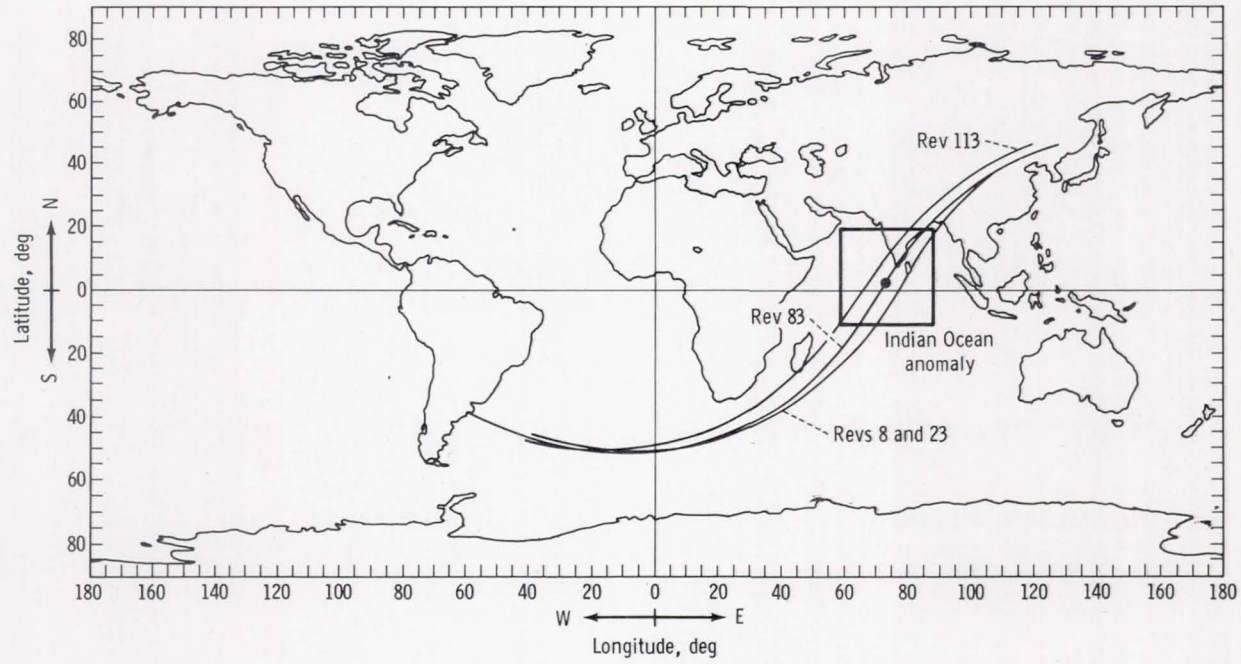

(a) Groundtrack.

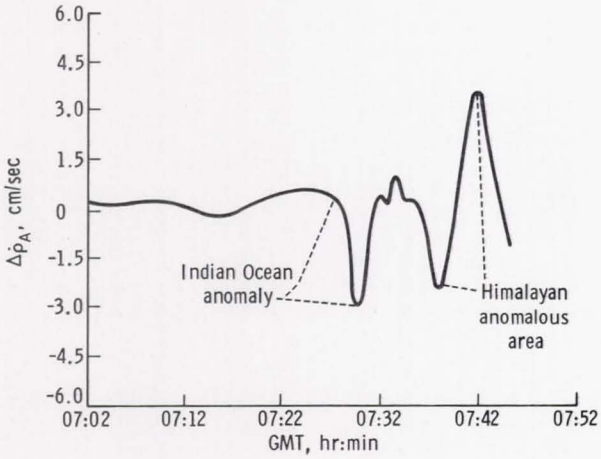

(b) Revolution 8, July 16, 1975.

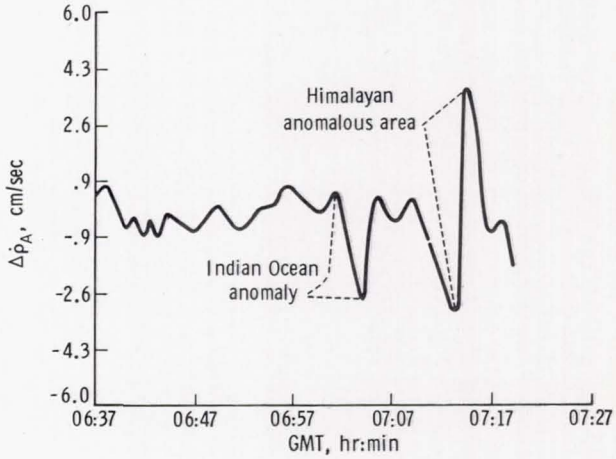

(c) Revolution 23, July 17, 1975.

Figure 12-6.- Range-rate signatures of four revolutions in the Indian Ocean and Himalayan areas.

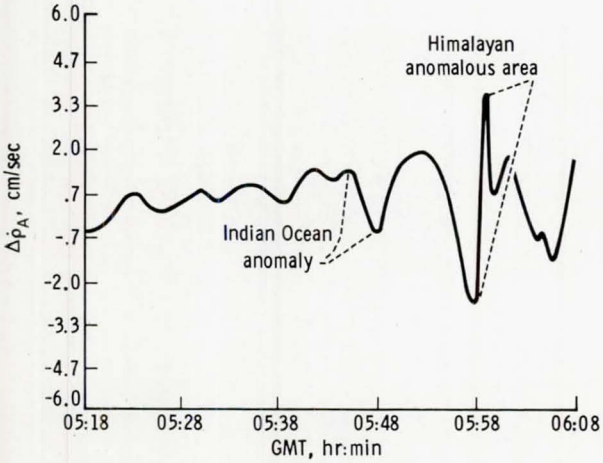

(d) Revolution 83, July 21, 1975.

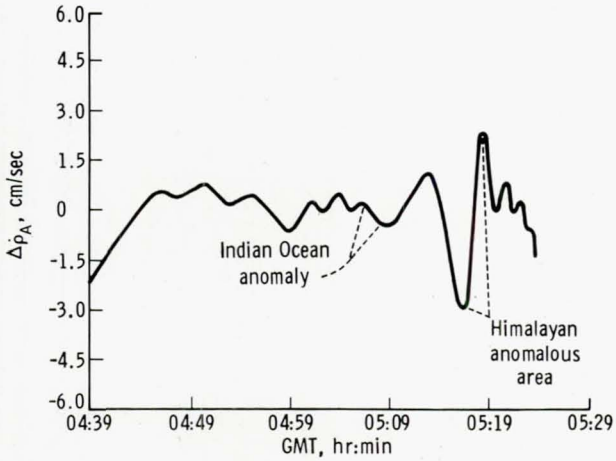

(e) Revolution 113, July 23, 1975.

Figure 12-6.- Concluded.

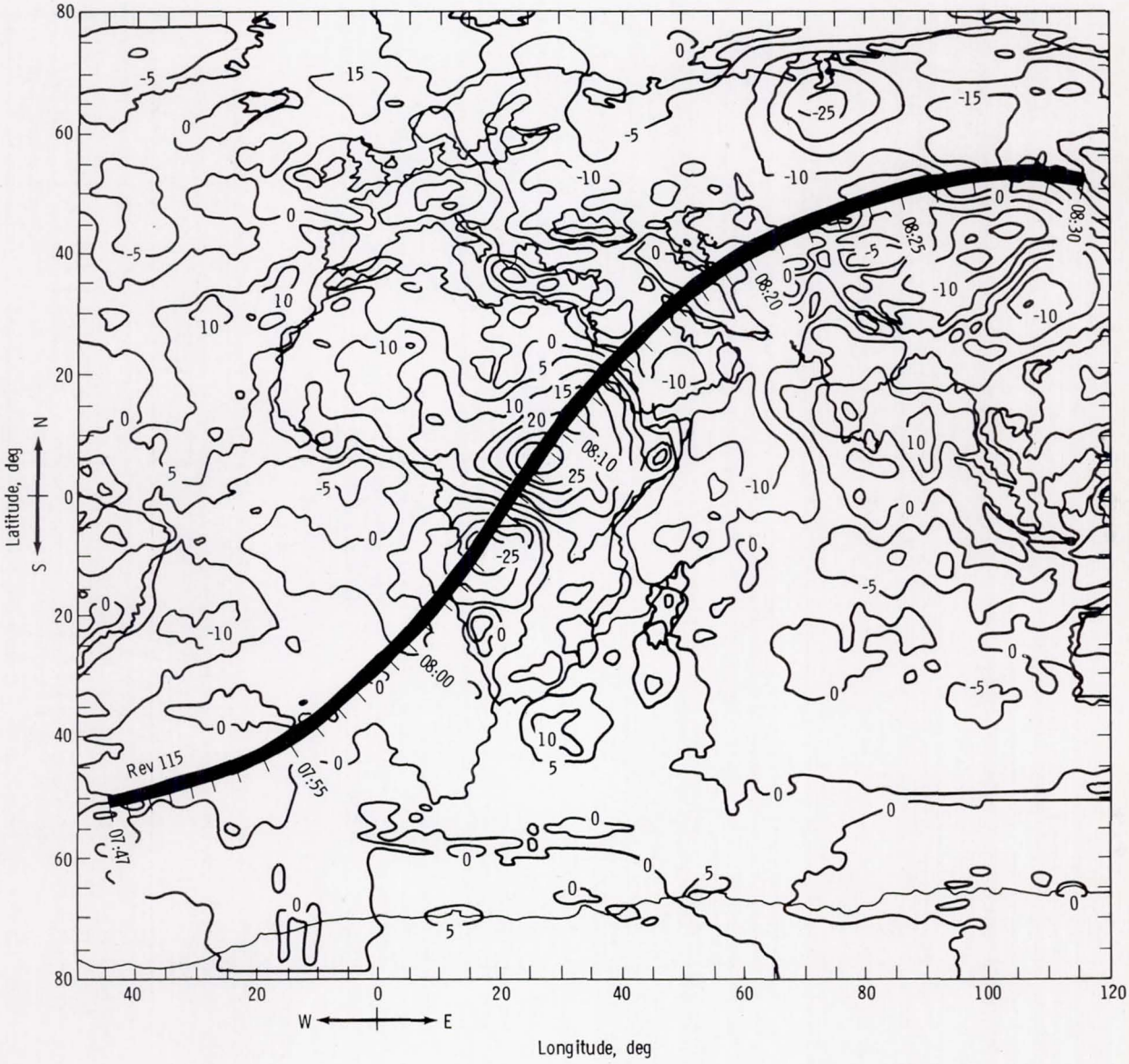

Figure 12-7.- Residual Earth surface undulations for the GEM-7 and GEM-8 models. Contour interval is 5 meters. Times are Greenwich mean times on July 23, 1975.

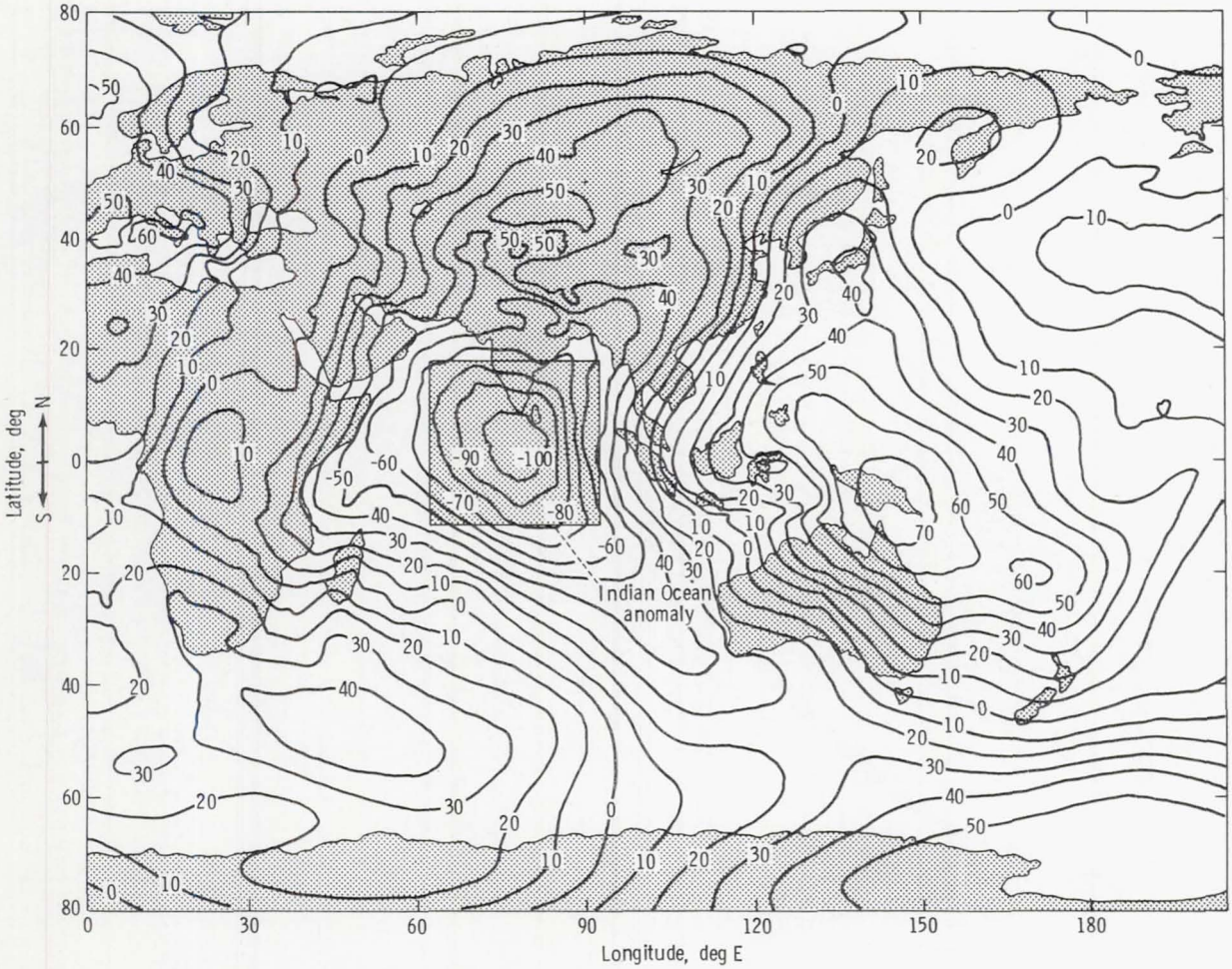

Figure 12-8.- Global detailed gravimetric geoid based on the GEM-6 Earth model and 1° by 1° surface gravity data. Contour interval is 10 meters.

13. QUANTITATIVE OBSERVATION OF LIGHT FLASH SENSATIONS

EXPERIMENT MA-106

T. F. Budinger,[a†] C. A. Tobias,[a] E. Schopper,[b] J. U. Schott,[b]
R. H. Huesman,[a] F. T. Upham,[a] T. F. Wieskamp,[c] J. M. Kucala,[c]
F. S. Goulding,[a] D. A. Landis,[a] J. T. Walton,[a] and R. E. Walton[a]

ABSTRACT

Light flashes caused by the interaction of cosmic particles with the visual apparatus have been observed by astronauts on all space missions since Apollo 11. The character of these flashes and the mechanism whereby they are elicited have been investigated both in flight and in ground laboratories for the past several years.

This Apollo-Soyuz Test Project experiment compared measurements of the observer's visual sensitivity with measurements of the ambient radiation environment and with the frequency and character of the flashes observed. The data obtained reveal a latitude dependence of the frequency of observed flashes. This distribution of flashes is correlated with the distribution of cosmic particles with stopping power >15 keV/μm in the eye. The interaction of dark adaptation, specific ionization, and range of particles in the retina as factors in the visualization of particle passage is discussed.

INTRODUCTION

This preliminary report records the quantitative observations of the light flash phenomenon seen by astronauts during the Apollo-Soyuz Test Project (ASTP). The experiment was conducted during two revolutions and consisted of the correlation of precisely reported visual phenomena noted by two astronauts with the measured and calculated cosmic particle environment near the astronauts' heads. This was the sixth mission during which planned observations of the light flash phenomenon were made.

---

[a]Lawrence Berkeley Laboratory, University of California at Berkeley.

[b]University of Frankfurt.

[c]Lawrence Livermore Laboratory.

[†]Principal Investigator.

BACKGROUND

Astronauts on Apollo 11 and subsequent missions (including Skylab) have observed randomly occurring visual phenomena that consist of the perception of tiny, brief, starlike flashes of white light or pencil-thin streaks of light. These observations were made when the interior of the spacecraft was darkened. Examples of the types of phenomena seen are shown in figure 13-1, which is based on descriptions by Apollo and Skylab crews as well as descriptions from Earth-based experiments with accelerated charged particles. Not all of these visual effects were seen during the ASTP mission. During the last six Apollo missions, and on a few occasions during Skylab, crews made both scheduled and unscheduled observations of the frequency and character of these events (refs. 13-1 to 13-6). These observations can be summarized as follows. After approximately 17 minutes of dark adaptation, tiny dots and thin streaks of white light were seen at frequencies of about 3 events/min by astronauts during the translunar or transearth coast phases of the Apollo missions or the polar part of Skylab orbits. Near the South Atlantic Anomaly (SAA), where the proton flux is 1000 times or more greater than in other parts of the orbit, the frequency increased to about 15 events/min (ref. 13-6) for Skylab altitudes of 443 kilometers.

The Apollo 11 lunar module pilot first reported these visual phenomena, which were predicted in 1952 by C. A. Tobias (ref. 13-7) who hypothesized that astronauts were likely to see flashes of light from cosmic particles when they were outside the shielding provided by the magnetic field of the Earth. The site of action of these cosmic particles, and whether cosmic particles actually caused the light flash phenomenon, were subjects of conjecture in 1970 when this phenomenon was first reported. Many known causes for luminous phosphenes exist, including ionizing radiation, mechanical pressure, electrical currents, magnetic fields, stimulation of the cerebral cortex, and central nervous system pathological conditions. For example, flashes can be seen during stages of retinal detachment, and the retina is sensitive to externally applied currents as small as 0.3 milliampere. In 1970, these phenomena were believed to be caused by carbon, nitrogen, and oxygen nuclei which traverse the spacecraft and the body at frequencies of 1 to 2 nuclei/min/cm^2 when outside the magnetic shielding of the Earth. Of continuing controversy is the conjecture that the major mechanism for these visual phenomena is Cerenkov radiation (refs. 13-8 to 13-11).

In 1970, a series of experiments was undertaken to determine whether carbon, nitrogen, and oxygen of approximately 300 MeV/amu and other ions with equivalent ionizing characteristics could cause qualitatively the same phenomena seen by astronauts. In a series of experiments using neutrons of 630 megaelectronvolt energy (ref. 13-12), neutrons of approximately 8 megaelectronvolt energy (ref. 13-13), helium ions from the 467-centimeter (184 inch) cyclotron at 230 MeV/nucleon (ref. 13-14), and nitrogen ions accelerated to approximately 260 MeV/nucleon at the bevatron (ref. 13-15), ionizing particles with a stopping power of approximately 10 keV/μm or greater caused similar phenomena. These experiments demonstrated that ionization or electronic excitation from cosmic particles could adequately account for the light flash phenomenon. Cerenkov light is produced by particles with velocities greater than those used in the experiments just described; therefore, it was concluded that whereas Cerenkov radiation might cause similar phenomena, it was not

the predominant mechanism. The exact mechanism whereby the retina is stimulated by ionizing particles at velocities below those necessary for emission of Cerenkov light is still unclear. Experiments in which nitrogen ions were stopped in nine positions in the cerebral cortex have shown that the brain and the optic nerve are not stimulated by ions (ref. 13-15). Possibilities are electronic excitation resulting in near-ultraviolet (uv) radiation in the vicinity of the retina, ionization in a confined region associated with delta rays around the ion track, or a shock wave phenomenon from energetic charged particles passing through the tissue matrix.

The purpose of this experiment was to ascertain quantitatively the frequency, character, latitudinal dependence, and identity of cosmic particles that cause the light flash phenomenon. The ultimate objective was the assessment of radiation hazards for long-term Earth-orbiting and interplanetary missions. The special features of this experiment included measurement of dark adaptation, measurement of the characteristics of the cosmic particle environment in the vicinity of the eye, and continuous onboard accumulation of the light flash observations from astronauts and particle detectors throughout one continuous revolution.

EXPERIMENT PROTOCOL

Two revolutions were devoted to this experiment. During revolution 110, the silicon telescope-spectrometer was deployed for the measurement of the trajectory, atomic charge Z, and velocity of cosmic particles with a stopping power of 10 keV/μm or greater. During revolution 111, the Apollo commander and the command module pilot made continuous observations of visual sensations while dark adapted. The docking module pilot (DMP) operated the experiment control unit, which received data from the silicon detectors as well as from silver chloride cadmium-doped (AgCl(Cd)) crystals that were used to register particle tracks in four sectors of the orbit corresponding to northern latitudes, equatorial latitudes, the SAA, and southern latitudes.

The experiment commenced with the detector-alone orbit according to the Flight Plan at approximately 13:40 GMT on July 22, 1975. The manned orbit, revolution 111, began according to the Flight Plan at approximately 14:45 GMT, at which time the spacecraft was maneuvering to proper attitude because the attitude for revolution 110 was not optimum. Approximately 10 minutes later, the observing crewmembers had reached dark adaption. The first light flash was reported at 15:00 GMT at latitude 49° N when the spacecraft was approaching the northernmost point of the orbit. At each event, a pushbutton signal from the observing astronaut was recorded on the digital tape and the verbal description was recorded on the onboard tape recorder. The DMP switched the lighting for the AgCl(Cd) crystal compartments according to the Flight Plan at 17, 39, and 54 minutes after commencement of revolution 111. The experiment was terminated at 16:50 GMT. In accordance with the Flight Plan, the digital tapes, voice tapes, detector boxes, and masks were returned to the experimenters. The digital tapes were transported to the Lawrence Berkeley Laboratory (LBL) for analysis, and the AgCl(Cd) crystals were transported to Frankfurt, Germany, where they had been produced and calibrated.

EQUIPMENT

The hardware for the experiment consisted of two dark adaption masks, two pushbuttons, two cosmic-particle detector boxes, and a control and power unit that housed a data tape. The masks and pushbuttons were manned by two astronauts and the control and power unit was controlled by the third astronaut, who monitored the experiment (figs. 13-2 to 13-4).

Dark Adaption Masks

Each dark adaption mask was made of Lexan plastic approximately 2 millimeters thick and was fitted with a light-emitting diode (LED) behind a pinhole aperture approximately 2 centimeters from one eye. The masks, held to the head by straps, were fabricated from molds of each astronaut's head. The head molds were made by the LBL group using techniques adapted from fabrication of similar molds used for head positioning in radiotherapy of the pituitary gland. Plaster of paris head casts were made from the molds. The Lexan masks were then made by pressing near-molten Lexan over these head casts. A foam rubber insert was used to ensure a perfect light-tight fit, and each mask was then custom fitted to each crewmember.

The effective brightness of the LED was controlled by the duration of a constant voltage. The duration ranged from 5 microseconds to 1.7 milliseconds in six different levels and produced the expected response on normal subjects in terms of the rapidity with which each level of dark adaption was reached. Level 5 was reached approximately 15 minutes after commencement of dark adaption.

Pushbuttons

Events noted by astronauts were recorded on digital tape by means of a handheld pushbutton switch.

Detector Boxes

Each of the two detector units contained AgCl(Cd) crystals and a silicon solid-state telescope-spectrometer. Each detector box was composed of two units. The first unit (4.1 by 5.5 by 12.7 centimeters) was an aluminum housing in which there were four compartments (each 1.84 by 3.5 by 2.75 centimeters) for AgCl(Cd) crystals and small lights. The AgCl(Cd) crystals were 1- by 2-centimeter wafers 0.03 centimeter thick. Two crystals were placed in each compartment on either side of two white 6-volt lights, which were filtered to give predominantly yellow light by using 0.06-centimeter-thick Kapton plastic sheets between the lights and crystals.

The AgCl(Cd) crystals are nuclear particle detectors developed in Germany (ref. 13-16). They are similar to nuclear emulsions but have a unique property that allows evaluation of the time at which a particle traverses the detector. A nuclear particle passing through the crystal leaves a latent track of dislocated electrons and displaced silver or cadmium atoms. Within a few minutes, the migration

of electrons and atoms will return the crystal to its original condition. However, if the crystal is exposed to visual spectrum photons, the latent track is fixed or stabilized. Hours or weeks later, if the crystal is exposed to ultraviolet light, the stabilized but still invisible tracks are developed, thus giving a permanent record of the nuclear particle track. The distribution of residual silver around the track is related to the charge and velocity of the ion as well as to the intensity and spectrum of the near-ultraviolet light used to develop the stabilized tracks. The time period between implantation of a latent track and fading is a few minutes, but the period between the time a stabilized track is made and fading is more than 1 week. Crystals were loaded into each of four compartments so that the particle environment could be measured in the four sectors of the orbit corresponding to the northern latitudes, the equatorial latitudes, the SAA, and the remaining minutes of the orbit over the Pacific Ocean.

The second unit (4.3 by 9.6 by 12.7 centimeters) of each detector box housed the electronic detector, which consisted of two sets of silicon solid-state wafers. Each set consisted of two individual wafers 1.7 centimeters in diameter and 0.03 centimeter thick. On each wafer were four active strips each 3 millimeters wide separated by 0.5 millimeter. The telescope was made by rotating one wafer 90° from the other. This set of two wafers gave 16 possible combinations (4 by 4) for particle position. The second set of two wafers was placed 1.5 centimeters from the first set, and a 0.5-centimeter-thick copper energy degrader was placed between the sets. This arrangement allowed measurement of the trajectory and energy loss of particles passing through the telescope.

The accuracy of energy and trajectory measurements is 5 percent. From these measurements, the most likely charge and velocity of the detected particle can be deduced, using the curves of figure 13-5. The threshold for the device is 10 keV/μm.

Control and Power Unit

The control and power unit consisted of power distribution, logic circuits, and a digital cassette tape recorder that received 16-bit word groups from the observer pushbuttons and the silicon detectors. The word groups from the silicon detectors contained information on the trajectory and energy loss of particles that passed through the silicon detector. Elapsed time and detector selector switch position information were also recorded.

PROCEDURES FOR DATA REDUCTION

Descriptions of the events observed by the crewmembers were recorded on the onboard voice recorder. The tapes were transcribed, and each event was related to the orbital position of the spacecraft. Events from the silicon detectors and pushbuttons and the status of the control unit were read from the digital tape by a specially constructed microprocessor. The pushbutton events and time marks were related to the verbal reports. The energy and trajectory information is being reduced in terms of particle velocity and most likely charge Z (fig. 13-5).

The AgCl(Cd) crystals were transported to Frankfurt, Germany, where they had been produced and calibrated. These crystals are being analyzed for the abundance of tracks that are related to protons, alpha particles, or heavier ions. The data are further separated into categories of stopping power and direction.

The characteristics of the cosmic particle environment inside the spacecraft were determined by converting the spectrum and abundance of particles outside the spacecraft to the number of particles with various stopping powers and residual ranges, using shielding data for 512 sectors of solid angle around the spacecraft. The shielding data were supplied by the NASA Lyndon B. Johnson Space Center.

The input abundances from free space for $Z > 3$ were obtained from Webber et al. (ref. 13-17), and the abundances for hydrogen and helium were obtained from Smith et al. (ref. 13-18). The spectra were assumed to be the same as those for carbon and oxygen, which were obtained from Juliusson (ref. 13-19). These free-space abundances were converted to the abundance outside the spacecraft at a 225-kilometer altitude using the spacecraft orbital parameters and B[1] and L[2] data obtained from the 99-term field of Hendricks and Cain (ref. 13-20) extrapolated to 1975. Vertical rigidity cutoffs were estimated by the empirical formula $P_c = 15.96\ L^{-2.005}$ from Smart and Shea (ref. 13-21). The present spacecraft orbit routine is based on the Flight Plan and assumed circular orbit because the ephemeris data are not yet available.

The energy-range relationship was derived from an empirical formula that gives range R as a function of kinetic energy:

$$R = \frac{\alpha A}{Z^2}\left(\frac{E}{A}\right)^{\beta} \tag{13-1}$$

where A is the atomic number, Z is the charge, and E is the kinetic energy in MeV/amu.

For passage of ions through the spacecraft, aluminum shielding is assumed. Thus, the constants are $\alpha = 2.811 \times 10^{-3}$ and $\beta = 1.775$. The stopping power S is given as

$$S = \frac{Z^2}{\alpha\beta}\left(\frac{E}{A}\right)^{1-\beta} \tag{13-2}$$

---

[1]Geomagnetic field strength.

[2]Distance from the center of the Earth in Earth radii.

Energy transfer in the eye is calculated using equation (13-2) and $\alpha = 1.88 \times 10^{-3}$ and $\beta = 1.802$.

RESULTS

The distribution of visual events reported by astronauts is shown along the track line in figure 13-6. Histograms depicting the frequency of events in time and with respect to latitude are shown in figures 13-7(a) and 13-7(b). Because the spacecraft transited latitudes for varying time intervals, normalization to equal time intervals is shown in figure 13-7(c).

A total of 82 events was reported by the two astronauts (table 13-I). No increased activity in the SAA and no graying of the darkened visual fields occurred. The relative expected distribution of cosmic particles with stopping power of greater than 15 keV/μm in the eye is superposed on the histogram of reported events in figure 13-8.

DISCUSSION

The results of the light flash experiment indicate that the abundance of ions that cause the light flash phenomena is minimal between latitudes 30° N and 30° S. The frequency of light flash events between latitudes 30° N and 50° N and 30° S and 50° S is 25 times that noted in equatorial latitudes. There were no reports of increased flash phenomena through the SAA, as might be expected from a Skylab 4 report of increased activity through the SAA (ref. 13-15). However, at the 225-kilometer altitude of the ASTP spacecraft, the proton flux is much less than at the Skylab altitudes, which were approximately 440 kilometers. Also, the shielding of the Apollo spacecraft is greater than that of Skylab.

Through the SAA, the number of protons with a stopping power of 15 keV/μm that would intersect the astronaut's eye was approximately 2 protons/min for each eye under the shielding conditions of the Apollo spacecraft. The range of these particles in the retina is approximately 100 micrometers. Based on the assumption that protons with a stopping power of this energy will produce visual phenomena and on the fact that two observers reported events at less than 1 event/min through the SAA, the efficiency is concluded to be approximately 10 percent. If the threshold is 10 keV/μm, then the efficiency is reduced to 5 percent. The efficiency should be a function of stopping power. Ground-based experiments with stopping protons are being conducted to corroborate these observations.

The expected flux of heavy particles in the northernmost and southernmost points of the orbits is 1 to 2 particles/min for each eye. Thus, the efficiency for seeing high charge energy (HZE) particles is approximately 50 percent for the dark-adapted eye. The abundance of heavy ions with various stopping powers is being calculated as previously described. The efficiency and character of light flashes should be a function of the stopping power and the velocity of the particle, because the range of the effective radiation around the particle track will increase as the

velocity increases. Thus, a slow helium ion with a stopping power of 20 keV/μm might give a thinner and less efficiently seen streak than an iron particle at the same stopping power, because the distribution of delta rays is much greater in the latter situation.

REFERENCES

13-1. Chapman, P. K.; Pinsky, L. S.; Benson, R. E.; and Budinger, T. F.: Observations of Cosmic Ray Induced Phosphenes. Proceedings of the National Symposium on Natural and Manmade Radiation in Space (E. A. Warren, ed.). NASA TM X-2440, 1972, pp. 1002-1006.

13-2. Budinger, T. F.; Tobias, C. A.; Lyman, J. T.; Chapman, P. K.; et al.: Light Flash Phenomenon Seen by Astronauts. Proceedings of the Colloquium on Space Biology Related to Post-Apollo Program. ESRO, Paris, France, 1971, p. 209.

13-3. Benson, R. E.; and Pinsky, L. S.: Visual Light Flash Phenomenon. Sec. 27, Part C, of the Apollo 16 Preliminary Science Report. NASA SP-315, 1972.

13-4. Pinsky, L. S.; Osborne, W. Z.; and Bailey, J. V.: Visual Light Flash Phenomenon. Sec. 27 of the Apollo 17 Preliminary Science Report. NASA SP-330, 1973.

13-5. Pinsky, L. S.; Osborne, W. Z.; Bailey, J. V.; Benson, R. E.; and Thompson, L. F.: Light Flashes Observed by Astronauts on Apollo 11 Through Apollo 17. Science, vol. 183, no. 4120, Mar. 8, 1974, pp. 957-959.

13-6. Pinsky, L. S.; Osborne, W. Z.; Bailey, J. V.; and Hoffman, R. A.: Light Flashes Observed by Astronauts on Skylab 4. Science, vol. 188, no. 4191, May 30, 1975, pp. 928-930.

13-7. Tobias, C. A.: Radiation Hazards in High Altitude Aviation. J. Aviation Med., vol. 23, 1952, p. 345.

13-8. Fazio, G. G.; Jelley, J. V.; and Charman, W. N.: Generation of Cerenkov Light Flashes by Cosmic Radiation Within the Eyes of the Apollo Astronauts. Nature, vol. 228, no. 5268, Oct. 17, 1970, pp. 260-264.

13-9. McNulty, P. J.: Light Flashes Produced in the Human Eye by Extremely Relativistic Means. Nature, vol. 234, no. 5323, Nov. 12, 1971, p. 110.

13-10. McNulty, P. J.; Pease, V. P.; Pinsky, L. S.; Bond, V. P.; et al.: Visual Sensations Induced by Relativistic Nitrogen Nuclei. Science, vol. 178, no. 4056, Oct. 13, 1972, p. 160.

13-11. McNulty, P. J.; Pease, V. P.; and Bond, V. P.: Visual Sensations Induced by Cerenkov Radiation. Science, vol. 189, no. 4201, Aug. 8, 1975, pp. 453-454.

13-12. Tobias, C. A.; Budinger, T. F.; and Lyman, J. T.: Radiation-Induced Light Flashes Observed by Human Subjects in Fast Neutron, X-ray, and Positive Pion Beams. Nature, vol. 230, Apr. 30, 1971, pp. 596-597.

13-13. Budinger, T. F.; Bichsel, H.; and Tobias, C. A.: Visual Phenomena Noted by Human Subjects on Exposure to Neutrons of Energies Less Than 25 Million Electron Volts. Science, vol. 172, no. 3978, May 21, 1971, pp. 868-870.

13-14. Tobias, C. A.; Budinger, T. F.; and Lyman, J. T.: Biological Effects Due to Single Accelerated Heavy Particles - Problems of Nervous System Exposure in Space. In Life Sciences and Space Research XI (P. H. A. Sneath, ed.). Academie-Verlag (Berlin), 1973, p. 233.

13-15. Budinger, T. F.; Lyman, J. T.; and Tobias, C. A.: Visual Perception of Accelerated Nitrogen Nuclei Interacting With the Human Retina. Nature, vol. 239, no. 5369, Sept. 22, 1972, pp. 209-211.

13-16. Schott, J.-U.: Eigenshaften von AgCl(Cd)-Kristallen als Teilchenspur-Detektoren. Ph. D. Thesis, Institut für Kernphysik der Johann Wolfgang Goethe-Universität Frankfurt Am Main, 1974.

13-17. Webber, W. R.; Damle, S. V.; and Kish, J.: Studies of the Chemical Composition of Cosmic Rays with Z = 3-30 at High and Low Energies. Astrophys. Space Sci., vol. 15, Feb. 1972, pp. 245-271.

13-18. Smith, L. H.; Buffington, A.; Smoot, G. F.; Alvarez, L. W.; and Wahlig, M. A.: A Measurement of Cosmic-Ray Rigidity Spectra Above 5 GV/c of Elements From Hydrogen to Iron. Astrophys. J., vol. 180, no. 3, Mar. 1973, pp. 987-1010.

13-19. Juliusson, E.: Cosmic Rays at Very High Energies. Vol. I, Proceedings of the 13th International Cosmic Ray Conference 1974, pp. 373-377.

13-20. Hendricks, S. J.; and Cain, J. C.: Magnetic Field Data for Trapped-Particle Evaluations. J. Geophys. Res., vol. 71, no. 1, Jan. 1, 1966, pp. 346-349.

13-21. Smart, D. F.; and Shea, M. A.: A Study of the Effectiveness of the McIlwain Coordinates in Estimating Cosmic-Ray Vertical Cutoff Rigidities. J. Geophys. Res., vol. 72, no. 13, July 1, 1967, pp. 3447-3454.

TABLE 13-I.- SUMMARY OF EVENTS

Track sector	Stars	Streaks	Commas	Total
Northernmost point of orbit to Florida	[a]12	[b]6	2	20
Florida to Brazil	2	3	0	5
SAA	2	1	0	3
SAA to completion of orbit	27	16	11	54

[a]Includes events expressed as supernova in figure 13-6.

[b]Includes events expressed as hotdogs in figure 13-6.

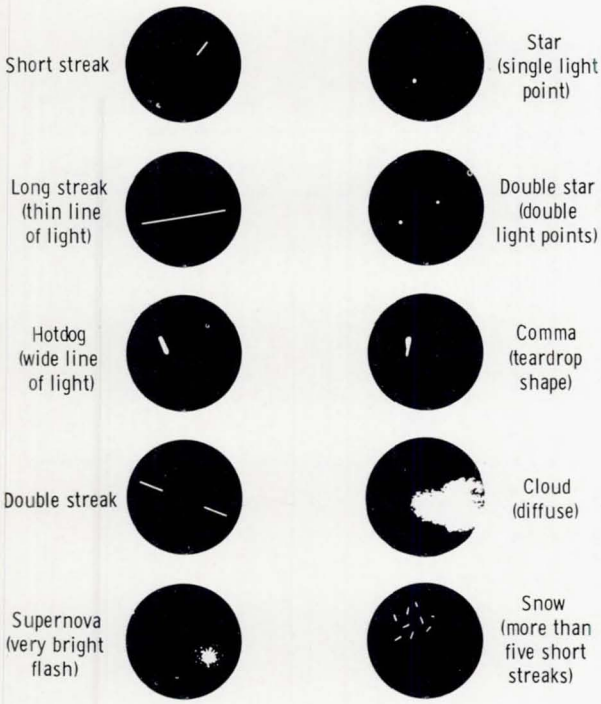

Figure 13-1.- Reproduction of visual events noted in space and in cyclotron experiments.

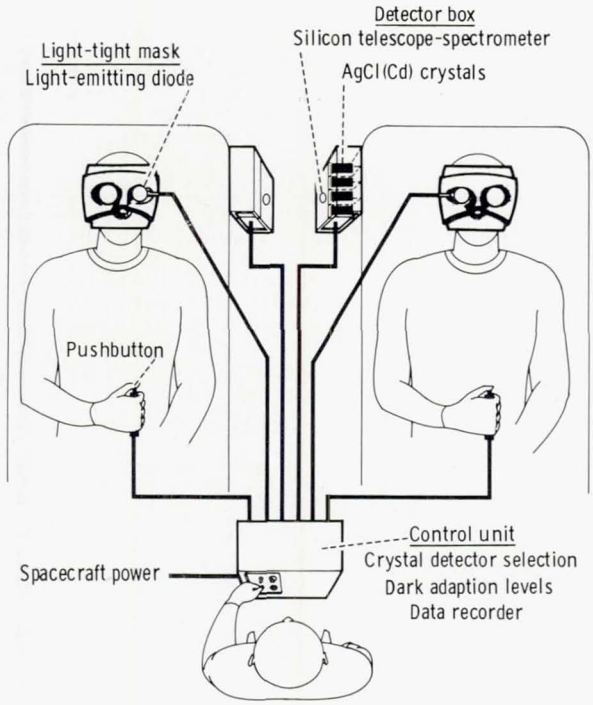

Figure 13-2.- Experiment layout.

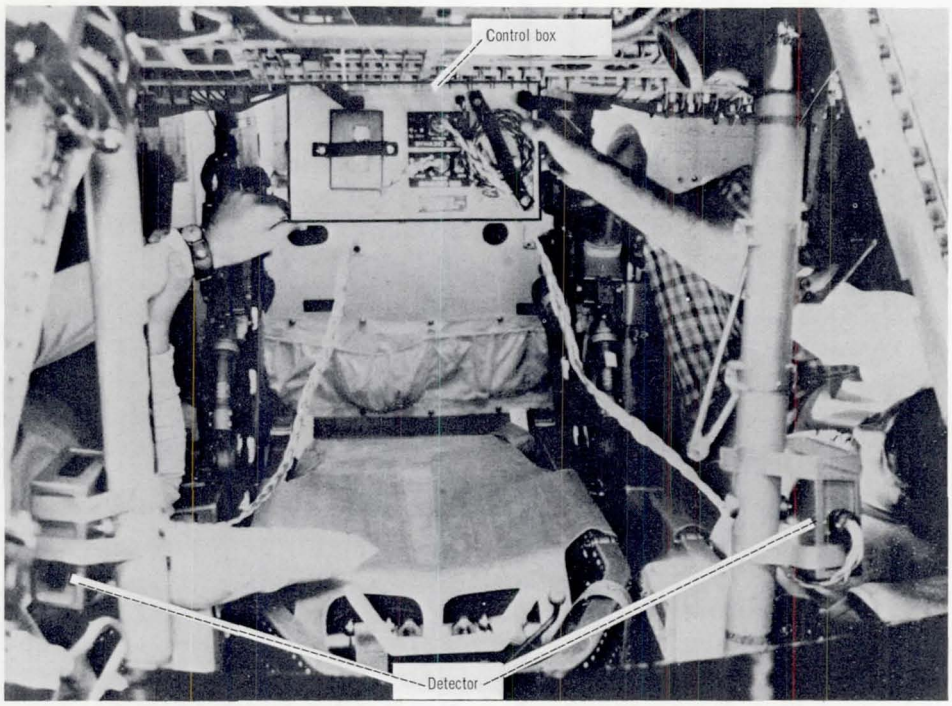

Figure 13-3.- Position of equipment in spacecraft.

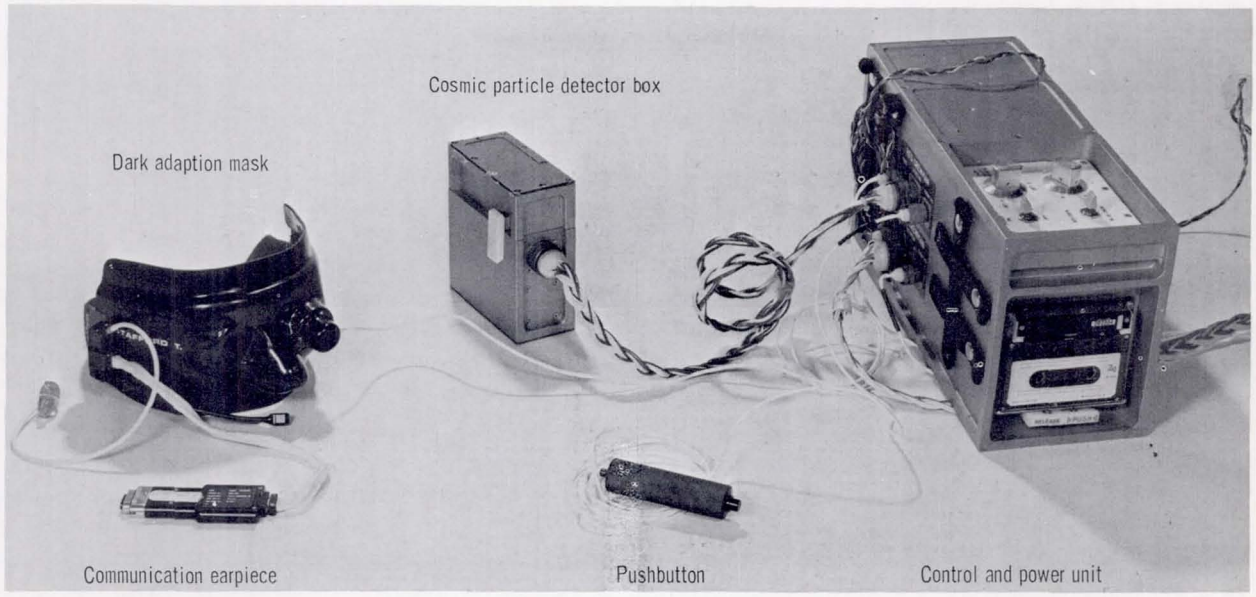

Figure 13-4.- Experiment hardware.

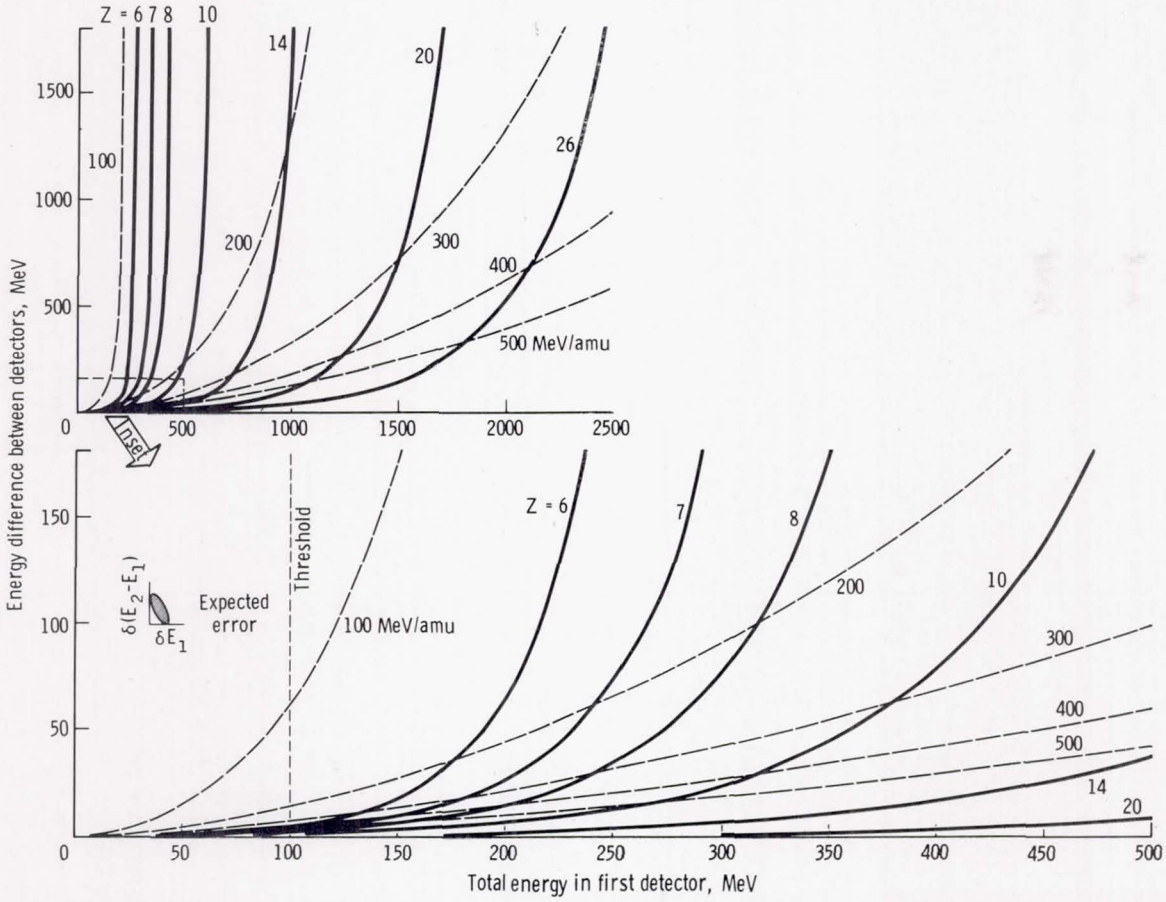

Figure 13-5.- Relationship between silicon detector response, particle charge, and velocity.

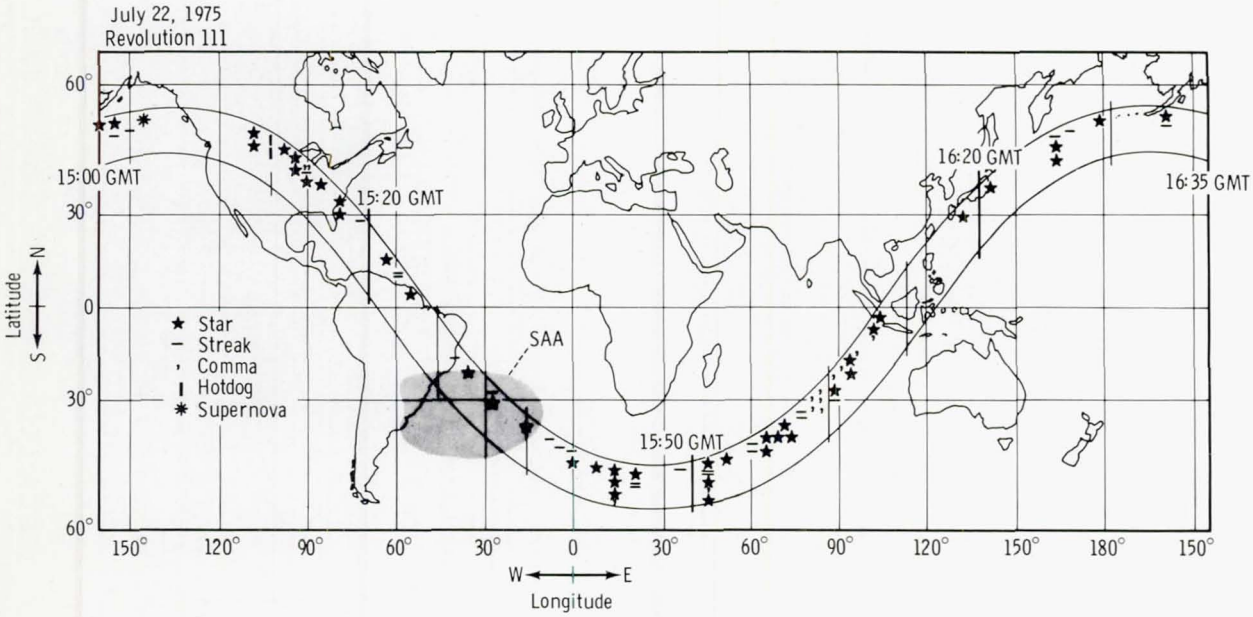

Figure 13-6.- Orbit track and distribution of reported events.

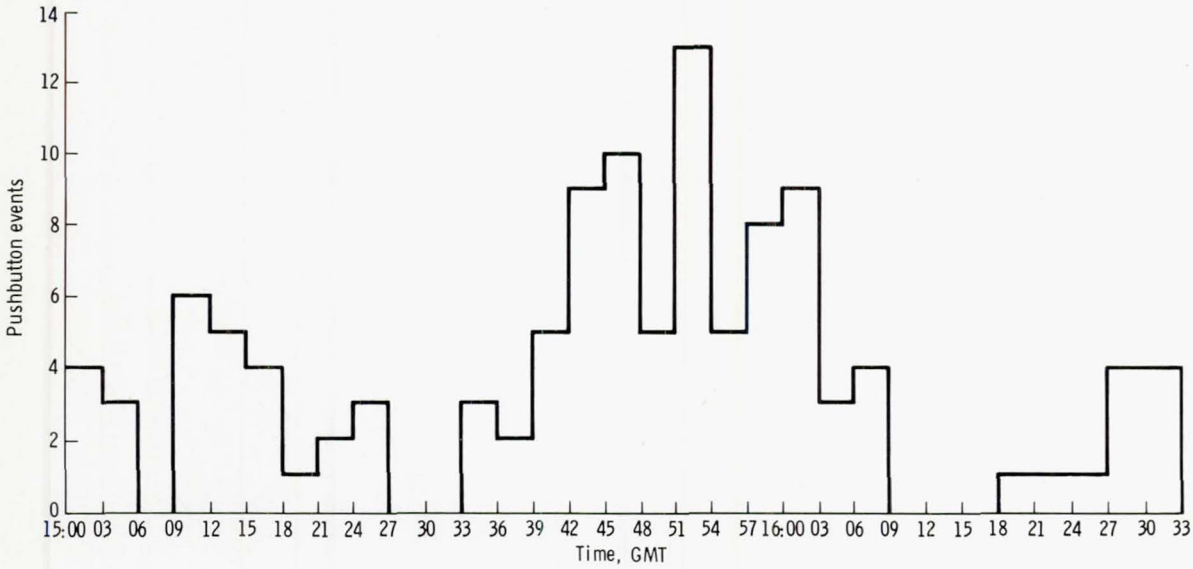

(a) Intervals of 3 minutes.

Figure 13-7.- Histograms of pushbutton events by time and latitude. Except for a few cases, pushbutton events agree with verbal reports.

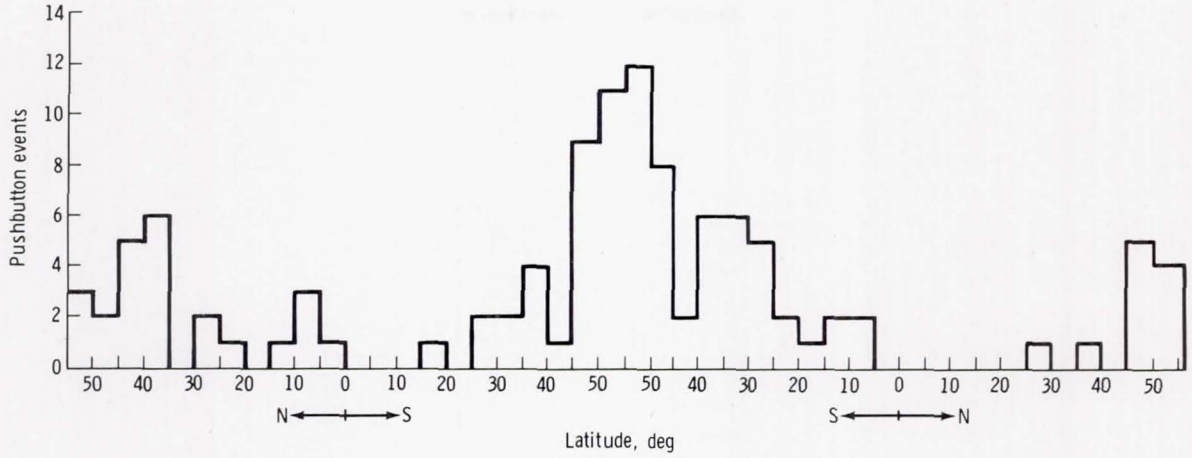

(b) Intervals of 5° latitude.

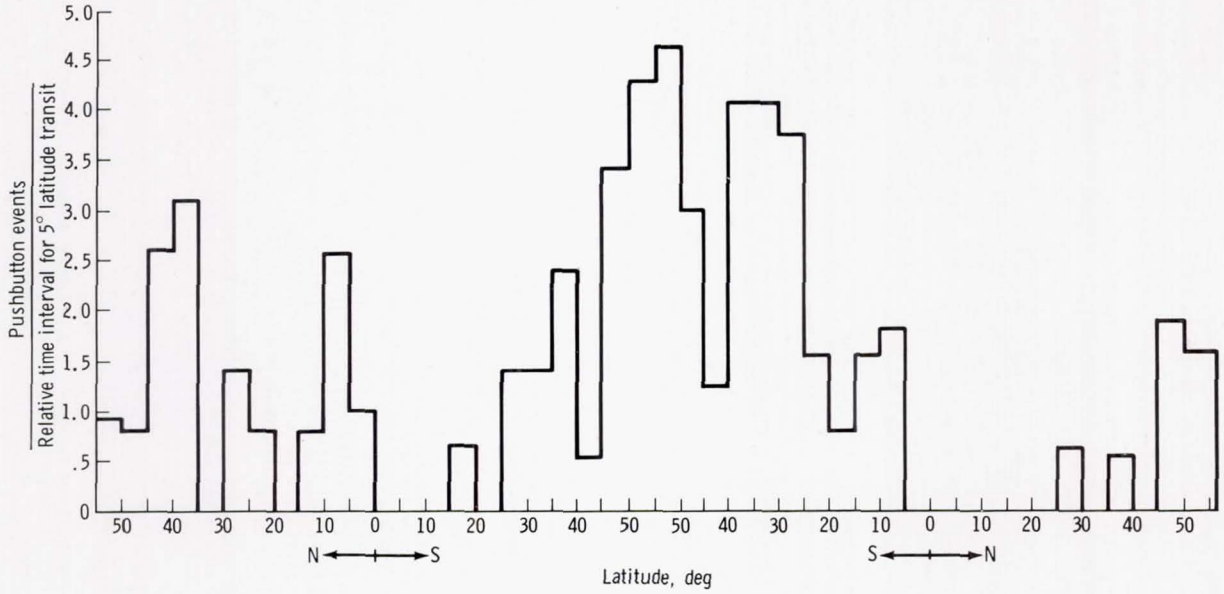

(c) Intervals of 5° latitude normalized by time intervals.

Figure 13-7.- Concluded.

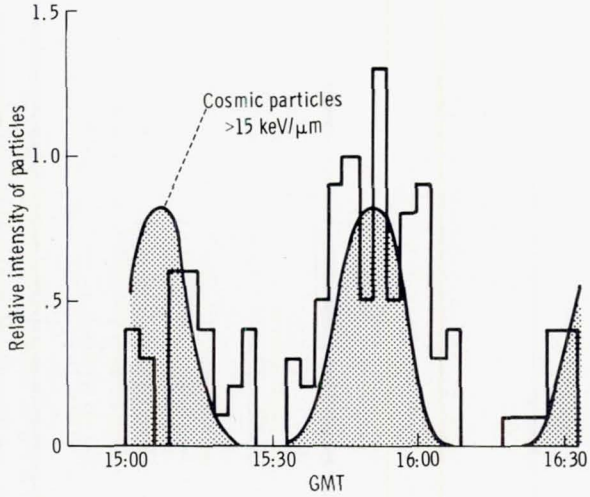

Figure 13-8.- Superposition of relative number of events with a stopping power of >15 keV/μm on histogram of reported events.

14. BIOSTACK III

EXPERIMENT MA-107

H. Bücker,[a†] R. Facius,[a] D. Hildebrand,[a] G. Horneck,[a] G. Reitz,[a]
U. Scheidemann,[a] M. Schäfer,[a] C. Thomas,[a] B. Toth,[a] A. R. Kranz,[a]
E. H. Graul,[b] W. Rüther,[b] M. Delpoux,[c] H. Planel,[c] J. P. Soleilhavoup,[c]
C. A. Tobias,[d] T. Yang,[d] E. Schopper,[a] J. U. Schott,[a] E. Obst,[a]
O. C. Allkofer,[e] K. P. Bartholomä,[e] R. Beaujean,[e] W. Enge,[e] W. Heinrich,[f]
H. François,[g] G. Portal,[g] R. Kaiser,[h] J. P. Massué,[i] R. Pfohl,[i] C. Jacquot,[i]
E. V. Benton,[j] and D. D. Peterson[j]

ABSTRACT

The Biostack III experiment onboard the Apollo spacecraft during the Apollo-Soyuz Test Project complemented the Biostack I and II experiments of the Apollo 16 and 17 missions. The objectives of these experiments were to study the biological effects of individual heavy cosmic particles of high-energy loss (HZE) not available on Earth, to study the influence of additional space-flight factors, to obtain knowledge on the mechanism by which HZE particles damage biological materials, to get information on the spectrum of charge and energy of the cosmic ions in the spacecraft, and to estimate the radiation hazards to man in space.

---

[a]University of Frankfurt.

[b]University of Marburg.

[c]University of Toulouse.

[d]University of California.

[e]University of Kiel.

[f]University of Siegen.

[g]Atomic Energy Commission, Republic of France.

[h]Ministre de l'Industrie et de la Recherches, Paris, France.

[i]University of Strasbourg.

[j]University of San Francisco.

[†]Principal Investigator.

For these purposes, the Biostack experiment includes a wide spectrum of biological objects, and various radiobiological end points are under investigation. Bacterial spores, protozoa cysts, plant seeds, shrimp eggs, and insect eggs were included in the Biostack experiment packages together with different physical radiation detectors (nuclear emulsions, plastics, silver chloride crystals, and lithium fluoride thermoluminescence dosimeters). The biological objects in the Biostack are stacked alternately between physical detectors of HZE particle tracks. By using special arrangements of biological objects and physical track detectors, individual evaluation of tracks was obtained that permitted the identification of each penetrating particle in relation to the possible biological effects on its path. A precision micromanipulator was developed that allowed the transfer of a single bacterial spore from the flight plates to the nutrient medium, thus permitting observation of the growth of known hit spores for changes in development, growth kinetics, and cell morphology. The response of the different biological objects to space flight and HZE particle bombardment varied in degree, presumably depending on the ability of the organism to replace the cells damaged by a hit. The results help to estimate the radiation hazard to astronauts during long-duration space missions.

INTRODUCTION

The Biostack III experiment was designed to study the biological efficiency of individual particles of galactic cosmic radiation that penetrate biologic matter during space flight. Of special interest were the heavy (high atomic number) high-energy (HZE) particles with a high loss of energy as the particles pass through material. To determine this biological efficiency and to correlate the biological effect with the energy deposition, layers of several biological species in resting states were stacked alternately with various track detectors (fig. 14-1). The possible interaction with other space-flight factors (e.g., weightlessness) can be recognized by comparing the results of spacecraft-borne, balloon-borne, and accelerator-exposed experiments.

The Biostack III experiment onboard the Apollo spacecraft during the Apollo-Soyuz Test Project (ASTP) complemented the Biostack I experiment of the Apollo 16 flight and the Biostack II experiment of the Apollo 17 flight. The Biostack I and II experiments have demonstrated several developmental disturbances and anomalies in different biological objects (fig. 14-2).

The biological damage by a single HZE particle was shown to be significant. The Biostack experiments thus yield the basic data (ref. 14-1) that are necessary to estimate the radiation hazards to man in space and that contribute to the establishment of radiation protection requirements for manned space flights.

The dose contribution of the HZE particles was only 0.5 percent of the total space radiation dose. Therefore, the results of the observed radiation effects required the development of new approaches to dosimetry. The objective of the ASTP Biostack experiment (Biostack III) was to confirm, complement, and enlarge the results of the Biostack I and II experiments by applying improved and advanced methods of localization and physical and biological evaluation, by performing advanced experiments based on the Biostack I and II data, and by including additional biological specimens and radiation detectors. This experiment will contribute

to a more complete knowledge of the biological effectiveness of the highly structured cosmic radiation. Furthermore, a comparison of the data of Biostack III with the data of Biostacks I and II will show the differences in radiation composition and the relative biological effectiveness of the radiation inside and outside the geomagnetic field. Generally, the viability of the flown biological objects did not appear to be affected by any additional random space-flight factors. From these observations, a scientifically profitable evaluation of the Biostack III experiment is anticipated.

CONSIDERATIONS ON THE DOSIMETRY OF HZE RADIATION

The determination of the relative biological effectiveness of cosmic radiation, and consequently the estimation of radiation hazards to man in space, requires an appropriate dosimetric approach. In this respect, the entire cascade of events following the impact in matter, not the primary composition of the cosmic radiation, is of interest. Thus, there are two separate categories of action:

1. The quasi-homogeneous radiation, which is the total spectrum of electromagnetic radiation and the low-energy particle radiation. Conventional dosimetric concepts are applicable to and valid for this category.

2. The highly structured radiation with high-energy deposition (HED) events. These HED events are HZE particle tracks, nuclear disintegration stars, recoil particle tracks, high-energy jets, and fission fragment tracks. A common characteristic of these events is that the main part of their energy is deposited in such a small volume (track core diameters of a few nanometers) and in such a short time ($\approx 10^{-13}$ sec) that comparison with other types of radiation is not possible (ref. 14-2).

Little is known about the action mechanisms of HED events on biological objects. The highly organized and differentiated structure of biological material complicates investigations in this connection. A total breakdown of lattice structure by HED events can be verified only in inorganic crystals by electron microscope investigations (ref. 14-3). Present knowledge about the interaction of HED events with matter is restricted to ionization and excitation patterns within a limited distance from the particle trajectories (refs. 14-4 to 14-6) and cautious assumptions about heat transfer and shock waves (refs. 14-7 and 14-8).

To appraise the hazards of cosmic radiation from HED events, dose equivalent indices are inadequate, as already outlined in 1966 by the International Commission for Radiation Protection (ICRP) Task Group on Biological Effects of High Energy Radiations (ref. 14-9) and in 1973 by the National Academy of Sciences (ref. 14-1). Recently, Schaefer (ref. 14-10) came to the conclusion that, in the absence of a dosimetric system and considering the urgent need for recordkeeping on HZE particle exposure in manned space operations, all that can be done is to measure the basic physical parameters of the exposure.

To determine all the physical, chemical, and biological consequences of an individual HZE particle penetration, a length of particle track is needed (for simple statistical reasons) that exceeds system dimensions of common radiobiological procedures. Also, in the region where the classical dose concept becomes valid, the question arises of what insight into biological consequences can be gained from examining living organisms that have experienced a "shotgun volley."

In every experiment with HZE particles, the "dose" is proportional to the density of particle tracks. The arguments can be refined using the stochastic distribution of specific energy to find the lower limit for the applicability of the quantity "dose" (ref. 14-11). However, the trend is the same, and there is no choice. To investigate the biological effects of HZE particles, it is necessary to use new techniques: the Biostack is one example. There is still the stochastic process of energy deposition along and lateral to the track. By the Biostack techniques, the sample space is reduced to individual specimens, which are affected with a high probability by the passage of a particle. It is necessary to correlate the observed effects with quantities determined by continuous model calculations, being well aware that the stochastic process of energy deposition leads to a statistical variation in the response of the biological specimen. The biological effects found in the Biostack I and II experiments were incurred at energy deposition levels of approximately 7 mJ/kg; 0.03 mJ/kg of this radiation was contributed by HZE particles.

EQUIPMENT AND PROCEDURES

Experiment Preparation

The Biostack III experiment consists of eight biological experiments (table 14-I) and seven dosimetric experiments (table 14-II). For flight, the biological objects (bacterial spores, plant seeds, and animal eggs) were arranged in monolayers, and most were embedded in polyvinylalcohol (PVA). These layers were stacked between track detector sheets so that (1) the particle tracks could be located in relation to the biological objects and (2) the physical quantities of these particles could be determined. In principle, each biological experiment had the same arrangement (fig. 14-3). The dosimetric experiments consisted solely of stacks of detector sheets.

The Biostack III experiment was contained in two cylindrical aluminum containers. Container A had the same design as the Biostack I and II experiments (fig. 14-1, refs. 14-12 and 14-13) and enclosed a stack of 277 sheets of biological and dosimetric experiments. Container B (fig. 14-4) was equipped with small lamps, a filter system, and batteries. It contained a stack of silver chloride (AgCl) crystals, which were illuminated by yellow light during flight to stabilize the particle tracks. This stack consisted of two dosimetric experiments and two biological experiments; some of the AgCl crystals were covered with monolayers of bacterial spores and animal eggs (table 14-I). Container B also contained two detector stacks for dosimetric investigations.

Flight Performance

The Biostack III experiment was stored in the R-1 compartment of the Apollo command module, the same storage area as used for Biostack I and II onboard the Apollo 16 and 17 spacecraft. The bottom of container A was directed toward space and the flange toward the cabin. Container B was positioned conversely (fig. 14-5). The backup units of the experiment were used as ground controls. The ASTP mission duration was approximately 218 hours. After the flight, the experiment was returned to Frankfurt. An external inspection of the Biostack experiment revealed no damage.

New Evaluation Techniques

In addition to the postflight procedures used for Biostack I and II (refs. 14-12 and 14-13), four new techniques were developed and used: micromanipulation of spores, pinpoint etching of plastic detectors, computer-supported track measurements, and track decoration by copolymerization in plastics.

Micromanipulation of spores.- A high-precision micromanipulation procedure was developed for the transfer of single bacterial spores, which are approximately 1 micrometer in length, from the flight layer onto the nutrient medium. The micromanipulation is carried out with an electromechanical device (fig. 14-6) driven in three axes by high-precision step motors. The movement pulses can be adjusted for duration and repetition rate, thus achieving steps smaller than 0.1 micrometer and translation rates of approximately 1 μm/sec in the manual mode. Beginning immediately after transfer, the development characteristics of the spores are watched periodically until a colony is formed (fig. 14-7). This method permits the observation of each spore near a particle track for changes in development, growth kinetics, and cell morphology as well as for genetic information manifested in its progeny.

Pinpoint etching of plastic detectors.- Pinpoint etching greatly improves the accuracy of locating particle tracks in relation to biological objects. The side of the detector that is covered with the biological objects embedded in PVA is sealed, and the other side is etched. The etch cones obtained by the overall etching are enlarged by etching the individual cones under microscopical control until they almost reach the opposite side (fig. 14-8). The situation is then photographed. After removing the biological objects around the calculated penetration point, e.g., by micromanipulating the spores (fig. 14-9(a)), the etching process continues until the opposite side is reached; it is stopped immediately after the breakthrough (fig. 14-9(b)). The situation again is photographed. The actual penetration point can then be determined in relation to the micromanipulated spores by superimposing the two photographs. The only limits of accuracy are given by Abbe's theory of the light microscope (approximately ±0.2 micrometer).

Each track can be evaluated with this new etching method. This is an advantage for the ASTP Biostack III experiment, which encountered a smaller flux than the Apollo 16 and 17 Biostack I and II experiments.

Computer-supported track measurements.- The evaluation of the plastic detectors is performed with a modified microscope; signal transducers allow the automatic recording of local position in three orthogonal axes. Online processing with a minicomputer results in several improvements compared to the method used for the Biostack I and II experiments. Measurement time is decreased. Appropriate data handling facilitates further analysis such as programed reconstruction of complete particle tracks or establishment of range/cone-length diagrams (needed for the linear energy transfer (LET) calibration). A further improvement concerns the determination of particle track location in the seeds of *Arabidopsis thaliana*. These seeds may be treated as a good approximation of rotational ellipsoids. Their size and orientation in three dimensions are determined together with the particle etch cone. If a particle penetrates a given grain, the coordinates of the points of intersection with its surface are given in the system defined by the main axis of the seed (fig. 14-10). Thus, it can be determined immediately whether the particle has crossed internal structures (e.g., cotyledons, radicles, or stem-meristems) because these structures can be recognized in the partly translucent seeds.

Track decoration by copolymerization in plastics.- After a polymer chain exposure to HED events, chemically active sites, such as trapped radicals or peroxidized elements, are formed along the tracks. By permeation with convenient monomers, copolymerization occurs along the tracks. The copolymerized parts of the tracks become visible when they are dyed with a fluorescent medium. Using this method, an attempt was made to detect HED events completely inside the detector (without interference with the surface) in a nearly tissue equivalent material.

The special procedure used was developed by Monnin and Blanford (ref. 14-14). Acrylic acid is copolymerized on cellulose triacetate (CTA) and dyed with rhodamine B. Figure 14-11 shows an example of the fluorescent fission fragment tracks obtained after irradiation with a californium-252 source.

Advanced Postflight Analysis

In a multiple factorial analysis, relations between parameters are detected and condensed into factors; correlations among the factors are then calculated. This analysis works even if colinearity among the parameters prevents the use of standard statistical procedures, such as multiple regression or correlation analysis. If the correlations between the factors and the parameters define the factors in an unequivocal way, the factors can be interpreted causally. The results of the multiple factorial analysis of the Biostack II *Bacillus subtilis* data are shown in figure 14-12. The point plots on the left show the original biological variables as functions of the physical parameters. The biological variables are condensed into factor A, which can be named "biological activity" according to the fraction to which the variables contribute to it. The plots on the right show the point plots of factor A as a function of the factors containing the physical data. Factor B can be named "particle characteristic," and factor C contains an environmental quantity. Both correlations A with B and A with C are now statistically significant with an error probability of 0.05 for A with B and of less than 0.001 for A with C. Two aspects of this analysis should be discussed.

First, the particles of LET_{350} that varied between approximately 1.8 and 5.5 GeV cm^2/g contribute only to a small degree to the "explained" variance of the biological factor. Second, the atomic number Z of the particle appears twice and is the most important component in both factors because it contains the physical characteristics of the event. This may indicate that, apart from the LET, a quantity that depends on the square of Z has to be looked for, a quantity that is possibly connected more directly to the biological effectiveness of these HZE particles. Alper et al.[1] recently reported that Z^2/β^2a^2 (where β is the particle velocity expressed as a fraction of the speed of light and a is the distance between the particle path and the center of the biological object) was a more appropriate parameter than LET for interpreting results of the oxygen enhancement ratio for heavy ions, which is at least consistent with the arguments mentioned previously. In the Biostack III experiment, an attempt has been made to use multiple factorial analysis for all biological objects.

PRELIMINARY RESULTS

Dosimetric Data

The total dose of the cosmic radiation was measured by thermoluminescence dosimeters (TLD) in five different layers of the Biostack III experiment (table 14-III). The tracks produced by HZE particles of cosmic radiation were counted in plastic detectors. The uncorrected values of track density are shown in table 14-IV. A preliminary integral LET_{1000} spectrum that depended on the measured particle density was estimated (fig. 14-13).

From a first partial evaluation of the AgCl detector foils 1-1 to 1-9, the flux of particles with LET of approximately 10 MeV cm^2/g is as follows:

All particles:	1500 ± 100 particles/cm^2
Stopping protons:	50 particles/cm^2
Stopping alpha particles:	70 particles/cm^2
Number of disintegration stars:	3500 stars/cm^3 AgCl or approximately 6300 stars/g

The first dosimetric data of Biostack III obtained from the plastic detectors were compared with those of Biostack I and II (table 14-V). The values measured during the ASTP Earth-orbital flight were essentially lower than those obtained during the Apollo 16 and 17 lunar missions, which are in agreement.

---

[1]Personal communication, 1975.

First Biological Observations

The etching of the cellulose nitrate (CN) sheets, which carried monolayers of biological objects, was performed by a specially developed procedure (ref. 14-13). The CN sheets showed well-developed etch cones (fig. 14-14). Determination of the localization of the tracks in relation to the biological objects is in progress. In the Bacillus subtilis experiment, tracks with $Z > 12$ have been selected; the point of their penetration through the spore layer has been determined with an accuracy of ±0.2 micrometer; and the spores near this penetration point have been evaluated in regard to changes in spore outgrowth, cell morphology, and growth kinetics. The new techniques of pinpoint etching and micromanipulation were applied and worked without complications. Deviations from normal development have been observed; e.g., monstrous swelling during growth of the first vegetative cell (fig. 14-15). Such anomalies have been reported to be produced by X-rays or deuterons (ref. 14-15). A multiple factorial analysis, which will be applied after the complete set of data is processed, will show the contribution of HED events to such phenomena.

The analysis of the CN layers for the Zea mays experiment indicates that 52 of 79 seeds were hit by HZE particles with $LET_{\infty} > 1.5$ GeV/cm. The first one-fourth of the flight seeds were planted approximately 90 days after the mission. No significant difference in seedling development between the flight seeds and the control seeds has been observed. The germination is 94.28 percent in the flight group and 96.97 percent in the control group. The average length of the embryonic leaf is 52.39 millimeters for the flight seeds and 52.00 millimeters for the control seeds. The average length of the first leaf is 115.42 millimeters for the flight group and 119.10 millimeters for the control group.

DISCUSSION

To determine the radiation hazards to man in space, theoretical calculations based on dose equivalent indices are not sufficient (ref. 14-10). The quality factors for HED events are mostly unknown, and their definition is very doubtful according to theoretical considerations. There are many indications that the action of HED events cannot be appraised by quality factors at all.

The Biostack experiment is a very effective and universal monitor of the physical parameters of cosmic radiation and of the biological effects produced by HED events of cosmic radiation during space flight. Although the Biostack technology was developed for the special task of a space flight, theoretical considerations endorse the use of the same experiment in ground-based accelerator experiments. Based on statistics from several Biostack experiments (including space flight, balloon, and accelerator experiments), an attempt will be made to find empirical parameters (e.g., by multiple factorial analysis) to be used for radiation protection guidelines. Conversely, predictions from established methods of radiation hazard calculation (both empirical (Katz) and theoretical (Rossi, Kellerer) approaches) can be compared with the Biostack results.

The Biostack II results on the development of Artemia salina eggs (table 14-VI) indicate that the biological importance of nuclear disintegration stars is comparable to that of HZE particles. Even those flight eggs that were not affected by HZE particles showed remarkable disturbances in development. The high level of embryonic lethality in these eggs compared with the flight eggs penetrated by HZE particles leads to the conclusion that the observed reduced emergence is a radiation effect. This hypothesis is supported by the fact that the 15 000 stars/cm^3 measured in the adjacent emulsions permit the calculation of a "dose" contribution by stars in Artemia salina eggs that is approximately the same as that of HZE particles.

The equivalence in rank of disintegration stars to HZE particles in regard to biological efficiency (fig. 14-16) would be, if proved, a strong argument for the use of pion (π^-) beams in cancer therapy. Usual dose measurement (ref. 14-16) strongly underestimates the star peak that covers the main part of the depth-dose peak of a pion beam. The most probable reaction $\pi^- + {}^{16}O \longrightarrow {}^{12}C + 3\,n$ (26 percent of the reactions) can even be approached as occurring between multipronged stars and a stopping HZE particle. The considerations are in good agreement with the relative biological effectiveness (RBE) measurements for pions of Akojew and Jurow (ref. 14-17).

For future biological experiments in space (e.g., Spacelab), simultaneous measurement of HED events is recommended. For supersonic transport (SST) travel, the stars as HED events have also been taken into account. Allkofer (ref. 14-18) found the maximum of disintegration stars at an altitude of approximately 20 kilometers, which is the actual altitude of SST travel. The hazards to embryos from stars are unknown.

CONCLUDING REMARKS

Causal interpretations of effects found during space flight are possible only if the influence of all known environmental factors is considered. The Biostack experiments proved that significant radiation damage has resulted from the passage of a single HZE particle (refs. 14-12 and 14-13). Some indications were found of the comparable effectiveness of other HED events. In view of these results, the influence of HED events may have to be incorporated into the interpretation of the observed effects in space biological studies. This assertion is strengthened by the assumed contribution of nuclear disintegration stars to biological radiation events in space.

The question remains of how relevant to man are the effects that have been shown to be produced by HZE particles in animal eggs, plant seeds, and bacterial spores. Table 14-VII compares the radiation sensitivity of man with that of some of the biological objects used in the Biostack experiments. Of this group, man is the most radiosensitive object. The sensitivity of the hatching of the two groups of insect eggs is of the same magnitude, but hatching of the Artemia salina shrimp eggs is approximately 10 times more resistant. In these animal eggs, developmental defects have been produced by a penetrating HZE particle. This confirms the

assumption that HZE-particle-induced damage might become manifest if nonreplaceable cells are destroyed. In manned space flight, the primary concern would be the nervous system, which consists of highly differentiated nonreplaceable cells. Occurrence of sublethally damaged cells that could possibly produce late radiation effects should also be considered. However, the risk to man from HZE particles during space flight can be sufficiently lowered if the maximum possible shielding against HZE particle bombardment is ensured in the design and construction of future space vehicles.

REFERENCES

14-1. Grahn, Douglas, ed.: HZE-Particle Effects in Manned Space-Flight. National Research Council, Radiobiological Advisory Council, National Academy of Sciences, Washington, D.C., 1973.

14-2. Bücker, H.; Horneck, G.; and Hildebrand, D.: Effects of Individual HZE-Particles in the Biostack Experiment. Proceedings of the 4th Symposium on Microdosimetry. Euratom EUR 5122 d-e-f, Sept. 1973, p. 1071.

14-3. Fleischer, R. L.; Price, P. B.; and Walker, R. M.: Tracks of Charged Particles in Solids. Science, vol. 149, no. 3682, July 23, 1965, pp. 383-393.

14-4. Paretzke, H. G.: Approaches to Physical Track Structure Calculations and Comparison of Track Structure Calculations With Experimental Results. Proceedings of the 4th Symposium on Microdosimetry. Euratom EUR 5122 d-e-f, Sept. 1973, p. 141.

14-5. Fain, J.: Energy Density Deposited by a Heavy Ion Around Its Path. Proceedings of the 4th Symposium on Microdosimetry. Euratom EUR 5122 d-e-f, Sept. 1973, p. 169.

14-6. Muga, M. L.: A New Model Describing the Energy Deposition Profile Along the Path of a Heavy Ion. Paper presented at 5th International Conference on Radiation Research (Seattle, Wash.), 1974.

14-7. Dessauer, Friedrich: Quantumbiologie; Einsührung in einen neuen Wissenszweig. (Quantum Biology; An Introduction to the New Science.) Second ed., Springer (Berlin), 1964.

14-8. Simmons, J. A.: Thermal Conductivity of Glycine. Nature, vol. 216, Dec. 30, 1967, p. 1302.

14-9. Upton, A. C.; Chase, H. B.; Hekhuis, G. L.; Mole, R. H.; et. al.: Radiobiological Aspects of the Supersonic Transport. Health Phys., vol. 12, 1966, pp. 209-226.

14-10. Schaefer, H. J.: Microdosimetric Structure of HZE Particle Tracks in Tissue. NASA CR-141935, Apr. 1975.

14-11. Kellerer, A. M.: Microdosimetry and the Theory of Straggling. Biological Aspects of Radiation Quality, International Atomic Energy Agency (Vienna), 1968, pp. 89-103.

14-12. Bücker, Horst; Horneck, G.; Reinholtz, E., Scheuermann, W.; et al.: Biostack Experiment. Sec. 27, Part A, of the Apollo 16 Preliminary Science Report. NASA SP-315, 1972.

14-13. Bücker, H.; Horneck, G.; Reinholtz, E.; Rüther, W.; et al.: Biostack Experiment. Sec. 25 of the Apollo 17 Preliminary Science Report. NASA SP-330, 1973.

14-14. Monnin, Michel M.; and Blanford, George E., Jr.: Detection of Charged Particles by Polymer Grafting. Science, vol. 181, Aug. 24, 1973, pp. 743-744.

14-15. Donnellan, J. Edward, Jr.; and Morowitz, Harold J.: The Effect of Charged Particle Irradiation on Germination of Bacillus subtilis. Radia. Res., vol. 12, no. 1, Jan. 1960, pp. 67-78.

14-16. Biomedical Applications and Dosimetry of Pions. Institute for Nuclear Research (SIN), Zurich, Switzerland, Oct. 1973.

14-17. Akojew, J. G.; and Jurow, S. S.: The Molecular Principles of the Action of High Energy Hadrones and the Results of Space Biological Investigations. Izvestija Academia Nauk, SSSR, Seria Biologiceskja. Nr. 1, 1975.

14-18. Allkofer, O. C.: Dosimetry at SST Altitude. Paper presented at 8th International Conference on Nuclear Photography and Solid State Track Detectors (Bucharest, Rumania), 1972.

TABLE 14-I.- BIOSTACK III BIOLOGICAL EXPERIMENTS

Biological system	Track detectors (a)	Effects under investigation	Investigators	Affiliation
Monocellular:				
Bacillus subtilis spores	AgCl CN Lexan	Influence on spore outgrowth, cell development, colony formation, and mutation induction	D. Hildebrand, R. Facius, B. Toth, G. Horneck, and M. Schäfer	University of Frankfurt
Plant:				
Arabidopsis thaliana seeds	CN Lexan	Influence on germination, plant development, and mutation induction	A. R. Kranz, U. Scheidemann, C. Thomas, and G. Reitz	University of Frankfurt
Negotiana tabaccum seeds	K2	Influence on germination, growth and development, and mutation induction	M. Delpoux	University of Toulouse
Zea mays seeds	CN Lexan	Influence on growth, differentiation and morphogenesis, and mutation induction	C. A. Tobias and T. Yang E. V. Benton	University of California University of San Francisco
Animal:				
Artemia salina eggs	K2	Influence on early steps of development	H. Planel and J. P. Soleilhavoup	University of Toulouse
Artemia salina, *Tribolium castaneum*, and *Carausius morosus* eggs	K2 CN Lexan AgCl	Influence on hatching, induction of development anomalies, and histological anomalies	W. Rüther and E. H. Graul W. Heinrich	University of Marburg University of Siegen

[a]AgCl - silver chloride, CN - cellulose nitrate, K2 - nuclear emulsion.

TABLE 14-II.- BIOSTACK III DOSIMETRICAL EXPERIMENTS

Detector	Description	Physical data investigated	Investigators	Affiliation
CN	Track detector Area sensitive Tissue comparable	Particles with $LET_{1000} > 1$ GeV cm^2/g energy, charge, pathlength, and LET_{1000}	W. Enge, O. C. Allkofer, K. P. Bartholomä, R. Beaujean, and K. Fukui W. Heinrich E. V. Benton R. Facius, D. Hildebrand, G. Reitz, and M. Schäfer	University of Kiel University of Siegen University of San Francisco University of Frankfurt
Lexan	Track detector Area sensitive Tissue comparable	Particles with $LET_{1000} > 3$ GeV cm^2/g energy, charge, pathlength, and LET_{1000}	W. Enge, O. C. Allkofer, K. P. Bartholomä, R. Beaujean, and K. Fukui W. Heinrich E. V. Benton	University of Kiel University of Siegen University of San Francisco
Cellulose triacetate (CTA)	Track detector Area sensitive Volume sensitive Tissue comparable	Particles with $LET_{1000} > 1.5$ GeV cm^2/g energy, charge, pathlength, and LET Primary particles with LET > 2.0 GeV cm^2/g Attenuated particles with LET > 0.5 GeV cm^2/g Stars and other HED-event indications	D. Hildebrand, C. Thomas, and G. Reitz	University of Frankfurt
K2	Track detector Volume sensitive	Particles with LET > 10 MeV cm^2/g LET, charge group, pathlength, dose contribution, and all HED events	R. Kaiser, J. P. Massué, and R. Pfohl	Center of Nuclear Research, Strasbourg
K5	Track detector Volume sensitive	Particles with LET > 10 MeV cm^2/g LET, charge group, pathlength, dose contribution, and all HED events Quasi-homogeneous component	R. Kaiser, J. P. Massué, and R. Pfohl	Center of Nuclear Research, Strasbourg
AgCl	Track detectors Volume sensitive	Particles with LET > 10 MeV cm^2/g LET, charge group, pathlength, and all HED events	E. Schopper, J. U. Schott, and E. Obst	University of Frankfurt
Thermoluminescence dosimeter (TLD)	Total dose measurement	Total dose	H. François and G. Portal	Atomic Energy Commission, Republic of France

TABLE 14-III.- TOTAL DOSE OF COSMIC RADIATION

MEASURED BY TLD IN BIOSTACK III

Container	Layer no.	Position in the container	Total absorbed dose, mJ/kg	Mission absolute dose, mJ/kg	Mission dose rate, μJ/kg hr
Flight unit					
A	K1	Bottom	1.10	0.99	4.54
	K7	Middle	1.21	1.10	5.04
	K14	Top	1.35	1.24	5.69
B	B1	Middle	1.15	1.03	4.72
	B2	Bottom	1.13	1.01	4.63
Ground control					
A	L1	Bottom	11.3	--	--
	L7	Middle	10.9	--	--
	L14	Top	10.6	--	--
B	B3	Middle	11.7	--	--

TABLE 14-IV.- PARTICLES RECORDED IN BIOSTACK III CELLULOSE NITRATE DETECTORS

Location	Layer no.	Detector	Restricted energy loss (LET_{1000}), GeV cm^2/g	Tracks/cm^2
Bottom	K2-54	CN_{Kodak}	≥ 0.8	6.4
	[a]K3-47, [a]K3-62	CN_{Daicel}	≥ 1.0	1.9
Top	K13-22	CN_{Daicel}	≥ 1.0	2.0

[a]Mean value.

TABLE 14-V.- DOSIMETRIC DATA ON COSMIC RADIATION RECORDED IN THE BIOSTACK I, II, AND III EXPERIMENTS

Space flight	Biostack experiment	Total cosmic radiation		HZE particle flux, tracks/cm^2/hr
		Dose, mJ/kg	Dose rate, μJ/kg hr	
Apollo 16	I	5.75 to 6.45	23.4	0.07
Apollo 17	II	7.15 to 7.50	24.1	.07
ASTP	III	1.10 to 1.35	5.0	.009

TABLE 14-VI.- RESULTS OF APOLLO 17 ARTEMIA SALINA EMERGENCE STUDY

Sample	Percent of eggs without development	Percent of eggs with development (eggshell cracked)		
		Membrane not torn		Membrane torn
		Basic shape of larva not formed	Basic shape of larva formed	Swimming nauplius
	Group 1	Group 2	Group 3	Group 4
Eggs hit by heavy primaries (822)	43.07	34.55	7.66	14.72
Eggs not hit by heavy primaries (background irradiated) (1200)	20.5	16.4	12.8	50.3
Ground controls (1600)	9.2	1.0	1.2	88.6

TABLE 14-VII.- SENSITIVITY OF DIFFERENT BIOLOGICAL OBJECTS TO X-IRRADIATION[a]

Biological object	Effect	LD_{50}, kJ/kg (krad)
Man	Death	0.004 (0.4)
Tribolium castaneum eggs	No hatching	.006 (.6)
Carausius morosus eggs	No hatching	.010 (1.0)
Artemia salina eggs	No hatching	.035 (3.5)
Bacillus subtilis spores	No colony formation	.900 (90.0)
Bacillus subtilis spores	No outgrowth	1.600 (160.0)

[a]Lethal dose producing the effect in 50 percent of the irradiated objects.

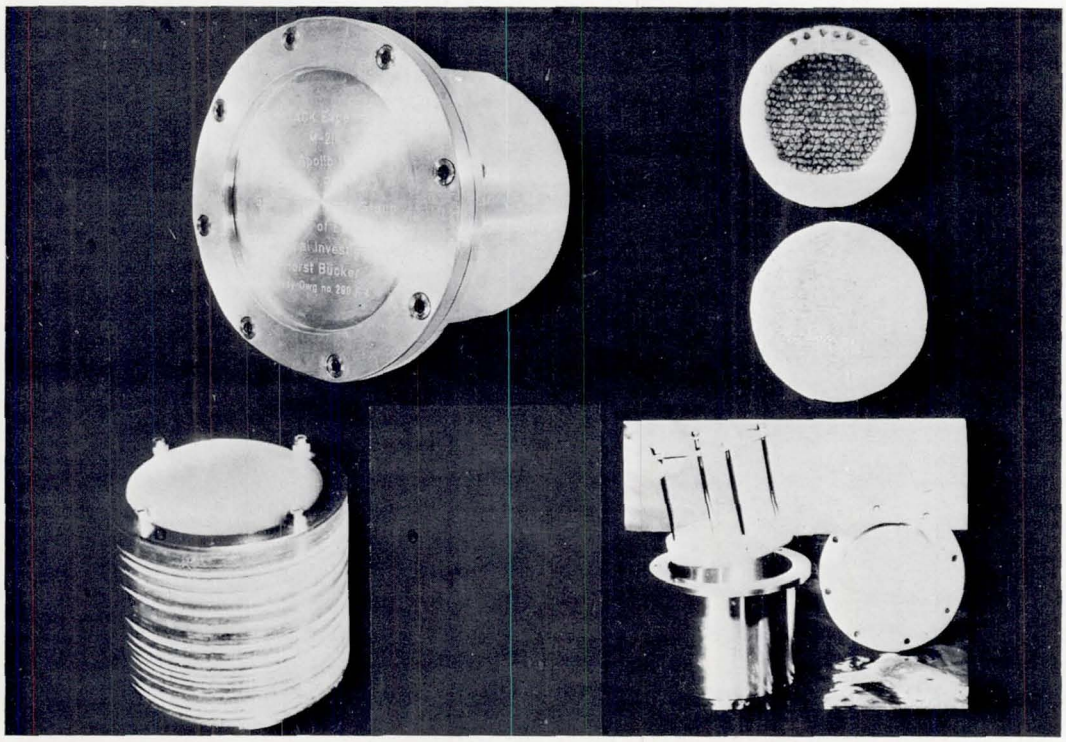

(a) Photograph of components.

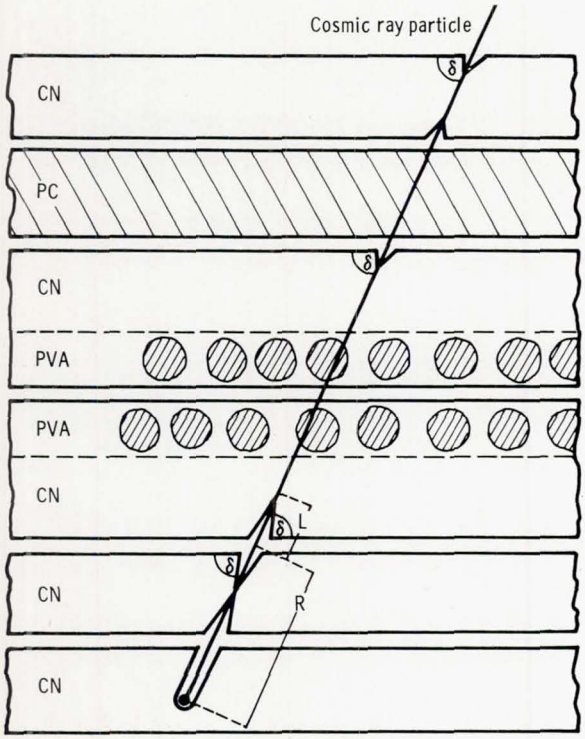

(b) Schematic of part of a biologic unit in fixed contact with the cellulose nitrate (CN) sheets. Measurement of the dip angle δ is made to determine (1) the hit biologic object, (2) the cone length L (to determine energy loss), and (3) the residual range R (to establish the particle charge). The biological objects are embedded in polyvinylalcohol (PVA). A layer of polycarbonate (PC) separates the CN sheets at the top.

Figure 14-1.- Biostack III container A.

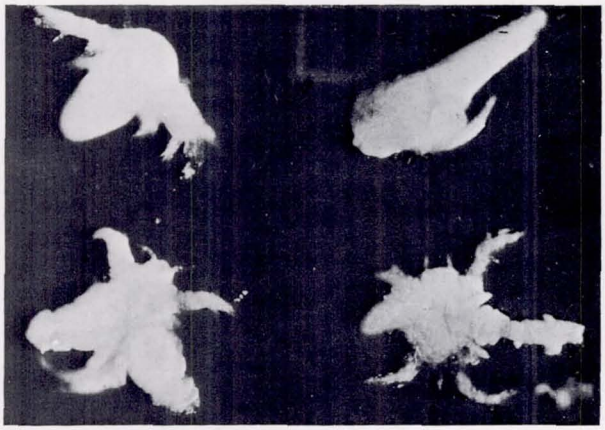

Figure 14-2.- Malformations of Artemia salina induced by HZE particles that penetrated their eggs.

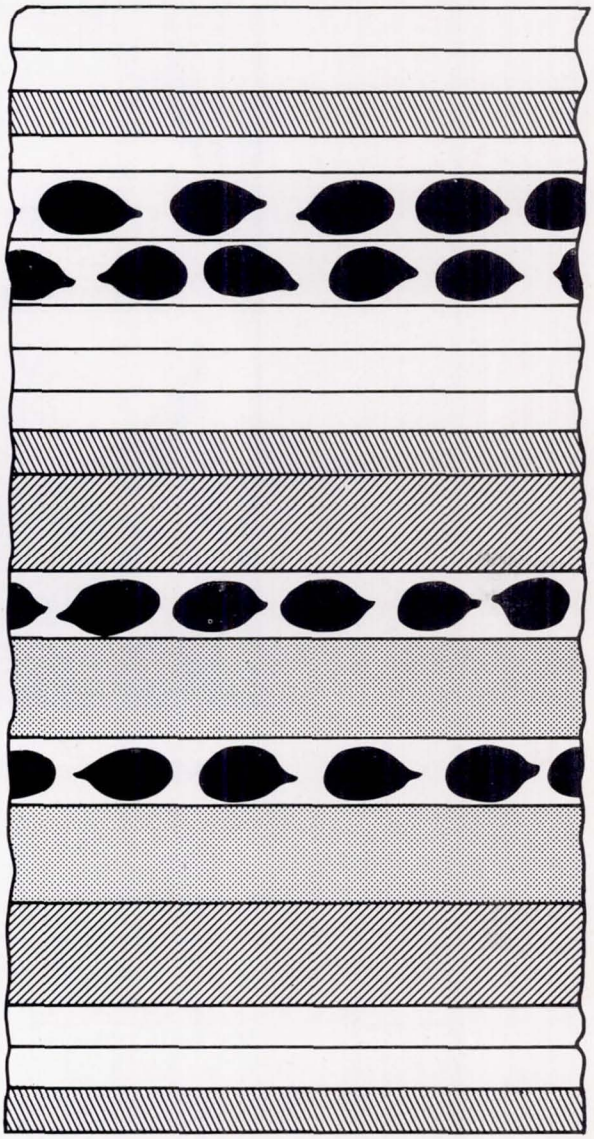

Figure 14-3.- Typical configuration of biological objects and track detectors in the Biostack.

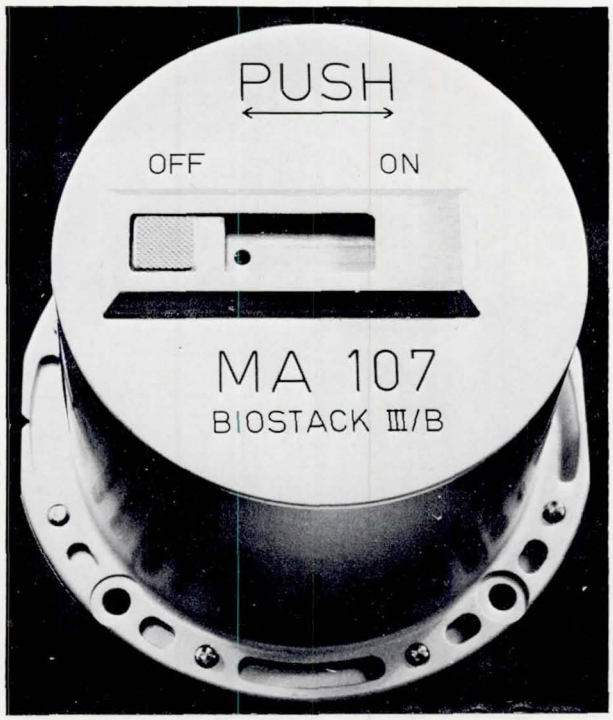

Figure 14-4.- Biostack III container B.

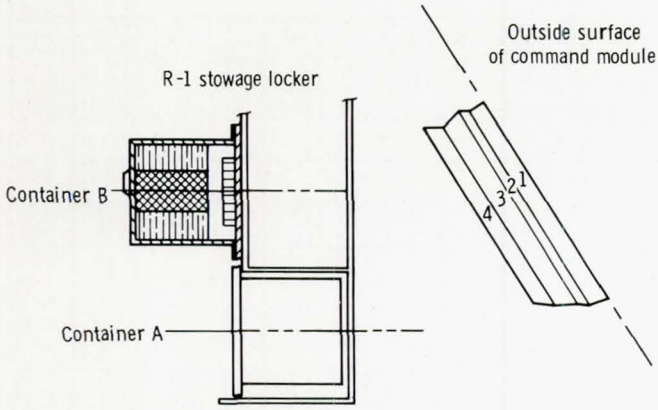

1 Ablator: 1.8 cm thick, 513 kg/m^3

2 Honeycomb:
Face sheet - 15-7 stainless steel, 0.020 cm thick
Core - 15-7 stainless steel, 1.229 cm thick;
cell diameter, 0.476 cm; cell wall, 0.0025 cm
Face sheet - 15-7 stainless steel, 0.020 cm thick

3 Insulation: TG 15000, 3.18 cm thick, 9.6 kg/m^3

4 Honeycomb:
Face sheet - 2014 T6 aluminum, 0.025 cm thick
Core - 5052 H39 aluminum, 2.286 cm thick;
cell diameter, 0.476 cm; cell wall, 0.0038 cm
Face sheet - 2014 T6 aluminum, 0.025 cm thick

Figure 14-5.- Stowage location of the Biostack experiment and structural shielding of the Apollo command module.

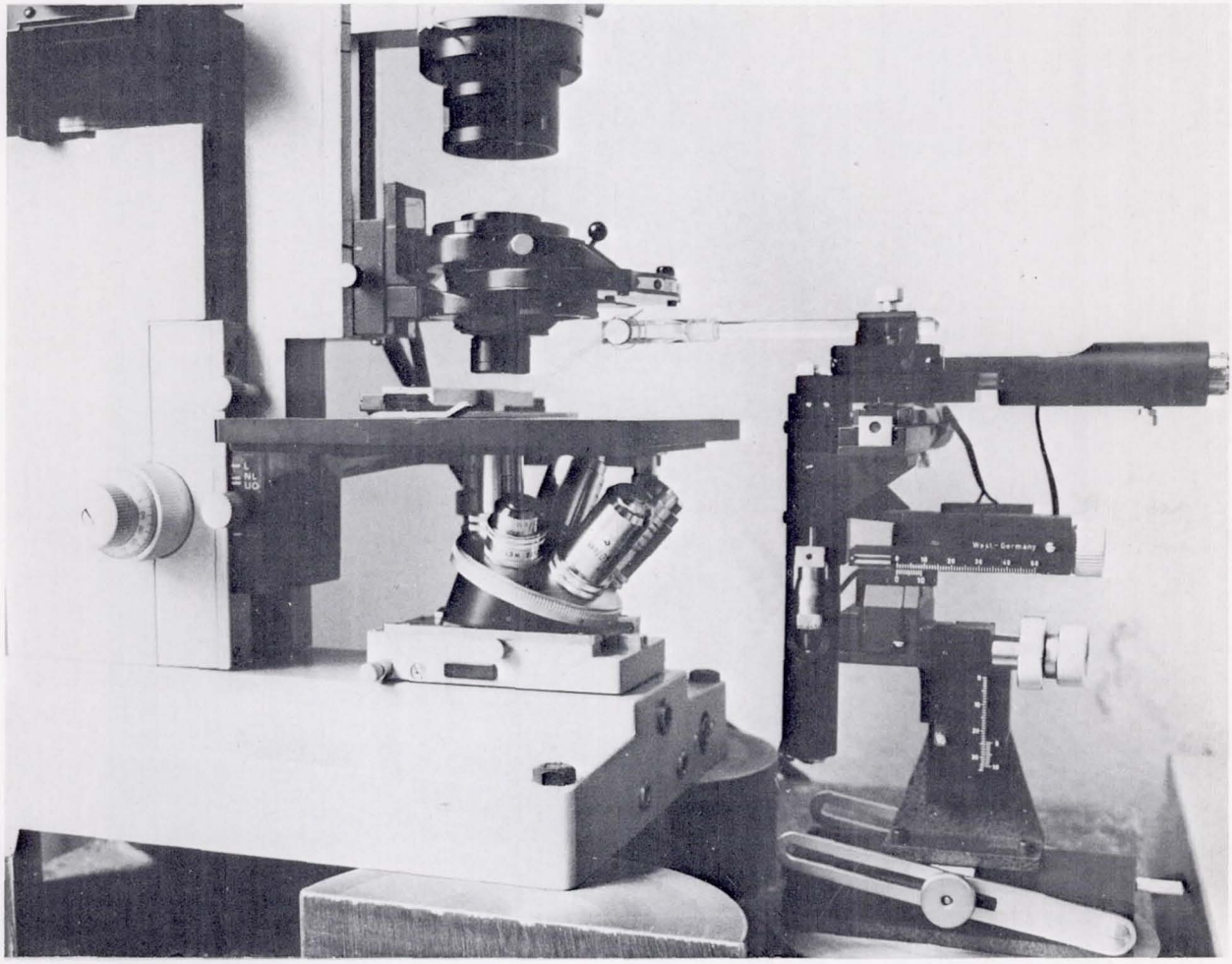

Figure 14-6.- Manipulation equipment.

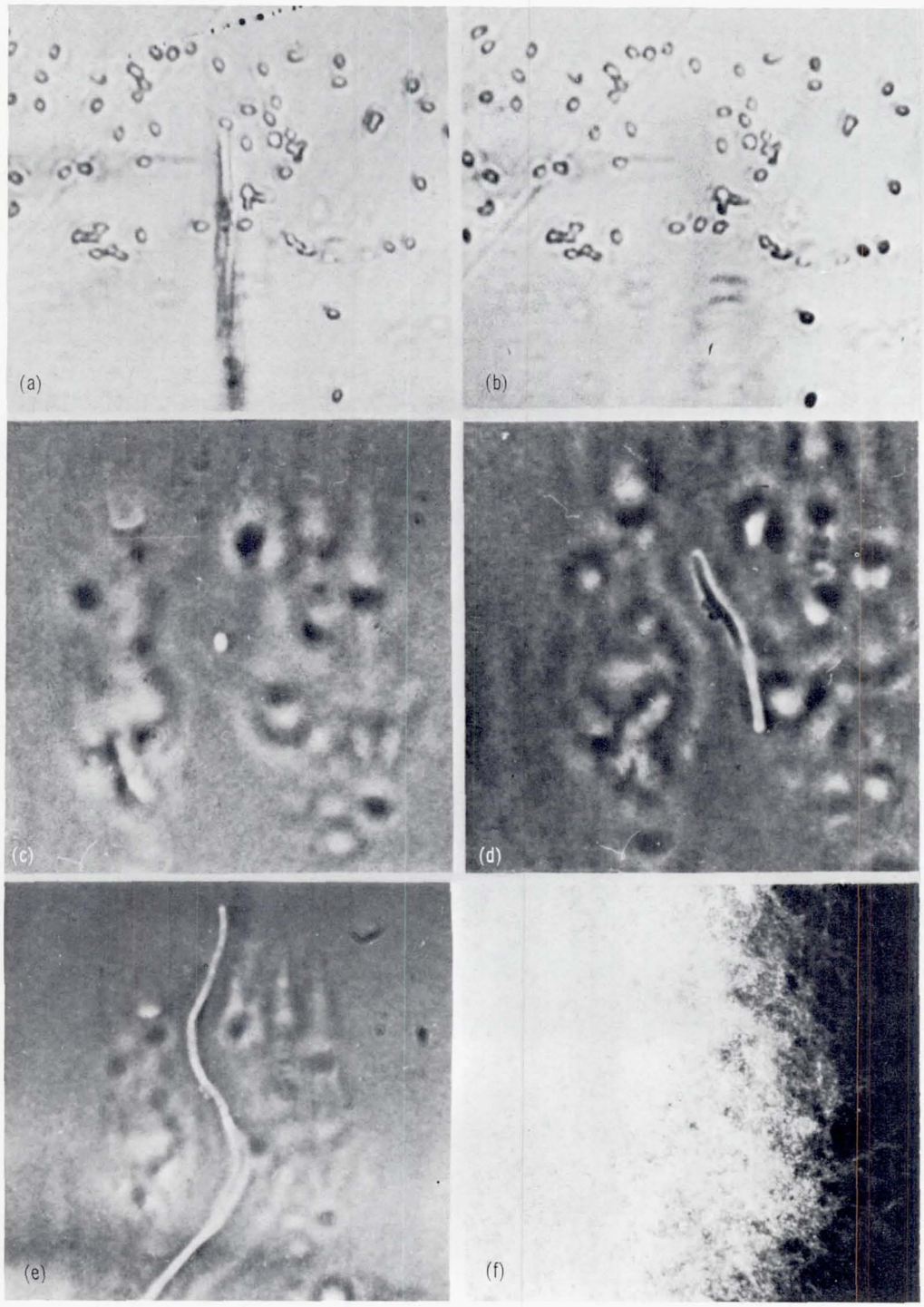

Figure 14-7.- Manipulation and growth of a single Bacillus subtilis spore. The spore to be removed is shown at the end of the needle in (a); the spore has been removed in (b). Increasing incubation times to 250 minutes are shown in (c), (d), and (e), and the colony after 24 hours is shown in (f).

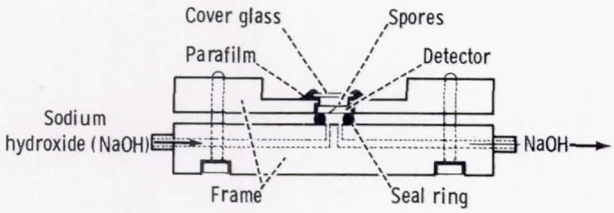

Figure 14-8.- Schematic of pinpoint etching device.

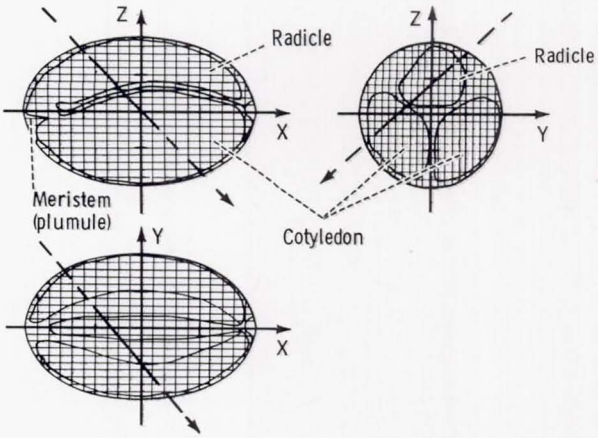

Figure 14-10.- Schematic of orthogonal projections of Arabidopsis thaliana seeds used for localization of HZE particle penetration.

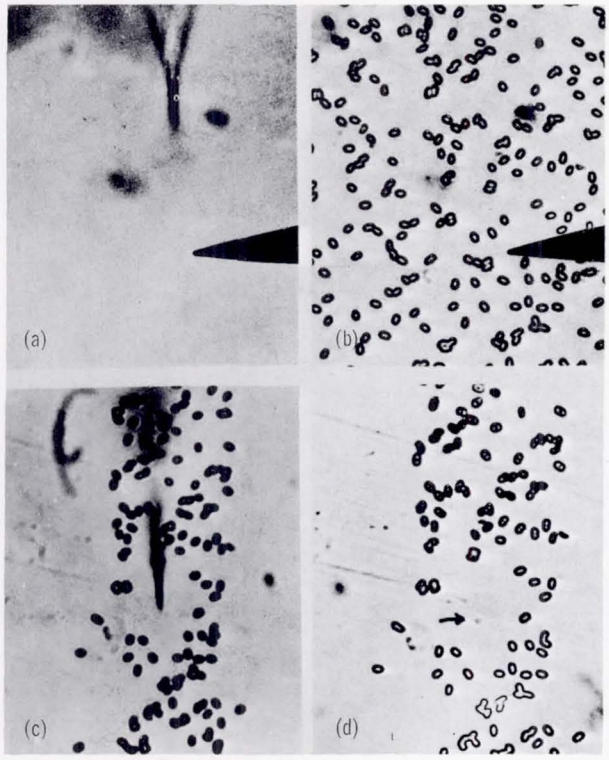

Figure 14-9.- Demonstration of pinpoint etching. The focus is on the tip of the etch cone in (a) and at the surface (spore layer) in (b). The spore is shown after being removed by manipulation and the breakthrough of the etch cone in (c) at low aperture and in (d) at high aperture.

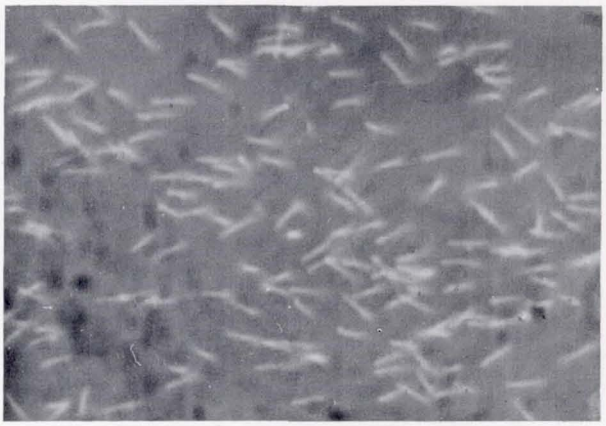

Figure 14-11.- Decorated fission fragment tracks in cellulose triacetate (polymergrafting).

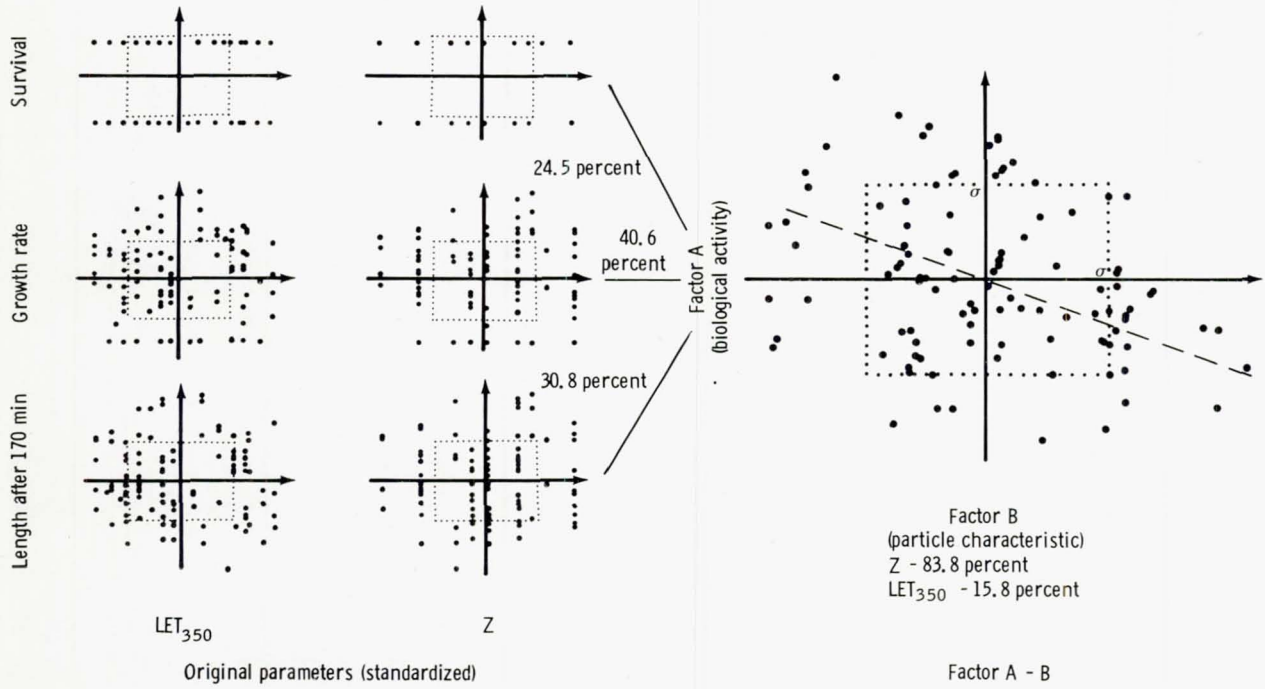

(a) Correlation of factor A with factor B.

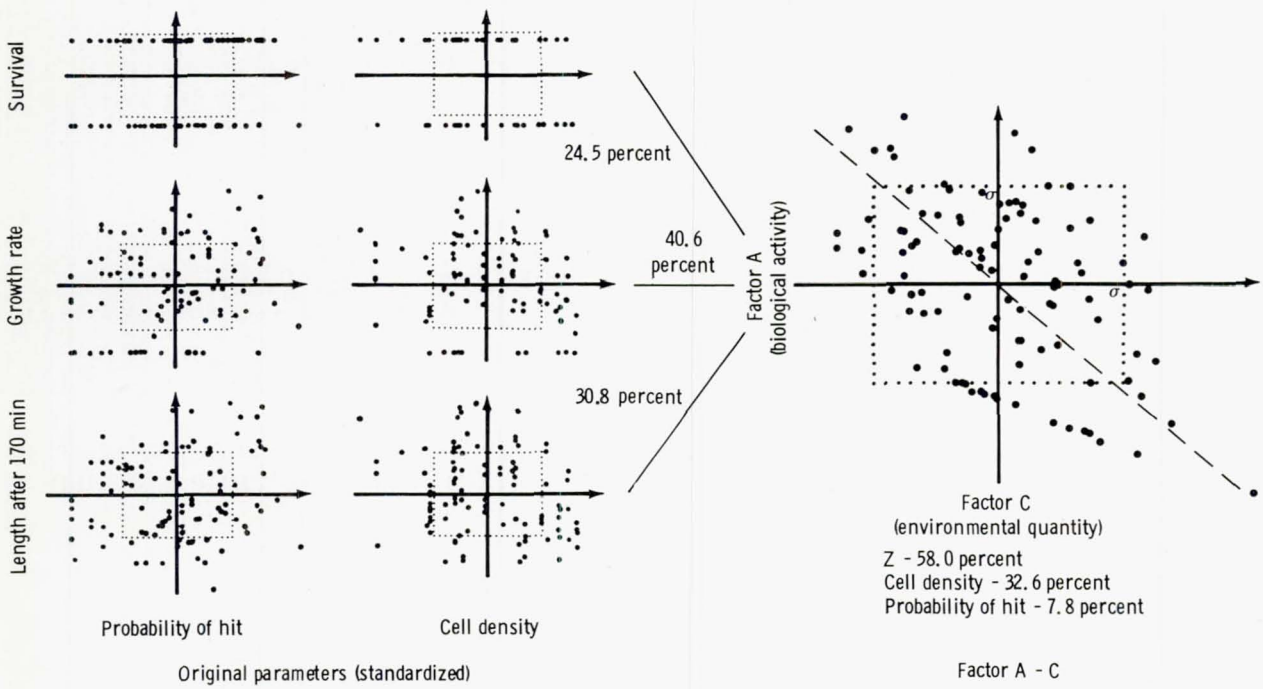

(b) Correlation of factor A with factor C.

Figure 14-12.- Multiple factorial analysis of Biostack III results (three-factor solution).

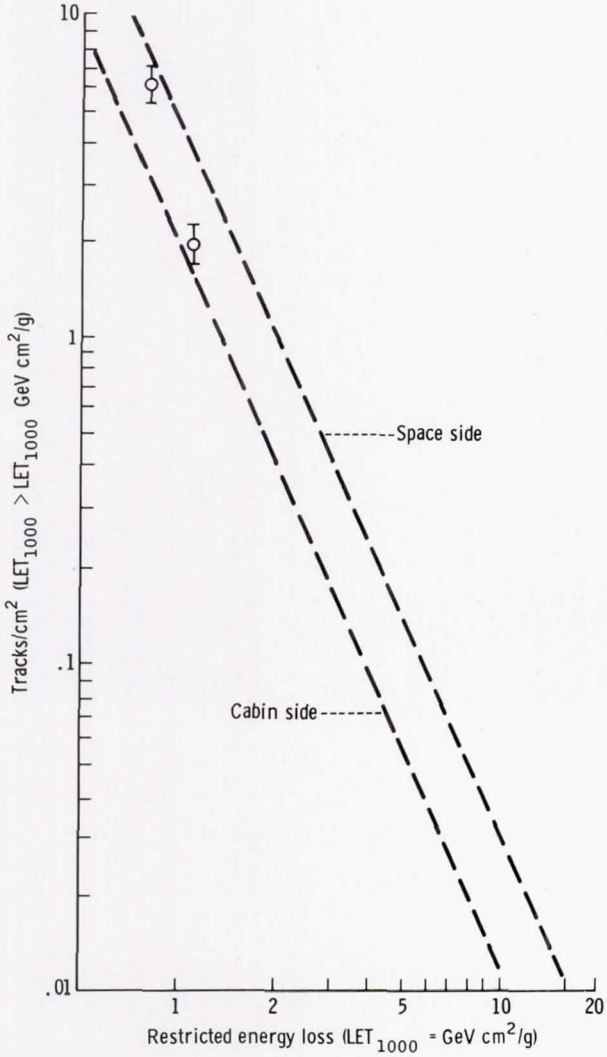

Figure 14-13.- Preliminary LET spectrum for Biostack III container A.

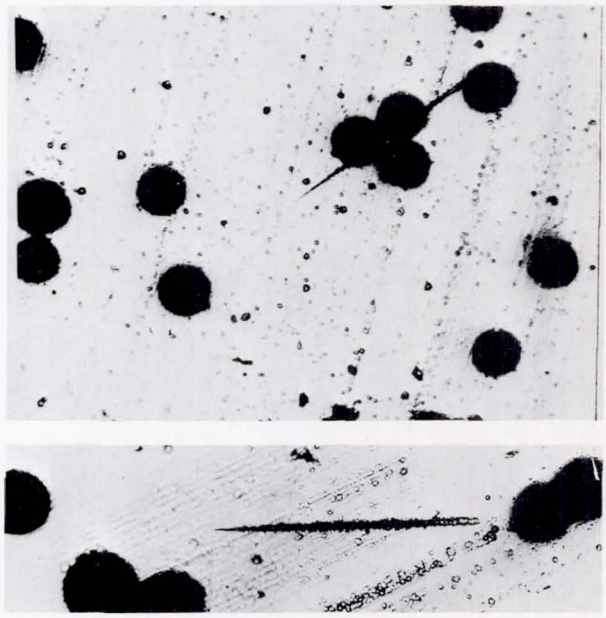

Figure 14-14.- Etch cones in a cellulose nitrate detector covered with Artemia salina eggs embedded in polyvinylalcohol.

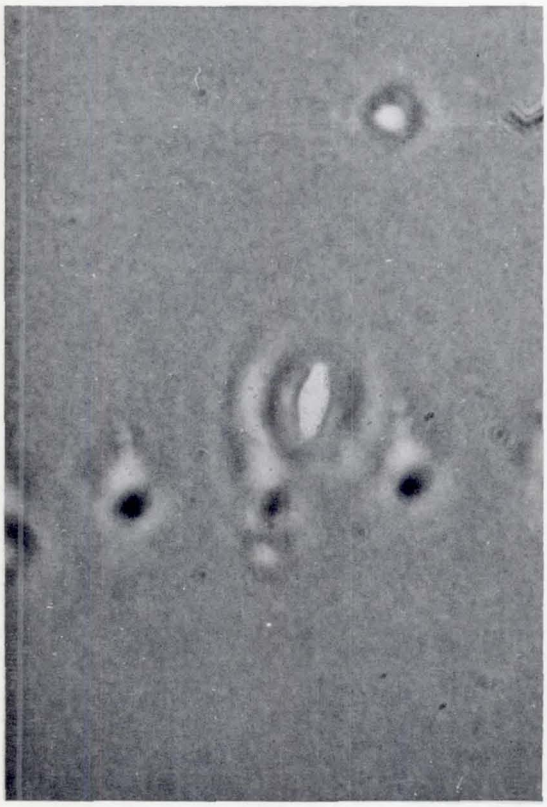

(a) Monstrous swelling in cell.

(b) Normal elongated cell.

Figure 14-15.- Deviation from normal development in Bacillus subtilis cells.

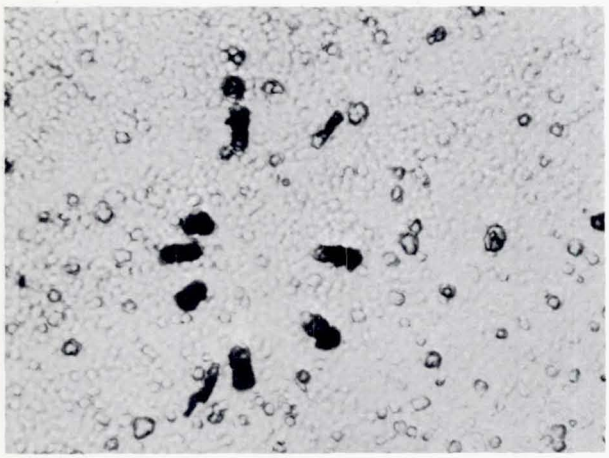

(a) Star in cellulose nitrate foil in Biostack II.

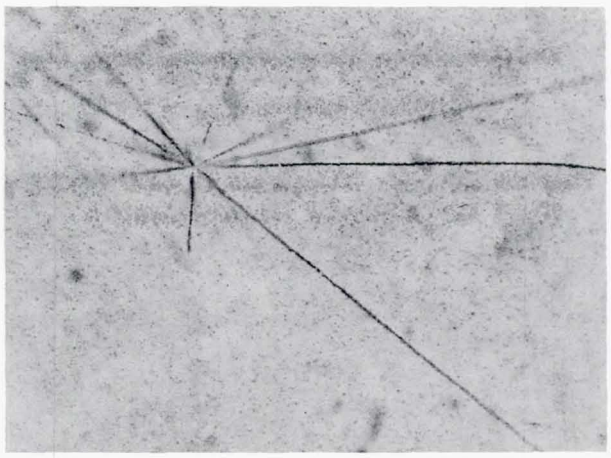

(b) Star in silver chloride foil in Biostack III.

Figure 14-16.- Stars discovered in plastic detectors.

15. ZONE-FORMING FUNGI

EXPERIMENT MA-147

T. D. Rogers,[a] G. R. Taylor,[b†] and M. E. Brower[a]

ABSTRACT

Streptomyces (Actinomyces in the U.S.S.R.) levoris was used as an experimental micro-organism during the Apollo-Soyuz Test Project to study specific biological considerations that may be influenced by space-flight factors. Preflight, in-flight, and postflight growth rates of the cultures were compared by photographing the specimens at regular intervals.

Preliminary results based on visual comparison of the photographic data indicate that an increased growth rate occurred during space flight in two of eight flight specimens. The increased growth rate continued in the two specimens during the postflight period until termination of the experiment. Radiation effects may be responsible for the absence of spores in two areas of the last spore ring that was formed during the in-flight period in one of the flight cultures; however, the radiation studies related to this experiment have not been completed. Distinct morphological differences in spore rings were observed when postflight spore rings were compared with in-flight spore rings. Factors that are related to space-flight recovery and reentry into Earth gravity may have effected these alterations. Studies are in progress to compare the secondary cultures from the respective spore rings.

INTRODUCTION

Streptomyces (Actinomyces in the U.S.S.R.) levoris was used as a test micro-organism to study specific biological aspects during space flight. The cultural characteristics of this organism permit in situ comparison of spore ring features and development rates in preflight, flight, and postflight periods of the Apollo-Soyuz Test Project (ASTP). The vegetative growth and degree of spore ring development during the respective periods could be observed within a single culture. Photographic documentation of growth characteristics in both the flight and control specimens was performed during the experiment.

---

[a]Northrop Services Inc., Houston, Texas.

[b]NASA Lyndon B. Johnson Space Center.

[†]Principal Investigator.

The objective of the experiment was to investigate the influence of spaceflight conditions on the rhythms of vegetative and spore phase characteristics of Streptomyces (Actinomyces) levoris. To assist in accomplishing this objective, five aspects of the experiment were studied.

1. Cultures that had been initiated with a 12-hour phase shift were exchanged during the flight.

2. The effects of local radiation factors (especially multicharged high-energy particles) on arrhythmia and injury areas of primary cultures were evaluated.

3. Similar effects of radiation on genetic changes of T4B r+ bacteriophage were studied.

4. Characteristics of secondary cultures that were derived from different sectors of the primary cultures (which were developed during preflight, flight, and postflight periods) were studied and compared.

5. Morphological and cultural properties of different nutrient media were recorded.

The results of radiation dosimetry and bacteriophage genetic studies were used for selection of specific areas of the primary Streptomyces cultures that may have been affected by local radiation factors. Secondary cultures from these areas will later be compared morphologically and genetically with secondary cultures from controls and secondary cultures of nonaffected areas of the flight specimens.

METHODS AND MATERIALS

Streptomyces (Actinomyces) levoris was used as the primary test specimen for this experiment. This species was isolated, named, and provided by the U.S.S.R. Optimum growth of the organism is achieved by incubating at 300 K (27° C) on an agar-base medium that consists of inorganic salts, glucose, and yeast extract.

From a single-point inoculation, radial vegetative growth of the organism was followed by sporulation, which formed a circular spore ring. When the organism was grown in 60- by 5-millimeter petri dishes at 300 K (27° C), one complete cycle (vegetative and spore phases) occurred at approximately 24 to 26 hours for 10 to 14 days. Thereafter, because of nutritional depletion and metabolic waste diffusion within the media, the rate of growth slowed.

Optimum phasing of the vegetative growth and spore production cycle was facilitated by using a 12-hour light-dark regimen of approximately 100 lux with the lighted phase occurring from 9 a.m. to 9 p.m. central daylight savings time. The light-dark cycle was maintained until the cultures were selected for the experiment and placed in the flight devices.

The bacteriophage T4B r+ was incorporated into an agar medium and dried to form a thin film. These films were placed in the flight devices beneath the lower layer of plastic dosimeters so that specific genetic alterations of the bacteriophage deoxyribonucleic acid (DNA), which were induced by the action of high-energy particles, could be studied (ref. 15-1).

Radiation Detectors

Radiation detectors of cellulose triacetate, cellulose nitrate, and Lexan were used for registration of particles that passed through the biological test systems. One radiation detector was situated in the movable cover of each flight device and another was placed directly under each of the petri dishes that contained the Streptomyces cultures.

Flight Devices

The flight devices for performing the experiment consisted of four containers (figs. 15-1 and 15-2). Each device was designed to hold two petri dishes (60 by 5 millimeters) that contained Streptomyces cultures. Radiation detectors were situated beneath the petri dishes as well as in the movable lid. A bacteriophage film was also placed beneath each of the radiation detectors under the petri dishes.

The main body of each device consisted of separable halves that were composed of anodized aluminum. A protective glass, fitted with a biologically nonreactive siliconized rubber ring, was inserted beneath the movable lid in the top half of each device. This glass served as a protective cover and permitted observation and photography of the cultures. The bottom half of the device, which included the petri dishes with cultures, spacing rings around the dishes, and siliconized rubber rings below the dishes, was fitted with the top half of the device to complete the assembly.

Portable Incubator

The "Thermocont" (fig. 15-3), which was used as a portable incubator for the cultures enclosed in the flight devices, had an ac/dc power capacity with a temperature range of 273 to 313 K (0° to 40° C) and was equipped with an electric digital thermometer. The Thermocont held four flight devices.

In the United States, the control cultures were maintained in the Thermocont during the entire course of the experiment, including transportation to and from the launch and recovery sites. The flight cultures were maintained in the Thermocont during the preflight and postflight periods.

In the U.S.S.R., the Thermocont was used to maintain and transport the control and flight cultures to and from the launch and recovery sites. During the mission, the controls were maintained in the Thermocont. Following recovery, both control and flight specimens were maintained in the Thermocont until the experiment was terminated.

Photography

Photography of the specimens was initiated after selection of the cultures and loading of the flight devices. All flight and control specimens were photographed at 12-hour (±3 hours) intervals from the time the cultures were selected for the experiment until termination of the experiment. Exceptions were made during space flight because of schedule time lines.

In the U.S.S.R., photography was with a 35-millimeter camera with an f/2.8 (50 millimeter) lens. Photographs were recorded on black-and-white film (type KH-z, ASA 55). In the United States, a Nikon 35-millimeter camera with an f/2.8 (55 millimeter) lens was used. All photographs were taken with Kodak SO-168 film (ASA-500). Special devices were used to position the cameras 30.4 centimeters from the specimens (figs. 15-4 and 15-5).

Preparation and Deployment of Specimens

Streptomyces (Actinomyces) levoris was inoculated on nutrient medium in petri dishes (60 by 5 millimeters) on July 9, 1975, at 14:00 GMT at the Lyndon B. Johnson Space Center (JSC) and at 06:00 GMT at the Baykonur Cosmodrome. The cultures were incubated at 300 K (27° C) with a 12-hour light-dark cycle of approximately 100 lux.

Before selection of the cultures, the flight devices were disassembled, cleaned, and autoclaved (with the exception of the protective glass inserts, which were washed in acetic acid, alcohol, and sterile distilled water).

At JSC on July 13, 1975, four flight and four control cultures were selected and assembled together with radiation detectors and the bacteriophage film. The devices and specimens were then placed in a Thermocont and transported to the launch site. Two devices (A-19 and A-22) were placed onboard the Apollo spacecraft approximately 13 hours before launch.

Four flight and four control cultures were selected at the Baykonur Cosmodrome on July 15, 1975, and assembled with radiation detectors and bacteriophage film. The devices and specimens (C-12 and C-31) were placed onboard the Soyuz spacecraft approximately 2 hours before launch. The controls were maintained in a Thermocont at the Baykonur Cosmodrome at 300 K (27° C) until July 21. After recovery, the flight and control specimens were transported from the recovery site and maintained in a Thermocont until the experiment was terminated on August 16.

After the launch of Apollo, the control specimens were returned to JSC and then transported to the Apollo recovery site on July 21. Both the flight and control specimens were then returned to JSC on July 26 and were maintained in the Thermocont until the experiment was terminated on August 11.

During the joint activities of the Apollo-Soyuz crewmembers, the U.S. culture A-19 was exchanged with the U.S.S.R. culture C-12 on July 17. On August 29, following termination of the experiment, the Thermocont and specimens from the United States were shipped to the laboratory in the U.S.S.R. On October 7, the

radiation detectors were marked for position and were removed from the flight and control devices in the presence of science representatives of both the United States and the U.S.S.R.

RESULTS AND DISCUSSION

The general scheme of the experiment was carried out according to the project outline. All the flight and control cultures of Streptomyces exhibited growth during the preflight, flight, and postflight periods of the experiment without apparent contamination.

Preliminary visual analyses of photographic documentation of culture growth rates during the experiment were performed. To facilitate preliminary comparison of data in the respective periods, August 1 was selected as the cutoff date for the postflight period, although the experiment was continued until August 11 in the United States and August 16 in the U.S.S.R.

Data on the total number of spore rings formed by the control and flight cultures at the end of the preflight, flight, and postflight periods are shown in table 15-I. Similar data are shown in table 15-II for the specimens that were exchanged during the mission. Photographs of the respective flight and control specimens (U.S.S.R. and U.S.) that were taken on August 1 are shown in figures 15-6 and 15-7.

Cultures were initiated for the experiment in both the U.S.S.R. and the United States on July 9. However, at the respective launch times on July 15, the rate of vegetative growth and subsequent spore ring development (biorhythm) was different (tables 15-I and 15-II). The difference in growth rate between cultures initiated in the United States and those initiated in the U.S.S.R. continued throughout the experiment. This growth-rate difference between the respective cultures reflects differences in the nutritional media used by the two laboratories, although all attempts were made to standardize procedures and components. In practice, the culture medium formula was identical, but specific chemicals were not obtained from the same sources. The variation in the number of spore rings in the U.S.S.R. cultures at the end of the preflight period may suggest inherent differences of growth rate rather than nutritional effects, because the cultures were grown on identical media (tables 15-I and 15-II). Studies are in progress to determine whether this difference was due to nutritional or genetic variation, or a combination of both.

The controls cultured in the United States grew at the same rate when compared with each other within a given time period (preflight, flight, or postflight), with the exception of number 2 of A-25, which exhibited a slight decrease in growth rate during the postflight period (table 15-I). In the U.S.S.R. controls, the two cultures of C-35 had three spore rings and C-36 had two spore rings at the end of the preflight period. At the time of Soyuz recovery on July 21, the number of spore rings of C-35 and C-36 was the same. During the postflight period, number 2 of C-36 exhibited a distinct increase in growth rate when compared with the other U.S.S.R. controls (table 15-I).

Differences in growth rate between flight and control cultures occurred (table 15-I). Either space-flight factors or the reduced temperature in both the Apollo and Soyuz spacecraft could have contributed to this slower growth rate.

During the in-flight period of Apollo, number 1 of A-22 developed four spore rings. When compared with the growth rate of the controls, and when considering the reduced temperature in Apollo, this growth rate appears as expected. In the postflight period, the growth rate of number 1 of A-22 was similar to that of the controls.

The most obvious alteration of growth rate was exhibited by number 2 of A-22 during the in-flight period. In the decreased temperature environment of Apollo, six spore rings were formed. This was two rings more than in number 1 of A-22 and one-half ring more than in the controls, which were continually maintained at 300 K (27° C). The increased growth rate continued during the postflight period (table 15-I). In number 2 of C-31, the preflight growth rate was slightly slower than in number 1 of C-31; during the in-flight period, the two cultures grew at the same rate. However, in the postflight period, the biorhythm was slightly decreased in number 2 of C-31 when compared with other flight specimens (tables 15-I and 15-II).

The morphologic appearance of the spore rings of the flight specimens that formed during the preflight and in-flight periods was distinct and generally uniform. The spore rings that developed during the postflight period were irregular and indistinct. This alteration of morphologic appearance between adjacent rings (the last in-flight ring and the first postflight ring) may suggest an influence of space-flight recovery factors on spore ring formation. The comparative aspects of these features are shown in figures 15-6 and 15-7.

In addition to the increased growth rate of number 2 of A-22 during flight, this culture developed an offset, which caused the formation of a spiral ring (fig. 15-8). Similar offsets and spirals were observed in the controls; however, they developed during the postflight period (figs. 15-6 and 15-7).

In number 1 of A-19, the last ring formed during the in-flight period exhibited two distinct areas in which spores failed to form (fig. 15-9). As subsequent spore rings developed, these two regions remained void of spores. As the next ring was formed (the double ring that developed in the early postflight period), a portion of the spore development occurred in part of the void region (fig. 15-10).

The first postflight spore rings that formed in both cultures of A-19 and in number 2 of C-31 were double rings (figs. 15-10 and 15-11). Based on the time of their formation, it appears that factors related to reentry and recovery resulted in this abnormal spore ring development. This feature was not observed in any of the subsequent spore rings of these cultures or in any of the other cultures during the remainder of the experiment.

After the exchange of the temperature profiles of Apollo and Soyuz, the influence of temperature on the characteristics of Streptomyces will be studied. Studies on the radiation detectors and bacteriophage aspects of the experiments are in progress. These data will be used for assessing the effects of radiation on

specific areas of the primary flight and control cultures. Studies are in progress for comparison of morphological and cultural characteristics of secondary cultures derived from the preflight, flight, and postflight growth regions. These studies will provide data with which to determine whether the noticeable changes of growth biorhythm observed in two of the eight specimens during the in-flight period are permanent or temporary alterations related to space-flight factors. As these data become available, they may help to achieve a better understanding of the biological effects of space-flight factors that may influence the biorhythm of vegetative growth and spore production of Streptomyces (Actinomyces) levoris.

REFERENCE

15-1. Akoev, I. G.; Yurov, S. S.; Leontyeva, G. A.; Kusin, I. A.; et al.: Mutagenic Action of Secondary Radiation of 70 GeV Protons. Studia Biophysica, vol. 41, 1973, pp. 167-180.

TABLE 15-I.- NUMBER OF RINGS FORMED BY STREPTOMYCES (ACTINOMYCES) LEVORIS

DURING THE RESPECTIVE PERIODS OF THE EXPERIMENT

Experiment period	U.S.S.R. culture							U.S. culture						
	Date	Control				Flight		Date	Control				Flight	
		C-35 (a)		C-36 (a)		C-31 (a)			A-24 (a)		A-25 (a)		A-22 (a)	
		1	2	1	2	1	2		1	2	1	2	1	2
Preflight	July 9 to 15	3.0	3.0	2.0	2.0	3.0	2.8	July 9 to 15	4.0	4.0	4.0	4.0	4.0	4.0
Flight	July 15 to 21	6.1	6.1	6.0	6.2	5.0	4.8	July 15 to 24	9.5	9.5	9.5	9.5	8.0	10.0
Postflight	July 21 to Aug. 1	9.5	9.3	9.2	11.5	9.3	8.5	July 24 to Aug. 1	13.0	13.0	13.0	12.5	12.0	15.0

[a]Numbers "1" and "2" designate petri dishes in the flight device as shown in figure 15-1.

TABLE 15-II.- NUMBER OF RINGS FORMED BY STREPTOMYCES (ACTINOMYCES) LEVORIS CULTURES THAT WERE EXCHANGED DURING JOINT ACTIVITIES

Experiment period	Date	[1]A-19		Date	[2]C-12	
		Culture no. (3)			Culture no. (3)	
		1	2		1	2
Preflight	July 9 to 15	4.0	4.0	July 9 to 15	2.5	2.3
Flight	July 15 to 21	7.0	7.0	July 15 to 24	7.3	6.3
Postflight	July 21 to Aug. 1	13.0	13.0	July 24 to Aug. 1	10.3	9.2

[1]Culture launched on Apollo and recovered from Soyuz.

[2]Culture launched on Soyuz and recovered from Apollo.

[3]Numbers "1" and "2" designate petri dishes in the flight device as shown in figure 15-1.

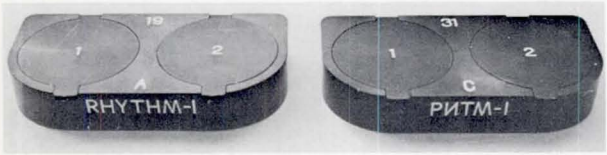

Figure 15-1.- Examples of flight devices. The "A" series was used by the United States and the "C" series by the U.S.S.R. Each device holds two petri dishes (60 by 5 millimeters), which are designated as "1" and "2".

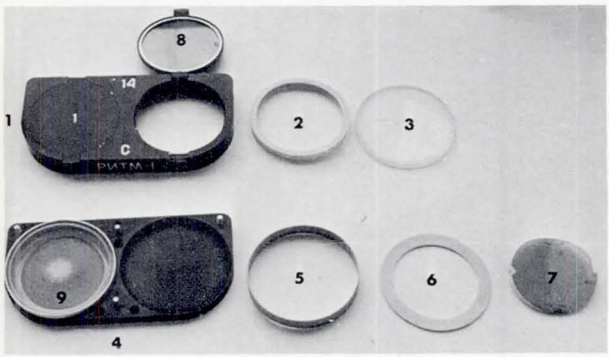

Figure 15-2.- Photograph of the components of a flight device. (1) Upper half of device with movable covers. (2) Siliconized rubber ring that fits around the protective glass. (3) Protective glass and rubber ring, which are inserted into the upper half of the device and serve to protect the specimen in the petri dish. (4) Bottom half of the device. (5) Metal spacing ring. (6) Siliconized rubber washer that fits in the well of the lower half. (7) Radiation detector that is placed in the bottom of the device under the petri dish. (8) Radiation detector in movable cover. (9) Petri dish and specimen.

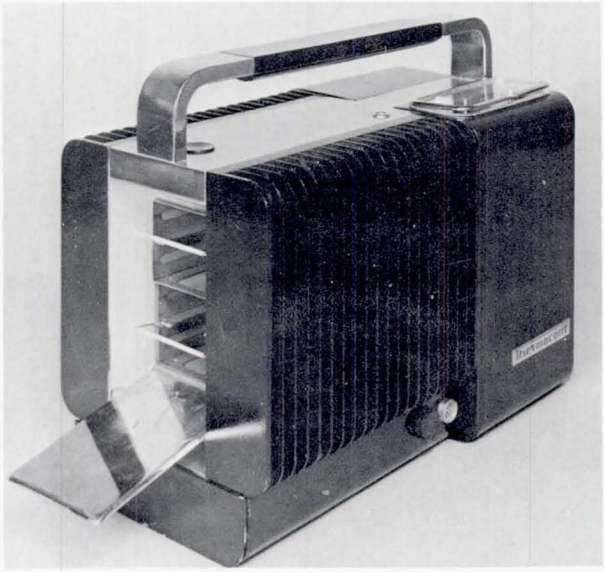

Figure 15-3.- The portable incubator (transport container) "Thermocont" that was used to maintain cultures at 300 K (27° C) during various phases of the experiment in the United States and the U.S.S.R. It has both ac/dc power capability.

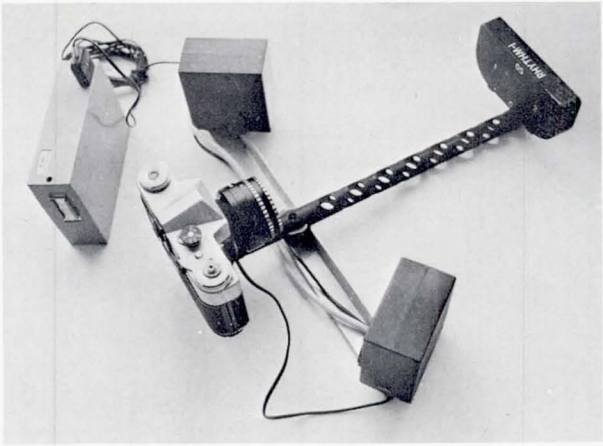

Figure 15-4.- Photographic apparatus used in the U.S.S.R. for ground-support photography of the experiment. A similar bracket was used in flight with another type of camera.

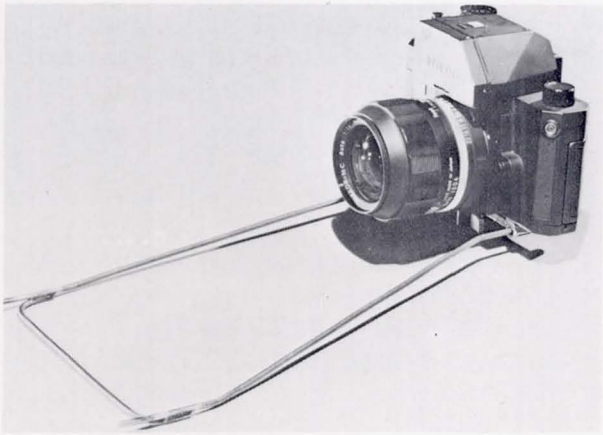

Figure 15-5.- Photographic apparatus used in the United States during both ground-support and Apollo in-flight photography of the experiment.

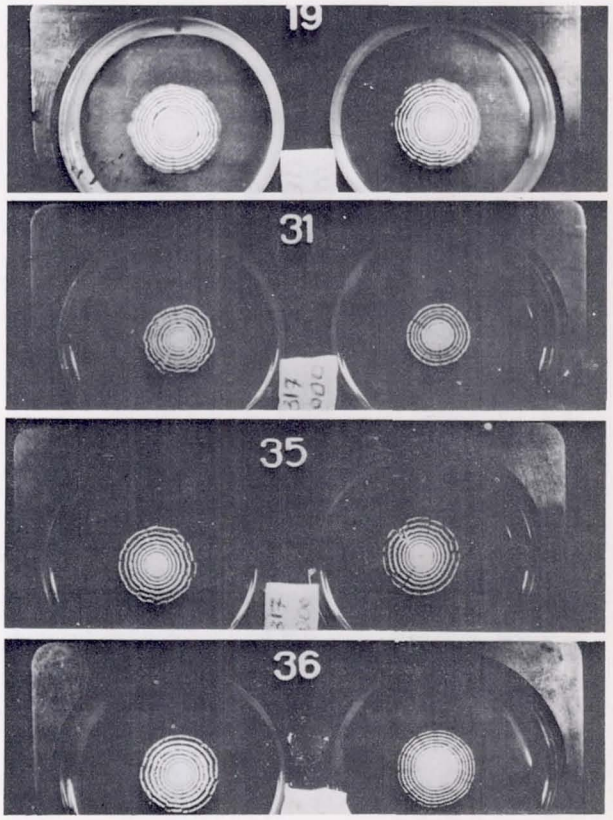

Figure 15-6.- Photographs of cultures of Streptomyces (Actinomyces) levoris in the U.S.S.R. taken on August 1, 1975. Device A-19 was launched in Apollo and recovered from Soyuz, whereas C-31 was both launched and recovered in Soyuz. Devices C-35 and C-36 were U.S.S.R. controls.

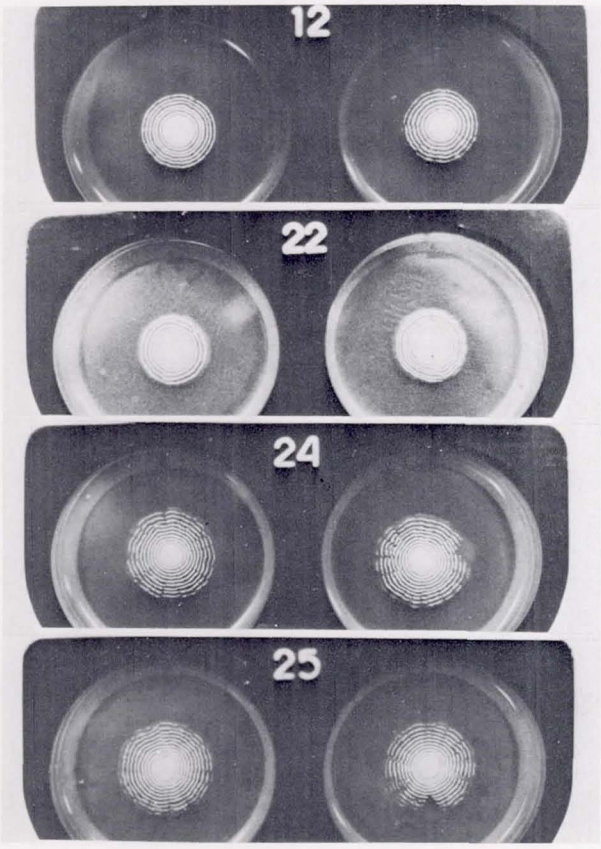

Figure 15-7.- Photographs of cultures of Streptomyces (Actinomyces) levoris taken in the United States on August 1, 1975. Device C-12 was launched in Soyuz and recovered from Apollo, whereas A-22 was both launched and recovered from Apollo. Devices A-24 and A-25 were U.S. controls.

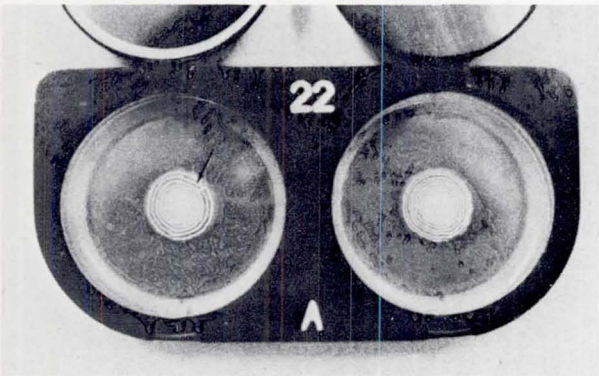

Figure 15-8.- Growth offset of a spore ring that formed during the in-flight period.

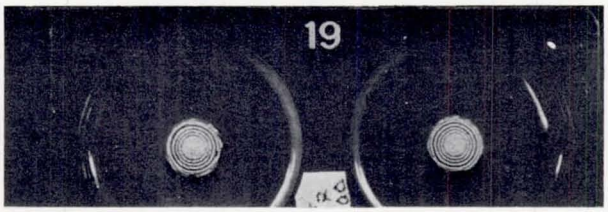

Figure 15-10.- Photograph of the first postflight spore ring showing an erratic attachment to the last in-flight ring and partial "filling in" of the void area. Note the occurrence of the double-ring formation.

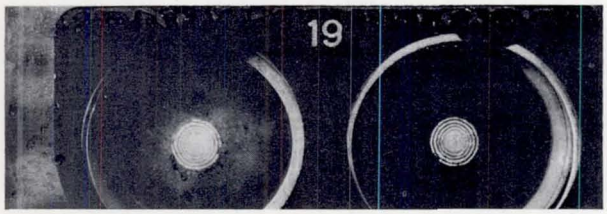

Figure 15-9.- Photograph of spore ring deletion that occurred in the last ring formed in flight.

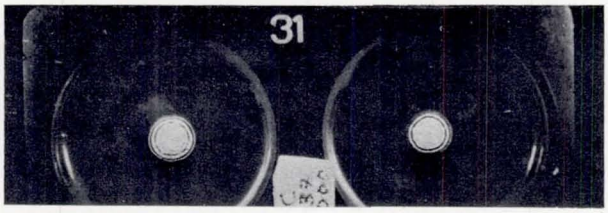

Figure 15-11.- Example of another culture exhibiting the double-ring formation.

16. MICROBIAL EXCHANGE

EXPERIMENT AR-002

G. R. Taylor,[a†] K. D. Kropp,[b] M. R. Henney,[b] S. S. Ekblad,[b]
T. O. Groves,[b] T. C. Molina,[b] J. G. Decelle,[b] C. F. Carmichael,[b]
N. J. Gehring,[b] and E. L. Young[b]

ABSTRACT

The purpose of the Microbial Exchange Experiment was to evaluate components of the infectious disease process in space flight by measuring alterations in three factors: (1) the composition of the microbial populations inhabiting the crewmembers and spacecraft, (2) the ability of each crewmember's defense mechanism to resist infection, and (3) the ability of certain micro-organisms to originate infections. The impetus for performing the experiment arose from the variety of in-flight and ground-based microbial studies in the United States and the U.S.S.R., which have indicated that the conditions of space flight alter man and micro-organisms in such a way that the normal fine balance between them may be adversely affected. The monitoring of two separate crews, which differed microbiologically and immunologically, provided an opportunity to study in-flight cross-contamination patterns. Because the Apollo-Soyuz Test Project crewmembers came from widely different geographical and ecological areas, it was possible to identify specific, naturally occurring, marker micro-organisms for detailed analysis.

This report evaluates the operational aspects associated with the experiment and the activities of medically important micro-organisms recovered from the Apollo crewmen. The majority of activities were performed as planned, and a large percentage of the anticipated data will be forthcoming. A variety of potential pathogens was recovered from each of the prime and backup crewmembers before and after flight. However, no disease events were reported. Candida albicans and Staphylococcus aureus (type 52, 52A, 80, 81) were shown to be transferred from one crewmember to another during the flight. No other medically significant changes in the microbial population were observed.

---

[a]NASA Lyndon B. Johnson Space Center.

[b]Northrop Services Incorporated, Houston, Texas.

[†]Principal Investigator.

INTRODUCTION

The problems concerning the occurrence of microbial contamination and infectious diseases during space flight have been evaluated repeatedly following U.S. and U.S.S.R. manned missions. Scientists in the U.S.S.R. have been concerned with crew microbiological profiles and natural bactericidal activity since their first manned mission. Twelve years ago, Alekseyeva (ref. 16-1) reported that the composition and properties of the autoflora of cosmonauts remained within normal limits during preflight evaluations but that there were occasional postflight changes. An increase in oral autoflora was accompanied by dysbacteriosis in which the normal throat flora were almost entirely crowded out by Gram-negative, nonhemolytic diplococci. It was also reported that an increase in the number of microbes in the deep layers of the skin was caused by the appearance of masses of hemolytic micrococci (ref. 16-1).

More recently, Nefedov et al. (ref. 16-2) have observed that alterations in microbial flora have been observed on several flights and appear to be dependent on "environmental parameters," the duration of the exposure to different environmental factors, and the work-rest schedules. The same authors point out that one of the most consistent phenomena appears to be the interchange of micro-organisms between subjects (ref. 16-2).

The interest of U.S.S.R. investigators in autoflora has not been restricted to cosmonauts. Alekseyeva and Volkova (ref. 16-3) have reported studies with "space dogs" (dogs that have experienced space flight) since 1960. They reported that whereas acceleration and vibration on the ground had no effect on the microflora, the space dogs had intestinal bacilli in their mouths after 2 days of flight. The authors interpreted the presence of intestinal bacilli to be a result of a space-flight-mediated decrease in the immunological activity of the subjects.

The advent of the U.S.S.R. space station, Salyut, enabled in-flight samples to be taken from the three crewmembers. Postflight analysis of these samples revealed changes in autoflora and microbial interchange.[1] However, the death of the crewmembers prevented postflight sampling and analysis.

The interest of the U.S.S.R. Space Agency concerning this research and their philosophy, which led to their participation in the Microbial Exchange Experiment, was offered during the first meeting of the U.S.-U.S.S.R. Joint Working Group in Space Biology and Medicine in Moscow.[2] During the meeting, U.S.S.R. investigators made the following observation.

---

[1] L. I. Kakurin, data presented at the second meeting of the U.S.-U.S.S.R. Joint Working Group in Space Biology and Medicine, NASA Lyndon B. Johnson Space Center, May 1972.

[2] Data presented at the first meeting of the U.S.-U.S.S.R. Joint Working Group in Space Biology and Medicine, Moscow, 1971.

The results of the study of the automicroflora of the integumentary tissues of the cosmonauts, indicating the development of dysbacteriotic changes in its composition during the space flight, have necessitated more detailed scientific studies in this area. Studies to clarify the role of the environment of objects in space in terms of the appearance of unfavorable changes in the composition of the automicroflora of the cosmonauts are most important in this respect.

The corresponding NASA studies began with comparisons between preflight and postflight specimens collected during one of the Gemini flights (ref. 16-4). In this first U.S. microbial analysis, the investigators reported a decrease in the number of types and an increase in the total number of micro-organisms recovered after the flight. Also, there was evidence of microbial transfer between the crewmembers. When evaluating these findings in reference to the total clinical picture, Berry (ref. 16-5) indicated that the observed microbial changes may not be compatible with the health and welfare of the astronauts.

In a survey of 26 chamber tests conducted by the National Academy of Sciences between 1962 and 1970, evidence was presented which indicates that microbial exchange is not infrequent and that it may contribute to medically significant events (ref. 16-6).

Detailed analyses of preflight and postflight samples from Apollo 14 crewmembers revealed (1) an intercrew transfer of S. aureus, (2) an 830-percent increase in the quantitation of aerobic bacteria, and (3) a transfer of micro-organisms from crewmembers to the command module hardware (ref. 16-7). A dramatic postflight reduction in the number of mycological species recovered from the Apollo 14 crewmembers was also observed with the Apollo 15 crew (ref. 16-8).

The review by Fox (ref. 16-9) indicates clearly that the results of the early NASA autoflora studies were analogous to those done in the U.S.S.R. Both studies have indicated significant alterations in the microbial population as well as definite transfer of species between crewmembers.

With the advent of the Skylab missions, it became possible to evaluate the microbial alterations resulting from space flights with durations as long as 85 days. Complete autoflora studies were conducted on each of the prime crews (refs. 16-10 and 16-11). Preliminary evaluations show that while gross contamination of the Skylab environment did occur and while there were several in-flight disease events (presumably of microbial origin), such events did not prove to be limiting hazards for long-term space flight. Evaluation of the major groups of micro-organisms, comprising the microbial population tested, tended to support the theory of microbial simplification for anaerobic bacteria (refs. 16-2, 16-12, and 16-13) but not for other microbes. Intercrew transfer of pathogens was indicated. The data did not support the theory of postflight microbial shock (refs. 16-13, 16-14, and 16-15).

The Microbial Exchange Experiment was designed to monitor quantitatively the microbial load of all crewmembers and of selected inner surfaces of both the Apollo and Soyuz spacecraft and to evaluate the status of certain components of the immune mechanism of each crewmember. To accomplish this objective, the normal

autoflora and immunocompetence level of each crewmember was established before flight through repeated sampling and analyses. Therefore, quantitative and qualitative changes occurring during or after flight could be measured and evaluated, and instances of intercrew transfer of marker organisms could be identified. In addition, selected micro-organisms recovered from the crew and spacecraft were examined to detect changes in the ability of the micro-organisms to become pathogenic, infective, or toxic to man. At the same time, certain immunological parameters of the blood and saliva of each crewmember were studied to detect changes in the ability of the individual to resist infection.

METHODS AND MATERIALS

Baseline Microbial Specimen Collection

Specimens were to be collected from the 5 prime and 5 backup crewmembers and from 15 areas on the inner surfaces of each spacecraft at specific times before, during, and after the flight as given in table 16-I.

During each preflight and postflight sampling period, 11 microbial specimens were collected from each crewmember (table 16-II). Calcium alginate swabs, wetted in 0.3-millimolar phosphate buffer, were used to sample each of the seven body surface areas. This swab technique was the only collection method compatible with the flight program. Although it is recognized that subsurface microbes may be overlooked by this method, procedures for sampling subsurface area were not acceptable. Dry calcium alginate swabs were used to sample the surfaces of the tonsils and the posterior pharyngeal vault before collection of the gargle specimen. For the latter sample, the subject gargled with 0.3-millimolar phosphate buffer followed by a repeated rinse of the teeth with the same solution. Fecal samples were collected into a sterile cardboard container at the convenience of the subject. Swabs were placed in 5 cubic centimeters of 0.3-millimolar phosphate buffer for transport to the laboratory. Analysis of all samples was initiated within 1 hour of specimen collection.

In-Flight Microbial Specimen Collection

In addition to the baseline samples previously described, in-flight samples were obtained from all five prime crewmembers and both spacecraft between 77:40 and 78:30 ground elapsed time (GET). A specially developed sample collection device was used for this set of samples (fig. 16-1). This device consisted of a cotton-tipped Teflon swab on a capillary tube that contained conservation fluid to keep the micro-organisms alive. Each swab was housed within an airtight case to prevent desiccation. Groups of swabs were organized in Beta-cloth retaining bags (fig. 16-2). One bag of this type was provided for each of the following: (1) swabs used for Soyuz spacecraft samples, (2) swabs used for Apollo spacecraft samples, (3) swabs used for Apollo commander (ACDR) and Soyuz commander (SCDR) samples that were taken in the Soyuz, (4) swabs used for Soyuz flight engineer (SFE), docking module pilot (DMP), and command module pilot (CMP) samples that were taken in the Apollo spacecraft.

All four sets of swabs were launched in the Soyuz spacecraft. The two kits to be used in the Apollo were transferred from the Soyuz at the end of the first joint activity (58: 20 GET) and returned to the Soyuz near the end of the last joint activity (79: 50 GET). All samples collected during flight were returned to Moscow for preliminary analysis and division between the U.S. and U.S.S.R. laboratories as outlined in the following discussion. In-flight samples consisted of the first six areas outlined in table 16-II as well as the spacecraft sites presented in table 16-III. It should be noted that Soyuz spacecraft samples C-7 through C-15 were taken from the part of the spacecraft not returned to Earth. Accordingly, these samples were not collected after the flight. To assist in spacecraft sample collection, black lines demarking a 100-square-centimeter area had previously been painted at each of the specified sites as shown in the two examples illustrated in figure 16-3.

Because the specimens collected during flight had to be returned to the laboratory for analysis, considerable delay was unavoidable. To equate results from these specimens with results of specimens collected before and after flight, a group of samples was collected the morning of launch and immediately upon return from the flight. These samples were held at room temperature for 4 days to simulate the delay imposed on the in-flight specimens. These comparative specimens were collected from all 10 crewmembers and both spacecraft using the same type swabs used during flight.

Collection of Salivary Parotid Fluid

Saliva from the parotid gland was collected from each of the 10 crewmembers before flight and from the 5 prime crewmembers after flight according to the schedule shown in table 16-I. The special saliva collection device, shown in figure 16-4, was attached by pressure to the inner surface of the oral cavity over the opening of the parotid duct. The parotid fluid was collected for 10 minutes with the flow being stimulated by a sour candy drop placed in the subject's mouth. The resulting saliva was frozen at 233 K (-40° C) and stored for future analysis. No saliva was collected during the flight.

Blood Collection and Serum Preparation

Venous blood was collected from the antecubital fossae of each of the 10 participating crewmembers before flight and from the 5 prime crewmembers after flight as outlined in table 16-I. From each sample, whole blood was smeared onto slides and subsequently treated with Wright's stain (ref. 16-16) for leukocyte differential counts. The remaining blood was allowed to clot for serum separation. The resulting serum was used to determine humoral antibody levels and bactericidal activity.

Preliminary Analysis of Microbial Specimens and Distribution of Test Materials

The contents of each swab, gargle sample, and fecal specimen were serially diluted under aseptic conditions and subsequently inoculated onto the surface of

the nutrient media (table 16-IV). The variety of media, number of plates inoculated, and dilution range were selected on the basis of what was required to isolate and quantitate the autoflora components present in each sampled area. The SAB plates were incubated at 303 K (30° C) for 5 days. The CMMY plates were incubated at 298 K (25° C) for 7 days, and all others were incubated at 310 K (37° C) for 48 hours.

Following incubation under the appropriate conditions, all resulting colonies on every culture plate were categorized and counted. Subsequently, one sample of each morphologically different colony type was transferred from each dilution series to the appropriate nutrient media and was stained according to the method of Gram (fig. 16-5). Following verification that a pure culture was obtained, one aliquot of each culture was stored by the laboratory in which it was identified (the host laboratory), and another complimentary aliquot was made available to the guest laboratory. The guest laboratory was to have had access to an isolate from each different type of colony grown on the plates outlined in table 16-IV.

A discrete specimen number was assigned to each isolate by the host laboratory, and a bilingual data sheet (fig. 16-6) was completed to accompany the specimen when it was transferred to the guest laboratory. A unique identification number and a bilingual data sheet were processed with each isolate so that unequivocal traceability of each isolate was established in a method intelligible to both U.S. and U.S.S.R. investigators.

Division of Responsibility for Specimen Analysis

The analytical procedures required for performance of the Microbial Exchange Experiment were divided between the laboratories in the United States and the U.S.S.R. (table 16-V). The U.S. Principal Investigator was responsible for identification of all filamentous fungi, nonlactose-fermenting Gram-negative rods, and members of the genus Haemophilus. The U.S.S.R. Principal Investigator was responsible for the identification of yeasts and yeastlike fungi, Gram-positive catalase-negative cocci, Gram-negative cocci, and lactose-fermenting Gram-negative rods. The responsibility for identification of Gram-positive catalase-positive cocci was shared by both laboratories. In addition to these microbial identifications, the responsibility for specific tests was divided as shown in table 16-V.

The proper collection of preflight and postflight samples from the cosmonauts and the Soyuz spacecraft was the responsibility of the U.S.S.R. Principal Investigator. The proper collection of preflight and postflight samples from the astronauts and the Apollo spacecraft was the responsibility of the U.S. Principal Investigator. The safe and expeditious return of samples collected during flight was the responsibility of the U.S.S.R. Principal Investigator. The preliminary analysis of all samples, culminating in and including distribution of specimens to both U.S. and U.S.S.R. investigators, was the responsibility of the Principal Investigator of the country in which the sample was collected. All preliminary specimen analyses conducted in the U.S.S.R. laboratories were to be conducted in the presence of a science representative of both the United States and the U.S.S.R. Although this arrangement was also available in U.S. laboratories, the U.S.S.R. investigators had the option of exercising this procedure. These joint activities were to include

dilution and plating of specimen materials, isolation of microbial colonies, and evaluation of growth properties on the initial isolation media. Crewmembers and spacecraft were sampled independently.

RESULTS AND DISCUSSION

For this report, analyses are limited to two areas: an analysis and evaluation of the operational aspects of the experiment and a thorough analysis of the activities of medically important micro-organisms recovered from U.S. crewmembers.

Analysis and Evaluation of Operational Activities

The extent to which each objective of the experiment was accomplished is evaluated together with a discussion of any reported anomalies.

1. The normal microbial autoflora level and the immunocompetence level of each crewmember were identified. The collection of five sets of preflight saliva and microbial samples and of two sets of serum samples for each of the prime and backup crewmembers provided adequate establishment of baselines for U.S. crewmembers. However, data pertaining to the total microbial load cannot be retrieved from microbiology specimens collected in the U.S.S.R. All serum samples, with the exception of those taken from the backup SCDR 15 days before launch, were received in a condition that permitted the required analysis. All the astronaut saliva samples, with the exception of the CMP samples, were collected as planned. (An alternate collection method was used for the CMP that provided an adequate but not optimum saliva sample.) All cosmonaut saliva samples were collected in a manner different from that agreed upon and therefore may not be usable in this study.

2. The identification of qualitative and quantitative changes in crew and spacecraft microbial populations and the evaluation of demonstrable intercrew microbial exchange occurring during flight are necessary for proper analysis. The most important marker micro-organisms were properly monitored in the U.S. and U.S.S.R. laboratories, allowing for a reasonably thorough evaluation of intercrew microbial exchange. Likewise, shifts in many of the major components of the autoflora can be evaluated. Variations in the total autoflora are calculated only for the Apollo crew.

3. Selected micro-organisms must be critically evaluated to detect postflight changes in their ability to be pathogenic, infective, or toxic in man. Several of the micro-organisms that are most useful for these evaluations have repeatedly been isolated from Apollo-Soyuz crewmembers. The prognosis for satisfying this objective is very good. Thirty-day postflight samples of cosmonauts were not collected.

4. Immunological parameters of blood and saliva must be evaluated to detect postflight changes in the ability of crewmembers to resist infection. The required astronaut specimens have been obtained, and analyses are proceeding as planned. Data from cosmonaut specimens will be less complete because of incomplete blood collection and different saliva collection techniques.

Most of the activities were performed as planned, and a large percentage of the cooperatively derived data will be preserved. At present, all samples have been collected and divided between the two laboratories, with the exceptions previously noted. Analyses of specimens are currently progressing according to the joint laboratory procedures previously approved by the U.S. and the U.S.S.R. investigators.

Medical Microbiological Analysis of Apollo Crewmembers

On early Apollo missions, before strict protective measures were instituted, in-flight infections were not unusual (ref. 16-17). In-flight illness of microbial origin was, however, completely absent from the Apollo 14 through 17 missions (ref. 16-18). There is no doubt that the implementation of extensive preventive measures (ref. 16-19), following the clinically significant Apollo 13 mission, was a contributing factor. Preflight monitoring of pathogenic and potentially pathogenic species identified certain potential problems so that appropriate prophylaxis or treatment could be administered before the flight or could be provided during the flight. This procedure was highly effective and was recommended for all future U.S. manned space flights (ref. 16-18). Similar analyses conducted during the three Skylab missions indicated that whereas there were several in-flight disease events and gross contamination of the orbital workshop did occur, such events did not prove to be limiting hazards for long-term space flight (ref. 16-11).

The Apollo-Soyuz Test Project (ASTP), a unique space flight in which two teams of crewmembers from different geographical areas joined in space with two different spacecraft, presented an unusual opportunity for cross-contamination. Accordingly, it was necessary to identify and trace all micro-organisms of potential medical importance present in the population. This report covers such an analysis of the three prime and three backup Apollo crewmen.

Gram-negative rods.- Gram-negative rods are composed of enteric micro-organisms and other Gram-negative rods.

Enteric micro-organisms: A number of different microbes that normally occur in the intestinal tract, or are associated with intestinal infection, are placed in the enteric group of bacilli. The normally occurring members of this group are generally considered to be of potential medical importance when they are recovered repeatedly, or in large numbers, from sites other than the lower digestive tract. The following members of this group were recovered from areas on the ASTP crewmembers other than the lower digestive tract. An outline of the total recovery pattern for the Apollo crewmembers is presented in tables 16-VI to 16-IX.

The *Escherichia coli* species is generally accepted as the most reliable evidence of fecal contamination. Outside the intestinal tract, under certain conditions, it often produces diseases such as the following: urinary tract infections (cystitis and pyelitis), peritonitis, gallbladder infection, wound infection, septicemia, and enteritis. This species was repeatedly recovered from the groin of the prime CMP and occasionally from the upper respiratory tract of the other two Apollo prime crewmembers. In all cases, neither the recovery pattern nor the quantitation indicated medical significance.

The Enterobacter aerogenes micro-organism often occurs in the large intestine of man, although the number present is considerably smaller than that of E. coli. The pathogenic significance of E. aerogenes is similar to that of E. coli. As indicated in tables 16-VI and 16-VII, this species was always carried in the nose and mouth of the prime CMP and DMP and was frequently isolated from the backup ACDR and DMP. Although this is not a common occurrence, it should be noted that this species was not shown to spread to the prime ACDR or to more sites on the carriers during the flight. Also, there was no postflight increase in quantitation. This occurrence is an excellent example of a potential pathogen, carried by two Apollo prime crewmembers, apparently being unaffected by the conditions of space flight.

Members of the genus Proteus may cause infections of the urinary tract and abscesses. Additionally, these microbes have been associated with outbreaks of enteric infection, particularly gastroenteritis. More often, they are secondary invaders of infections of the middle ear, mastoid process, meninges, wounds, and urinary tract. P. mirabilis is the most frequent species of this genus found in human clinical material. This species was carried, in low numbers, in the nasal passage of the prime ACDR throughout the monitoring period. As with E. aerogenes previously described, this unusual event provides a good model system for analyzing the response of Gram-negative rods to space-flight conditions. The ASTP mission had no detectable affect on the qualitative or quantitative presence of this micro-organism.

Other Gram-negative rods: Nonenteric Gram-negative rods discussed in this section include the Moraxella genus, Acinetobacter calcoaceticus organisms, and four species of Haemophilus.

Members of the Moraxella genus are parasites of the mucous membranes of humans and are frequently involved in pathogenic activity such as conjunctivitis. Although carried in the oral cavity of the prime DMP for 45 days before the flight, no discernible alteration was demonstrated following the mission.

Acinetobacter calcoaceticus (synonym: Mima polymorpha) is a species of minor potential medical importance. Isolated infrequently from multiple sites on the prime CMP, it did not contribute significantly to the load of Gram-negative rods recovered from ASTP prime crewmembers.

Four species of Haemophilus were isolated from the oral cavity of each ASTP astronaut as outlined in tables 16-VIII and 16-IX. Although each of these is to some degree a common inhabitant of the human mouth, each is a strict parasite requiring certain growth factors present in blood. A discussion of the potential medical importance of each follows.

H. influenzae is found in lesions and in the upper respiratory tract of carriers. It may be either a primary or a secondary invader. As a primary incitant of disease, it is responsible for meningitis, septicemia, conjunctivitis, and upper respiratory tract infections. It is commonly a secondary invader in cases of influenza and pertussis. This species was isolated from each crewmember before flight in quantitations ranging from 10 000 to 600 000 viable cells/cm^3 of gargle. The postflight loss

from two Apollo crewmembers and the quantitative reduction in contamination of the ACDR is contraindicative of a space-flight-mediated increase in infective potential.

H. haemolyticus and H. parahaemolyticus are often associated with acute pharyngitis when present in high numbers. As with the H. influenzae, the overall quantitation and incidence decreased following the ASTP flight.

H. parainfluenzae is the most benign of the four recovered species and is used largely as a marker organism because of its almost ubiquitous appearance.

Candida albicans.- This well-recognized component of the indigenous autoflora of man (ref. 16-20) has been recovered from astronaut specimens collected in association with each Apollo and Skylab mission (refs. 16-11, 16-18, and 16-21). Because C. albicans has been identified as the causative agent for serious oral cavity diseases (refs. 16-20 and 16-22), the presence of this micro-organism in the mouth of astronauts was carefully monitored. As previously reported (ref. 16-8), C. albicans was recovered from crewmembers following the Apollo 14 and 15 missions whereas other fungal species, present before flight, were absent from samples obtained immediately after recovery. Analysis of the ASTP data presented in table 16-X indicates an in-flight transfer of this species to the ACDR. No such transfer occurred with the backup crew, although C. albicans was carried in the mouth of the backup CMP. These events demonstrate the importance of this species in space flight. C. albicans could become even more important during in-flight use of antibiotics because this could provide the opportunity for a loss of competing bacterial species and eventual overgrowth with C. albicans (refs. 16-22, 16-23, and 16-24).

Staphylococcus aureus.- Although S. aureus micro-organisms are not uncommon skin and nasal contaminants, all strains are potential pathogens. They have been shown to be the causative agent of a wide range of infection and intoxications including boils, abscesses, meningitis, furunculosis, pyemia, osteomyelitis, suppuration of wounds, and food poisoning (ref. 16-25). Several space-flight-simulation studies (refs. 16-2, 16-26, and 16-27) have indicated increases in the toxigenic activity, virulence, or pathogenicity of this species with stressful confinement of the human host. If these events were to be duplicated during space flight, the resulting lesions could be especially important because of their interference with close-contact surfaces, such as the tight-fitting and abrasive pressure suits. Accordingly, the presence and activity of this species were monitored before and after each of the recent U.S. space flights. Data from the Apollo 13, 14, and 15 missions and from the Skylab missions confirm in-flight cross-contamination with S. aureus (refs. 16-11 and 16-18).

The recovery of this species from ASTP crewmembers in connection with previous space flights is presented in table 16-XI. The prime DMP had not previously been assigned to a space flight, rendering such data nonapplicable. Strains of S. aureus were recovered from all the other five ASTP astronauts in connection with at least one previous space flight.

The recovery of strains of S. aureus during the ASTP monitoring period is presented in table 16-XII. These strains are expressed as numbered bacteriophage types. The data show that each prime and backup crewmember carried a different

strain of S. aureus. Type 52, 52A, 80, 81 was carried by the prime DMP and was transferred to the prime ACDR during flight. Apparently, colonization did not ensue because this strain was not recovered again from the prime ACDR.

A postflight increase in the incidence of S. aureus isolation (refs. 16-11 and 16-18) has been previously reported. In the ASTP mission, this increase did not occur among the astronaut population. Likewise, and contrary to some previous missions (ref. 16-11), no disease events resulted from the ubiquitous presence of S. aureus before and during the flight.

Total load of potential pathogens.- Several investigators have suggested that returning space travelers may experience a "microbial shock" and may respond negatively to renewed contact with potentially pathogenic micro-organisms that are absent in the space-flight environment (refs. 16-13, 16-15, 16-17, and 16-28). These warnings were based on the assumption that contact with potential pathogens during space flight would be very limited, resulting in a reduction of immunocompetence. However, there was no demonstrable decrease in the incidence of medically important micro-organisms recovered from the astronauts on recovery day. This finding supports results reported earlier (refs. 16-7, 16-18, and 16-29). If a reduction in total immunocompetence occurred during this mission, it was not in response to decreased contact with medically important components of the resident microflora.

SUMMARY

The major portion of the planned postflight laboratory activities is continuing. Analysis of the specimen collection and distribution activities indicates that most of the experiment objectives will be satisfied. Analyses of the recovery of medically important micro-organisms from U.S. crewmembers have shown in-flight intercrew transfer of potential pathogens but no other changes of medical significance. Alterations leading to microbial simplification and microbial shock did not occur.

REFERENCES

16-1. Alekseyeva, O. G.: Some Natural Immunity Factors and Cosmonaut Autoflora During the Training Period and Following the Flights of "Vostok," "Vostok 2," "Vostok 3," and "Vostok 4." Problemy Kosmicheskoi Biologii (Problems in Space Biology), Vol. IV. U.S.S.R. Academy of Sciences Publishing House (Moscow), 1964, pp. 278-289.

16-2. Nefedov, Yu. G.; Shilov, V. M.; Konstantinova, I. V.; and Zaloguyev, S. N.: Microbiological and Immunological Aspects of Extended Manned Space Flights. Life Sciences and Space Research, IX, COSPAR, Akademie-Verlag (Berlin), May 1971, pp. 11-16.

16-3. Alekseyeva, O. G.; and Volkova, A. P.: Influence of Space Flight Factors on the Bactericidal Activity of the Body. Problemy Kosmicheskoi Biologii (Problems in Space Biology), Vol. I. U.S.S.R. Academy of Sciences Publishing House (Moscow), 1962, pp. 201-209.

16-4. Wheeler, H. O.; Kemmerer, W. W.; Dietlein, L. F.; and Berry, C. A.: Effects of Space Flight Upon Indigenous Microflora of Gemini Crew Members. Bacteriological Proceedings, 1967, p. 16.

16-5. Berry, Charles A.: Preliminary Clinical Report of the Medical Aspects of Apollo 7 and 8. NASA TM X-58027, 1969.

16-6. Vargosko, Andrew J.; Gordon, Francis B.; and Wilkins, Judd R.: Microbiological Studies on Man in Closed Environmental Systems. App. B of Infectious Disease in Manned Spaceflight. National Academy of Sciences (Washington, D.C.), 1970, pp. 137-211.

16-7. Taylor, Gerald R.: Apollo 14 Microbial Analysis. NASA TM X-58094, 1972.

16-8. Taylor, Gerald R.; Henney, Mary R.; and Ellis, Walter L.: Changes in the Fungal Autoflora of Apollo Astronauts. Appl. Microbiology, vol. 26, no. 5, Nov. 1973, pp. 804-813.

16-9. Fox, Leo: The Ecology of Microorganisms in a Closed Environment. Life Sciences and Space Research, IX, COSPAR, Akademie-Verlag (Berlin), May 1971, pp. 69-74.

16-10. Brown, Lee R.; Frome, William J.; Handler, Sandra; Wheatcroft, Merrill G.; and Rider, Linda J.: Skylab Oral Health Studies. The Proceedings of the Skylab Life Sciences Symposium. NASA TM X-58154, 1974, pp. 75-97.

16-11. Brockett, R. M.; Ferguson, J. K.; Graves, R. C.; Groves, T. O.; et al.: Skylab Environmental and Crew Microbiology Studies. The Proceedings of the Skylab Life Sciences Symposium. NASA TM X-58154, 1974, pp. 121-143.

16-12. Lebedev, K. A.; and Petrov, R. V.: Immunological Problems of Closed Environments and Gnotobiology. Uspekhi Sovremennoy Biologii, vol. 71, no. 2, 1971, pp. 235-252. (Translation available from Joint Publications Research Service, Washington, D.C.)

16-13. Luckey, T. D.: Potential Microbic Shock in Manned Aerospace Systems. Aerospace Med., vol. 37, no. 12, Dec. 1966, pp. 1223-1228.

16-14. Dobronravora, N. M.; Kortayev, M. M.; Kozar, M. I.; Mikhaylovskiy, G. P.; and Tsiganova, N. I.: Variation in Overall Body Tolerance During a 62-Day Exposure to Hypokinesia and Acceleration. Space Biol. & Med., vol. I, no. 6, Mar. 1968, pp. 101-108. (Primary source - Kosmickeskaya Biologiya i Meditsina, vol. 1, 1967, pp. 66-70. (In Russian.))

16-15. Spizizen, J.: Microbiological Problems of Manned Space Flight. Life Sciences and Space Research, IX, COSPAR, Akademie-Verlag (Berlin), May 1971, pp. 65-68.

16-16. Bauer, John D.: Staining Techniques and Cytochemistry. Gradwohl's Clinical Laboratory Methods and Diagnosis, vol. 1, ch. 27, seventh ed., C. V. Mosby Co., 1970, pp. 506-507.

16-17. Berry, Charles A.: Summary of Medical Experiences in the Apollo 7 Through 11 Manned Spaceflights. Aerospace Med., vol. 41, no. 5, May 1970, pp. 500-519.

16-18. Taylor, Gerald R.: Recovery of Medically Important Microorganisms From Apollo Astronauts. Aerospace Med., vol. 45, no. 8, Aug. 1974, pp. 824-828.

16-19. Wooley, Bennie C.: Apollo Experience Report - Protection of Life and Health. NASA TN D-6856, 1972.

16-20. Rosebury, T.: Microorganisms Indigenous to Man. Blackiston Division, McGraw-Hill, 1962.

16-21. Taylor, G. R.: Space Microbiology. Ann. Rev. Microbiol., vol. 401, 1974, pp. 23-40.

16-22. Marwin, R. M.: Relative Incidence of Candida albicans on the Skin of Persons With and Without Skin Disease. J. Investigative Dermatology, vol. 1, 1949, pp. 229-241.

16-23. Ginsberg, H. S.: Immune States in Long-Term Space Flights. Life Sciences and Space Research, IX, COSPAR, Akademie-Verlag (Berlin), May 1971, pp. 1-9.

16-24. Huppert, M.; Cazin, J., Jr.; and Smith, H., Jr.: Pathogenesis of Candida albicans Infections Following Antibiotic Therapy. J. Bacteriol., vol. 70, no. 1, July 1955, pp. 440-447.

16-25. Buchanan, Robert E.; and Gibbons, Norman E.: Bergey's Manual of Determinative Bacteriology. Eighth ed., Williams & Wilkins Co. (Baltimore), 1974.

16-26. Chukhlovin, B. A.; Ostrovmov, P. B.; and Ivanova, S. P.: Development of Staphylococcal Infections in Human Subjects Under the Influence of Some Spaceflight Factors. Space Biol. & Med., vol. 5, no. 6, 1971, pp. 91-98. (Primary source - Kosmicheskaya Biologiya i Meditsina, vol. 5, 1971, pp. 61-65. (In Russian.))

16-27. Borisova, O. K.; Lizko, N. N.; Prokhorov, V. Ia.; and Shilov, V. M.: Changes in the Microflora of Man During Long-Term Confinement. Life Sciences and Space Research, IX, COSPAR, Akademie-Verlag (Berlin), May 1971, pp. 43-49.

16-28. Wilkins, Judd R.: Man, His Environment, and Microbiological Problems of Long-Term Spaceflight. Biotechnology. NASA SP-205, 1967, pp. 133-143.

16-29. Zaloguyev, S. N.; Shinkareva, N. M.; and Utkina, T. G.: State of the Automicroflora of Skin Tissues and Certain Natural Immunity Indices in the Astronauts A. G. Nikolaev and V. I. Sevast'ianov Before and After Flight. Kosmicheskaya Biologiya i Meditsina, vol. 4, no. 6, 1970, pp. 54-59. (Translation available from Joint Publications Research Service, Washington, D.C.)

TABLE 16-I.- SAMPLE COLLECTION SCHEDULE

Sample	Day of collection											
	Before flight						During flight	After flight				
	F-45	F-30	F-15	F-7	F-1	F-0		R+0	R+3	R+7	R+15	R+30
Blood		X	X					X[a]	X[a]			
Spacecraft microflora					X		X	X				
Saliva	X	X	X	X		X		X		X[a]	X[a]	X[a]
Crew microflora	X	X	X	X		X	X	X		X[a]	X[a]	X[a]

[a]Prime crewmembers only. No samples were taken from backup crewmembers after R+0.

TABLE 16-II.- SAMPLE COLLECTION AREAS

Sample no.	Sample designation	Sample area
1	Hair	20-cm^2 area of hair (and scalp) on top of head
2	Ears	Right and left external auditory canals with 2 revolutions of each swab in each ear canal
3	Neck	20-cm^2 area below hairline at base of neck
4	Nose	Internal area of both nostrils
5	Throat swab	Surfaces of tonsils and posterior pharyngeal vault
6	Hands	20-cm^2 area on right and left palms
7	Axilla	20-cm^2 area below hair on each side
8	Groin	5-cm strip from rear to front on right and left inguinal area between legs
9	Toes	Area between the two smallest toes of each foot
10	Feces	Two 100-mg samples taken from center of the fecal specimen
11	Gargle	10 cm^3 of phosphate buffer used as gargle and washed through oral cavity 3 times

TABLE 16-III.- LOCATION OF SAMPLING SITES ON INNER SURFACES OF APOLLO-SOYUZ TEST PROJECT SPACECRAFT

Sample no.	Location in Soyuz	Sample no.	Location in Apollo
C-1	SCDR couch seat	A-1	Left X-X headstrut
C-2	SFE couch seat	A-2	Right X-X footstrut
C-3	Control panel in the descent vehicle	A-3	Crew couch, right stabilizer beam
C-4	Surface of gas mixture regulator	A-4	Tunnel area
C-5	Surface near bulkhead hatch in descent vehicle	A-5	Right floodlight
C-6	Descent vehicle hatch cover under the handwheel	A-6	Left rotational hand controller pistol grip (both sides)
C-7	Flush side of sanitary device in the orbital module (OM)	A-7	Right girth shelf above panel 278
C-8	Top of food locker table in OM	A-8	Panel 325 below window
C-9	Couch seat in OM	A-9	Above left girth shelf (above U-3)
C-10	Surface of food locker in OM near panel	A-10	Cover plate, ORDEAL stowage locker (U-3)
C-11	Front surface of the couch backrest in the OM	A-11	B-6 door behind waste stowage bag
C-12	Grid near fan in OM	A-12	Inside door of food locker (L-3)
C-13	Floor surface near OM food locker	A-13	Top of video tape recorder module
C-14	Transfer hatch under the handwheel	A-14	Panel 251, waste management dump
C-15	Surface of transfer hatch	A-15	Forward of panel 225

TABLE 16-IV.- ISOLATION MEDIA

Sample designation	Media	Number of plates	Dilution range
Back of neck	Blood[a]	2	[b]10^0 to 10^4
Hair	Mannitol[c]	3	10^0 to 10^1
Hands	CMMY[d]	4	10^0
Axilla	BTB[e]	3	10^0
Ears	SAB[f]	5	10^0
Gargle (natural)	Blood	2	10^0 to 10^5
	Mannitol	3	10^0 to 10^1
	CMMY	4	10^0 to 10^2
	Rogosa[g]	3	10^0 to 10^3
	Choc[h]	3	10^0 to 10^5
Gargle (centrifugate)	CMMY	4	10^0
	BTB	3	10^0
	SAB	5	10^0

[a]Blood agar.

[b]Sample in 5 cm^3 of phosphate-buffered physiological saline solution.

[c]Mannitol salts agar.

[d]Cornmeal, malt-extract, yeast-extract agar.

[e]Bromthymol blue agar.

[f]Sabouraud's dextrose agar.

[g]Rogosa agar.

[h]Chocolate bacitracin agar.

TABLE 16-IV.- Concluded

Sample designation	Media	Number of plates	Dilution range
Nose	Blood	2	10^0 to 10^4
	Mannitol	3	10^0 to 10^3
	CMMY	4	10^0
	BTB	3	10^0
	SAB	5	10^0
	Choc	3	10^0 to 10^1
Toes and groin	Blood	2	10^0 to 10^5
	Mannitol	3	10^0 to 10^1
	CMMY	4	10^0
	BTB	3	10^0 to 10^1
	SAB	5	10^0
Throat swab	Blood	2	10^0 to 10^5
	Mannitol	3	10^0 to 10^1
	CMMY	4	10^0 to 10^2
	BTB	3	10^0 to 10^1
	SAB	5	10^0
	Choc	3	10^0 to 10^5
	Rogosa	3	10^0 to 10^3
Feces	BTB	2	10^3 to 10^{10}
	SAB	5	10^0 to 10^3
Internal surfaces of ASTP spacecraft	Blood	3	10^0 to 10^4
	Mannitol	3	10^0
	CMMY	4	10^0
	BTB	3	10^0
	SAB	5	10^0

TABLE 16-V.- DIVISION OF RESPONSIBILITY FOR SPECIMEN ANALYSIS

Activity	Responsible laboratory	
	U.S.	U.S.S.R.
Collection of specimens from astronauts and Apollo spacecraft	X	
Collection of specimens from cosmonauts and Soyuz spacecraft		X
Identification of filamentous fungi	X	
Identification of yeasts and yeastlike fungi		X
Identification of Gram-positive catalase-positive cocci	X	X
Identification of Gram-positive catalase-negative cocci		X
Identification of Gram-negative cocci		X
Identification of nonlactose-fermenting Gram-negative rods	X	
Identification of lactose-fermenting Gram-negative rods		X
Identification of *Haemophilus* species	X	
Bacteriophage typing of *Staphylococcus aureus*	X	
Antibiotic sensitivity testing of *Staphylococcus aureus*		X
Determination of immunoglobulin levels in parotid fluid	X	
Determination of steroid, urea nitrogen, uric acid, calcium, and potassium levels in parotid fluid	X	
Determination of lysozyme levels in parotid fluid		X
Determination of bactericidal activity of serum		X
Measurement of viral antibody titers in serum		X
Measurement of specific microbial antibody levels in serum	X	
Determination of leukocyte differential count	X	

TABLE 16-VI.- RECOVERY OF GRAM-NEGATIVE RODS FROM ASTP APOLLO PRIME CREWMEMBERS

(GENERA OTHER THAN HAEMOPHILUS)

Genus and species	Crew-member	Location and quantity of bacteria, $\log_{10}$ colony-forming units/cm^3 of gargle or swab diluent							
		Days before flight					Days after flight		
		F-43	F-29	F-18	F-5	F-0	R+0	R+18	R+29
Enterobacter aerogenes	ACDR	0	0	0	0	0	0	0	0
	CMP	Axilla 1.95 Nose 2.00 Mouth 1.60	Nose 1.95 Mouth 1.84	Nose 2.23 Mouth 4.00	Nose 1.47 Mouth 3.00	Nose 3.30 Mouth 2.20	Nose 2.78 Mouth 2.60	Nose 2.48 Mouth 2.00	Axilla 1.00 Nose 1.30
	DMP	Nose 1.69 Mouth 1.30	Nose 2.00 Mouth 1.48	Mouth 2.07	Nose 1.47 Mouth 1.47	Nose 2.78 Mouth 2.00	Nose 1.00 Mouth 1.00	Nose 2.40	Mouth 1.95
Escherichia coli	ACDR	0	Mouth 2.00	0	0	0	0	Nose 1.30	0
	CMP	Groin 2.00	Groin 2.60	Groin 1.60	0	Groin 2.30	0	0	0
	DMP	0	0	Nose 2.07	0	0	0	Nose 1.78	Nose 1.00
Moraxella species	ACDR	Hands 1.00	0	0	0	0	0	0	0
	CMP	Mouth 5.00	Ear 1.30	0	Mouth 6.47	0	0	0	0
	DMP	Mouth 2.43	0	Mouth 3.77	Mouth 2.68	Mouth 2.30	Mouth 2.00	0	0
Proteus mirabilis	ACDR	Nose 2.85	Nose 2.00	Nose 2.84	Nose 2.56	Nose 1.30	Nose 1.30	Nose 1.00	Nose 3.04
	CMP	0	0	0	0	0	0	0	0
	DMP	0	0	0	0	0	0	0	0
Acinetobacter calcoaceticus	ACDR	0	0	0	0	0	0	0	0
	CMP	0	Neck 2.00 Hand 2.60	0	0	0	0	0	Hair 1.30 Neck 3.00 Mouth 2.60
	DMP	0	0	0	0	0	0	0	0

TABLE 16-VII.- RECOVERY OF GRAM-NEGATIVE RODS FROM ASTP APOLLO BACKUP CREWMEMBERS

(GENERA OTHER THAN HAEMOPHILUS)

Genus and species	Crew-member	Location and quantity of bacteria, $\log_{10}$ colony-forming units/cm^3 of gargle or swab diluent					
		Days before flight					Day of recovery
		F-45	F-32	F-18	F-5	F-0	
Enterobacter aerogenes	ACDR	Nose 1.00	Nose 1.00	Nose 1.00	0	0	Nose 1.60
	CMP	0	0	0	0	0	0
	DMP	Nose 2.00 Mouth 2.47 Neck 1.00 Groin 1.69	Mouth 2.69 Groin 3.69	0	Mouth 2.00	0	Axilla 1.78
Escherichia coli	ACDR	0	0	0	0	0	0
	CMP	0	0	0	0	0	0
	DMP	0	0	0	0	0	0
Moraxella species	ACDR	Hair 2.11 Neck 3.17 Axilla 2.86 Hands 2.17	0	Neck 1.00	0	0	Nose 2.00 Axilla 1.00
	CMP	0	0	0	0	0	0
	DMP	0	0	0	0	0	Toes 2.00
Proteus mirabilis	ACDR	0	0	0	0	0	0
	CMP	0	0	0	0	0	0
	DMP	0	0	0	0	0	0
Acinetobacter calcoaceticus	ACDR	0	0	0	0	Groin 3.00	Ear 3.00
	CMP	0	0	0	0	0	Neck 2.00 Axilla 1.60
	DMP	Axilla 1.30 Hands 1.60	0	0	0	Nose 2.30 Axilla 1.30 Hands 1.70	0
Klebsiella pneumoniae	ACDR	0	0	0	0	0	0
	CMP	0	0	0	0	0	0
	DMP	0	0	Mouth 3.00 Groin 3.38 Hands 1.30	Mouth 3.48 Groin 3.38 Hands 1.00	Mouth 3.78 Groin 4.00	Mouth 1.48 Groin 3.30

TABLE 16-VIII.- RECOVERY OF GRAM-NEGATIVE RODS FROM ASTP APOLLO PRIME CREWMEMBERS (GENUS HAEMOPHILUS)

Crew-member	Species of Haemophilus	Quantity of bacteria, $\log_{10}$ colony-forming units/cm^3 of gargle or swab diluent							
		Days before flight					Days after flight		
		F-43	F-29	F-18	F-5	F-0	R+0	R+18	R+29
Throat swab									
ACDR	H. haemolyticus	0	0	4.47	0	0	0	0	0
	H. influenzae	0	0	4.90	0	0	3.34	0	0
	H. parahaemolyticus	0	0	0	0	0	0	0	0
	H. parainfluenzae	4.50	5.04	5.36	5.17	5.20	3.49	4.62	2.18
CMP	H. haemolyticus	5.60	5.47	0	0	0	3.30	0	0
	H. influenzae	5.77	0	0	0	0	0	0	0
	H. parahaemolyticus	0	0	4.00	5.90	0	0	0	0
	H. parainfluenzae	5.69	6.04	5.14	5.90	5.36	3.84	5.87	5.49
DMP	H. haemolyticus	0	0	4.47	0	0	0	0	0
	H. influenzae	0	0	0	0	4.00	0	0	0
	H. parahaemolyticus	0	0	0	0	0	0	5.11	0
	H. parainfluenzae	5.41	5.23	4.84	6.46	5.45	4.77	4.90	4.00
Gargle									
ACDR	H. haemolyticus	0	0	6.49	0	0	5.30	0	0
	H. influenzae	0	4.90	5.77	0	0	0	0	1.48
	H. parahaemolyticus	0	0	0	0	0	5.00	0	0
	H. parainfluenzae	5.54	5.99	6.77	6.53	6.53	5.95	5.08	4.18
CMP	H. haemolyticus	0	6.30	0	6.90	0	0	0	0
	H. influenzae	5.69	0	0	0	0	0	0	0
	H. parahaemolyticus	0	0	6.30	7.11	0	0	0	0
	H. parainfluenzae	6.23	7.08	7.20	7.39	6.48	5.15	6.48	7.00
DMP	H. haemolyticus	0	0	5.77	0	0	0	5.78	0
	H. influenzae	0	0	0	0	0	0	0	0
	H. parahaemolyticus	4.69	0	0	5.30	0	5.30	5.00	0
	H. parainfluenzae	5.44	6.04	6.43	6.80	6.28	5.52	6.25	5.46

TABLE 16-IX.- RECOVERY OF GRAM-NEGATIVE RODS FROM ASTP APOLLO BACKUP CREWMEMBERS (GENUS HAEMOPHILUS)

Crew-member	Species of Haemophilus	Quantity of bacteria, $\log_{10}$ colony-forming units/cm^3 of gargle or swab diluent					
		Days before flight					Day of recovery
		F-45	F-32	F-18	F-5	F-0	
Throat swab							
ACDR	H. haemolyticus	0	4.60	0	0	0	0
	H. influenzae	0	0	0	0	0	0
	H. parahaemolyticus	4.30	0	4.11	0	0	0
	H. parainfluenzae	5.32	4.95	7.95	5.81	6.05	5.38
CMP	H. haemolyticus	0	0	0	0	0	0
	H. influenzae	0	0	0	0	0	0
	H. parahaemolyticus	0	0	4.65	4.65	4.57	0
	H. parainfluenzae	4.34	2.30	3.95	3.60	4.48	4.57
DMP	H. haemolyticus	0	0	0	5.04	0	0
	H. influenzae	0	4.00	0	3.00	3.00	0
	H. parahaemolyticus	0	0	0	0	0	0
	H. parainfluenzae	2.44	5.20	4.41	4.69	4.04	4.15
Gargle							
ACDR	H. haemolyticus	5.47	0	0	0	0	5.00
	H. influenzae	0	0	0	0	0	0
	H. parahaemolyticus	0	0	0	0	0	0
	H. parainfluenzae	5.95	6.54	6.60	0	6.49	6.36
CMP	H. haemolyticus	0	0	0	0	0	0
	H. influenzae	0	0	0	0	0	0
	H. parahaemolyticus	0	0	6.00	6.77	0	5.30
	H. parainfluenzae	4.70	0	6.43	6.36	5.86	6.41
DMP	H. haemolyticus	0	0	0	0	0	0
	H. influenzae	3.00	0	0	0	0	0
	H. parahaemolyticus	4.25	0	0	0	4.00	4.30
	H. parainfluenzae	0	6.73	7.43	7.43	5.81	5.00

TABLE 16-X.- RECOVERY OF CANDIDA ALBICANS FROM THE MOUTHS OF APOLLO CREWMEMBERS

Crewmember	Days before or during flight						Days after flight		
	F-45	F-30	F-15	F-5	F-0	F+5	R+0	R+15	R+30
Prime crew									
ACDR	A[a]	A	A	A	A	A	P[b]	A	A
CMP	P	P	P	P	P	P	P	P	P
DMP	A	P	P	P	P	A	P	P	P
Backup crew									
ACDR	A	A	A	A	A	NS[c]	A	NS	NS
CMP	P	P	P	P	P	NS	P	NS	NS
DMP	A	A	A	A	A	NS	A	NS	NS

[a]Absence of C. albicans.

[b]Presence of C. albicans.

[c]No sample taken.

TABLE 16-XI.- STAPHYLOCCUS AUREUS RECOVERY FOR U.S. CREWMEMBERS COLLECTED BEFORE ASTP FLIGHT

Crewmember	Flight	Sampling period	Sample area	Phage type
Prime ASTP crew				
ACDR	Apollo 10	F-30	Hands	NA[a]
CMP	Apollo 15	F-30	Scalp Nose	NT[b] 85
		F-5	Nose Mouth	85 NT
	Skylab 3	F-30	Groin Nose	NT 75/85
		F-14	Groin	NT
		F-5	Mouth Nose	75/85 NT
	Skylab 4	F-30	Groin Nose	NT 75/85
		F-14	Nose, groin Mouth	NT 75/85
		F-5	Ear, groin Nose Mouth, scalp	NT 29/75 29/47/75
DMP	Clinic	- -	Mouth	83-A
Backup ASTP crew				
ACDR	Apollo 12	F-30	Scalp, ears, axilla, hands, nose, inguinal	NA
		F-14	Nose	NA
		F-0	Toes, nose	NA
		R+0	Nose	NA
	Skylab 3	F-45	Nose, mouth	3-A
		F-14	Scalp, navel, nose, groin	3-A
		F-5	Nose	3-A
		F-0	Nose	3-A
		R+0	Hands Nose	3-A 3-A/3-C
		R+8	Nose, hands, navel Groin	3-A 3-A/3-C
		R+15	Scalp Nose, axilla, hands Navel	3-A/3-C 3-A 3-C
CMP	Apollo 14	F-14	Nose, hands	6/47/53/54/77/79/80/81
DMP	Skylab 3	F-45	Scalp Groin Nose	29/79 29/79/80 29/53/54/79/80
		F-14	Nose	29/53/54/79/80
		F-5	Hands Nose	29/79 NT
		R+0	Mouth, scalp, feces Hands Nose	29/79 3-A 29/53/54/79/80
		R+8	Mouth	29/53/79/80
		R+18	Nose Mouth	29/79 29/53/79/80

[a]Not applicable (typing not done).

[b]Nontypable.

TABLE 16-XII.- RECOVERY OF STAPHYLOCOCCUS AUREUS BACTERIOPHAGE TYPES FROM ASTP APOLLO CREWMEN

Crew-member	Sample collection period								Carrier status
	Days before flight					Days after flight			
	F-45	F-30	F-15	F-7	F-0	R+0	R+15	R+30	
Prime crew									
ACDR	0	Mouth (NT[a])	Mouth (NT) Mouth (6)	Mouth (NT) Toes (85)	Mouth (NT) Hand (42E)	Mouth (52, 52A, 80, 81)	Mouth (NT)	Mouth (NT)	(NT)
CMP	Mouth 85 (83A)	Mouth 85 (53, 83A)	Mouth 83A, 85 (6, 42E, 53, 79, 80, 81) Nose 71 (6, 75, 80, 81)	Mouth 85 (53, 79, 83A)	Mouth 85 (53, 83A)	0	Mouth (83A, 85)	Mouth (85)	53, 83A, 85
DMP	0	Mouth 52, 52A, 80, 81 Mouth 29 (42E, 53, 75, 81, 83A)	0	Mouth 52, 52A, 80, 81	Mouth 52, 52A, 80, 81 Nose (6, 42D, 42E, 47, 53, 75, 81)	Mouth (52, 52A, 80, 81)	0	0	52, 52A, 80, 81
Backup crew									
ACDR	Mouth 3A (3C)	Mouth 3A (3C)	Mouth 3A (3C)	0	0	0	NS[b]	NS	3A, 3C
CMP	Hands (NT) Nose 71 (55)	Nose (55, 71) Hair (55, 71)	0	0	Nose (55, 71)	Nose (54, 55, 71) Hand (NT) Nose (NT) Hair (81)	NS	NS	55, 71
DMP	Nose (75, 79, 84)	Mouth 29 (53, 54, 75, 79, 80, 81) Nose (29, 53, 54, 75, 79, 80)	Mouth 29, 75, 79 (42E, 53) Nose 29, 75, 79 (6, 42E, 53, 80) Neck 29, 75, 79 (42E, 53, 54, 80, 81)	Mouth (29, 42E, 53, 75, 79, 80) Nose 29 (42E, 53, 75, 79, 80, 81, 85)	Mouth (29, 53, 75, 79, 80) Nose (29, 53, 75, 79)	Mouth (29, 53, 54, 75) Nose (29, 53, 75, 80)	NS	NS	29, 53, 54, 75, 79, 80

[a]Nontypable.

[b]No sample taken.

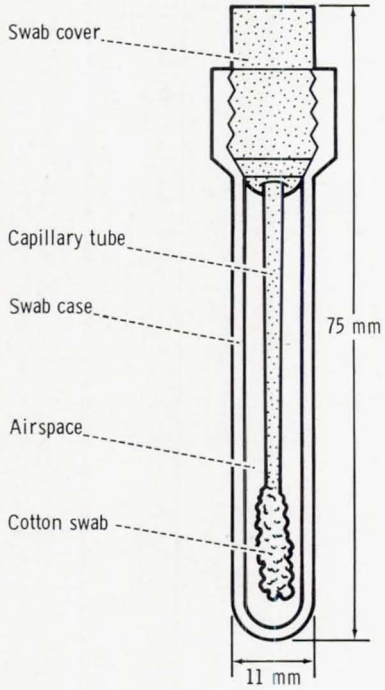

Figure 16-1.- In-flight microbial sample collection device.

(a) Closed kit.

Figure 16-2.- Beta-cloth sample collection kit used for crewmember samples in the Apollo spacecraft.

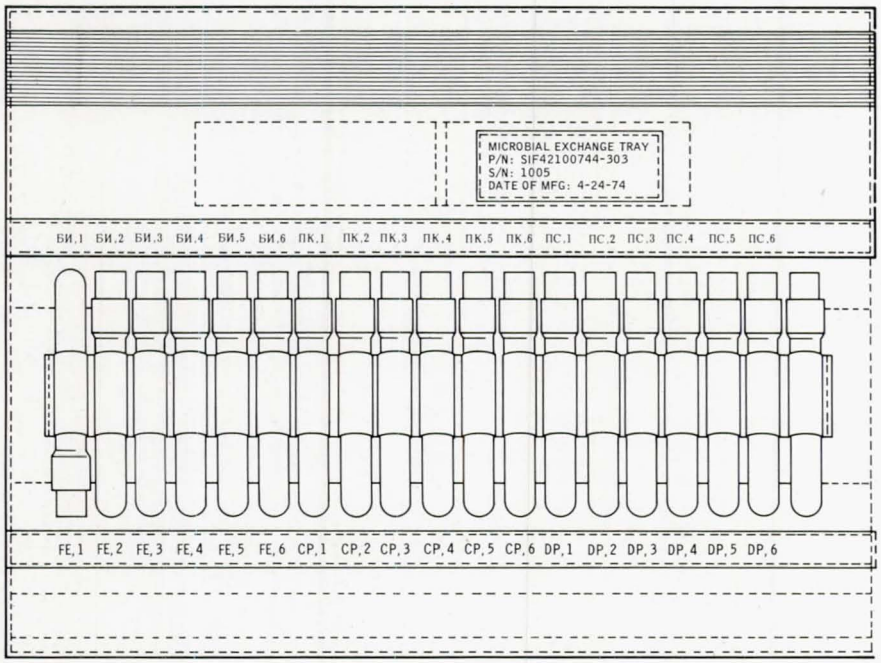

(b) Open kit showing sample collection devices in place.

Figure 16-2.- Concluded.

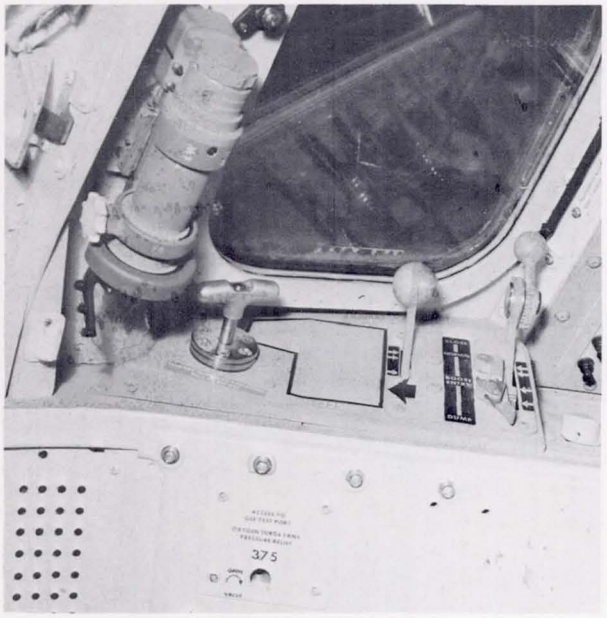

(a) A-8: panel 325 below window (S-74-33254).

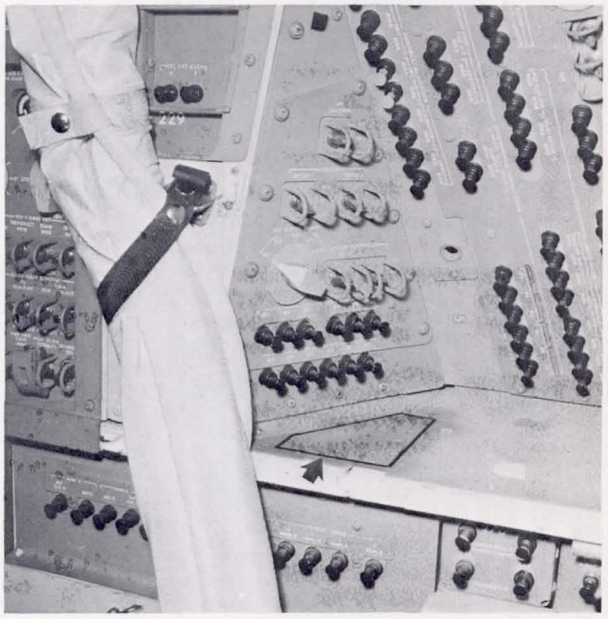

(b) A-7: right girth shelf above panel 278 (S-74-33259).

Figure 16-3.- Demarcation lines on internal surfaces of Apollo spacecraft.

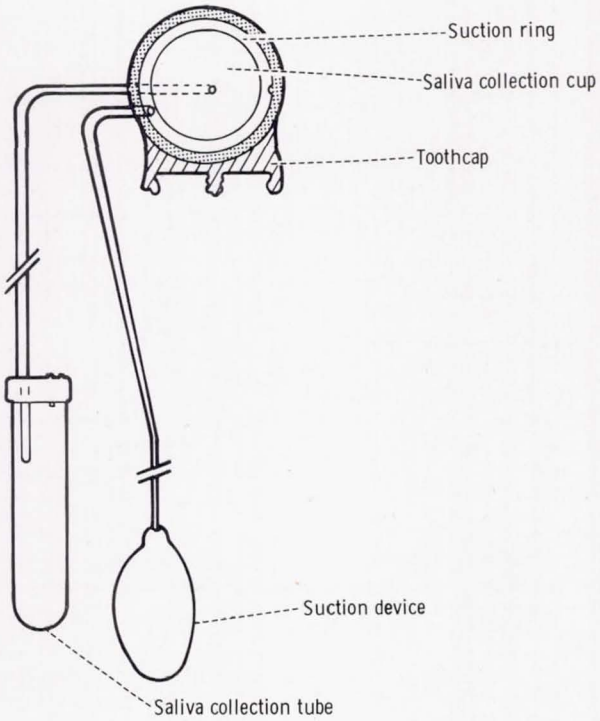

Figure 16-4.- Saliva collection device used to obtain salivary parotid fluid.

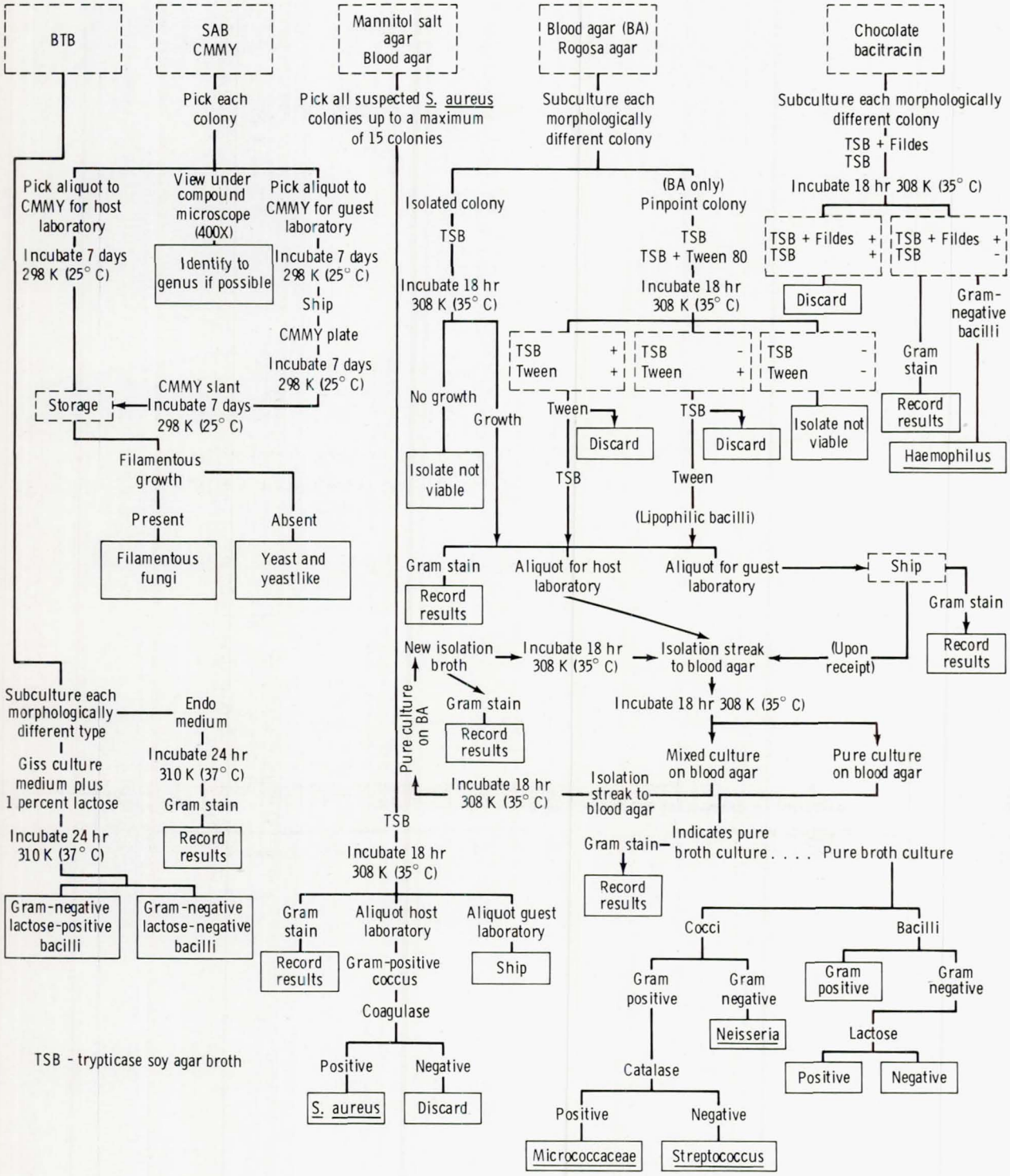

Figure 16-5.- Schematic diagram for identifying micro-organisms.

ASTP BACTERIOLOGY DATA FORM

ФОРМУЛЯР БАКТЕРИОЛОГИЧЕСКИХ ДАННЫХ ЭПАС

IDENTIFICATION NUMBER _____
ИДЕНТИФИКАЦИОННЫЙ НОМЕР

- ☐ **Stafford** Стаффорд
- ☐ **Slayton** Слейтон
- ☐ **Brand** Бранд
- ☐ **Leonov** Леонов
- ☐ **Kubasov** Кубасов
- ☐ **Bean** Бин
- ☐ **Evans** Эванс
- ☐ **Lousma** Лусма
- ☐ **Filipchenko** Филипченко
- ☐ **Rukavishnikov** Рукавишников

Area _____
Место забора

Count: _____
Счет:

Dilution: _____
Разведение:

Sample Period _____
Время забора

Sample Date _____
Дата забора

MEDIUM:
ПИТАТЕЛЬНАЯ СРЕДА:

- ☐ **Blood Agar** Кровяной агар
- ☐ **Mannitol Salt** Маннитолово-солевой агар
- ☐ **Chocolate Bacitracin** Шоколадный агар /Бацитрацин/
- ☐ **CMMY** С.М.М.У
- ☐ **SAB** Среда Сабуро
- ☐ **Ragosa** Рагоза
- ☐ **BTB** Среда БТБ

CELL MORPHOLOGY
МОРФОЛОГИЯ КЛЕТОК

Size _____ **mm.**
Размер мм

Pigment _____
Пигмент

Form:
Форма:

- ☐ **Round** Круглая
- ☐ **Elongated** Продолговатая
- ☐ **Irregular** Неровная

Hemolysis:
Гемолиз:

- ☐ **Alpha** Альфа
- ☐ **Beta** Бета
- ☐ **Gamma** Гамма

Surface:
Поверхность:

- ☐ **Smooth** Гладкая
- ☐ **Rough** Шероховатая
- ☐ **Wrinkled** Морщинистая

Elevation:
Возвышенность:

- ☐ **Convex** Выпуклая
- ☐ **Raised** Приподнятая
- ☐ **Flat** Плоская

Gram Stain:
Окраска по Граму:

- ☐ **Gram positive rod** (02)
  Грамположительная палочка /02/
- ☐ **Gram positive sporulating rod** (08)
  Спорообразующая грам-положительная палочка /08/
- ☐ **Gram positive branching rod** (13)
  Ветвистая грам-положительная палочка /13/
- ☐ **Gram positive cocci in pairs and chains** (04)
  Цепочные и парные грам-положительные кокки /04/
- ☐ **Gram positive cocci in clusters** (06)
  Гроздевидные грам-положительные кокки /06/
- ☐ **Gram negative cocci in pairs and clusters** (05)
  Гроздевидные и парные грамотрицательные кокки /05/
- ☐ **Gram negative rod** (03)
  Грамотрицательная палочка /03/

Figure 16-6.- ASTP bacteriology data form.

17. CELLULAR IMMUNE RESPONSE

EXPERIMENT MA-031

B. S. Criswell[a]

ABSTRACT

Significant changes in phytohemagglutinin (PHA) lymphocytic responsiveness occurred in the cellular immune response of three astronauts during the 9-day flight of the Apollo-Soyuz Test Project. Parameters studied were white blood cell concentrations, lymphocyte numbers, B- and T-lymphocyte distributions in peripheral blood, and lymphocyte responsiveness to PHA, pokeweed mitogen, Concanavalin A, and influenza virus antigen.

INTRODUCTION

The cellular immune response of the three astronauts of the Apollo-Soyuz Test Project (ASTP) space flight was studied before and after the 9 days of flight. The findings are to be correlated in the future with lymphocytic changes that were noted during the Skylab space flight. Briefly, the functional capacity of lymphocytes at splashdown of Skylab 3 and 4 was depressed along with a suppression in the T-lymphocyte numbers. No changes of this type were noted following a 14-day bed-rest study. In the present study, which involved a shorter flight, functional suppression was again noted but no quantitative changes in lymphocytes occurred.

METHODS AND MATERIALS

Samples of heparinized peripheral venous blood (10 cubic centimeters) were obtained and were processed within 1 to 24 hours after collection. Before separation, total leukocyte (white blood cell (WBC)) counts were performed using a hemacytometer and/or a Coulter counter, and differential counts were determined using slide preparations stained with Wright's stain.

Lymphocyte Preparation

Lymphocytes were also separated by Ficoll-Hypaque gradient centrifugation according to Böyum's method (ref. 17-1) or by using a Technicon lymphocyte

---

[a]Baylor College of Medicine; Principal Investigator.

separator. Cells in the resulting suspension of mononuclear cells were washed three times in minimum essential medium (MEM); they were then adjusted to a final concentration of 1×10^6 cells/ml.

Lymphocyte Classification

The B-lymphocyte distributions were determined by enumerating the percent of 200 mononuclear cells with surface immunoglobulins detected by the immunofluorescent antibody technique described in reference 17-2.

The E-rosette forming lymphocytes (T-cells) were determined by the method of Jondahl et al. (ref. 17-3). A concentration of 1×10^6 lymphocytes was mixed in 0.25 milliliter of MEM and added to 0.25 milliliter of a 0.5-percent sheep red blood cell (SRBC) suspension. After mixing, the tubes were incubated at 310 K (37° C) for 5 minutes, centrifuged at 500g for 3 minutes, and incubated in ice water for 2 hours. Approximately half the supernatant was removed and the top layer of cells was gently resuspended; 200 lymphocytes were counted with three or more adhering SRBC used as criteria for E-rosetted lymphocyte.

Lymphocyte Responsiveness in Microculture to PHA, PWM, and Con A

Purified lymphocytes (1×10^5 cells) in MEM containing 40-percent fetal calf serum (FCS) were placed in culture plates, and the antigens were diluted in MEM (containing Pen-Strep and L-glutamine) in the following concentrations: 0.01 ml phytohemagglutinin (PHA)/ml MEM; 0.01 and 0.05 ml pokeweed mitogen (PWM)/ml MEM; and 25 and 50 μg Concanavalin A (Con A)/ml MEM. The diluted antigens in 0.1-milliliter aliquots (in duplicate) were placed in the appropriate well. The cultures were incubated in a humidified carbon dioxide atmosphere at 310 K (37° C) for the following periods: 3 days for PHA and 5 days for Con A and PWM. On the day of harvest, samples were treated as described in the following section on the influenza virus antigen cultures.

Lymphocyte Responsiveness to Influenza Virus Antigen by Thymidine Incorporation

An inactivated monovalent type A influenza virus vaccine containing 1600 chick cell agglutinating units/ml of a Hong Kong strain (H_3N_2) was dialyzed against phosphate-buffered saline (PBS) and stored at 203 K (-70° C) until used for tests. Separated lymphocytes were added in 0.1-milliliter aliquots (in duplicate) for each dilution of influenza antigen, and the cultures were incubated in a humidified carbon dioxide incubator at 310 K (37° C) for periods of either 2 or 3 days. On the day of harvest, the cells were pulsed for 2 hours with 1 microcurie of methyl ^{3}H-thymidine and then harvested with an automated harvester onto glass-fiber filter strips; they were then counted in a liquid scintillation counter. Data were expressed as counts per minute (CPM)/1×10^6 lymphocytes, and the stimulation index (SI) was calculated by dividing the mean result for stimulated cultures by that for

the unstimulated cultures. Allantoic fluid was used separately as a control on reactivity of each individual crewman to chick embryo proteins.

RESULTS

White Blood Cell Quantitation

Table 17-I shows the mean and one standard deviation (SD) of the WBC count, lymphocyte count, and lymphocyte percentages for respective days preflight and postflight. Significant increases in WBC numbers were noted on R+0 (day of splashdown) and R+1, which represented polymorphonuclear leukocyte increases. Normal laboratory values are given for comparison.

Table 17-II gives the results of the T-lymphocytes, B-lymphocytes, and nonreactive lymphocytes. Fluctuations are indicated but values remain within the one SD for normal laboratory values.

Lymphocyte Responsiveness in Culture to PHA, PWM, and Con A

Table 17-III shows the culture findings for the nonspecific mitogens. The stimulation indexes for PHA dropped at R+0 and at R+1 for all three astronauts. By R+8, the three astronauts were back within normal ranges. Interestingly, a reverse situation is indicated for the Apollo commander (ACDR) at R+0 with Con A stimulation enhanced. Other crewmembers began and remained at low-level ranges for Con A throughout the preflight and postflight periods. Considerable individual variation was noted in the PWM data and no consistent trend was obtained.

Influenza Virus Antigen Stimulation

One of the three astronauts responded to influenza virus Hong Kong strain antigen in cultures. All three astronauts responded to influenza virus England strain preflight. Because these antigens are quite variable in response patterns even in known and diagnosed influenza illnesses, changes or losses in reactivity are not significant. Total lack of reactivity may reflect influenza susceptibility.

DISCUSSION

Significant changes were found for all three crewmen in PHA responsiveness of the lymphocytes. No significant quantitative changes were noted among the lymphocytic population. Variations were noted in the stimulation indexes of the subjects for Con A and PWM; however, because of the rapid exchange of cells between different compartments in the body, variation in the indexes may be expected.

It has been noted during space flight in Skylab 4 that PHA responsiveness of lymphocytes was extremely depressed on splashdown. Previous bed-rest data showed no significant change in PHA reactivity for a 14-day period. Because a depression was observed in this 9-day ASTP mission, one must conclude that time in space may not be the controlling factor in the functional suppressiveness of the lymphocytes. Perhaps, because no quantitative changes were noted in lymphocytes for ASTP but were present for the Skylab 3 and 4 missions, these changes in B- and T-lymphocyte numbers may reflect the longer period in space.

REFERENCES

17-1. Böyum, A.: Separation of Leukocytes From Blood and Bone Marrow. Scand. J. Clin. Lab. Invest., vol. 21, suppl. 97, 1968, p. 7.

17-2. DeFazio, Sally R.; Criswell, B. Sue; South, Mary A.; Kimzey, S. L.; and Montgomery, J. R.: A Paraprotein in Severe Combined Immunodeficiency Disease Detected by Immunoelectrophoretic Analyses of Plasma. J. Clin. Exp. Immunol., vol. 19, no. 3, 1975, pp. 563-570.

17-3. Jondahl, M.; Holm, G.; and Wigzell, H.: Surface Markers on Human T and B Lymphocytes. 1. A Large Population of Lymphocytes Forming Nonimmune Rosettes With Sheep Red Blood Cells. J. Exp. Med., vol. 136, no. 2, Aug. 1, 1972, pp. 207-215.

TABLE 17-I.- PREFLIGHT, POSTFLIGHT, AND "NORMAL VALUE" WHITE BLOOD COUNT, LYMPHOCYTE COUNT, AND LYMPHOCYTE PERCENT

Sample day (a)	WBC/mm^3, mean ± 1 SD	Lymphocyte count/mm^3, mean ± 1 SD	Lymphocyte percent, mean ± 1 SD
F-30	6 640 ± 1830	2820 ± 480	43 ± 5
F-15	5 830 ± 2020	2420 ± 440	43 ± 7
F-5	6 530 ± 560	3040 ± 550	47 ± 11
R+0	11 110 ± 4210	1950 ± 490	20 ± 10
R+1	13 530 ± 610	3020 ± 810	22 ± 6
R+8	9 560 ± 2580	3500 ± 900	37 ± 1
R+13	6 600 ± 1510	2270 ± 400	35 ± 5
Normal laboratory value	7 110 ± 2400	3000 ± 1200	43 ± 13

[a]F-30 is 30 days before lift-off, R+0 is recovery (splashdown) day, R+1 is recovery plus 1 day, etc.

TABLE 17-II.- RESULTS OF THE T-LYMPHOCYTES, B-LYMPHOCYTES, AND NONREACTIVE LYMPHOCYTES

Sample day	T-lymphocytes, 1×10^5/ml (mean ± 1 SD)	B-lymphocytes, 1×10^5/ml (mean ± 1 SD)	Nonreactive lymphocytes, 1×10^5/ml (mean ± 1 SD)
F-30	16.5 ± 6.1	7.1 ± 0.4	4.7 ± 2.1
F-15	12.9 ± 4.9	4.7 ± 0.2	6.7 ± 0.5
F-5	17.9 ± 2.8	5.4 ± 0.9	7.1 ± 3.7
R+0	13.0 ± 5.6	5.3 ± 1.2	1.2 ± 1.2
R+1	19.1 ± 3.8	7.0 ± 3.5	4.2 ± 1.8
R+8	25.3 ± 4.4	5.8 ± 1.9	3.9 ± 3.6
R+13	14.4 ± 3.2	5.6 ± 1.2	2.6 ± 1.0
Normal laboratory value	15.9 ± 6.3	5.1 ± 3.0	8.5 ± 5.6

TABLE 17-III.- LYMPHOCYTIC RESPONSE TO PHA, PWM, AND CON A

Sample day	Subject (a)	Stimulation indexes		
		PHA	Con A	PWM
F-30	ACDR	34	3	5
	CMP	34	26	50
	DMP	41	16	114
	Mean of three	36 ± 4	15 ± 12	56 ± 55
F-15	ACDR	65	25	43
	CMP	47	11	14
	DMP	95	12	41
	Mean of three	69 ± 24	16 ± 8	33 ± 16
F-5	ACDR	66	12	27
	CMP	46	32	29
	DMP	74	6	34
	Mean of three	63 ± 15	17 ± 14	30 ± 4
R+0	ACDR	38	151	100
	CMP	11	11	24
	DMP	12	12	11
	Mean of three	20 ± 15	58 ± 80	45 ± 48
R+1	ACDR	9	20	40
	CMP	21	49	11
	DMP	5	6	4
	Mean of three	12 ± 8	25 ± 22	25 ± 15
R+8	ACDR	72	12	11
	CMP	45	18	11
	DMP	18	8	9
	Mean of three	45 ± 27	13 ± 5	10 ± 1
Normal laboratory value	Mean	69	67	50
	Range	10 to 282	10 to 277	10 to 170

[a]ACDR, CMP, and DMP mean Apollo commander, command module pilot, and docking module pilot, respectively.

18. THE EFFECTS OF SPACE FLIGHT ON POLYMORPHONUCLEAR LEUKOCYTE RESPONSE

EXPERIMENT MA-032

R. R. Martin[a]

ABSTRACT

In a series of studies performed at intervals from 30 days before flight to 30 days after recovery, blood samples were obtained from the three astronauts of the Apollo-Soyuz Test Project and from eight control subjects. To determine the effects of space flight on polymorphonuclear leukocytes, tests were performed onboard the recovery ship U.S.S. New Orleans on blood samples obtained as quickly as possible after splashdown and on the day following recovery. The astronauts' inhalation of propellent gases and the inception of corticosteroid therapy 1 day after recovery provided an additional opportunity to investigate the possible effects of these factors on leukocyte function. Data were obtained during each time period on the total leukocyte count, differential count, leukocyte adhesion, leukocyte migration and chemotaxis, phagocytosis, and histochemical staining for leukocyte acid and alkaline phosphatase. These observations present a variety of in vitro correlates to white blood cell function within the body. Taken together, they serve as a reasonable approximation of the effects of space flight on leukocyte function.

INTRODUCTION

Various physiological, hematological, and serological measurements have been performed on astronauts throughout the manned spacecraft program. No previous formal effort has been made to investigate the possible effects of space flight and weightlessness on polymorphonuclear leukocyte (PMN) function. Because these phagocytic cells are important in the defense of the body against disease and because situations in which the function of these leukocytes is abnormal are associated with increased susceptibility to infection, a variety of experiments was designed to observe changes in the PMN's of astronauts in relationship to the events of the Apollo-Soyuz Test Project (ASTP). The goal of this experiment was to identify any measurable PMN alterations that might be significant in planning future, longer duration space missions.

The results of this experiment are being analyzed and correlated with a large amount of normal data in which the same laboratory methods were used. The experiment went as planned, and all blood samples were obtained during baseline, postflight, and later convalescent periods. The unplanned inhalation of

---

[a]Baylor College of Medicine; Principal Investigator.

propellent gases and subsequent hospitalization of the astronauts with the administration of adrenal corticosteroid therapy provided an opportunity to evaluate these factors in relation to leukocyte function.

Overall, this experiment was successful in documenting that no consistent, potentially serious abnormalities in PMN function (detectable by the methods used) were produced in the ASTP crewmembers. A broader experience, including similar studies on future space-flight missions, will be required before definite conclusions can be drawn.

BASIC THEORY

The PMN is a critical cell in the defense of the host against infections. The ultimate function of the PMN is the phagocytosis and killing of micro-organisms that invade the tissues of the body. To carry out this function, however, a sequence of earlier steps is important. Because the majority of leukocytes at some time pass through the bloodstream, they must be able to leave the circulating blood and reach the tissue spaces where potential infections occur. To do this, the leukocyte must adhere to the surface of the blood vessel, work its way through the walls of the small blood vessels, migrate through the tissue spaces, and collect in the area of inflammation accompanying early infection. Abnormalities in function leading to the impairment of any one of these steps can potentially cause increased susceptibility to infection.

The PMN is present in the circulating blood for a matter of hours, as the cells travel from the production sites in the bone marrow to the tissues where they function to protect the host from invasion of foreign organisms. As a result of this rapid turnover, changes in the well-being of the host may be reflected in alterations in circulating leukocytes. The usual clinical data of total white blood cell counts and differential counts can be considerably supplemented by a variety of functional tests.

The in vitro techniques used in the present studies have been adapted from methods in widespread use among investigators of leukocyte function. These tests have been standardized by using a large number of normal subjects. This experiment was performed using concurrent controls.

The total white blood cell counts and differential counts have been useful to clinicians for many decades as indices of the status of the host. The leukocyte counts are well recognized to fluctuate with infections (ref. 18-1) and with stress reactions (ref. 18-2). Histochemical staining for acid phosphatase and for alkaline phosphatase can correlate with leukocyte "activation" (ref. 18-3) and fluctuate with physiological abnormalities (ref. 18-4). The property of leukocyte adhesion can be quantitated in vitro and is altered with several clinical states associated with increased susceptibility to infection, such as alcohol ingestion, and corticosteroid administration (ref. 18-5). Chemotaxis experiments were performed using a variation of the Boyden chamber technique developed in this laboratory (ref. 18-6). Similarly, phagocytosis studies were conducted using tissue chamber slides and previously described techniques (ref. 18-7).

RESULTS AND DISCUSSION

The experiment was successfully carried out as planned. All blood samples were obtained from the Apollo commander (ACDR), command module pilot (CMP), and docking module pilot (DMP) during the interval from 30 days before flight (F-30) to 30 days after recovery (R+30). The backup crew was studied during the preflight period and served as a normal control for this interval. Three other subjects (A, B, C) were studied both in preflight testing and during recovery testing onboard the U.S.S. New Orleans. Two other subjects (D, E) who had been tested repeatedly served as internal controls.

The total white blood cell counts were fairly stable and reproducible for each subject (table 18-I). Abnormalities include low preflight values for the DMP (particularly on day F-5) and the occurrence of elevated leukocyte counts in all three astronauts for 2 days after recovery and on day R+8 (when steroid administration was a factor).

The differential leukocyte counts for the study group are given in table 18-II. These values are used to calculate the total PMN counts in table 18-III. Note that the total PMN counts are extremely reproducible among the group of normal controls.

The leukocyte alkaline phosphatase is a histochemical test that generally correlates with the amount of PMN activation. The numbers of positive cells for this enzyme generally paralleled the total number of PMN's (table 18-IV). A weighted value can be assigned to positive leukocytes by grading the reaction of individual cells from 0 through 4+. A number of cells of each degree of reactivity are multiplied by the activity score, and the total value for 100 representative cells is calculated. When this is done, the astronauts are noted to have somewhat elevated values during both the preflight and postflight periods (table 18-V). This higher value is also noted in the backup CMP. A further weighted value can be calculated by determining the mean staining characteristics of the positive leukocytes (table 18-VI). Again, the astronauts tend to have somewhat higher values than the normal controls, but these differences are not significant.

The total number of PMN's staining for the lysosomal enzyme, acid phosphatase, were similarly determined (table 18-VII). The DMP again had low values during the preflight period; the number decreased to a level of 990 positive cells on day F-5. All crewmembers showed an elevation in the number of cells that stain for acid phosphatase during the postflight interval. The total leukocyte acid phosphatase scores (table 18-VIII) and the mean acid phosphatase scores (table 18-IX) were not significantly different from the values found in the concurrent controls.

To test leukocyte adhesion, samples of heparinized blood were passed through nylon columns and the percentage of leukocytes adhering to the columns was calculated (table 18-X). This test is usually reproducible if followed linearly, but it is known to be influenced by high levels of steroids, aspirin ingestion, alcohol ingestion, and inflammation. Two of the three astronauts (the CMP and the DMP) showed a decrease in leukocyte adherence on day F-5. However, the concurrent controls also showed decreased adherence values on that same day, although decreases did not occur to the same extent in all control individuals. The control

tests were much more stable on the day of recovery (R+0) and on day R+1, possibly making the decreases in PMN adherence in members of the prime crew significant. However, because of the fluctuations, the serial values in the prime crew are not significantly different from those obtained for the controls.

The ability of leukocytes to migrate in a modified Boyden chamber was measured both without a chemotactic stimulus (table 18-XI) and in response to the chemotactic agent casein (table 18-XII). A chemotactic index, expressed as the ratio of migration with casein compared to migration with no chemotactic agent, is presented in table 18-XIII. In general, the migration of leukocytes as quantitated in this manner remained within the normal range throughout the period of observation. Slightly decreased migration was noted on day R+8, but this decrease was also noted in the normal control. Because this test was performed at a temporary facility in Honolulu, comparative values obtained under the same field conditions are not available to determine whether migration was actually depressed or whether this decrease was a result of the testing conditions. The chemotactic index was preserved normally in the tests performed on day R+8.

The phagocytic capacity of PMN's was measured by allowing the leukocytes to form monolayers and then adding heat-killed staphylococci. The percentage of PMN's that were phagocytic was determined microscopically (table 18-XIV). Although some fluctuations occurred, the leukocytes retained the ability to ingest staphylococci in cells from the prime crew. When the total number of phagocytic PMN's was calculated, increased numbers of phagocytes were found in the prime crew following recovery (table 18-XV). This increase reflects the total increase in the leukocyte count. When the number of leukocytes containing large numbers of staphylococci (five or more) was calculated, the values for the prime crew were not as markedly elevated when compared to the controls (table 18-XVI). The conclusion concerning the phagocytosis test would be that no impairment in PMN phagocytic function was demonstrable using these techniques. In fact, because of the increased numbers of circulating leukocytes, the phagocytic capacity of the blood was enhanced.

SUMMARY

The studies summarized in this report constitute the first comprehensive effort to evaluate the effects of space flight and weightlessness on PMN function. Because of limitations imposed by the mission, blood samples obtained during weightlessness could not be tested. The values obtained for day R+0 reflect the effects both of the reentry stresses and of the unplanned inhalation of propellent gases. The sample obtained on day R+1 was drawn before the first dose of corticosteroid therapy was given, but the pulmonary changes in the astronauts were becoming evident at this time. The results of the tests performed on day R+8 must be interpreted in the context of corticosteroid therapy being administered to the astronauts for the pulmonary reaction following gas inhalation.

Despite these limitations and reservations, a comprehensive survey of leukocyte function is possible if performed serially in both the crew and control individuals. The data reported herein are still being analyzed in the context of larger groups of normal control individuals. The tentative conclusion, however, is that no consistent abnormality attributable to the period of weightlessness and space

flight was detected. Before the effects of space flight on polymorphonuclear leukocytes can be accurately determined, however, testing of samples obtained during flight without the influences of reentry, gas inhalation, and corticosteroid therapy will be necessary.

REFERENCES

18-1. Wintrobe, M. H.: The Leukocytes in Clinical Hematology. Lea and Febiger (Philadelphia), 1962, p. 214.

18-2. White, A.: Hormonal Steroids, Biochemistry, Pharmacology, and Therapeutics. Proceedings of the First International Congress of Hormonal Steroids, vol. I, Academic Press (New York), 1964, p. 571.

18-3. McCall, C. E.; Katayama, I.; Cotran, R. S.; and Finland, M.: Lysosomal and Ultrastructural Changes in Human "Toxic" Neutrophils During Bacterial Infection. J. Exp. Med., vol. 129, Feb. 1969, pp. 267-293.

18-4. McCall, C. E.; Caves, J.; Cooper, R.; and DeChatelet, L.: Functional Characteristics of Human Toxic Neutrophils. J. Infect. Dis., vol. 124, July 1971, pp. 68-75.

18-5. McGregor, R. R.; Spagnuolo, P. J.; and Lentnek, A. L.: Inhibition of Granulocyte Adherence by Ethanol, Prednisone, and Aspirin, Measured With an Assay System. N. Engl. J. Med., vol. 291, Sept. 1974, pp. 642-646.

18-6. Martin, R. R.; Warr, G. A.; Couch, R.; and Knight, V.: Chemotaxis of Human Leukocytes: Responsiveness to Mycoplasma Pneumoniae. J. Lab. Clin. Med., vol. 81, Apr. 1973, pp. 520-529.

18-7. Cline, M. J.: A New White Cell Test Which Measures Individual Phagocyte Function in a Mixed Leukocyte Population. I. A Neutrophil Defect in Acute Myelocytic Leukemia. J. Lab. Clin. Med., vol. 81, Feb. 1973, pp. 311-316.

TABLE 18-I.- TOTAL LEUKOCYTE COUNTS

[Cells per standard volume]

Subject	Day of observation						
	Before flight			After recovery			
	F-30	F-15	F-5	R+0	R+1	R+8	R+30
ACDR	8512	5567	9605	7 192	11 427	7 200	7076
CMP	6005	6375	4913	13 448	14 395	10 000	5304
DMP	5157	4324	3631	7 036	11 582	9 800	4127
A	7495	5139	5453	6 880	7 673	--	--
B	6757	8210	7429	5 329	6 344	--	--
C	7967	6306	5209	4 502	5 390	--	--
D	--	5364	[a]6991 [b]7397	[a]7 259 [b]7 479	7 074	--	[a]6012 [b]6384
E	6549	--	--	--	--	5 500	--
ACDR[c]	7736	5209	6009	--	--	--	--
CMP[c]	8679	8613	7516	--	--	--	--
DMP[c]	6043	7298	4592	--	--	--	--

[a]Morning sample.

[b]Afternoon sample.

[c]Backup crewmember.

TABLE 18-II.- DIFFERENTIAL LEUKOCYTE COUNTS

[Cells per standard volume]

Subject	Cell type	Day of observation						
		Before flight			After recovery			
		F-30	F-15	F-5	R+0	R+1	R+8	R+30
ACDR	Lymphocyte	51	40	55	23	25	27	46
	Neutrophil	46	57	42	74	73	64	46
	Eosinophil	2	1	1	1	1	6	3
	Basophil	0	1	1	0	1	0	1
	Monocyte	1	1	1	2	0	3	4
CMP	Lymphocyte	40	56	51	12	19	39	43
	Neutrophil	55	38	46	86	77	53	52
	Eosinophil	3	2	0	0	2	3	3
	Basophil	0	0	0	0	0	0	1
	Monocyte	2	4	3	2	2	5	1
DMP	Lymphocyte	56	60	68	14	17	42	42
	Neutrophil	38	36	29	79	80	52	52
	Eosinophil	3	2	1	0	0	2	3
	Basophil	1	1	0	0	0	0	0
	Monocyte	2	1	2	7	3	4	3
A	Lymphocyte	65	32	53	66	54	--	--
	Neutrophil	24	51	34	23	38	--	--
	Eosinophil	8	13	10	3	3	--	--
	Basophil	1	1	0	1	3	--	--
	Monocyte	2	3	3	7	2	--	--

TABLE 18-II.- Continued

Subject	Cell type	Day of observation						
		Before flight			After recovery			
		F-30	F-15	F-5	R+0	R+1	R+8	R+30
B	Lymphocyte	45	38	42	45	41	--	--
	Neutrophil	49	58	51	51	52	--	--
	Eosinophil	3	2	2	0	2	--	--
	Basophil	2	0	0	0	1	--	--
	Monocyte	1	2	5	4	4	--	--
C	Lymphocyte	39	20	31	52	47	--	--
	Neutrophil	58	65	61	41	48	--	--
	Eosinophil	2	3	5	5	3	--	--
	Basophil	0	1	2	0	0	--	--
	Monocyte	1	1	1	2	2	--	--
D	Lymphocyte	--	38	50/48	41/42	38	--	47
	Neutrophil	--	59	46/49	50/54	56	--	48
	Eosinophil	--	0	0/1	4/0	2	--	2
	Basophil	--	0	0/0	0/0	1	--	0
	Monocyte	--	3	4/2	5/2	3	--	3
E	Lymphocyte	33	--	--	--	--	38	--
	Neutrophil	63	--	--	--	--	56	--
	Eosinophil	2	--	--	--	--	2	--
	Basophil	0	--	--	--	--	0	--
	Monocyte	2	--	--	--	--	4	--

TABLE 18-II.- Concluded

Subject	Cell type	Day of observation						
		Before flight			After recovery			
		F-30	F-15	F-5	R+0	R+1	R+8	R+30
ACDR[a]	Lymphocyte	46	41	54	--	--	--	--
	Neutrophil	45	53	42	--	--	--	--
	Eosinophil	2	4	1	--	--	--	--
	Basophil	2	0	1	--	--	--	--
	Monocyte	5	2	2	--	--	--	--
CMP[a]	Lymphocyte	44	36	42	--	--	--	--
	Neutrophil	51	61	55	--	--	--	--
	Eosinophil	1	0	1	--	--	--	--
	Basophil	1	1	0	--	--	--	--
	Monocyte	3	2	2	--	--	--	--
DMP[a]	Lymphocyte	49	52	50	--	--	--	--
	Neutrophil	46	43	45	--	--	--	--
	Eosinophil	1	1	0	--	--	--	--
	Basophil	2	0	0	--	--	--	--
	Monocyte	2	4	5	--	--	--	--

[a]Backup crewmember.

TABLE 18-III.- TOTAL PMN COUNTS

[Cells per standard volume]

Subject	Day of observation						
	Before flight			After recovery			
	F-30	F-15	F-5	R+0	R+1	R+8	R+30
ACDR	3916	3173	4034	5 322	8 342	4608	3255
CMP	3303	2423	2260	11 565	11 084	5300	2758
DMP	1960	1557	1053	5 558	9 266	5096	2146
A	1799	2621	1854	1 582	2 916	--	--
B	3311	4762	3789	2 718	3 299	--	--
C	4621	4099	3177	1 846	2 587	--	--
D	--	3165	[a]3215	[a]3 360	3 961	--	[a]3487
			[b]3625	[b]4 039			[b]3064
E	4126	--	--	--	--	3080	--
ACDR[c]	3481	2761	2524	--	--	--	--
CMP[c]	4426	5254	4134	--	--	--	--
DMP[c]	2780	3138	2066	--	--	--	--

[a]Morning sample.

[b]Afternoon sample.

[c]Backup crewmember.

TABLE 18-IV.- LEUKOCYTE ALKALINE PHOSPHATASE: TOTAL NUMBER OF POSITIVE PMN'S

[Cells per standard volume]

Subject	Day of observation						
	Before flight			After recovery			
	F-30	F-15	F-5	R+0	R+1	R+8	R+30
ACDR	3564	2665	3066	4630	7841	4986	3255
CMP	2246	1696	1379	6708	8867	4876	2758
DMP	1274	1246	853	3390	8710	4790	2146
A	1673	1835	1224	886	1866	--	--
B	1788	3000	1819	1250	1188	--	--
C	3050	2090	1334	591	905	--	--
D	--	[a]3023 [b]2216	[a]2348 [b]2683	[a]1742 [b]2585	3129	--	[a]2301 [b]1900
E	[a]2630 [b]3260	--	--	--	--	2587	--
ACDR[c]	1949	2098	1565	--	--	--	--
CMP[c]	4116	4729	3307	--	--	--	--
DMP[c]	2029	2479	1364	--	--	--	--

[a]Morning sample.

[b]Afternoon sample.

[c]Backup crewmember.

TABLE 18-V.- LEUKOCYTE ALKALINE PHOSPHATASE: TOTAL SCORE OF POSITIVE PMN'S

[Cells per standard volume]

Subject	Day of observation						
	Before flight			After recovery			
	F-30	F-15	F-5	R+0	R+1	R+8	R+30
ACDR	144	128	96	138	133	158	117
CMP	106	89	69	68	95	130	101
DMP	91	119	94	90	129	160	88
A	93	103	72	80	87	--	--
B	58	82	48	50	45	--	--
C	89	60	43	33	37	--	--
D	--	[a]93 [b]94	[a]89 [b]88	[a]63 [b]83	104	--	[a]71 [b]73
E	[a]101 [b]111	--	--	--	--	113	--
ACDR[c]	67	104	74	--	--	--	--
CMP[c]	151	145	96	--	--	--	--
DMP[c]	95	117	82	--	--	--	--

[a]Morning sample.

[b]Afternoon sample.

[c]Backup crewmember.

TABLE 18-VI.- LEUKOCYTE ALKALINE PHOSPHATASE: MEAN SCORE OF POSITIVE PMN'S

[Cells per standard volume]

Subject	Day of observation						
	Before flight			After recovery			
	F-30	F-15	F-5	R+0	R+1	R+8	R+30
ACDR	158	152	126	159	141	166	144
CMP	156	127	113	117	119	141	120
DMP	140	149	116	148	137	170	117
A	141	147	109	143	136	--	--
B	107	130	100	109	125	--	--
C	135	118	102	103	106	--	--
D	--	[a]126 [b]134	[a]122 [b]119	[a]131 [b]130	132	--	[a]108 [b]118
E	[a]131 [b]141	--	--	--	--	135	--
ACDR[c]	120	137	119	--	--	--	--
CMP[c]	162	161	120	--	--	--	--
DMP[c]	130	148	124	--	--	--	--

[a]Morning sample.

[b]Afternoon sample.

[c]Backup crewmember.

TABLE 18-VII.- LEUKOCYTE ACID PHOSPHATASE: TOTAL POSITIVE PMN'S

[Cells per standard volume]

Subject	Day of observation						
	Before flight			After recovery			
	F-30	F-15	F-5	R+0	R+1	R+8	R+30
ACDR	3877	2697	3711	2759	6090	5196	3255
CMP	3303	2399	1966	9715	9754	5194	2758
DMP	1960	1557	990	4724	7413	5096	2146
A	1799	2569	1557	1187	2295	--	--
B	3311	4619	3334	2419	2705	--	--
C	4621	4099	2828	1329	2173	--	--
D	--	[a]4085 [b]3165	[a]3216 [b]3625	[a]3630 [b]4039	3961	--	[a]3487 [b]3063
E	[a]3415 [b]3507	--	--	--	--	3080	--
ACDR[c]	3481	2733	2297	--	--	--	--
CMP[c]	4426	5201	3473	--	--	--	--
DMP[c]	2780	3138	1756	--	--	--	--

[a]Morning sample.

[b]Afternoon sample.

[c]Backup crewmember.

TABLE 18-VIII.- LEUKOCYTE ACID PHOSPHATASE: TOTAL PMN SCORE

[Cells per standard volume]

Subject	Day of observation						
	Before flight			After recovery			
	F-30	F-15	F-5	R+0	R+1	R+8	R+30
ACDR	117	91	100	79	74	124	156
CMP	124	116	95	92	98	107	151
DMP	130	121	99	91	87	134	159
A	125	123	88	78	92	--	--
B	124	112	93	97	84	--	--
C	116	145	99	80	86	--	--
D	--	[a]99 [b]96	[a]108 [b]93	[a]89 [b]84	87	--	[a]155 [b]156
E	[a]126 [b]89	--	--	--	--	125	--
ACDR[c]	124	122	100	--	--	--	--
CMP[c]	150	120	106	--	--	--	--
DMP[c]	120	129	91	--	--	--	--

[a]Morning sample.

[b]Afternoon sample.

[c]Backup crewmember.

TABLE 18-IX.- LEUKOCYTE ACID PHOSPHATASE: MEAN PMN SCORE

[Cells per standard volume]

Subject	Day of observation						
	Before flight			After recovery			
	F-30	F-15	F-5	R+0	R+1	R+8	R+30
ACDR	118	107	109	110	101	125	156
CMP	124	117	109	110	111	141	151
DMP	130	121	105	107	109	134	159
A	125	126	105	104	103	--	--
B	124	115	106	109	102	--	--
C	116	145	111	111	102	--	--
D	--	[a]116 [b]114	[a]117 [b]109	[a]110 [b]105	102	--	[a]155 [b]156
E	[a]126 [b]105	--	--	--	--	125	--
ACDR[c]	124	123	110	--	--	--	--
CMP[c]	150	121	126	--	--	--	--
DMP[c]	120	129	107	--	--	--	--

[a]Morning sample.

[b]Afternoon sample.

[c]Backup crewmember.

TABLE 18-X.- PERCENTAGE OF PMN ADHERENCE

Subject	Day of observation						
	Before flight			After recovery			
	F-30	F-15	F-5	R+0	R+1	R+8	R+30
ACDR	94.1	--	89.6	88.1	77.3	91.4	74.2
CMP	81.3	78.8	53.2	61.6	80.3	65.4	56.2
DMP	87.0	89.5	62.3	76.9	77.0	81.9	74.4
A	96.8	89.0	81.0	88.5	90.9	--	--
B	89.2	89.6	81.6	83.1	89.4	--	--
C	94.0	93.8	78.7	81.6	85.3	--	--
D	--	[a]84.4	[a]56.4	[a]81.4	75.6	--	[a]77.9
		[b]84.2	[b]85.5	[b]94.3			[b]72.6
E	76.8	--	--	--	--	70.9	--
ACDR[c]	80.5	75.2	67.2	--	--	--	--
CMP[c]	80.5	93.1	67.4	--	--	--	--
DMP[c]	80.4	84.1	52.0	--	--	--	--

[a]Morning sample.

[b]Afternoon sample.

[c]Backup crewmember.

TABLE 18-XI.- LEUKOTAXIS: RANDOM PMN MIGRATION

[Cells per high-power microscopic field]

Subject	Day of observation						
	Before flight			After recovery			
	F-30	F-15	F-5	R+0	R+1	R+8	R+30
ACDR	9.6	2.3	10.67	10.0	6.93	3.87	6.33
CMP	22.27	13.4	16.03	7.37	12.87	5.6	10.25
DMP	19.47	3.6	10.85	7.70	12.8	1.67	--
A	5.6	7.8	9.93	4.23	3.93	--	--
B	4.7	13.87	5.3	6.07	5.6	--	--
C	6.4	5.0	29.2	5.2	3.2	--	--
D	--	[a]31.47 [b]16.27	[a]11.1 [b]6.5	[a]4.77 [b]5.2	9.33	--	10.57
E	7.7	--	--	--	--	2.73	--
ACDR[c]	2.43	9.0	25.87	--	--	--	--
CMP[c]	7.97	20.93	9.17	--	--	--	--
DMP[c]	2.47	1.65	7.55	--	--	--	--

[a]Morning sample.

[b]Afternoon sample.

[c]Backup crewmember.

TABLE 18-XII.- LEUKOTAXIS: PMN CHEMOTAXIS TO CASEIN

[Cells per high-power microscopic field]

Subject	Day of observation						
	Before flight			After recovery			
	F-30	F-15	F-5	R+0	R+1	R+8	R+30
ACDR	70.93	76.4	70.8	45.2	82.93	27.2	50.26
CMP	48.4	41.2	73.47	88.67	65.2	40.9	44.67
DMP	76.0	8.25	50.2	78.67	64.53	17.6	--
A	22.6	41.6	63.5	73.47	81.6	--	--
B	29.87	33.2	35.87	56.4	38.8	--	--
C	37.87	21.8	45.7	12.17	60.8	--	--
D	--	[a]68.5 [b]52.57	[a]100.4 [b]93.2	[a]68.0 [b]74.67	72.8	--	76.1
E	79.7	--	--	--	--	20.4	--
ACDR[c]	20.13	28.2	83.07	--	--	--	--
CMP[c]	24.03	48.0	82.8	--	--	--	--
DMP[c]	12.07	29.0	114.4	--	--	--	--

[a]Morning sample.

[b]Afternoon sample.

[c]Backup crewmember.

TABLE 18-XIII.- CHEMOTACTIC INDEX OF LEUKOTAXIS

[Stimulated migration/random migration]

Subject	Day of observation						
	Before flight			After recovery			
	F-30	F-15	F-5	R+0	R+1	R+8	R+30
ACDR	7.38	33.2	6.64	4.52	11.97	7.03	7.94
CMP	2.17	3.07	4.58	12.03	5.07	7.31	4.36
DMP	3.90	2.29	4.63	10.22	5.04	10.54	--
A	4.04	5.33	6.40	17.37	20.76	--	--
B	6.36	2.39	6.77	9.29	6.93	--	--
C	5.92	4.36	1.57	2.34	19.0	--	--
D	--	[a]2.18 [b]3.21	[a]9.04 [b]14.4	[a]14.26 [b]14.36	7.80	--	7.20
E	10.35	--	--	--	--	7.47	--
ACDR[c]	8.28	3.13	3.21	--	--	--	--
CMP[c]	3.02	2.29	9.03	--	--	--	--
DMP[c]	4.89	17.58	15.2	--	--	--	--

[a]Morning sample.

[b]Afternoon sample.

[c]Backup crewmember.

TABLE 18-XIV.- PERCENTAGE OF PHAGOCYTIC PMN'S

[Cells per standard volume]

Subject	Time, min	Day of observation						
		Before flight			After recovery			
		F-30	F-15	F-5	R+0	R+1	R+8	R+30
ACDR	3	9	5	5	30	1	22	10
	6	15	14	21	70	5	38	15
	10	7	24	19	72	19	38	21
	15	26	41	18	89	30	51	12
CMP	3	5	4	6	3	4	4	13
	6	11	9	7	5	4	23	17
	10	13	15	9	31	11	29	21
	15	23	28	18	37	22	15	9
DMP	3	7	6	8	6	6	3	7
	6	8	13	11	10	9	8	5
	10	6	12	8	23	17	15	25
	15	13	28	16	20	23	27	18
A	3	6	6	9	3	18	--	--
	6	13	4	15	3	31	--	--
	10	11	17	31	8	41	--	--
	15	14	29	45	28	31	--	--
B	3	14	9	20	25	13	--	--
	6	25	10	20	54	17	--	--
	10	18	16	10	89	25	--	--
	15	30	26	16	96	29	--	--

TABLE 18-XIV.- Continued

Subject	Time, min	Day of observation						
		Before flight			After recovery			
		F-30	F-15	F-5	R+0	R+1	R+8	R+30
C	3	14	4	9	6	6	--	--
	6	15	8	23	12	20	--	--
	10	41	16	10	15	29	--	--
	15	20	20	14	14	57	--	--
D	3	--	$^{a}6$ $^{b}12$	$^{a}14$ $^{b}9$	$^{a}4$ $^{b}7$	5	--	$^{a}3$ $^{b}10$
	6	--	$^{a}7$ $^{b}12$	$^{a}14$ $^{b}17$	$^{a}9$ $^{b}15$	8	--	$^{a}8$ $^{b}11$
	10	--	$^{a}10$ $^{b}25$	$^{a}22$ $^{b}12$	$^{a}18$ $^{b}16$	7	--	$^{a}24$ $^{b}13$
	15	--	$^{a}22$ $^{b}24$	$^{a}12$ $^{b}17$	$^{a}35$ $^{b}38$	32	--	$^{a}15$ $^{b}19$
E	3	10	--	--	--	--	18	--
	6	16	--	--	--	--	27	--
	10	22	--	--	--	--	48	--
	15	18	--	--	--	--	42	--
ACDR[c]	3	4	3	3	--	--	--	--
	6	15	8	14	--	--	--	--
	10	20	13	18	--	--	--	--
	15	18	25	19	--	--	--	--

TABLE 18-XIV.- Concluded

Subject	Time, min	Day of observation						
		Before flight			After recovery			
		F-30	F-15	F-5	R+0	R+1	R+8	R+30
CMP[c]	3	6	2	5	--	--	--	--
	6	12	14	10	--	--	--	--
	10	22	15	11	--	--	--	--
	15	13	20	18	--	--	--	--
DMP[c]	3	5	--	8	--	--	--	--
	6	7	--	11	--	--	--	--
	10	22	--	12	--	--	--	--
	15	17	--	9	--	--	--	--

[a]Morning sample.

[b]Afternoon sample.

[c]Backup crewmember.

TABLE 18-XV.- NUMBER OF PHAGOCYTIC PMN'S

[Cells per standard volume]

Subject	Time, min	Day of observation						
		Before flight			After recovery			
		F-30	F-15	F-5	R+0	R+1	R+8	R+30
ACDR	3	352	159	202	1597	83	1155	326
	6	587	444	847	3725	417	1994	488
	10	274	762	767	3832	1585	1994	684
	15	1018	1303	726	4737	2502	2676	391
CMP	3	165	97	154	359	443	212	359
	6	363	218	179	599	443	1219	469
	10	429	264	230	3710	1219	1537	579
	15	760	678	461	4429	2438	795	248
DMP	3	137	100	84	342	556	153	150
	6	157	217	116	569	834	408	107
	10	118	201	84	1310	1575	764	537
	15	255	468	169	1140	2131	1376	386
A	3	108	157	167	47	525	--	--
	6	234	105	278	47	904	--	--
	10	199	446	575	127	1196	--	--
	15	252	760	834	443	904	--	--
B	3	464	429	758	679	429	--	--
	6	794	476	758	1468	561	--	--
	10	596	762	379	2419	825	--	--
	15	993	1238	606	2609	957	--	--

TABLE 18-XV.- Continued

Subject	Time, min	Day of observation						
		Before flight			After recovery			
		F-30	F-15	F-5	R+0	R+1	R+8	R+30
C	3	647	164	286	111	155	--	--
	6	693	328	731	222	518	--	--
	10	1895	656	317	277	751	--	--
	15	924	820	445	258	1476	--	--
D	3	--	[a]245 [b]379	[a]489 [b]326	164	198	--	[a]105 [b]306
	6	--	[a]286 [b]379	[a]489 [b]616	370	317	--	[a]279 [b]337
	10	--	[a]409 [b]791	[a]769 [b]435	740	277	--	[a]837 [b]398
	15	--	[a]899 [b]760	[a]386 [b]616	1439	1286	--	[a]523 [b]582
E	3	206	--	--	--	--	554	--
	6	330	--	--	--	--	832	--
	10	412	--	--	--	--	1478	--
	15	742	--	--	--	--	1294	--

[a]Morning sample.

[b]Afternoon sample.

TABLE 18-XV.- Concluded

Subject	Time, min	Day of observation						
		Before flight			After recovery			
		F-30	F-15	F-5	R+0	R+1	R+8	R+30
ACDR[c]	3	139	83	76	--	--	--	--
	6	522	221	353	--	--	--	--
	10	696	359	454	--	--	--	--
	15	626	690	479	--	--	--	--
CMP[c]	3	266	105	207	--	--	--	--
	6	531	736	413	--	--	--	--
	10	974	788	455	--	--	--	--
	15	575	1051	744	--	--	--	--
DMP[c]	3	139	--	165	--	--	--	--
	6	195	--	227	--	--	--	--
	10	612	--	248	--	--	--	--
	15	473	--	186	--	--	--	--

[c]Backup crewmember.

TABLE 18-XVI.- NUMBER OF PHAGOCYTIC PMN'S WITH FIVE OR MORE STAPHYLOCOCCI

Subject	Time, min	Day of observation						
		Before flight			After recovery			
		F-30	F-15	F-5	R+0	R+1	R+8	R+30
ACDR	3	0	0	0	426	0	367	33
	6	0	64	0	852	334	840	0
	10	0	159	81	1277	834	525	98
	15	157	571	121	2076	1501	1102	163
CMP	3	0	0	0	120	0	0	28
	6	33	24	0	120	111	106	0
	10	33	97	51	2513	443	265	110
	15	33	145	26	3351	1108	424	28
DMP	3	0	0	0	57	278	0	0
	6	0	17	0	0	278	0	0
	10	20	0	11	456	648	204	64
	15	0	117	0	513	1019	204	129
A	3	0	0	0	0	58	--	--
	6	18	0	37	0	117	--	--
	10	18	26	297	63	233	--	--
	15	0	184	222	233	204	--	--
B	3	33	48	0	163	132	--	--
	6	0	0	0	462	330	--	--
	10	0	286	0	1142	495	--	--
	15	331	667	75	1359	627	--	--

TABLE 18-XVI.- Continued

Subject	Time, min	Day of observation						
		Before flight			After recovery			
		F-30	F-15	F-5	R+0	R+1	R+8	R+30
C	3	92	0	0	0	0	--	--
	6	0	0	0	55	129	--	--
	10	508	82	0	148	285	--	--
	15	231	328	32	148	751	--	--
D	3	--	[a]0 [b]0	[a]70 [b]0	41	0	--	[a]0 [b]0
	6	--	[a]0 [b]0	[a]70 [b]0	0	40	--	[a]35 [b]61
	10	--	[a]82 [b]32	[a]0 [b]0	205	119	--	[a]105 [b]92
	15	--	[a]286 [b]379	[a]0 [b]0	1234	634	--	[a]105 [b]30
E	3	0	--	--	--	--	92	--
	6	0	--	--	--	--	185	--
	10	0	--	--	--	--	400	--
	15	7	--	--	--	--	462	--

[a]Morning sample.

[b]Afternoon sample.

TABLE 18-XVI.- Concluded

Subject	Time, min	Day of observation						
		Before flight			After recovery			
		F-30	F-15	F-5	R+0	R+1	R+8	R+30
ACDR[c]	3	0	0	0	--	--	--	--
	6	104	0	25	--	--	--	--
	10	104	0	25	--	--	--	--
	15	104	110	101	--	--	--	--
CMP[c]	3	44	0	0	--	--	--	--
	6	133	53	0	--	--	--	--
	10	133	158	83	--	--	--	--
	15	89	158	83	--	--	--	--
DMP[c]	3	28	--	0	--	--	--	--
	6	28	--	0	--	--	--	--
	10	167	--	0	--	--	--	--
	15	83	--	0	--	--	--	--

[c]Backup crewmember.

19. *KILLIFISH HATCHING AND ORIENTATION*

EXPERIMENT MA-161

H. W. Scheld,[a†] J. F. Boyd,[b] G. A. Bozarth,[b] J. A. Conner,[c]
V. B. Eichler,[d] P. M. Fuller,[e] R. B. Hoffman,[f] J. R. Keefe,[e]
K. P. Kuchnow,[g] J. M. Oppenheimer,[h] G. A. Salinas,[b]
and R. J. von Baumgarten[i]

ABSTRACT

In the Apollo-Soyuz Test Project Killifish Hatching and Orientation Experiment, the killifish Fundulus heteroclitus was used as a model system for study of embryonic development and vestibular adaptation in orbital flight. The experiment package consisted of two parts: a series of staged embryos in five individual compartments of a polyethylene bag and a series of preconditioned juvenile fish in a similar bag. Embryos at 32, 66, 128, 216, and 336 hours after fertilization at the time of launch were chosen to represent key stages of development; development occurred at a constant temperature of 295 K (22° C). Juvenile fish were reared from hatching for 21 days in specific visual environments.

Experiment packages were mounted on the docking module wall and photographed periodically during the mission to record the swimming activity of the fish and the condition of the eggs. At splashdown, vestibular sensitivity of the juvenile fish and of hatchlings from the eggs was tested in a rotating, striped drum. Subsequently, additional vestibular orientation tests during parabolic-trajectory flight, light orientation tests, and geotaxis tests were performed. Samples of juveniles

---

[a]Baylor College of Medicine.

[b]Northrop Services Inc.

[c]Rice University.

[d]Wichita State University.

[e]University of Louisville.

[f]NRC-NASA Resident Research Associate.

[g]Texas A. & M. University.

[h]Bryn Mawr College.

[i]University of Mainz, Germany.

[†]Principal Investigator.

and hatchlings/embryos were fixed for microscopic examination at splashdown and at selected times thereafter. Sampling for microscopy and testing of vestibular function will be continued through maturity of the fish.

Juvenile fish in a null-gravity environment exhibited looping swimming activity similar to that observed during the Skylab 3 mission. Hatchlings from the 336-hour egg stage also were observed to loop. At splashdown, both juveniles and hatchlings exhibited a typical diving response suggesting relatively normal vestibular function. The juveniles exhibited swimming patterns suggestive of abnormal swim bladders. Rotating drum tests confirmed that no radical changes in vestibular function had occurred, but more subtle changes may be apparent after careful analysis of motion picture records. The embryos exhibited no apparent gross abnormalities resulting from development in a null-gravity environment. Extensive light and electron microscopic analyses of flight and control animals are currently underway.

INTRODUCTION

The Apollo-Soyuz Test Project (ASTP) killifish experiment was the second in a series of experiments to evaluate the hazards inherent in the exposure of living organisms to the space environment during critical portions of the life cycle or for extended periods. The points of primary emphasis were the function and development of the vestibular system and calcium metabolism, particularly as it relates to otolith development.

The experimental organism was Fundulus heteroclitus (Walbaum), a small shallow-water minnow common along the Atlantic coast. This organism has been used in experimental embryology for many years, and its biology and developmental relationships are well known (refs. 19-1 to 19-3). Fundulus was used as a test organism at the NASA Lyndon B. Johnson Space Center (JSC) during the lunar quarantine. Subsequently, the methodology for continuous laboratory production of fertile eggs was developed in this laboratory (ref. 19-4). The Beaufort, North Carolina, strain of Fundulus produces an egg having a transparent chorion that is extremely tough. Development may thus be observed from the first cleavage to hatching, and during this time, the egg may be manipulated extensively without undue stress on the developing embryo. The approximately 2-week period of development is convenient for most laboratory experiments, and the resulting hatchling is relatively large (approximately 1 centimeter long) with much of the length taken up by the head. The vestibular region, the eyes, and the brain are relatively large at this stage. Overall, the Fundulus embryo offers a high-quality system for flight experimentation under available flight conditions.

EXPERIMENT BACKGROUND AND DESCRIPTION

A Fundulus experiment was included on the Skylab 3 mission in an abbreviated and informal demonstration form. The Skylab package consisted of a plastic bag containing 2 juvenile fish in a compartment with 250 milliliters of synthetic seawater

(21 parts per thousand dissolved solids) and 50 fertilized eggs (5 days past fertilization) in a separate compartment with 50 milliliters of seawater. Initially, the juveniles exhibited obvious disorientation reactions (swimming rapidly in loops and circles), but over a period of several days in orbit, they gradually adapted to the weightless environment and to dependence on visual cues for orientation. In this state of adaptation, the locker door surface to which the plastic aquarium was attached served as "down." Adaptation was not complete, however, and occasional disoriented swimming activity occurred. Nearly all the 50 eggs hatched in space, and because of a delay in hatching of the flight fish, several returned alive to Earth. However, a series of unfortunate events resulted in the death of these animals shortly after return. The space-hatched Fundulus fry exhibited no observable tendency toward disoriented swimming activity, and their apparent dependence on visual orientation cues both onboard the Skylab spacecraft and on the recovery ship suggested the possible absence of vestibular input. Preservation of the returned hatchlings was insufficient to prevent deterioration and did not permit definite conclusions regarding the condition of the vestibular system. Typical otoliths, however, were not visible in microscopic sections of the flight fish.

The ASTP killifish experiment was designed to confirm and extend the Skylab 3 observations of vestibular disturbance and embryonic development. Calcium loss has been observed in humans after exposure in space, and otolith development is, in fact, largely concerned with calcium metabolism. Therefore, observations of otolith development are important not only because of the importance of the vestibular system in balance but also because of the possible use of the otolith as a model for space research on calcium metabolism in general.

The Skylab observations also raised several questions regarding mechanisms of vestibular disturbance and adaptation in the Fundulus and its usefulness as a model for vestibular research. The primary questions asked in the ASTP experiment were related to the rate of adaptation, which is only sketchily known from the Skylab experiment, and the role of the visual system in orientation and adaptation to null-gravity conditions.

Experimental Design

The experiment consisted of a two-part experimental package (package A, fig. 19-1) that was exposed in orbital flight and of four control treatment packages. Except for the treatment designated "launch control," all packages contained the experimental materials enumerated in table 19-I. The following control packages were used.

1. Transport control (package C-I): This package was transported with the flight package. During the mission, it was exposed to a constant temperature (296 K (23° C)) and to the predicted atmospheric pressure and oxygen (O_2) partial pressure profile of the ASTP spacecraft. Recovery processing and return to JSC paralleled those of the flight treatment package.

2. Laboratory air control (package C-II): Immediately after packing, the fish and egg packages were placed in a 295-K (22° C) incubator under standard atmospheric conditions until recovery. Subsequent handling was similar to that for the flight treatment package.

3. The 48-hour lag control in ASTP-simulated air (package C-III): Eggs were fertilized and packages prepared on a schedule precisely 48 hours behind the flight schedule. All timing and conditions of preparation of flight packages were duplicated. At launch time, the package was exposed to a simulated launch vibration profile and then placed in an atmosphere chamber for exposure to simulated spacecraft atmosphere. Atmosphere (O_2 partial pressure) and temperature were programed to duplicate the averaged readings of the spacecraft sensors. Recovery activities paralleled those of the flight treatment package.

4. Launch control: Smaller samples of eggs (10) and fish (2) were prepared in parallel to the flight controls and the 48-hour lag controls and were transported with these treatment packages. At lift-off, these samples were killed and fixed to provide a record of developmental condition at lift-off.

Experiment Theory

The embryo development portion of the experiment was designed to isolate the effects of exposure to a null-gravity environment in progressively more advanced stages of embryo development. The ages were selected as probable average times for the onset of key stages of development with particular reference to the vestibular system and otolith development. Development time varies somewhat within the population but is essentially complete by 9 to 11 days, and most of the eggs may be stimulated to hatch at the end of 14 days under standard laboratory conditions. Thus, in a majority of the flight treatment eggs, all subsequent embryogenesis was completed in the near-null-gravity conditions of orbital flight. The three later stages, 128, 216, and 336 hours, theoretically were fully developed and capable of hatching in orbit. One experiment objective was to observe and record swimming activities of the hatchlings from these eggs to confirm the apparent adaptation of the Skylab hatchlings.

Embryos of different ages (table 19-I) were obtained by stripping ova and milt from adult Fundulus (ref. 19-4) and combining these to effect fertilization at the given prelaunch times. Fertilized eggs were then incubated in plastic petri dishes containing synthetic seawater (21 parts per thousand dissolved solids) at a constant temperature of 295 K (22° C). Each petri dish contained a maximum of 50 eggs that were washed daily with filter-sterilized synthetic seawater to ensure removal of metabolic products and contaminating micro-organisms. Between 30 and 26 hours before launch, all eggs were sorted, given a final wash, and sealed into the compartments of the plastic flight package.

The vestibular adaptation portion of the experiment was designed to extend previous observations of Fundulus swimming behavior in a null-gravity environment. The cause of the observed disorientation in the fish is largely unknown, although the vestibular system is presumed to be primarily responsible. The observed adaptation during the Skylab 3 mission was apparently based partly on a

switch to dependence on the visual system for orientational cues. The entire process is of more than passing interest because it parallels in many ways the patterns reported for human adjustment to weightlessness, and findings regarding vestibular adaptation in fish could usefully be applied to humans (ref. 19-5). Because of time and space limitations, the experimental scheme was not intended to produce profound conclusions; it was simply an attempt to refine previous measurements of rate of adaptation and to define the nature of the visual stimulus (light direction or background surface) in the apparent habituation of fish to null-gravity conditions. Of equal importance was the observation of readaptation of the partly space-adapted fish to one-g conditions.

The experiment package consisted of several small plastic-film bags (fig. 19-1), each containing a number (table 19-I) of Fundulus fry (immature fish 21 days old at time of launch) that had been reared from hatching in tanks presenting different visual environments (table 19-I). The swimming activity of the fish was recorded with a motion picture camera at various times during the flight with the objective of measuring general rate of adaptation as well as orientation patterns and relative rates of adaptation of the visually conditioned fish.

Data Collection

The data yield of the experiment consisted of visual observations from the flight, motion picture recordings of the condition and activity of experimental animals during and after the flight, animals for microscopic examination that were killed and fixed at recovery and at subsequent selected sampling times up to maturity, and results of vestibular sensitivity tests taken at recovery and for an indeterminate time after recovery.

The primary objective of the histological sampling was to detect anatomical differences in the flight animals that could be correlated with behavioral differences and to record any observable readjustments that might occur in the developing animals after their return. Samples of juvenile fish were fixed at splashdown and several weeks later following completion of behavioral testing. Hatchlings and unhatched eggs were sampled at recovery, at approximately daily intervals for the first week after splashdown, and again at 2 weeks, 1 month, and 6 months to provide a picture of progressive changes. Analysis involved, as a first stage, serial sectioning of the fixed animals for light and electron microscopy of the head and particularly the vestibular organs. Key points of interest were development of the otolith and the associated sensory tissue. Subsequent study will depend on initial results, but probable further areas of interest are general calcium deposition and development of other sensory systems.

Postflight testing was performed on both fry and hatchlings from the flight and control treatment packages with the objective of detecting and measuring differences in orientation behavior attributable to null-gravity exposure during development. The tests used were the rotating striped-drum test, the light orientation test, the geotaxis test, and brief exposure to null-gravity conditions during parabolic-trajectory flight. In each case, the response of the vestibular system was measured.

The classical fish otolith tests (ref. 19-6) are based on measurements of the fish longitudinal-axis tilt from the horizontal when the direction of water currents or of illumination is varied. At the University of Mainz, an additional otolith test that works especially well with very young and small fish has been developed. The fish tank containing the unrestrained fish is placed inside first a vertical and later a horizontal rotating striped drum. In the vertical drum, the fish visually lock with the stripes and swim around inside the drum keeping pace with the moving stripe (fig. 19-2(a)). In the horizontal drum, the fish are prevented from looping solely by action of the otolith system (fig. 19-2(b)). However, if the fish face the stripes, their bodies are tilted in the direction of stripe movement. The fish that are turned 90° away from the stripes roll to a measurable degree in the direction of the drum rotation, but again are prevented from tilting further by the action of their otolith system. Abnormal tilt indicates a lowered sensitivity of the otolith system. The fish tested were inside a sealed tank, which was placed inside the drum for varying times of at least 1 minute in both horizontal and vertical drum positions. Tilt angle and movements were recorded by a motion picture camera for later single-frame analysis.

In addition to the rotating striped-drum test, a light orientation test was given to the juvenile fish. The purpose of this test was to further evaluate the ability of the juvenile fish to orient in the geogravitational environment after a 9-day exposure to weightlessness. Although it is well known that fish maintain their relative vertical orientation by integrating sensory information from the influences of both gravity and light (ref. 19-6), it was not known whether the exposure only to light cues during a 9-day period would affect this integration when the fish were reintroduced into the normal one-g environment.

In the normal geogravity environment, fish maintain their equilibrium orientation by static and optic stimuli. If these stimuli do not operate in the vertical direction, the fish takes a position between the vertical plane and the incidence of the light (ref. 19-7). For example, if a light is placed in a darkened chamber at a 90° angle relative to the vertical plane, the fish will roll about its body axis toward the light and the dorsal fin will form a 30° to 60° angle relative to the vertical plane. (The exact magnitude of the angle varies with species of fish and other environmental factors such as light intensity and dark adaptation.) Normally, fish live in an environment in which light is overhead and therefore represents a reference for the vertical in addition to the sensing of gravity. The fish rolls toward the light source to accommodate its sensory inputs in the new 90° test environment. If the light intensity is increased, the fish will roll even farther toward the light up to a point. If gravity is increased (as in a centrifuge), the fish will roll back toward the gravitational vertical. The static vestibular sense is the more dominant of the two systems, but if it is damaged (as in ablation studies), the fish will orient strictly with respect to the dominant light direction. Therefore, the light orientation test was an attempt to measure a possible modification of the gravitational receptors due to a 9-day exposure to null-gravity conditions.

In this test, each juvenile fish was placed in a clear Plexiglas cylinder and its dorsal fin orientation was measured after a 40-watt bulb was placed 14 centimeters to the right of the fish (90° relative to the vertical plane) for 30 minutes and then to the left for the same period. One minute of dark adaptation was permitted before each test interval, and right and left tests were randomized. Each fish was

given one trial (left and right orientations) in any given test day. All fish were tested sequentially until four trials per fish were made over a period of several days.

A geotaxis test for small fish has been developed at JSC. In this test, a fish is gently placed just below the meniscus of the synthetic seawater in a graduated cylinder filled to the 500-milliliter mark. The amount of time spent in the upper half of the cylinder is recorded over a 2-minute interval as a measure of the geotaxis response. This diving response is very strong in the majority of Fundulus heteroclitus; therefore, the test was a measure of whether or not this innate vestibular program was modified by an exposure to null-gravity conditions during embryonic development.

Experiment Execution

Execution of the flight portion of the experiment was, relatively, the simplest part. The prepared flight package was transported to the launch site in a T-38 aircraft between 26 and 23 hours before launch and placed in a storage locker of the command module approximately 9 hours before launch. At approximately 30 hours after launch, the metal and glass cloth flight container was opened and the experimental packages were mounted on the docking module wall for the duration of the mission. Motion pictures were taken of the fish package at this time. No photography or observations were scheduled during the joint phase of the mission because of the heavy demands placed on the crew during that time. Daily observations were recorded in the flight notes, and motion pictures were made on mission day 6 and all subsequent days of the mission. Following photography on mission day 9, the packages were returned to the flight container and stored for reentry.

Eight hours after recovery, the flight package was removed from the command module and photographed to record initial swimming activity. Hatching was induced by agitation on a rotary shaker, and samples of eggs, hatchlings, and juvenile fish were killed and fixed for microscopic examination. Additional samples were fixed at selected intervals after recovery. Upon return of experimental materials to the laboratory 2 days after recovery, selected specimens were injected with tritiated thymidine and killed after a 1-hour exposure.

Testing for vestibular sensitivity by the rotating drum method was begun as soon as the fish and hatchlings were removed from the flight packages and was continued for several days after splashdown. Following return to the laboratory, testing of light orientation response was initiated and continued for several weeks. The first test of orientation in parabolic-trajectory flight was completed 5 days after recovery.

Continuation of the experiment will involve rearing the remaining hatchlings to maturity and eventually producing a new generation from the flight-developed animals. Additional periodic observations will be made to assess vestibular function in the maturing fish. Limited numbers of animals will be killed for anatomical studies.

RESULTS

The experiment was accomplished as scheduled. The only major loss of data was the initial photography, apparently because of an improperly seated camera magazine. Looping swimming activity similar to that on the Skylab 3 mission was observed in juveniles and in hatchlings from the 336-hour egg group. Some adaptation to null-gravity conditions apparently occurred during the 9-day mission, but when the flight package was opened 8 hours after splashdown, all juveniles and hatchlings initially exhibited a typical diving response suggesting that vestibular systems were in relatively good working order. After recovery from their initial fright, most fish swam in a manner that indicated low buoyancy, probably as a result of deflated swim bladders. No radical alterations in orientation behavior or vestibular function were observed. Any alterations were relatively subtle and will be apparent only from careful statistical treatment of the data.

Films from the flight, from postflight testing in the rotating drum, and from tests in parabolic-trajectory flight are currently undergoing single-frame analysis. Results from these tests will be reported when the analyses are complete.

The results of light orientation tests on the juvenile fish are presented in table 19-II as the group means of the roll angles for the light orientations. The C-I group was omitted because only four juveniles survived and two died midway through the test period. The roll angles were highly variable for all groups, and the mean values for each group for four trials were similar. There were no significant differences. The ASTP flight juveniles were slightly more variable, particularly for 90° light orientations on the right side of the fish, but this deviation is mentioned only for the sake of data completeness.

The light orienting of the Fundulus heteroclitus appears to be much more stable (unpublished observations) in adults than in juveniles. Several competing responses in the juvenile Fundulus apparently increase the difficulty of obtaining a reliable measure of the roll orientation. It is possible to place an adult in a Plexiglas cylinder and position its body perpendicular to the light rays for 30 minutes and thereby to enable observation of a slow roll to a final angle toward the light. However, the juvenile will frequently bend itself into a U-shape or become wedged upside down in the same type of tube. The light orientation is most reliable in the adult of the Fundulus heteroclitus when measured on an individual basis. On mission day 9, an attempt was made in orbit to measure the light-orienting responses of the groups of juveniles in each of the five compartments. The lights were turned off in the spacecraft and the camera photolight was held at a 45° angle from the camera line of sight to the fish packages. The astronauts reported that the fish did not orient themselves with respect to light direction but seemed to be alining their bodies with respect to the "bottom" of the fish packages adjacent to the spacecraft wall. It is difficult to believe that light direction was not the major influence for orientation while the fish were in a weightless environment, but it may be possible that a contrast gradient due to the cards in the "bottom" of the package or some type of tactile reference was the major influence. The crew reported that this light orientation experiment was photographed but this cannot be confirmed from present techniques for viewing the flight films. A frame-by-frame analysis may clarify this question.

The geotaxis tests on the hatchlings are in progress.

Embryonic development appeared to be normal in all flight animals. In-flight hatching occurred only in the 336-hour embryos, which were theoretically ready to hatch at the time of launch. This result was not surprising in view of the Skylab 3 experience and of ground-based experiments indicating that hatching occurs readily only following a change in the state of vestibular stimulation. A similarly low hatching rate was also observed in controls that were exposed to minimum disturbance.

Exposure of the eggs to agitation during the recovery procedures, which involved routine shaking on a rotary shaker for 20 minutes each day, resulted in extensive hatching in all treatment groups. The cumulative hatching curve in figure 19-3 is typical of the results obtained. If hatching rate and ultimate hatch can be considered an index of health and development rate, it is safe to conclude that the flight animals did not suffer in any case. Temperature and atmosphere profiles of the flight environment were duplicated relatively closely in the ground controls, and baseline experiments indicate that relatively large deviations would be required to produce the observed results. Photographs of the egg packages in flight show a remarkably even distribution of eggs throughout the packages. It is known that crowding of eggs results in slowed development, and it seems likely that the even distribution resulted in improved dissipation of toxic metabolites and thus in increased development rate. No significance is attached to this result other than as an indication that poor health is not a causal agent in any possible morphological anomalies uncovered by the histological studies in progress.

ACKNOWLEDGMENTS

The investigators wish to acknowledge the significant contributions made to this research by Mr. Thomas B. McKee and his associates of the Nutrition-Physiology Section, Fish Commission, Clackamas, Oregon, and Mr. Thomas J. Price and his associates of the National Marine Fisheries Service, Atlantic Estuarine Research Center, Beaufort, North Carolina. Without their interest and assistance, respectively, in trapping wild Fundulus breeding stock and in providing the diet for the breeding colony, the Fundulus research program and the resultant flight experiments would not have been possible.

REFERENCES

19-1. Armstrong, Philip B.; and Child, Julia Swope: Stages in the Normal Development of Fundulus heteroclitus. Biol. Bull., vol. 128, no. 2, Apr. 1965, pp. 143-168.

19-2. Oppenheimer, Jane Marion: The Normal Stages of Fundulus heteroclitus. Anatomical Record, vol. 68, no. 1, Apr. 25, 1937, pp. 1-15.

19-3. Trinkaus, J. P.: Fundulus. Methods for Study of Development, N. K. Wessells and F. Wilt, eds., Thomas Y. Crowell (New York, N.Y.), 1967, pp. 113-122.

19-4. Boyd, John F.; and Simmonds, Richard C.: Continuous Laboratory Production of Fertile Fundulus heteroclitus (Walbaum) Eggs Lacking Chorionic Fibrils. J. Fish. Biol., vol. 6, no. 4, 1974, pp. 389-394.

19-5. Von Baumgarten, R. J.; Simmonds, R. C.; Boyd, J. F.; and Garriott, O. K.: Effects of Prolonged Weightlessness on the Swimming Pattern of Fish Aboard Skylab 3. Aviation, Space and Environmental Medicine, vol. 46, no. 7, July 1975, pp. 902-906.

19-6. Von Holst, E.: Uber den Lichtrackenreflex bei fischen. Publ. Staz. Zool. Napoli., vol. 15, 1935, pp. 143-158.

19-7. Pfeiffer, Wolfgang: Equilibrium Orientation in Fish. Int. Rev. Gen. Exp. Zool., vol. 1, 1964, pp. 77-111.

TABLE 19-I.- EXPERIMENTAL PACKAGES

(a) Egg package with 5 compartments

Compartment	Number of eggs		Age of embryos at launch, hr (a)	Nominal stage of embryogenesis
	Launch	Return		
1	100	100	32	Early gastrulation
2	100	100	66	Otic vesicle closure
3	100	100	128	Completed vestibular development
4	100	100	216	Vestibular system functional
5	50	50	336	Full development; able to hatch

(b) Fish package with 5 compartments

Compartment	Number of fish		Preconditioning	Flight background
	Launch (b)	Return		
1	6	5	Neutral background	White
2	6	5	Vertical bars	Barred
3	6	5	Horizontal bars	Barred
4	6	[c]0	Black overhead	Black
5	6	6	Blinded	White

[a]Development occurred at a constant temperature of 295 K (22° C).

[b]Age of fish at launch was approximately 21 days.

[c]All fish in this compartment were dead.

TABLE 19-II.- GROUP RESPONSES TO LIGHT ORIENTATION TESTS OF JUVENILE FUNDULUS HETEROCLITUS

Group	N[a]	Roll angle about body axis, deg				
		Trial 1	Trial 2	Trial 3	Trial 4	Mean
Left						
A	7	34.3	27.9	36.4	-10.7	22.0 ± 19.2
C-II	12	12.1	34.6	22.5	30.4	24.9 ± 8.6
C-III	6	23.3	2.5	35.8	35.8	24.4 ± 13.6
Right						
A	7	-8.6	7.1	-21.4	-20.7	-10.9 ± 12.6
C-II	12	-26.2	-23.8	-7.9	-18.3	-19.1 ± 7.1
C-III	6	-3.3	-39.2	-16.7	-29.2	-22.1 ± 13.5

[a]Number of samples.

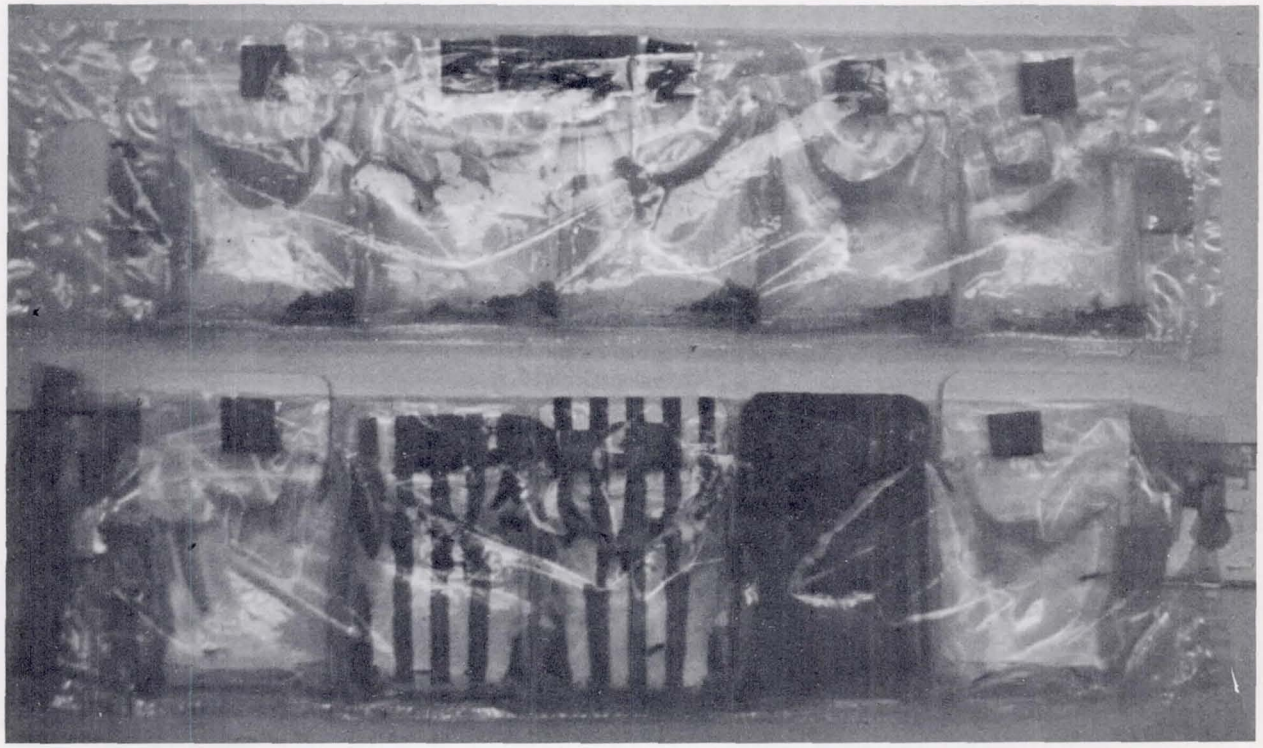

Figure 19-1.- Experiment package consisting of fish packet and egg packet.

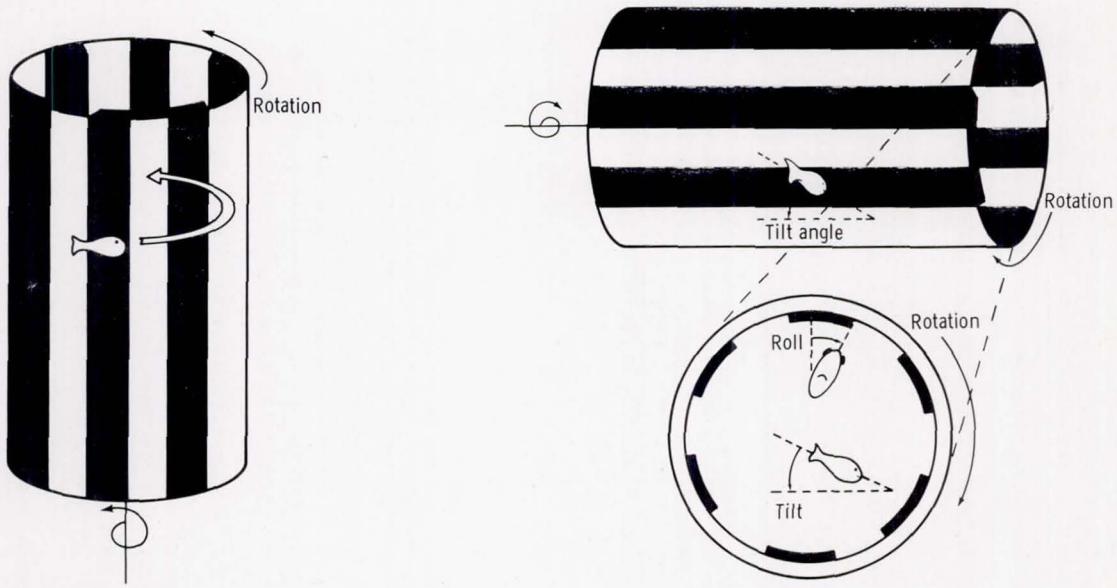

(a) Vertical position.

(b) Horizontal position.

Figure 19-2.- Orientation in rotating drum.

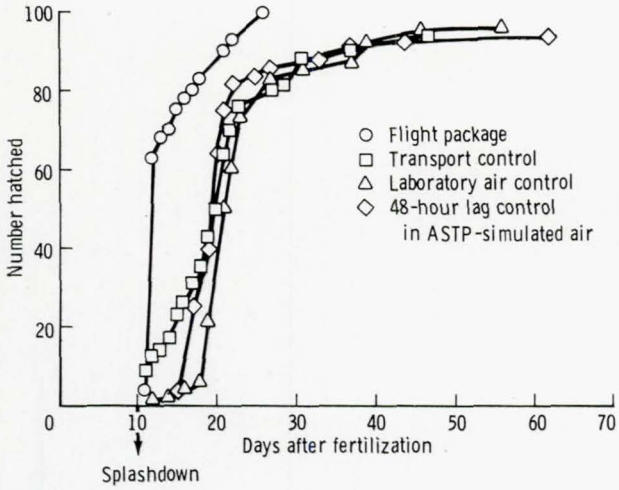

Figure 19-3.- Cumulative hatching curve of 32-hour eggs from the flight and control treatment packages.

20. ELECTROPHORESIS TECHNOLOGY

EXPERIMENT MA-011

R. E. Allen,[a†] G. H. Barlow,[b] M. Bier,[c] P. E. Bigazzi,[d]
R. J. Knox,[e] F. J. Micale,[f] G. V. F. Seaman,[e] J. W. Vanderhoff,[f]
C. J. Van Oss,[d] W. J. Patterson,[a] F. E. Scott,[a] P. H. Rhodes,[a]
B. H. Nerren,[a] and R. J. Harwell[a]

ABSTRACT

Experiment MA-011, Electrophoresis Technology, was designed to test electrophoresis hardware that would continue the development of technology for electrophoretic separation of materials in the near-zero-g environment of space. Experimental difficulties identified during the Apollo 14 and Apollo 16 electrophoresis demonstrations, if not successfully eliminated, would have severely limited any future separations by electrophoresis of biological materials in space.

The experimental hardware generally functioned as planned. Frozen live cells were successfully transported into space, electrophoretic processing was performed, and viable cells were returned to Earth. A separation of the three types of fixed red blood cells (rabbit, human, and horse) was demonstrated. The human lymphocytes, however, showed no apparent migration. Problems relating to this experiment will be discussed in detail in this report.

The separation of human kidney cells produced the most exciting data. Analysis shows electrophoretic separation throughout the entire column with at least four bands of viable cells. The isotachophoresis experiment definitely demonstrated the isotachophoretic separation of biological cells in a near-zero-g environment.

---

[a]NASA George C. Marshall Space Flight Center.

[b]Abbott Laboratories, Chicago, Illinois.

[c]Veterans Administration Hospital, Tucson, Arizona.

[d]State University of New York, Buffalo, New York.

[e]University of Oregon Health Sciences Center, Portland, Oregon.

[f]Lehigh University, Bethlehem, Pennsylvania.

[†]Principal Investigator.

INTRODUCTION

The Electrophoresis Technology Experiment was performed to demonstrate the concept of static free-fluid electrophoresis in the unique environment of space and to verify electrophoresis experiment concepts by operation in this environment. The following objectives were set forth.

1. To conduct engineering and operational tests of a space-rated static electrophoresis separation apparatus

2. To further current research efforts through separation of similar cellular species

3. To reduce or eliminate electro-osmosis through the application of a low zeta potential coating to the inner surfaces of the columns

4. To apply biological samples precisely without perturbing the subsequent electrophoresis

5. To maintain viable biological samples during all phases of the experimental procedure

6. To demonstrate isotachophoresis of red blood cells in space

The experiment equipment consisted of four major elements: (1) an electrophoresis unit (EU), (2) a cryogenic freezer (CF), (3) eight experiment columns (six electrophoresis, two isotachophoresis), and (4) eight sample insertion slides.

The following biological materials were contained in the sample slides for the eight experiment stages.

1. Columns 1 and 5, three species of fixed red blood cells: rabbit, human, and horse

2. Columns 2 and 6, human peripheral blood lymphocytes

3. Columns 3 and 7, human fetal kidney cells

4. Column 4 (isotachophoresis), fixed rabbit and human red blood cells; column 8, (isotachophoresis), fresh rabbit and human red blood cells.

To perform the experiment, a crewmember removed an electrophoresis or isotachophoresis column from its storage location and installed it in the EU. Fluid couplings were secured to each electrode chamber of the electrophoresis columns only. The slide containing a specific frozen sample was next removed from the cryogenic freezer and inserted into the column. A camera mounted on the EU cover photographed critical control positions and digital readouts during each column operation. Following each electrophoresis separation, the electrophoresis columns were frozen by the thermoelectric (TE) module and then removed from the cradle. The crewman then quickly removed each electrode chamber from the frozen columns

and placed the column in the CF for return to Earth. The isotachophoresis columns were neither frozen nor returned but only photographed in orbit during their operation.

BACKGROUND

Most biological materials, when dissolved or suspended in a selected aqueous medium, have a characteristic electric charge, and the migration velocity per unit electric field strength (defined as the electrophoretic mobility of the material) is thus fixed (ref. 20-1). If the mobility difference between biological species is small, separation can be enhanced by increasing the length of the column. Electrophoresis was originally conducted in liquid media, or free solutions, but problems arose because of disturbances in the bulk of the fluid. Two major causes of these disturbances were sedimentation of the particles or solute being separated and thermal convection generated by Joule heating of the column during electrophoresis. Although various techniques have been developed to overcome these problems on Earth, the elimination of gravity-induced sedimentation and thermal convection can be accomplished best in the near-zero-g environment of space.

Electrophoresis in a free fluid was first demonstrated in space during the Apollo 14 mission. Three materials of different molecular weight, deoxyribonucleic acid (DNA), hemoglobin, and soluble dyes, were to be photographed periodically during electrophoresis in 10-centimeter (4 inch) long by 0.64-centimeter (0.25 inch) diameter cylindrical columns. Before operation of the apparatus, the sample materials were isolated in small cavities in a plastic slide that was arranged for insertion in a slot intersecting the separation columns. The experiment was initiated by pushing the slide so that the sample cavities coincided with the separation columns. The diameter of the sample cavity was made slightly smaller than the column diameter so that electrophoresis of the sample would occur away from the walls, where electro-osmotic streaming would be less intense.

Particular problems encountered during the demonstration included a misalined sample insertion assembly which injected the samples near the column walls, poor photography from a hand-held camera, and bacterial degradation of the DNA and hemoglobin because of the long storage time. However, a separation was measured between two dyes, and operation of the fluid and electrical systems was normal. The overall results indicated the validity of fluid electrophoresis investigation; therefore, plans were made and apparatus was developed for a second demonstration during the Apollo 16 mission.

The Apollo 16 electrophoresis demonstration was performed using the basic operating elements of the Apollo 14 demonstration, but a nonbiological sample material, polystyrene latex, was used (ref. 20-2). These stable, nondegradable particles were used as models for living cells. Two sizes of latex particles were run separately and collectively to provide comparative data (ref. 20-3). An automatically operated camera, mounted rigidly on the apparatus, photographed a clock, a thermometer, a column current meter, and the position of the migrating materials. These photographs provided better technical data on electrophoresis in space than had been obtained previously. The sample insertion mechanism was redesigned to

provide more reliable release of the samples in the columns. Although each sample was inserted correctly, the insertion mechanism allowed buffer to leak out of the columns before the electrophoresis began, and a bubble formed in each column. The sample bands were severely distorted by electro-osmosis, which caused buffer flow along the walls of the columns counter to the direction of electrophoretic migration of the latex particles. Although the parabolic bands observed in space were explained by subsequent analysis, a clear separation of the two sizes of polystyrene latex particles was not obtained because of the electro-osmosis. Electrophoresis according to size did occur in the columns containing single species of the latex, and the photographs clearly show distinct boundaries and sharply defined fronts. The deleterious effects of gravity-induced sedimentation and thermal convection on particle electrophoresis can be seen by comparing the results of the Apollo 16 electrophoresis demonstration with those of ground experiments.

For the Apollo-Soyuz Test Project (ASTP), experiment plans included reuse of the parts of the Apollo 14 and Apollo 16 systems that operated correctly, improvement of the techniques used to accomplish sample insertion, elimination of the charge condition along the column walls, and avoidance of bacterial degradation by using proven sterile techniques. A sample insertion technique was devised to ensure precise injection of the sample into the electrophoresis column without affecting the properties of the sample or disturbing the fluid column. The Apollo 14 method of inserting a thin rectangular vane containing cylindrical sample disks into the column was slightly modified and used. Buffer leakage and bubble formation were avoided by specific design techniques. Each sample disk was kept frozen, and the entire insertion slide was stored in a CF that was kept at liquid-nitrogen (77 K (-196° C)) temperatures.

The advantages of a separate insertion vane containing frozen samples are as follows.

1. The frozen disks can be inserted into the column and allowed to thaw in contact with the buffer while any fluid disturbances induced by the sample insertion are damped.

2. Agglutination and sedimentation of the sample material in storage can be avoided by rate freezing a well-mixed sample on the ground.

3. The freezing preserves the viability of the live biological materials.

To assess the resolution and sharpness of the bands formed by electrophoresis in space, a well-characterized particle specie is required. Although polystyrene latexes were the model particles for the Apollo 16 demonstration, the red blood cells used on the ASTP flight (erythrocytes fixed in a formaldehyde fixative) provide an almost indestructible sample material resistant to mechanical stress, hemolytic agents, and surface modification. These fixed red blood cells are stable for months under varying temperature conditions, and extensive electrophoresis mobility measurements of the cells using a variety of buffers have been published (ref. 20-4). Each type of cell was selected to be morphologically distinguishable under microscopic examination. The red color of the cells make them clearly distinguishable on the photographs made in orbit.

Isotachophoresis

Isotachophoresis is a relatively new technique of electrophoretic separation in which a discontinuous electrolyte system is used at the site of sample injection (ref. 20-5). The boundaries between species of different mobility are sharply defined and stabilized by electrical forces. Adjacent compartments of sample components that may not be distinguishable by zone electrophoresis may be resolved by isotachophoresis. The boundaries are highly self-recuperative and will reform if stirred or disrupted by other factors, including convection. The concentration of each substance within a compartment is uniform and remains constant throughout the run once the separation has been achieved. Because of this uniformity, higher concentrations of components can be handled with no deterioration of the sharp boundaries.

Lymphocytes

The interest in specific lymphocytes stems from the increased emphasis in the field of immunology. Initial interest in immunology grew out of the knowledge that persons who survive an infectious disease seldom contract that disease again. The two major types of immune mechanisms are humoral and cellular. Humoral immunity is characterized by the circulating antibodies that originate from B lymphocytes. Cellular immunity is mediated by means of T lymphocytes and is responsible for delayed allergic and transplant-rejection reactions. With the increasing emphasis on cell interactions and the cellular basis of immunology, a simple method of obtaining pure fractions of cells from heterogeneous populations is desirable. From examination of microelectrophoretic data, differences in cell surface charge are known to exist (ref. 20-6), and differences in electrophoretic mobility have been measured. The significance of the cell separation is of great practical and theoretical importance. Many unresolved questions in immunology depend on the availability of pure lymphocyte subpopulations; such subpopulations are needed to study the nature of the interaction between T and B cells in antibody formation and the nature of the recently described interaction between the classes of T cells in reactions of cell-mediated immunity. More specifically, interest has developed in the clinical use of various soluble lymphocyte products (lymphokines) in a manner analogous to the use of antisera. Several other lymphocyte products, such as the factors modifying inflammatory cell behavior, are also important. The fractionation of these different lymphokines depends on the earlier separation of the specific lymphocyte populations responsible for their production. To date, none have been fractionated to any significant extent.

Kidney Cells

The isolation and production of the enzyme urokinase (UK) has interested biomedical laboratories for more than 20 years (ref. 20-7). This enzyme is capable of effecting the conversion of plasminogen to plasmin. This conversion is necessary to accomplish blood clot lysis. Originally, UK was extracted from urine; however, at least 1500 liters of urine were required to produce a single UK unit dose consisting of 4 million CTA (Committee on Thrombolytic Agents) units. The production cost was $1200/CTA unit dose. Another source was subsequently discovered; UK

has been isolated from cultures of cells located in the cortex of the kidney as follows. Human fetal kidneys are trypsinized to disperse the cells and then tested for viability. The cells are grown out in cultures on mass tissue propagators from which the UK is harvested. Currently, the demand for UK greatly exceeds the capability to produce it. Bernik and Kwaan (ref. 20-8) in 1969 observed that only approximately 5 percent of the cells in the cortex of the kidney produce UK. Obviously, if these "producing cells" could be isolated and subjected to subculturing techniques, a twentyfold increase in the yield and a corresponding reduction in the cost of this lifesaving drug might result. Electrophoresis has been used to try to isolate these "producing cells." The disadvantages of separation on Earth are the loss of resolving power due to sedimentation of the cells and convective mixing due to the heating effects of electrophoresis. Under zero-g conditions, these disadvantages should be eliminated or minimized.

As outlined, the kidney cell portion of Experiment MA-011 consisted of taking to orbit a mixture of frozen human kidney cells, separating them by electrophoresis, refreezing the resulting bands, and returning them to Earth. They were then grown out in tissue culture and assessed for UK production. In addition, extensive analyses were conducted to characterize the separated cells. The information from these analyses, as well as the data from the tissue culturing, has contributed extensively to the understanding of this very important source of UK.

EQUIPMENT

The experiment equipment consisted of four major elements: (1) an EU, (2) a CF, (3) eight experiment columns (six for electrophoresis and two for isotachophoresis), and (4) eight sample slides containing the experiment specimens. In addition to this experiment hardware, performance of the experiment required the following items of support equipment: (1) a 70-millimeter electric camera, (2) an 80-millimeter lens and extender tube, (3) an intervalometer, and (4) an EU power cable. As stated, the materials used as samples in the experiment consisted of fixed red blood cells of three different types (rabbit, human, and horse), lymphocytes, and human kidney cells. In addition to the slides processed, several control slides containing samples of the biological materials were stored in the CF at launch and remained there throughout the ASTP mission to allow assessment of the effects of space flight on the biological materials.

A general description of experiment operation follows. An electrophoresis or isotachophoresis column was removed from its storage location and installed on the EU column cradle. Fluid couplings were secured to each electrode chamber of the electrophoresis columns only. Then, the proper sample slide with a frozen sample was removed from the CF and inserted into the column. The 70-millimeter camera, mounted on the EU cover, photographed the experiment column during a run. After each electrophoretic separation was completed, the column was frozen in place on the EU by the TE module. The frozen column was removed from the column cradle, the electrode chambers were removed and discarded, and the column was placed in the CF for return to Earth. Isotachophoresis specimens were neither frozen nor returned but only photographed. Duplicate electrophoretic separations were performed using each of the three sample materials. The two isotachophoretic

separations (runs 4 and 8) were performed using rabbit and human red blood cells. Run number 4 contained formalin-fixed red blood cells and run number 8, fresh red blood cells.

A detailed description of each major hardware element and its subelements is provided in the following paragraphs.

Electrophoresis Unit

The EU (fig. 20-1) was the apparatus in which the experiment was performed. External envelope dimensions of the unit (cover closed), excluding mounting lugs and fasteners, were 20.32 by 20.32 by 40.64 centimeters (8 by 8 by 16 inches). Launch weight was 13.61 kilograms (30 pounds). The EU was designed to be mounted to the Electrophoresis Experiment (MA-014) adapter rack near command module locker A-6 with four thermally stable fasteners. Subassemblies provided by the EU were as follows.

1. Controls and displays

2. Fluorescent light assembly for illumination of the experiment columns during processing

3. Thermoelectric module for cooling and freezing the electrophoresis columns

4. Self-contained power supplies that required only an external 208-volt ac (115-volt line-to-neutral), three-phase, 400-hertz connection

5. Buffer solution reservoir

6. Buffer solution circulation pump

7. Phase separator assemblies for removing gases liberated in the buffer solution

8. Electrical circuitry and plumbing required by the experiment

9. Cover with one knurled screw fastener latch to protect the EU when not in use

10. Camera attachment assembly for mounting the camera to the EU cover

11. Individual storage compartments for eight experiment column assemblies

The EU control and display panel (fig. 20-2) is described as follows. In the ON position, the POWER switch energizes the fluorescent light assembly and the EU digital displays and also activates the TE module cooling blower.

The TEMP SELECT switch has positions FREEZE, COOL, and OFF. The FREEZE position is selected to freeze the electrophoresis column after each electrophoresis separation has been accomplished. A thermoelectric temperature controller allows a minimum temperature of approximately 233 K (-40° C). When the COOL position of the switch is selected, the temperature controller will control the TE units to temperatures as high as 278 K (5° C). The switch is placed in this position at the beginning of viable cell electrophoresis separations and remains in COOL until the separation is accomplished. Because performance of the isotachophoresis portion of the experiment required neither cooling nor freezing of the column, the OFF position was used for isotachophoresis.

The MODE SELECT switch has positions ELECTRO, OFF, and ISOTACH. The ELECTRO position is selected to perform the electrophoresis. When the ISOTACH position of the switch is used to perform the isotachophoresis, the buffer pump, which is not needed for this part of the experiment, does not operate.

The TIME SELECT (MIN) switch is used to select a time period of 45, 60, or 75 minutes for experiment operation.

The CURRENT SELECT switch is used to select the level of current flow through the experiment column to either 4.00 milliamperes (HI) or 1.31 milliamperes (LO). The electrophoresis samples were processed with the switch in the HI position, while the LO position was used for isotachophoresis.

The COLUMN VOLT (DC) digitally displays the voltage sensed across the experiment column electrodes. The range of the display is from 0 to 99 volts in increments of 1 volt, with an accuracy of ±2 percent.

The COLUMN TEMP (°C) displays the buffer solution temperature in the electrophoresis column. The range of the display is from -99° to 99° C in increments of 1° C, with an accuracy of ±2 percent.

The TE TEMP (°C) displays the temperature of the thermoelectric module assembly cold plate. The range of this display is from -99° to 99° C in increments of 1° C, with an accuracy of ±2 percent.

The purpose of the EU clock (a commercial panel-mounted wristwatch) is to enable time correlation of the photographs taken during the experiment process. A metric scale is mounted next to the experiment column cradle. The scale is marked from 0 to 130 millimeters in 1-millimeter increments to provide distance information in photographing the biological specimens as the specimens move through the column during the experiment. A portable fluorescent light assembly mounted on the EU cover supplied the illumination required both for viewing the electrophoresis and isotachophoresis processes in the experiment columns and for photography. The fluorescent light tube, contained inside a polycarbonate tube for protection, is permanently bonded to its electrical receptacles.

The EU contains a TE assembly consisting of four three-stage thermoelectric coolers to remove heat from the electrophoresis columns during the experiment and to freeze the columns after each separation has been performed. The four coolers are mounted on a heat sink that is cooled by a flow of 0.09 m^3/sec (190 ft^3/min)

free air by a 208-volt ac, three-phase blower. The cradle holding the electrophoresis columns during the experiment is attached to the TE assembly cold plate. The cold plate contains a thermistor device to sense the cold plate temperature. A thermal cover joins the column cradle to provide thermal continuity around the periphery of the column. The thermal cover is designed to remain in place for all freezing operations and during electrophoresis of lymphocytes and human kidney cells. The column assemblies can be isolated from the TE cradle by using special thermal spacers or slide devices.

A buffer solution reservoir is mounted on a removable tray that forms a part of the EU structure. The tray is attached to the EU by screw fasteners. The reservoir contains a cylindrical rubber diaphragm with a hemispherical end and has a buffer solution capacity of 57.7 milliliters. The buffer solution enters the reservoir from a phase separator assembly and is then delivered from the reservoir to the buffer solution pump. The reservoir was covered with a hydrophobic felt cover to ensure containment of the buffer solution if the diaphragm ruptured.

A double peristaltic pump, mounted on one side of the EU removable tray assembly next to the buffer solution reservoir, circulates the buffer solution through the fluid system to allow removal by the phase separators of gas bubbles generated at the electrophoresis column electrodes. The pump receives buffer solution from one side of the fluid system (e.g., the column anode side) and circulates it to the other end of the column (fig. 20-3). The capacity of the pump is 35 ml/min.

Two phase separator assemblies were located on the EU removable tray assembly. The phase separators are identical and consist of two cylindrical membranes. One membrane is hydrophilic (porous polyethylene) and the other is hydrophobic (porous polytetrafluoroethylene). The buffer and gas mixture enters between the membranes. The hydrophobic membrane allows passage of gas to either the cabin atmosphere or the hydrogen adsorber, and the hydrophilic membrane allows passage of liquid to the storage reservoir. One separator is connected to the column anode side of the fluid system and removes the oxygen gas liberated in the buffer solution at the anode. The oxygen is vented to cabin air. The other separator is connected to the cathode side of the fluid system and removes hydrogen gas liberated at the cathode. The hydrogen is then routed to the hydrogen adsorber assembly. The separator assemblies return the liquid buffer solution to the reservoir.

The hydrogen adsorber assembly is connected to the phase separator assembly to remove hydrogen bubbles from the buffer solution. The hydrogen gas is adsorbed on a mixture of precipitated palladium (palladium black) and silica gel contained in a fine-filament fiberglass bag in the adsorber canister.

Cryogenic Freezer

The CF (fig. 20-4) was used to freeze the experiment samples before insertion into the experiment columns for processing and to maintain the frozen electrophoresis columns after the separations had been accomplished. The sample slides were launched in the CF, and the frozen electrophoresis columns were returned to Earth in the CF.

The CF consists of two flasks (one contained within the other). The space between the flasks is evacuated for thermal insulation. The inner flask has an outside diameter of 31.12 centimeters (12.25 inches) and has a cavity to accommodate a cylindrical sample storage canister with dimensions of 4.98 centimeters (1.96 inches) diameter and 48.26 centimeters (19 inches) length. The maximum launch weight of the CF, when charged with liquid nitrogen, is 10.4 kilograms (22.9 pounds).

The cooling medium used in the CF was liquid nitrogen, which was contained in the inner flask and surrounded the sample canister cavity. The CF maintained the samples at a temperature no higher than 188 K (-85° C) for 20 days. The sample canister had space for eight experiment sample slides with samples, one experiment sample column for the German Electrophoresis Experiment (MA-014), and three cylindrical cavities for return of the electrophoresis columns (two columns per cavity).

Electrophoresis Columns

Six electrophoresis columns were stowed in individual compartments at one end of the EU. Each column consisted of a transparent Pyrex glass tube 0.953 centimeter (0.375 inch) outside diameter by 0.635 centimeter (0.25 inch) inside diameter. The tube was 15.24 centimeters (6 inches) long and was split lengthwise and rejoined with a flexible adhesive (RTV 140) to allow for expansion of the buffer solution when the electrophoresis columns were frozen. A thermistor bonded to the tube wall at the center of the length of each tube was used to monitor the column temperature for display on the EU COLUMN TEMP (°C) display.

The inside surfaces of the glass columns were stringently cleaned, coated with Z-6040 (γ-glycidoxypropyltrimethoxysilane, Dow Corning) and then coated with methylcellulose in order to obtain a stable, biocompatible surface with close to zero zeta potential. Confirmation of the adequacy of the coating was obtained by experimentally determining the electrophoretic velocity of fixed red blood cells in the coated columns. The ends of the tubes were plugged with a fritted glass disk containing a 3 percent agarose gel. The columns were filled before flight with a sterile buffer solution. Each column was sealed in a polyvinylidene chloride bag that was then placed in a fine-filament fiberglass bag. Attached to the polyvinylidene chloride bag was a wiper used to wipe the female electrical connectors before column installation. Each end of the electrophoresis column has an electrode chamber assembly containing a platinum electrode, a printed circuit electrical connector, and a mating EU buffer solution connector.

The electrode chamber assemblies were removable for disposal after the column had been frozen in the EU. The electrode chamber assembly containing the column cathode had a cavity into which the sample slide was inserted for experiment operation. A blank slide was contained in the cavity before experiment operation. The blank slide had a 0.13-centimeter (0.05 inch) inside diameter threaded hole used for preflight filling of the column with buffer solution. The opening was sealed after filling.

A drawing of the electrophoresis column assembly is provided in figure 20-5. The assembly electrical schematic is shown in figure 20-6.

The buffer used in the electrophoresis columns consisted of a mixture of 1.76 mmol Na_2HPO_4, 0.367 mmol KH_2PO_4, 6.42 mmol NaCl, 0.336 mmol Na_2EDTA, 222 mmol glucose, and 514 mmol glycerol in water.[1] It had a hydrogen-ion concentration (pH) of 7.30 ± 0.10 at 293 K (20° C) and a calculated ionic strength of 0.0097 mol/liter. At 298 K (25° C), the conductivity was 0.96 mmho/cm; the density, 1.022; and the dynamic viscosity, 0.00111 N-sec/m^2 (0.0111 poise). The buffer was demonstrated to be compatible with the column coating, all components of the EU system, and the candidate materials to be flown on the mission. The mobilities of fixed rabbit, human, and horse red blood cells in this buffer were 1.60, 1.96, and 2.60 μm/sec/V/cm, respectively.

Isotachophoresis Columns

Two isotachophoresis columns (fig. 20-5) were stowed in individual compartments in the EU. Each column consisted of a glass tube having dimensions of 0.97 centimeter (0.38 inch) outside diameter, 0.64 centimeter (0.25 inch) inside diameter, and 15.24 centimeters (6 inches) length. Each end of the tube had an assembly containing a flat, disk-shaped, three-lobed electrode (one electrode assembly with a silver anode and the other with a palladium cathode), a rubber diaphragm, and a printed circuit electrical connector.

The assembly containing the palladium cathode had a cavity into which the sample slide was inserted for experiment operation. A blank slide was contained in the cavity before processing the column. The blank slide had two 0.13-centimeter (0.05 inch) inside-diameter threaded holes used to fill the column with buffer solution before flight.

The isotachophoresis occurred in a column containing a leader buffer of 0.62 milliliter of 85 percent phosphoric acid in 500 milliliters water, with 42 grams of dextrose and 276 grams of glycerol, adjusted to a pH of 7.4 in 1 liter of distilled water. The terminator buffer contained 2 grams of serine, 42 grams of dextrose, and 276 grams of glycerol, adjusted to pH 8.2 in 1 liter of glass distilled water.

Sample Slides

Each sample to be processed during the experiment was mounted in a slide assembly. Before processing, the slides were stowed in the CF sample canister. Each slide assembly was contained in a tetrafluoroethylene cover 0.13 millimeter (0.005 inch) thick that had a removal tab 5.08 centimeters (2 inches) long of the same material. The slides were removed from the CF sample canister by grasping

---

[1]Na, sodium; H, hydrogen; P, phosphorus; O, oxygen; K, potassium; Cl, chlorine; and EDTA, ethylenediaminetetraacetic acid.

the removal tab and pulling the slide out of the canister. Every two slides removed from the canister exposed a return storage space in the canister for two electrophoresis columns. In addition to the slides to be processed, four "control" slides with sample material were stowed in spaces on the circumference of the sample canister. Two control slides contained lymphocytes and two contained kidney cells. These "control" slides were designed to assess the effects of the flight environment on the viable sample materials; they were returned to Earth without processing.

Each sample slide was numbered to correspond to the appropriate column. The slides were removed from the canister and inserted into the experiment column electrode (cathode) chamber assembly for processing in numerical order. Each slide was discarded together with the electrode chamber assemblies after each electrophoresis column was frozen for return. The entire isotachophoresis column was discarded after processing.

RESULTS

The EU, the CF, and the data collection assembly met the required objectives with satisfactory experimental results. The fluid connect lines (located in the electrode housings) of some of the columns were clogged during assembly. Without a fluid washout of the electrode housing, chemical and gas products of electrolysis accumulated in the electrode region. This accumulation triggered changes in the buffer which were manifested as column voltage fluctuations and pH changes in the column fluid. These anomalies were seen in columns 2, 5, and 6. Operation of the remaining columns appeared normal.

In the laboratory, the frozen buffer containing the processed samples was separated from the glass electrophoresis columns. These frozen ice columns were sliced into sections (5 millimeters in width) for processing by each Co-Investigator. The results of the analyses available to date are presented in the following sections.

Fixed Red Blood Cells

The fixed red blood cells were selected as a standard, or control. The photographic record clearly demonstrates separation of the sharp bands of cells in column 1. The volume of cells loaded in the sample slide was 5.22×10^6 rabbit cells/0.06 ml, 3.44×10^6 human cells/0.06 ml, and 7.26×10^6 horse cells/0.06 ml. The volume of the sample slide was 0.06 milliliter for an electrophoresis slide. The bands appeared to spread during separation. Histograms have been completed showing less than 43-percent recovery of cells in column 1 and a 54-percent recovery of cells in column 5 with a 60-minute operation time. To identify specific cells, mobility data for column 1 (fig. 20-7) were collected using microelectrophoresis techniques. The highest mobility was shown by horse cells, the next highest by human cells, and the lowest by rabbit cells.

The pH of column 1 was 7.2; however, column 5 had a pH range of 6.0 to 9.2. This condition, together with an unexplained dispersion of the bands, was responsible for the lack of distinct bands in column 5. Mobility data for column 5 (fig. 20-8) indicate the occurrence of cellular separation, but not to the concentration necessary to show distinct bands in the photographs. The pH problems were induced by the fluid line blockage already discussed.

In column 5, two specific instances of sudden disruption of boundaries can be seen in the flight photographs (figs. 20-9 to 20-12). These dispersions occurred between the time of the photographs shown in figures 20-9 and 20-10 and between the time of the photographs shown in figures 20-11 and 20-12. The disruptions probably were caused by random motion of the apparatus or perhaps of the spacecraft.

Human Lymphocytes

Approximately 1.5×10^7 human lymphocyte cells were loaded into the 0.06-milliliter volume of the sample slide. Migration of the cells was not detected in either column. In column 2, current was established for less than 3 minutes because of fluid line blockage, which resulted in the formation of gaseous products around the electrodes. These gas bubbles blocked current and prevented operation of the experiment. In addition, the cell viability was only 6 percent. No explanation can be found for this observation, as the pH of the column fluid varied from 6.69 to 6.85.

In column 6, current existed for approximately 30 minutes. In this case, the electrode housings were returned, and a failure analysis confirmed that the right electrode chamber fluid lines were blocked. This condition resulted in an acid pH throughout the column. The pH of the fluid in column 6 was 2.54 on the left end, 2.28 in the center, and 2.21 on the right end. As would be expected, the viability of the lymphocytes was only 1 percent.

Human Kidney Cells

In the human kidney cell experiments, approximately 2.0×10^6 cells were loaded into the sample slide. Only column 3 was electrophoresed in orbit. Analysis showed that the electrophoretic separation proceeded throughout the entire column (fig. 20-13). The experiment was active for approximately 75 minutes. All the cells returned were viable. The pH was 7.45 ± 0.40. All returned samples were planted on culture media on August 28, 1975, and showed attachment characteristic of growing cell cultures. Controls were planted 1 day later. However, after approximately 1 month, only sample slices 11, 13, 15, and 17 were capable of producing an assayable product. The lack of assayable byproducts from the other slices has not been explained. The only product assayed to date has been UK. Because the number of cells differs for each sample, an assay was performed on September 26, 1975, to determine the number of CTA units and the number of UK units per 100 cells being produced (table 20-I). These data show that the amount of UK produced per 100 cells is higher than the amount seen in the mixed culture controls. Assays for other products of interest from these same cells are in progress.

Isotachophoresis

Isotachophoresis column 4 was processed using rabbit and human formalin-fixed red blood cells. The concentration of these cells, when loaded, was the same as that for columns 1 and 5. The volume of live red blood cells loaded into the sample slide (number 8) was provided in the following manner. Human and rabbit cells were prepared at a 40-percent hematocrit each. Equal volumes of each concentration were loaded into the sample slide. The final concentration was 450×10^6 cells/0.098 ml. The isotachophoresis sample slides had a slightly larger volume (0.098 milliliter) than that of the electrophoresis slides (0.06 milliliter).

Both of the isotachophoresis experiments were essentially successful. Unfortunately, however, full expectations were not realized. Thus, there is only evidence of frontal boundaries, but not of any separation or details of the rear boundaries. In retrospect, the duration of the run, 45 minutes, was insufficient to bring the isotachophoretic bands into full view. The 45-minute duration was based on the calculated and experimentally observed temperature rise in ground-based experiments. A better photographic record might have provided some indications of possible emergence of the rear boundary or the expected intercompartmental boundaries in the fresh cell sample.

The predicted overall migration rate was 1 mm/min for both samples. The last four frames of the fixed cells have confirmed this migration rate, but the overall migration rate appears to be substantially lower than expected (0.68 mm/min). With the fresh cells, the migration rate was still lower, ranging from 0.55 to 0.64 mm/min depending on mode of calculation. Interpretation of these mobility differences is made difficult by several possible contributing factors such as possible variation in time, power, and starting position.

CONCLUSIONS

With the successful separation of the standard particles (fixed red blood cells) and the human kidney cells, it has been shown that electrophoresis can be performed under zero-g conditions. The absence of significant electro-osmosis, the loading and returning of a sterile system, the capture of the resulting separation, and the preservation of the viable cells in orbit and during the subsequent return represents many "firsts" for space electrophoresis. In addition, the newer methods of separation represented by the isotachophoresis runs proved the feasibility of conducting large-particle processing by this method. The red blood cells in both columns demonstrated sharp front boundaries indicative of successful isotachophoresis. However, the experiment was not totally successful because the fluid lines in some of the columns were blocked. Although each column was thoroughly tested before even being considered for flight, the fluid lines could not be checked without contaminating the encased sterile buffer.

Significant steps have been made toward future plans for providing a separation facility in orbit for space-processing experiments. Important areas necessary for future operations were considered in the Electrophoresis Technology Experiment.

In both zonal electrophoresis columns (1 and 5), sharpness of boundaries deteriorated with time, as evident from the photographic record. In column 5, two specific instances of sudden disruption of boundaries can be pinpointed.

Operating time of the two isotachophoresis experiments was insufficient to permit visualization of rear or intercompartmental boundaries. Nevertheless, the experiments show the great advantage of isotachophoresis in displaying the sharpness of boundaries and the concentration of the migrating zones. Thus, the main potential advantage of isotachophoresis is the quantity of sample it may fractionate within comparable instruments. With cells, the future of isotachophoresis depends on finding proper spacers; however, with other substances, the use of a zero-g environment for large-scale fractionation can be foreseen.

SUMMARY

The basic objectives of the Electrophoresis Technology Experiment were to conduct engineering and operational tests of a space-rated static electrophoresis separation apparatus and to further current research efforts through separation of similar cellular species. In addition, special effort was made to improve existing concepts in several areas. A method was needed that would allow for the precise application of the sample without affecting the subsequent electrophoresis. This improvement was accomplished by inserting the sample as a frozen disk. Attempts were made to separate and return viable lymphocytes and kidney cells. This goal was accomplished with the kidney cells but not with the lymphocytes. A technique was needed to demonstrate viable candidate preservation after separation. This preservation was accomplished for the first time in space by using a thermoelectric module to freeze the sample at a prescribed rate after separation was completed. The experiment allowed, therefore, the testing and evaluation of many important aspects related to space-flight electrophoresis. In almost all cases, the concepts developed were proven operationally or shown to offer significant improvements over past efforts. Of particular interest was the low zeta potential coating. The minimization of electro-osmosis in this experiment provided a breakthrough sought since before the Apollo 14 separation attempts.

In summary, this experiment provided a significant step forward in the development of a biological processing facility in space. All areas of concern — i.e., sample preservation, sample collection and return, biocompatible systems, and sterile operating environment — were considered in this experiment. The accomplishments were significant and encouraging. The performance of electrophoretic separations in space without sedimentation and heat convective-mixing problems has been demonstrated. The isotachophoresis of large living biological particles can be achieved. Scientists limited by Earth gravity problems can now use space-flight operations in the processing of particles that are difficult to separate or purify on Earth.

REFERENCES

20-1. Shaw, Duncan J.: Electrophoresis. Academic Press (New York), 1969.

20-2. Snyder, R. S.: Electrophoresis Demonstration on Apollo 16. NASA TM X-64724, 1972.

20-3. Wiersema, P. H.; Loeb, A. L.; and Overbeek, J. Th. G.: Calculation of the Electrophoretic Mobility of a Spherical Colloid Particle. J. Colloid & Interface Sci., vol. 22, no. 1, July 1966, pp. 78-99.

20-4. Seaman, G. V. F.: Electrokinetic Behavior of Red Cells. Red Blood Cell, Vol. 2, Douglas N. Surgenor, ed., Academic Press (New York), 1975.

20-5. Bier, M.; Hinckley, J. O. N.; and Smolka, A. J. K.: Potential Use of Isotachophoresis in Space. Protides of the Biological Fluids: 22nd Colloquium, H. Peeters, ed., Pergamon Press (New York), 1975, pp. 673-678.

20-6. Donald, D.; Hutchinson, F.; Macleod, T. M.; and Raffle, E. J.: Electrophoretic Mobility of Human Lymphocytes — An Investigation of the Technique of Cytopherometry. J. Immunological Methods, vol. 6, nos. 1 and 2, 1974, pp. 151-156.

20-7. White, Wilfrid F.; Barlow, Grant H.; and Mozen, Milton M.: The Isolation and Characterization of Plasminogen Activators (Urokinase) From Human Urine. Biochemistry, vol. 5, no. 7, July 1966, pp. 2160-2169.

20-8. Bernik, Maria B.; and Kwaan, Hau C.: Plasminogen Activator Activity in Cultures From Human Tissues. An Immunological and Histochemical Study. J. Clin. Invest., vol. 48, no. 7, Apr. 24, 1969, pp. 1740-1753.

TABLE 20-I.- UROKINASE PRODUCTION FROM A SELECTED POPULATION OF HUMAN KIDNEY CELLS

Slice	No. of cells	UK activity,[a] CTA units	UK units per 100 cells
Flight[b]			
11	28 000	90	0.32
13	69 600	535	.77
15	12 000	240	2.00
17	74 000	225	.30
Control[c]			
B	--	61	0.28
D	--	81	.40

[a]All activity quenched by urokinase antisera.

[b]26 days after planting.

[c]25 days after planting.

Electric camera

Camera mount

Electrophoresis unit

Figure 20-1.- Electrophoresis unit with camera.

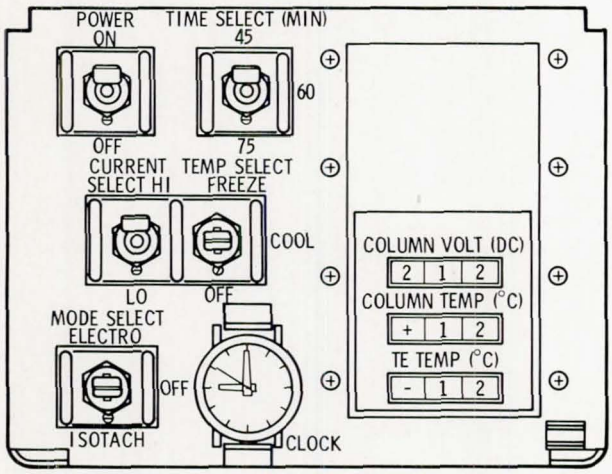

Figure 20-2.- Electrophoresis unit control and display panel.

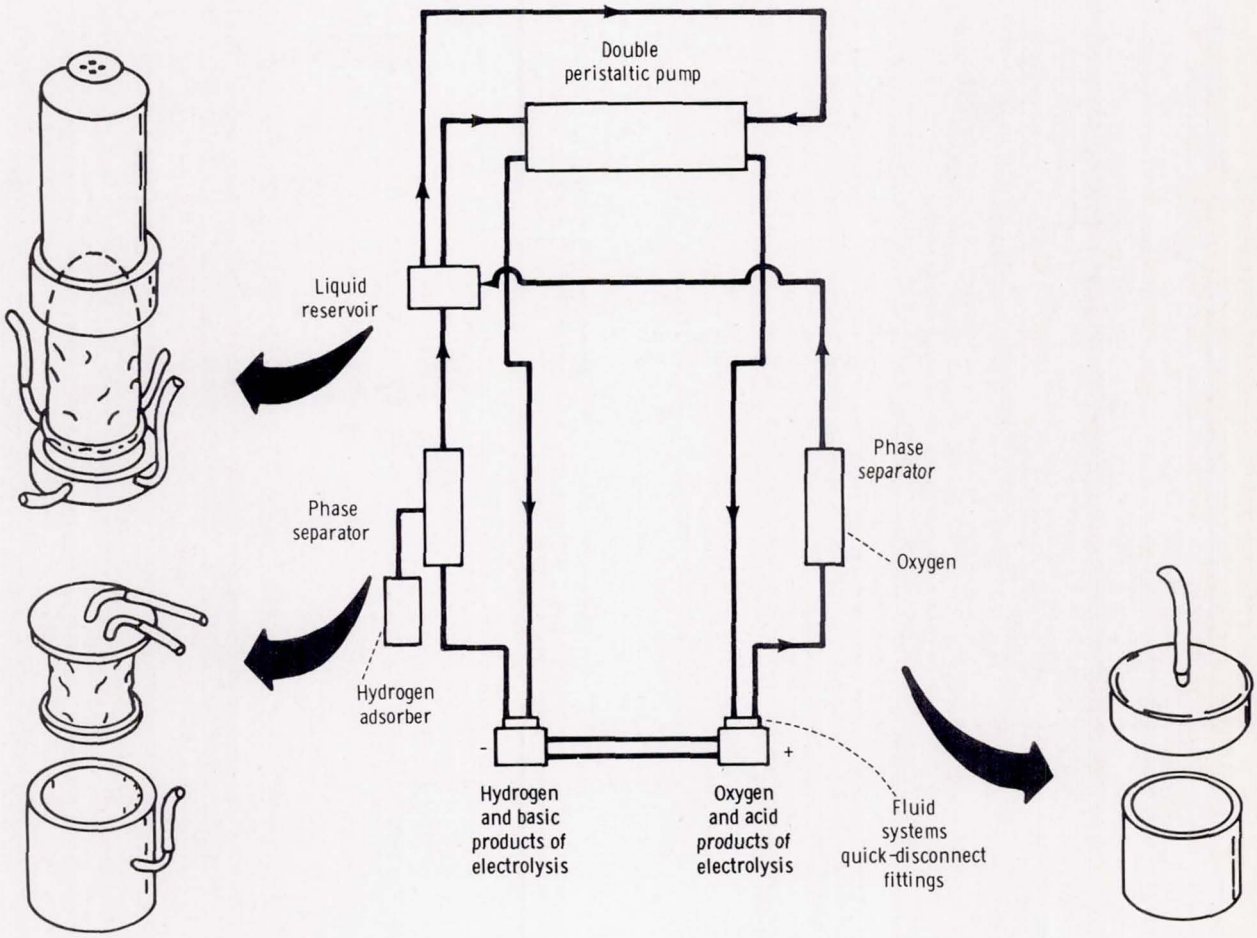

Figure 20-3.- Electrophoresis fluid system schematic.

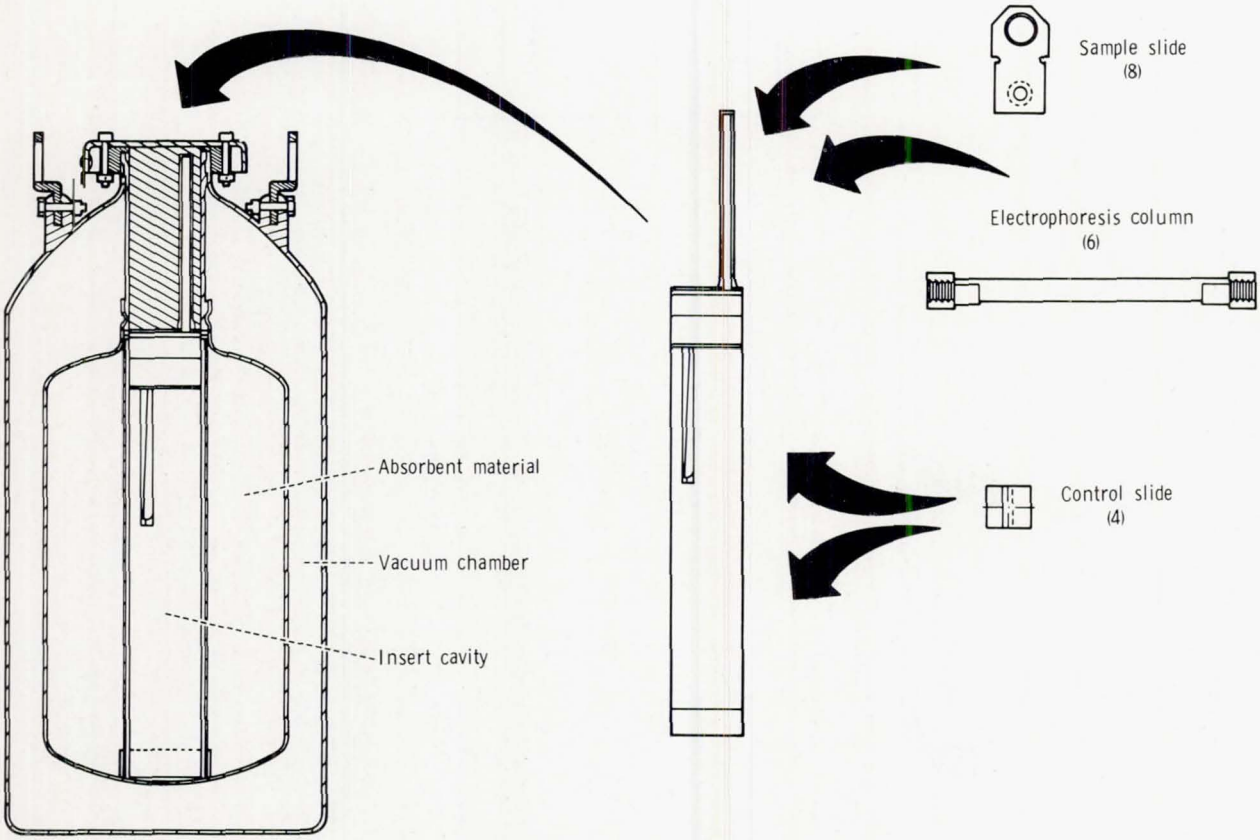

Figure 20-4.- Cryogenic freezer.

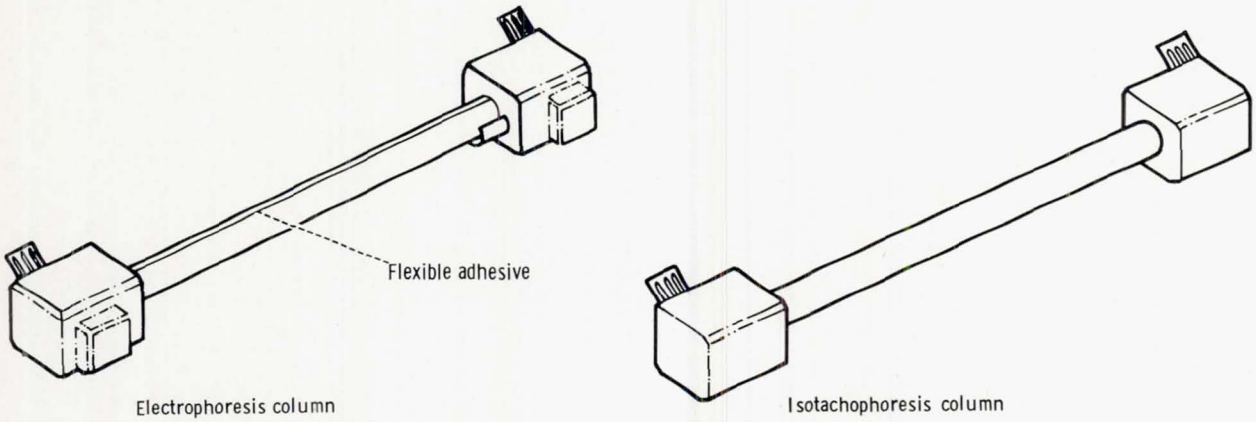

Figure 20-5.- Electrophoresis and isotachophoresis column assemblies.

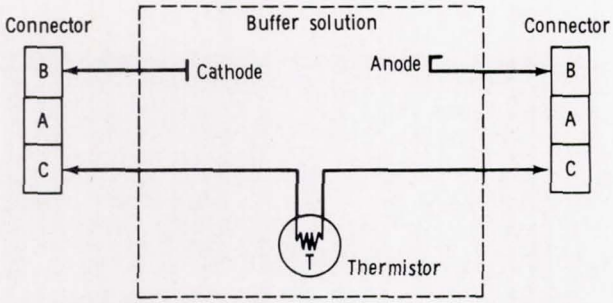

Figure 20-6.- Electrophoresis column electrical schematic.

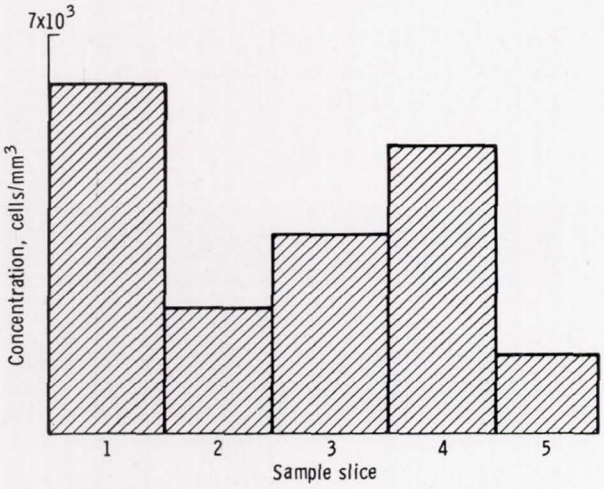

Sample slice	Cell type		
	Rabbit	Human	Horse
Mobility, percent			
1	19	22	59
3	11	17	72
4	12	38	50
Morphology per 100 cells			
1	17	26	57
3	19	48	33
4	15	31	54

Figure 20-7.- Mobility and morphological data from column 1.

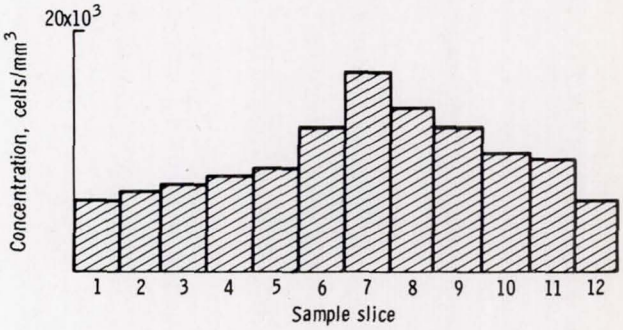

Sample slice	Cell type		
	Rabbit	Human	Horse
Mobility, percent			
5	18	60	22
8	24	48	28
11	23	42	35
Morphology per 100 cells			
1	56	38	6
2	66	31	3
3	60	40	0
4	64	36	0
5	36	57	7
6	47	41	12
7	31	32	37
8	17	41	41
9	12	27	61
10	11	23	66
11	10	34	56

Figure 20-8.- Mobility and morphological data from column 5.

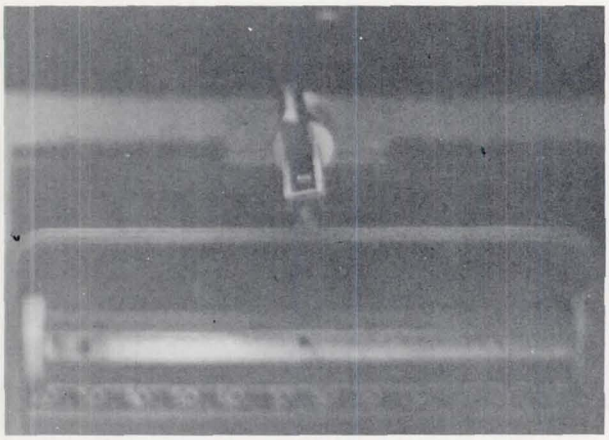

Figure 20-9.- Flight photograph of electrophoresis column 5 (AST-26-2182).

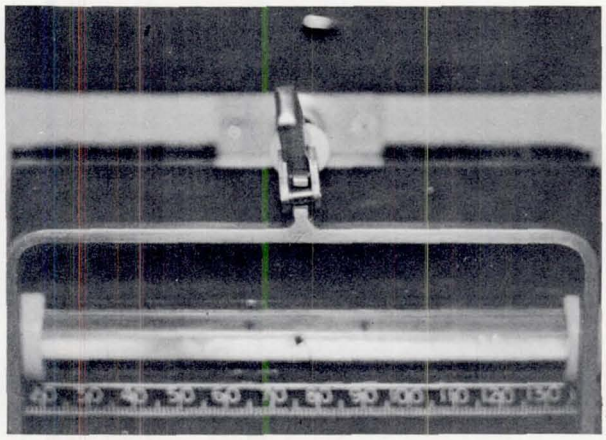

Figure 20-11.- Flight photograph of electrophoresis column 5 (AST-26-2186).

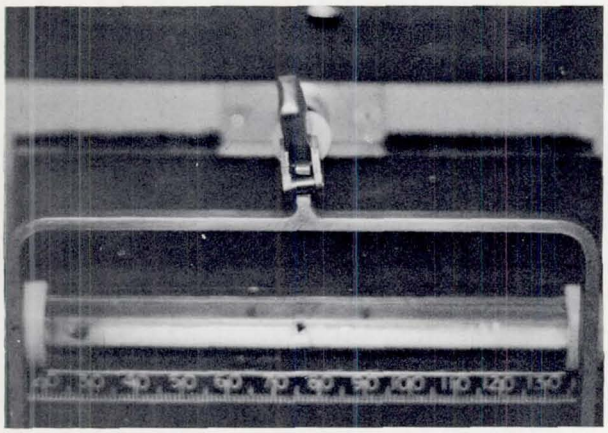

Figure 20-10.- Flight photograph of electrophoresis column 5 showing disruption of boundaries seen in figure 20-9 (AST-26-2183).

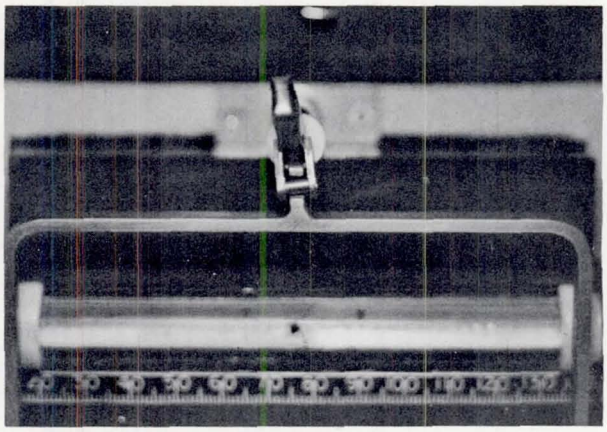

Figure 20-12.- Flight photograph of electrophoresis column 5 showing disruption of boundaries seen in figure 20-11 (AST-26-2187).

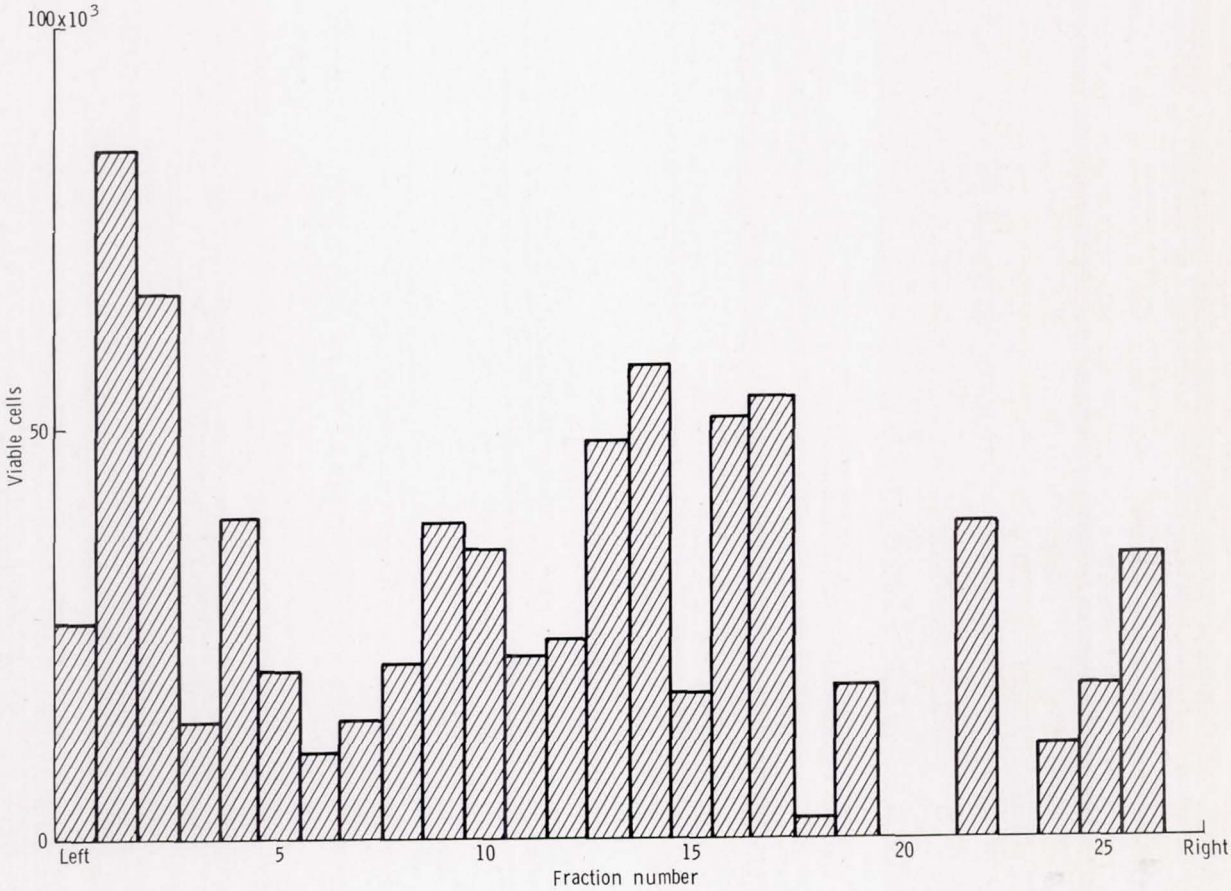

Figure 20-13.- Histogram of viable kidney cells for each sample slice in column 3.

21. ELECTROPHORESIS EXPERIMENT

EXPERIMENT MA-014

K. Hannig[a†] and H. Wirth[a]

ABSTRACT

A continuous, free-flow electrophoresis study was conducted during the Apollo-Soyuz Test Project mission to investigate and evaluate the increase in sample flow rate and sample resolution achievable in space. This electrophoresis technique is one of the most valuable methods to separate and analyze biological particles, such as living cells, without decreasing their biological activity. Gravity-induced thermal convection and sedimentation limit the effectiveness of separation by this method. The electrophoresis equipment was designed for the separation of four mixtures of biological cells with variable sample flow rates, buffer flow rates, and electric field gradients. Separation quality was assessed by measuring the light from a quartz lamp through the electrophoresis channel and on to a photodiode system.

The preliminary results indicate that all monitored systems operated correctly during the experiment. The optical system produced a light that was too bright to discern true cell distributions, but data were received that show a distribution of separated cells.

INTRODUCTION

The scientific requirements of the Electrophoresis Experiment (EPE) on the Apollo-Soyuz Test Project (ASTP) flight resulted from a study concerning the application of electrophoresis in future biological experiments on Spacelab. That study examined the possibility of separating vital cells or other biological materials in the space environment.

To understand the specific function of cells and their membrane systems, research is needed concerning the problem of separation and characterization of particles performing individual functions. Of particular importance in studying cooperative interactions in biological processes is the isolation of the interacting systems in the most homogeneous and still functioning form. These problems are not only of a fundamental theoretical interest but are also of practical importance to elucidate normal and pathological processes in biology.

---

[a]Max Planck Institut für Biochemie, Munich.

[†]Principal Investigator.

The reason for using electrophoresis to investigate these problems concerns the properties of the cell membrane surface, which is the site of many important biological phenomena. Transformation and differentiation processes are often accompanied by changes of the cell surface charge density. Charge density, however, determines the electrophoretic behavior; i.e., the electrophoretic mobility. Therefore, electrophoresis is a highly efficient method of separating cells or other biological particles according to functional criteria. Furthermore, cell electrophoresis is one of the few physicochemical processes that can be applied to living cells without producing damage or loss of viability.

Because electrophoresis is established as one of the most effective separation methods used in biological study, it is considered an essential tool for investigation in space. The expectation was that the separation capability would be increased at zero-g, resulting in new applications that depend on improved resolution.

The EPE concept was based on a new electrophoretic principle known as "carrier-free continuous-deflection electrophoresis" (free-flow electrophoresis). The technique was developed by K. Hannig at the Max Planck Institut and is patented in Germany and the United States. By this method (fig. 21-1), the sample to be separated is introduced continuously into a separation chamber, in which a buffer solution flows laminarly. An electric field is generated perpendicular to the direction of flow. Particles having different surface charge densities are deflected from the flow direction of the buffer by an angle determined by the flow rate and the electrophoretic mobility of the particles. After leaving the lower end of the separation chamber, the separated zones can be collected continuously or analyzed by evaluating the deflection and the density distribution of the fractions.

Because this electrophoresis system is a continuous procedure, it should be applicable for routine use in solving a variety of separation problems in a future Spacelab. The EPE was designed to verify the theoretically expected better and higher-capacity separations in the free-flow electrophoresis system under zero-g conditions.

EFFICIENCY OF FREE-FLOW ELECTROPHORESIS

The decisive advantages of free-flow electrophoresis result from the principle of continuous operation in a flowing medium. In contrast to most of the usually applied foil- or gel-electrophoresis methods, this method does not accomplish stability by an open-pore carrier medium, but rather permits the medium to flow freely in a narrow gap. To obtain the necessary stability, the capillary forces at the gap walls are used. Under one-g conditions, this method succeeds when the gap width is less than 1.0 millimeter. This width is also sufficient for an undisturbed electrophoretic migration of larger particles in the electrical field. Unlike the discontinuous electrophoresis method that is stabilized by porous media, the range of application of electrophoresis for preparative purposes can be expanded to include bulk-colloidal mixtures such as suspensions of viruses, bacteria, and cells and their membrane systems. A further advantage of electrophoresis in flowing medium with continuous operation is that the samples to be examined can be quickly exchanged without interrupting the experimental process.

The capability of quickly switching to the optimal experimental conditions combined with a completely automated operation makes this electrophoretic principle applicable to routine analytical separation problems. Thus, it would be possible to separate as many as 100 samples/hr to obtain analytical data concerning the composition of the samples to be examined.

As in every physical process, the effectiveness of free-flow electrophoresis is limited by some methodologically determined disturbances. In the use of electrophoresis under zero-g conditions, it is necessary to distinguish between effects caused by gravitation (i.e., sedimentation and thermal convection) and effects independent of gravitation. Under zero-g conditions, sedimentation and convection can be eliminated and thus a higher throughput with larger separation chamber gap dimensions can be obtained.

The resolution of electrophoretic separation is, however, hindered by a methodologically caused band broadening, which also exists under zero-g conditions. The band-broadening effects result mainly from (1) the Poisseuille velocity profile of the liquid curtain, (2) the electro-osmotic velocity profile, and (3) the temperature gradient through the liquid curtain thickness; the temperature gradient increases with liquid curtain thickness and electric power (fig. 21-2). The thermal diffusion caused by the extremely short separation times in free-flow electrophoresis can be ruled out.

The extent of the previously mentioned effects on the resulting band broadening has been theoretically and experimentally examined. The results are reported in reference 21-1, from which the following remarks were taken.

> An analytical Free-Flow Electrophoresis apparatus permitted easy observation of all these parameters. It could be shown that the opposing tailing effects of electro-osmosis, and the temperature gradient to the effect of the velocity profiles can be compensated for by appropriate adjustment of the chamber wall zeta potential. (The velocity profile of the liquid curtain flow causes a tailing of the separated bands in the direction of electrophoretic migration, whereas the electro-osmotic velocity profile counteracts this effect.) The experiments showed that there are additional broadening effects due to other not clearly defined parameters. It was observed that the sample inlet geometry plays a considerable role in band broadening. The practical relevance of this observation is that band broadening is reduced if samples are centered in the middle of the liquid curtain. Furthermore, sample bandwidth should be adjusted to values with a starting bandwidth of less than half the liquid curtain thickness. Under such conditions, the bandwidth was reduced so as to approach theoretical values.

These considerations and the experimental results reveal decisive advantages of free-flow electrophoresis, as opposed to static systems, regarding obtainable separation sharpness and sample throughput. However, one limitation occurs if the method of "isoelectric focusing" or "isotachophoresis" is applied for special separation problems. Because of the discontinuous buffer systems required (pH or ion strength gradients), the free-flow system appears to be less suitable.

ELECTROPHORESIS UNDER ZERO-G CONDITIONS

The efficiency of electrophoresis under one-g conditions is limited. Gravity effects such as heat convection, sedimentation, and buoyancy limit the application with respect to flow rates and resolution. To avoid convection under one-g conditions, the cross section and dimensions of the electrophoresis separation chamber must be kept small. (The thickness of the buffer film is normally 0.5 to 1 millimeter.) Under zero-g conditions, there are theoretically no limits in this respect. However, one limit is set by the need for effective removal of the Joule heat, especially when working with biological materials. (Depending on environmental conditions, this limit occurs at a layer thickness of 5 to 10 millimeters.) Considering this limitation, with a possible tenfold larger buffer film thickness, an increase of up to tenfold in sample throughput can be achieved because of the lack of convection disturbances.

A simultaneous improvement of separation sharpness is, however, not to be expected. As previously discussed, the factors influencing separation sharpness in the EPE are essentially methodological and are not dependent on gravitation. An optimization of separation sharpness can be achieved under one-g conditions if the experimental requirements are fulfilled (suitable separation chamber wall potential and less sample throughput).

The significance of applying electrophoresis in the Spacelab as the preferred separation method for sensitive biological material becomes particularly evident in connection with important biological experiments conducted under zero-g conditions. The use of electrophoresis may assist in clarifying many phenomena, such as growth, metabolism, genetics, and immune responses, which occur differently in zero-g conditions than in one-g conditions. The two main purposes for conducting electrophoretic experiments in space are (1) to analyze purity and to isolate samples for medical and biological research, and (2) to develop separation methods for commercial and other applications on a preparative scale.

Many proposals also merit further investigation. These proposals concern the effect of gravity on cell functions and the ability of cells or whole organisms to adapt to changes in gravity. One example is the cultivation of cells, the investigation of their synthesis efficiency, and their contact inhibition without gravity. Assuming that it is possible to isolate highly purified cell populations grown under zero-g conditions, the state of weightlessness will offer an excellent opportunity to examine the phenomena of cell differentiation and the exchange of information between different cells.

Some of the necessary operational conditions can be tested only with complete absence of sedimentation. The clarification of these phenomena is not only of great scientific interest but also of practical significance for the regulation of detailed biological processes.

The importance of new findings of this kind for medicine can be anticipated. These investigations require a separation method that allows separation of the carriers of specific syntheses or of the synthesis products themselves. This purpose may be fulfilled in Spacelab by using electrophoretic separation methods. However, the applicability of space electrophoresis for the production of biological material

for commercial purposes cannot yet be predicted. At this point, researchers are just learning how electrophoresis in space is to be used. The EPE can therefore be essentially regarded as a pilot experiment.

The main purposes of EPE and the problems to be clarified were as follows.

1. Applicability of electrophoresis in space

2. Performance of separation experiments with greater throughput

3. Investigation of temperature and velocity effects with a chamber of larger gap width

4. Investigation of separation capability in zero-g conditions

5. Proof of the possibility of separating preparative quantities of living cells

6. Determination of necessary modifications in the construction of the apparatus for use in space

METHODS AND PROCEDURES

Equipment Design

The design goal for the EPE apparatus (fig. 21-3) was to develop experimental equipment meeting the ASTP spacecraft requirements. The apparatus functions automatically, requiring minimal crew intervention. Known biological samples were used and it was not necessary to collect the separated biomaterial fractions. An optoelectronic analysis of the separation was performed. A preparative separation was not used. A quantitative evaluation (by use of an optical system) is sufficient to determine the applicability of the method and to study the sharpness of separation.

The separation chamber is the main part of the apparatus. It consists of two cooling plates that are adjusted to be exactly parallel to supply laminar flow and form a gap of approximately a 28- by 3.8-millimeter cross section. Along the sides, electrodes (180 millimeters long) provide the electric field perpendicular to the cell buffer flow. The electrodes are separated from the cell buffer by ion-exchange membranes. The electrodes are located in channels purged by the electrode buffer to remove the hydrogen and oxygen (H_2 and O_2) gases generated by the electrolytic processes. The gases are separated from the fluid and absorbed by means of catalysis. The fluid flow is kept constant by controlled pumping at a rate sufficient to transport the total volume of gas generated. The electrode buffer is separated from the cell buffer, which has a lower concentration, by the two ion-exchange diaphragms.

The separation buffer flow was achieved by means of a peristaltic pump. Before starting the experiment, the buffer was pumped through the heat exchanger, which is in contact with a cold plate of the spacecraft, and cooled to the appropriate

operation temperature of 278 ± 3 K (5° ± 3° C). The buffer leaves the storage container and enters the cell somewhat upstream of the sample inlet to achieve a constant laminar flow in the cell parallel to the electrodes. After having passed the separation chamber, the mixture of sample and cell buffer entered the waste container, which is combined with the storage container but separated by a membrane. The angle of deflection for a particular particle was determined by the separation buffer flow rate and the field gradient. The program included two flow rates for each sample so that the influence of buffer velocity could be studied.

The sample containers were designed so that no air entered the circuit and none of the samples were split when the containers were inserted into the equipment. The containers have a volume of 2 milliliters, consist of a metal tube with handling knob, and are totally gold plated. On the upper end, they are closed by a pressure exchange membrane and sealing. The lower end has a bore connected to a needle with a valve that is opened by inserting the container into the sample inlet closed by a rubber sealing.

The sample containers were stored in a freezer at 273 to 278 K (0° to +5° C). For experimental operation, they were removed from the freezer and inserted into the equipment so that the sample flow entered the buffer flow. This flow was directed by a peristaltic pump similar to that of the buffer flow circuit.

The separation was evaluated by optoelectronic methods. By this method, a narrow slit across the downstream end of the separation chamber, parallel to the electric field, is illuminated. The light passes through the quartz plates of the separation chamber and is attenuated as a function of the density of the biomaterial distribution. On the other side of the chamber, the light intensity, related to the cell density, is measured with a photodiode array.

Experiment Sequencing

The experiment equipment was programed and controlled by electronic units that performed the following functions.

1. Control of the flow rates; i.e., motor speeds for driving the pumps

2. Power supply

3. Program sequencing, which provided the program of the experiment operations and was triggered by the parameters of the experiment

4. Thermoelectric temperature control

5. Self-check

6. Data acquisition, evaluation, and processing

7. Data recording

8. Switching and displaying of experiment operations and experiment states

The main purpose of the program sequencer was to operate the experiment automatically as much as possible, thereby reducing crewmember participation. The program sequencer was designed to perform the following functions (fig. 21-4).

1. Timing of functions such as precooling or purging

2. Generating nominal values for voltage and flow rates according to the sequence step

3. Collecting and processing GO/NO GO information from experiment subsystems

4. Switching subunits "on" or "off" according to a fixed test program

5. Providing time, frequency, and voltage references

6. Initiating and performing an in-flight self-check program

All experimental data were recorded in digital form by two tape recorders that were integrated into the experiment. Both recorded digital data at a bit rate of 2.5 kilobits/sec.

Cell Sample Preparation

The following samples were prepared for the electrophoresis experiment.

1. Rat bone marrow cells

2. Mixture of human and rabbit erythrocytes

3. Rat spleen cells

4. Rat lymph node cells with the addition of human erythrocytes as markers (Sample 4 was the only frozen sample.)

With the exception of sample 2 (erythrocytes), all samples were freshly prepared on July 14, 1975, 15 to 20 hours before lift-off. They were stored at 277 K (4° C) for approximately 45 hours before the start of the experiment. Sample 2 (erythrocytes) had been prepared 2 weeks in advance at the Max Planck Institut für Biochemie in Munich, and the cells were preserved by fixation in 2 percent glutaraldehyde. The preparation of cells from different lymphatic organs was accomplished under sterile conditions (autoclaved material, clean bench) at 277 K (4° C) in the NASA John F. Kennedy Space Center (KSC) laboratory.

Bone marrow cells of rats (Wistar) were prepared, and cells were flushed out of the bones with Puck TC solution combined with 2.5 percent bovine serum albumin (33 percent) by using a syringe. A single-cell suspension was prepared by passing the cells several times through a plastic syringe without a needle. The cells were then washed twice (150 grams, 10 minutes) with the same buffer and finally resuspended in ampholine buffer.

Cells from spleen and lymph nodes of the rats were prepared by teasing the organs in Puck TC solution at 277 K (4° C) with injection needles. Cells were washed twice with the same solution (150 grams, 10 minutes), filtered through cotton wool, and resuspended in ampholine buffer.

For sterile tests, cell suspensions and buffer solution were spread on blood-agar dishes and incubated for 5 hours at 301 K (28° C). This test, as well as light microscopical control, showed no bacterial contamination of cell suspensions and buffer solutions. The viability of the prepared cells (tested with trypan-blue exclusion test) was more than 90 percent in each sample.

All containers of the flight unit were sterilized with formaldehyde (2.5 percent) and washed five times with 20 milliliters of sterile ampholine buffer. A special apparatus for filling the sample containers was sterilized in the same way. At 4 days before Apollo lift-off, the special "deep freezing container" was filled with a 0.8-milliliter mixture of rat lymph node cells (25×10^6 cells/ml) and human erythrocytes (30×10^6 cells/ml) and kept in liquid nitrogen. At 14 hours before Apollo lift-off, the other three sample containers were filled with 1.4 milliliters of the following preparations.

1. A mixture of fixed human erythrocytes (30×10^6 cells/ml) and fixed rabbit erythrocytes (50×10^6 cells/ml)

2. Native bone marrow cells of the rat (80×10^6 cells/ml)

3. Native spleen cells of the rat (80×10^6 cells/ml)

The exact composition of all buffer systems used for cell preparation and for electrophoretic separation is shown in table 21-I.

RESULTS

The experiment began on schedule on July 16, 1975, at 32:40 ground elapsed time (GET) and lasted for one complete Earth orbit until 34:25 GET. Radio communication from the Apollo spacecraft confirmed that, according to the signal lamps, all functions were operating properly.

Analysis of the Tapes

The first playback took place at the Max Planck Institut with the aid of a so-called "unit tester." All housekeeping data correspond to the expected course except for the chamber temperature, which for unknown reasons was indicated as being too high. Nevertheless, the measurements were within the tolerable range for biological material.

The scientific data revealed that the light for the optical detection of the separation must have been too bright. The lamp check showed excessive lighting resulting in a saturation of the photodiodes in the optical detection system. The quantitative estimate of error revealed that the light must have been 42 percent too bright, although the lamp check indicated normal functioning during the preinstallation check. For this reason, only absorptions above 30 percent were registered. This amount corresponds to the maximum expected absorption of a separated fraction zone.

In the entire separation process, no "true" cell distribution curve was obtained. The baseline of registration in all cases was above the maximum absorption obtained in the peaks. Because of this finding, an analysis of the experiment seemed at first to be impossible. However, during the stationary phase of the separation (after adjustment to constant experimental conditions), i.e., during 90-second separation time, irregularly occurring pulses (called "events") were recorded. This pattern reflected the expected course of the separation curves (fig. 21-5). These pulses seemed to be caused by cell aggregation in the region of the separated bands. This assumption was confirmed in the following two ways.

1. An aliquot of the sample used in the ASTP flight was separated under the same conditions on mission day at KSC in an identical apparatus under one-g conditions (electrophoresis engineering model (EM) with a 0.7-millimeter buffer film thickness). In addition to the expected cell distribution curves (fig. 21-5), analysis of this undisturbed tape showed stray pulses caused by cell aggregation that had a greater absorption. The accumulation at the same location (frequency distribution of the events) during a separation time of approximately 2 minutes yielded distribution curves similar to normal separation curves (fig. 21-5).

2. To check this finding and to obtain a reliable interpretation, such separations were repeated many times with the EM apparatus, and each experiment was performed and evaluated with normal and increased lighting. It was clearly established that only the analysis of the periodically occurring cell aggregations at the measuring location was representative of the actual cell distribution. The difficult evaluation and coordination of indirect information was performed with the aid of a data-processing computer.

Based on these studies, assertions can be made regarding the following samples.

1. Bone marrow cells: Although only a few events (73) could be analyzed because of the tendency of these cells to form no aggregations, the distribution curve is that of an excellent separation.

2. Mixture of human and rabbit erythrocytes: Because of the weak tendency of these fixed cells to form aggregations, insufficient information was available for computation.

3. Spleen cells: The best result was obtained with this sample. The amount of information (358 events) was sufficient to identify fine details of the separation. The separation in erythrocyte peak can sometimes be indicated in good separations under normal one-g conditions as well. This finding indicates an essentially good separation sharpness under zero-g conditions.

4. Lymph node cells with the addition of human erythrocytes (frozen sample): A large number of events (549) were detected. A good separation effect, similar to sample 3, was inferred here as well as under zero-g conditions.

Postflight Examination

Postflight examination of the flight unit, which took place in Munich, yielded the following information.

1. All housekeeping data were within the tolerance range.

2. The buffer and sample amounts corresponded to the required specification according to the volume measurements carried out.

3. Buffer samples collected in the container revealed no extraordinary bacterial contamination despite the long storage period. Microscopic investigation for the presence of cell particles in the separation buffer (collection container) was positive.

4. The expected remainder of the cell suspension, more than 3 months old, was found in the examined sample containers. However, the gold-plated containers revealed unexpected corrosion.

5. All buffer tube systems were intact and penetrable. The pump systems were still fully operational.

This information clearly reveals that the course of buffer and sample and the electronic system must have operated accurately. Surprisingly, the error in the optical detection system shown by the tape (saturation of the photodiodes) was at first not identifiable. Both the current and the voltage of the lamp were normal. By contrast, the light intensity measured by the diode array was, as expected, too low, because of turbidity. The cause for this phenomenon can be considered as either a fault in the electrical contact arising during the flight or an increase in lamp helix temperature arising under zero-g conditions. The latter could be explained by the absence of thermal convection in the gas-filled tube.

SUMMARY

The applicability of free-flow electrophoresis under zero-g conditions of the space flight was confirmed. The technical problems arising from the special environmental conditions in a Spacelab can be controlled. This observation applies to the technical concept of the EPE apparatus as well as the manual operation by crewmembers. In particular, it was demonstrated that the buffer flow systems operated despite the more difficult conditions imposed by a closed system. The effective removal of gases from the electrode buffer (electrolytic products) by the measures used was a necessary part of this experiment.

In a separation chamber of large cross section, the temperature conditions required for biological material could be fulfilled. The same applies for the correct laminar buffer flow.

A sample throughput greater than tenfold was achieved by the expansion of the separation chamber cross section possible in space flight and with otherwise similar chamber dimensions. (In the fast sequence (fig. 21-4, step 1), 7×10^6 cells/min were separated.) Despite the error that occurred in the optical detection system, it was demonstrated that the separation sharpness corresponded at least to that of analytical separations under one-g conditions. Whether an improved separation sharpness is possible with a fivefold decreased sample insertion rate (fig. 21-4, steps 2 and 3), in contrast to one-g conditions, could not be determined because of the reduced source of information (sensitivity) caused by the lamp error. This is of little importance because such measurements can also be conducted under one-g conditions, as already shown. Also, the separation sharpness depends on other influences as well (e.g., zeta potential on the wall).

The possibility of separating living cells under zero-g conditions was demonstrated. The cell aggregations that formed in the cell suspensions need not correspond to a decrease in cell viability.

REFERENCE

21-1. Hannig, K.; Wirth, H.; Neyer, B.; and Zeilter, K.: Theoretical and Experimental Investigations of the Influence of Mechanical and Electrokinetic Variables on the Efficiency of the Method. Z. Physiol. Chem., vol. 356, Aug. 1975, pp. 1209-1223.

TABLE 21-I.- BUFFER SOLUTIONS[a]

Description	Electrode buffer	Chamber buffer	Ampholine buffer
Substance, g/liter			
Triethanolamine	5.16	1.71	--
Potassium acetate	0.90	0.30	0.61
Glucose	0.90	14.61	--
Sucrose	--	7.88	--
Calcium acetate	--	0.033	0.05
Magnesium acetate	--	0.46	--
Glycine	--	--	21.55
Ampholine (pH 3.5 to 10)	--	--	20 000
Characteristic			
Conductivity, μmho	2500	900	900
Osmolarity, mOsmol	--	≈300	≈300
pH	7.2	7.2	7.2

[a]Buffer solutions mixed with distilled water.

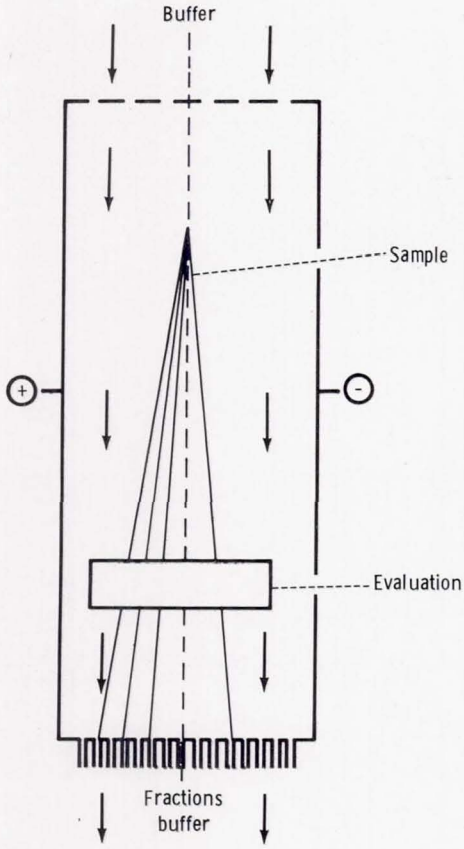

Figure 21-1.- Illustration of the principle of free-flow electrophoresis.

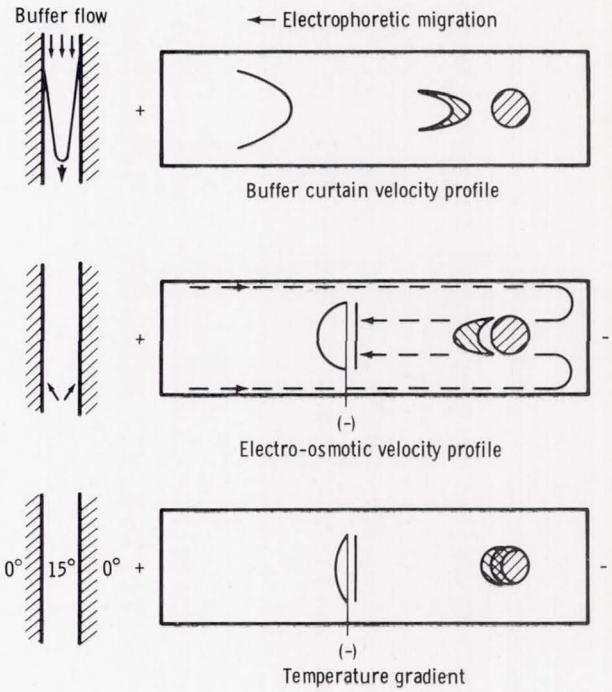

Figure 21-2.- Band-broadening effects in free-flow electrophoresis.

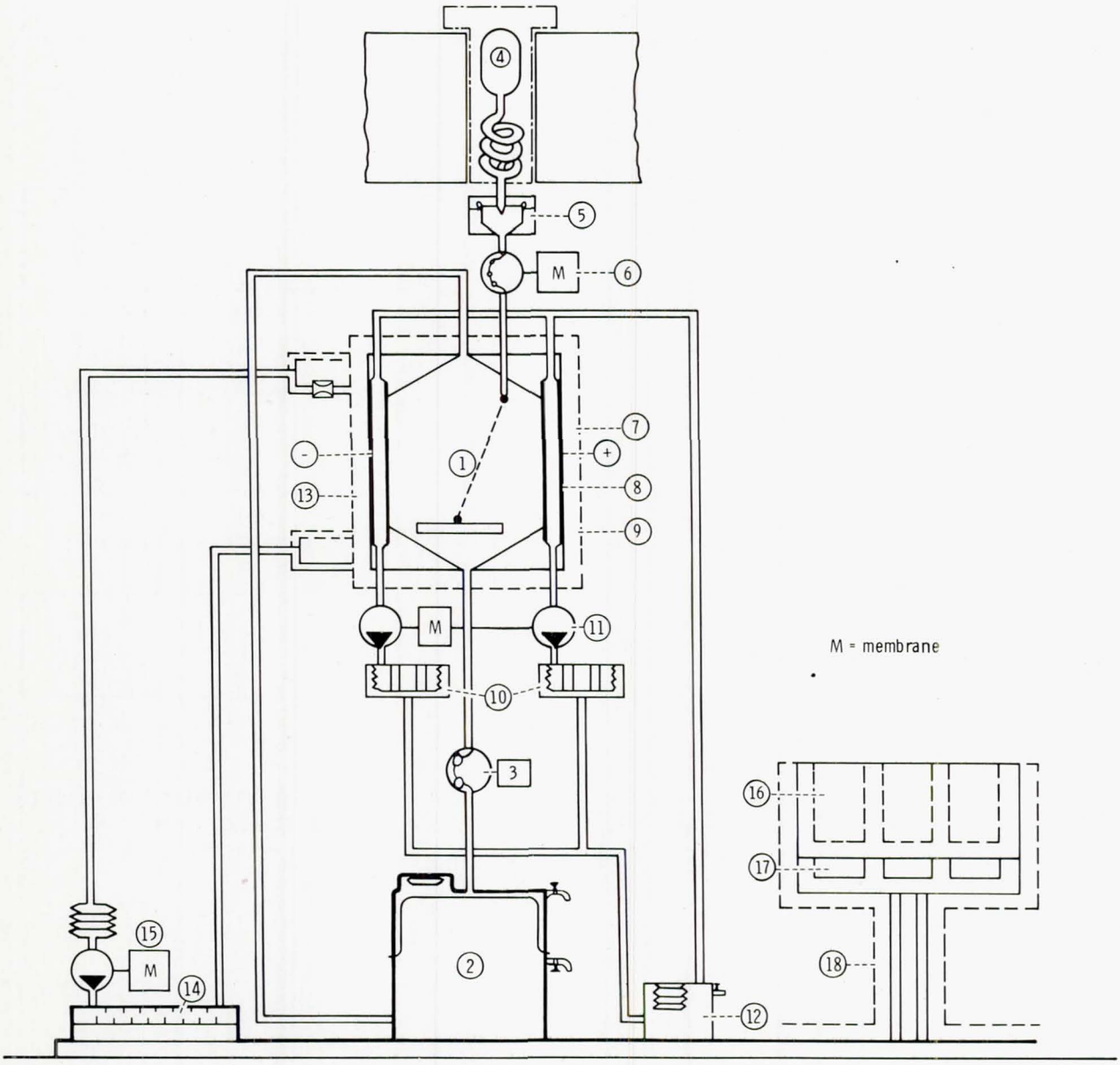

Figure 21-3.- Functional diagram of experimental setup. Buffer system: (1) cell, (2) cell buffer, waste container, (3) pipe pump, motor, pipe. Sample system: (4) sample container (exchangeable), (5) separation membrane, (6) pipe-pump, motor. Electrode wash system: (7) electrode chamber, (8) electrode, (9) diaphragm (membrane), (10) phase-separation $O_2 + H_2$ (catalytic burner), (11) pump, motor, (12) electrode buffer container. Cell cooling system: (13) cell cooling tank, (14) Peltier cooling tank, (15) pump, motor. Freezer system: (16) samples container, (17) Peltier cooling unit, (18) heat radiation plate.

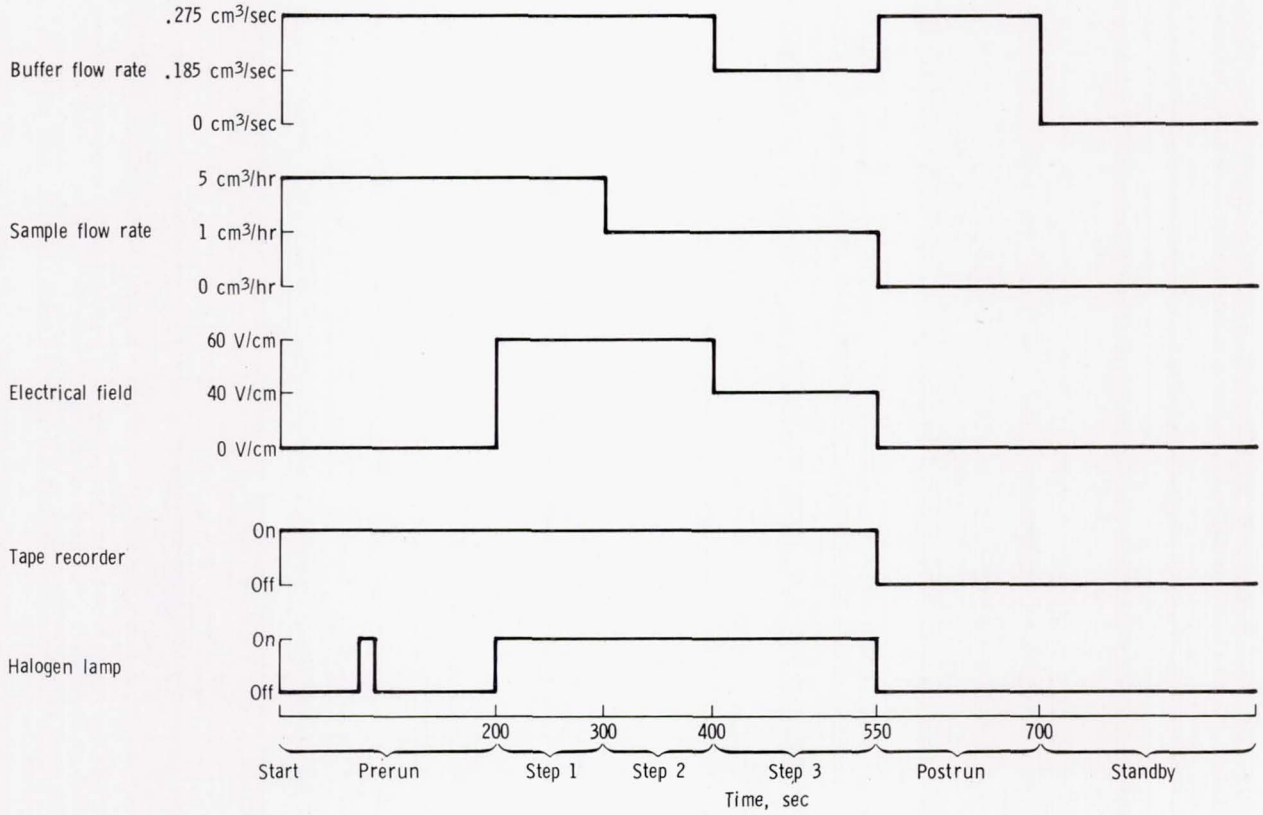

Figure 21-4.- Electrophoresis experiment sequence.

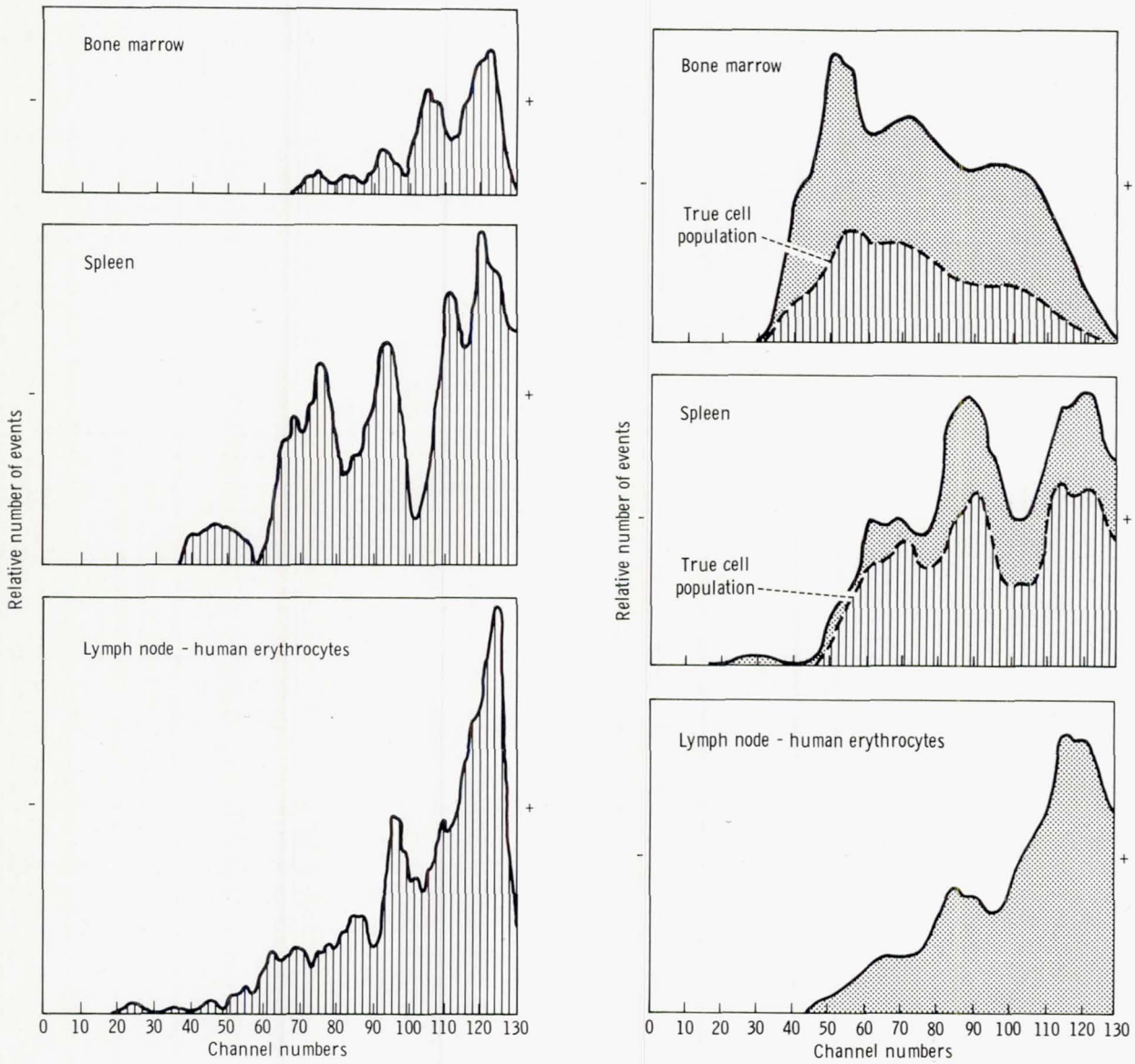

(a) Zero-g conditions.

(b) One-g conditions.

Figure 21-5.- Sample separation under zero-g and one-g conditions.

22. MULTIPURPOSE ELECTRIC FURNACE

EXPERIMENT MA-010

A. Boese,[a†] J. McHugh,[b] and R. Seidensticker[b]

ABSTRACT

Experiments on solidification, crystal growth, and other processes involving phase changes in various type materials were performed in the multipurpose electric furnace developed for the Apollo-Soyuz Test Project. Phase changes were conducted at elevated temperatures (as high as 1423 K (1150° C)) in systems comprising selected combinations of solid, liquid, and vapor phases. Because of the near-zero-g environment aboard the spacecraft, the liquid and vapor phases were essentially quiescent, and phases of different density had little or no tendency to separate.

INTRODUCTION

The Multipurpose Electric Furnace Experiment facility for the Apollo-Soyuz Test Project (ASTP) was based on a similar furnace (denoted M-518) that was operated onboard the Skylab. The furnace was used to heat and cool material samples in space and thereby take advantage of the lack of thermal convection and sedimentation during the liquid or gaseous phase of the material. Seven experiments in solidification and crystal growth from vapor or melts were performed: Surface-Tension-Induced Convection (MA-041), Monotectic and Syntectic Alloys (MA-044), Interface Markings in Crystals (MA-060), Zero-g Processing of Magnets (MA-070), Crystal Growth From the Vapor Phase (MA-085), Halide Eutectic Growth (MA-131), and Multiple Material Melting (MA-150). These experiments are described in sections 23 to 29, respectively.

The motivating concept for the MA-010 experiment was that, at the present stage of the space-processing program, there are many useful preliminary space experiments that can be performed simply by applying prescribed heating and cooling programs and/or known temperature distributions to selected experimental samples of materials. For example, the simple process of growing a Bridgman crystal of a pure metal by directional solidification becomes an interesting new experiment

---

[a]NASA George C. Marshall Space Flight Center.

[b]Westinghouse Research Laboratories, Pittsburgh, Pa.

[†]Principal Investigator.

in space because convective heat and mass transport will be largely suppressed in the melt. Many other similar examples exist.

The guiding design requirement for the multipurpose electric furnace system was to produce an apparatus that provided the widest possible flexibility in applying predetermined temperature distributions and temperature/time sequences within the constraints imposed by existing interfaces. Although the Skylab multipurpose furnace met all expectations of performance and reliability, it was apparent that improvement in function could be obtained with some specific modifications for ASTP. The system consisted of three essential parts: the furnace, a programmable electronic temperature controller that provided the desired temperatures, and a helium rapid cooldown system (fig. 22-1).

SYSTEM DEVELOPMENT

Furnace

The design of the ASTP multipurpose furnace was prompted by two major considerations: the need for higher operating temperatures and the desire for reduced power requirements. The variety of materials experiments proposed for the ASTP mission required temperatures in excess of the approximately 1273 K (1000° C) limit of the Skylab system. Furthermore, the reduced heat dissipation capability of the ASTP vehicles dictated that these higher temperatures be obtained with no increase in power requirements.

Experience with the Skylab furnace facility indicated that somewhat higher temperature operation would be possible without any modification; however, the power requirements would be excessive. Therefore, the initial effort of the redesign was to reduce the intrinsic heat loss. The predicted performance of the redesigned system was sufficiently encouraging that even higher temperature operation appeared feasible if it were compatible with the furnace materials, especially the heating elements. Accordingly, the high-temperature components of the furnace were carefully evaluated and, where necessary, materials were changed or assembly techniques modified to provide reliable operation.

Analysis of the Skylab furnace indicated that one significant source of heat loss was the "piping" of radiation between the heat shields. This loss could be reduced by providing a "mitered" closure of the radiation shields at both the cold and hot ends of the furnace. This type of construction would, in essence, provide a "nested can" shield configuration in which radiation leaks would occur only through the necessary clearance gaps in the shields. The efficiency of the shield system was also increased by using two interstitial shields of 0.0127-millimeter (0.0005 inch) thick molybdenum foil between adjacent main shields.

Conductive heat loss through the heat leveler support tubes was also reduced. In the Skylab system, the heat leveler assembly was mechanically supported by three stainless steel (Type 310) gradient tubes that had outside diameters of 2.223 centimeters (0.875 inch) and walls that were 0.040 centimeter (0.016 inch) thick. These tubes had a combined thermal conductance of approximately 0.15 W-cm/K,

which would result in a conductive loss of approximately 21 watts with a furnace temperature of 1423 K (1150° C). In the modified furnace, the wall thickness of the support tubes was cut to 0.020 centimeter (0.008 inch), which would reduce the loss by half.

The design target maximum temperature of 1423 K (1150° C) for the heat leveler necessitated a reexamination of the heater elements. The first characteristic considered was the specific loading of the heater wires. This parameter controls the temperature difference between the wire and the workpiece; e.g., the graphite heat leveler. If the loading is too large, then the heater wire may be forced to run too hot in order to transfer the requisite power to the work. Several variations of heater design, including single and multiple ribbon heaters, were investigated. It was found, however, that the double, noninductive winding used for the Skylab furnace was nearly optimum when the additional constraint of heater resistance was imposed. The specific loading of approximately 1 W/cm^2 would impose a wire temperature only approximately 50 K (50° C) greater than the heat leveler temperature.

The next factor investigated was the suitability of Kanthal A-1 as heater material. Although this material is suitable for use to 1598 K (1325° C) in air, it is not recommended for use in vacuum at temperatures over 1273 K (1000° C). This warning is based on the rapid evaporation of a component from the alloy and was verified by tests performed on bare wires in ultrahigh vacuum. Sample filaments burned out after 2 hours or less at a surface temperature of 1473 K (1200° C). The heater winding, however, is not a bare wire operating in ultrahigh vacuum.

A second test was performed with a Kanthal A-1 heater wound on a salvaged Skylab heater form. In this configuration, the wire is completely surrounded by high-purity alumina. In the test facility, this heater form was filled with a graphite block to simulate the heat leveler and heavily insulated with Fiberfrax to reduce heat losses. After 144 hours of operation, the windings were still operating; however, the heater resistances had changed considerably. Examination of the disassembled unit revealed that evaporation of a volatile component had occurred and the wire was seriously degraded.

A further modification of the configuration was considered, namely embedding the heater wires in high-purity alumina cement. The life test was then repeated. The Kanthal was wound on the heater form and fired in air at 1273 K (1000° C) to form a surface oxide. A slurry of alumina powder was applied and air dried, and the heater form was then fired at 1273 K (1000° C). Finally, the test setup was reassembled. After 100 hours of operation at approximately 1473 K (1200° C), the heater resistances had changed by only 1.3 percent. Because the test time was roughly 10 times longer than the anticipated operating requirements, this design was adopted for incorporation in the prototype furnace.

Coincident with the requirement for higher temperature operation of the modified furnace, it became necessary to evaluate the higher temperature suitability of the structural materials used in the Skylab furnace design. It was immediately obvious that the only portion of the design that might be doubtful was that part of the structure in close thermal proximity to the heating element. Furthermore, it was clear that the limiting condition was that of the combined effects of graphite,

alumina, and stainless steel as they exist at higher temperature in the multipurpose furnace atmosphere and pressure environment. In the Skylab furnace design, these materials are in direct physical contact.

To evaluate the limiting of this materials combination, a series of compatibility tests was carried out under conditions that approximated the multipurpose furnace environment. Alumina was promptly shown to be inert in these conditions at the intended temperature. The margin of safe temperature for the graphite-stainless steel combination, however, was found to be very small. The intended maximum design temperature for graphite and stainless steel is 1423 K (1150° C) in the modified design. The tests indicated that this materials combination exhibited no harmful degradation at 1498 K (1225° C) but degraded seriously at 1523 K (1250° C). Thus, a furnace overtemperature of approximately 75 K (75° C) would be allowable insofar as graphite and stainless steel reaction is a concern. Although a margin of that value is probably adequate, it was desirable to provide a better choice of materials.

As a consequence, nickel was proposed as a replacement for the stainless steel, and the graphite and nickel combination was evaluated. This combination exhibited no harmful degradation even at 1560 K (1287° C), and it was deemed unnecessary to extend the evaluation to higher temperatures. The conclusion was that the graphite-nickel-alumina combination was safe to at least 1560 K (1287° C) and that the resulting overtemperature margin of 137 K (137° C) was more than adequate. The stainless steel was thus replaced with nickel in the temperature-critical areas in the modified multipurpose furnace.

A predictable consequence of increased multipurpose furnace temperature is increasingly reduced thermocouple electrical isolation resistance. This occurrence is a natural property of the magnesia insulation in the prefabricated swaged thermocouples and has the effect of reducing the resistance between the Chromel-Alumel wires and the Inconel sheaths, which, in the Skylab furnace, were electrically grounded to the furnace structure. This effect was acceptable at the 1273 K (1000° C) maximum temperature for which the Skylab furnace was designed. Because this effect is strongly temperature dependent, however, it was unacceptable at the higher (1423 K (1150° C)) maximum furnace temperature and thus required compensating design changes.

Greatly increased thermocouple resistance to a ground was obtained by electrically insulating the Inconel sheaths from the grounded furnace structure. This was accomplished in the high-temperature region by the installation of high-purity alumina sleeves and in the low-temperature region by Teflon sleeves. Additionally, the control thermocouple Inconel sheaths were electrically connected to the regulated 10-volt supply that biases the control thermocouples. This arrangement in effect applies a guard potential to the sheaths and thus eliminates the effect of the small remaining electrical leakage which exists with the insulating sleeves. The Inconel sheaths of the four measuring thermocouples were allowed to float electrically.

Experience disclosed that the seals of the access ports for the Skylab multipurpose electric furnace were not suitable for repeated use because of the excessive force required for removal. No seal leakage was ever detected. Because rotating and reciprocating seals are used routinely in high-vacuum systems, it appeared

very likely that the problem with the Skylab furnace was not a fault of design principle but was rather a fault of design detail dimensions. A new design was developed.

The Skylab furnace was evacuated by evacuating the chamber in which it was situated. The ASTP furnace was evacuated through a pump line leading from the furnace through the docking module wall to space. The furnace vacuum connection was redesigned to allow for this change. The Skylab fitting was replaced by a 2.54-centimeter (1 inch) diameter elbow that terminated in a welded connection to the docking module pump line.

Helium Package

The Skylab multipurpose furnace was evacuated during the entire time period required for each experiment. The modified furnace, if evacuated, required as much as 20 hours of passive cooling to reach the allowed touch temperature. For the ASTP mission, cooldown periods of such duration would seriously limit the number of experiments that could be fitted into the permitted time frame. To minimize this problem, a helium rapid cooldown system was developed. With this system, the time required for cooldown was reduced to as little as 3 hours.

Rapid cooling may be provided through selective control of the heat loss of the furnace. For minimum thermal transfer, the heat shields require a high-vacuum environment, but the thermal transfer will be greatly increased if the vacuum environment is replaced by helium. Fortunately, only a very small amount of helium is required for this purpose; approximately 1.01 kN/m^2 (0.01 atmosphere) approaches the maximum effectiveness. For the multipurpose furnace, the volume required to produce 1004.13 kN/m^2 (9.91 atmospheres) is approximately 0.16 cubic centimeter of helium at standard conditions. Within the 1.01-kN/m^2 (0.01 atmosphere) range, the thermal transfer is weakly dependent on pressure, and it is consequently not necessary to provide a precise volumetric measure for each dosage. The helium package was designed so that successive doses of helium would be provided at slightly reduced volume.

A schematic representation of the helium package is shown in figure 22-2. During each experiment before rapid cooldown, all helium package valves must be closed. Immediately before operation of the package, the docking module valve in the overboard vacuum line to the furnace must be closed. To initiate rapid cooldown, two valve operations are required: (1) valve B must be opened momentarily to pressurize the helium dosage cavity from the helium storage tube, and (2) valve A must be opened momentarily to release the helium dosage into the furnace. No further valve manipulation is required during the rapid cooldown period.

When cooldown is completed and the allowed touch temperature has been reached, the experiment cycle is completed. Before the furnace is opened, it should be pressurized to the same value as the docking module. This is accomplished with the helium package by momentarily opening valves A and C simultaneously and thus allowing the docking module atmosphere to flow into the furnace until the pressure is equilibrated.

Control Package

The control package for the multipurpose electric furnace system (fig. 22-3) was modified to meet a new set of requirements for the ASTP mission. These modifications included several changes of the system operating functions; mechanical modifications were also made to meet new interface requirements. A listing of these modifications and a brief description of each is presented in the following paragraphs. In addition to these items, a number of minor electronic component changes were made to provide additional safety margins in circuitry operation.

Increase in maximum control temperature.- To facilitate higher temperature experiments, the gain of the control thermocouple amplifier was altered to permit a maximum controlled heat leveler temperature in excess of 1423 K (1150° C).

Variable controlled cooldown rate.- To provide more constant solidification velocities in the experiments, circuitry was incorporated to decrease the cooldown rate continuously during the controlled cooldown portion of the experiment. A control was provided to enable selection of the amount of cooldown rate variation.

Shorted control thermocouple protection.- To protect the furnace from overheating should the control thermocouple become shorted, an additional shutdown circuit was incorporated in the control package. This circuit continuously monitors both HOT-1 and HOT-2 measuring thermocouples and automatically shuts off the furnace heaters if either of these thermocouples exceeds a preset limit temperature (nominally set at 1463 K (1190° C)).

Mechanical interface modifications.- A new mounting mechanism and a new control cable between the control package and the furnace were designed to facilitate the ASTP system configuration. The input power and telemetry cable was provided by the vehicle integration contractor.

The operation of the ASTP control package is very similar to the operation of the Skylab control package described previously.

SUMMARY

The entire multipurpose electric furnace system performed perfectly, as had been predicted from the ground-based testing, with one minor exception. The rapid cooldown helium system did not respond during the first experiment. It could not be ascertained whether this was a facility or an operational problem, but the system performed nominally on all subsequent experiments. Table 22-I describes the thermal cycles for the flight experiments and shows how they compare with the ground-based tests. The soak temperatures were well within the tolerances requested by the Principal Investigators.

TABLE 22-I.- EXPERIMENT THERMAL CYCLES

Experiment	Heat-up time, hr: min		Soak temperature, K (°C)		Cooldown
	Ground test	Flight	Ground test	Flight	
MA-041	1: 10	1: 37	962 (689)	965 (692)	Extended
MA-044	2: 45	3: 15	1428 (1155)	1422 (1149)	Normal
MA-060	3: 15	3: 45	1393 (1120)	1396 (1123)	Normal
MA-070	2: 30	3: 07	1348 (1075)	1354 (1081)	Normal
MA-085	1: 12	1: 15	898 (625)	898 (625)	Normal
MA-131	2: 10	2: 23	1293 (1020)	1293 (1020)	Normal
MA-150	3: 12	2: 52	1338 (1065)	1339 (1066)	Normal

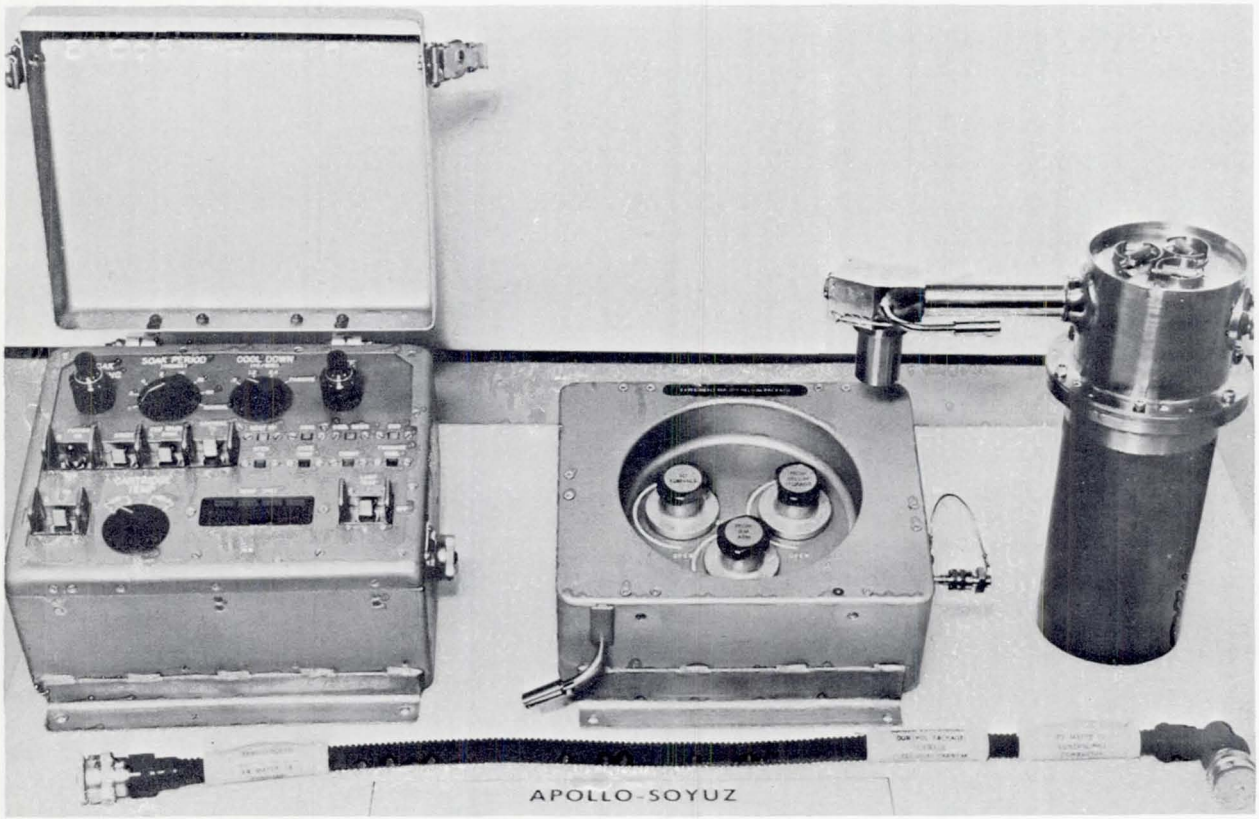

Figure 22-1.- Multipurpose electric furnace system.

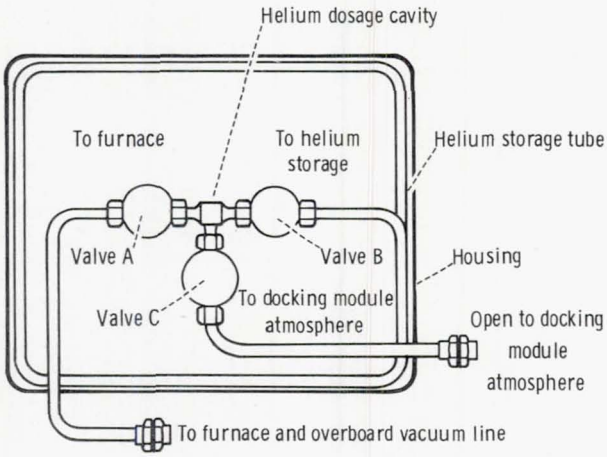

Figure 22-2.- Schematic representation of the helium rapid cooldown system.

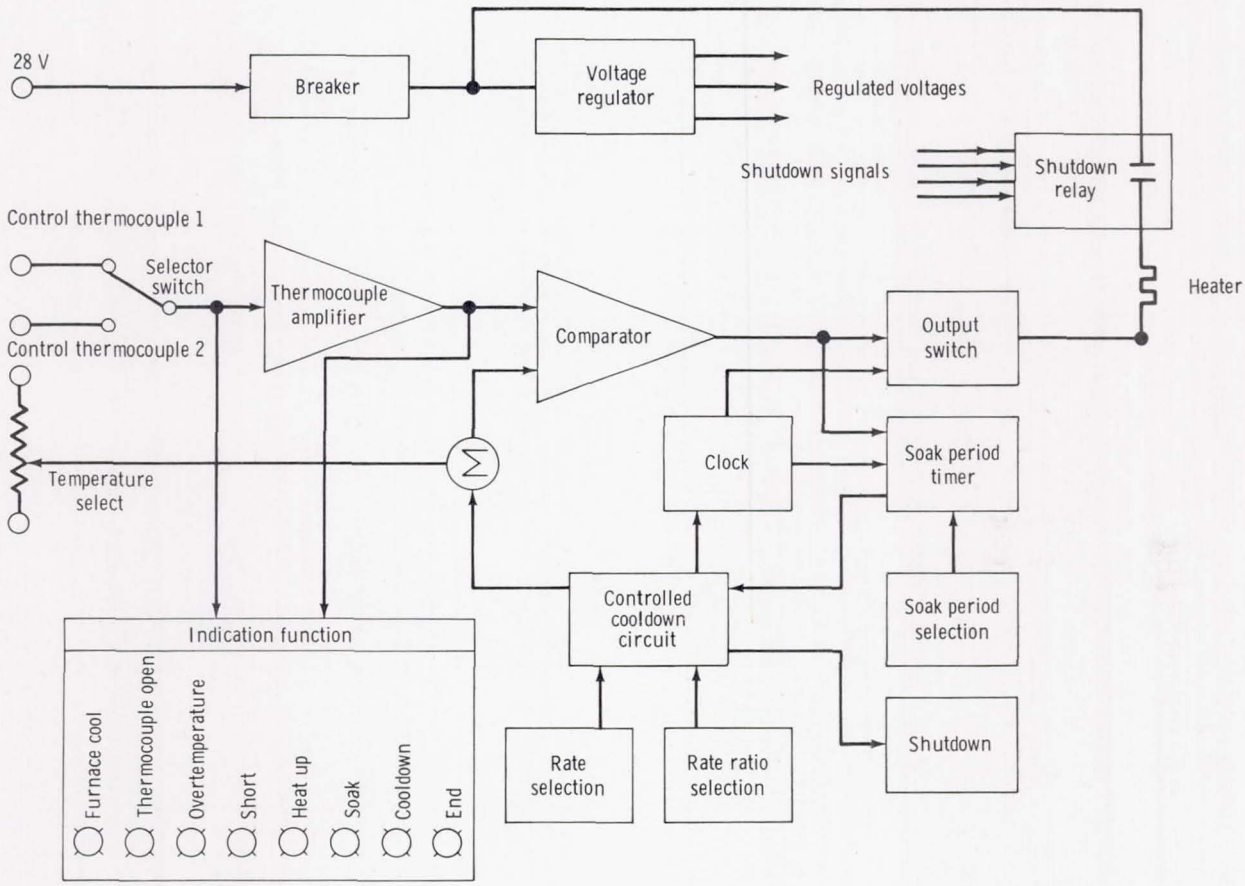

Figure 22-3.- Schematic representation of the furnace control system.

23. SURFACE-TENSION-INDUCED CONVECTION

EXPERIMENT MA-041

R. E. Reed[a]

ABSTRACT

This experiment was designed to detect possible surface-tension-induced convection caused by a steplike compositional variation in a liquid metal contained in both wetting and nonwetting ampoules with minimum temperature gradients. The concept of the investigation was to set up a liquid diffusion couple of lead and lead-0.05 atomic percent gold alloy in a microgravity environment. The liquid diffusion couple was contained in two types of ampoules, a steel container which the liquid metal would wet and a graphite container that the liquid metal would not wet.

In the absence of gravity, stirring in a liquid is suppressed because of density differences caused by thermal or compositional gradients. However, other mechanisms resulting in natural convection in a microgravity environment exist. One of the most important mechanisms for liquid metals is surface-tension-driven convection, which becomes predominant in the low-gravity environment. In this case, surface tension differences caused by compositional or temperature gradients have been demonstrated to cause stirring in liquids during experiments performed onboard Skylab. Compositional gradients were created by adding a soap solution to a large water globule, which caused vigorous fluid motion for some moments after the addition.

INTRODUCTION

The purpose of this investigation was to set up a liquid diffusion couple of lead (Pb) and Pb-0.05 atomic percent (at. %) gold (Au) alloy in a microgravity environment. The liquid diffusion couple was contained in two types of ampoules, a 1015 steel container that the liquid metal would wet and an LTJ graphite container that the liquid metal could not wet. The couples were in the molten state for approximately 2 hours to allow the Au to diffuse approximately 2.5 centimeters. If there were no convective stirring effects due to the surface tension difference between the Pb and Pb-0.05 at. % Au alloy, then a normal concentration-distance profile for the Au could be found in the diffusion couples. Because there were two diffusion temperatures (923 and 743 K), the liquid diffusion parameters for Au in Pb can be

---

[a]Oak Ridge National Laboratory; Principal Investigator.

estimated. If there were convective stirring effects due to the surface tension variations caused by the Au additions, then these effects could also be found by the autoradiographic technique used for the diffusion analysis. The role of the two ampoules will be examined in evaluating the extent of these stirring effects.

EXPERIMENT DESIGN

The specimen ampoule preparation for this experiment is described in reference 23-1 and illustrated in figure 23-1. Because of the longitudinal heat flow in the furnace upon heating and cooling, the specimens probably melted from left to right in this schematic and solidified in the reverse direction. The results described in this report are based entirely on observations of flight cartridge 2.

The dimensions of the actual specimen are shown in figure 23-2. The total specimen length was approximately 3 centimeters, and the diameter was approximately 1 centimeter. The 3-millimeter-thick Pb-0.05 at. % Au alloy disk was cold-pressure welded to the pure Pb. It should be noted that the total diffusion distance available was approximately 3 centimeters.

The ampoule used for the specimens described in this report is illustrated in figure 23-3. In addition to the graphite liner on the interior of this ampoule, quartz cloth disks were placed at each end to provide some padding for normal handling movements and to adjust the void space in the ampoule.

OBSERVATIONS AND DISCUSSION

Thermal Characteristics of the Multipurpose Electric Furnace

The temperature-time data monitored on the mission were taken on the heat-leveler block of the multipurpose furnace. After the flight, another ground-based test (GBT) was made to duplicate the space-flight (SF) furnace operation because it varied from the original experimental plan. Thermal characterization analyses to obtain the temperature-time history for the specimen ampoules from these data have not been completed. However, it was estimated that the samples were molten 105 minutes and 35 to 40 minutes for the hot and cold positions, respectively.

The prototype test data and a thermal analysis of the GBT for the original experimental plan allowed additional estimates of the thermal history of the specimen ampoules. These parameters are shown in table 23-I. It should be noted that, during the prototype test, thermal arrests due to the heat of fusion were observed at the melting point. The estimated slope of this arrest is the lower limit of the heating and cooling rates given in table 23-I.

Because the thermal analysis giving the temperature-time record for the specimens during the mission is not available at this time, the best estimates of the thermal parameters are as follows. Thermal gradients along the specimen during heating, soaking, and cooling were similar and were approximately 2 K/cm and

3 K/cm for the hot and cold ampoules, respectively. The heating rates at the melting point were approximately 2 K/min and 3 K/min for the hot and cold ampoules, respectively. Similarly, the cooling rates were 4 K/min and approximately 5 K/min. An estimate for the solidification rate was 2 cm/min.

Postmission Examination of Samples

After removal from the ampoule, the specimens were potted in araldite epoxy for longitudinal sectioning. A high-torque, low-speed diamond blade wheel was used for the sectioning. The epoxy was then redissolved from the sample. The sample half with four calibration Pb-Au disks was then remounted in a 5.1-centimeter-diameter araldite epoxy mount. The entire mount was then metallographically polished.

The mounts were prepared for irradiation as follows. Two mounts were irradiated at the same time. A polyethylene ring separator separated the epoxy specimens when they were placed face to face. The mounts, face to face with the separator in position, were placed in a 0.24-liter plastic bag, and the bag was twisted until the mounts were held rigidly secure. The bag was then heat sealed, and the mounts were placed in a 0.12-liter polyethylene bottle by slitting the side of the bottle. After the mounts were in place, the side of the bottle was sealed, using a soldering pencil. The samples were then irradiated in the Bulk Shielding Reactor East (deuterium oxide) tank. After the irradiation, the sample was allowed to decay from 4 to 8 hours, and the mounts were then removed from the bottle. The mounts at this time read approximately 100 mrads/hr. This operation was conducted using plastic gloves in a hood. After about a 24-hour decay, the mounts were ready for autoradiography.

Autoradiographs were made in complete darkness in the same darkroom in which the film was processed. The polished face of the mount was placed face down on Kodak industrial type R X-ray film. This single-emulsion ultrafine-grain film is suitable for autoradiographs. Exposures were made for 15-, 20-, and 30-minute durations. In addition, an overexposed autoradiograph of 4 hours 15 minutes was made to emphasize the penetration of the Au. It should be noted that the film was recording a β emission from the Au in the Pb. Also, the Pb has such a high cross section that the Au activity from the very near surface is the only activity seen by the film. Additional details of the autoradiographic technique can be found in reference 23-1.

Hot-End Specimens

Specimens from the hot end of the electric furnace were photographed in color to record the outward appearance. The GBT and SF specimens were directly compared. Figure 23-4 shows the side view of the 17-A GBT specimen and the 11-A SF specimen. These specimens were solidified from the bottom to the top. The original bond interface of the Pb-Au disks can still be seen at the top of each specimen. The outward surface of the 11-A SF specimen shows indication of cellular structure, which is especially noticeable at the top of the specimen. The 17-A GBT specimen shows the expected sharp corners at the bottom; conversely, the SF specimen has rounded corners at each end of the ingot.

The top ends of the two specimens are shown in figure 23-5. The 17-A GBT specimen shows evidence of a solidification pipe, whereas the 11-A SF specimen indicates the cellular or substructure walls typical of a lightly alloyed metal. There is no evidence of outward high-angle grain boundaries on the surface of either casting.

Figure 23-6 shows the bottom ends of the same two specimens. The ripple marks seen on the 17-A GBT specimen were caused by an impression of the quartz spacer cloth. The 11-A SF specimen does not show these ripple marks and exhibits a rounded edge.

A study of the metallographically polished cross section of the 11-A SF specimen shows some additional features. A macrograph of the autoradiographic mount is shown in figure 23-7. This figure shows that the 11-A SF specimen was almost entirely a single crystal with the exception of the section near the top. In addition, there is some indication of intercellular porosity at the very top. The Pb-Au calibration disks, which were as-cast structures, show the typical elongated grains pointing toward a direction of freezing. Also, there is some porosity in these rods that shows up as dark spots on the autoradiographs.

A similar study of a macrograph (fig. 23-8) taken of the mounted 17-A GBT specimen also shows that this specimen is very large grained. There are apparently three grains in the entire sample. The solidification pipe at the top does not extend very far into the casting. Again, the calibration disks show some porosity.

The autoradiograph taken of the 11-A SF specimen shows some interesting features. A print of such an autoradiograph that was deliberately overexposed to show the extent of Au diffusion is shown in figure 23-9. In this figure, (1) the lighter areas indicate the Au activity, (2) the total diffusion distance is approximately 2.2 centimeters, and (3) the Au diffusion interface is curved, with the Au apparently diffusing faster at the center of the melt. However, this interface could be an artifact if for some reason the original interface became curved upon melting. In this particular autoradiograph, there are some straight markings resulting from scratches made on the mount during irradiation. The original experimental plan estimated the diffusion distance for the high temperature and the expected time during the mission. These estimates show that the distance based on liquid diffusivities for zinc self-diffusion was to be approximately 2.5 centimeters. Thus, the diffusivity of Au in Pb may be found to be in the typical liquid diffusion range.

A similar print of an overexposed autoradiograph taken of the 17-A GBT specimen is shown in figure 23-10. This autoradiograph exhibits a surprising feature. It was expected that the Au would be evenly distributed throughout the ingot. However, figure 23-10 clearly shows that there is more Au activity in the bottom half of the ingot. The Pb-Au phase diagram predicts an equilibrium distribution coefficient during solidification of <1. Hence, if it is assumed that the Au was evenly distributed in the melt and the solidification front passed up the ingot, a heavier concentration of Au could be expected near the top. The distribution shown in the autoradiograph cannot be explained by this effect. Again, the straight markings were caused by scratches made on the mount during irradiation.

Cold-End Specimens

Photographs were also taken of the outside surface of the 14-A GBT specimen and the 21-A SF specimen, which had been positioned in the cold end of the multipurpose electric furnace (fig. 23-11). The same observations will be made on these specimens. The original Pb-Au disk bond interface is again evident as the line near the top of the ingot. The 14-A GBT specimen shows the typical sharp-cornered bottom and the slightly rounded top. In this particular specimen, there is no solidification pipe. The 21-A SF specimen shows rounded corners at the bottom and a highly rounded top. There is no solidification pipe in this ingot either. Evidence of high-angle boundaries is not present on either specimen. A much finer cellular structure is faintly evident near the top of the 21-A SF specimen.

A photograph of the bottom ends of these two specimens is shown in figure 23-12. Again, the ripple markings caused by the quartz spacer cloth are evident on the 14-A GBT specimen. These markings are not so evident on the 21-A SF specimen, which also shows a distinctly rounded corner.

The autoradiographs of the 21-A SF specimen show the same features seen on the previous autoradiographs. A print of a deliberately overexposed autoradiograph of the 21-A SF specimen is shown in figure 23-13. Again, (1) the light areas indicate Au activity, (2) the Au diffusion interface is curved, (3) the total Au diffusion distance is approximately 1.2 centimeters, and (4) in this particular autoradiograph, there appears to be some indication of surface diffusion of Au along the ingot. This surface diffusion could be a possible explanation for the curved interface, if a depletion of the Au at the surfaces as it diffuses along the melt interface is considered.

A print of the overexposed autoradiograph for the 14-A GBT specimen is shown in figure 23-14. It is again evident that there is more Au activity near the bottom half of the ingot, which is very similar in appearance to the GBT specimen that had been processed at the hot end of the electric furnace.

CONCLUSIONS

It is difficult to make any definite conclusions until all the specimens from the mission have been studied. For example, if the curved Au diffusion interface is due to a melting effect upon heating, then it may be possible to see a difference on the reversed specimens that have not been studied yet. However, several conclusions can be made from the one flight cartridge that has been studied. (It must be remembered that no Au concentration-distance data have been obtained yet.)

1. The SF samples that were almost entirely single crystals exhibited a cellular structure near the top, typical of lightly alloyed metals solidified in a unidirectional manner. Such a structure is not readily evident on the surfaces of the GBT specimens; however, the surfaces of these specimens were in close contact with the container material.

2. The Au distribution, as indicated by the autoradiographs, showed no extensive stirring in the SF samples. Instead, they showed primarily a typical

liquid diffusion profile. However, two features were quite striking: the curved Au diffusion interface and some evidence of diffusion along the surface of the melt.

3. The GBT specimens also showed an unusual feature, that of increased Au activity at the bottom half of the ingot. This activity is unexplained by a unidirectional redistribution of Au due to solidification from bottom to top, because the predicted equilibrium distribution coefficient is probably <1.

4. The total diffusion distances measured from the autoradiographs of the SF samples compare favorably with those distances predicted in the experimental plan, using Zn self-diffusion liquid diffusivities from Skylab results, which means that the diffusion of Au in Pb will be in the typical liquid diffusion range.

REFERENCE

23-1. Reed, R. E.: Progress Report of Apollo-Soyuz Test Project Experiment No. MA-041 for the Period, Sept. 1 - Dec. 31, 1974. ORNL TM-4812, April 1975.

TABLE 23-I.- THERMAL CHARACTERISTICS OF SPECIMEN AMPOULE IN THE MULTIPURPOSE ELECTRIC FURNACE

Characteristic	Prototype test		Ground-based test	
	Hot position[a]	Cold position[b]	Hot position	Cold position
Thermal gradient along ampoule, K/cm	[c]0	[c]2 to 3	[d]2	[d]3
Heating rate at [e]600 K, K/min	[f]2 to 7	[f]3 to 5	- -	- -
Cooling rate at [e]600 K, K/min	[f]2 to 9	[g]15	[h]4	[h]5

[a]Copper thermal insert in heat-leveler block.

[b]Copper thermal insert in temperature gradient section.

[c]Electric multipurpose furnace at equilibrium.

[d]Thermal gradient during heating and cooling.

[e]Melting point of sample.

[f]Lower limit estimated from slope of thermal arrest.

[g]Thermal arrest insufficient for lower-limit estimate.

[h]Rate taken from slope of calculated cooling curve.

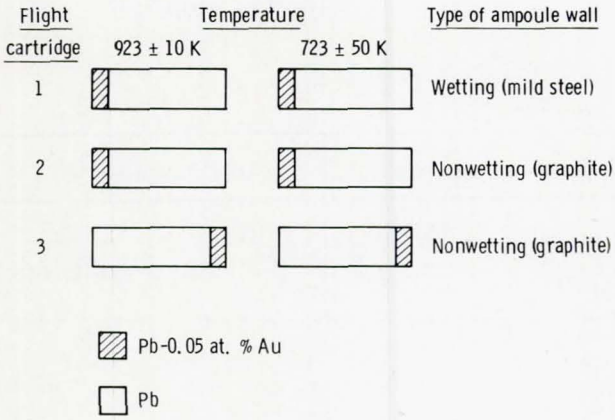

Figure 23-1.- Schematic arrangement of specimens.

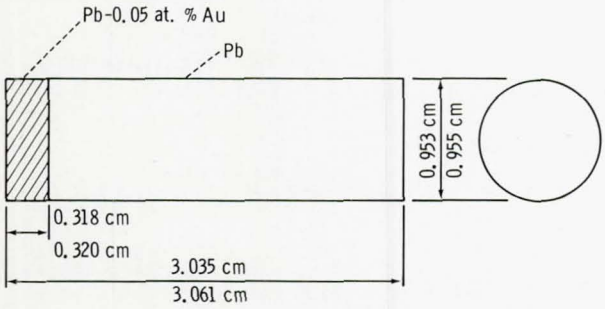

Figure 23-2.- Dimensions of MA-041 specimen.

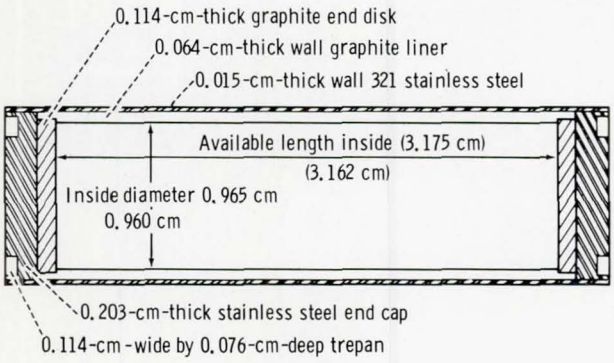

Figure 23-3.- Stainless steel-graphite ampoule assembly.

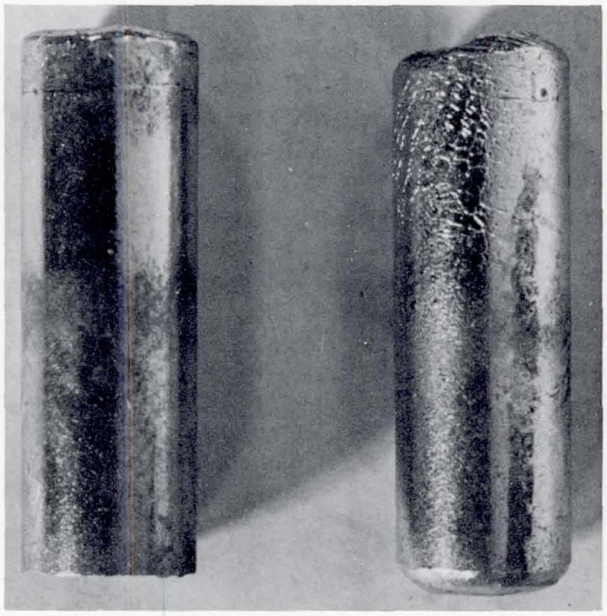

Figure 23-4.- Photograph of the 17-A GBT (left) and the 11-A SF specimens from the hot end of the electric furnace. Specimens solidified from bottom to top in ampoules with nonwetting walls. Specimens are approximately 1 centimeter in diameter.

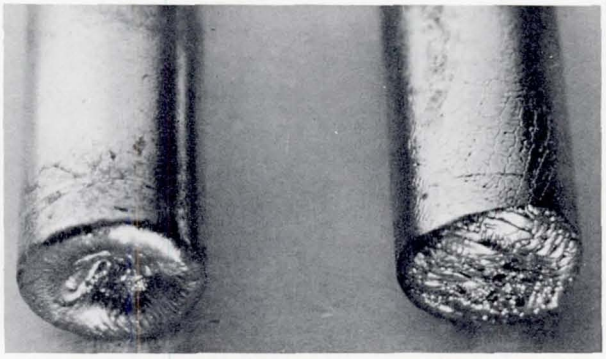

Figure 23-5.- Photograph of the top ends of the 17-A GBT (left) and the 11-A SF specimens.

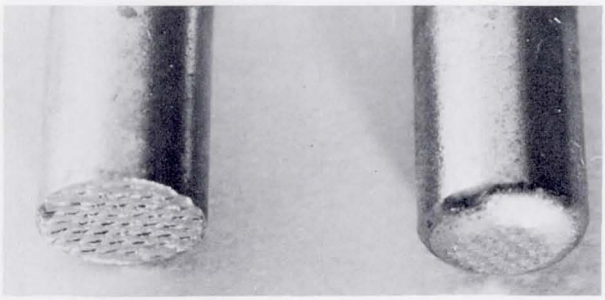

Figure 23-6.- Photograph of the bottom ends of the 17-A GBT (left) and the 11-A SF specimens. Ripple marks evident on the 17-A GBT specimen bottom are an imprint of the quartz spacer cloth in the ampoule.

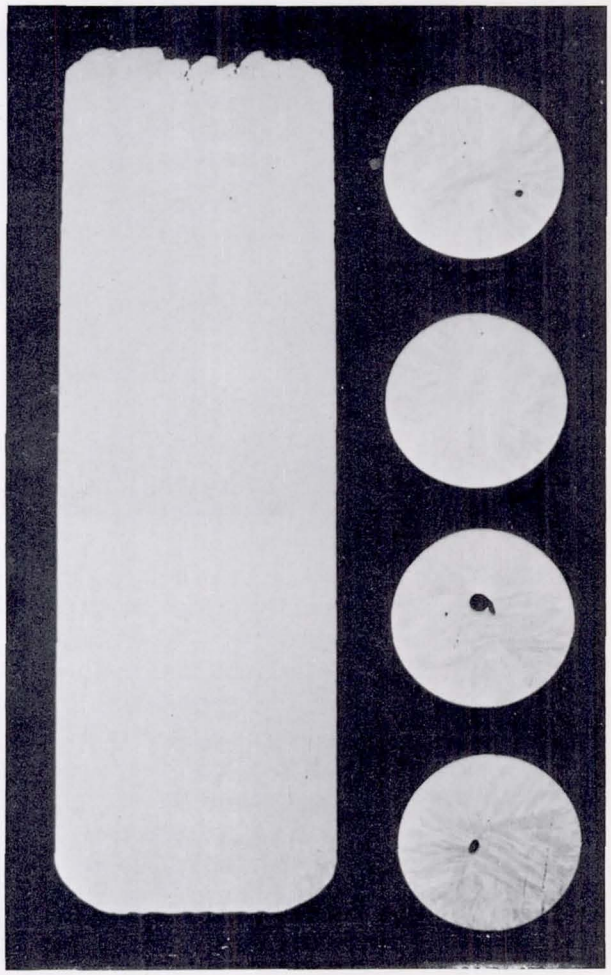

Figure 23-7.- Macrograph of the as-polished 11-A SF specimen, mounted with four Pb-Au calibration disks. Specimen was in the hot end of the multipurpose furnace and solidified from bottom to top in a nonwetting ampoule. Specimen is approximately 1 centimeter in diameter.

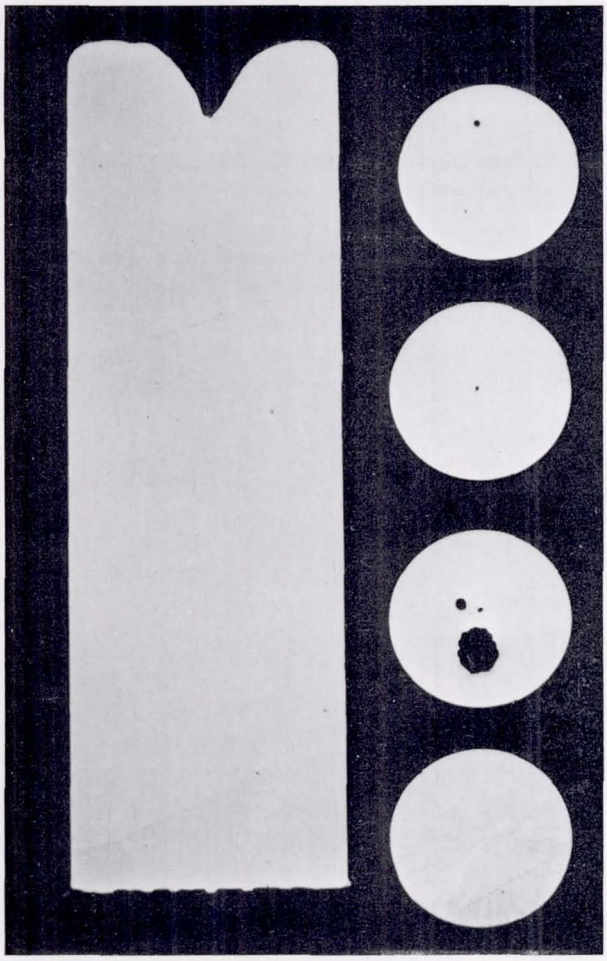

Figure 23-8.- Macrograph of the as-polished 17-A GBT specimen, mounted with four Pb-Au calibration disks. Specimen was in the hot end of the multipurpose furnace and solidified from bottom to top in a nonwetting ampoule. Specimen is approximately 1 centimeter in diameter.

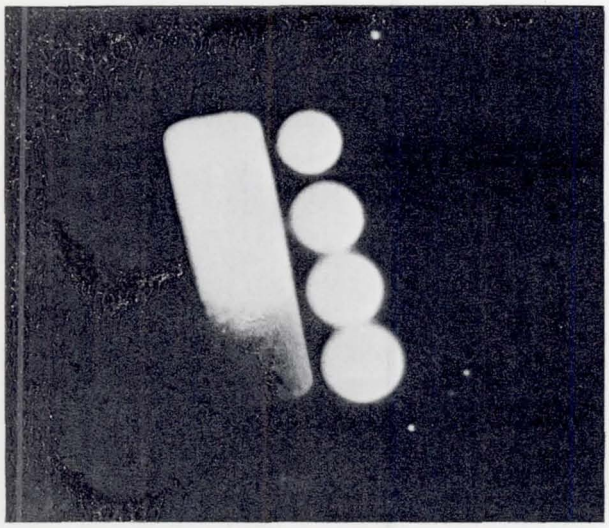

Figure 23-9.- Print taken from a deliberately overexposed (4 hours 15 minutes) autoradiograph to emphasize the extent of Au diffusion in the 11-A SF specimen. Light areas indicate Au activity. Mount was scratched during neutron irradiation; the scratches show up as line markings. Apparent increase in diameter of the calibration disks with increasing Au content is due to long exposure time allowing "side-scatter" activity that also darkens the film.

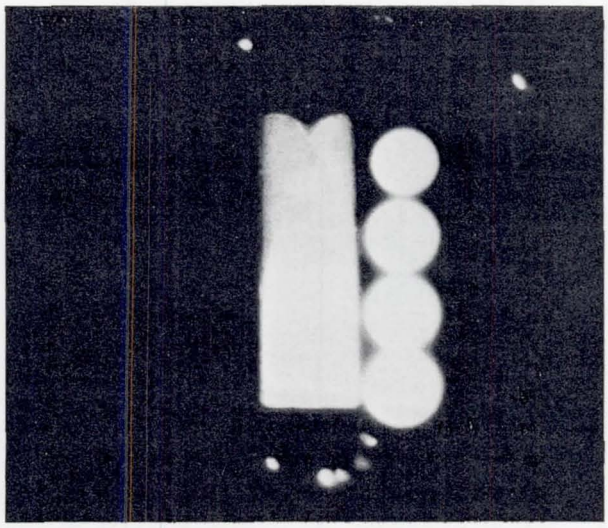

Figure 23-10.- Print taken from deliberately overexposed (4 hours 15 minutes) autoradiograph to emphasize the extent of Au diffusion in the 17-A GBT specimen. Light areas indicate Au activity. Mount was scratched during neutron irradiation; the scratches show up as line markings. Apparent increase in the size of the calibration disks and sample diameter with increasing Au content is due to long exposure time allowing "side-scatter" activity that also darkens the film.

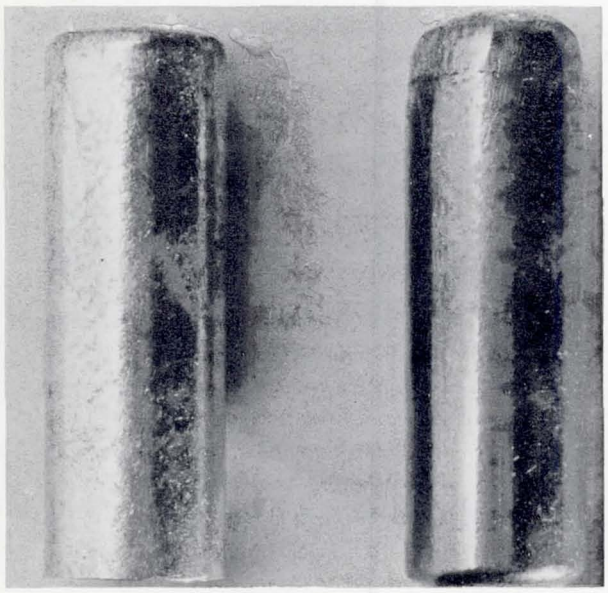

Figure 23-11.- Photograph of the 14-A GBT (left) and the 21-A SF specimens from the cold end of the electric furnace. Specimens solidified from bottom to top in ampoules with non-wetting walls. Specimens are approximately 1 centimeter in diameter.

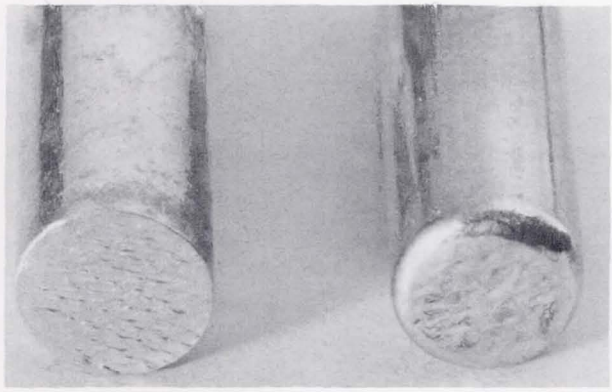

Figure 23-12.- Photograph of the bottom ends of the 14-A GBT (left) and the 21-A SF specimens. Ripple marks evident on the 14-A GBT specimen bottom are an imprint of the quartz spacer cloth in the ampoule.

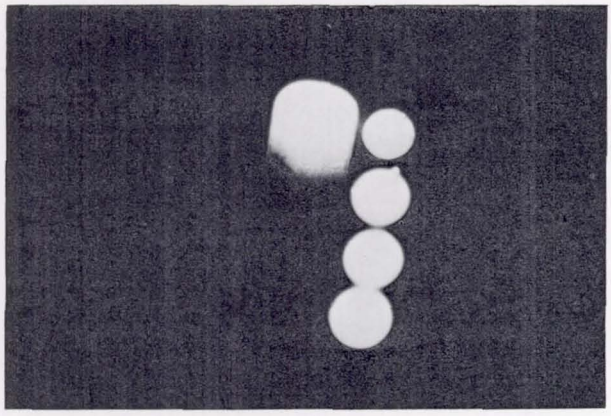

Figure 23-13.- Print taken from a deliberately overexposed (4 hours 15 minutes) autoradiograph to emphasize extent of Au diffusion in the 21-A SF specimen. Light areas indicate Au activity. Apparent increase in diameter of the calibration disks with increasing Au content is due to long exposure time allowing "side-scatter" activity that also darkens the film.

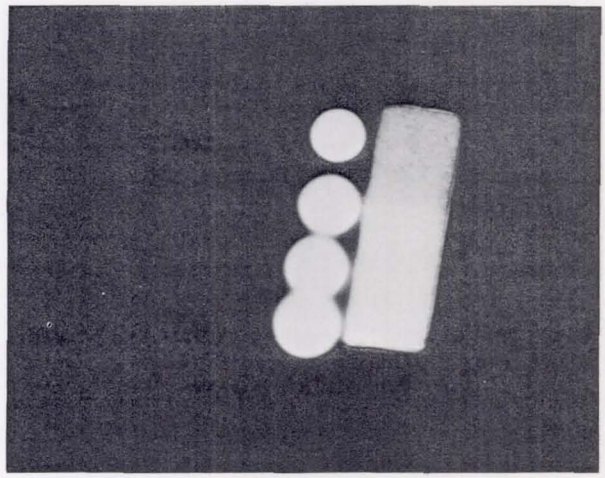

Figure 23-14.- Print taken from a deliberately overexposed (4 hours 15 minutes) autoradiograph to emphasize the extent of Au diffusion in the 14-A GBT specimen. Light areas indicate Au activity. Apparent increase in diameter of the calibration disks with increasing Au content is due to long exposure time allowing "side-scatter" activity that also darkens the film.

24. MONOTECTIC AND SYNTECTIC ALLOYS

EXPERIMENT MA-044

C. Y. Ang[a] and L. L. Lacy[a]

ABSTRACT

The flight test furnace run of the Monotectic and Syntectic Alloys Experiment was successfully performed during the Apollo-Soyuz Test Project mission. All three experiment cartridges were returned intact. A second ground-based test was conducted after the mission to provide one-g samples with an equivalent thermal history. The examinations of all flight and ground-based cartridges and ampoules have been completed. Formal characterization of the flight and ground samples began after the initial postflight quick-look efforts had been completed and a characterization plan had been developed. Encouraging results have been obtained in the preliminary analysis of one flight aluminum antimonide sample as compared to ground-based and prototype-test counterparts. In terms of reduction of the unwanted second phase, the low-g sample shows a homogeneity improvement by a factor of 5 to 20. Furthermore, small amounts of the second phase were formed only along parts of the grain boundaries of the flight sample, whereas the ground-based samples show major grains of the second phase. Preliminary examination of one lead zinc flight sample shows a dispersion of lead in the zinc matrix. However, complete homogenization of the material did not occur. A thermal analysis of flight data shows that the average soak temperature for the lead zinc ampoules was 20 K (20° C) lower than planned but 35 K (35° C) above the published consolute temperature. Further indepth analysis and characterization will be performed to study lead zinc diffusion and to identify differences between the flight and ground-processed samples.

INTRODUCTION

The purpose of this experiment was to investigate the effects of weightlessness on the melting and solidification of two material systems, lead zinc (PbZn) and aluminum antimonide (AlSb). The objectives were (1) to investigate phase segregation effects in low g for the immiscible binary PbZn and (2) to determine the influences of low-g solidification on the microstructural homogeneity and stoichiometry of the semiconducting compound AlSb.

---

[a]NASA George C. Marshall Space Flight Center; Co-Principal Investigators.

This report presents an updated (ref. 24-1) preliminary evaluation of the returned samples of AlSb syntectic compound and PbZn monotectic immiscible processed during the Apollo-Soyuz Test Project (ASTP) mission. Postflight data have been used to develop a tentative characterization plan for evaluating the limited number of available samples. This plan will be modified if new observations at each stage require specialized analysis.

EXPERIMENT CONCEPT

Certain potentially useful alloys or material systems are difficult to synthesize on Earth because of sizable differences in specific gravity of the constituents in a molten state, which results in undesirable buoyancy and convection influences on solidification. Consequently, the near-zero-g conditions in space processing were the primary motivation for this experiment. Furthermore, significant discoveries related to microsegregation and kinetics of lattice defects, made as a result of the Skylab experiments, have strengthened the belief in the value of continuing space processing experimentation for future space manufacturing activities.

The PbZn system (ref. 24-2, fig. 24-1) is characterized by the large miscibility gap $L_1 + L_2$ and the monotectic point at 99.7 atomic percent (at.%) Zn where the immediate transformation upon solidification is from one liquid to a second liquid plus a solid. This system is also characterized by a large density difference between Pb (11.7 g/cm^3) and Zn (7.14 g/cm^3). In the Earth's gravity field, preventing gravity separation between Pb and Zn upon solidification is difficult. Negating the effects of gravity in space processing should lead to a degree of mixing of the two phases, resulting in a dispersion of fine particles of superconducting Pb in a Zn matrix. The composition selected for the experiment was 20 at.% Pb and 80 at.% Zn as shown by the dashed line in figure 24-1. This composition is equivalent to a weight percent of 44.2 Pb and 55.8 Zn or a volume percent of 33.2 Pb and 66.8 Zn.

The AlSb system (fig. 24-2) has been neglected for many years among the III-V semiconducting compounds that are characterized upon solidification by a syntectic transformation of two molten constituents to a constant composition intermetallic compound (at.% of 50 Al and 50 Sb). The reasons for this neglect have been difficulties (ref. 24-3) in synthesizing a stoichiometrically homogeneous compound and the problems of high reactivity of the material to moisture. Some reported properties of AlSb are given in table 24-I. With an energy gap of 1.62 electronvolts, AlSb has been theoretically analyzed as a highly efficient solar energy converter (refs. 24-4 and 24-5). However, because of the aforementioned problems in crystal synthesis, experimental verification is lacking.

In space processing, the compositional homogeneity may be enhanced by minimizing the very large density difference (2.7 g/cm^3 for Al and 6.62 g/cm^3 for Sb) between constituents in the molten state and during crystallite formation upon cooling. Electromotive potential considerations suggest that the Al- and Sb-rich phases observed in polycrystalline AlSb synthesized on Earth could cause the high reactivity to moisture.

SAMPLE PREPARATION AND TESTING

Thermal Cycling Considerations

One AlSb sample and one PbZn sample were to be processed in each of three flight cartridges. Homogenization (soaking) for 4 hours in the molten state at 1123 K (850° C) for PbZn and 1373 K (1100° C) for AlSb was originally proposed. The soaking temperature for AlSb was later raised to 1403 K (1130° C) because of the lack of complete melting at 1373 K (1100° C) in laboratory tests. Higher temperatures could not be readily obtained in the multipurpose furnace. Serious AlSb sample leakage problems that necessitated a reduction of the soaking time to 1 hour were evidenced during ground-based testing. Including the heatup and cooldown times for the multipurpose furnace, this adjustment resulted in an estimated effective soaking time of 1.5 hours for both PbZn and AlSb.

Temperature and sample crucible reactivity considerations led to the selection of high-purity graphite as the crucible material for both PbZn and AlSb. For the latter, the use of graphite was not an optimum choice, but fabrication of alumina crucibles with hermetic sealing to contain Al and/or Sb vapor was difficult. The reaction between molten AlSb and graphite and the slow carbide formation were recognized and considered in comparing ground and flight samples.

Starting Materials

All starting constituents were composed of material of at least five-nines purity (i.e., total impurities were less than 10 ppm). Zinc, obtained in disk form, was machined from zone-refined rods. Lead was obtained in both pellet and powder forms. Aluminum antimonide, obtained in granular form, was processed from zone-refined polycrystalline ingots.

Ampoule Configuration and Sample Loading

The ampoule configurations for PbZn and AlSb samples are shown in figure 24-3. The materials were loaded in the graphite crucibles and sealed with graphite cement in an argon glove box. Before capping and sealing, the AlSb samples were premelted at 1423 K (1150° C) in uncapped graphite crucibles under argon. Tungsten inert gas welding of the stainless steel ampoule containers was also completed in a glove box with approximately 100 000 N/m^2 (1 atmosphere) of ultra-high-purity argon. Both fabricated AlSb and PbZn ampoules were further heated for 10 minutes at 1423 K (1150° C) and 1123 K (850° C), respectively. The AlSb ampoules were heated by a high-frequency induction furnace, and the thermometry was determined by an optical pyrometer. The PbZn ampoules were heated in a 30.5-centimeter hot-zone tube furnace.

Ampoule weighing and American Society of Testing Materials bubble-leak testing were performed before and after heating. Graphite boats were used to carry from four to nine ampoules per furnace load, with one ampoule of each furnace load

used as a control sample. An ampoule might fail the heating test because of either dimensional distortion or leakage. The control samples were again thermally tested for 4 hours at the respective temperatures. If a control failed, the entire boatload was rejected. It should be noted that all PbZn ampoules passed, but one of the five AlSb control ampoules failed. Of the 33 AlSb ampoules processed for prototype, qualification, ground-based, and flight tests and for laboratory studies, 6 failed, including the control sample. In addition, three good ampoules were rejected because of the failure of the control sample.

Cartridge Construction

A simplified schematic of the cartridge is shown in figure 24-3. Ampoule temperatures were determined during prototype testing by using an instrumented cartridge as shown in figure 24-4(a). This figure also presents an exposed view of the components of a cartridge, including the A and B ampoules and the graphite, copper, and stainless steel inserts. Figure 24-4(b) shows the same exposed components for a flight cartridge.

Scheduled Preflight Tests

All required ampoules were fabricated without simulation and prototype testing. When ground-based testing was conducted, two out of three AlSb ampoules failed. The failure mode was determined to be cracking of the graphite crucibles similar to cracking that occurred during ampoule fabrication and testing. These failures did not leave sufficient time to introduce and develop changes in crucible materials or new ampoule designs. The decision was made to adapt the previously mentioned shortening of the soaking time from 4 hours to 1 hour for the flight test and to use X-radiography in the selection of flight test cartridges for increased reliability.

As a result of this last-minute change, no true one-g samples were thermally treated identically to the flight samples (table 24-II). A second ground-based test (GBT) has been conducted to perform the primary experiment objective of comparative characterization of samples.

IN-FLIGHT AND GROUND-BASED TESTS

This experiment was the last furnace test run during the ASTP mission. The initial heatup was started at 175:30 ground elapsed time (GET), which corresponds to 14:50 GMT on July 23, 1975. The run was completed (cartridges extracted) on the morning of July 24, just before the jettison of the docking module (and the furnace).

A computer-generated plot of the telemetered furnace temperatures for the graphite heat leveler (hot end) and the heat extractor (cold end) is presented in figures 24-5(a) and 24-5(b). The change of slopes shown in the cooling curves of figure 24-5(b) is caused by the injection of helium into the multipurpose furnace to

increase the cooling rate. In figure 24-6, the time-temperature profile of the flight cartridges is compared with a similar profile obtained from the second GBT. As indicated in figure 24-6, the GBT has essentially duplicated the thermal profile of the flight sample.

A computer analysis[1] of the thermal histories revealed that the AlSb samples were in the homogenization region (i.e., in the liquid state) for 1.5 hours and that the PbZn samples were in the miscible region (i.e., above the consolute temperature) also for 1.5 hours. During the cooldown period, it is estimated that PbZn was in the two-liquid phase region (i.e., the miscibility gap) for 3.4 hours.

The flight cartridge and ampoule numbers are identified in table 24-II. Based on the temperature calibration data obtained in prototype testing and computer analysis, the AlSb ampoule temperature at soak is estimated to be 1399 K (1126° C). Because of thermal lag, the PbZn ampoule temperature at soak was estimated to be below the specified minimum of 1123 K (850° C). The thermal analysis indicated that indeed the PbZn ampoules were soaked for 1 hour at an average temperature of 1107 K (834° C).

PRELIMINARY EVALUATION RESULTS AND DISCUSSION

A summary of the postflight evaluation and characterization plan for the returned samples and various ground samples is given in table 24-III. An earlier report (ref. 24-1) describes efforts performed in tasks 1 and 2 and a quick-look assessment of some samples (task 3). This report contains a preliminary characterization of flight and ground-based samples performed in task 3. The samples characterized to date include one AlSb flight sample, one PbZn flight sample, a pair of GBT-2 counterparts, and one prototype-tested AlSb sample. Characterization of the AlSb and PbZn samples has been completed through the scanning electron microscopy (SEM) energy dispersive X-ray analysis (EDAX) evaluations.

Figure 24-7 is a photograph of the two AlSb and three PbZn flight samples. Figure 24-8 is a photograph of the GBT-2 samples. Part of the graphite crucible was left attached to one of the flight and one of the GBT-2 AlSb samples so that later microstructure analysis could be correlated with potential contamination by the graphite crucible. Visual observation of the exposed surfaces of the AlSb samples indicated that melting and recrystallization did occur. A macrophotograph (5X) of one of the AlSb samples (A-164) is shown in figure 24-9 where large crystallites of the polycrystalline sample can be seen. Part of the graphite crucible is shown at the bottom of the sample.

Complete melting also occurred with the three PbZn samples. Macrophotographs (10X) of the samples are shown in figure 24-10. As shown in figure 24-10, an interface exists between the smaller and larger parts of the samples. This interface may correspond to the original Pb/Zn interface. Overflow regions can be seen on the surface of the sample where a liquid phase flowed over the first solidified surfaces.

---

[1]W. Key, Brown Engineering Co., personal communication, 1975.

Each of the samples appears to have solidified first on the cold end (temperature gradient of 4.5 K/cm) and, because of shrinkage away from the container walls, part of the remaining liquid then flowed around the solid surface. The topography of sample B-186 appears to be different from the other two samples. In sample B-186, the liquid flow appears to be symmetric about the axis of the sample, whereas an asymmetric flow channel apparently developed on sample B-164. Sample B-181 also has an asymmetric flow that can be seen in figure 24-11(a), which is a photograph of its cold end.

Closer examination of B-181 in figure 24-10 reveals small parallel grooves or strata around the circumference of the sample. These grooves are believed to be caused by machining marks in the graphite crucible. A more detailed view of the topography of B-181 is shown in the SEM photographs of figure 24-12. A shrinkage cavity is visible on the hot end of the sample (fig. 24-12(a)), and the interface region is shown in figure 24-12(c). A preliminary EDAX of B-181 reveals that both Pb and Zn are present at both the hot and cold ends of the sample and that the concentration of Zn is more pronounced at the cold end.

For a preliminary microstructural examination, one longitudinal section each of the A-185 AlSb sample and the B-186 PbZn sample was mounted and cut for metallography. Similarly, one GBT-2 AlSb sample (A-141) and one GBT-2 PbZn sample (B-142) were extracted and sectioned for metallography.

The flight AlSb sample appears to have an overall homogeneous compound phase with a small amount of a second phase along the grain boundaries. Figure 24-13(a) illustrates this typical feature (unetched). With all the AlSb samples processed on the ground, including the as-received AlSb granules, at least two phases, one rich in Al or Sb and the other the compound AlSb, can be seen. Figure 24-13(b) shows this feature of large amounts of two phases present in one-g solidified samples. The one-g solidified sample (A-127) was obtained in a prototype test that had approximately the same thermal history as the ASTP solidified sample except for a slightly lower soak temperature. Figures 24-14(a) and 24-14(b) are pseudocolored photographs of figures 24-13(a) and 24-13(b) in which surface artifacts have been eliminated and the computer-aided technique of digital imaging analysis (DIA) has been used to more clearly present compositional homogeneity. The red areas of the photograph represent the AlSb compound, and the blue areas represent a second phase. Likewise, figure 24-15 is a graphical presentation of the digitized data depicting the low-g effects of reducing the unwanted second phase from 21.6 to 1.7 percent.

Figures 24-16(a) and 24-16(b) are photomicrographs of another area of flight sample A-185 as compared with GBT-2 sample A-141. Major improvements in microscopic homogeneity are again evident in the flight sample. An EDAX of the samples reveals that the gray phase is the compound AlSb and that the white phase is an Al-rich phase. An analysis of the area fraction of the second phase for these two photomicrographs reveals that the flight sample has 1.1 percent of the Al-rich phase as compared to 25.2 percent for the GBT-2 sample. Thus, for these two selected areas, the Al-rich phase has been reduced by a factor of 23 in the flight sample.

To compare the homogeneity of the flight and the GBT-2 samples on a macroscopic scale, a continuous series of photomicrographs (100X) was taken across each sample. An area analysis for the second phase, obtained from the photomicrographs, is shown in figure 24-17 as a function of position for the two samples. As indicated in figure 24-17, the GBT sample contains significantly more of the second phase across the sample face. It is also interesting to note that, unlike the flight sample, the second phase of the GBT sample is macroscopically inhomogeneously distributed across the sample.

A quantitative comparison of the microscopic homogeneity of the two samples is shown in figure 24-18 where the area fractions of the unwanted second phase are plotted as a function of increasing area for two of the photomicrographs. Because the second phase grows as major grains in the ground-based samples, the material is also microscopically inhomogeneous. Conversely, the ASTP solidified material contains the second phase only as small particles located on selected portions of the grain boundaries. Figure 24-18 indicates that the second phase for the flight sample is homogeneously distributed throughout the measured area. Additional analysis, presently in progress, will be done to examine the microscopic homogeneity of the two samples at other locations and for smaller measuring areas.

The flight sample of PbZn (B-186) exhibits a macrostructure similar to that of the ground samples; i.e., a Zn-rich portion and a Pb-rich portion, the latter entrapping one large and several small zinc particles (fig. 24-19). On a macroscopic scale, the separation of Zn and Pb portions due to gravity can be seen in the GBT-2 sample B-142 (figs. 24-20(a) and 24-20(b)). Some striking (5 percent nitric acid etched) microscopic formations in the Zn-rich areas of the flight sample can be seen in figure 24-19. The small particulate inclusions have been identified by a preliminary EDAX scan as Pb particles.

INTERIM CONCLUSIONS

1. The flight and ground-based tests have essentially the same thermal history. The combined flight and various ground-based tests have provided low-g and one-g samples with identical and different thermal histories for indepth scientific study.

2. Comparing the microstructure of the flight and ground solidified samples of AlSb reveals major microscopic and macroscopic homogeneity improvements in the low-g solidified material. The flight solidified material contains 5 to 20 times less of the unwanted second phase. An Al-rich phase is found only along parts of the grain boundaries for a flight sample, whereas the ground-based samples show major grains of the Al-rich or Sb-rich phase.

3. Incomplete homogenization between Pb and Zn has been observed in one flight sample. A thermal analysis shows that the samples were soaked at a temperature above the published consolute temperature for over 1 hour. Although complete homogenization was not achieved in the PbZn system, the presence of fine Pb particles was detected in the Zn matrix by a preliminary microstructural study. Further indepth analysis and characterization will be performed to study PbZn diffusion and to identify differences between the flight and ground-processed samples.

REFERENCES

24-1. Ang, Choh-Y.; and Lacy, Lewis L.: Monotectic and Syntectic Alloys: ASTP Experiment MA-044. NASA TM X-64956, 1975.

24-2. Hansen, Max: Constitution of Binary Alloys. McGraw-Hill, 1959.

24-3. Willardson, R. K.; and Beer, Albert C., eds.: Semiconductors and Semimetals. Physics of III-V Compounds. Vol. 4. Academic Press (New York), 1968, p. 59.

24-4. Rittner, E. S.: Use of p-n Junctions for Solar Energy Conversion. Phys. Rev., vol. 96, no. 6, Dec. 15, 1954, pp. 1708-1709.

24-5. Loferski, J. J.: Theoretical Considerations Governing the Choice of the Optimum Semiconductor for Photovoltaic Solar Energy Conversion. J. Appl. Phys., vol. 27, no. 7, July 1956, pp. 777-784.

TABLE 24-I.- REPORTED PROPERTIES OF AlSb[a]

Property	Value
Density, g/cm^3	4.27
Melting point, K (°C)	1323 to 1353 (1050 to 1080)
Energy gap at 293 K (20° C), eV . . .	1.62
Hall mobility at 293 K (20° C)	
Electrons, cm^2/V sec	200
Holes, cm^2/V sec	420
Dielectric constant	11
Conductivity (p-type), ohm/cm	10^{-2} to 10^{-1}

[a]Crystal structure is Zn blend.

TABLE 24-II.- THERMAL HISTORY OF AlSb and PbZn SAMPLES

Test origin	Cartridge no.	AlSb			PbZn		
		Ampoule no.	Thermal history		Ampoule no.	Thermal history	
			Soak time, hr	Temperature, K (°C)		Soak time, hr	Temperature, K (°C)
Flight	7	A-185	1	1399 (1126)	B-186	1	1107 (834)
	9				B-181	1	1107 (834)
	10	A-164	1	1399 (1126)	B-164	1	1107 (834)
GBT-1	1	A-163	4	1405 (1132)	B-160	4	1138 (865)
	2	- -	- -	- -	B-161	4	1138 (865)
	3	- -	- -	- -	B-162	4	1138 (865)
GBT-2	5	A-141	1	1401 (1128)	B-141	1	1107 (834)
	6	A-142	1	1401 (1128)	B-142	1	1107 (834)
	11	A-165	1	1401 (1128)	B-165	1	1107 (834)
Prototype-1	- -	A-127	1.2	1385 (1112)	B-127	1.2	1208 (935)
Prototype-2	1	A-124	5.6 plus 1.3	1322 (1049) 1405 (1132)	B-124	5.6 plus 1.3	1014 (741) 1138 (865)
	2	A-132	1.2 plus 1.3	1385 (1112) 1405 (1132)	B-125	1.2 plus 1.3	1208 (935) 1138 (865)
	3	A-126	1.2 plus 1.3	1385 (1112) 1405 (1132)	B-105	1.2 plus 1.3	1208 (935) 1138 (865)

TABLE 24-III.- POSTFLIGHT EVALUATION AND CHARACTERIZATION PLAN

Evaluation	AlSb	PbZn
Cartridge examination (task 1)		
Photography	X	X
Radiography (preflight and postflight)	X	X
Disassembly	X	X
Ampoule examination (task 2)		
Photography	X	X
Radiography	X	X
Leak tests (helium)	X	X
Weighing	X	X
Sample characterization (task 3)		
Removal	X	X
Weighing	X	X
Stereoscopic examination (10X to 100X)	X	X
Macrophotography (2X to 10X)	X	X
SEM[a] topography (60X to 1000X)	(b)	X
Surface EDAX[c]	(b)	X
Microstructure (metallography)	X	X
Quantitative microstructural analysis	X	X
SEM/EDAX (qualitative and quantitative)	X	X
Microhardness testing	X	(b)
Resistivity (four-point probe)	X	X
Superconductivity	(b)	X
X-ray diffraction	X	X
Chemical and spectral analysis	X	X
Impurity analysis (ion microprobe)	X	X
Humidity oven testing	X	(b)
Diffusion analysis	X	X

[a]Scanning electron microscope.

[b]No evaluation.

[c]Energy dispersive X-ray analysis.

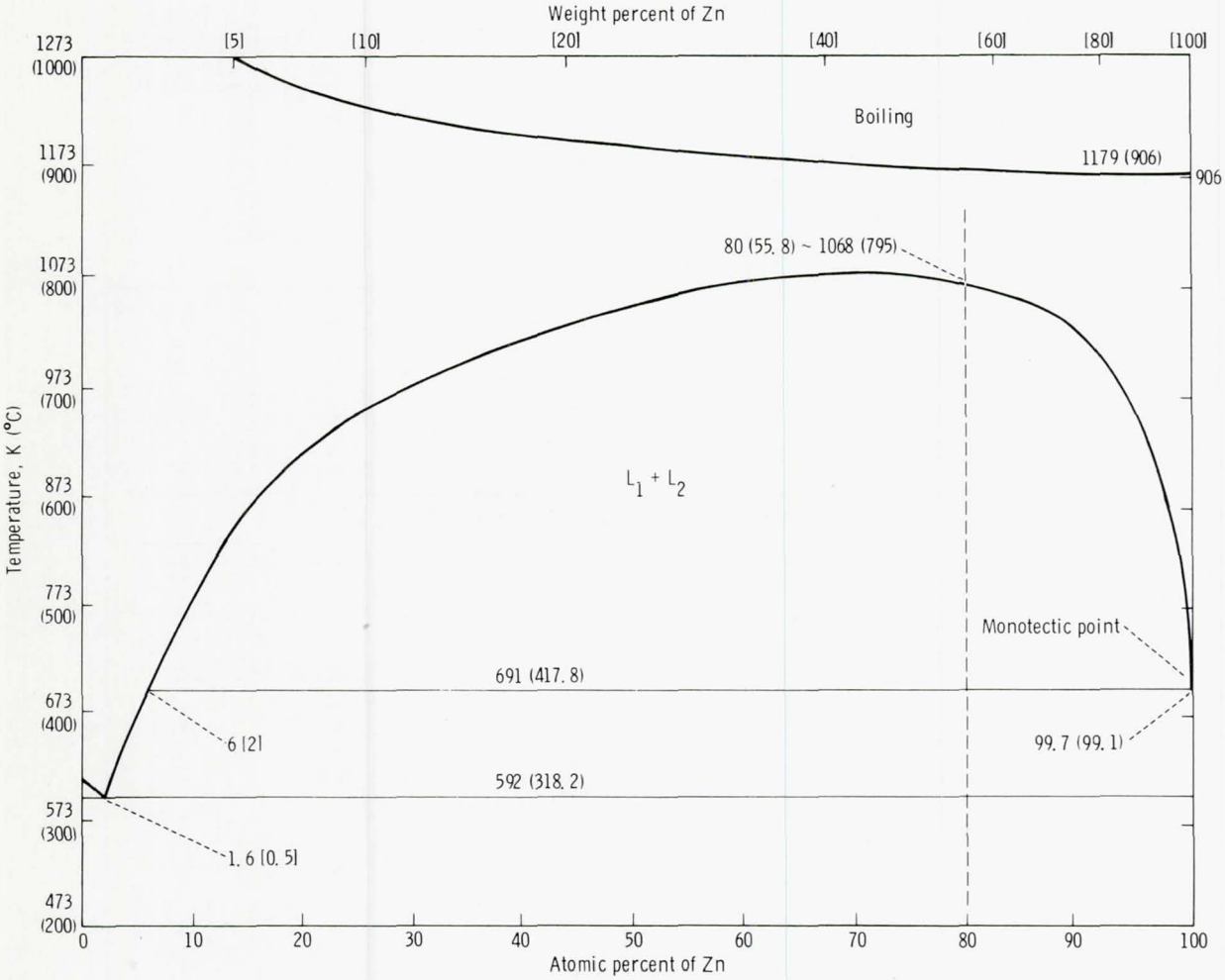

Figure 24-1.- Phase diagram for PbZn.

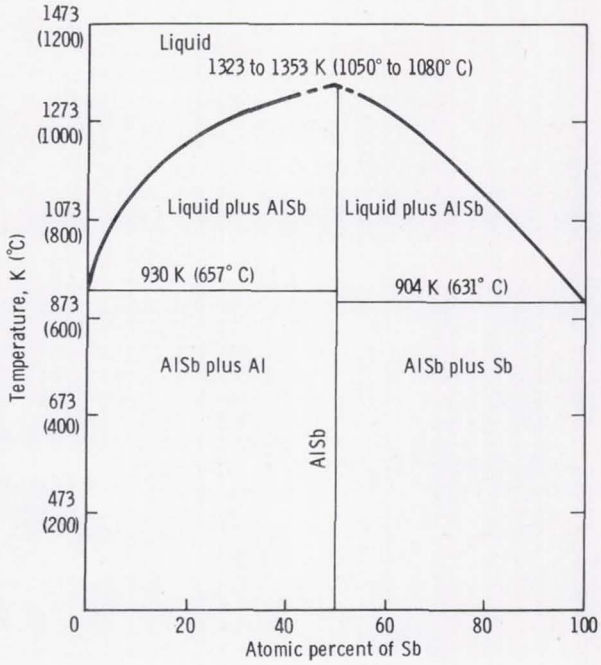

Figure 24-2.- Phase diagram for AlSb.

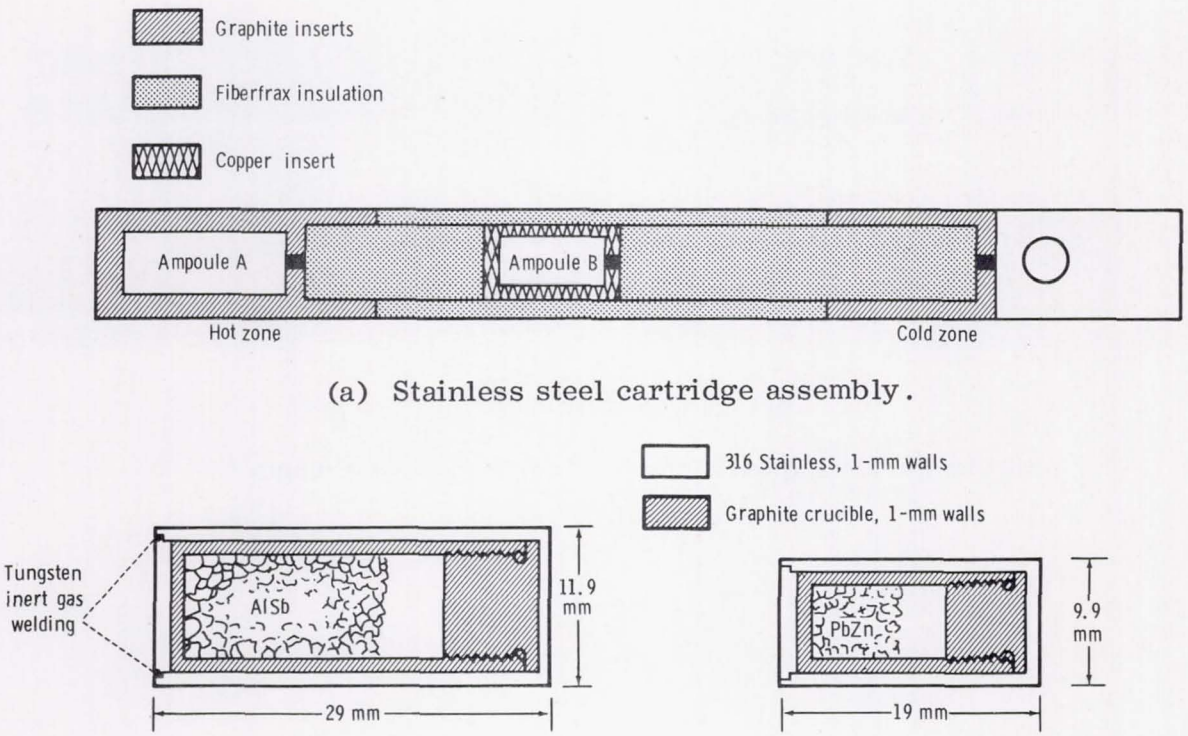

(a) Stainless steel cartridge assembly.

(b) Ampoule A.

(c) Ampoule B.

Figure 24-3.- Schematic of cartridge assembly and ampoules.

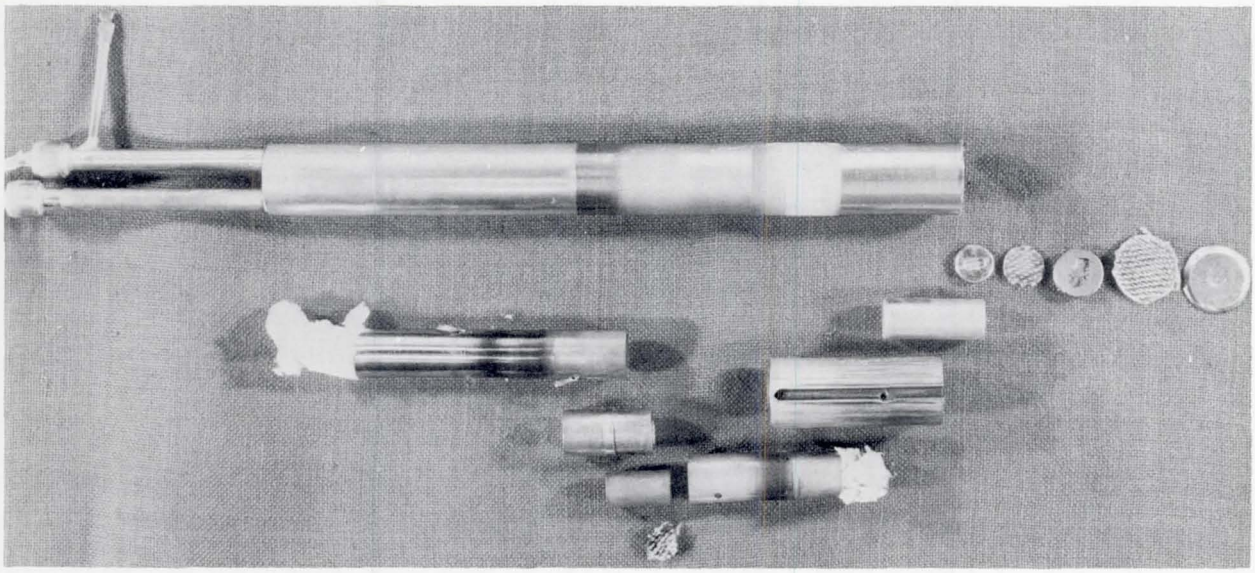

(a) Instrumented prototype equipment.

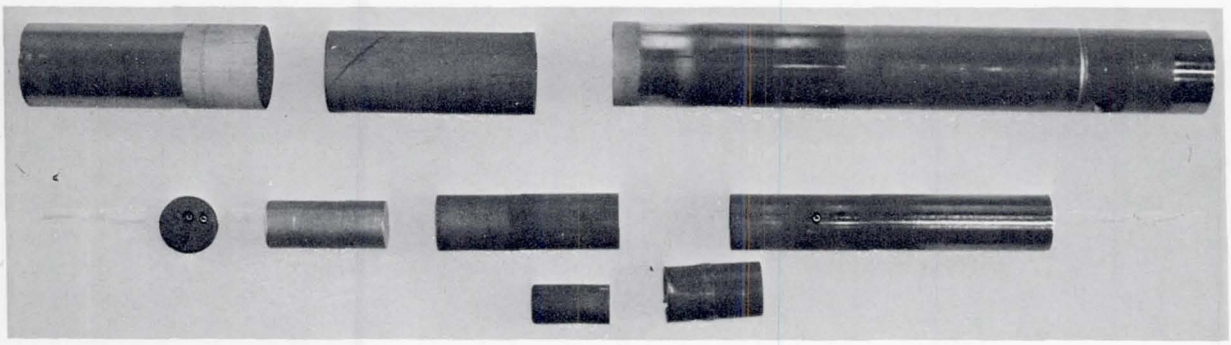

(b) Flight equipment.

Figure 24-4.- Exposed views of cartridges and ampoules.

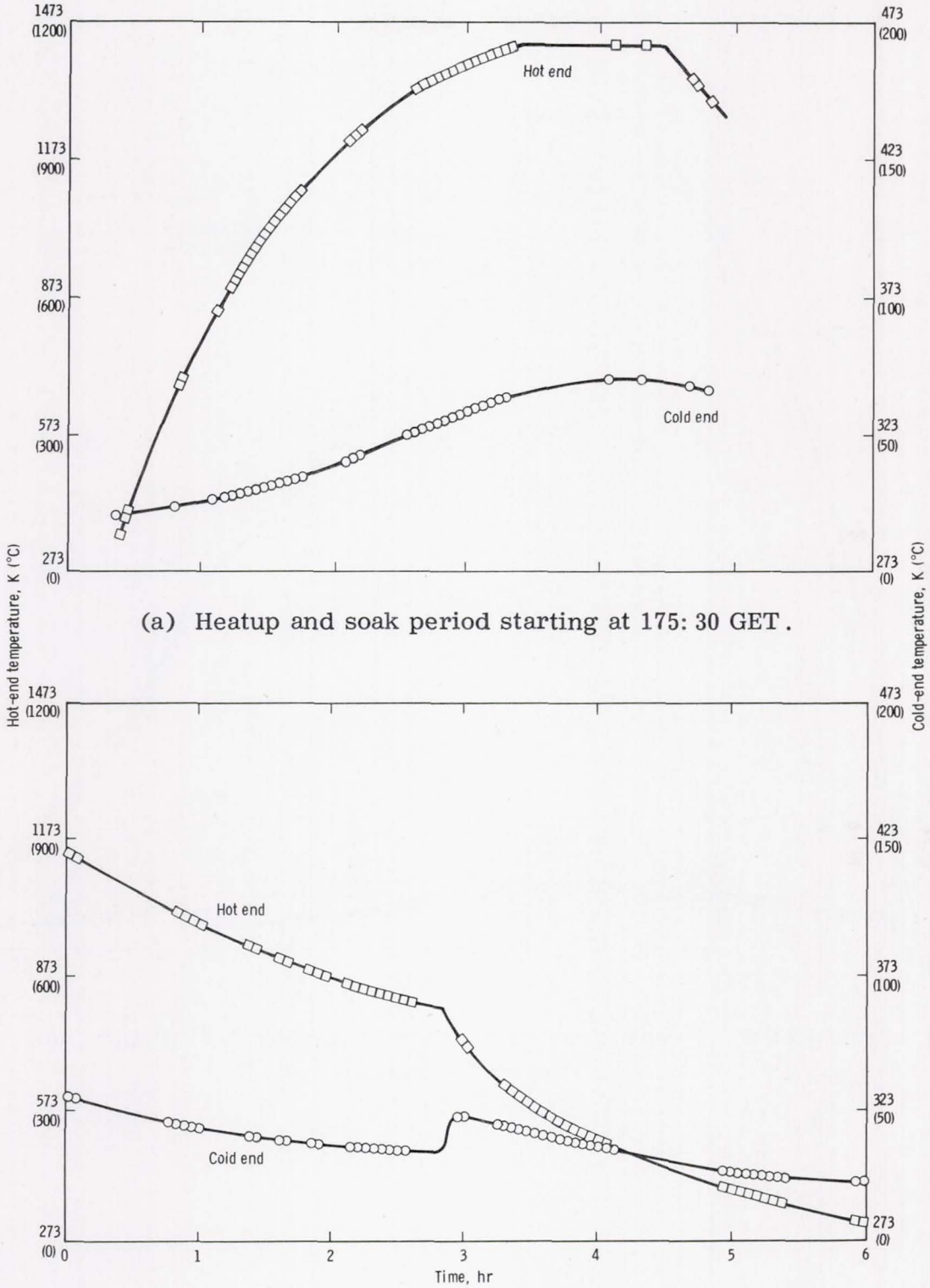

(a) Heatup and soak period starting at 175: 30 GET.

(b) Cooldown period starting at 181: 00 GET.

Figure 24-5.- Furnace telemetry data.

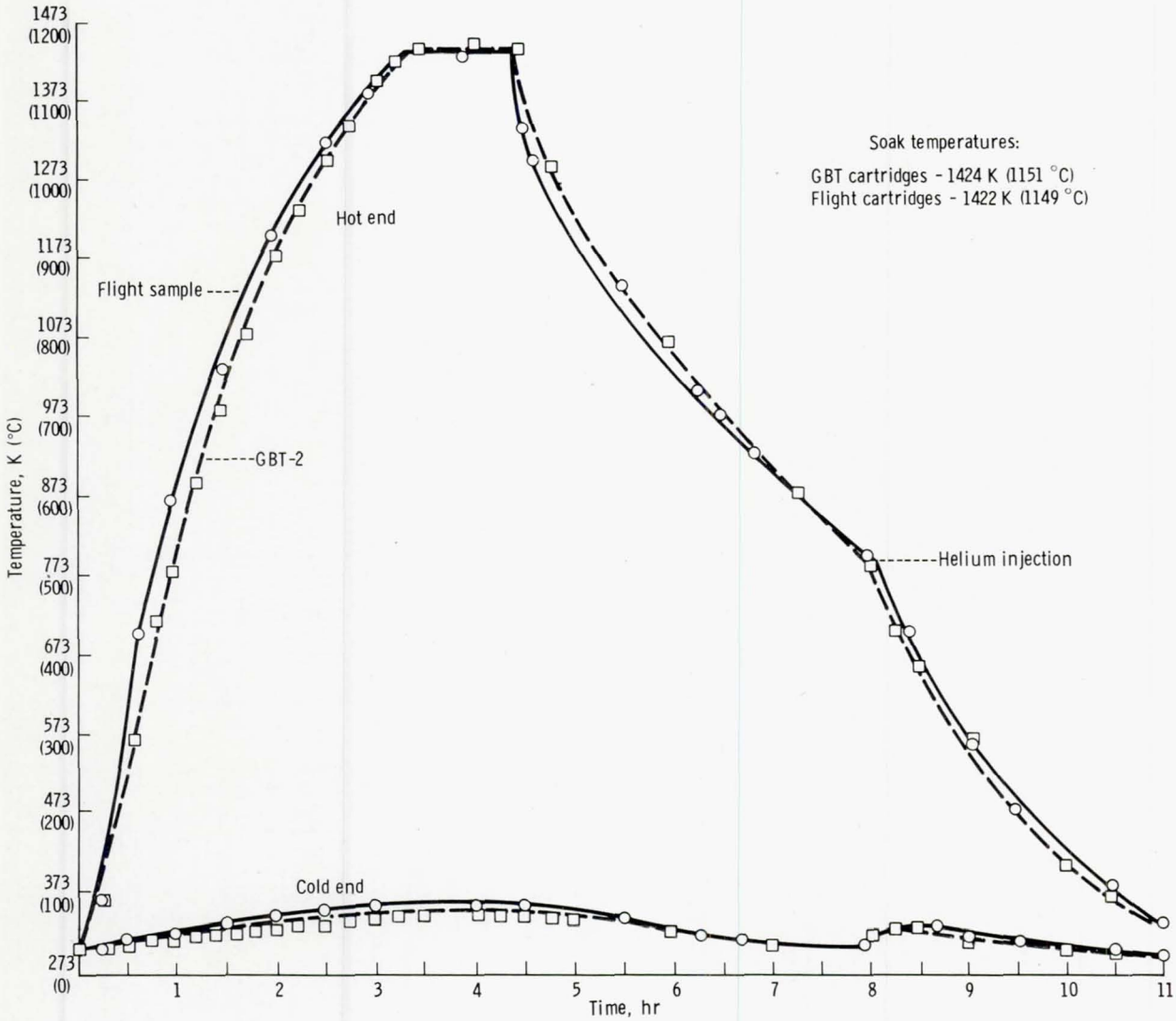

Figure 24-6.- A comparison of the thermal profiles for the flight and the GBT samples.

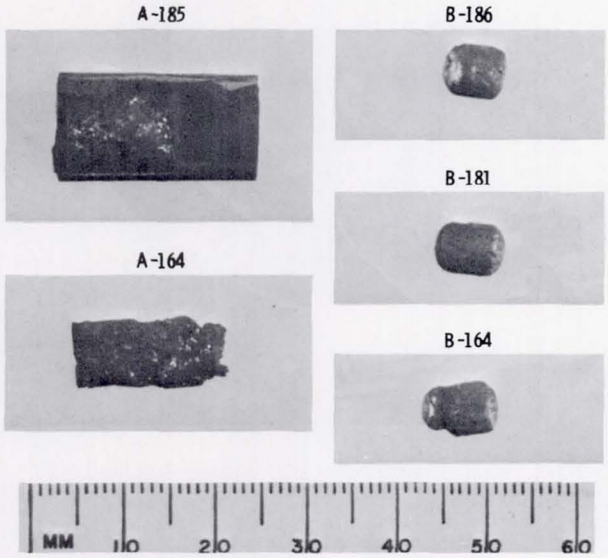

Figure 24-7.- Photograph of the flight samples.

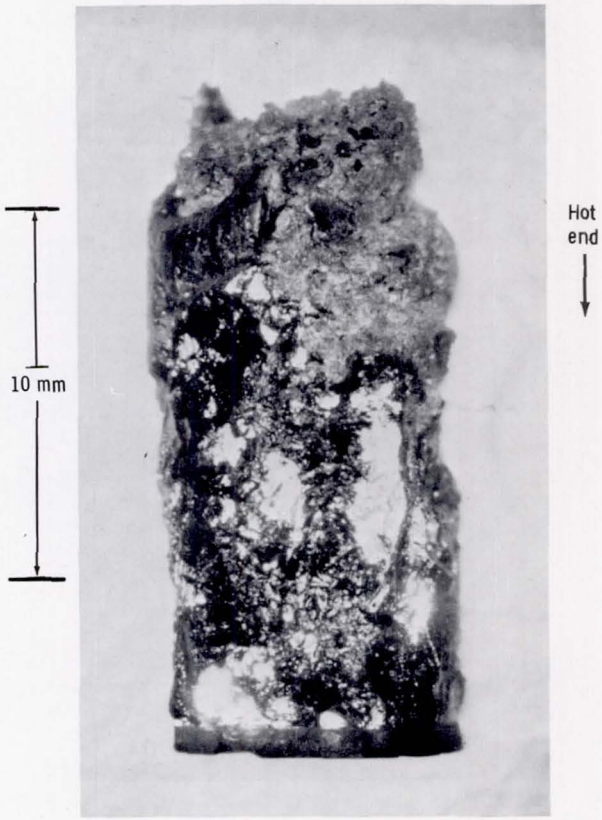

Figure 24-9.- Macrophotograph (5X) of AlSb flight sample.

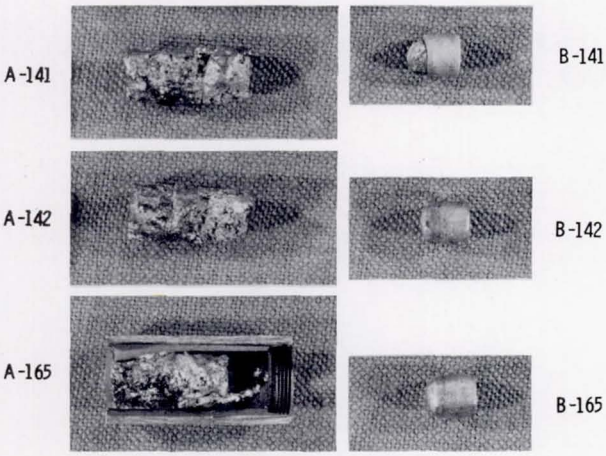

Figure 24-8.- Photograph of the GBT-2 samples.

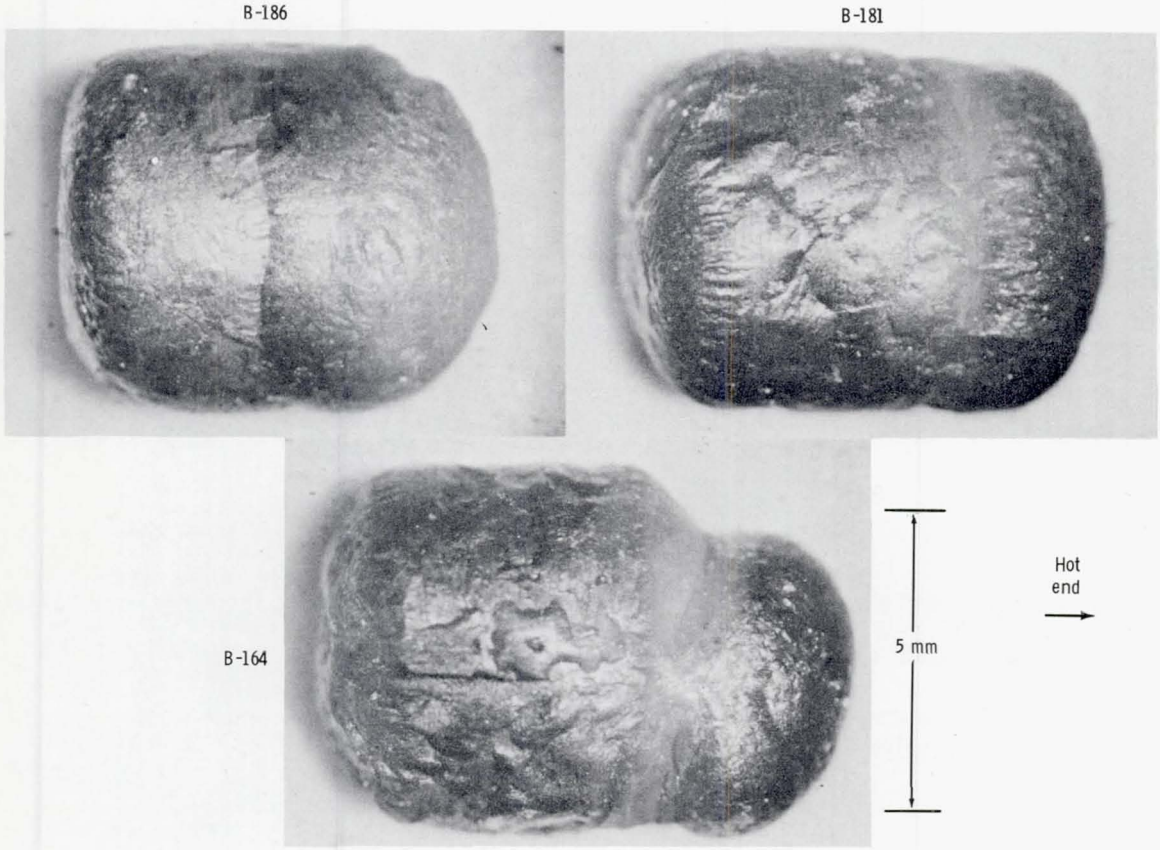

Figure 24-10.- Macrophotograph (10X) of the three PbZn samples identified by ampoule number.

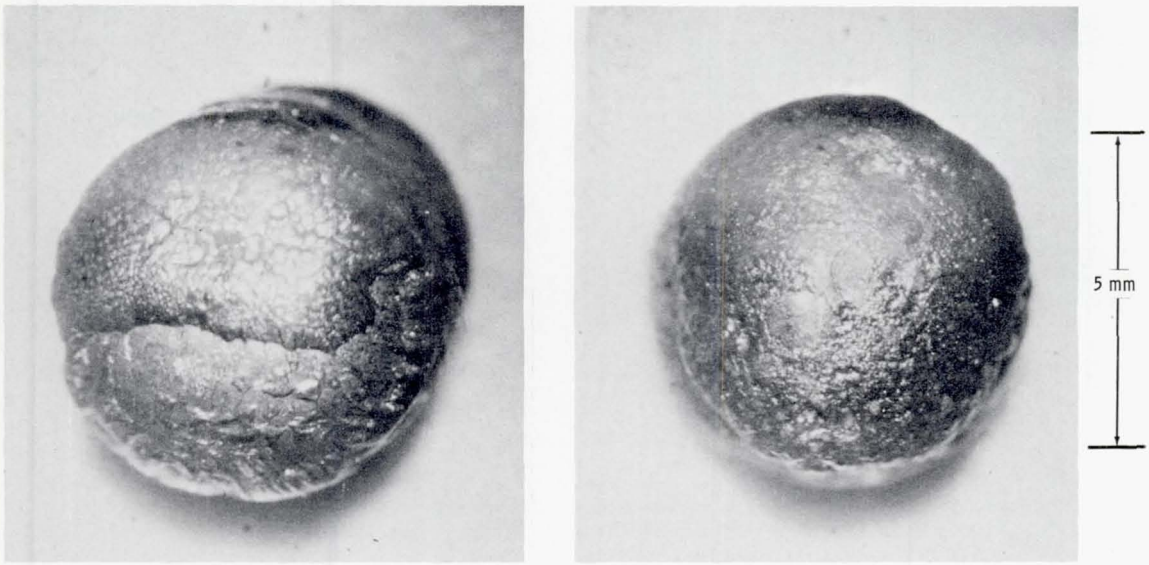

(a) Cold end. (b) Hot end.

Figure 24-11.- Macrophotograph (10X) of the two ends of the PbZn flight sample B-181.

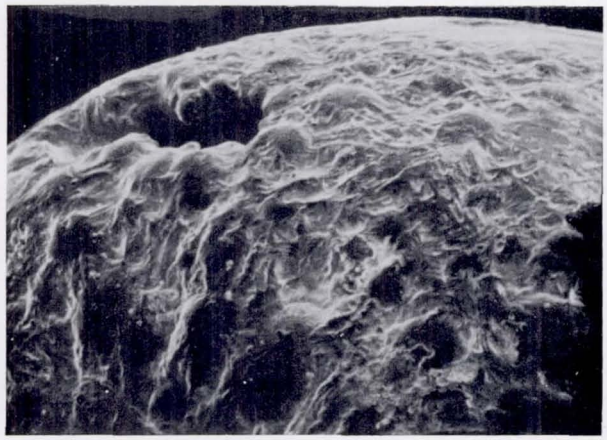

(a) Hot end.

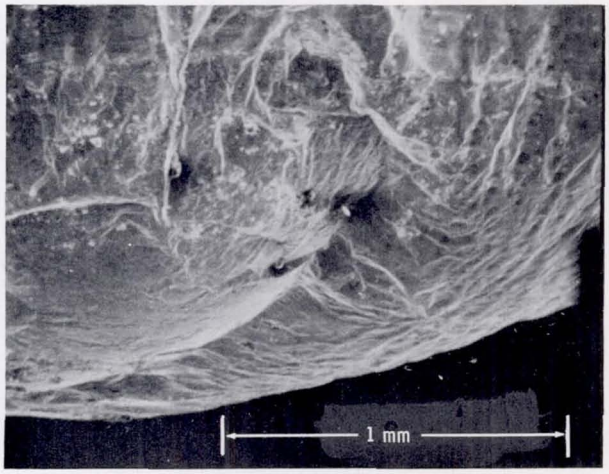

(b) Cold end.

(c) Interface.

Figure 24-12.- SEM photographs of surface features of PbZn flight sample B-181.

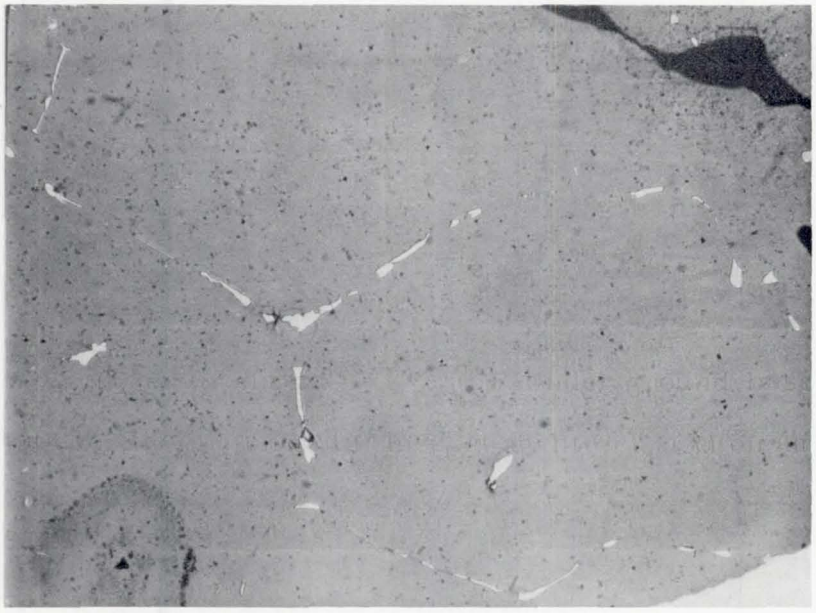

(a) Low-g sample (A-185).

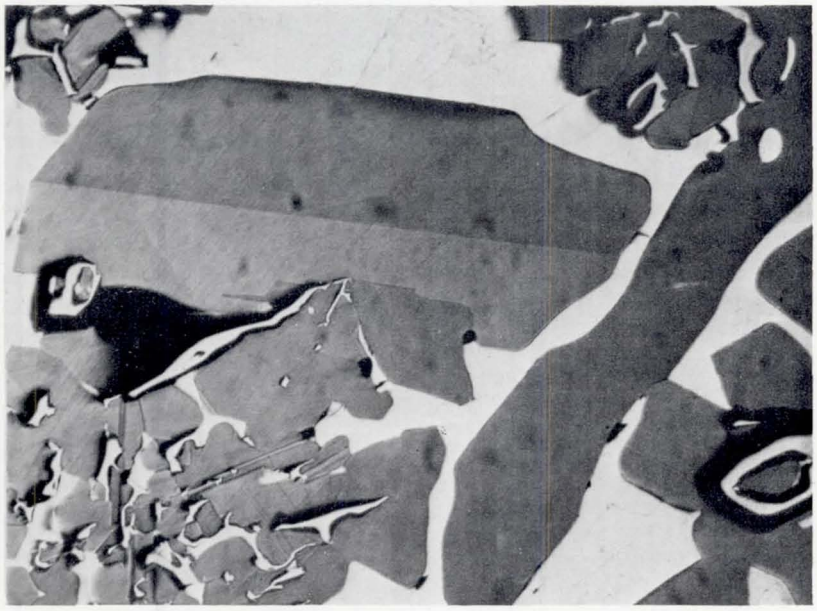

(b) One-g sample (A-127).

Figure 24-13.- Comparison of the microstructure of AlSb samples tested in low-g flight and one-g prototype furnace conditions (100X).

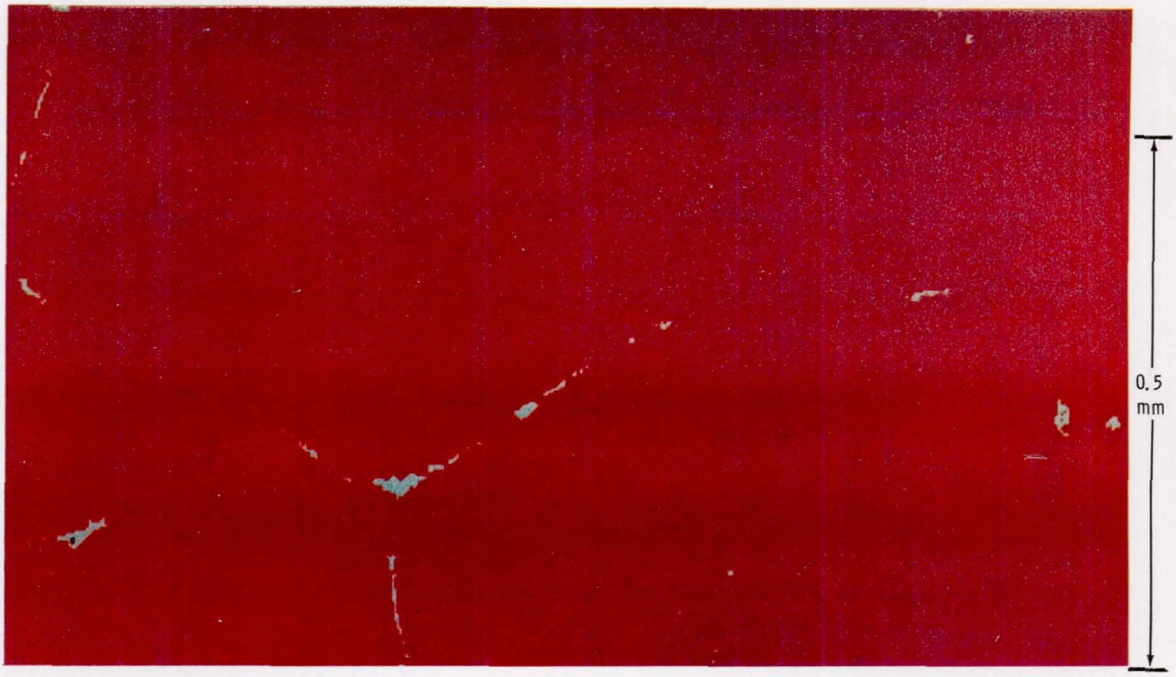

(a) Flight sample. The blue areas are rich in Al.

(b) Laboratory sample. The blue areas are rich in Sb.

Figure 24-14.- Pseudocolored presentation of microstructures shown in figures 24-13(a) and 24-13(b) using DIA. The red areas represent the AlSb compound.

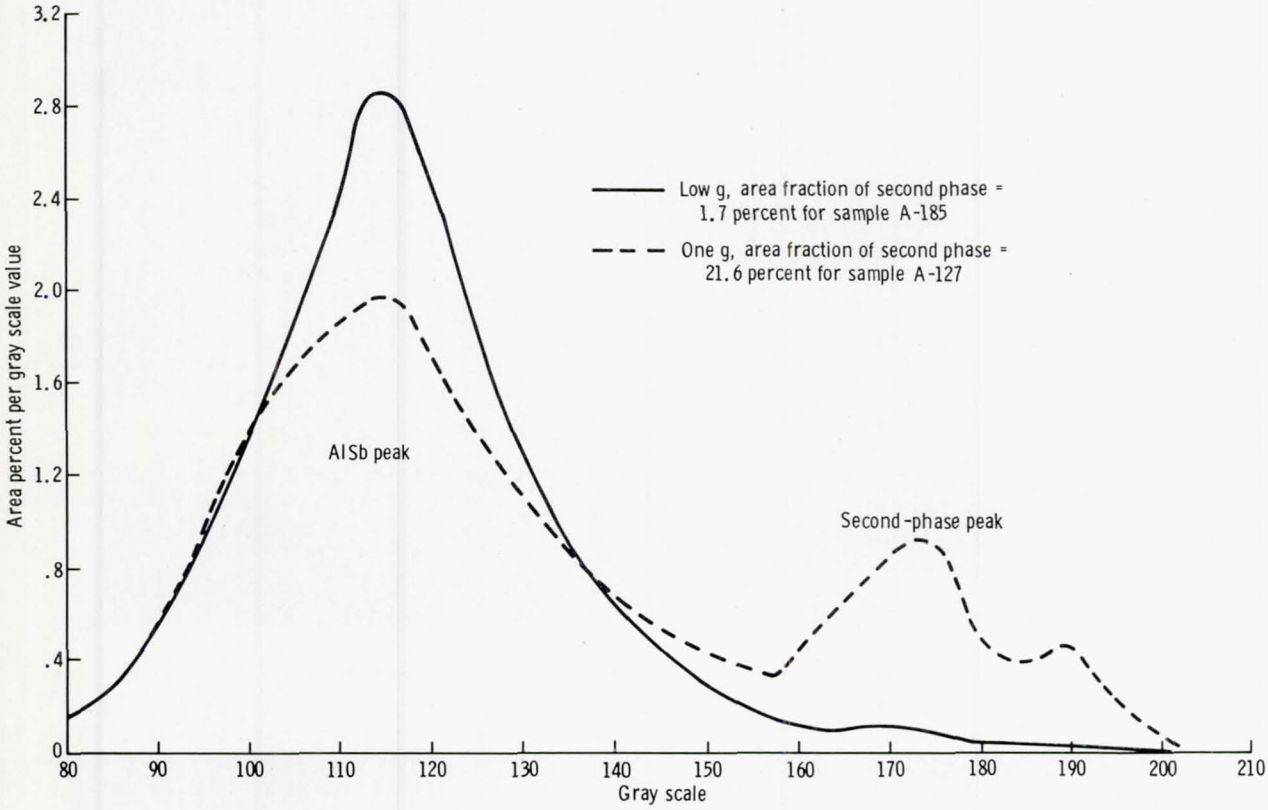

Figure 24-15.- Quantitative comparison of AlSb microstructures using DIA.

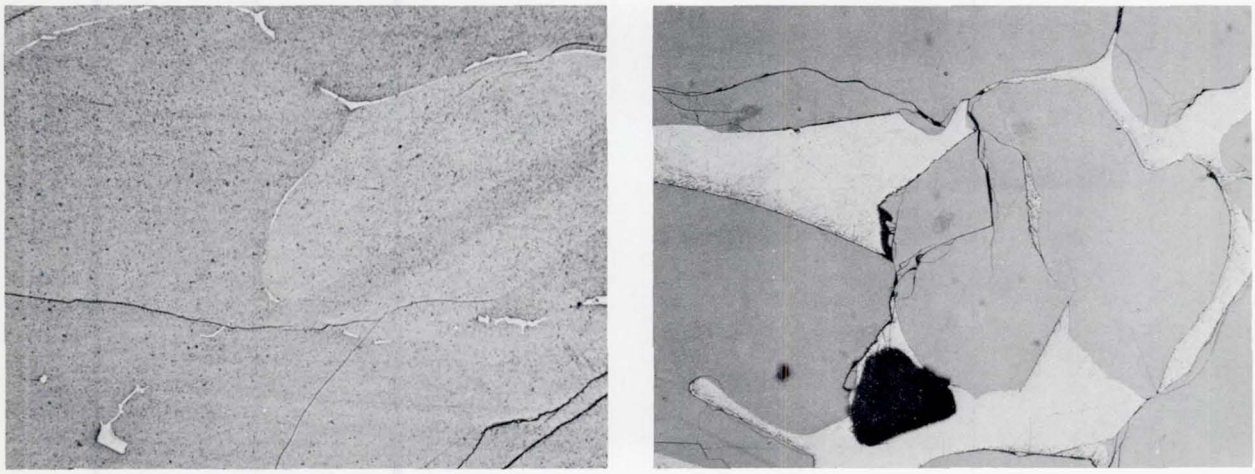

(a) Low-g sample (A-185).

(b) One-g sample (A-141).

Figure 24-16.- Comparison of the microstructure of AlSb samples tested under flight and equivalent GBT conditions (100X).

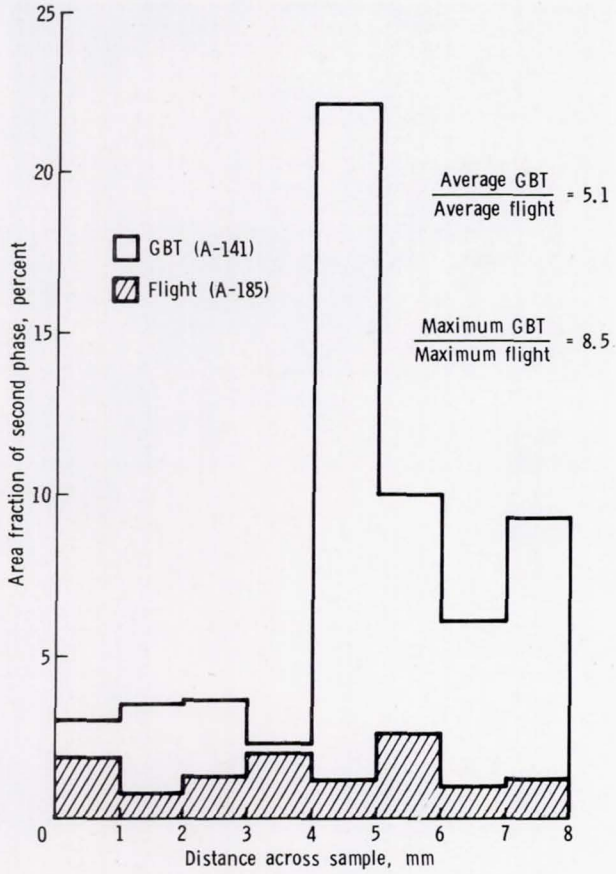

Figure 24-17.- Comparison of AlSb macrostructural homogeneity across sample sections.

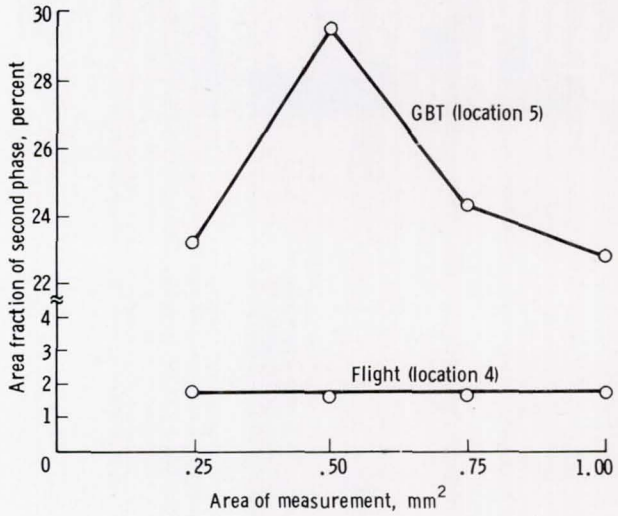

Figure 24-18.- Comparison of AlSb microstructural homogeneity as a function of area of measurement.

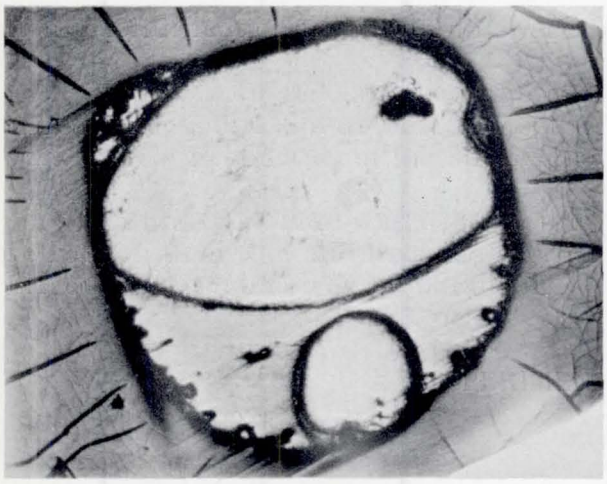

(a) 10X.

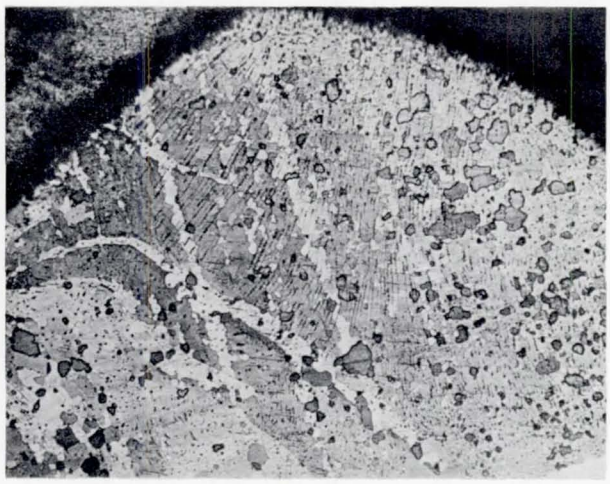

(b) 50X.

(c) 500X.

Figure 24-19.- Microstructure of PbZn flight sample B-186.

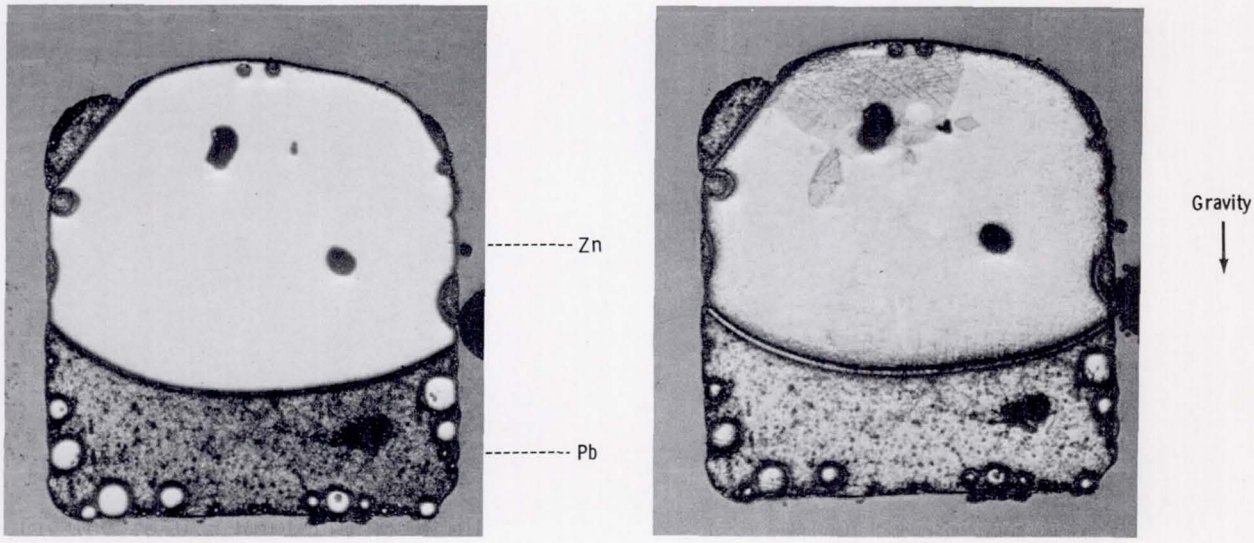

(a) Unetched (10X).

(b) Etched (10X).

Figure 24-20.- Macrophotograph of the longitudinal section of GBT-2 PbZn sample B-142.

25. INTERFACE MARKINGS IN CRYSTALS

EXPERIMENT MA-060

H. C. Gatos[a†] and A. F. Witt[a]

ABSTRACT

Doped germanium single crystals with interface demarcation were successfully grown during the Apollo-Soyuz Test Project mission. Interface demarcation permitted the determination of the microscopic growth behavior from the onset to the termination of solidification. Preliminary segregation analysis shows striking differences in segregation in the presence and the absence of gravity. The correlation between microscopic growth-rate behavior and the composition of the solid on the microscale is being evaluated.

INTRODUCTION

The purpose of the germanium (Ge) crystal growth experiment was to study quantitatively the basic solidification behavior of high-temperature melts in near-zero-g conditions. It was specifically designed to establish (1) the growth-rate behavior on the microscale, (2) the morphology of the crystal-melt interface and its changes during solidification, (3) the dopant segregation behavior and its functional dependence on the microscopic growth rate, (4) the absence or presence of convection phenomena, and (5) the heat-transfer characteristics of a solidification system in the absence of free convection.

To achieve these objectives, the growth system was equipped for interface demarcation during solidification through 20-ampere current pulsing (20A) at 4-second intervals. The experiment, involving the growth of gallium (Ga) doped and antimony (Sb) doped Ge of <111> and <100> orientation, was conducted to permit in all solidified crystals the direct comparison of solidification behavior on Earth with that in near-zero-g conditions.

The data obtained from the experiments were used to assist in establishing a quantitative framework for solidification and to provide a basis for feasibility studies of zero-g processing experiments to be conducted in the Space Shuttle. The results were also intended to establish guidelines for designing space-processing instrumentation.

---

[a]Massachusetts Institute of Technology.

[†]Principal Investigator.

Preliminary analysis of the experiments indicates that the basic objectives were realized. Further analysis of several phenomena is in progress.

BASIC THEORY

Solidification conditions require the establishment of thermal gradients (in melts), which are inherently destabilizing in the presence of gravity. Generally, the resulting thermal convection leads to uncontrollable variations in solidification rates and significant perturbations of the segregation-controlling diffusion boundary layer at the solidification front (crystal-melt interface). Thus, gravity effects make it essentially impossible to produce materials with compositional homogeneity on the microscale and macroscale; furthermore, in many systems, such gravity effects may contribute significantly to the formation of structural defects in single crystals.

The adverse conditions generated by gravity effects do not permit the experimental establishment of "theoretical" ideal experimental solidification conditions. Thus, a gap exists between theory and experiment in crystal growth. This gap must be bridged if optimization of processing conditions on Earth is to be achieved. Specifically, several approaches have been taken to obtain solutions for the segregation-controlling diffusion equation

$$D \frac{\partial^2 c_L}{\partial x^2} + R \frac{\partial c_L}{\partial x} = \frac{\partial c_L}{\partial t}$$

for transient and steady-state growth conditions where D is the diffusion coefficient, c_L is the concentration in liquid, R is the speed of advance of interface, x is the distance along the crystal, and t is time. The proposed solutions vary, and, because of convective interference, experimental confirmation of the validity of the proposed theoretical approaches has as yet been impossible.

These experiments provide solidification conditions that are applicable, in principle, to the theoretical work previously mentioned and permit the first analysis of basic solidification theory through experimental results.

EQUIPMENT

The Ge crystal growth experiment was conducted in the multipurpose furnace originally designed for the Skylab Program and further developed for the Apollo-Soyuz Test Project (ASTP). To provide for growth interface demarcation through current pulsing, the internal structure of the encapsulated quartz ampoule configuration that had been used for indium-Sb had to be redesigned. The centerless ground Ge single crystals, 1.0 centimeter in diameter, were reduced in diameter

at both ends to 0.8 centimeter to permit the insertion of high-purity graphite cup electrodes for current flow across the growth system. The graphite electrodes were in contact with current-carrying platinum wires, 0.1 centimeter in diameter, connected to the pulsing power supply (fig. 25-1). The pulsing unit provided pulses of 60 milliseconds duration at 4-second intervals. The electrical pulses for interface demarcation were applied to the three growth ampoules, containing one Ga-doped <111> Ge crystal and one (each) Ga-doped and Sb-doped <100> Ge crystal, connected in series to the power supply.

The growth conditions used in space were determined by a series of ground-based tests that also served as a basis for comparison of the growth behavior encountered in one-g and near-zero-g conditions. Based on these tests, the following space-growth conditions were established. The furnace was brought to growth temperature (1383 K (1110° C)) over a period of 3.5 hours by applying full power at a 100-percent duty cycle. At this temperature, the encapsulated Ge crystals were expected to melt back to a length of approximately 3.5 centimeters. The system was subsequently allowed to reach thermal equilibrium (soaking period) for 2 hours. Equilibration was obtained by applying full power with an approximate 90-percent duty cycle. Current pulsing was applied to the growth system throughout the heatup, thermal-soaking, and ensuing cooling cycle. After thermal equilibration, the power system was switched to the cooldown position, resulting in a decreasing duty cycle with a cooling rate of 2.4 K/min (2.4° C/min). This cooling rate was expected to yield a microscopic growth rate ranging from 5 μm/sec at the beginning to 10 m/sec at the end of the controlled cooldown period.

The crystals grown in space were subjected to exhaustive growth and segregation analysis based on procedures determined during the ground-based tests. The primary techniques used in the analysis involve high-resolution etching, Hall-effect measurements, spreading-resistance measurements, and ion-microprobe analysis.

RESULTS

The preliminary results of the Ge crystal growth experiment are as follows.

1. All three space-grown Ge segments were single crystals with a length exceeding 3 centimeters. Breakdown of single crystallinity during the late stages of growth was expected and was attributed to constitutional supercooling. The experiment thus confirmed the adequacy of the ampoule design. The original regrowth interface appeared approximately 3.5 centimeters from the cold end of the Ge crystal, confirming on the macroscale the proper functioning of the growth furnace (figs. 25-2 and 25-3).

2. High-resolution etching analysis of longitudinal cuts of the regrown crystals revealed the presence of interface demarcation lines, confirming the functioning of the electrode design and pulsing power unit (fig. 25-4). Visual inspection of the region about the original regrowth interface indicates that before controlled cooldown (top part of fig. 25-5), the systems experienced uncontrolled, irregular, slow

growth, which resulted in the formation of a growth band approximately 300 micrometers wide. The growth of this band must have occurred during the thermal soaking period and reflects thermal instability in the form of a slow, irregular, downward temperature drift. This thermal drift is attributed to a slight imbalance of heat input and heat loss in the growth systems.

3. Interface demarcation permitted, by spacing the successive demarcation lines, a quantitative microscopic growth-rate analysis of the space-grown crystal (fig. 25-6). The results indicate an exponential increase of the growth rate, which reached a value of approximately 9 μm/sec after a growth length of approximately 2 centimeters. The observed growth-rate behavior in space, which is virtually identical with that encountered during ground-based testing, varies from the predicted behavior. This variance will have a significant impact on the theoretical approach to growth and segregation analysis. The results of the growth-rate analysis also indicate that the heat-transfer characteristics of the system are virtually identical in zero-g and one-g conditions. This finding indicates that conductive heat transfer dominates and that the contribution of laminar convection to heat transfer, which was present in the ground-based experiments, is negligible. Interface demarcation further indicates that the growth interface morphology (shape of the solidification isotherm) remained constant over a growth distance exceeding 2.5 centimeters. Changes in the morphology of the crystal-melt interface were observed only after approximately 3.5 centimeters of growth, when the presence of the graphite electrodes, which have significantly different thermal conduction characteristics, altered the basic heat flow in the system. This finding is important because it provides a means of controlling the growth interface morphology during the materials processing in space.

4. The quantitative compositional analysis of the space-grown crystal, based on spreading-resistance measurements and ion-microprobe measurements, is in progress. Preliminary results indicate the absence of compositional fluctuations on the microscale, and the data thus far obtained indicate that compositional homogeneity (steady-state segregation) on the macroscale was not obtained during growth. In fact, the compositional analysis indicates the occurrence of unpredicted dopant concentration decreases at distances of approximately 3 centimeters from the original regrowth interface (fig. 25-7). The validity of these preliminary data obtained through spreading-resistance measurements is checked by means of ion-microprobe analysis to verify the absence of unpredictable contamination. The quantitative microsegregation analysis and comparison of that analysis with theoretical treatments will be performed after verification of the compositional analysis.

SUMMARY

Based on preliminary results, interface demarcation constitutes an indispensable tool for quantitative investigation of growth and segregation behavior at zero-g conditions. Preliminary results obtained are as follows.

1. The microscopic growth rate is subject to an initial transient that reaches approximately 8 μm/sec after 2 centimeters of growth.

2. The microscopic growth-rate behavior observed during the ASTP mission is identical to behavior encountered during ground-based testing.

3. Compositional fluctuations on the microscale are absent in the space-grown Ge crystals.

4. The basic segregation behavior observed in the space-grown material is fundamentally different from that observed in ground-based tests.

Conclusions concerning the qualitative relationship between microscopic growth rates and composition will follow further experimental analysis.

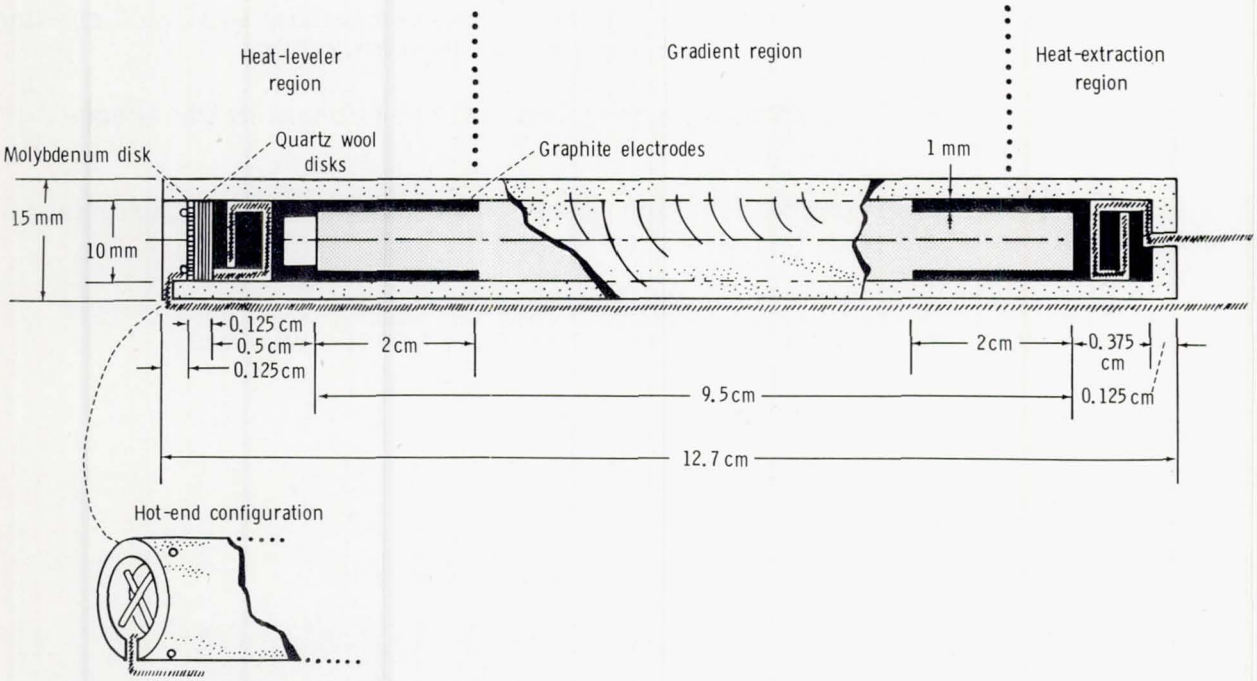

Figure 25-1.- Schematic diagram of the growth ampoule.

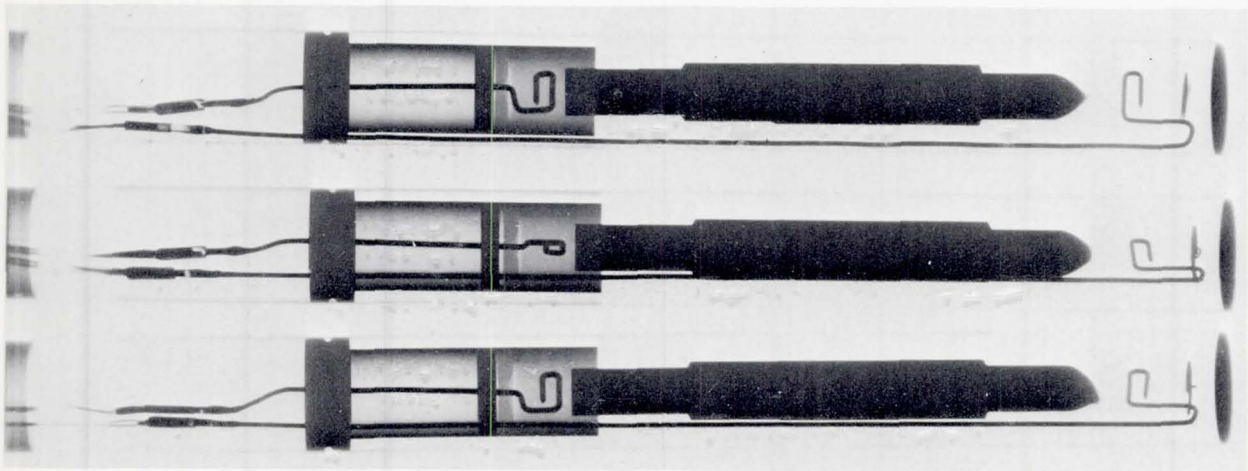

Figure 25-2.- Radiogram of Ge crystals regrown in space.

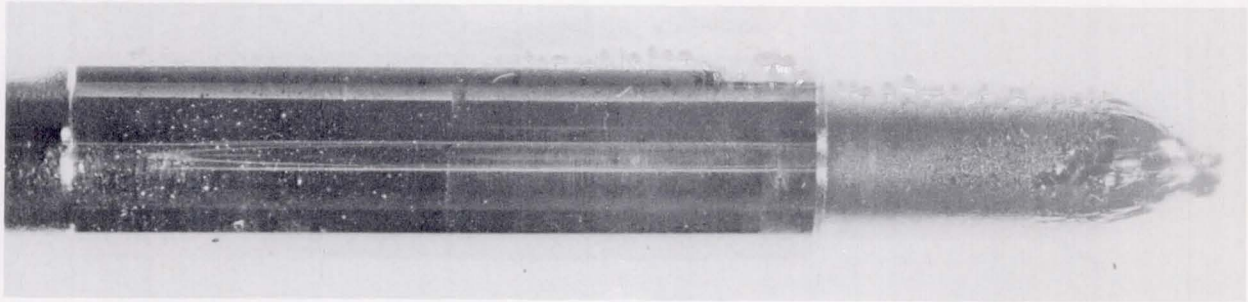

Figure 25-3.- Ge crystal regrown in space.

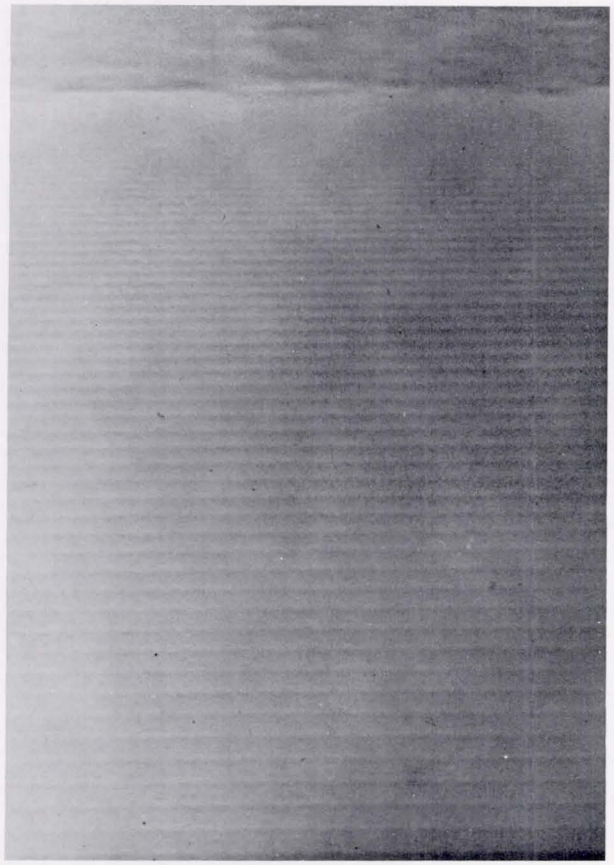

Figure 25-4.- Interface demarcation lines in the initial portion of regrowth.

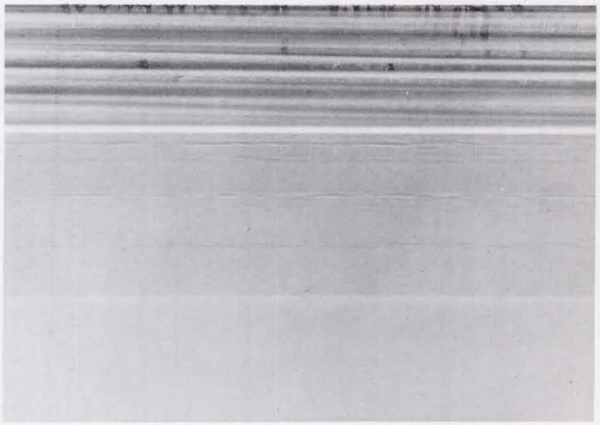

Figure 25-5.- Segregation effects in the region of the original regrowth interface.

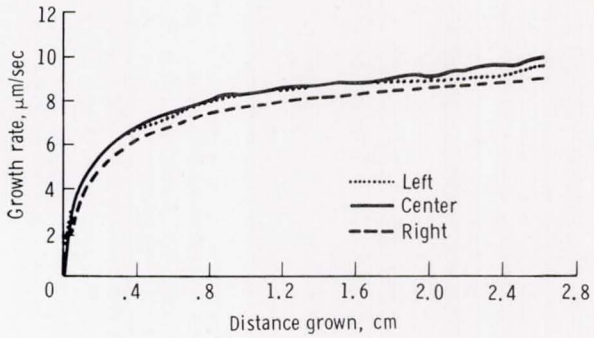

Figure 25-6.- Microscopic growth-rate analysis of Ga-doped <111> Ge crystal regrown in space.

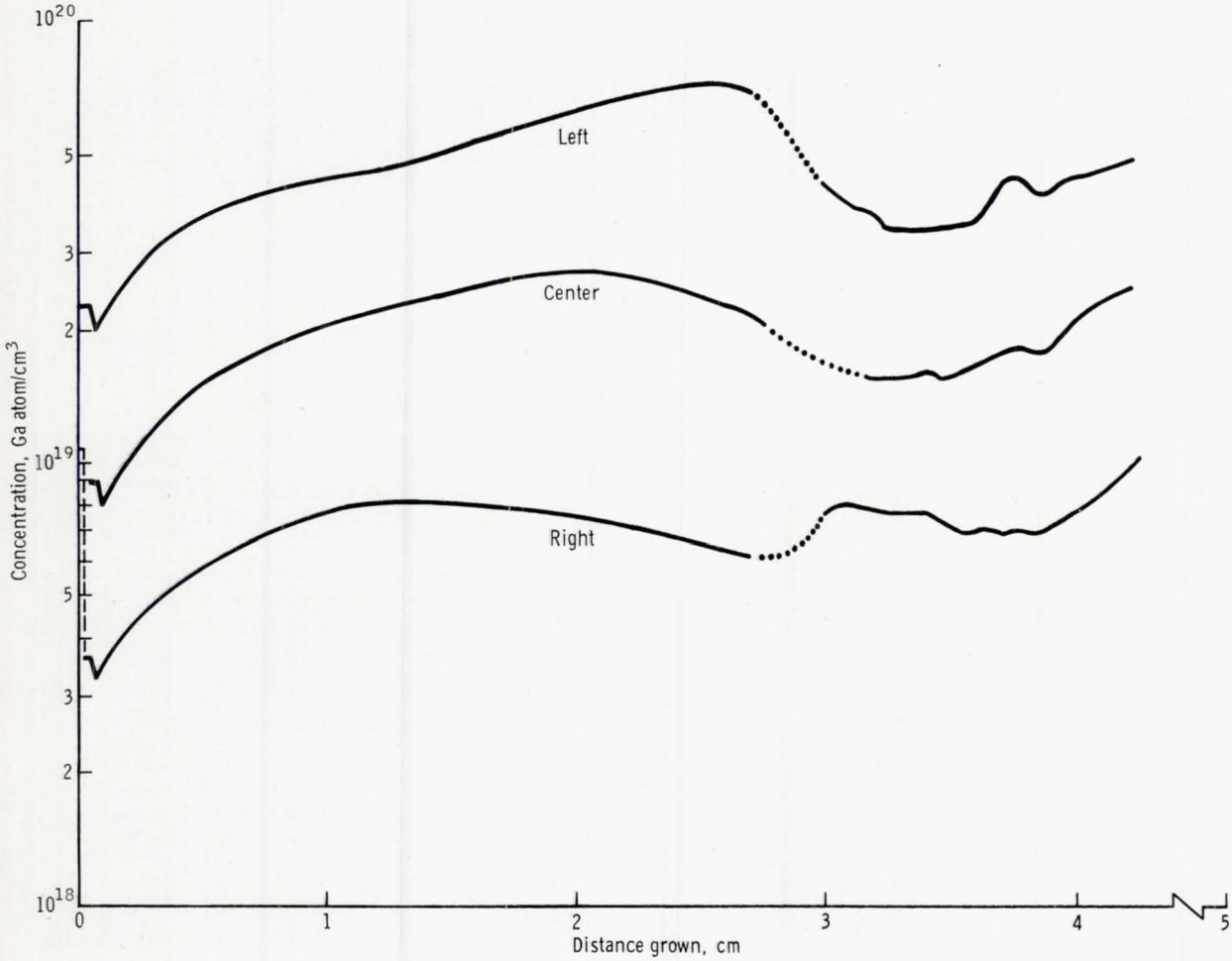

Figure 25-7.- Preliminary compositional analysis of Ga-doped <111> Ge crystal regrown in space.

26. ZERO-G PROCESSING OF MAGNETS

EXPERIMENT MA-070

D. J. Larson, Jr.[a]

ABSTRACT

The Zero-g Processing of Magnets Experiment (MA-070) was conducted to study the solidification of magnetic materials in the low-gravity orbital environment. The magnetic compounds under study, manganese bismuth (MnBi) and copper-cobalt-cerium ($(Cu, Co)_5 Ce$), both have the potential for the development of high coercive strength. The results of this experiment will determine whether space processing offers the opportunity to substantially improve critical magnetic properties by improving chemical homogeneity, morphological perfection, crystalline perfection, or magnetic substructure.

Preliminary results indicate that static fluid configurations, in the absence of the gravitational body force, differ substantially from the documented terrestrial behavior. Chemical homogeneity is substantially enhanced on a macroscopic and microscopic level. Single crystal matrices have been grown in the coordinated growth regions of the flight samples. Primary crystals one order of magnitude greater than those grown terrestrially have been noted and are limited in size by the ampoule dimensions.

INTRODUCTION

The purpose of this experiment was to increase the fundamental understanding of contained solidification in the low-gravity, orbital environment. In addition, tests will be conducted on a number of specific results obtained during the Skylab materials science experimentation and analysis. Specifically, an order of magnitude reduction in the twin density was reported in the Skylab mixed crystal growth experiment (M563) (ref. 26-1); this finding will be tested within the bismuth matrix that surrounds the manganese bismuth (MnBi) particles. In addition, an analysis of the Skylab immiscible alloy (M557) experiment results (refs. 26-2 and 26-3) indicates that several significant points were not considered quantitatively; these

---

[a]Grumman Aerospace Corporation, Bethpage, New York; Principal Investigator.

points will be considered in the course of this investigation.[1] The Skylab results indicate a significantly larger primary crystallite size and a nonuniform chemical distribution within the primary crystallites. The former result is of critical importance to solution crystal growth in orbit, and the latter is of critical importance to both solution crystal growth and fundamental solidification theory, if it is actually a bulk and not just a surface effect. Lastly, investigators will evaluate crystalline and morphological perfection of directionally solidified eutectics that led to conflicting conclusions within the Skylab copper-aluminum eutectics (M566) and metal and halide eutectics (M564) experiments[2] (refs. 26-3 and 26-4).

BASIC THEORY

The fluid state before the initiation of thermally controlled solidification is of fundamental importance to crystal growth and directional solidification experiments. This fluid state has both static and dynamic considerations; however, the measurements required to conduct in situ or postflight dynamic analysis of the flight samples, processed during the Apollo-Soyuz Test Project (ASTP) flight, were deemed impossible and thus only static analysis is to be conducted. Previous crystal growth experiments, conducted onboard Skylab, indicated that the static fluid shape in low-g was appreciably different from the static fluid shape documented terrestrially (refs. 26-5 and 26-6). If the fluid configuration is changed, the heat flux or thermal profile, which is critical to the success or failure of the experiment, may be changed. Prior work conducted in the drop tower facility at NASA Lewis Research Center (LeRC) has identified the fluid-crucible variables that are of primary consideration in a reduced gravity environment. These variables are the fluid-crucible wetting angle θ, the thermal gradient G, the crucible taper, the fluid-crucible volume fill factor, and the diameter to length ratio D/L of the cylindrical crucible (refs. 26-7 to 26-9). The LeRC results on fluid displacement in the reduced gravity environment are reproduced in figure 26-1, and the fluid configurations within a cylindrical crucible ("tank" in LeRC terminology) are illustrated in figure 26-2. In the current experiments, fluid-crucible fill-factor studies and solidification studies were conducted in the isothermal portion of the experiment. Fluid displacement studies were conducted in the gradient regions of the experiment. In addition, the isothermal and elevated temperature thermal gradient experiments were conducted with metallic liquids that wet their containers, whereas the low-temperature thermal gradient experiment was conducted with a nonwetting fluid-crucible system. Results, presented in the section entitled "Results and Discussion," were, for the most part, consistent with theory. Information on the theory of crystal growth and directional solidification, or coordinated growth of eutectics, is available in references 26-10 to 26-12.

---

[1] J. L. Reger, "Experiment No. M557 Immiscible Alloy Compositions, Final Report," TRW Systems Group, Apr. 1975.

[2] Ibid.

EQUIPMENT

This experiment used the multipurpose furnace facility located in the ASTP docking module. The experiment used three discretely different thermal zones (one isothermal and two gradient). The thermal profile of the furnace is shown in figure 26-3 at three stages of the prototype test, and the data used to make this drawing are presented in table 26-I. Note that the isothermal region of the furnace had a slight thermal gradient of 2 to 3 K over the range of solidification of this alloy, and that the thermal gradients in the gradient regions were, respectively, approximately 30 K/cm and 50 K/cm. The furnace required approximately 3.25 hours to reach the soak temperature. It was held at the soak temperature for 0.75 hour and then cooled passively over a 10.5-hour period. The measured soak temperature during the flight was 1348 K (1075° C), the helium injection was conducted at 673 K (400° C), and the air quench was performed at approximately 523 K (250° C). Controlled solidification was accomplished during an astronaut sleep period to minimize vehicular vibration and to avoid control maneuvers.

Three experiment cartridges (types 1, 2, and 3) of the design shown in figure 26-4 were used in the experiment. The sample materials were selected for compatibility with the thermal capabilities of the furnace, and the ampoule materials were selected with both experiment and safety criteria in mind. The final experiment was such that ampoules 1 and 2 were pyrolytic boron nitride and ampoule 3 was quartz. Ampoule 1 contained a 50-50 atomic percent alloy of bismuth and manganese, ampoule 2 contained a copper copper-cobalt cerium ($Cu-(Cu, Co)_5Ce$) eutectic alloy, and ampoule 3 contained a bismuth manganese-bismuth (Bi-MnBi) eutectic alloy. These ampoule-sample selections were adequate for both the fluid-statics studies and the solidification studies.

RESULTS AND DISCUSSION

It should be immediately noted that conclusions based on the flight samples are preliminary, with the exception of the fluid statics, and that they are based on surface and near-surface measurements only. No bulk measurements have been made to date because the materials are being conserved for magnetic analysis. Once the magnetic results are completed, then the internal morphological, chemical, microstructural, and crystallographic measurements will be made. Whenever bulk measurements are critical to a conclusion, this fact will be pointed out.

The macroscopic fluid configurations are visible in the X-ray radiograph (fig. 26-5), and the reader can infer the anticipated fluid configurations and displacement from figures 26-1 and 26-2.

The three number 1 ampoules (fig. 26-4) contained wetting fluids, each with a different fill factor; the other factors are assumed constant. The fill factors were such that one ampoule was anticipated to give a type 1 configuration, one ampoule a type 2 configuration, and one ampoule a configuration (type 3) somewhere close to the transition between the two. Unfortunately, the type 2 sample was lost because of a vibrational failure of the inner ampoule; however, the other ampoules

agreed with theory. The type 1 sample is shown in figure 26-6. The pore has been revealed by breaking away a portion of the metallic shell surrounding the large pore. All the ground-based fluids assumed a bottom position with a flattened meniscus that was due to the dominant gravitational body force.

The number 2 ampoules contained a wetting fluid; however, the fluid was positionally constrained by the unmelted seed portion of the sample. These samples all had high fill factors, and cross-sectional analysis is required to define any fine differences between the samples.

The number 3 ampoules were intended to represent an unconstrained, nonwetting fluid, in parallel walled capillaries, with a superimposed thermal gradient. Two unanticipated results took place during the flight experiment. First, the number 3 ampoules were backfilled with inert gas to suppress cavitation of the bismuth-rich fluid and, apparently, a small amount of contaminant oxygen was also injected into the type 3 ampoule of the middle cartridge (fig. 26-5). This small amount of contaminant oxygen was sufficient to change the system from a nonwetting to a wetting system, with concomitant differences in displacement behavior. The nonwetting fluid moved toward the hot end of the ampoules, whereas the wetting fluid moved away from the hot end. This fluid displacement is indicated by the comparative positions of the solidified samples in figure 26-5. The manifestation of the fluid motion within the nonwetting ampoules was such that, as the bismuth-rich fluid expanded upon solidification, it caused an internal stress to build up ahead of the solidification front that was sufficient to cause these two ampoules to crack. Close inspection of figure 26-5 shows that a small amount of fluid was lost within one of the cartridges.

Another fluid effect was unexpectedly discovered in the ground-based studies. Inspection of the thermal profile imposed upon the number 3 ampoules, when the furnace was at peak temperature, reveals that the hot end of the number 3 ampoule appreciably superheated the bismuth-rich fluid. This superheating necessitated the backfilling of these ampoules with inert gas to suppress cavitation. To check ampoule-fluid compatibility, the quartz-bismuth system was superheated within a differential thermal analysis (DTA) unit. This testing discovered a liquid phase transition that took place at 988 K (715° C) on heating and 858 K (585° C) on cooling. Cyclic studies within the DTA ascertained that these transitions were one and the same, with large hysteresis. Similar fluid state transitions have been reported for other semimetals, but not previously for bismuth (ref. 26-13).

The isothermally processed ground-based samples demonstrated appreciable gravitationally dependent segregation. This chemical segregation resulted in almost all the properitectic Mn particles being at the top of the sample and a continuously decreasing area percentage of MnBi particles on progressing from top to bottom. This area fraction varied from 42 percent at the top to less than 1 percent at the bottom. The Mn, MnBi, and Bi phases were evident at the surface of the ground-based samples.

Surface analysis of the internal pore shown in figure 26-6 revealed no primary Mn particles that could be identified by X-ray energy dispersive analysis. There appeared to be extremely large MnBi particles that were arrayed in a Bi-MnBi matrix. The major MnBi particles were few in number and an order of magnitude

greater in extent than those documented within the ground-based samples. Comparison with Skylab samples revealed, unexpectedly, that these results occurred within the Skylab samples but they had not been quantitatively evaluated (ref. 26-2). The extent of these crystallites was limited by the dimensions of the ampoule.

Chemical surface analysis of these particles, by X-ray energy dispersive analysis and microcompositional mapping techniques, gave a highly anomalous result. The particles seen optically and the two-phase matrix are isocompositional. This compositional result may be a surface effect, and it can be readily explained as such. However, reference 26-2 (fig. 5, p. 143) shows a bulk micrograph that would also account for this compositional result. Within the bulk, it would be anticipated that these large crystallites would be monolithic slabs of uniform composition. The sectioning of the samples will determine whether this characteristic is a bulk effect. If this is true, the structure is an extremely difficult one to explain with respect to solidification theory.

The X-ray surface analysis of the type 2 samples indicates a single crystalline matrix, which is an ideal result. However, no conclusions about the dispersion of the secondary particles can be drawn at this time because the necessary bulk analysis has not yet been performed.

The type 3 ground-based samples revealed gravitational segregation to a lesser extent than the type 1 samples. The segregation was sufficient, from bottom to top, to result in three discrete regions of growth. At the bottom of the samples was a bismuth-rich region that consisted of a proeutectic array of Bi dendrites and interdendritic eutectic (fig. 26-7). This morphology abruptly changed to a coordinated growth (fig. 26-8). The abrupt change in morphology may have been chemically or thermally driven; but, if it were chemically driven and the chemical gradient due to gravitational segregation, then one would not expect to observe this abrupt change in the flight samples. If it were imposed thermally, then one might anticipate similar behavior, but with the transition somewhat displaced. Surface techniques are not sufficient to adequately define the location of the transition point in the flight samples. However, it appears that the transition does occur, and thus it is thermally driven or driven by both chemical and thermal parameters. The latter is the most likely. Internal chemistry and morphology have not yet been defined.

SUMMARY AND CONCLUSIONS

The intent of this program was to study the fluid-static configurations in low-g by variation of fundamental parameters such as fill factor, diameter to length ratio of the cylindrical crucible, fluid-crucible wetting angle, and crucible taper. These goals were accomplished and the results were found to agree well with theory. Of equal importance was the study of solidification in the low-g environment. Because this is a preliminary report, definitive conclusions within the latter area are not included, but it appears that sufficient data exist to conclude that chemical and morphological distributions are appreciably different in the low-g processed materials.

The following conclusions are made with a high degree of certainty.

1. Bismuth undergoes a liquid phase transition at elevated temperatures.

2. Equiatomic manganese bismuth alloys undergo severe gravitational segregation. However, segregation does not appear to occur in the flight processed samples.

3. The number and size distribution of orbitally processed primary crystals is greatly different than the same properties of terrestrially processed samples.

4. Static fluid configurations in the orbital environment are greatly different from those monitored terrestrially.

5. Anomalous surface chemical results have been monitored in areas of primary crystallization.

REFERENCES

26-1. Wilcox, William R.; Yee, James F.; Sen, Sanghamitra; Samra, Kalluri; and Lin, Mu-Ching: Directional Solidification of InSb-GaSb Alloys. Proceedings of the Third Space Processing Symposium - Skylab Results. NASA TM X-70252, 1974, pp. 301-373.

26-2. Reger, J. L.: Experiment No. M-557 Immiscible Alloy Compositions. Proceedings of the Third Space Processing Symposium - Skylab Results. NASA TM X-70252, 1974, pp. 133-158.

26-3. Hasemeyer, Earl A.; Lovoy, Charles V.; and Lacy, L. L.: Skylab Experiment M566 Copper-Aluminum Eutectic. Proceedings of the Third Space Processing Symposium - Skylab Results. NASA TM X-70252, 1974, pp. 457-461.

26-4. Yue, A. S.; and Yu, J. G.: Halide Eutectic Growth. Proceedings of the Third Space Processing Symposium - Skylab Results. NASA TM X-70252, 1974, pp. 469-489.

26-5. Witt, A. F.; Gatos, H. C.; Lichtensteiger, M.; Lavine, M. C.; and Herman, C. J.: Steady State Growth and Segregation Under Zero Gravity: InSb. Proceedings of the Third Space Processing Symposium - Skylab Results. NASA TM X-70252, 1974, pp. 275-288.

26-6. Walter, H. U.: Seeded, Containerless Solidification of Indium Antimonide. Proceedings of the Third Space Processing Symposium - Skylab Results. NASA TM X-70252, 1974, pp. 257-265.

26-7. Clodfelter, Robert G.; and Lewis, Roger C.: Fluid Studies in a Zero Gravity Environment. Technical Note 61-84, Wright-Patterson A.F.B., June 1961.

26-8. Clodfelter, Robert G.: Fluid Mechanics and Tankage Design for Low Gravity Environments. ASD-TDR-63-506, Wright-Patterson A.F.B., Sept. 1963.

26-9. Clodfelter, Robert Glen: Low Gravity Pool Boiling Heat Transfer. APL-TDR-64-19, Wright-Patterson A.F.B., Mar. 1964.

26-10. Chalmers, Bruce: Principles of Solidification. John Wiley and Sons, 1964.

26-11. Flemings, Merton C.: Solidification Processing. McGraw-Hill, 1974.

26-12. Hurle, D. T. J.: Mechanisms of Growth of Metal Single Crystals From the Melt. Pergamon Press, 1962.

26-13. Vezzoli, Gary C.: Electrical Resistance of Liquid Sulfur to 420° C and of Liquid Selenium to 700° C. American Ceram. Soc. J., vol. 55, no. 2, Feb. 1972, pp. 65-67.

TABLE 26-I.- PROTOTYPE TEST THERMAL DATA

Thermocouple	Temperature, K (°C)		
	Data set 1	Data set 2	Data set 3
AT-1	873 (600)	1092 (819)	1328 (1055)
AT-2	869 (596)	1088 (815)	1322 (1049)
AT-3	788 (515)	962 (689)	1152 (879)
AT-4	543 (270)	610 (337)	678 (405)
Heat leveler	909 (636)	1126 (853)	1362 (1089)

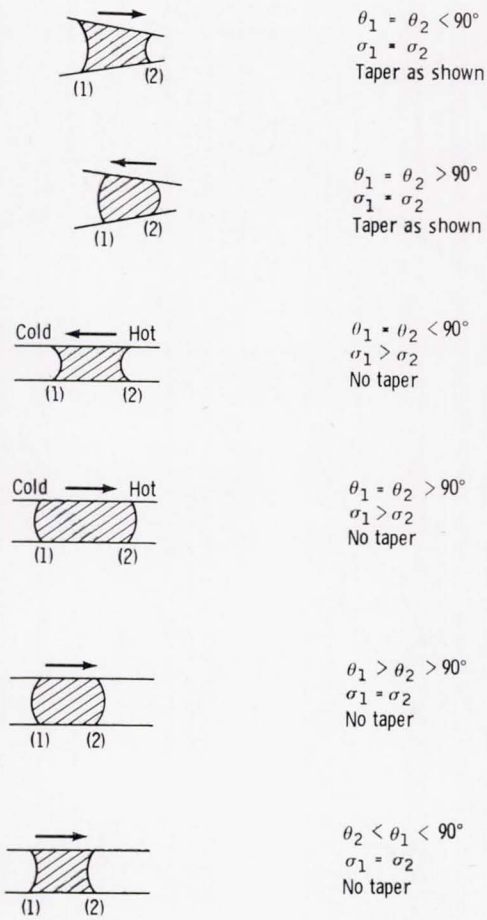

Figure 26-1.- Results on fluid displacement in the reduced gravity environment where σ is surface tension.

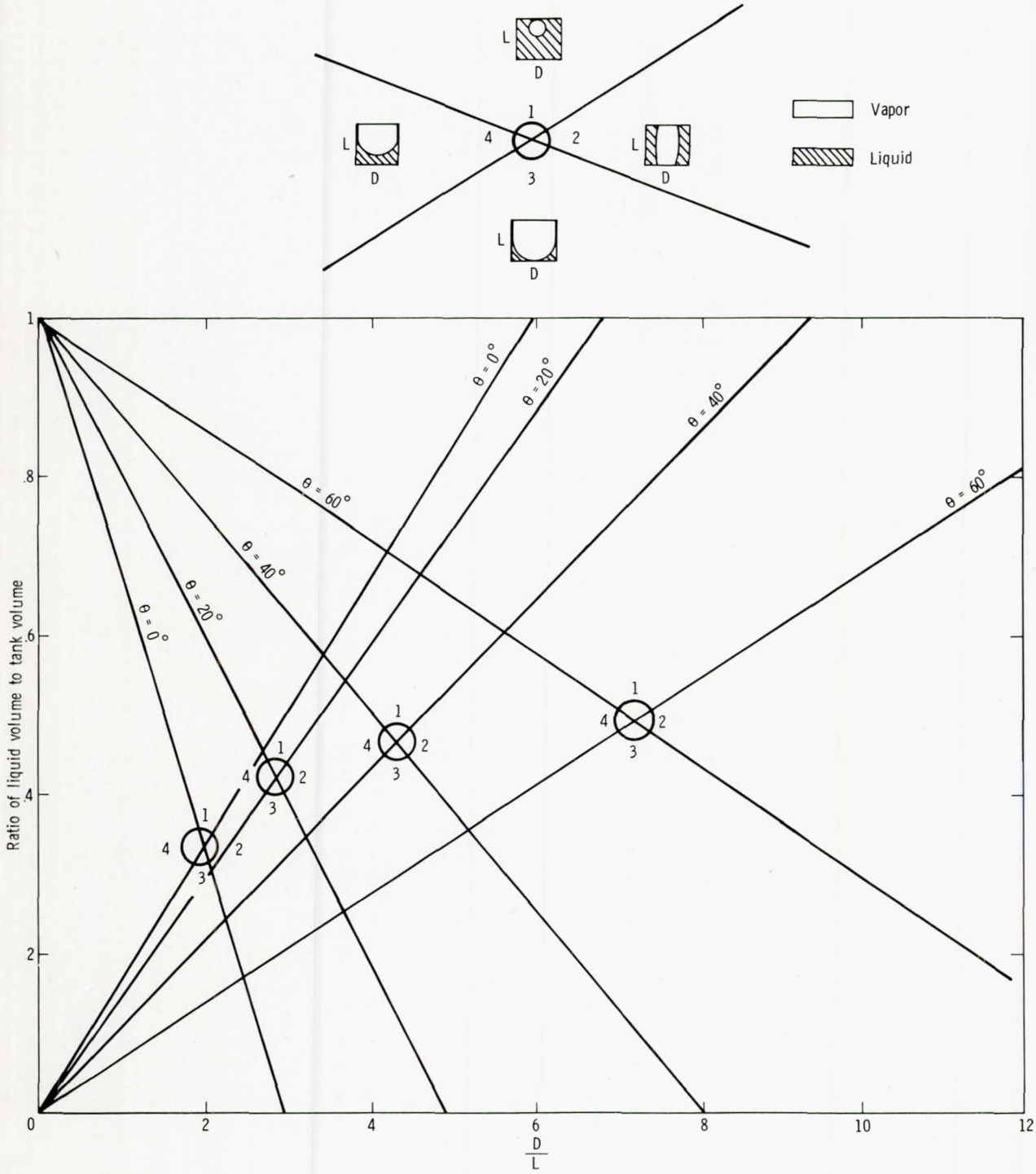

Figure 26-2.- Wetting fluid configurations in a cylindrical tank.

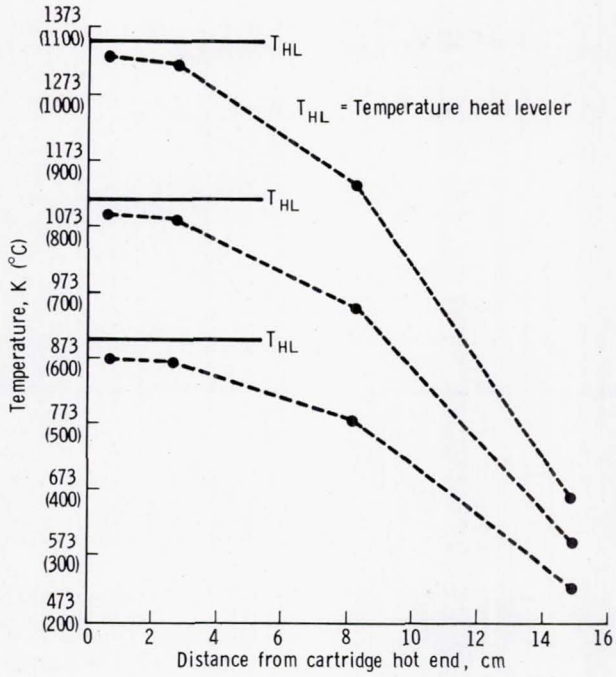

Figure 26-3.- Thermal profile of the furnace at the three stages of the prototype test.

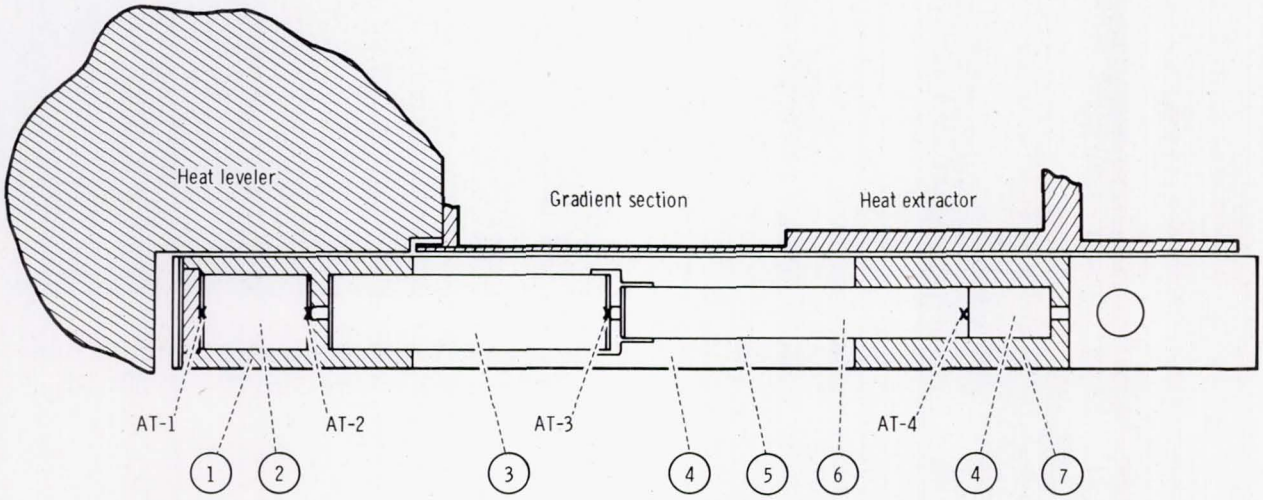

1. Thermal insert, ZTA graphite
2. Ampoule 1
3. Ampoule 2
4. Insulation
5. Support tube, 321 stainless steel
6. Ampoule 3
7. Thermal insert, ZTA graphite

Figure 26-4.- Experiment cartridge.

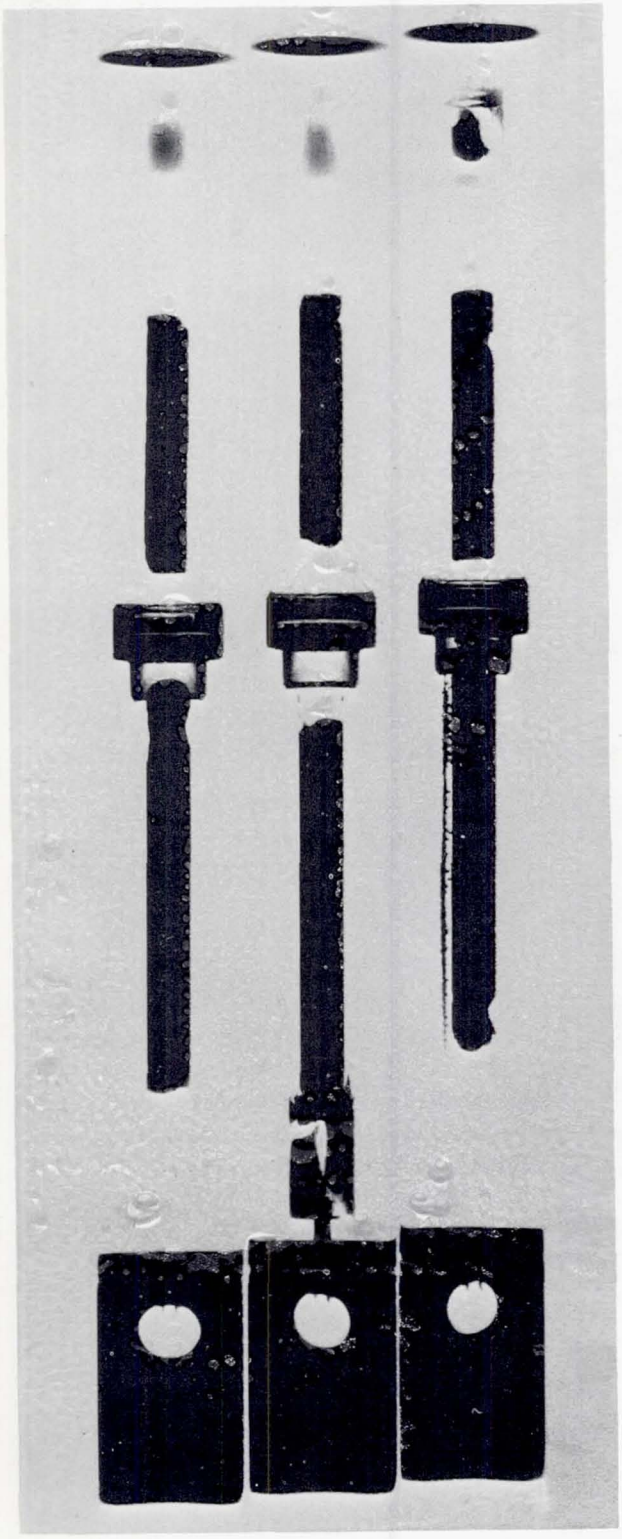

Figure 26-5.- X-ray radiograph of the three flight cartridges (1X).

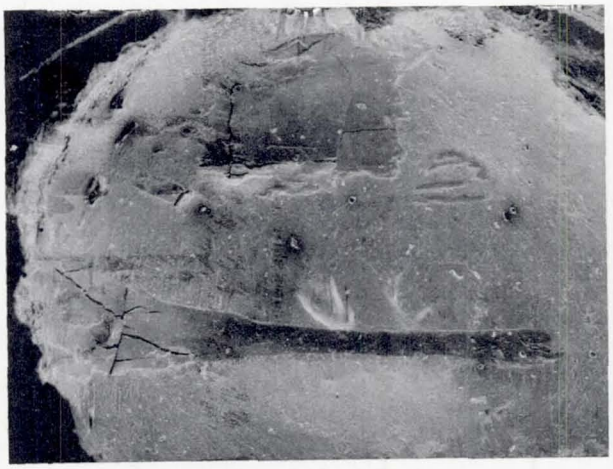

Figure 26-6.- Large pore formed by flow of the wetting fluid over all inner surfaces of the ampoule (120X).

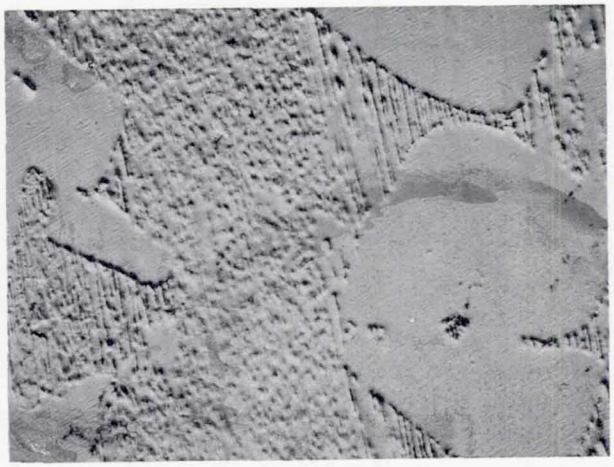

Figure 26-7.- Proeutectic bismuth dendrites and interdendritic Bi-MnBi eutectic (40X).

Figure 26-8.- Transition from dendritic to coordinated growth (75X).

27. CRYSTAL GROWTH FROM THE VAPOR PHASE

EXPERIMENT MA-085

H. Wiedemeier,[a†] H. Sadeek,[a] F. C. Klaessig,[a] and M. Norek[a]

ABSTRACT

Three vapor transport experiments on multicomponent systems were performed during the Apollo-Soyuz mission to determine the effects of microgravity forces on crystal morphology and mass transport rates. The mixed systems using germanium selenide, tellurium, germanium tetraiodide (transport agent), germanium monosulfide, germanium tetrachloride (transport agent), and argon (inert atmosphere) were

1. System A: $GeSe_{0.99}Te_{0.01} - GeI_4$
2. System B: $GeS_{0.98}Se_{0.02} - GeCl_4$
3. System C: $GeS - GeCl_4 - Ar$

The materials were enclosed in evacuated sealed ampoules of fused silica and were transported in a temperature gradient of the multipurpose electric furnace onboard the Apollo-Soyuz spacecraft.

The preliminary evaluation of systems A and B shows improved quality of the space-grown crystals in terms of growth morphology and bulk perfection. This conclusion is based on a direct comparison of space-grown and ground-based (prototype) crystals by means of X-ray diffraction, microscopic, and chemical etching techniques. The observation of greater mass transport rates than predicted for a microgravity environment by existing vapor transport models indicates the existence of non-gravity-caused transport effects in a reactive solid-gas phase system. Present results are in close agreement with those of a similar Skylab experiment and extend the findings to mixed systems and different experimental conditions. The completed analysis of the Apollo-Soyuz Test Project crystal growth by vapor transport experiment, in combination with the Skylab results, will yield a conclusive interpretation of the crystal growth and transport phenomena under microgravity conditions for a series of technologically useful materials.

---

[a]Rensselaer Polytechnic Institute.

[†]Principal Investigator.

INTRODUCTION

Crystal growth by chemical vapor transport is of technological importance for the production of bulk- and layer-type single crystalline materials used in various electronic devices. That the performance characteristics of electronic materials are critically dependent on the degree of chemical homogeneity and crystalline perfection is well known. These properties are affected by the transport and growth conditions of a given chemical system. Complete control of these growth parameters under ground-based conditions is limited because of the presence of gravity-driven convection. Under otherwise optimum growth conditions on Earth, convective interference with the transport process causes crystalline imperfections.

Crystal growth in a microgravity environment without convective interference should produce crystals of improved quality and yield fundamental data for the vapor transport process. These expectations were confirmed by the results of Skylab Experiment M556 (Vapor Growth of IV-VI Compounds). In the Skylab experiment (ref. 27-1), representative compounds of Group IV-VI materials, germanium selenide (GeSe) and germanium telluride (GeTe), were transported with germanium tetraiodide (GeI_4) as a transport agent. The single crystals grown in space are of considerably improved structural perfection compared to corresponding ground-based specimens. The second major result of the Skylab studies is the observation of greater mass transport rates in a microgravity environment than predicted for a diffusion-controlled transport process. Because of the far-reaching scientific and technological implications of these two observations, the Skylab results served as a basis for the definition of the Apollo-Soyuz Test Project (ASTP) experiments. The primary objectives of the ASTP crystal growth by vapor transport experiment were to extend and generalize microgravity crystal growth for a class of compounds and to characterize the unexpected gas motion observed during Skylab missions. Hence, new compounds and doped materials were transported with different transport agents in higher temperature gradients. Also, an inert atmosphere was used in one of the transport ampoules. Details of the experimental design and chemical systems are discussed as follows.

This report is based on the preliminary analysis of two of the three vapor transport experiments performed in space. Present data reveal improved crystalline perfection for the space-grown material compared to ground-based samples. These results confirm the Skylab observations and extend the conclusions drawn to more complex systems. In addition, the present evaluation of mass transport rates for two systems shows considerably greater mass fluxes than predicted by theory. The latter result not only confirms Skylab data, but could provide evidence for determining the cause of the higher than predicted transport rates.

Because of the technological importance of single crystals for solid-state devices and because of their high yield-to-weight ratio, crystal growth by vapor transport is a primary candidate for space-processing applications. Therefore, the long-range goal of microgravity transport studies is to provide the scientific and technical basis for actual space manufacturing. In addition, the knowledge gained from these experiments will be of practical use for the improvement of crystal growth techniques on Earth.

GROUND-BASED STUDIES

Basic Theory

In a chemical transport reaction (ref. 27-2), a gaseous (g) transport agent B(g) reacts at a given temperature with the solid (s) source material A(s) to form exclusively gaseous products C(g). This process is represented by the following reaction.

$$x\,A(s) + y\,B(g) = z\,C(g) + ---- \qquad (27\text{-}1)$$

The number of different gaseous products formed depends on the particular chemical system. The vapor species migrate in the reaction vessel from the source to the condensation region, where, at a different temperature, the reverse reaction occurs with formation of the solid. The necessary concentration gradient is established by means of a temperature gradient, which yields different equilibrium constants for the reaction of equation (27-1) and, thus, yields different partial pressures of the gaseous species in the source and condensation zones of the system. According to equation (27-1), the solid A is transported by way of the gas phase through a chemical reaction; this method is distinctly different from transport by sublimation. Under optimal experimental conditions, well-defined single crystals of the source material are obtained by the condensation reaction. Depending on the thermodynamic properties of the transport reaction, a chemical transport can occur from high to low temperature or from low to high temperature. This aspect is of practical importance with respect to the choice of transport agent and condensation temperature. The transport reaction is performed in evacuated, sealed ampoules of fused silica that are conventionally subjected to the desired temperature gradient in a horizontal, two-zone, tubular resistance furnace.

The migration of gas phase species can be described by diffusion and by gravity-driven convection. In a gravitational field and temperature gradient, both transport modes occur simultaneously. It is a unique feature of the vapor transport technique to select experimental conditions so that one or the other mode can be predominant. Under ground-based conditions, the convective contribution to the overall transport process can be minimized but not eliminated. Based on present models for diffusive and convective gas motion (ref. 27-2), the material flux from the source to the condensation region is affected by the pressure in the transport ampoule. At very low pressures of the transport agent, the mass transport rate is controlled by the rate of the heterogeneous solid-gas phase reaction in the source or the condensation region, or both. Under these conditions, the material flux is proportional to the concentration of the transport agent. At medium pressures, the transport rate is inversely proportional to the total pressure. In this range, the overall transport is diffusion controlled. At higher pressures, the material flux increases with increasing total pressure and thus indicates the predominance of the convective transport mode. For the conditions of the diffusion- and convection-controlled transport modes, the heterogeneous solid-gas phase reactions in the source and condensation zones occur rapidly.

Transport Properties of Group IV-VI Compounds

Mass transport rate studies on GeTe (ref. 27-3) and GeSe (ref. 27-4) confirmed the previously described models. Details of the experimental procedures and results have been discussed previously (refs. 27-3 and 27-4). The most important observation of these studies is the decrease in crystal perfection with increasing contribution of the convective component to the overall transport process. Transport studies in the Rensselaer Polytechnic Institute (RPI) laboratory on germanium monosulfide (GeS) using germanium tetrachloride ($GeCl_4$) as a transport agent and different temperature gradients show the diffusion- and convection-controlled transport regimes in agreement with those of the previous systems (refs. 27-3 and 27-4). In particular, the changes in crystal morphology and habit of GeS as a function of transport mode reveal the negative effects of convective interference on crystal quality. The previous ground-based studies and the solution properties of solids used in these binary systems led to the definition of mixed systems for two of the three transport experiments performed during the ASTP mission and discussed in this report. (The third transport ampoule contained GeS and a mixture of $GeCl_4$ and argon (Ar)). The chemical composition of the mixed systems is given by the formulas $GeSe_{0.99}Te_{0.01}$ (system A) and $GeS_{0.98}Se_{0.02}$ (system B), respectively. In the RPI laboratory, quantitative mass transport rate studies in terms of flux as a function of pressure were performed on these systems in the temperature gradient of approximately 873 → 773 K (600° → 500° C). The transport agents used were GeI_4 for system A and $GeCl_4$ for system B. The flux is calculated from the quantity of crystals recovered, the cross section of the ampoule, and the duration of the experiment. The pressure is computed for the mean temperature from the amount of transport agent added, assuming ideal conditions and use of $GeI_4(g)$ or $GeCl_4(g)$, respectively. The results are illustrated in figure 27-1, together with those for the system GeS - $GeCl_4$ (C). The flux curves of all three systems have the same shape as those observed earlier (ref. 27-4). The diffusion-controlled region at lower pressures shows a decrease in flux with increasing pressure. The range of predominantly convective transport is characterized by an increase in flux with increasing pressure. The leveling of the flux curve for system A at higher pressures is due to the precipitation of the transport agent and the resultant establishment of a constant saturation pressure in the ampoule. The flux curves in figure 27-1, determined in the RPI laboratory, serve as a basis for the evaluation of the space experiments. For the direct comparison of mass transport rates and crystals obtained on Earth and in space, a set of three ampoules containing the same amounts of starting materials and transport agent as the corresponding ampoules used on the ASTP mission was processed in the prototype furnace. This furnace and the prototype transport conditions were identical to the furnace and conditions used in space, except for gravity.

EXPERIMENTAL ASTP PROCEDURES

Apparatus

The transport experiments were performed in the multipurpose electric furnace, which consisted essentially of a cylindrical furnace chamber and an instrumentation compartment. The furnace chamber contained three tubular reaction cavities for the individual metal cartridges and quartz ampoules discussed subsequently. Because the furnace was heated resistively in one zone at the source region, the desired temperature gradient and stability were achieved by heat shields surrounding the quartz ampoules in the metal cartridges and by appropriate heat shields in the furnace. The temperature gradient employed for these experiments in space was 877 → 780 K (604° → 507° C) with a shallow gradient in the hot zone and a nearly linear gradient between the hot and cold zones of the reaction chamber. During the performance of the transport experiments, the furnace temperatures were constantly monitored at the outside of the metal cartridges in the hot and cold zones. The relationship between furnace and actual ampoule temperatures was calibrated under identical ground-based conditions by using thermocouples.

Ampoule and Sample Preparation

The transport ampoules were made of fused silica tubing of 13.7 millimeters inside diameter and 150 millimeters length. Near the rounded end, the ampoules contained two thin silica rods to hold the source material in place. The other ampoule end was sealed after loading at a pressure of 0.1333 mN/m^2 (10^{-6} torr) or less. Before loading, the cleaned ampoules (refs. 27-3 and 27-4) were outgassed at a temperature of approximately 1273 K (1000° C) and a pressure of 0.1333 mN/m^2 (10^{-6} torr) for 10 hours. The polycrystalline starting materials were synthesized by the repeated annealing at approximately 873 K (600° C) of stoichiometric mixtures of the binary compounds GeS, GeSe, and GeTe. The compounds were prepared from high-purity elements (99.999 percent) by annealing and subsequent sublimation of the product (refs. 27-3 and 27-4). The crystallographic identity of all materials was established by means of X-ray diffraction techniques. High-purity GeI_4 (99.999 percent) and $GeCl_4$ (99.999 percent) were used as transport agents. Ultra-high-purity Ar was employed as inert gas in one system. The ampoule designated as 3A in this experiment contained 1.50 grams of $GeSe_{0.99}Te_{0.01}$ and 123.5 milligrams of GeI_4. Ampoule 3B was loaded with 1.50 grams of $GeS_{0.98}Se_{0.02}$ and 59.1 milligrams of $GeCl_4$. The third ampoule (3C) contained 1.50 grams of GeS, 61.8 milligrams of $GeCl_4$, and 193.53 kN/m^2 (1.91 atmospheres) of Ar at the mean temperature of the gradient. The ampoules used for the ground-based prototype tests (2A, 2B, and

2C) were of the same dimensions and contents. The chemical transport reactions for the binary compounds are shown in the following equations.

$$GeSe(s) + GeI_4(g) = 2\ GeI_2(g) + 0.5\ Se_2(g) \tag{27-2}$$

$$GeTe(s) + GeI_4(g) = 2\ GeI_2(g) + 0.5\ Te_2(g) \tag{27-3}$$

$$GeS(s) + GeCl_4(g) = 2\ GeCl_2(g) + 0.5\ S_2(g) \tag{27-4}$$

The experimental conditions for the ASTP mission are summarized as follows for a temperature gradient of 877 → 780 K (604° → 507° C).

$GeSe_{0.99}Te_{0.01}$ (3A)	$P(GeI_4(g))$	$= 70.93\ kN/m^2$ (0.70 atm)
$GeS_{0.98}Se_{0.02}$ (3B)	$P(GeCl_4(g))$	$= 95.25\ kN/m^2$ (0.94 atm)
GeS (3C)	$P(GeCl_4(g))$	$= 97.27\ kN/m^2$ (0.96 atm)
	$P(Ar)$	$= 193.53\ kN/m^2$ (1.91 atm)

where P indicates component gas pressure. The transport reactions of the mixed systems are analogous. The total pressures in terms of $GeI_4(g)$ or $GeCl_4(g)$ are calculated for the mean temperature of the gradient and for ideal gas conditions.

Heating Cycle and Return of Ampoules

The transport ampoules were enclosed in metal cartridges, which were inserted into the multipurpose furnace by the astronauts. After a heatup period of approximately 2 hours, the desired temperature gradient was achieved and maintained for 16 hours. Following termination of the experiment, cooling of the cartridges to ambient temperatures occurred over a period of approximately 4 hours, during which a helium quench was used.

Examination of the opened cartridges at the NASA George C. Marshall Space Flight Center revealed that none of the ampoules had any mechanical damage and that the source material in all the ampoules was firmly attached to the ampoule wall in the source region. The ampoules were brought to the RPI laboratory for analysis. An opened cartridge and a prototype ampoule (2A) are shown in figure 27-2. The residual source material is at the left end of the ampoule; the onset of crystallization and the deposition zone extend to the right end of the ampoule. The ampoule fit

into the upper section of the cartridge, which was inserted into the lower part of the cartridge and sealed at the right edge of the wider section (left part) of the upper cartridge.

RESULTS AND DISCUSSION

The preliminary evaluation of two transport experiments performed on the ASTP mission is based on X-ray diffraction analyses, flux measurements, and microscopic and chemical etching techniques. Present results are summarized as follows.

Crystallographic Identification of Transport Products

The crystallographic identification of space-grown crystals was established by means of Debye-Scherrer and Laue X-ray diffraction techniques. For the Debye-Scherrer method, randomly selected crystals were finely powdered, sealed in thin-walled glass capillaries, and exposed to copper (Cu) Kα radiation in a 114.59-millimeter-diameter camera. For the Laue method, individual single-crystal platelets were mounted on the crystal holder of a conventional Laue camera and exposed to Cu Kα radiation. The results in terms of lattice parameters (Debye-Scherrer) and crystallographic orientation of as-grown predominant faces (Laue) are summarized in table 27-I together with corresponding data for ground-based crystals.

A comparison of the data in table 27-I shows that the lattice constants of the respective systems are in excellent agreement. There is no change in the orientation of predominant native faces of single crystals. Within the detection limits of X-ray diffraction techniques, there is no measurable effect of microgravity forces on the crystallographic parameters of space-grown crystals. These results are expected in view of the relative magnitude of chemical bonding and gravitational forces.

Transmission Laue photographs of $GeS_{0.98}Se_{0.02}$ ground (2B) and space (3B) crystals revealed major differences, as illustrated in figure 27-3. The diffraction pattern of the ground-based crystal (fig. 27-3(a)) shows considerable strain and multiplicity of individual diffraction spots, an indication of distortion and structural inhomogeneities of the ground specimens. The diffraction pattern of the space crystal (fig. 27-3(b)) clearly reveals the twofold symmetry of the predominant (001)-oriented growth face. The considerably better defined diffraction spots indicate a higher degree of crystallographic perfection compared to the ground-based sample. These differences in crystallinity are observed for most samples that have been investigated. Similar observations are made for ground (2A) and space (3A) crystals of the $GeSe_{0.99}Te_{0.01}$ system. The combined results of the present diffraction studies demonstrate the improved structural homogeneity of the crystals obtained in a microgravity environment.

Mass Transport Rates

The determination of the mass transport rates observed in a microgravity environment is based on the mass of the transported crystals and on the mass loss of the source materials. The same procedures were applied to determine the flux of the ground-based (prototype) systems. The experimental uncertainties connected with the recovery of crystals and the separation of crystals from the transport agent were combined to yield lower values for the mass flux observed under microgravity conditions. The extrapolated values are based on a graphical extrapolation of the diffusion-controlled region of the respective ground-based experimental flux curves shown in figure 27-1. Therefore, selected data on flux as a function of pressure were plotted in double logarithmic scales. The resulting straight line was extended to the flux that corresponded to the pressure employed in the space experiment. The data of the diffusion-controlled region used for the extrapolation were selected to obtain upper values for the predicted fluxes. The extrapolation is based on the assumption that vapor transport in a microgravity environment is by gas phase diffusion. The numerical results are listed in table 27-II.

A comparison of these data reveals a rather significant result. For system A, the flux observed in a microgravity environment is lower than that observed under ground-based (prototype) conditions, but is approximately three times greater than predicted for a diffusion-limited transport. For system B, the ground-based flux and the microgravity flux are apparently the same, but the latter is approximately three times higher than the transport rate predicted by theory. In view of the previously discussed evaluation procedures, the discrepancy between observed and predicted microgravity fluxes is outside error limits. Despite the differences in experimental conditions between the ASTP and Skylab missions, the observed trends for the mass transport rates in a microgravity environment are in perfect agreement for both missions.

The consistency of the flux data (ASTP and Skylab) obtained for different chemical systems with two transport agents, seven pressures, and three temperature gradients strongly supports the validity of these observations. The combined results suggest the existence of non-gravity-caused transport effects in a microgravity environment. These unexpected phenomena could be related to thermochemical effects of gas phase reactions; these effects have not been considered in existing vapor transport models. A further interpretation of the combined data will be attempted after completion of the current evaluation. However, it is justifiable to conclude that the transport phenomena observed on the ASTP and Skylab missions are of scientific and technological significance. Furthermore, clarification of these observations is of great practical importance for space-processing applications.

Morphological Characterization of Crystals

Optical photomicrographs of representative $GeSe_{0.99}Te_{0.01}$ (A) ground (prototype) and space crystals show qualitative differences in surface morphology as illustrated in figure 27-4. Most of the prototype crystals (fig. 27-4(a)) reveal ragged edges, intergrowth, and stepped surfaces. The space crystals (fig. 27-4(b)) have smoother surfaces and, in general, have better defined edges. The average dimensions of the ground specimens range from approximately 2 to 8 millimeters in

edge length. The slightly smaller sizes of the space material are in agreement with the lower microgravity transport rates observed for this system (table 27-II).

The deposition patterns of transport agent GeI_4 on the system A ampoule walls, shown in figure 27-5, differ significantly. The transport agent in the space ampoule (fig. 27-5(a)) has condensed in the form of well-developed, transparent single-crystal platelets and a few needles. The GeI_4 deposition in the ground-based ampoule (fig. 27-5(b)) consists of dendritic material with a distinct curvature of individual dendrites that are as long as approximately 8 millimeters. The absence of any distinct curvature in the deposition pattern of the space ampoule (fig. 27-5(a)) reflects the more homogeneous gas motion in a microgravity environment.

Optical photomicrographs of representative $GeS_{0.98}Se_{0.02}$ (B) ground (prototype) and space crystals in figure 27-6 reveal distinct morphological differences. The prototype crystals (fig. 27-6(a)) show considerable aggregation, undefined edges, and rough surfaces. The distinct morphological improvement in terms of surfaces and edges of the space crystals is apparent from figure 27-6(b). The average dimensions of the space material range from approximately 1 to 7 millimeters in edge length. Because the transport rates for system B (table 27-II) are the same under both ground and space conditions, the external morphological differences reflect the absence of convective interference in a microgravity environment.

To investigate the effects of microgravity forces on crystalline perfection for the bulk of the material, internal faces of ground and space crystals were examined by means of chemical etching and optical microscopy. For this purpose, crystal platelets were cleaved parallel to the (001) plane.

An optical photomicrograph (200X) of the cleaved face of a ground (prototype) cyrstal of $GeSe_{0.99}Te_{0.01}$ (system A) shows the presence of large cavities in the bulk of the material (fig. 27-7(a)). After chemical etching, the same area of the crystal is covered with etch pits (fig. 27-7(b)). It is interesting to note that the areas which appear to be mirror smooth at this magnification (fig. 27-7(a)) show a high etch-pit density (fig. 27-7(b)). Etch pits along the walls of the main cavity are also clearly visible. The concentration of etch pits indicates the degree of structural or chemical imperfections in the ground-based material. Similar observations were made for the majority of the investigated crystals.

Application of the same cleaving and etching procedures to space-grown crystals of system A yields rather different results, as shown in figure 27-8. The photomicrograph (100X) of the cleaved crystal reveals that most of the space material is structurally very uniform (fig. 27-8(a)). The photomicrograph (200X) of a cleaved space crystal platelet after etching (fig. 27-8(b)) shows very few etch pits and thus indicates a high degree of microhomogeneity. The striation pattern of both crystals, showing (001) planes of different depth with respect to the native surface, is due to cleavage. (The edge damage was caused by handling.)

Similar differences in cleavage and etch patterns were observed for ground-based (prototype) and space-grown $GeS_{0.98}Se_{0.02}$ (B) crystals as shown in figures 27-9 and 27-10. Elongated channels and irregular cleavage of the ground crystal (fig. 27-9(a), 100X) indicate nearly macroscopic crystallographic imperfections for the bulk of the material. Chemical etching of the same crystal (fig. 27-9(b)) reveals additional random imperfections in other areas of the cleaved face. This is contrasted by optical photomicrographs (100X) of the native, cleaved, and etched (001) face of a space-grown crystal platelet (B) in figure 27-10. The spotty appearance of the native surface (fig. 27-10(a)) is due to condensation of residual gas phase on the crystal during the cooldown period of the ASTP furnace. The cleaved face (fig. 27-10(b)) reveals a high degree of structural quality for the bulk of the space material. The line pattern is due to cleavage and marks the border of a series of (001) planes of different depth relative to the native surface. Except for an isolated area in the lower left corner of the same crystal platelet (fig. 27-10(c)), the space crystal is practically unaffected by chemical etching, an indication of considerably improved structural and chemical microhomogeneity of the crystal relative to the corresponding ground-based material.

The previously described differences after cleaving and etching were observed for the majority of presently investigated space and ground specimens. The combined morphological observations demonstrate the improved crystallographic quality of the crystals grown in a microgravity environment.

SUMMARY AND CONCLUSIONS

The original objectives of the crystal growth by vapor transport experiment were to investigate the effects of microgravity forces on the morphology of single crystals of mixed systems and to determine the mass transport rates of these systems using the chemical transport technique. Therefore, three vapor transport experiments were performed during the Apollo-Soyuz mission using three chemical compounds, two transport agents, and one inert gas in one common temperature gradient. The preliminary evaluation of two of the three experiments performed during the Apollo-Soyuz mission has yielded positive results. This conclusion is based on a direct comparison of macroscopic crystal habits, optical microscopy, and chemical etching of cleaved crystals obtained under ground-based (prototype) and microgravity conditions. Present data indicate improved structural homogeneity of the space-grown materials. In addition to the crystallographic data, the observation of greater mass transport rates in a microgravity environment than predicted by existing transport models is significant and represents the second important result of this experiment.

Despite the preliminary nature of presently available analysis data, the results are in close agreement with those of the similar Skylab experiment. Considering the experimental differences between the Apollo-Soyuz and Skylab missions in terms of chemical systems, pressures, and temperature gradients, the agreement demonstrates the validity of the combined results. This agreement confirms initial predictions concerning the suitability of the vapor transport technique for the growth of better quality crystals, and the observation of unexpected phenomena in a microgravity environment. Crystals of structurally improved homogeneity have

been produced, and the transport rates in space were rather unexpected. When the analysis of this experiment has been completed, the combined information available from the Apollo-Soyuz and Skylab missions will represent the crystal growth and transport properties in a microgravity environment for a class of technologically useful materials. These results are of scientific and practical significance for future space-processing applications.

REFERENCES

27-1. Wiedemeier, H.; Klaessig, F. C.; Wey, S. J.; and Irene, E. A.: Vapor Growth of GeTe Single Crystals in Micro-Gravity. Proceedings of the Third Space Processing Symposium on Skylab Results, vol. 1, June 1974, pp. 235-256.

27-2. Schaefer, Harald: Chemical Transport Reactions. Academic Press (New York), 1964.

27-3. Wiedemeier, H.; Irene, E. A.; and Chaudhuri, A. K.: Crystal Growth by Vapor Transport of GeSe, $GeSe_2$, and GeTe and Transport Mechanism and Morphology of GeTe. J. Crystal Growth, vol. 13-14, 1972, pp. 393-396.

27-4. Wiedemeier, H.; and Irene, E. A.: The Chemical Transport Rates and Crystal Morphology of GeSe. Z. Anorg. Allgem. Chem., vol. 400, 1973, pp. 59-66.

TABLE 27-I.- CRYSTALLOGRAPHIC PARAMETERS OF GROUND-BASED AND ASTP SPACE-GROWN CRYSTALS

Location	Lattice parameter, nm (Å)			Orientation
	a_o	b_o	c_o	
$GeSe_{0.99}Te_{0.01}$ (A)				
Ground	0.4385 (4.385) ± 0.0008 (0.008)	0.3838 (3.838) ± 0.0007 (0.007)	1.0791 (10.791) ± 0.0019 (0.019)	(001)
Space	.4386 (4.386) ± .0008 (.008)	.3839 (3.839) ± .0007 (.007)	1.0793 (10.793) ± .0020 (.020)	(001)
$GeS_{0.98}Se_{0.02}$ (B)				
Ground	0.4301 (4.301) ± 0.0009 (0.009)	0.3651 (3.651) ± 0.0008 (0.008)	1.0431 (10.431) ± 0.0020 (0.020)	(001)
Space	.4302 (4.302) ± .0012 (.012)	.3652 (3.652) ± .0010 (.010)	1.0432 (10.432) ± .0022 (.022)	(001)

TABLE 27-II.- MASS TRANSPORT RATES UNDER GROUND-BASED AND MICROGRAVITY CONDITIONS

System	Mass flux, $\mu g/(cm^2\ sec)$		
	Condition		Extrapolated diffusion mode
	Normal gravity	Microgravity	
$GeSe_{0.99}Te_{0.01}$ (A)	1.2	≈0.64	≈0.21
$GeS_{0.98}Se_{0.02}$ (B)	2.3	≈2.3	≈0.68

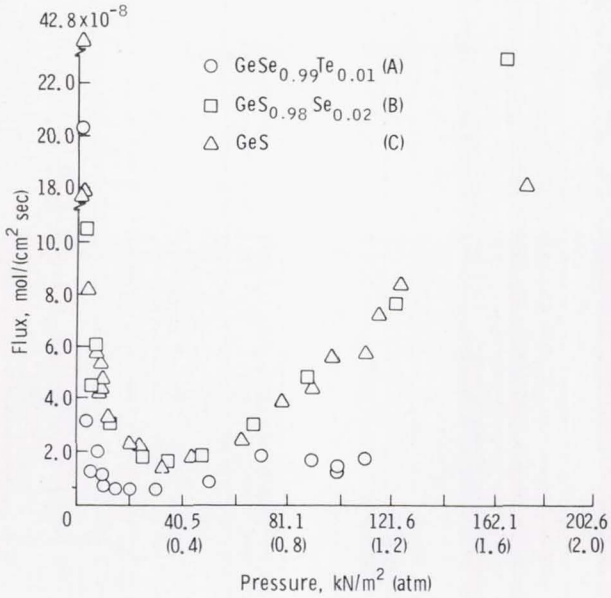

Figure 27-1.- Mass transport rates in terms of flux as a function of pressure for the temperature gradient 873 → 773 K (600° → 500° C) determined under ground-based conditions.

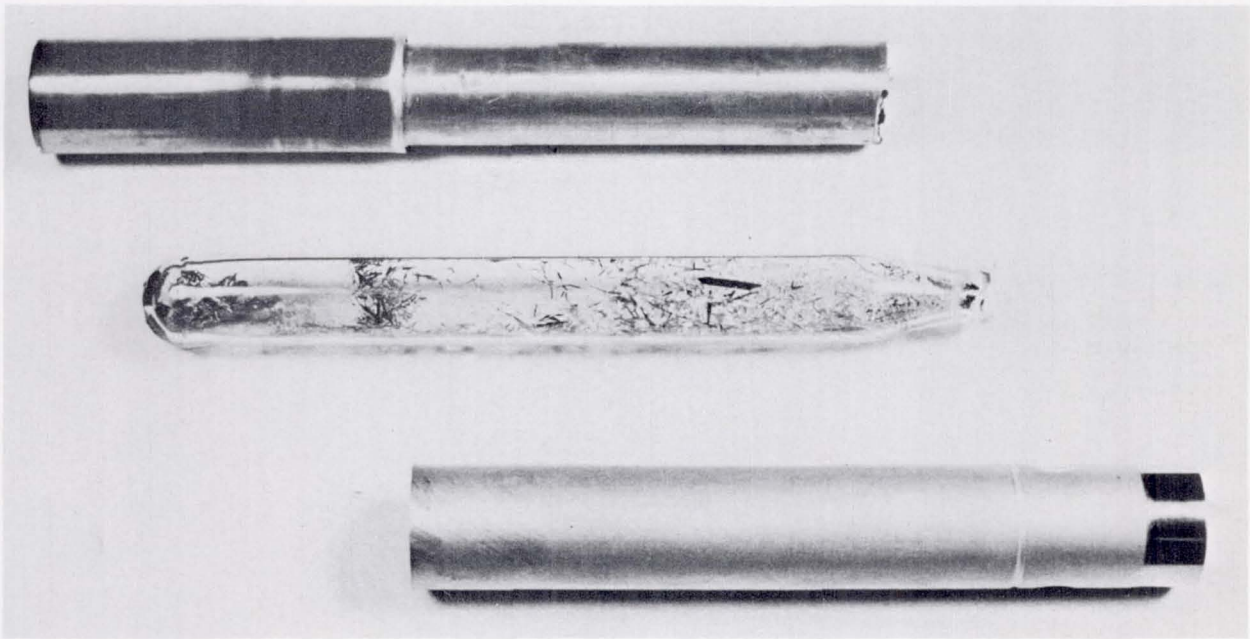

Figure 27-2.- Metal cartridge and ground-based (prototype) transport ampoule (2A).

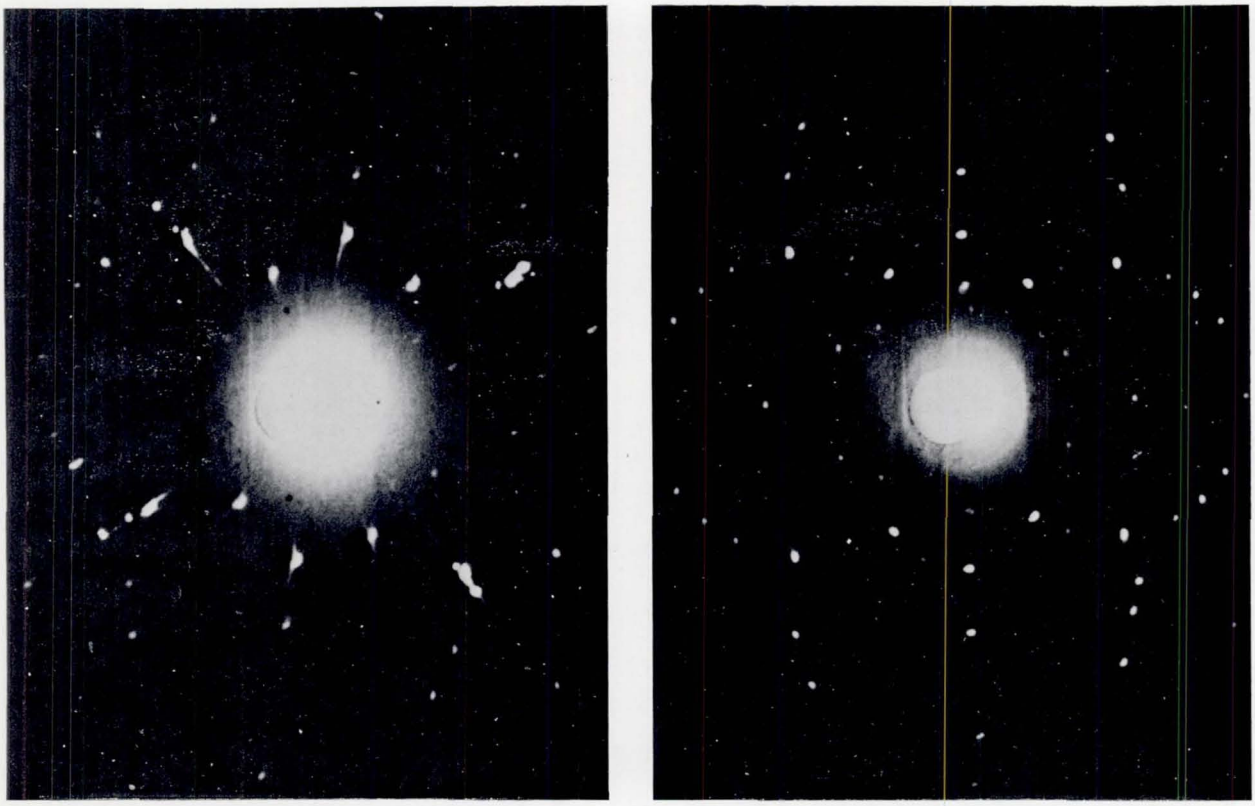

(a) Ground-based (prototype).

(b) Space-grown.

Figure 27-3.- Laue X-ray diffraction transmission photographs of $GeS_{0.98}Se_{0.02}$(B) single-crystal platelets.

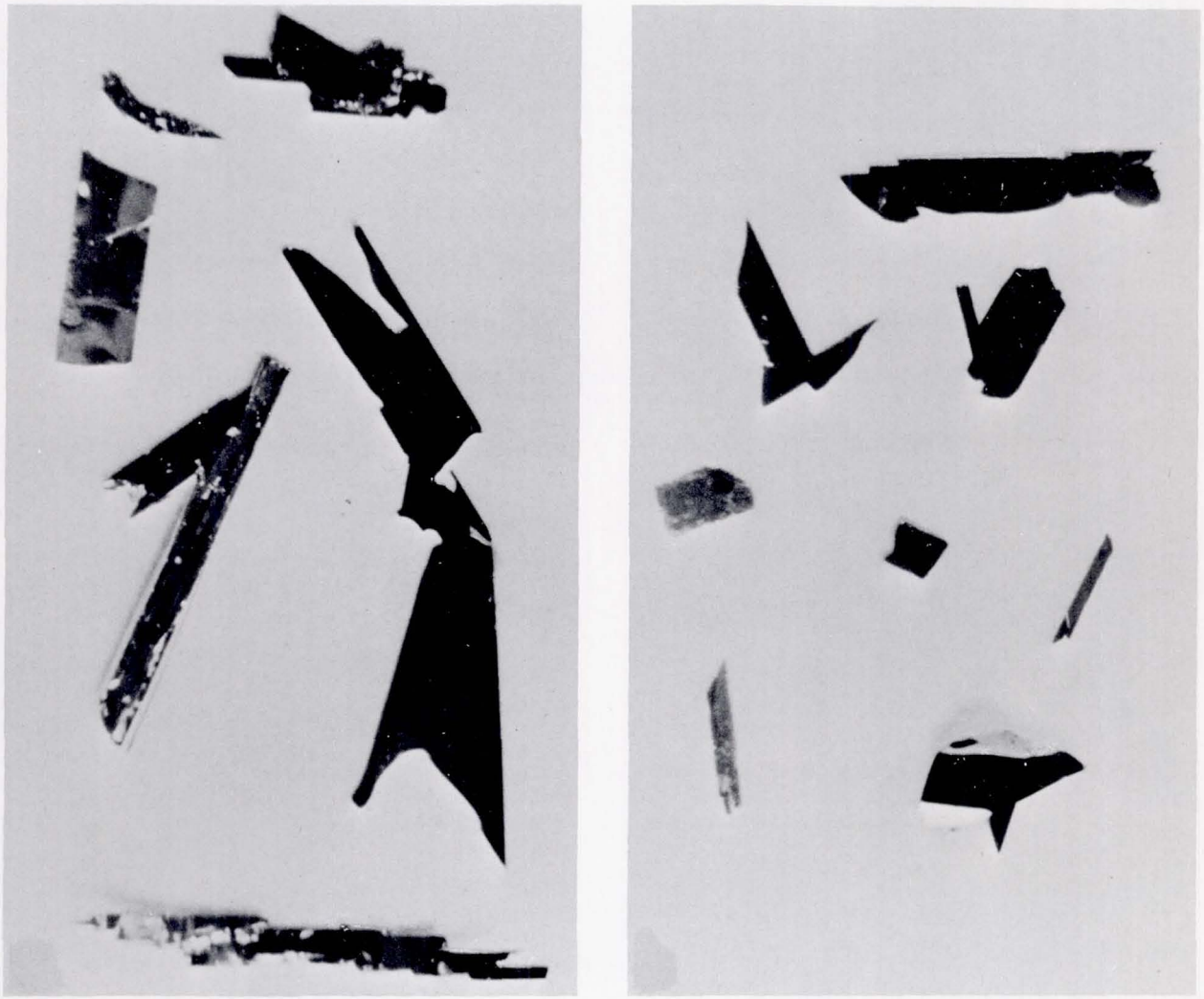

(a) Ground-based (prototype). (b) Space-grown.

Figure 27-4.- Representative crystals of $GeSe_{0.99}Te_{0.01}$ (A).

(a) In microgravity environment.

(b) Under ground-based conditions.

Figure 27-5.- Deposition pattern of transport agent GeI_4 (A) on ampoule walls.

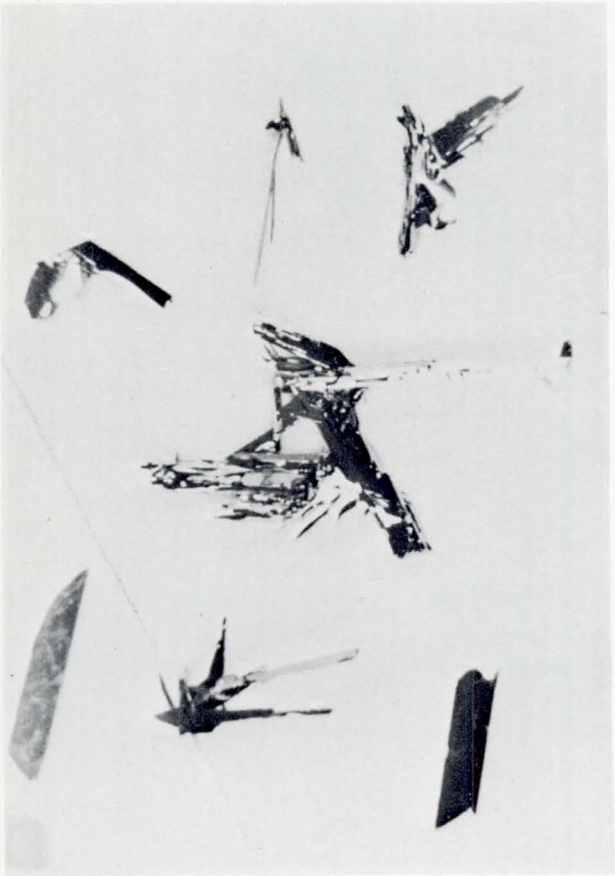

(a) Ground-based (prototype).

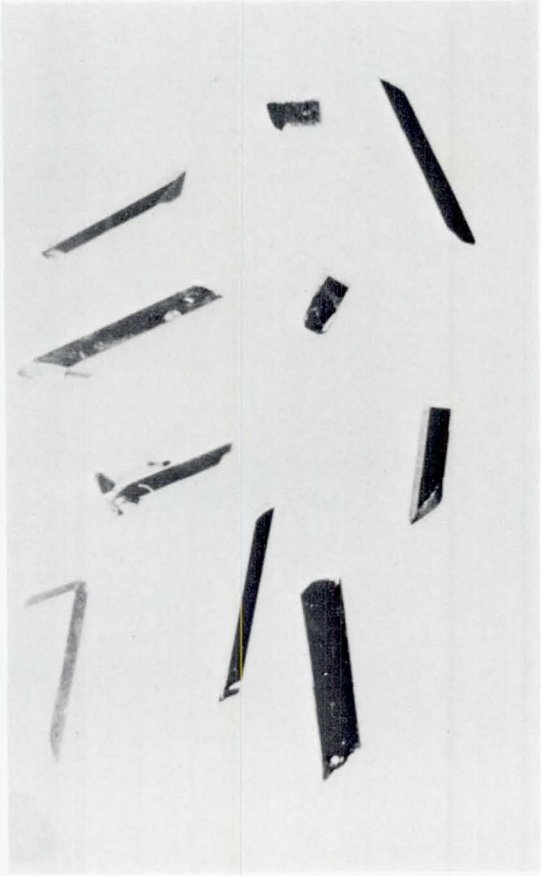

(b) Space-grown.

Figure 27-6.- Representative crystals of $GeS_{0.98}Se_{0.02}$ (B).

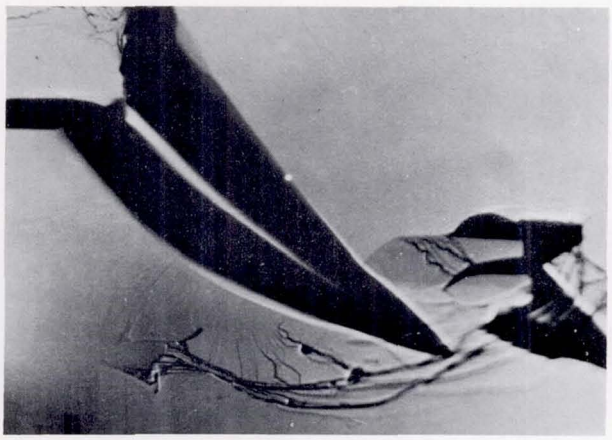

(a) Cleaved.

(b) Cleaved and etched.

Figure 27-7.- Optical photomicrographs of a cleaved and etched (001) face of a ground-based (prototype) $GeSe_{0.99}Te_{0.01}$ (A) crystal platelet.

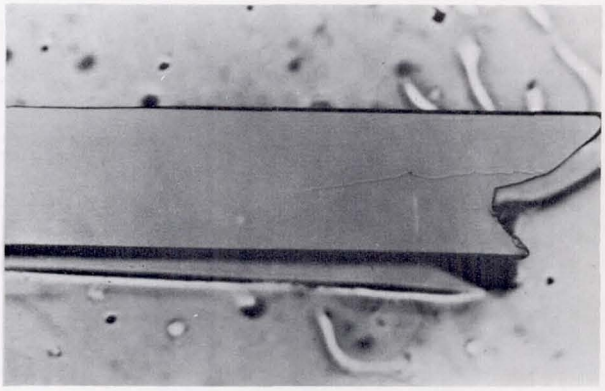

(a) Cleaved.

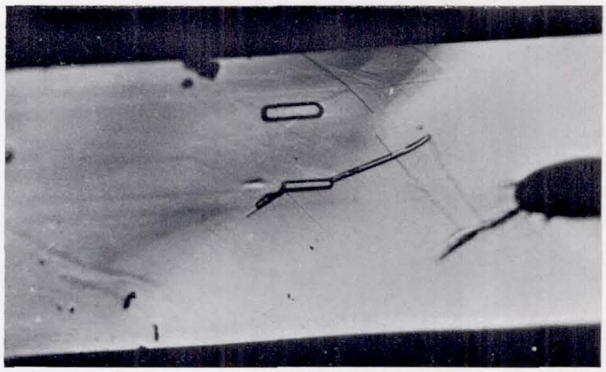

(b) Cleaved and etched.

Figure 27-8.- Optical photomicrographs of cleaved and etched (001) faces of space-grown $GeSe_{0.99}Te_{0.01}$ (A) crystal platelets.

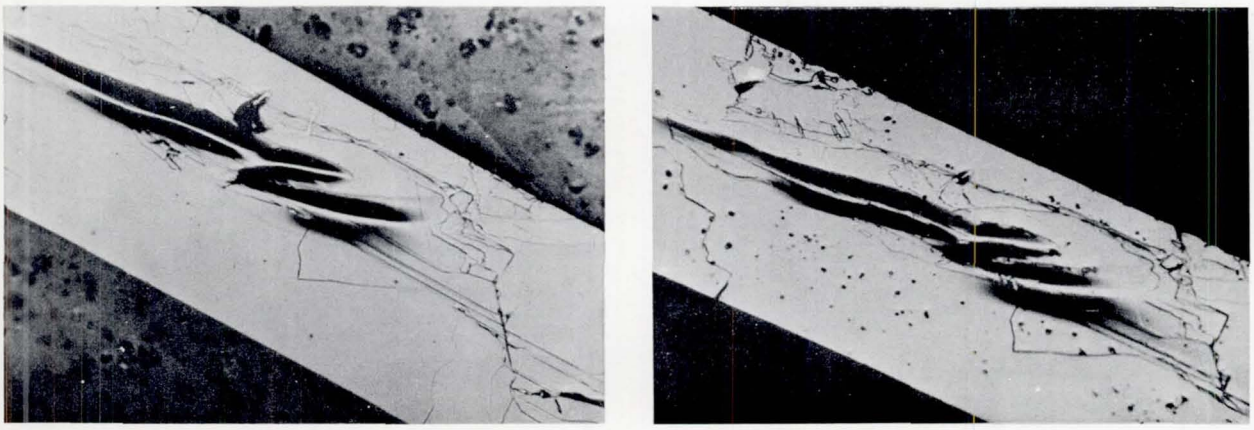

(a) Cleaved. (b) Cleaved and etched.

Figure 27-9.- Optical photomicrographs of a cleaved and etched (001) face of a ground-based (prototype) $GeS_{0.98}Se_{0.02}$ (B) crystal platelet.

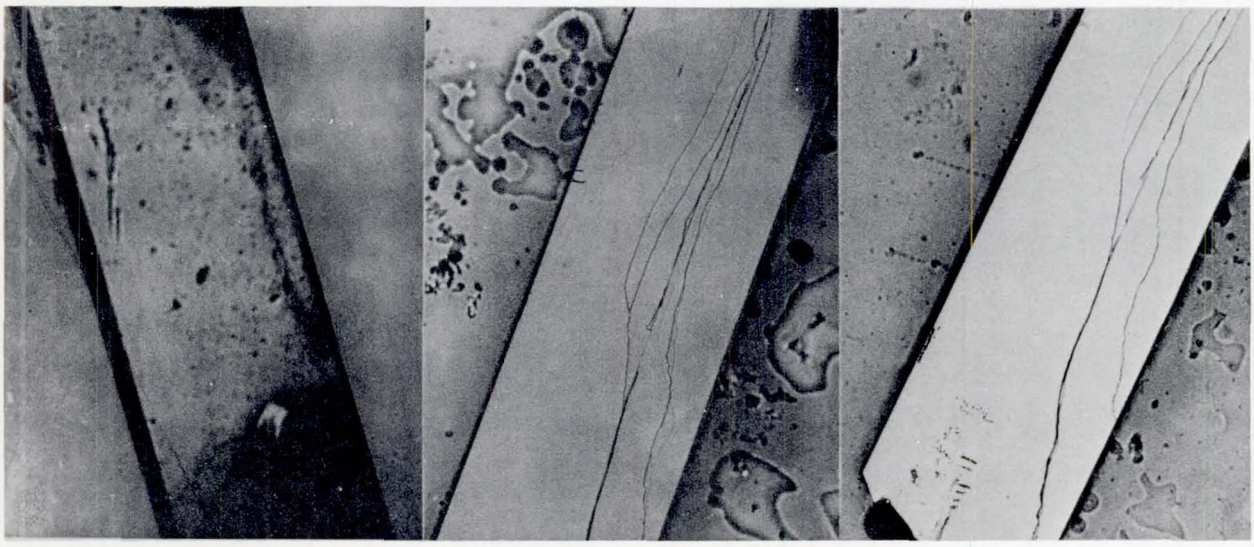

(a) As-grown. (b) Cleaved. (c) Cleaved and etched.

Figure 27-10.- Optical photomicrographs of the as-grown, cleaved, and etched (001) faces of a space-grown $GeS_{0.98}Se_{0.02}$ (B) crystal platelet.

28. HALIDE EUTECTIC GROWTH

EXPERIMENT MA-131

A. S. Yue,[a†] B. K. Yue,[a] and J. Y. M. Lee[a]

ABSTRACT

Fiberlike sodium chloride-lithium fluoride eutectic mixtures have been produced on Earth and in space by the directional solidification technique. Macroscopic and microscopic examinations were made on longitudinal and transverse sections of Apollo-Soyuz Test Project space-grown and Earth-grown ingots. It was found that samples grown in space have a higher percentage of fibers alined with the growth axis. The enhanced alinement of fibers is attributed to the absence of convection currents in the liquid during solidification.

Optical transmittance measurements of transverse sections of the space-grown and Earth-grown ingots were performed with an infrared spectrometer. For a given sample thickness, the highest transmittance was obtained from ingots grown in space. For samples of different thicknesses, grown either in space or on Earth, it was found that the thinner the sample, the higher the transmittance. This is in agreement with the general optical property of transparent materials.

INTRODUCTION

When certain binary eutectic mixtures solidify, one of the two phases can form fibers or platelets in a matrix of the second phase. For example, when a eutectic liquid of sodium chloride (NaCl) and sodium fluoride (NaF) solidifies, fibers of NaF form in a matrix of NaCl. Similarly, when a liquid of NaCl and lithium fluoride (LiF) solidifies, LiF will form the fiber phase in the NaCl matrix.

Fiberlike and platelike eutectics produced on Earth are limited in perfection by the presence of a banded structure (refs. 28-1 and 28-2), by discontinuity (ref. 28-3), and by faults (refs. 28-4 and 28-5) due, at least in part, to vibration and convection currents in the melt during solidification. The presence of these defects renders the solid-state eutectic devices inefficient and useless (ref. 28-6).

If the solidification process is performed in a space environment, where there are no vibration and convection currents in the melt, there is reason to believe that continuous fiberlike eutectic microstructures can be produced. The electric, thermomagnetic, optical, and superconducting characteristics of such fibers will be

---

[a]University of California.

[†]Principal Investigator.

strongly anisotropic, which suggests the possibility of exciting device applications. A Skylab experiment (ref. 28-7) of NaCl-NaF eutectic demonstrated that continuous oriented fibers of NaF embedded in an NaCl matrix could be grown by the directional solidification technique in space.

This paper describes (1) the results of the NaCl-LiF eutectic grown in space during the Apollo-Soyuz Test Project (ASTP), and (2) the measurements of the relevant optical properties of the space-grown and Earth-grown eutectics.

Lithium fluoride was used in this experiment because it has a higher index of refraction than NaF and because a greater volume of fraction of fibers in the NaCl-LiF eutectic system may be obtained.

EXPERIMENTAL PROCEDURES

The NaCl-28.8 weight percent (wt%) LiF eutectic mixtures were made from 99.96-wt% NaCl and 99.99-wt% LiF and were solidified in an induction heating unit under a protective atmosphere. The ampoule assembly was similar to that used in the Skylab experiment with the exception that a copper tube was not used.

Ingots of NaCl-LiF eutectics, 0.79 centimeter (0.31 inch) in diameter and 6.4 centimeters (2.5 inches) long, have been grown unidirectionally on Earth and in space in the ASTP spacecraft in a multipurpose furnace at one freezing rate and at a steep temperature gradient similar to that described in reference 28-7.

RESULTS AND DISCUSSION

The experimental results are divided into two parts: (1) the macroscopic and microscopic examinations of the samples that were grown in space and on Earth, and (2) the optical property of the NaCl-LiF eutectic.

Macroscopic and Microscopic Examinations of Microstructures

The appearance of one of the three opened ampoules and the eutectic sample after completion of the ASTP experiment is shown in figure 28-1. The surfaces of the stainless steel cylinders were in perfect condition, which indicates that no reaction occurred between the ampoules and the cartridges. Inspection of the sample surface revealed no reaction between the NaCl-LiF eutectic and the graphite container.

The remelt-back interface is shown in figure 28-2. The resolidified portion of the sample is on the right and the unsolidified portion on the left. In this particular sample, the remelt-back interface is 0.28 centimeter (0.11 inch) from the left end of the sample, whereas the same melt-back distances of the other two samples are approximately 0.51 centimeter (0.20 inch). This may indicate a slight offset in the positioning of the heat zones in the furnace. Figure 28-3 is a photograph of the region of the remelt-back interface which shows that, at the beginning of the growth,

the LiF fibers were grown in a direction perpendicular to the growth direction during the soaking period. However, the LiF began to aline toward the growth direction a short distance from the initial solid-liquid interface.

A representative photomicrograph of alined continuous fibers is given in figure 28-4, which shows that the LiF fibers are regularly spaced and parallel to the growth axis. The eutectic microstructure that resulted when the NaCl-LiF eutectic was grown on Earth with convection current is shown in figure 28-5, which shows that the solidified LiF fibers are short and discontinuous.

The orientation of the LiF fibers in the NaCl matrix, however, varies along the length of the sample. Optical metallographic results show that the LiF fibers are straight and parallel to the growth direction for approximately one-half the total length of the sample. The LiF fibers in the remaining half of the NaCl-LiF eutectic, however, change gradually from a parallel direction to a direction that is perpendicular to the growth axis. This change indicates that the direction of heat extraction during the latter half of the solidification process is normal to the growth direction in contrast to what was originally designed. Figure 28-6 is a photomicrograph showing the change of direction of fibers along the length of the sample.

A photomicrograph of the transverse section of an ASTP-grown sample is shown in figure 28-7, which reveals that the shapes of the LiF fibers are preferentially circular. This circular shape is different from the preferentially rectangular shape of the NaF fibers in the NaCl-NaF eutectic grown in the Skylab experiment.

A single-grain eutectic has not been achieved in the presence of microgravity in space in this ASTP experiment. However, the fibers grown in space are alined more regularly and are more parallel to the growth direction than those grown on Earth. Evidence supporting this observation is shown in figure 28-8 and also in the optical transmittance results shown in figure 28-9. In figure 28-8, filtered light was incident at the end of the sample. Light can be seen to transmit farther through the ASTP space-grown sample than through the sample grown on Earth because of better alinement of the fibers. Light was not transmitted through the upper portion of the ASTP sample because, in that portion of the sample, the LiF fibers were not alined well enough to the growth direction, as discussed previously.

Optical Property

Image transmission properties similar to those of fiber optic materials were obtained with an NaCl-NaF eutectic (ref. 28-8). This eutectic was found to be a far-field infrared transmitting medium for wavelengths longer than the interfiber distance. Because the NaCl-NaF eutectic used for optical measurement has discontinuous NaF fibers embedded in NaCl matrix, better results should be observed if continuous fibers are obtained. That this is indeed the case was demonstrated in the Skylab experiment (ref. 28-7). Similar experiments comparing transmission properties of NaCl-LiF eutectic grown in space and on Earth were conducted for ASTP. The far-field infrared transmissions of transverse sections of three NaCl-LiF eutectic samples are compared in figure 28-9. The ASTP space-grown sample is shown to have the highest transmittance over nearly the entire wavelength range, which indicates that it has the highest percentage of fibers parallel to the growth direction.

The transmittance result also shows that the sample grown in the prototype furnace has a lower transmittance over part of the wavelength range than the eutectic sample grown in the laboratory.

The effect of thickness on the transmission curve is shown in figure 28-10 for the prototype furnace and the ASTP space-grown samples. In both cases, the thinner the sample, the higher the transmittance for a fixed wavelength. This observation is in agreement with absorption laws as expected.

CONCLUSIONS

The following conclusions can be drawn from this investigation.

1. Eutectic samples grown in space have a higher percentage of fibers parallel to the growth direction than samples grown on Earth.

2. Larger transmittance over a wider range of wavelength was obtained from the ASTP space-grown ingots because of the better alinement of LiF fibers embedded in the NaCl matrix.

REFERENCES

28-1. Yue, A. S.; and Clark, J. B.: Determination of Eutectic Composition by Zone-Melting Method. Trans. TMS-AIME, vol. 221, no. 2, Apr. 1961, pp. 383-389.

28-2. Lemkey, F. D.; and Thompson, E. R.: Nickel and Cobalt Eutectic Alloys Reinforced by Refractory Metal Carbides. Met. Trans., vol. 2, no. 6, June 1971, pp. 1537-1544.

28-3. Crossman, F. W.; and Yue, A. S.: Unidirectionally Solidified Ti-TiB and Ti-Ti_5Si_3 Eutectic Composites. Met. Trans., vol. 2, no. 6, June 1971, pp. 1545-1555.

28-4. Yue, A. S.: Microstructure of Magnesium-Aluminum Eutectic. Trans. TMS-AIME, vol. 224, no. 5, Oct. 1962, pp. 1010-1015.

28-5. Kraft, R. W.; and Albright, D. L.: Structural Characteristics of Fe-FeS Eutectic. Trans. TMS-AIME, vol. 236, no. 7, July 1966, pp. 998-1003.

28-6. Weiss, H.: Electromagnetic Properties of Eutectic Composites (A Critical Review). Met. Trans., vol. 2, no. 6, June 1971, pp. 1513-1521.

28-7. Yue, A. S.; and Yu, J. G.: Solidification of NaCl-NaF Eutectic in Space. AIAA/ASME Conference on Thermophysics and Heat Transfer. AIAA Paper 74-646, July 1974.

28-8. Batt, J. A.; Douglas, F. C.; and Galasso, F. S.: Optical Properties of Undirectionally Solidified NaF-NaCl Eutectic. American Ceram. Soc. Bull., vol. 48, no. 6, June 1969, pp. 622-626.

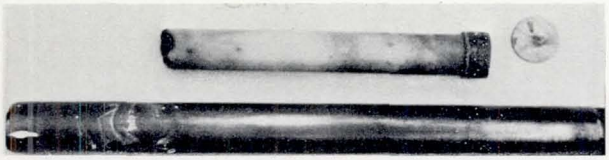

Figure 28-1.- Macrophotograph of opened ampoule and eutectic sample.

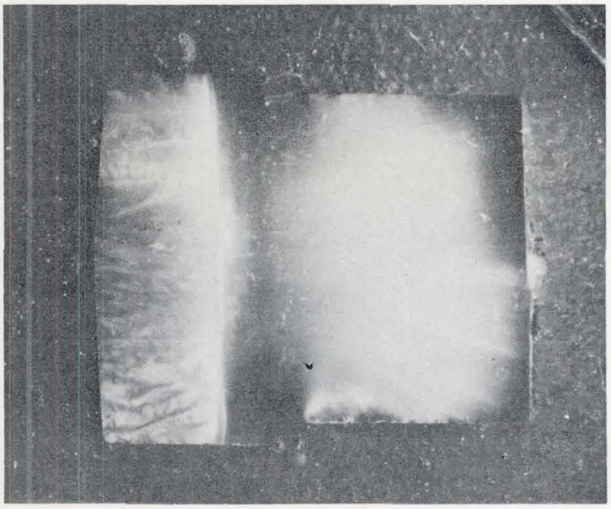

Figure 28-2.- Macrophotograph showing the remelt-back interface of the ASTP space-grown NaCl-LiF eutectic (6.4X).

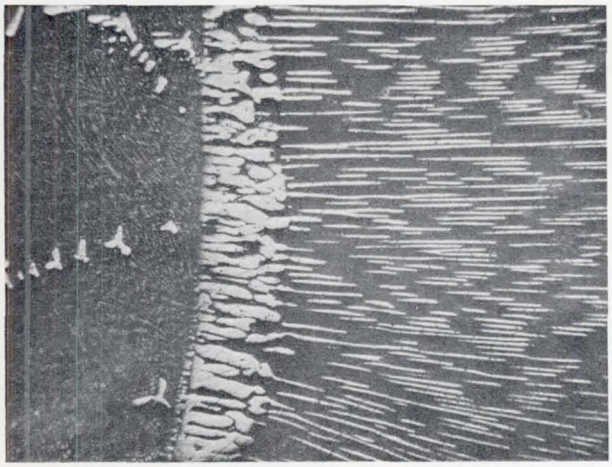

Figure 28-3.- Enlarged portion of the remelt-back interface (56X).

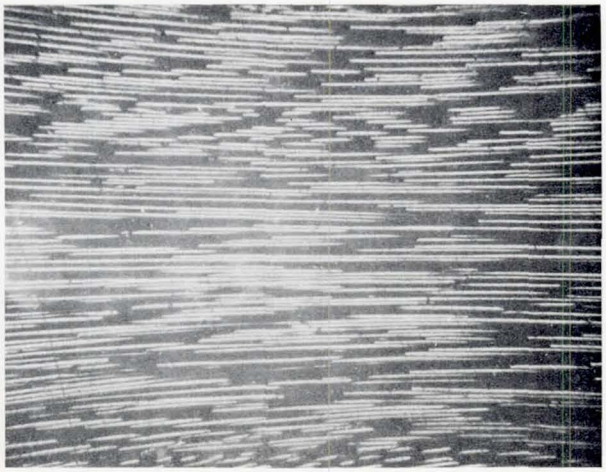

Figure 28-4.- Photomicrograph of the longitudinal section of the ASTP space-grown NaCl-LiF eutectic showing continuous LiF fibers (56X).

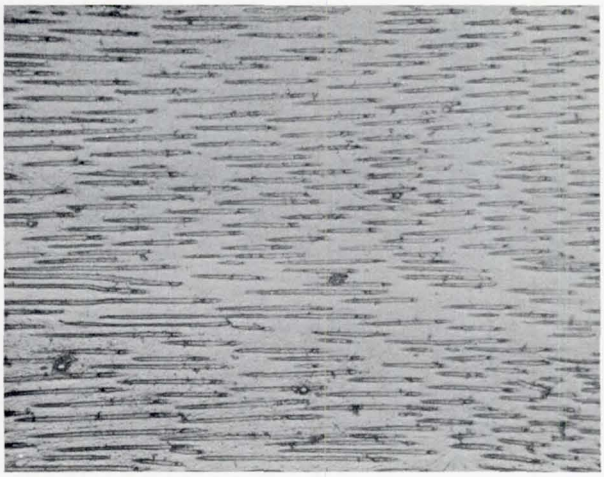

Figure 28-5.- Photomicrograph of the longitudinal section of Earth-grown NaCl-LiF eutectic showing discontinuous LiF fibers (210X).

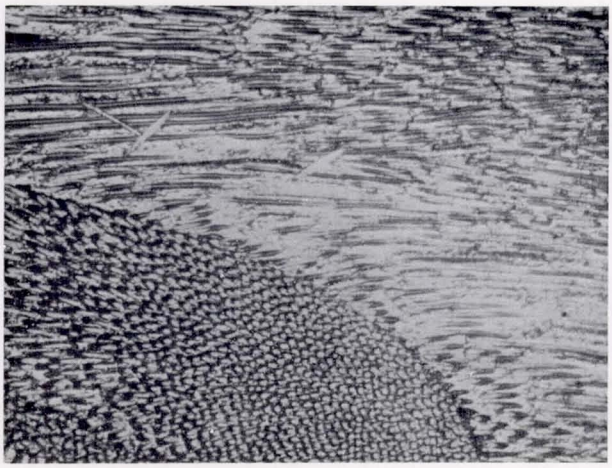

Figure 28-6.- Photomicrograph showing the change of direction of fibers (210X).

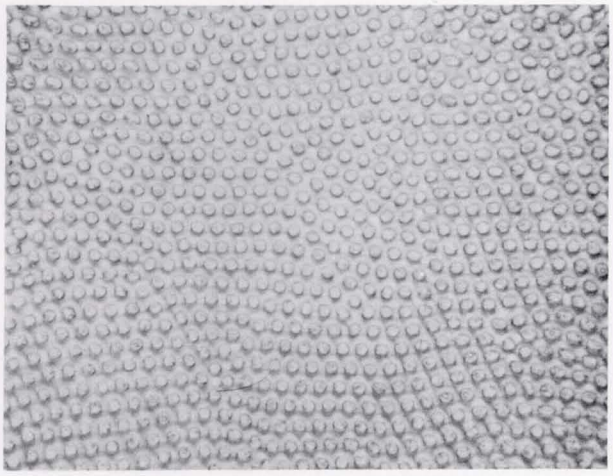

Figure 28-7.- Photomicrograph of the transverse section of ASTP space-grown eutectic (410X).

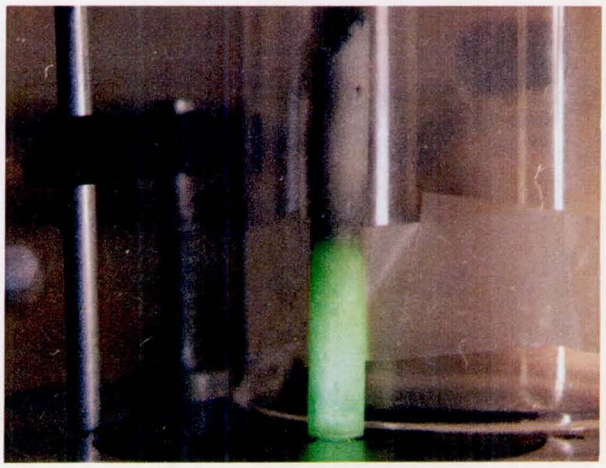

(a) Space grown.

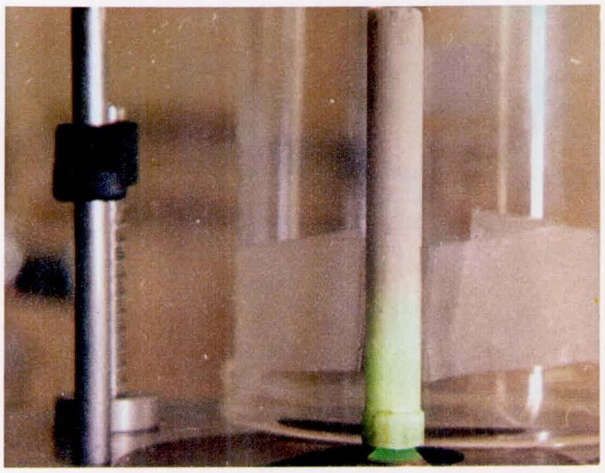

(b) Earth grown.

Figure 28-8.- Macrophotographs of ASTP NaCl-LiF eutectics.

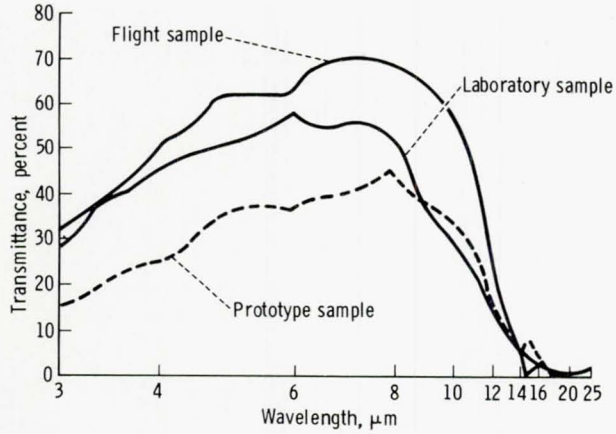

Figure 28-9.- Far-field infrared transmission curve of transverse sections of NaCl-LiF eutectics grown on Earth and in space. The sample thickness was 0.0536 centimeter (0.0211 inch).

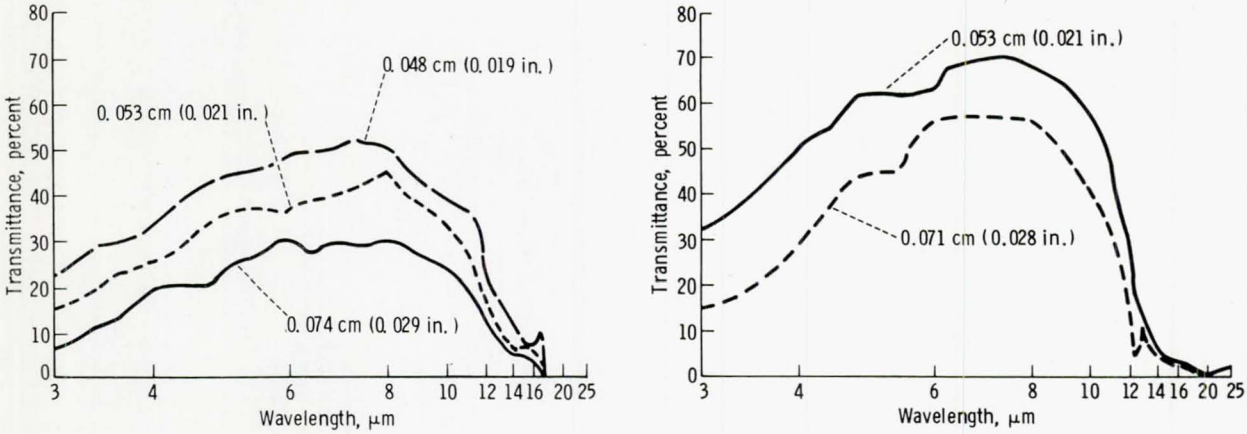

(a) Prototype sample.

(b) Flight sample.

Figure 28-10.- Far-field infrared transmission curves of transverse sections of NaCl-LiF eutectics with different thicknesses.

29. MULTIPLE MATERIAL MELTING

EXPERIMENT MA-150

R. S. Snyder[a] and A. Boese[a]

ABSTRACT

Three different experiments to reveal the effect of weightlessness on some metallurgical and crystalline processes in metals and semiconductors were prepared by I. Ivanov and his coworkers at the Institute for Metallurgy, U.S.S.R., for the Apollo-Soyuz Test Project mission. The experiment materials were fabricated in the U.S.S.R., assembled in three stainless steel cartridges of U.S. design, taken into space for processing in the multipurpose furnace, and returned to the U.S.S.R. for analysis. Analysis of the samples and comparison with the ground-based test results are in progress.

INTRODUCTION

The Multiple Material Melting Experiment was a U.S.S.R. experiment that processed three different materials systems (aluminum with tungsten spheres, germanium with 2 atomic percent (at.%) silicon, and powdered aluminum) in each of three identical cartridges. The experiment cartridges were carried into space with the other furnace cartridges adjacent to the multipurpose furnace. The experiment was performed during the joint U.S.S.R.-U.S. phase of the mission; upon completion of the experiment, the three cartridges were returned by Soyuz to the U.S.S.R. for analysis.

BACKGROUND

The U.S.S.R. interest in the use of space to conduct materials experiments for investigation of technological processes has been active for approximately 2 years. Extensive experiments in electron beam welding were reported to have occurred during an early Soyuz space station mission. Analysis of the space-welded specimens has been published in the scientific literature (ref. 29-1). The report cites improved metallurgical characteristics of the welds and evidence of decreased movement of the molten material in space compared with similar specimens welded on Earth. There is extensive interest in composite materials of two

---

[a]NASA George C. Marshall Space Flight Center.

or more materials that differ greatly in density. Similarly, weightlessness is of interest for manufacturing new metal and semiconducting materials formed of elements with substantially different densities by careful crystallization from the liquid state.

EXPERIMENT OBJECTIVES

Each of the three materials systems selected for this experiment had a different objective. Placing tungsten spheres in aluminum powder on the ground and then melting and solidifying in space was planned to investigate composite materials with one phase meltable and the second phase heavier and more refractory. The tungsten spheres for the second phase were carefully distributed in the laboratory and, presumably, this distribution did not move in space. Ground-based testing clearly showed the sedimentation of the heavier tungsten spheres. Other important scientific objectives of this experiment are the actual rate of dissolving solid refractory metals in various liquid systems, the actual rate of metal crystallization from a liquid phase, and the actual rate for growing new phases from the melt. Determination of the actual rates of such processes is not possible on Earth because of gravity-induced fluid convection. Metallurgical reactions will thus be more controllable with the knowledge of actual rate values.

The investigation of single crystal growth of semiconductors used germanium containing 2 at.% of silicon. Because of convection flow in the melt on Earth, fabrication of such germanium monocrystals with a uniform distribution of silicon throughout the bulk is very difficult.

Ball formation in weightlessness was to be investigated by melting aluminum powder. This technique for forming spheres of fused metals or semiconducting compounds should produce different results in space and should be significant for such space technological procedures as welding and treatment of biochemically active raw materials.

EQUIPMENT AND OPERATIONS

The Multiple Material Melting Experiment was begun soon after the Apollo and Soyuz space vehicles joined together. The three materials specimens were in different locations in the cartridge, were contained in their own quartz ampoules, and were subjected to different temperatures during the furnace heatup, soak, and cooldown. An outline of the cartridge is shown in figure 29-1. Ampoule 1 contained the aluminum with tungsten spheres. It was heated to approximately 1325 K (1050° C). Ampoule 2 contained the germanium with silicon and was partly melted by the furnace heatup. During furnace cooldown, the solid/liquid interface slowly caused the entire melt to resolidify directionally. This method was selected to yield monocrystals with improved properties. Ampoule 3 contained the aluminum powder, and the 973 K (700° C) temperature at this cartridge location was sufficient to melt the sample. The maximum temperature of the hot end of the furnace was maintained

for 1 hour to "soak" the sample. The three-stage cooldown gave the necessary thermal profile in the cartridge and allowed the experiment to be completed in approximately 10 hours.

REFERENCE

29-1. Kubasov, V. M.; and Paton, B. E.: Experiment in Metal Welding in Outer Space. J. Acad. Sci. Ukrainian S.S.R., vol. 34, 1970, pp. 37-44.

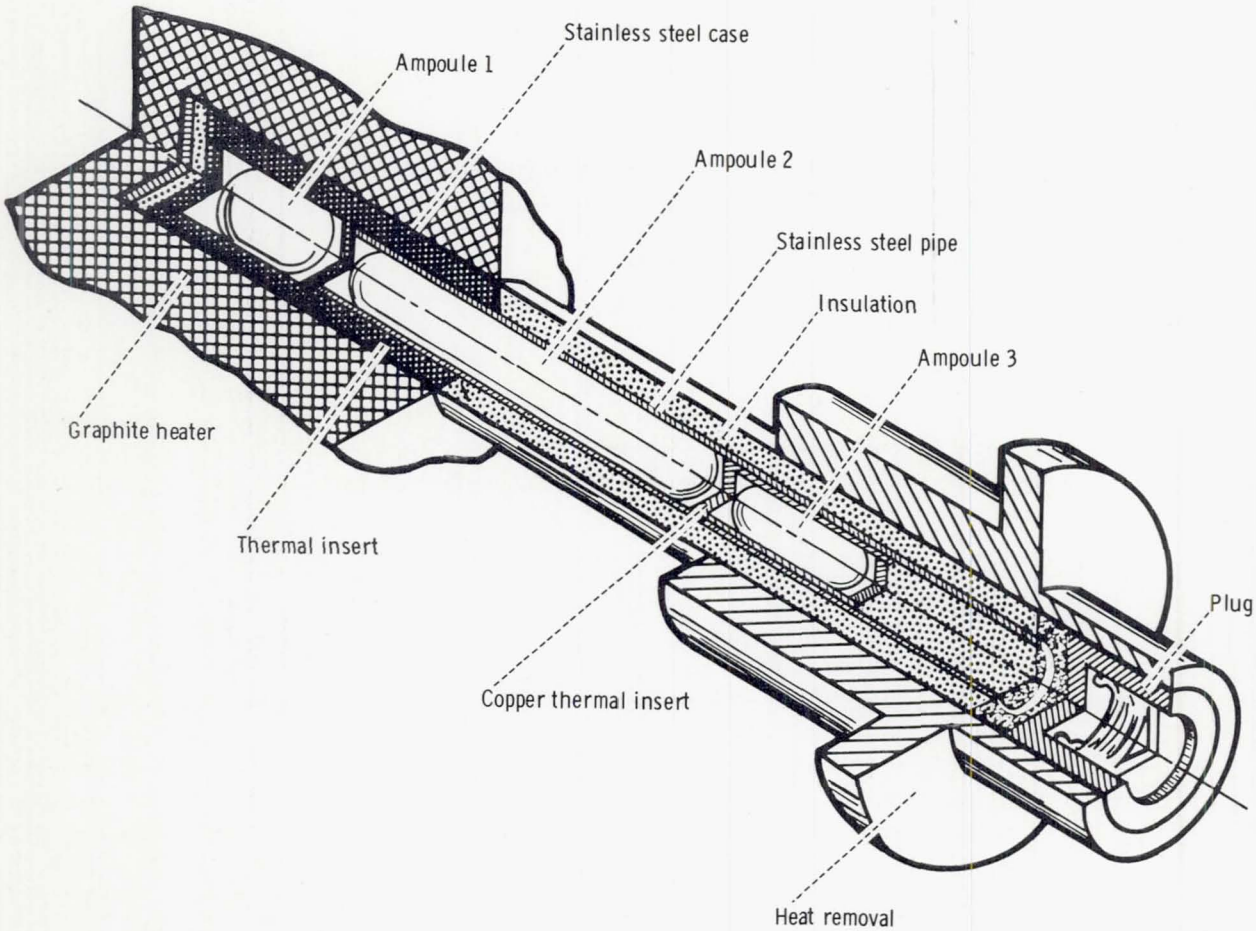

Figure 29-1.- Cartridge used in the Multiple Material Melting Experiment.

30. CRYSTAL GROWTH

EXPERIMENT MA-028

M. D. Lind[a]

ABSTRACT

The Crystal Growth Experiment assessed a novel process for growing single crystals of insoluble substances by allowing two or more reactant solutions to diffuse toward each other through a region of pure solvent in zero g. The experiment was entirely successful and yielded crystals of about the expected size, quality, and number. Photographs were taken in orbit to record the progress of the crystal growth.

INTRODUCTION

The objective of this experiment was to investigate the growth of single crystals of insoluble substances by a process in which two or more reactant solutions are allowed to diffuse toward each other through a region of pure solvent. This is a novel method of crystal growth conceived for orbital space flights to take advantage of the absence of gravity-driven convection that, on Earth, predominates over diffusion as a mechanism of material transport. The experiment performed during the Apollo-Soyuz Test Project (ASTP) mission was designed both as a first attempt to determine the feasibility of the method and as a starting point for further development.

BASIC THEORY

Because the method of crystal growth used for this experiment is closely related to gel methods of crystal growth, it is appropriate to present a brief review of gel methods. Gel methods are particularly applicable to the growth of crystals that have very small solubility in the solvent (usually water) that is used. In these methods, two or more reactant solutions, separated by a gel, diffuse slowly together and react according to a chemical equation of the following type as the crystal grows:

$$A\ (\text{soluble}) + B\ (\text{soluble}) + \ldots \rightleftharpoons C\downarrow\ (\text{slightly soluble}) + D\ (\text{soluble}) + \ldots$$

---

[a]Rockwell International Science Center; Principal Investigator.

The three reactions chosen for experiments on the ASTP flight are examples of this type reaction.

Calcium tartrate: $CaCl_2 + NaHC_4H_4O_6 + 4H_2O \rightleftharpoons CaC_4H_4O_6 \cdot 4H_2O\downarrow + NaCl + HCl$

Calcium carbonate: $CaCl_2 + (NH_4)_2CO_3 \rightleftharpoons CaCO_3\downarrow + 2NH_4Cl$

Lead sulfide: $PbCl_2 + CH_3CSNH_2 + H_2O \rightleftharpoons PbS\downarrow + CH_3CONH_2 + 2HCl$

Typical experimental arrangements for gel methods are shown schematically in figure 30-1. In the U-tube arrangement, the crystals normally grow within the gel or at the interfaces with the reactant solutions. In the second arrangement, the crystals can grow in the pure solvent at the center.

The primary functions of the gel are suppression of gravity-driven convection and support of the growing crystal. Diffusion is the predominant mechanism for mixing of the reactant solutions. The crystal grows in a cell of solution, is exposed to the solution on all sides, and has no contact with container surfaces except those of the flexible gel structure.

The hypothesis for this experiment was based on the assumption that, in an environment of sufficiently low gravity, convection and sedimentation become negligible. Therefore, the gel is not needed for suppressing these processes and can be replaced by a region of pure solvent. Diffusion becomes the predominant mixing mechanism even with no gel present.

The advantage of allowing diffusion to be the predominant mechanism for material transport, whether in gel processes on Earth or in low-gravity processes in space flights, is that the rate of transport can be controlled by varying the concentrations of the diffusing substances and the length of the diffusion path. This is important because the rate of material transport must be compatible with the rate of crystal growth, which may also depend on other kinetic or heat-transfer factors. A diffusion-controlled process can result in better crystal quality through better prediction and control of the parameters involved. It can also result in a better understanding of crystal growth processes through simplification of theoretical treatments and a clearer comparison of the experiment with the theory.

The gel methods of crystal growth, like most aqueous solution growth methods, are advantageous because crystal growth occurs at ambient (room or spacecraft) temperature. This minimizes problems of thermally or mechanically induced strain, phase transformations, volatility of components, contamination by the container, etc., often inherent in high-temperature growth methods. However, gel methods also have certain disadvantages, including excessive nucleation that results in small crystal sizes, contamination of the crystals by gel constituents or impurities in the gel, and gel instability. The method used for this experiment is expected to overcome all these disadvantages while retaining the advantages.

Much research has been done concerning gel methods of crystal growth. This research has provided much of the background for the design of the ASTP experiment. Information particularly relevant to this experiment can be found in references 30-1 to 30-12. The three crystals (calcium tartrate, calcium carbonate, and lead sulfide) investigated in the ASTP experiments were chosen for the following reasons:

1. They are easy to grow in gel systems.

2. There has been much investigation of their growth in gel systems so that growth conditions are well known, and terrestrial results are readily available for comparison with ASTP results.

3. Calcium tartrate has been an especially important subject for investigations of gel growth mechanisms.

4. Calcium carbonate and lead sulfide have technological importance.

5. Calcium carbonate is a typical example of crystals that are contaminated by gel constituents and therefore can be improved by growth without the gel.

The experimental conditions for the ASTP experiments were based on results of previous gel growth experiments. It was assumed that the diffusion and crystal growth processes would not be very different if the gel was replaced by a region of pure solvent. Because typical gels are 95 to 96 percent solvent and only 4 to 5 percent solid, this assumption was reasonable and appears to have been validated by the ASTP results. To simplify the ASTP experimental apparatus, the usual requirement for precise temperature control was eliminated by choosing crystals that can be grown at ambient temperature without precise temperature control. The other important experimental parameters are selection and concentrations of reactant solutions, reactor dimensions, and hydrogen-ion concentration (pH) of the growth medium (water). The values of these parameters used in the ASTP experiments are summarized in table 30-I.

As previously implied, much of the behavior of these crystal growth systems could be calculated from known laws of thermodynamics, diffusion, and heat transfer. In general, the required parameters, including equilibrium solubilities as functions of temperature and pH, heats and entropies of fusion, specific heats, diffusion coefficients, thermal conductivity coefficients, etc., were reasonably well known or could be determined in experiments on Earth. However, relationships between supersaturation and nucleation are more difficult to understand, and incomplete knowledge in this area precludes a complete prediction of the behavior of the crystal growth systems chosen for study. Consequently, it was necessary to estimate the best growth conditions on the basis of results of experimental gel growth studies.

EQUIPMENT

The experimental apparatus consisted of six specially designed and fabricated reactors (fig. 30-2). The entire set of flight hardware is illustrated in figure 30-3.

Each reactor had three compartments that were separated by valves operated by the knobs at each end. Each compartment had a separate filling port. The compartments varied in length, as indicated in table 30-I. The reactor covers were flat and transparent to permit photographing the progress of diffusion and crystal growth. The reactors were constructed of Lexan polycarbonate resin with silicone rubber gaskets and seals, porous high-density polyethylene diaphragms between the compartments, and aluminum knobs.

Before delivery of the hardware to the launch facility, the reactors (with the intercompartment valves in the closed positions) were filled with the various solutions. The reactant solutions were placed in the outer compartments of each reactor, and the central compartment was filled with water.

The six reactors were mounted in the U-4 locker in the command module. They were accessible in this location, yet out of the way of other operations.

After the joint phase of the flight, at approximately 109 hours ground elapsed time (GET), a crewman activated the experiments by opening the intercompartment valves to allow the reactants to begin diffusing toward the center. A wrench (fig. 30-3) that was included as a contingency measure was not required.

Beginning at the time of activation and at approximately 12-hour intervals for the remainder (116 hours) of the flight, a crewman took color photographs of the six reactors with the Nikon 35-millimeter camera used for various other photography. A framing device designed and fabricated at the NASA Lyndon B. Johnson Space Center was used to place the camera properly.

Throughout the flight, the experiment progressed as planned with no problems or anomalies. The performance of the reactors was most satisfactory. There was no evidence of leakage through the intercompartment valves before activation of the experiment, and the valves were opened easily at the proper time to begin the experiment. Photographs of the reactors taken during the flight appear to be of excellent quality and verify that the framing device, camera settings, and lighting were entirely satisfactory.

DISCUSSION AND RESULTS

Crystals of about the expected size, quality, and number formed in all six reactors. Figures 30-4 to 30-6 are photographs of the results taken before postflight analysis. Before opening the reactors, the crystals were examined thoroughly through the reactor faces by using a microscope. Then, the center filling port caps were machined out, and representative crystals were removed and identified by single-crystal X-ray diffraction data. As expected, the X-ray diffraction data appeared to be identical to that of Earth-grown crystals.

Also as expected, the largest crystals obtained were calcium tartrate (fig. 30-4). Both calcium tartrate reactors produced numerous well-formed and very clear platelike crystals as long as 5 millimeters and a few crystals as long as 10 millimeters but of somewhat poorer quality. The platelike morphology differs

markedly from the prismatic habit usually obtained in gel experiments, but the reasons for this difference and its significance are unknown at this time. The two calcium carbonate reactors each produced numerous well-formed clear rhombohedral crystals as long as 0.5 millimeter on an edge (fig. 30-5). These crystals are very similar in appearance to Earth-grown calcium carbonate crystals. Although small, they are large enough to exhibit birefringence. The two lead sulfide experiments were less successful, but both produced crystals as long as 0.1 millimeter (fig. 30-6).

The crystals grown during the flight are at least as good in size, quality, and number as those obtained by gel methods on the surface of the Earth in the same length of time. All six reactors contained crystals suitable for the planned detailed postflight analysis. However, nucleation was excessive in all six reactors, which indicates the need for considerable refinement of the experimental parameters to suppress nucleation and improve crystal size.

No finely divided precipitate was observed in the calcium tartrate or calcium carbonate reactors, which indicates that, in these four reactors, mixing of the reactant solutions and crystal growth were complete by the time of spacecraft reentry. This complete mixing was the desired result. In the case of lead sulfide, a similar result was not obtained although there was sufficient mixing to produce at least a few small crystals.

The calcium carbonate crystals are easily visible in the series of photographs taken at 184 hours GET (75 hours after activation of the experiment) and in subsequent photographs. The calcium tartrate crystals also appear in these photographs but less clearly. Thus far, only transparencies have been examined. Enlarged prints will be necessary for following the progress of the experiment in detail.

During the flight, the cabin temperature varied more than had been anticipated and more than was desirable for solution growth. In designing the experiment, it was decided not to provide temperature control to simplify the hardware. As part of the experiment results analysis, the effects of the temperature variations are being considered.

Further detailed analysis of the experiment results is planned. An important aspect of this analysis will be the detailed comparison of the ASTP-grown crystals and typical crystals grown on Earth. The experimental results will also be compared to theoretical calculations.

CONCLUSIONS

The experiment has successfully proven the feasibility of a novel method of crystal growth, both for producing superior crystals of a variety of compounds and for promoting a better understanding of the theory of crystal growth.

REFERENCES

30-1. Henisch, Heinz K.: Crystal Growth in Gels. Pennsylvania State Univ. Press, 1970.

30-2. Henisch, H. K.; Dennis, J.; and Hanoka, J. I.: Crystal Growth in Gels. J. Phys. Chem. Solids, vol. 26, no. 3, Mar. 1965, pp. 493-500.

30-3. Nickl, H. J.; and Henisch, H. K.: Growth of Calcite Crystals in Gels. J. Electrochem. Soc., vol. 116, no. 9, 1969, pp. 1258-1260.

30-4. Barta, Cestmir; and Zemlicka, Jan: Growth of Calcium Carbonate and Calcium Sulfate Dihydrate Crystals in Gels. J. Cryst. Growth, vol. 10, no. 2, 1971, pp. 158-162.

30-5. Blank, Zvi; and Brenner, Walter: The Growth of Group II-VI Crystals in Gels. J. Cryst. Growth, vol. 11, no. 3, 1971, pp. 255-259.

30-6. Blank, Zvi; and Brenner, Walter: Research Directed Toward Preparation of Compound Semiconductors by Controlled Diffusion Mechanism in Gels. AFCRL-70-0252, Air Force Cambridge Res. Labs., L. G. Hanscom Field, Mass., Mar. 1970.

30-7. Blank, Zvi; Brenner, Walter; and Okamoto, Yoshiyuki: The Growth of Lead Sulfide in Silica Gels at Ambient Temperatures - Preliminary Characterization and Effect of Various Organic Compounds as Sulfide Ion Donors. Mater. Res. Bull., vol. 3, no. 7, 1968, pp. 555-561.

30-8. Swift, Ernest H.; and Butler, Eliot A.: Precipitation of Sulfides From Homogeneous Solutions by Thioacetamide. Anal. Chem., vol. 28, no. 2, Feb. 1956, pp. 146-153.

30-9. Armington, Alton F.; DiPietro, Mary A.; and O'Connor, John J.: A Study of Some Factors Which Influence the Growth of Cuprous Chloride in Silica Gel. AFCRL-67-0445, Phy. Sci. Res. Paper no. 334, Air Force Cambridge Res. Labs., L. G. Hanscom Field, Mass., July 1967.

30-10. Armington, Alton F.; and O'Connor, John J.: Some Factors Influencing the Growth of Crystals in Gel by the Complex Dilution Method. Mater. Res. Bull., vol. 3, no. 12, 1968, pp. 923-931.

30-11. Kirov, G. K.: On the Diffusion Method for Growing Crystals. J. Cryst. Growth, vol. 15, no. 2, 1972, pp. 102-106.

30-12. Torgesen, John L.; and Peiser, Herbert S.: Method and Apparatus for Growing Single Crystals of Slightly Soluble Substances. U.S. Patent 3,371,036, Feb. 27, 1968.

TABLE 30-I.- REACTANT SOLUTIONS

Reactor serial number	Compartment B		Compartment A		Compartment C	
	Reactant	Length, cm	Reactant	Length, cm	Reactant	Length, cm
005	0.1M CH_3CSNH_2	3.30	H_2O adjusted to pH = 1.0 with HCl	5.08	Saturated $PbCl_2$	3.30
006	0.5M $CaCl_2$	3.30	H_2O	5.08	0.45M $NaHC_4H_4O_6$	3.30
007	0.5M $CaCl_2$	3.30	H_2O	5.08	0.5M $(NH_4)_2CO_3$	3.30
008	0.1M CH_3CSNH_2	3.30	H_2O adjusted to pH = 0.5 with HCl	5.08	Saturated $PbCl_2$	3.30
012	0.5M $CaCl_2$	4.19	H_2O	4.19	0.5M $(NH_4)_2CO_3$	3.30
013	0.5M $CaCl_2$	4.19	H_2O	4.19	0.45M $NaHC_4H_4O_6$	3.30

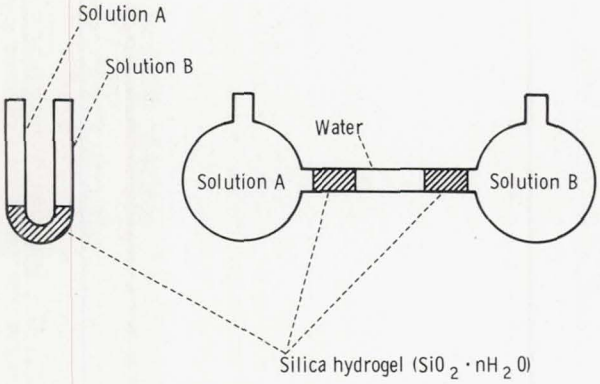

Figure 30-1.- Typical experimental arrangements for gel methods of crystal growth.

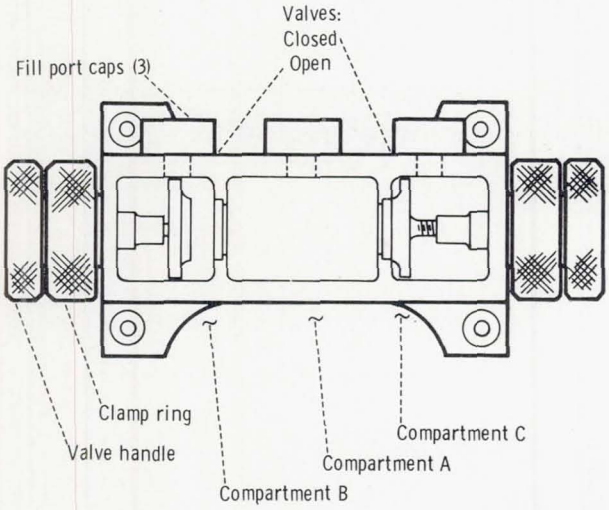

Figure 30-2.- Schematic diagram of a reactor.

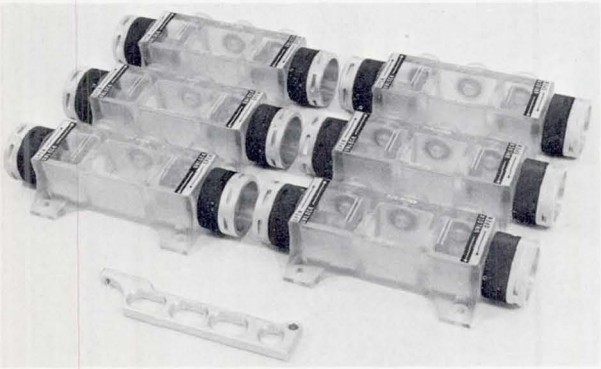

Figure 30-3.- Flight hardware.

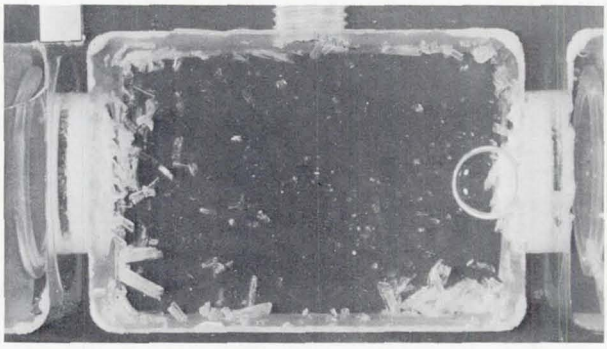

(a) Serial number 006.

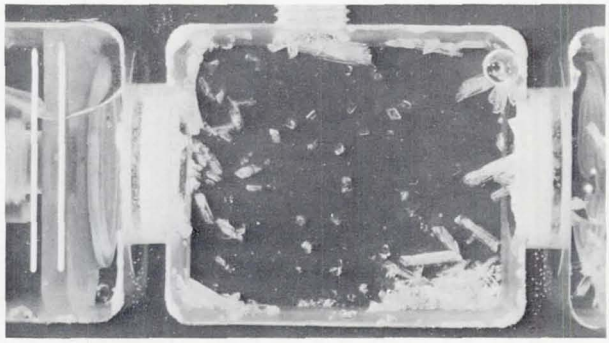

(b) Serial number 013.

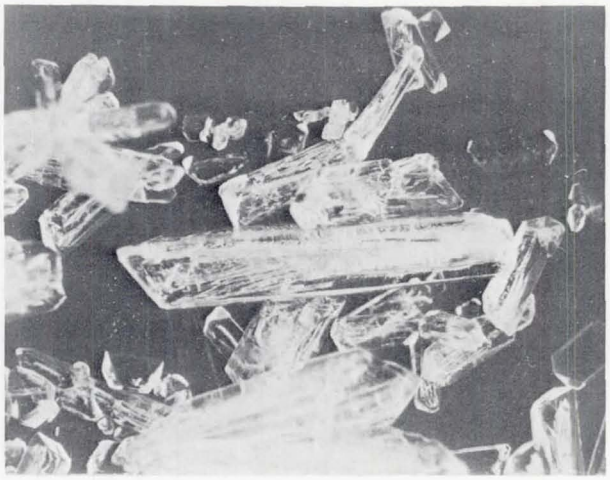

(c) Magnified view of calcium tartrate crystals.

Figure 30-4.- Calcium tartrate.

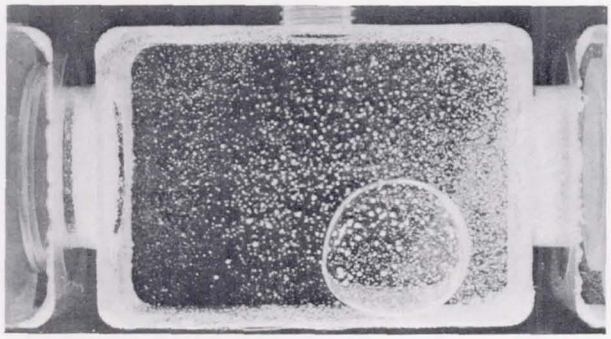

(a) Serial number 007.

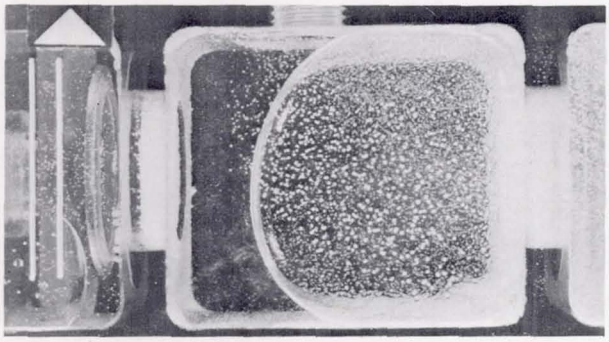

(b) Serial number 012.

(c) Magnified view of calcium carbonate crystals.

Figure 30-5.- Calcium carbonate.

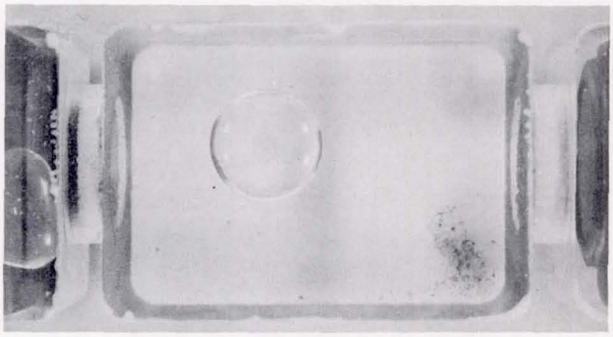

(a) Serial number 005.

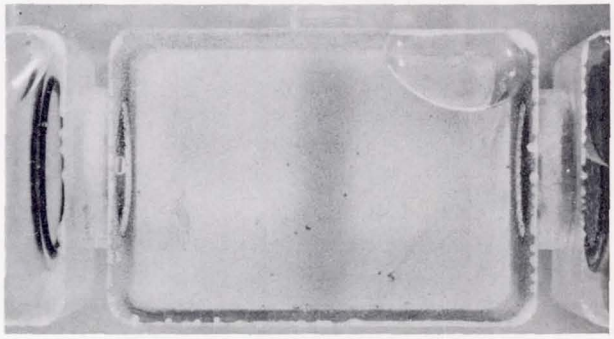

(b) Serial number 008.

Figure 30-6.- Lead sulfide.

31. SCIENCE DEMONSTRATIONS

R. S. Snyder,[a] K. S. Clifton,[a] B. Facemire,[a]
A. F. Whitaker,[a] P. G. Grodska,[b] and S. Bourgeois[b]

ABSTRACT

Three demonstrations of scientific concepts concerning liquids were performed during the Apollo-Soyuz Test Project mission. Chemical foaming, spreading of liquids, and capillary wicking were the subjects of each demonstration photographed in space. The results clearly illustrated the basic principles, and films suitable for educational uses are now available from the first author.

INTRODUCTION

Three science demonstrations with liquids were performed during the last part of the Apollo-Soyuz Test Project (ASTP) mission. The demonstrations were chemical foaming, liquid spreading, and capillary wicking, and all dealt with phenomena that occur at the boundary surface, or interface, between solids, liquids, and gases. The manner in which one surface interacts with another can be described by intermolecular surface forces that result in adhesion or cohesion and in wetting or nonwetting conditions. These surface forces cause such well-known phenomena as the shape of raindrops, the detergent action of soaps, and the lubrication of complex machinery.

Although basic theories of interfacial phenomena exist, detailed observations and measurements have been difficult to obtain on practical systems. In particular, gravity interferes with systems that include liquids and gases because the interface conditions are changed by sedimentation or buoyancy and the interface configuration of interest may not be obtainable in a gravity environment. The interaction on Earth of liquids with gases or solids has been especially difficult to model or predict because the gravity force influences each phase differently.

Gravitational force can only be circumvented on Earth by modifying the system being studied. For example, the addition of surface-active agents, such as detergents, enables the formation of stable foams in liquids, and solid surfaces can be coated or treated to change interactions with a second phase. However, these modifying agents may change the system being studied to the extent that significant

---

[a]NASA George C. Marshall Space Flight Center.

[b]Lockheed Missiles and Space Company.

data cannot be obtained relative to the original system. A zero-g environment is necessary to measure and assess the fundamental interactions in many important systems. The study of these systems led to the demonstrations proposed for ASTP.

The demonstrations required no power and had no impact on other experiments or on basic ASTP operations. Each was small, lightweight, and easy to perform. The demonstrations illustrated basic principles of science involving concepts with which people deal in everyday life. The action of wicking, for example, may be found in oil lamps, candles, or even paper towels. The action of foaming is seen in shaving creams and detergents, and the influence of liquid spreading is seen in the action of oils as well as in water-repellent garments and soldering materials.

The ASTP science demonstrations, although dealing with common terrestrial concepts, cannot totally be accomplished outside the zero-g environment of space, and not one can be described definitively on the basis of experience. Although the investigators understood the general action of each demonstration, detailed knowledge that enabled prediction of the phenomena was not available. Therefore, interesting and unanticipated results were obtained from each demonstration.

DEMONSTRATION OBJECTIVES AND RESULTS

Chemical Foams

The purpose of the chemical foam demonstration was to illustrate the stability of foams in space and to determine the change in reaction times of certain chemical mixtures when altered from bulk liquid form to a stable foam. Some foams are of interest because many chemical and pharmaceutical reactions occur predominantly in the thin surface layer of a liquid.

A foam consists of bubbles of gas encased by walls of thin liquid films. Although some foams can be made rigid or flexible and durable, the characteristic foam is not stable on Earth. Foams collapse primarily as a result of the gravity-induced drainage of liquid in the bubble walls. As the liquid drains from the bubble, the film walls become increasingly thin until, at a thickness of approximately 10 nanometers (100 angstroms), they are ruptured by random molecular motion. Thus, the foam gradually dissipates as more of the liquid drains away to bulk form and leaves less to support the bubble walls. In the zero-g environment of space, drainage is substantially reduced; therefore, a longer lasting foam is provided. Drainage, however, is only one of the mechanisms contributing to the dissipation of foams. Evaporation and liquid spreading also act to dissipate bubble walls. Thus, the full extent of foam stability is still uncertain.

Forming a foam in space yields a very large surface area-to-volume ratio of the liquid that should be retained for a relatively long period. This large, stable surface area should enable surface-sensitive chemical reactions to occur differently than they would on Earth. The sensitivity of some chemical reactions to the size of the interface area has long been known. Freundlich (ref. 31-1) reported that a hydrogen-ion-concentration indicator solution acquired different color intensities depending on the vigor with which the solution was shaken (or the size and number

of droplets formed). Likewise, test results have indicated that some reactions occur faster in a foam or froth. However, the precise change taking place at the interface has not been precisely determined, and definitive theories on the characteristics of a stable foam in space have not been generated. Nevertheless, it was anticipated that a chemical reaction dependent on the surface area of the air-to-liquid interfaces, such as the one demonstrated, would proceed differently in a foam in a zero-g environment than would normally occur on Earth.

Foams are currently used in such diverse applications as the separation of proteins by the fractionation of foams and the origination of rigid structures such as foamed polystyrene and foam rubber. It has been suggested (ref. 31-2) that such unique products as reinforced rigid foams could be formed in space without the influence of gravity. In such foams, metal fibers would be alined along the surface of a stable foam strictly by adhesion. When cured, the foam could have a lightweight durability possibly unknown with earthbound processes. It has also been suggested that space-originated foams could act as the basis of porous metal electrodes. Such new products and synthesis procedures are potential applications of foam technology in space.

In the foaming demonstration, the chemical change consists of the simultaneous occurrence of three homogeneous reactions proceeding at different rates. These three reactions are as follows.

1. The addition of bisulfite ion to formaldehyde:

$$HCHO + HSO_3^- \longrightarrow CH_2OHSO_3^- \quad \text{(rate constant = 2.8 liters/mol sec)}$$

2. The reaction of sulfite ion and water with formaldehyde yielding OH^-:

$$SO_3^= + H_2O + HCHO \longrightarrow CH_2OHSO_3^- + OH^- \quad \text{(rate constant = 0.14 liter/mol sec)}$$

3. The instantaneous reaction of OH^- with bisulfite ion:

$$OH^- + HSO_3^= \longrightarrow SO_3^= + H_2O$$

Thus, excess OH^- becomes available for reaction with the indicator, phenolphthalein, only after the bisulfite ion has been completely used.

This demonstration of chemical foams in space illustrated simple principles involving foams in a zero-g environment. The demonstration was divided into two portions, the first of which visually portrayed the stability of a foam in space. The crewmember shook a tube containing a premixed solution of water, thymol blue indicator, and a small amount of ethyl alcohol in front of the camera. The resulting foam turned bright pink, which contrasted sharply with the gold of the solution in bulk form. As the pink foam dissipated, this contrast was evident.

The second portion of the demonstration illustrated the influence of a stable foam on the reaction time of a chemical solution. The crewmember inserted prepared solutions of sodium sulfite, sodium metabisulfite, formaldehyde, and phenolphthalein indicator into a small tube. The tube was then shaken vigorously for approximately 5 seconds to thoroughly mix the reactants and simultaneously produce the foam. After the tube was held before the camera for 20 to 30 seconds, the colorless foamed mixture quickly changed to a vivid red.

Demonstrations using two tubes of pink foam and four tubes to illustrate the color change of foam were performed during the ASTP mission. Because the 16-millimeter motion picture was out of focus, detailed knowledge of foam dissipation in the pink foam has not been obtained. Although details of the foam structure are also lacking for the second part of this demonstration, the color change was dramatic and of unexpected configuration. During zero-g flights in a KC-135 aircraft with development hardware, uniform color change appeared to occur more rapidly in zero-g conditions. Reaction timing will not be possible with the ASTP films, but the color change began between the gas-liquid interface and the polycarbonate tube. The color change began as a red ring and rapidly spread throughout the liquid (fig. 31-1).

The results of this demonstration illustrate that foams can be used to change the rate of particular chemical reactions. It is anticipated that, in the future, such foams produced under zero-g conditions can be used as media for conducting chemical reactions, in which not only the rates but possibly also the end products may be changed.

Liquid Spreading

The purpose of the liquid spreading demonstration was to illustrate and determine the behavior of liquids spreading over both solid and liquid surfaces in a zero-g environment. In particular, the rate of spreading and the change of shape and thickness of a spreading liquid layer with time were examined.

Liquids, when brought in contact with solid surfaces, have a tendency to spread over the entire surface if the cohesive forces between the molecules of the liquid are smaller than the adhesive forces between the molecules of the liquid and the molecules of the solid. Under the influence of gravity, this wetting action occurs only when the flow of the liquid along the surface proceeds in a horizontal or downward direction; the liquid will not be distributed evenly over an object in opposition to gravity. However, in a zero-g environment, a wetting liquid will spread evenly over a surface irrespective of the orientation. The driving force for the initial spreading is the solid-liquid-gas surface energies. Further intrinsic spreading of the remaining liquid is produced by liquid-gas interfacial energy. This latter spreading will be much slower, or may stop completely. No data exist for predicting the intrinsic bulk spreading rate, but the time required to approach uniform thickness may exceed the time available to perform the demonstration in space.

The important parameters that characterize the solid-liquid interface are the contact angle formed at the boundary and the surface tension, which determines the work required to increase the surface by unit area at constant temperature, pressure, and composition. A spreading coefficient S can be defined as $S = \sigma_{SG} - \sigma_{SL} - \sigma_{LG}$, where σ_{SG}, σ_{SL}, and σ_{LG} represent the surface tension at the solid-gas, solid-liquid, and liquid-gas interfaces, respectively. Spreading will occur if S is greater than or less than zero.

To perform the demonstration, the crewmember injected small amounts of oil or water from a prepared syringe onto the bottom inside surface of a transparent cube. Additional oil or water was added as the spreading of the liquid progressed over the internal horizontal and vertical surfaces of the box. One surface that had been treated to be nonwetting was marked and placed facing the camera. The top of the box had also been treated to prevent fluid from creeping over the edge. Blue dye was mixed with the oil to increase visibility, and the water was dyed red for contrast. Figure 31-2(a) portrays one of the cubes in space, and the spreading oil can be observed. In addition to the measures enabling observation of liquid spreading over vertical and horizontal walls, a small anvil-shaped solid was used in the bottom of a transparent box to illustrate the manner in which a fluid spreads over sharp corners.

Only one box was photographed during the ASTP mission. The photographs clearly show that the oil placed at the center of the bottom surface quickly spread to the corners and climbed the vertical walls. The oil accumulated in the corners of the cube in a manner that would minimize the exposed surface area. When red water was added to the oil surface, repulsion of oil and water was followed by an equilibrated configuration of water droplets surrounded by an oil film (fig. 31-2(b)). Data concerning spreading, such as rates and observed mechanisms, are being compared with results of ground and KC-135 experiments as well as with relevant theories.

The information derived from this demonstration will result in a better understanding of the process of liquid spreading. In particular, the demonstration will contribute to the basis of a fully consistent hydrodynamic theory of liquid spreading independent of the effects of gravity. Discrepancies in the existing theory of spreading may also be resolved. Such information is pertinent to various applications involving the quickness of spreading or the uniformity of liquid layers. These applications cover a wide range of processes and products including coatings, soldering, brazing, lubrication, laminated microelectronic circuits, and insecticides.

Capillary Wicking

The purpose of the capillary wicking demonstration was to illustrate wicking phenomena in a zero-g environment. Three stainless steel wicks and one cloth wick were used simultaneously to determine the efficiency and rate of wicking in a zero-g environment. Two different fluids, a low-surface-tension water-soap solution and silicone oil, were used as wicking solutions.

In the absence of gravity, the behavior of fluids is unusual because of the predominance of surface properties (such as adhesion) over bulk properties (such as mass). The fluid behavior that is unique to space has been used to advantage; fluids can be easily maneuvered and maintained in a zero-g environment by passive devices that do not require spacecraft power. Capillary wicking principles have been used in spacecraft for containment of fuel/cryogen fluids, separation of liquid-vapor phases, and expulsion of propellants. Little is known, however, about the efficiency of transfer and the wicking rate of the stainless steel wicks used during space missions, and short-duration zero-g tests, such as those performed from drop towers and during KC-135 flights, have not provided sufficient time to generate basic design data. Attempts have been made to simulate zero-g conditions by wicking horizontally in a one-g environment. However, it is impossible in this simulation to eliminate both the fluid pressure head and the small gravity force.

The effect, called capillarity, is due to surface and interfacial forces acting on a liquid. If a cylindrical tube with a bore of small cross section is placed vertically in a container of liquid that wets the tube, the liquid will rise within the tube to a height that varies inversely with the diameter of the bore. Flow up the tube continues until the pressure difference created by the forces disappears. The pressure exerted by the column of liquid depends on the weight of the liquid. If gravity is reduced, the capillary rise will increase.

A capillary wick is a cloth or metal fabric structure used to absorb a liquid for storage or transfer to another location. For example, a blotter or towel will absorb a liquid and then disperse it from the contact area. The movement and spread of the liquid can be calculated for ideal, evenly spaced, parallel fiber wicks. Although the gravity force limits the liquid rise in a capillary or ideal wick, equations are available to describe the phenomenon. However, calculations cannot be used for practical wicks having variable properties. For example, common wicks have small channels that divert the liquid from the main channels. Similarly, wicking depends on the uniform, close spacing of solid surfaces. The large number of capillary paths available in a wicking material adds to the complexity of any analysis.

The use of capillary wicks is an important part of everyday life. The natural cross-linked weave of most fabrics makes them suitable as wicks for many liquids, as can be observed with the spreading of wet spots following contact of water on cloth. Treatments that are available to retard wicking are beneficial. Efficient wicking is also required to clean up liquid spills in the home. Industry and research require efficient wicks to absorb and retain oil during tanker spills at sea, to transfer liquid, for application in heat-pipe technology, and to position liquids (such as cryogens) in containers.

The apparatus for the wicking demonstration is shown in figure 31-3(a). The wicks were attached to an assembly that was affixed to a tetrafluoroethylene base plate. A small well was cut from the center of the tetrafluoroethylene plate, and the fluids were inserted into this well. A rough aluminum surface covering the bottom of the well ensured better retention of the fluid. Early plans to enclose the entire apparatus in a transparent cover were discarded after zero-g tests onboard

a KC-135 aircraft indicated that the fluid remained within the well despite considerable variation in gravitational forces experienced during the tests. It was also noted during these tests that the fluid was inserted best into the well with the syringe held vertically rather than at an angle.

Four identical wicking assemblies, each containing four different wicking materials, and two base plates were carried onboard the spacecraft. The three stainless steel wicks differed in the pattern of weave and the size of mesh. They included a 325 by 2300 Dutch twill weave, a 200 by 200 Plain weave, and a 200 by 600 Plain Dutch weave. A fourth wick of nylon was added for comparative purposes. Blue dye was added to both water and oil solutions for better visibility. Because silicone oil has a lower contact angle with respect to stainless steel than soapy water has, the wicking rates with oil were expected to be somewhat faster than with the water-soap solution.

The wicking of both oil and water proceeded much faster during the ASTP mission than had been anticipated on the basis of ground tests and KC-135 zero-g experiments. The dominant flow was up the crease between the wick and the tetrafluoroethylene post (fig. 31-3(b)).

SUMMARY

The three science demonstrations were successfully accomplished during the Apollo-Soyuz Test Project and useful data were generated. The results will be analyzed in depth and compared with available theory and similar experiments performed on the ground and during KC-135 aircraft flights.

REFERENCES

31-1. Freundlich, H.: Surface Forces and Chemical Equilibrium. J. Chem. Soc., 1930, p. 170.

31-2. Lacy, L. L.; and Otto, G. H.: The Stability of Liquid Dispersions in Low Gravity. Paper No. 74-1242, AIAA/AGU Conference on Scientific Experiments of Skylab (Huntsville, Ala.), Oct. 30-Nov. 1, 1974.

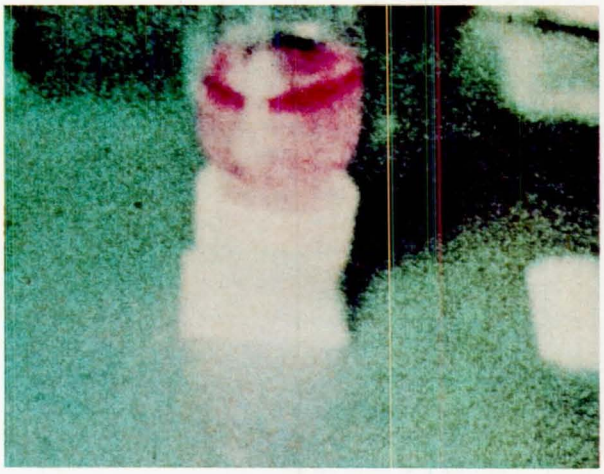

(a) During early part of reaction.

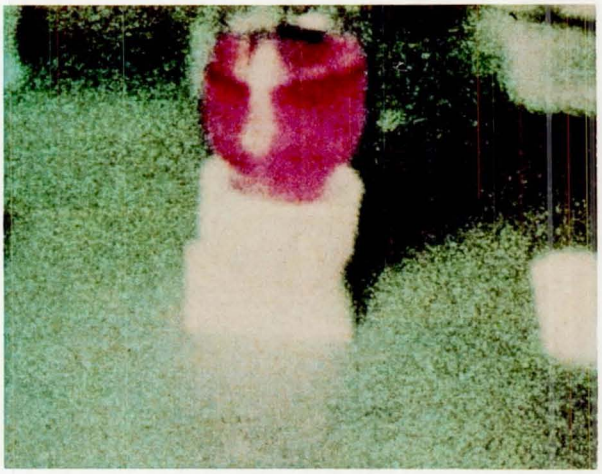

(b) Later in reaction.

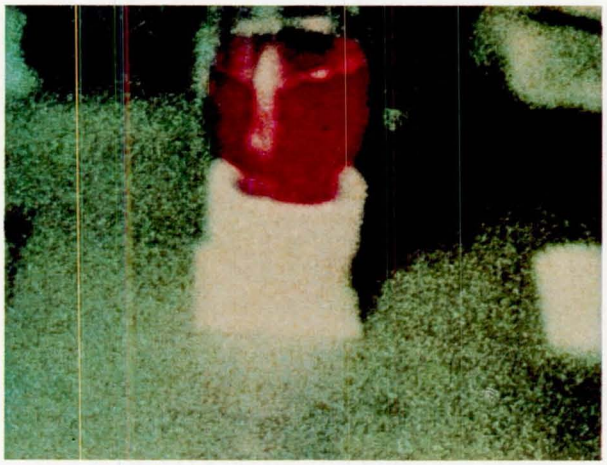

(c) At completion of reaction.

Figure 31-1.- Demonstration of the color change of foam.

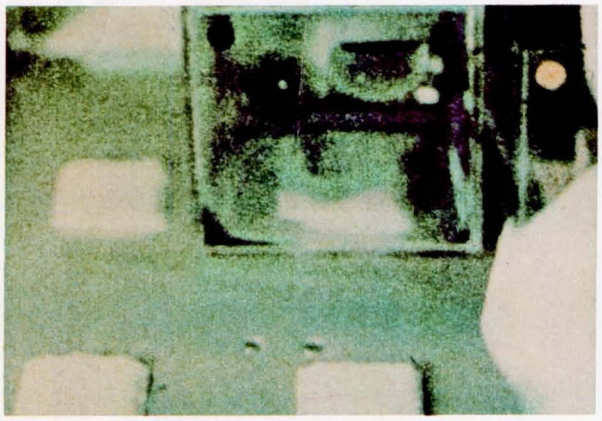

(a) Spreading oil film in cube.

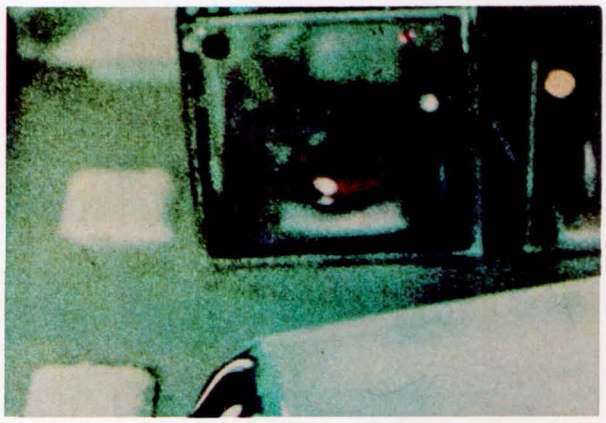

(b) Red water on blue oil in cube.

Figure 31-2.- Liquid spreading demonstration.

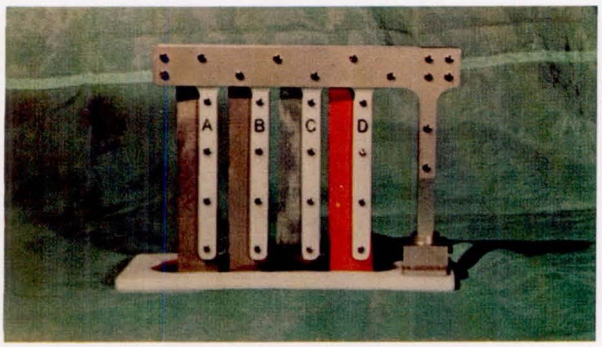

(a) Apparatus.

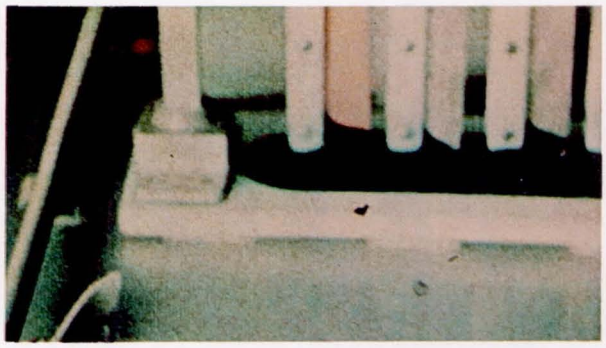

(b) Capillary wicking in space.

Figure 31-3.- Capillary wicking demonstration.

APPENDIX A

ABBREVIATIONS AND ACRONYMS

ac	alternating current
ACDR	Apollo commander
A-D	analog to digital
amu	atomic mass unit
ANZUS	Australia-New Zealand-United States
ASTP	Apollo-Soyuz Test Project
at.%	atomic percent
ATS	Applications Technology Satellite
ATSR	Applications Technology Satellite ranging
BTB	bromthymol blue agar
CF	cryogenic freezer
CGE	Crystal Growth Experiment
CM	command module
CMC	command module computer
CMMY	corn-meal, malt-extract, yeast-extract agar
CMP	command module pilot
CN	cellulose nitrate
COAS	crew optical alinement sight
Co-I	Co-Investigator
Con A	Concanavalin A
CPM	counts per minute
CSM	command and service module
CTA	cellulose triacetate
D-A	digital to analog
DAC	data acquisition camera
dc	direct current
D/L	diameter to length ratio
DM	docking module
DMA	Defense Mapping Agency
DMP	docking module pilot
DNA	deoxyribonucleic acid
DTA	differential thermal analysis
ECE	electrical checkout equipment
ECS	environmental control system
EMI	electromagnetic interference
EPE	Electrophoresis Experiment
EU	electrophoresis unit
EUV	extreme ultraviolet
FCS	fetal calf serum
FOV	field of view
FWHM	full width, half maximum
GBT	ground-based test
GEM	Goddard Earth Model
GET	ground elapsed time
GMT	Greenwich mean time
HDC	Hasselblad data camera

HED	high-energy deposition
HeG	helium glow
HGD	helium glow detector
HRC	Hasselblad reflex camera
HVPS	high-voltage power supply
HZE	high-charge energy
ICRP	International Commission for Radiation Protection
IF	intermediate frequency
IR	infrared
ISM	interstellar medium
JSC	NASA Lyndon B. Johnson Space Center
KSC	NASA John F. Kennedy Space Center
LaRC	NASA Langley Research Center
LBL	Lawrence Berkeley Laboratory
LED	light-emitting diode
LeRC	NASA Lewis Research Center
LET	linear energy transfer
LFE	Light Flash Experiment
lidar	laser radar
MEM	minimum essential medium
NOAA	National Oceanic and Atmospheric Administration
NRL	Naval Research Laboratory
OM	orbital module
PBS	phosphate-buffered saline
PGS	preliminary Goddard solution
PHA	phytohemagglutinin
PI	Principal Investigator
PMN	polymorphonuclear leukocyte
PVA	polyvinylalcohol
PWM	pokeweed mitogen
QT	quantum efficiency and transmission
RBE	relative biological effectiveness
RCS	reaction control system
RF	radiofrequency
RPI	Rensselaer Polytechnic Institute
SAA	South Atlantic Anomaly
SAB	Sabouraud's dextrose agar
SAM	stratospheric aerosol measurement
SAO	Smithsonian Astrophysical Observatory
SAS	small astronomy satellite
SCDR	Soyuz commander
SD	standard deviation
SEM	scanning electron microscope
SF	space flight
SFE	Soyuz flight engineer
SI	simulation index
SIM	scientific instrument module
SM	service module
SRBC	sheep red blood cells
SST	supersonic transport or satellite-to-satellite tracking
STDN	Spaceflight Tracking and Data Network

TE	thermoelectric module
TLD	thermoluminescence dosimeter
TV	thermal vacuum or television
UK	urokinase
USB	unified S-band
UVA	ultraviolet absorption
VCO	voltage-controlled oscillator
VHF	very high frequency
VTR	video tape recorder
WBC	white blood cell
wt.%	weight percent
XBT	expendable bathythermograph
Z	atomic number
ZFF	zone-forming fungi

APPENDIX B

UNITS AND UNIT-CONVERSION FACTORS

In this appendix are the names, abbreviations, and definitions of International System (SI) units used in this report and the numerical factors for converting from conventional units to SI units.

Names and Symbols of SI Units

Quantity	Name of unit	Symbol	Definition of symbol
	SI Base Units		
Length	meter	m	
Mass	kilogram	kg	
Time	second	sec	
Electric current	ampere	A	
Thermodynamic temperature	kelvin	K	
Luminous intensity	candela	cd	
Amount of substance	mole	mol	
	SI Derived Units		
Area	square meter	m^2	
Volume	cubic meter	m^3	
Frequency	hertz	Hz	s^{-1}
Mass density (density)	kilogram per cubic meter	kg/m^3	
Speed, velocity	meter per second	m/sec	
Angular velocity	radian per second	rad/sec	
Acceleration	meter per second squared	m/sec^2	
Angular acceleration	radian per second squared	rad/sec^2	
Force	newton	N	$kg \cdot m/sec^2$
Pressure (mechanical stress)	pascal	Pa	N/m^2
Kinematic viscosity	square meter per second	m^2/sec	
Dynamic viscosity	newton-second per square meter	$N \cdot sec/m^2$	
Work, energy, quantity of heat	joule	J	$N \cdot m$
Power	watt	W	J/sec
Quantity of electricity	coulomb	C	$A \cdot sec$
Potential difference, electromotive force	volt	V	W/A
Electric field strength	volt per meter	V/m	
Electric resistance	ohm	Ω	V/A
Capacitance	farad	F	$A \cdot sec/V$
Magnetic flux	weber	Wb	$V \cdot sec$
Inductance	henry	H	$V \cdot sec/A$
Magnetic flux density	tesla	T	Wb/m^2
Magnetic field strength	ampere per meter	A/m	
Magnetomotive force	ampere	A	
Luminous flux	lumen	lm	$cd \cdot sr$
Luminance	candela per square meter	cd/m^2	
Illuminance	lux	lx	lm/m^2
Wave number	1 per meter	m^{-1}	
Entropy	joule per kelvin	J/K	
Specific heat capacity	joule per kilogram kelvin	$J/(kg \cdot K)$	
Thermal conductivity	watt per meter kelvin	$W/(m \cdot K)$	
Radiant intensity	watt per steradian	W/sr	
Activity (of a radioactive source)	1 per second	s^{-1}	
	SI Supplementary Units		
Plane angle	radian	rad	
Solid angle	steradian	sr	

Unit Prefixes

Prefix	Abbreviation	Factor by which unit is multiplied
giga	G	10^9
mega	M	10^6
kilo	k	10^3
centi	c	10^{-2}
milli	m	10^{-3}
micro	μ	10^{-6}
nano	n	10^{-9}
pico	p	10^{-12}

Unit Conversion Factors

The following table expresses the definitions of units of measure used in the Apollo-Soyuz Test Project Preliminary Science Report as exact numerical multiples of coherent SI units and provides multiplying factors for converting to SI units. The first two digits of each numerical entry represent a power of 10. An asterisk follows each number which expresses an exact definition.

To convert from -	To -	Multiply by -
angstrom	meter	-10 1.00*
atmosphere	newton/meter^2	+05 1.013 25*
Celsius (temperature)	kelvin	$t_K = t_C + 273.15$
foot	meter	-01 3.048*
gram	kilogram	-03 1.00*
inch	meter	-02 2.54*
pound mass (lbm avoir-dupois)	kilogram	-01 4.535 923 7*
torr (0° C)	newton/meter^2	+02 1.333 22

APPENDIX C

HARDWARE VENDORS

Experiment	Equipment supplied	Vendor
Microbial Exchange (AR-002)	Experiment hardware	General Electric Company Houston, Tex.
Stratospheric Aerosol Measurement (MA-007)	Experiment hardware	University of Wyoming Laramie, Wyo.
Multipurpose Electric Furnace (MA-010)	Experiment hardware	Westinghouse Astronuclear Pittsburgh, Pa.
Electrophoresis Technology (MA-011)	Experiment hardware	Teledyne Brown Engineering Huntsville, Ala.
	Thermoelectric assembly	Ohio Semitronics Columbus, Ohio
	Column assemblies	NASA George C. Marshall Space Flight Center Huntsville, Ala.
Electrophoresis (MA-014)	Experiment hardware	Messerschmitt-Bölkow-Blohm Ottobeuren, West Germany
Crystal Growth (MA-028)	Experiment hardware	Rockwell International Science Center Thousand Oaks, Calif.
	Camera equipment and accessories	NASA Lyndon B. Johnson Space Center Houston, Tex.
Soft X-ray Observation (MA-048)	Experiment and ground-support equipment (GSE)	Ball Brothers Research Corporation Boulder, Colo.
	Data subsystem	New Mexico State University Las Cruces, N. Mex.
Ultraviolet Absorption (MA-059)	Experiment, optical system, and GSE	Johns Hopkins University Applied Physics Laboratory Laurel, Md.
	Retroreflector optics (built and tested)	Precision Lapping and Optical Company Valley Stream, N.Y.
	Ultraviolet (UV) light source (built)	Intraspace International Inc. Toronto, Ontario, Canada
	UV light assembly (design and assembly)	Lockheed Electronics Houston, Tex.
	Retroreflector mount, UV and incandescent light sources, and GSE	NASA Lyndon B. Johnson Space Center Houston, Tex.
Extreme Ultraviolet Survey (MA-083)	Experiment and GSE	Ball Brothers Research Corporation Boulder, Colo.
	Telescope	Applied Optics Center Burlington, Mass.
	UV filters	Luxel Corporation Santa Barbara, Calif.

Experiment	Equipment supplied	Vendor
Interstellar Helium Glow (MA-088)	Experiment and GSE	Ball Brothers Research Corporation Boulder, Colo.
	Helium pressure vessel	Supplied by NASA
	Helium system valves	Sterer Valves Engineering & Manufacturing Los Angeles, Calif.
	UV filters	Luxel Corporation Santa Barbara, Calif.
Doppler Tracking (MA-089)	Transmitter, receiver, and GSE	Raytheon Company Equipment Division Sudbury, Mass.
	Ultrastable oscillators for transmitters and receivers, crystal filters for transmitters	Frequency Electronics, Inc. New Hyde Park, N.Y.
	Transmitter battery development	Eagle Picher Joplin, Mo.
	Receiving antenna (design and development)	Ball Brothers Research Corporation Boulder, Colo.
	Data recording system	NASA Lyndon B. Johnson Space Center Houston, Tex.
Light Flash (MA-106)	Experiment hardware	Lawrence Livermore Laboratory University of California Berkeley, Calif.
Biostack (MA-107)	Experiment hardware	Messerschmitt-Bölkow-Blohm Ottobeuren, West Germany
Earth Observations and Photography (MA-136)	70-mm cameras, magazines, lenses, and accessories for photography	Victor Hasselblad, Aktiebolag Sweden
	20X binoculars for visual observations	Tasco Sales, Inc. Miami, Fla.
	Standard color chips for visual color comparisons	Munsell Color Company Macbeth Division Baltimore, Md.
	Zoom telescope for visual observations	Bushnell Optical Corporation Pasadena, Calif.
	Variable intervalometer for sequencing photography; 16-mm camera equipment for complementary strip mapping	Perkin Elmer Corporation Aerospace Division Pomona, Calif.
Crystal Activation (MA-151)	Experiment hardware	NASA Goddard Space Flight Center Greenbelt, Md.
Science Demonstrations	Experiment hardware	NASA George C. Marshall Space Flight Center Huntsville, Ala.

APPENDIX D

POINTS OF CONTACT

Experiment no.	Engineering development manager	Science coordinator
NASA Lyndon B. Johnson Space Center		
AR-002	--	G. R. Taylor, DD7
MA-007	--	J. R. Bates, TN3
MA-028	C. J. LeBlanc, ED6	J. R. Bates, TN3
MA-031	--	S. L. Kimzey, DB7
MA-032	--	S. L. Kimzey, DB7
MA-048	E. L. Weeks, ED6	S. N. Hardee, TN3
MA-059	L. W. McFaden, ED6	S. R. Mansur, TN3
MA-083	J. M. Sanders, ED6	R. R. Baldwin, TN3
MA-088	J. M. Sanders, ED6	R. R. Baldwin, TN3
MA-089	A. R. Cunningham, EE6, and J. S. Kelley, EE3	P. E. Lafferty, TN3
MA-106	J. D. Lem, DE4	R. A. Hoffman, DD6
MA-107	H. S. Anton[a]	J. V. Bailey, DD6
MA-128	--	P. E. Lafferty, TN3
MA-147	--	G. R. Taylor, DD7
MA-148	--	R. T. Giuli, TN3
MA-151	--	S. R. Mansur, TN3
MA-161	--	R. A. Hoffman, DD6
NASA George C. Marshall Space Flight Center		
MA-010	A. Boese, EL55	A. Boese, EL55
MA-011	R. E. Allen, EH35	R. E. Allen, EH35
MA-014	R. S. Snyder, EH12	R. S. Snyder, EH12
MA-041	A. Boese, EL55	R. C. Ruff, ES12
MA-044	A. Boese, EL55	L. L. Lacy, ES24
MA-060	A. Boese, EL55	C. F. Schafer, ES12
MA-070	A. Boese, EL55	C. S. Griner, EH12
MA-085	A. Boese, EL55	M. C. Davidson, ES12
MA-131	A. Boese, EL55	M. H. Johnston, EH12
MA-150	A. Boese, EL55	A. Boese, EL55

[a]Ministry of Research and Technology, Federal Republic of Germany, Gesellschaft Fuer Weltraumforschung, 505 Porz-Wahn, Linder Hoehe, West Germany.

☆ U.S. GOVERNMENT PRINTING OFFICE 1976—0—675—606